

Investigating the fate of petroleum fluids released in the marine environment with comprehensive two-dimensional gas chromatography and transport models

THÈSE N° 6883 (2016)

PRÉSENTÉE LE 30 MARS 2016

À LA FACULTÉ DE L'ENVIRONNEMENT NATUREL, ARCHITECTURAL ET CONSTRUIT
LABORATOIRE DE MODÉLISATION DE LA CHIMIE ENVIRONNEMENTALE
PROGRAMME DOCTORAL EN GÉNIE CIVIL ET ENVIRONNEMENT

ÉCOLE POLYTECHNIQUE FÉDÉRALE DE LAUSANNE

POUR L'OBTENTION DU GRADE DE DOCTEUR ÈS SCIENCES

PAR

Jonas GROS

acceptée sur proposition du jury:

Prof. A. Buttler, président du jury
Prof. J. S. Arey, directeur de thèse
Dr C. M. Reddy, rapporteur
Prof. S. A. Socolofsky, rapporteur
Prof. A. J. Wüest, rapporteur



ÉCOLE POLYTECHNIQUE
FÉDÉRALE DE LAUSANNE

Suisse
2016

Résumé

Les déversements anthropiques ponctuels de fluides pétroliers, lesquels contiennent des milliers de composés, représentent une menace pour les environnements marins. Cependant, des modèles capables d'expliquer le comportement de ces nombreux composés dans l'environnement marin manquent cruellement dans différents domaines. Ceci est particulièrement vrai pour les relâchements de fluides pétroliers en eaux profondes. Dans cette thèse nous avons tâché d'y remédier, en présentant de nouveaux modèles permettant de prédire le partitionnement de centaines de composés du pétrole lors d'un déversement dans l'environnement marin, en surface ou à grande profondeur. Nous introduisons également des améliorations aux techniques d'analyse des données.

Dans le but de répondre à ce besoin de modèles à même de prédire le comportement de centaines de composés pétroliers, la chromatographie en phase gazeuse à deux dimensions (GC×GC) est utilisée dans ce travail. La GC×GC permet une analyse quantitative et détaillée de la composition du pétrole et permet également d'estimer les propriétés chimiques de certains de ses composants. Néanmoins, la présence de variations incontrôlées de temps de rétention des composés au sein des chromatogrammes à deux dimensions limite la possibilité d'effectuer des comparaisons quantitatives. Pour cette raison, un nouvel algorithme d'alignement a été développé afin de réduire ces variations et de faciliter certaines des comparaisons quantitatives effectuées dans cette thèse. Notre algorithme présente des performances supérieures en comparaison de deux autres algorithmes préexistants.

Lors des premières heures après le déversement de fluides pétroliers à la surface de la mer, certains hydrocarbures vont rapidement être transférés dans l'air et dans l'eau. Cependant la communauté scientifique manque de données détaillées au niveau de la composition en ce qui concerne cette période initiale, en raison de l'incapacité de prendre des échantillons si rapidement lors d'un déversement involontaire. Nous avons développé un modèle applicable à l'entier d'un chromatogramme à deux dimensions ainsi qu'à des composés individuels. Ce modèle a été validé sur la base de données récoltées lors d'un déversement volontaire non-confiné de 4,3 m³ de pétrole en mer du Nord, mené conjointement par notre laboratoire et divers instituts de recherche européens. Notre modèle nous a permis d'étudier le partitionnement des hydrocarbures durant cette période initiale, et de prédire l'effet de la variation de certains paramètres environnementaux sur ce partitionnement.

Des modèles validés sont nécessaires afin de simuler le comportement des composés du pétrole lorsque ce dernier est déversé dans l'eau à grande profondeur. Afin de répondre à ce besoin, nous avons développé un modèle thermodynamique permettant la prédiction du partitionnement des composés d'un fluide pétrolier entre le gaz, le liquide, et l'eau. Le modèle

permet également d'estimer les densités et viscosités des différentes phases, le tout en fonction de la composition, de la pression et de la température. Ceci nous a permis de fournir des estimations pour plusieurs propriétés des fluides pétroliers émis durant la marée noire *Deepwater Horizon*, en 2010, ceci aux conditions ambiantes où ces fluides ont été relâchés : à environ 1500 mètres de profondeur dans le Golfe du Mexique. Ce modèle nous a permis également d'étudier l'effet de la profondeur sur la solubilité dans l'eau de mer des différents composés du pétrole.

Toujours pour la marée noire *Deepwater Horizon*, le partitionnement des hydrocarbures rapporté par plusieurs auteurs n'a pas reçu d'explication mécanistique. Afin de remédier à cet état de fait, nous avons développé un modèle décrivant le comportement du panache de bulles et gouttelettes (formées de composés du pétrole) et d'eau entraînée, incluant la cinétique de dissolution dans l'eau de mer et les principaux effets liés aux pressions élevées rencontrées à grande profondeur. Ce modèle constitue la première démonstration mécanistique de l'importance majeure de la dissolution pour expliquer le partitionnement documenté d'hydrocarbures vers les eaux profondes durant la marée noire, avec ~27% de la masse émise qui a été dissoute, selon les prédictions du modèle pour le 8 juin 2010. Notre modèle permet également d'apporter des éléments de réponse à une des grandes questions non-résolues : déterminer si une large fraction des fluides pétroliers émis a pu être retenue en profondeur pour une durée prolongée sous forme de minuscules gouttelettes.

La biodégradation joue un rôle majeur pour la dégradation des résidus pétroliers dans l'environnement après une marée noire. Cependant, seules des informations limitées sont disponibles concernant la biodégradation des hydrocarbures saturés dans l'environnement en surface, bien que le pétrole soit composé principalement de composés saturés. En collaboration avec la Woods Hole Oceanographic Institution, nous avons étudié des résidus pétroliers récoltés 12 à 19 mois après le début de la marée noire *Deepwater Horizon*. Nous avons pu déterminer les différences de susceptibilité à la biodégradation des hydrocarbures saturés dans l'intervalle n -C₂₂ (hydrocarbure saturé non branché avec 22 atomes de carbone) à n -C₂₉.

En résumé, nous avons montré dans cette thèse qu'une modélisation détaillée du devenir des nombreux composés du pétrole dans l'environnement marin est possible, permettant d'améliorer la compréhension des niveaux de pollution auxquels les organismes marins sont exposés lors de marées noires, particulièrement durant les premières heures.

Mots-clés

Chromatographie en phase gazeuse à deux dimensions, GC×GC, marée noire, pétrole, transfert de masse, biodégradation, eaux profondes, *Deepwater Horizon*, puits de Macondo

Abstract

Anthropogenic releases of petroleum fluids, which contain thousands of compounds, represent a threat to marine environments. However, there was a lack of models able to explain the independent behaviors of the numerous compounds of a spilled petroleum fluid, in particular for a release in deep waters that is subjected to elevated pressures. In this thesis, we present new models to predict the behavior of hundreds of petroleum compounds upon release in the environment, both at the sea surface and in deep waters. We also propose advances to data-analysis techniques.

Comprehensive two-dimensional gas chromatography (GC×GC) is used for quantitative and detailed analysis of petroleum composition, enabling the development of models able to predict the independent behavior of numerous petroleum compounds. Nevertheless, uncontrolled run-to-run variations of analyte retention times are encountered in GC×GC chromatograms and this hampers quantitative comparisons. Therefore a new alignment algorithm was developed, enabling improved analysis in subsequent chapters.

During the early period after release at sea surface (first hours), several petroleum hydrocarbons fractionate into air and water. However there is a lack of detailed compositional data for this early period, which cannot usually be sampled. We developed a model of evaporation and aqueous dissolution applicable to a whole GC×GC chromatogram and to individual compounds. This model was validated using data recorded previously during a 4.3 m³ oil release experiment conducted on the North Sea. Our model enabled us to investigate the fractionation of hydrocarbons during this early period, and to estimate the expected outcome when several environmental conditions are varied.

The thermodynamic properties of petroleum gas and liquid phases released in deep waters are poorly known. To address this need, we present a thermodynamic model of the gas-liquid-water partitioning, densities, and viscosities of petroleum mixtures with varying composition, as a function of pressure, temperature, and water salinity. This enabled us to provide estimates for poorly characterized properties at ambient conditions encountered at emission depth during the 2010 *Deepwater Horizon* disaster, and to investigate the effect of depth on equilibrium aqueous solubility.

The hydrocarbon fractionation reported during the *Deepwater Horizon* disaster had not been mechanistically explained. To address this need, we developed a model of the combined effects of buoyant plume dynamics and aqueous dissolution kinetics, including relevant deep-water effects. This is the first study to demonstrate mechanistically that aqueous dissolution was a major process, with ~27% of the emitted mass dissolved during ascent. Our model pre-

dictions also provide insight in the debate on whether the injection of dispersant at the emission source led to the formation of $<300\ \mu\text{m}$ droplets that stayed submerged for weeks or months.

Biodegradation plays a major role in the natural attenuation of oil spills. However, limited information is available about biodegradation of different saturated hydrocarbon classes, despite that oils are composed mostly of saturates. In collaboration with the Woods Hole Oceanographic Institution, we studied weathered oil samples collected on Gulf of Mexico beaches 12–19 months after the *Deepwater Horizon* disaster. We determined the difference in susceptibility to biodegradation for different saturates in the $n\text{-C}_{22}\text{--}n\text{-C}_{29}$ range.

Keywords

Comprehensive two-dimensional gas-chromatography, GC \times GC, oil spill, petroleum, mass transfer, biodegradation, deep water, *Deepwater Horizon*, Macondo well

Acknowledgements

During these four years, I have been mostly sitting on a bad rolling chair, my eyes fixed on a computer screen. To be able to do that and work on actual oil spill data requires the help of numerous people that performed the practical work (sampling and analysis), gave advice, or did both. I am deeply indebted to all these people, and want to specifically acknowledge the contributions of several of them, below.

First of all, I want to warmly thank Sam Arey for his thoughtful help and guidance, and for enabling me and pushing me to go to interesting conferences, make presentations in front of many people, and make very helpful stays in the United States, and, well, basically, simply to allow me to spend these four years on the bad rolling chair in front of the computer.

I also want to thank Chris Reddy, who somehow made all this possible too, by finding some funding, by his deep knowledge on oil spills, and by sharing the necessary part of the gigantic pile of data on the *Deepwater Horizon* disaster that his lab has accumulated. Also, it has been a pleasure to spend a few months visiting his lab and discovering that better rolling chairs do actually exist, on the other side of the Atlantic. It was also very nice to have been given the opportunity to take part in a field sampling trip on Gulf of Mexico beaches.

Similarly, I want to thank Scott Socolofsky. Having the opportunity to have my contributions implemented into his larger model simply made possible things that would otherwise have remained beyond the reach of a single Ph.D. student. Our discussions have been very fruitful, and it has also been nice visiting his lab.

I want to profoundly acknowledge Deedar Nabi and Bob Nelson, who, on both sides of the Atlantic, performed the GC×GC work without which all this would never have been possible. Deedar has also contributed to the North Sea field experiment (into which I did not take part), and we had fruitful discussions on property estimation methods. Petros Dimitriou-Christidis also provided some of the GC×GC chromatograms used in my work. And Bob is simply the Woods Hole Oceanographic Institution king of GC×GC.

I also thank all my colleagues at EPFL, especially Saer, for not staring too strangely at me when they saw me reading articles sitting on the floor, or sitting on my bad rolling chair in weird positions. In addition, I want to thank Daniela for watering all the plants when I was absent: without her the plants would have died, and I would have sunk into such a deep nervous breakdown that all this would (possibly) never have come to an end. Merci notamment à Karine, Daniela, et Daniel de m'avoir permis de ne pas oublier, durant toutes ces années, que, malgré les apparences contraires, je travaillais en Suisse francophone. Et merci à Charlotte et à l'Ancêtre pour la relecture de la version française du résumé et pour leurs conseils d'amélioration.

I also want to thank all the WHOI and TAMU nice people that I met during my stays and with whom I had fruitful interactions: Karin, Christoph, Jagos, Catherine, new Bob, Anusha, In Ok, Franke, Binbin, Chris (Lai), etc. Especially, interactions with Karin, Christoph, and In Ok have been very helpful, and the collaboration with Anusha in the last months of this work enabled us to get relatively converged and reasonable assumptions for the modeling of the *Deepwater Horizon* disaster in Chapter 5.

Lin Zhao and Michel Boufadel kindly accepted to re-run their model using the properties that I estimated at emission depth, leading to updated predicted size distributions that I could use in my work for the modeling of the *Deepwater Horizon* disaster (Chapter 5).

Johny Wüest has also provided very helpful guidance, during my first year exam and occasionally during the thesis.

Many other people shared data, replied to my questions, or participated to some extent to the work presented here: Oliver C. Mullins, Julian Zuo, Per Daling, Paul Eilers, Dabao Zhang, Robert E. Synovec, Jeremy S. Nadeau, Qingping Tao, Stephen E. Reichenbach, Jan van der Meer, Corina Brussaard, Sjon Huisman, Louis Peperzak, Julien Guyomarch, the crew of the R/V *Arca*, Dustin Baum, Birgit Würz, Lukas Y. Wick, Flavio Comino, Aaron A. Zick, Aniela Burant, Marcia McNutt, Paul Hsieh, Rich Camilli, Tom Ryerson, Pete Carragher, Jeffrey Short, Sean Sylva, Jeff Seewald, Peter Brewer, Peter Walz, Svein Ramstad, Helen White, Yasuyuki Zushi, Rob Modini, Damien Bouffard, Christophe Pache, Mauro Lattuada, Giovanni Cangiani, Alex Bonvin, et Auréline Grange.

Et finalement, merci à David Meylan et Samuel Bancal, de l'ENAC IT, pour m'avoir aidé à être un responsable informatique du LMCE pas trop calamiteux.

Vevey, le 11 février 2016

Contents

Résumé	i
Mots-clés	ii
Abstract	iii
Keywords	iv
Acknowledgements	v
Chapter 1 Introduction	15
1.1 What is <i>oil</i> : an imprecise word for incompletely characterized fluids.....	15
1.2 Liquid petroleum fluids in the marine environment.....	16
1.2.1 Sea-surface spills	17
1.2.2 The <i>Deepwater Horizon</i> disaster as a deep-water release	19
1.3 Comprehensive two-dimensional gas chromatography (GC×GC).....	21
1.3.1 Baseline correction for GC×GC data	23
1.4 Aim of this work.....	26
Chapter 2 A robust algorithm for aligning two-dimensional chromatograms	29
2.1 Abstract	30
2.2 Introduction.....	30
2.3 Experimental section	32
2.3.1 Sample analysis.	32
2.3.2 Data pretreatment.	33
2.3.3 Alignment algorithm.	33
2.3.4 Parameters used for the different alignment algorithms.....	37
2.4 Results and discussion	37
2.4.1 Extent of misalignment observed in the original, unaligned chromatograms.	37
2.4.2 Visual comparison of alignment results using different algorithms.....	38
2.4.3 Improvement in peak retention time deviations after alignment, using different algorithms.	41
2.4.4 Improvement in quality of difference chromatograms after alignment, using different algorithms.	42
2.4.5 Peak volumes alterations induced by alignment, using different algorithms.	42
2.5 Conclusions.....	44

2.6	Acknowledgment	46
2.7	Appendix.....	46
2.7.1	GC×GC analysis methods.....	46
2.7.2	Weighted average used in Sibson’s natural-neighbor interpolation	48
2.7.3	Bicubic convolution interpolation	49
2.7.4	Alignment points used for each chromatogram.....	50
2.7.5	Visual comparison of difference chromatograms, after alignment.....	52
2.7.6	Visual comparison of alignment results for chromatograms resulting from the analysis of the same wastewater sample with different temperature programs.....	55
2.7.7	Dependence of alignment quality on the number of alignment points used.....	55
2.7.8	Sums of the absolute values of the pixels of the difference chromatograms, after alignment	58
2.7.9	Changes in total chromatogram signal resulting from alignment	58
Chapter 3	First day of an oil spill on the open sea: Early mass transfers of hydrocarbons to air and water	61
3.1	Abstract	62
3.2	Introduction	62
3.3	Experimental and computational methods	64
3.3.1	Open sea oil spill experiment	64
3.3.2	Analysis of oil slick and oil sheen samples.....	65
3.3.3	Analysis of water column samples	66
3.3.4	Mass transfer model	66
3.4	Results and discussion	72
3.4.1	Compositional changes in oil slick and oil sheen samples.....	72
3.4.2	Diagnosing evaporation and dissolution of hydrocarbons using Mass Loss Tables	76
3.4.3	Hydrocarbon contamination of the water column at 1.5 m depth	79
3.4.4	Simulated hydrocarbon mass apportionments to air and water	79
3.4.5	Hydrocarbon evaporation predicted by the expressions of Fingas and by the ADIOS model	81
3.4.6	Implications for early mass transfer processes and resulting ecological exposures during oil spills.....	81
3.4.7	Funding sources	83
3.4.8	Acknowledgments.....	83
3.5	Appendix.....	84
3.5.1	Grane crude oil properties	84
3.5.2	Field sample collection	86
3.5.3	Concentrations of individual analyzed hydrocarbons in the water column and neat oil ...	88
3.5.4	GC–FID and GC–MS analysis of water column samples and neat oil.....	89
3.5.5	Mass transfers at interfaces: basis of Equation 3-1 and Equation 3-2 and similarity to other equations used in oil spill modeling	90

3.5.6	Estimation of the vertical turbulent mixing coefficient in the water column.	94
3.5.7	Estimation of hydrocarbon partitioning properties from GC×GC retention time information	96
3.5.8	Comparisons of different models for the evaporation mass loss of the oil slick during the field experiment.....	96
3.5.9	Measured mass losses of individual compounds based on GC×GC–FID data for oil slick and oil sheen samples.....	98
3.5.10	Comparison of model predictions and measured hydrocarbon concentrations in the water column.....	99
3.5.11	Effect of temperature on oil mass fractions apportioned to air and water.....	100
3.5.12	Mass loss tables for oil sheen samples.....	103
3.5.13	Effect of wind speed on oil mass fractions apportioned to air and water.....	104
3.5.14	Modeled evolution of oil slick thickness during the experiment.....	105
Chapter 4	Gas-liquid-water partitioning and fluid properties of petroleum mixtures under pressure: Implications for deep-sea blowouts.....	107
4.1	Abstract.....	108
4.2	Introduction.....	108
4.3	Modeling Approach.....	112
4.4	Results.....	116
4.4.1	Model compositions of MRF.....	116
4.4.2	Estimation of input parameters for the thermodynamic model.....	118
4.4.3	New proposed correlations for prediction of \bar{v}^L and K_{salt} for hydrocarbons.....	120
4.4.4	Validation of gas-liquid predictions of the thermodynamic model for MRF.....	120
4.4.5	Domain of applicability of the thermodynamic model.....	121
4.5	Implications for deep-sea petroleum fluid releases.....	122
4.5.1	Estimated state of the MRF at the Macondo well stub.....	122
4.5.2	Gas-liquid-water partitioning equilibrium in the deep sea.....	123
4.5.3	Expected changes in liquid and gas densities due to pressure and aqueous dissolution.....	124
4.5.4	Implications for Macondo well flow rate estimates.....	125
4.6	Outlook.....	126
4.7	Acknowledgement.....	126
4.8	Funding Sources.....	126
4.9	Appendix.....	127
4.9.1	Procedure for gas-liquid-water equilibrium calculation.....	127
4.9.2	Comparison of the composition of light compounds in MW-1 versus pre-spill downhole single-phase Macondo reservoir fluid samples.....	129
4.9.3	Combining light hydrocarbon and dead oil composition data.....	130
4.9.4	GC×GC analysis method.....	134

4.9.5	Approximate structures assigned to pseudo-components derived from GC×GC–FID	134
4.9.6	Definition of pseudo-components for single carbon number intervals $\geq n-C_{26}$ based on simulated distillation data	137
4.9.7	Definition of model composition of MW-1 dead oil, $MC_{1,do}$	137
4.9.8	Definitions of model compositions MC_2 and MC_3	137
4.9.9	Procedure for selection of Henry’s law constant values from Sander	138
4.9.10	Validation of group-contribution methods used for estimation of the chemical properties	140
4.9.11	Literature measurement data used to derive the correlations of Equation 4-19 and Equation 4-20	144
4.9.12	Methodological differences between the thermodynamic model of the present study and the Zick model	146
4.9.13	Thermodynamic model validation against laboratory data and comparison with the Zick model	148
4.9.14	Model domain of validity (extended discussion)	155
4.9.15	Predicted density of Macondo dead oil and live oil as a function of dissolution and evaporation extent	155
4.9.16	Component properties	157
Chapter 5	Controls on the aqueous dissolution of petroleum emitted into the Gulf of Mexico during the <i>Deepwater Horizon</i> disaster	171
5.1	Abstract	173
5.2	Introduction	173
5.3	Computational methods	177
5.3.1	Overview of TAMOC-c: a model for deep-water releases of petroleum fluids	177
5.3.2	Boundary conditions of the ambient water column: current velocity, temperature, and salinity profiles	180
5.3.3	The detailed model composition of the Macondo reservoir fluid (279 components)	181
5.3.4	The simplified model composition of the Macondo reservoir fluid (14 components)	181
5.3.5	Boundary conditions at the emission source: size distributions, compositions, and volumetric flow rates of droplets and bubbles	182
5.3.6	Modeling two-phase fluid particles in TAMOC-c	185
5.3.7	Simulation of aqueous dissolution kinetics for petroleum compounds in TAMOC version 0.1.17	186
5.3.8	Model of the deep-water hydrocarbon plume in TAMOC-c	189
5.3.9	Modelling the sea surface boundary and processes happening at the sea surface outside of the TAMOC-c model boundary	189
5.4	Results and implications	190
5.4.1	Size distributions of droplets and bubbles emitted at the emission source boundary	190
5.4.2	Time and location of arrival at the sea surface for fluid particles emitted from the broken Macondo riser stub	191

5.4.3	Apportionment of total mass flow rates of petroleum fluids to the deep water column, the upper water column, and the sea surface.....	194
5.4.4	Apportionments of the mass flow rates of individual petroleum compounds to the deep water column, the upper water column, and the sea surface	196
5.4.5	Stripping of aqueously dissolved nitrogen and oxygen from ambient seawater by ascending petroleum fluids	201
5.4.6	Predicted influence of subsurface dispersant injection on the trajectories and aqueous dissolution of petroleum fluids in the sea	202
5.4.7	Implications for deep-water petroleum fluid releases	205
5.4.8	Acknowledgements	206
5.5	Funding Sources.....	206
5.6	Appendix.....	207
5.6.1	The 14-component model compositions: MC _{1,14c} , MC _{2,14c} , and MC _{3,14c}	207
5.6.2	Comparison of measured and predicted velocities of currents in the water column near the Macondo well.....	209
5.6.3	Influence of temperature at the emission source boundary on predicted aqueous dissolution extent of petroleum compounds based on MC _{1,14c}	211
5.6.4	Effect of the start/end of dispersant injection on the fraction of mass surfacing.....	212
5.6.5	Effect of reservoir fluid composition on predicted aqueous dissolution extent of petroleum compounds based on MC _{1,14c} , MC _{2,14c} , and MC _{3,14c}	214
5.6.6	Effect of estimated water current velocity at >1184 m depth on predicted aqueous dissolution extent of petroleum compounds based on MC _{1,14c}	216
5.6.7	Binary interaction parameters used to describe oxygen interactions with petroleum compounds.....	218
5.6.8	Numerical values of the predicted fractionation indices and fraction of aqueously dissolved mass for petroleum compounds during ascent of petroleum fluids to the sea surface...	220
5.6.9	Comparison of TAMOC-c model predictions (assuming no dispersant addition) with field observations for the fraction of aqueously dissolved mass during ascent and fractionation indices of several individual petroleum compounds.....	222
5.6.10	Estimation of the fraction of the mass flow rate of petroleum fluids trapped in the deep-water hydrocarbon plume as small droplets having slow rise velocities	223
5.6.11	Estimated concentration of dispersant in live oil at the emission source boundary on different days during the <i>Deepwater Horizon</i> disaster	224
Chapter 6	Resolving biodegradation patterns of persistent saturated hydrocarbons in weathered oil samples from the <i>Deepwater Horizon</i> disaster.....	227
6.1	Abstract	228
6.2	Introduction.....	228
6.3	Methods	230
6.3.1	Sample collection	230
6.3.2	Sample extraction	231
6.3.3	Chemicals	231
6.3.4	GC-FID.....	231

6.3.5	GC×GC–FID	232
6.3.6	Data analysis of GC×GC–FID chromatograms	232
6.4	Results and Discussion	235
6.4.1	GC–FID and GC–MS chromatograms of weathered samples	235
6.4.2	GC×GC chromatograms of weathered samples	235
6.4.3	Percent mass losses of saturates compound classes	237
6.4.4	A new biodegradation index for oil weathering in surface environments	238
6.4.5	Implications for oil weathering in the environment.....	240
6.4.6	Acknowledgement	242
6.5	Appendix.....	243
6.5.1	Samples information	243
6.5.2	GC×GC–TOF-MS.....	244
6.5.3	GC–FID chromatograms	245
6.5.4	Alignment points	247
6.5.5	Investigation of GC-MS ability to separate the compounds studied	248
6.5.6	GC×GC–TOF-MS chromatogram.....	251
6.5.7	Percentage of each saturate class in the samples studied	252
6.5.8	Evolution of the saturates biodegradation index with respect to sampling time	253
6.5.9	Comparison of the saturates biodegradation index with the n-C ₁₈ /phytane ratio	254
6.5.10	Estimation of the fraction of the original oil load remaining in sample B93	255
Chapter 7	Conclusions.....	259
7.1	Main findings	259
7.2	Open questions.....	262
Chapter 8	References.....	265
Chapter 9	Curriculum Vitae	287

Chapter 1 Introduction

Acute and chronic accidental releases of petroleum fluids in the environment remain unfortunately unavoidable in the near foreseeable future, because liquid and gaseous fossil fuels currently comprise a large part of the primary energy supply of humankind (55% in 2007).¹ As the numerous compounds that constitute petroleum fluids can have both acute and long-term toxic effects on marine ecosystems, it is crucial to understand the fate of petroleum compounds once they enter the environment, in order to guide response action and to study damages. Especially, there is a lack of quantitative models that are able to predict the fate of thousands of petroleum compounds, and explain the underlying processes. The limitations of the pre-existing knowledge are discussed further in this chapter. This work investigates poorly studied aspects of several processes that play a role in the fate of petroleum fluids in the marine environment: mass transfers of petroleum compounds from a petroleum phase to the atmosphere and water, which dominate in the early weathering of petroleum, and biodegradation which plays a role on the longer term.

In this chapter, I will: discuss the meaning of the word “oil”; introduce the different processes known to affect petroleum fluids in the marine environment and the pre-existing knowledge gaps; present an important tool used to analyze the composition of oil and oil residues—comprehensive two-dimensional gas chromatography—and discuss some of its limitations; and finally define more specifically the scope of this work.

1.1 What is *oil*: an imprecise word for incompletely characterized fluids

Petroleum compounds result from the slow transformation of the buried remains of living organisms over millions of years.² Over geological time scale, these compounds can migrate through permeable rock layers and remain trapped below impermeable rock layers, forming reservoirs in which wells may be drilled for extraction. The compositions of these petroleum mixtures differ amongst reservoirs, and can encompass several thousands of compounds, ranging from methane to molecules with >100 carbon atoms.³ Whereas the lighter molecules are mostly hydrocarbons (including the potential presence of CO₂, N₂, and H₂S), some of the molecules with larger molecular weight also contain heteroatoms. In fact, petroleum fluids are so complex that a complete compound-by-compound characterization of any petroleum fluid remains highly improbable.⁴

Petroleum fluids include molecules that would be gaseous, liquid, or even solid as pure compounds at atmospheric conditions. Petroleum fluid mixtures are found as two-phase (gas and liquid) or single-phase fluids in reservoirs. In addition, some petroleum compounds will partition to the water-rich phase, if formation water is present. Usually, upon extraction and after having been brought to surface pressure and temperature conditions, petroleum fluids will

separate into a gas phase (including compounds $<C_5$) and a liquid phase (with a possible dissolved fraction within the formation water that might be extracted concomitantly). The term *oil* refers to the liquid petroleum phase. The liquid (or single-phase) fluid in reservoirs is sometimes referred to as *live oil*, and the liquid petroleum phase at surface condition is *dead oil*. However, the exact process by which reservoir fluids are brought to surface conditions (single or multi-stage separation) will modify the resulting partitioning of compounds between the gas phase and the liquid petroleum phase, at surface conditions.⁵ Hence, the term *oil* is imprecise and will be avoided in Chapter 4, Chapter 5, and throughout the thesis when we describe a release in deep waters, where the changes in pressure and temperature conditions make this term ambiguous. The early literature on *Deepwater Horizon*, during which a petroleum fluid was released at ~1500 m depth in the ocean, was often unclear on this terminology, and we aim to clarify these aspects in this thesis.

For the case of a surface spill, *oil* can be used unambiguously as a term referring to the liquid petroleum phase released. This is usually a relatively well-defined mixture, because the gas-liquid separation of the reservoir fluids occurred prior to the release in the environment. When the discussion is focused clearly on surface spills, *oil* will frequently be used with this meaning.

1.2 Liquid petroleum fluids in the marine environment

Liquid petroleum fluids are released into the marine environment through several pathways. Chronic, slow natural seepage through the seafloor has been occurring probably for millions of years,^{2,6} and its annual input into the marine environment was estimated worldwide as $6 \cdot 10^8$ kg per year for the period 1990–1999, or approximately half of the estimated total input of liquid petroleum compounds to marine environments.⁷ Anthropogenic emissions include many diffuse pathways (e.g. runoff from land-based consumption or atmospheric deposition), and some large, localized releases, for example oil spills from damaged ships, or offshore oil-well blowouts. These large, localized spills receive particular attention due to their frequently important detrimental effects on ecosystems. In this work, we will consider the case of a sea-surface localized oil spill and a deep-water oil-well blowout. Specifically, we sought to provide compositionally detailed information on the fate of petroleum compounds in marine environment, which is lacking. We aimed to do so by investigating the processes underlying petroleum compound fractionations through models, and by using new data analysis techniques. Ultimately, these models could be helpful for developing emergency plans, guiding response action, or performing damage assessment. In particular, model predictions need to be obtainable fast during an emergency situation, possibly at the cost of reduced accuracy. To the contrary, more detailed models can be applied to damage assessment, and such models can be used to validate predictions of simpler models. However, a single model of the underlying physical processes can often be used. For example, we developed two different model compositions of the petroleum fluids emitted during the *Deepwater Horizon* disaster, enabling faster yet less precise predictions to be obtained within a timeframe compatible with the needs of an emergency response when using the simpler model composition. A more detailed

model composition was used to get a deeper understanding as would be necessary for damage assessment. Finally, detailed model predictions can also serve to develop a better intuition of the potential outcomes which is helpful during an emergency situation.

Oil-well blowouts occur when the control of an oil well is lost: the pressure of the petroleum fluids within the well cannot be counterbalanced anymore, and, if all countermeasures fail, this can lead to a massive release of petroleum fluids (frequently including both a liquid and a gaseous petroleum phase) into the environment that will last until the damaged well can finally be capped. Gas-well blowouts do also happen, as at the *Elgin* rig in the North Sea in 2012. Dramatic blowouts from offshore platforms are fortunately not so common, but when they have occurred they have led to the largest accidental marine releases to date, each lasting for months (*Ixtoc I* in 1979, *Deepwater Horizon* in 2010, both in the Gulf of Mexico). For example, the quantity of stock tank oil that was released during the *Deepwater Horizon* blowout in the Gulf of Mexico over a three-month period,⁸⁻¹⁰ probably $4.7\text{--}6.9 \cdot 10^8$ kg,^{8,9} is similar in magnitude to the estimated anthropogenic mean annual input of liquid petroleum compounds into the marine environment *worldwide* ($\sim 6.7 \cdot 10^8$ kg per year for the 1990–1999 period).⁷

1.2.1 Sea-surface spills

After the release of oil on the sea surface, several physical processes, including evaporation, aqueous dissolution, sorption, emulsification, and dispersion, together called *weathering*, can modify oil composition and properties.⁷ Evaporation usually dominates the early fractionation of petroleum compounds after a spill, typically affecting compounds with boiling points lower than the *n*-C₁₅ alkane.¹¹ Evaporation can remove up to 75% of the oil volume within a few days for light crude oils (high API gravities), up to 40% for medium crude oils, and about 5% for heavy or residual oils (low API gravities).¹² Compared to evaporation, aqueous dissolution removes less mass from the oil phase during early weathering.¹³⁻¹⁶ However dissolution partly determines aquatic ecotoxicological impacts, because several individual soluble hydrocarbon compounds as well as hydrocarbon mixtures are toxic to aquatic species.^{7,17-20} It is challenging to apportion mass transfers of hydrocarbons from the oil phase into both water and air, because these two processes act simultaneously on many of the same compounds.¹⁵ Evaporation and aqueous dissolution dominate the first hours to day of an oil spill, and there is a lack of data for this early period due to the logistical challenge of sampling an unanticipated release and because the main focus is on limiting damages. In this thesis, based on previous experimental data by colleagues, I investigated this early period, showing that a compositionally detailed modeling of the processes of evaporation and aqueous dissolution is possible for the early hours.

From the moment of the release, the oil will tend to spread on the sea surface, and at a certain point it will break into patches.²¹ Some oils will tend to form water-in-oil emulsions depending on sea conditions. The emulsions contain up to 85% water,⁷ thus increasing the volume of the slick by up to about 550% and increasing the oil density so that it becomes much closer to the water density. The emulsification also leads to a large increase in oil viscosity, typically by two to three orders of magnitude.^{7,22} Emulsion formation can slow the other weathering processes and, especially due to the viscosity increase, greatly influences the oil recovery techniques

that can be used. Depending on the sea state, part or all of the oil may get dispersed as small droplets within the water column,^{23,24} where they may initially harm marine organisms. Partial to total oil dispersion was reported to happen under breaking wave conditions, which are assumed to be present when the wind speed is superior to 3 m s^{-1} in the ADIOS model.²⁵ The ADIOS model is an open-source oil weathering model for sea surface oil spills developed by the American National Oceanic and Atmospheric Administration (NOAA), designed to be used as a response tool. The other well-known oil spill weathering model is OSCAR, developed by SINTEF; the two models are compared in Table 1-1.

Table 1-1. Comparison of the OSCAR and ADIOS oil spill models.

	OSCAR	ADIOS
Developer	SINTEF	NOAA
Code status	proprietary/needs to buy a license	open source/can be downloaded for free from http://response.restoration.noaa.gov/oil-and-chemical-spills/oil-spills/response-tools/adios.html
Processes modeled	spreading, evaporation, emulsification, dispersion, aqueous dissolution , response actions (chemical dispersion, mechanical recovery, burning)	spreading, evaporation, emulsification, dispersion, response actions (chemical dispersion, mechanical recovery, burning)
Applicable to guide response actions	yes	yes
Oil database included	yes	yes
Pseudo-component type	25 pseudo-components, enables estimation of aqueous dissolution	varied number of distillation cuts

Several other processes act usually on a longer term. Photodegradation is a negligible process in terms of mass loss from the oil slick,⁷ but it can transform some of the oil compounds, leading to more toxic and water-soluble products.^{7,26} Biodegradation is negligible during the first days following an oil spill and probably only becomes a noticeable process after approximately a week or more.²⁷ The extent of biodegradation will vary widely depending on local conditions, but it plays usually a large role for the long-term degradation of petroleum compounds. Existing knowledge on oil biodegradation in the environment has focused so far on minor components of oils with acute toxicities, like polycyclic aromatic hydrocarbons (PAHs).^{7,28} However, saturated hydrocarbons are less studied, despite their prominent contribution to petroleum fluid compositions. Saturated hydrocarbons also participate into the narcotic-based toxicity of unresolved complex mixtures.²⁹ In this thesis, we will specifically investigate the biodegradation of saturated hydrocarbons in the surface environment in the aftermath of the *Deepwater Horizon* disaster.

1.2.2 The *Deepwater Horizon* disaster as a deep-water release

Deepwater Horizon

Background

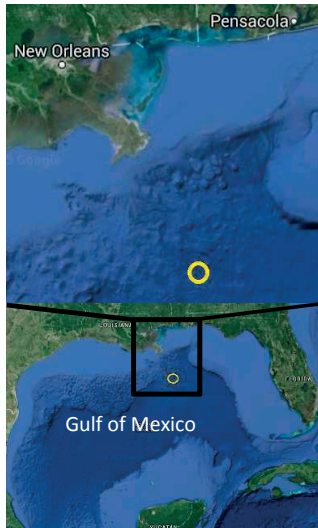
During the morning of April 20, 2010, following a series of risky decisions and misjudgments, the situation went out of control on Transocean's *Deepwater Horizon* drilling platform, leased by BP. A blow-out occurred, the platform burned during the following day and a half and eventually sank. As a consequence, eleven human lives were lost and the second largest marine oil spill ever caused by human beings was starting.³⁰ Oil leaked during 87 days from the broken Macondo well, at the sea floor level, approximately 1500 meters below the sea surface. More than half a million tonnes of total petroleum compounds were emitted in the environment (here and throughout this thesis: 1 tonne = 1,000 kilograms); however, determination of the exact amount of petroleum fluids emitted is difficult.^{10,31}

Specificities

- Deep-water release (elevated pressures)
- Presence of a deep-water hydrocarbon plume
- large extent of aqueous dissolution

Previous knowledge gaps

- Mechanistic explanation to the large extent of aqueous dissolution
- Contribution of droplets having low rise velocities
- Effect of dispersant



Location of the *Deepwater Horizon* disaster (yellow circle).
The maps are from Google map.

As a deep-water release, the *Deepwater Horizon* disaster presented several features that differentiate it from traditional, sea-surface releases, as explained below.

A plume of dissolved hydrocarbons at ~1100 meters depth in the water column was first noticed in late May 2010 by scientists aboard the R/V *Pelican*,³⁰ and rapidly scientific publications arose to document the finding.^{31,32} It became obvious that a portion of the oil compounds mass did not reach the surface and remained in the deep sea.^{8,31–33} In particular, the ~100,000 tonnes of methane released did not naturally surface.^{8,34} This finding is coherent with other reports about the fate of methane released in the Black Sea,³⁵ as well as modeling results for massive methane inputs also in the Black Sea.³⁶ The light hydrocarbon compounds ethane and propane, which would occur as gases at surface conditions, became also significantly aqueously dissolved in the deep-water hydrocarbon plume.⁸ In the same way, >99% of the benzene became aqueously dissolved during ascent, which limited the risks at the surface linked with the toxicity of this compound (a human carcinogen), but which led to exposures of aquatic

organisms to toxic hydrocarbons in the deep water column of the Gulf of Mexico.^{8,37} The possible presence of droplets having small diameters that would have stayed dispersed in the water column for prolonged times has remained uncertain in the available literature to date.

Another feature of deep-water petroleum fluid releases is the potential creation of hydrates, a buoyant solid material generated when light compounds (principally methane, ethane, propane, carbon dioxide) become trapped in a crystal-like structure of water molecules, formed under low temperature and high pressure conditions typically encountered at depths larger than ~500 m in the ocean. Hydrate formation contributed to the failures of early attempts to contain the release of petroleum fluids emitted from the Macondo well after the blowout of the *Deepwater Horizon* platform,³⁸ because hydrates clogged pipes designed to pump the emitted fluids.

In summary, a deep-water petroleum fluid release is very unlike a conventional sea-surface oil spill. After a sea-surface spill, evaporation is the dominant mechanism of mass removal from the oil slick during the initial hours to days,¹¹ impacting the compounds with low boiling points (<270 °C). Evaporation competes with aqueous dissolution to remove hydrocarbon compounds from the liquid petroleum phase,^{13,39–42} including toxic compounds like PAHs. However, during a deep-water hydrocarbon release, evaporation is suppressed during ascent in the water column, and this is expected to dramatically increase the fraction of soluble hydrocarbon mass that is transferred to the water column.^{8,40,43,44} As a result, the deep marine ecosystem experiences substantially increased hydrocarbon exposures.⁸ Pressure, temperature, and salinity influence the equilibrium distribution of hydrocarbons between water, liquid petroleum, and gas bubbles in the deep sea.⁴⁵ Additionally, thin⁴⁶ hydrate shells may form around hydrocarbon gas bubbles or liquid droplets under deep-water conditions.^{47–52} These thin hydrate shells are expected to impact mass transfer rates of hydrocarbons dissolving into the water column.⁴⁷

Globally, despite partial knowledge that was available when this thesis was started, there was a lack of understanding of the behavior of the petroleum fluids once emitted in the deep waters surrounding the broken Macondo well. The gas-liquid partitioning of the emitted petroleum fluid remained poorly characterized, as well as the physical properties of the hydrocarbon phases at emission depth, which are different from that at the surface and require specific estimation methods. In particular, there has been no attempts prior to this thesis to use the broad spectrum of the detailed composition of the emitted fluids to estimate these properties and to mechanistically explain the hydrocarbon partitioning noticed during the event.

1.3 Comprehensive two-dimensional gas chromatography (GC×GC)

Several analytical techniques are used to study the compositions of petroleum fluids. These techniques are mostly based on chromatographic procedures. In one-dimensional gas chromatographic analysis, the extract is eluted by passing a gas through a column, and compounds are separated due to their differences in affinity with the stationary phase coated to the inside of the column, which is regulated using a temperature ramp applied to the column. A gas chromatographic technique used to quantify approximate carbon number intervals in a petroleum liquid is simulated distillation.⁵³ It is designed to approximate the true boiling point distillation, which is more tedious, requiring especially larger sample volumes. One mature technique that has proved useful for the quantification of individual analytes is gas chromatography coupled to a mass-spectrum detector (GC–MS). However, since the diversity of chemical structures increases with carbon number, this method can separate only a very limited fraction of the large compounds. Addition of a second chromatographic dimension of separation can improve the ability to resolve compounds, providing much more detailed compositional data for further analysis.

Comprehensive two-dimensional gas chromatography (GC×GC), used widely to analyze complex mixtures, is based on two sequential separation steps: material eluting from a first chromatographic column is trapped and then released at discrete intervals into a second column (Figure 1-1). Transport in the second column is fast compared with the first column, which allows the compounds to be separated further without significant loss of resolution from the first separation. Compared to one-dimensional gas chromatography, GC×GC improves the signal to noise ratio⁵⁴ and allows the separation of thousands of compounds.⁵⁵ Since its inception two decades ago,⁵⁶ this technique has proven effective in domains involving very complex mixtures, such as petroleum, volatile organic compounds in air, fragrances, plant and animal extracts, food and alcoholic beverages, and pesticides in environmental samples.^{57–59} In GC×GC, all of the analytes are subjected to the two separation steps; this is different from two-dimensional “heart cut” chromatography where only a fraction of the analytes are subjected to a second separation (hence the “comprehensive” in the name).⁶⁰

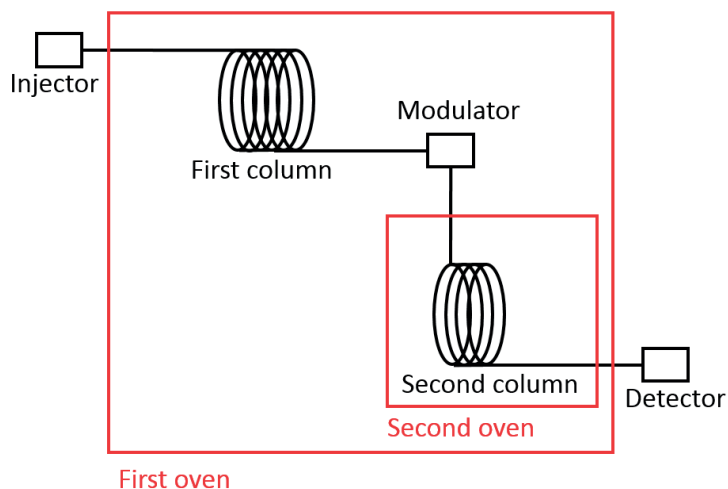


Figure 1-1. Schematic representation of a typical comprehensive two-dimensional gas chromatography (GCxGC) instrument. The detectors used are often a flame ionization detector (FID), which provides a signal approximately proportional to the mass of hydrocarbon analytes,^{61–63} or a mass spectrum detector (MS).

In short, GCxGC chromatograms are three-dimensional data structures that contain, for each data point, the retention time in the first column, the retention time in the second column, and the signal intensity value measured by the detector, which is generally linearly related to the amount of analyte eluting from the device (e.g. FID for hydrocarbons). GCxGC chromatograms are often visualized as two-dimensional surfaces, with the signal intensities represented by use of a color scale (Figure 1-2). GCxGC is a powerful tool for studying the evolution of oil composition, however some aspects require careful handling for quantitative use of the data, especially baseline (section 1.3.1 below) and small run-to-run retention time shifts (discussed below and in Chapter 2). GCxGC analyzes a compositional window that generally spans the normal alkanes $n\text{-C}_8$ to $n\text{-C}_{45}$, approximately, and that contains most of the compounds susceptible to undergo rapid fractionation in the environment, except for light compounds ($<n\text{-C}_8$). Compounds outside of this window must be studied by other means.

Some uncontrollable processes in the GCxGC instrument, such as small pressure and temperature variations and column degradation,⁶⁴ lead to variations of analyte retention times from run to run. This variability complicates the ability to make effective and automated comparisons between analyzed samples. There is therefore a need for effective alignment tools, designed to increase the similarity of analyte retention times in a target chromatogram with respect to a reference chromatogram, which is done in order to enable improved analysis (Chapter 2). Good alignment enables to draw difference chromatograms,⁶⁵ which selectively displays the difference in composition among two GCxGC chromatograms (if normalized); to compare the content of thousands of compounds among differently weathered samples;⁵⁵ to compute mass loss tables¹⁵ (Chapter 3); or to perform more easily any other quantitative comparison of whole GCxGC chromatograms.

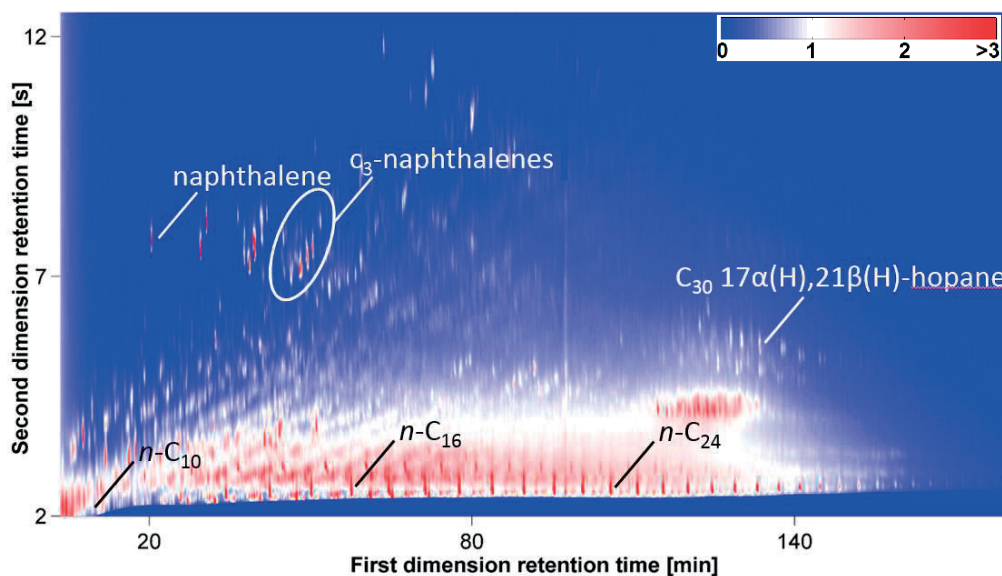


Figure 1-2. A typical GCxGC-FID chromatogram of a crude oil (Grane crude oil from the North Sea). A few compounds are labelled. The color scale on the upper right indicates FID signal response (arbitrary units).

1.3.1 Baseline correction for GCxGC data

Baseline correction is a necessary step prior to quantitative use of GCxGC data. In this section, we will introduce what is meant by the ambiguous term *baseline*, which is operationally defined depending on the aim. In general, the signal measured by a GCxGC detector can be separated into three main contributions: noise, instrument background signal, and the signal resulting from the analyzed sample.⁶⁶ The latter can be separated into analyte signal (resolved compounds) and unresolved signal (unresolved compounds).⁶⁶ The instrument background signal is the signal produced by the detector in the absence of sample.

If one is interested in quantifying analyte signal (resolved compounds), it is necessary to remove instrument background signal and unresolved signal (type I baseline on Figure 1-3). In order to study analyte signal + unresolved signal, another baseline correction method is necessary, which aims at removing only the instrument background signal, shown as the type II baseline correction algorithm on Figure 1-3.

In practice, we have found^{40,62,66,67} that applying our two-dimensional extension of the Eilers' baseline correction code (<https://github.com/jsarey/GCxGC-baseline-correction>)^{68,69} is pertinent for type I baseline applications, whereas the Reichenbach et al. method,⁷⁰ implemented in GC Image,⁷¹ is adequate for type II baseline applications. These are the two baseline correction techniques applied to whole chromatograms in this thesis. In addition, a local (linear) type I baseline-correction code, the Arey et al. Gaussian-peak fit code,¹⁵ implemented in Matlab, was used for quantification of individual analytes in some circumstances.

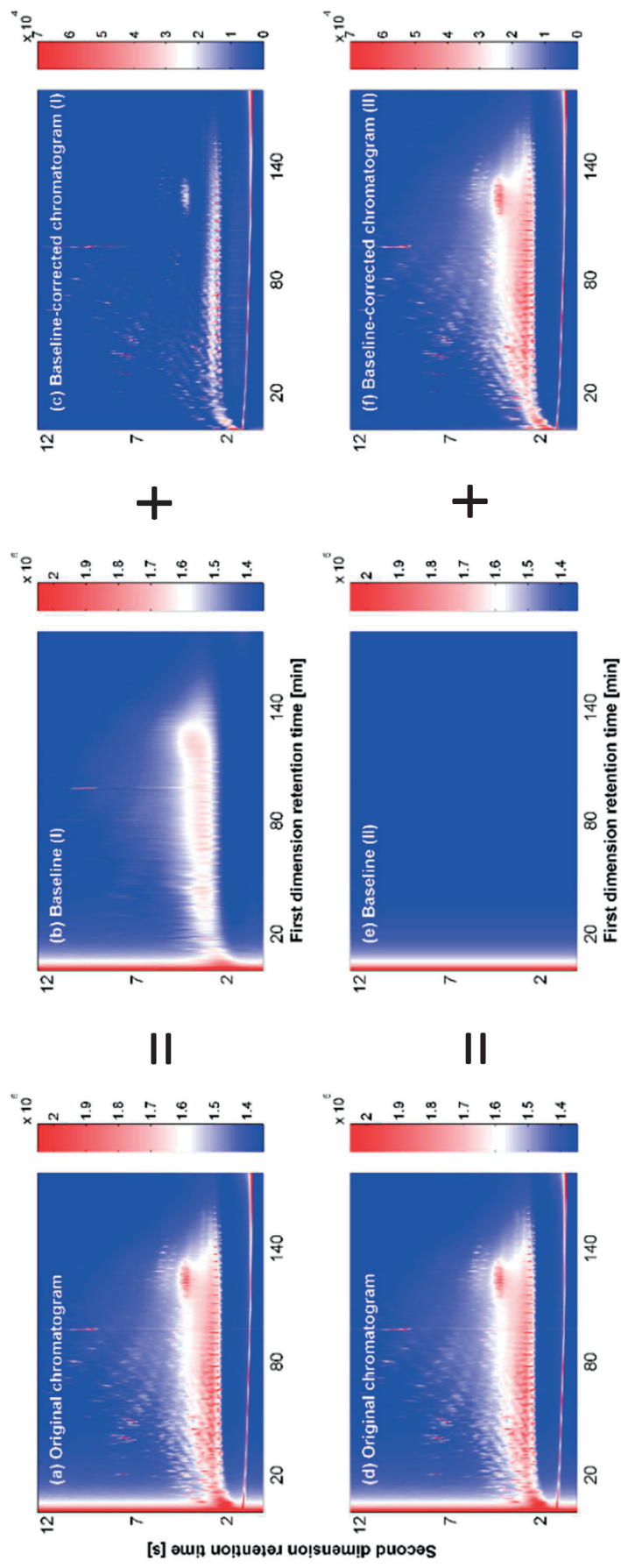


Figure 1-3. Schematic representation of the two types of baseline considered in this work, for a crude oil GCxGC chromatogram. (a-c) Baseline of type I (Eilers type) is useful to isolate the signal corresponding to analyte signal (resolved compounds), (d-f) whereas baseline of type II (Reichenbach type) is useful to isolate the signal corresponding to analyte signal + unresolved signal (resolved + unresolved compounds). (Color bars for FID signal for panels a, b, d, and e differ from color bars for panels c, and f; all color bars span a range of 70,000 FID signal units, but the first set of color bars starts at 135,000 whereas the latter set starts at 0.) The nearly horizontal line eluting at approximately one second in the second dimension (panels a, c, d, f) correspond to modulated column bleed.

1.4 Aim of this work

As discussed in section 1.2, several different processes affect petroleum fluids once released in the marine environment, and together they largely determine the pollutant exposure endured by marine ecosystems. This thesis aims to improve the understanding of some of these processes: the early processes of evaporation and aqueous dissolution during surface releases; aqueous dissolution and related high-pressure processes during deep-water releases; and biodegradation. Early transport and mass transfer processes control rapid exposures leading to acute toxic effects, whereas biodegradation is a major process for the long-term natural attenuation of petroleum in the marine environment. In particular, available compositional knowledge is often limited, based on techniques able to quantify only a limited fraction of petroleum fluid compositions. In this work, I sought to use the detailed compositional data on petroleum fluids that are made available by modern analysis tools, such as GC×GC, in order to study the fate of petroleum fluids in the environment not only for selected minor compounds but for a broader compositional range. This was done through models that explain the underlying processes and allow to make predictions of the individual behavior of a broad range of petroleum compounds and pseudo-components.

One recurrent analytical technique that is used throughout this thesis is GC×GC–FID, because it provides detailed compositional information for the n -C₈ to n -C₄₅ range. Additionally, it is a precious tool owing to its ability to separate petroleum compounds approximately according to boiling point and air-water partition coefficient (Figure 1-4),^{39,72} which makes it a natural tool for modeling of evaporation and aqueous dissolution.^{14,73,74,40} However, one technical limitation of GC×GC is the presence of uncontrollable, small run-to-run retention time shifts that hamper proper comparisons of whole chromatograms. Chapter 2 is dedicated to the development of a post-processing solution to this problem, enabling improved quantitative analyses in the other chapters of this thesis. The hypothesis underlying our alignment algorithm is that there is a correlation between the shifts of neighboring peaks, and that this can be corrected using a reasonably sized selection of peaks as alignment points. The aim is that better alignment between chromatograms can enable to use the detailed compositional information offered by GC×GC to make improved quantitative comparisons among samples.

Disentangling the coupled evaporation and dissolution mass transfers of petroleum hydrocarbons during the first hours to day after a sea-surface spill allows us to gain insight into the exposures of the different parts of the marine ecosystem. Despite that the highest concentrations of toxic compounds in the water column below oil slicks are expected in this early period, data describing aqueous dissolution and evaporation of oil hydrocarbons during the first hours to day are usually lacking for accidental spills. The lack of understanding of these two processes is further complicated by the fact that evaporation and aqueous dissolution both act on many of the same compounds. To establish a better understanding of the combined effects of these two processes, mass transfer models are required. In Chapter 3, we aim to predict the evolution of the oil slick composition, to apportion the mass losses to water and atmosphere, and to clarify the predicted effect of environmental conditions (temperature and wind speed) on the early apportionment of petroleum hydrocarbons, which are processes

that had been debated in earlier literature. To support this effort, we provide unprecedentedly detailed compositional predictions for the partitioning of hydrocarbons during this early stage (initial 25 hours) of a sea surface oil spill. The alignment algorithm (Chapter 2) was used in this work to enable improved quantitative comparisons.

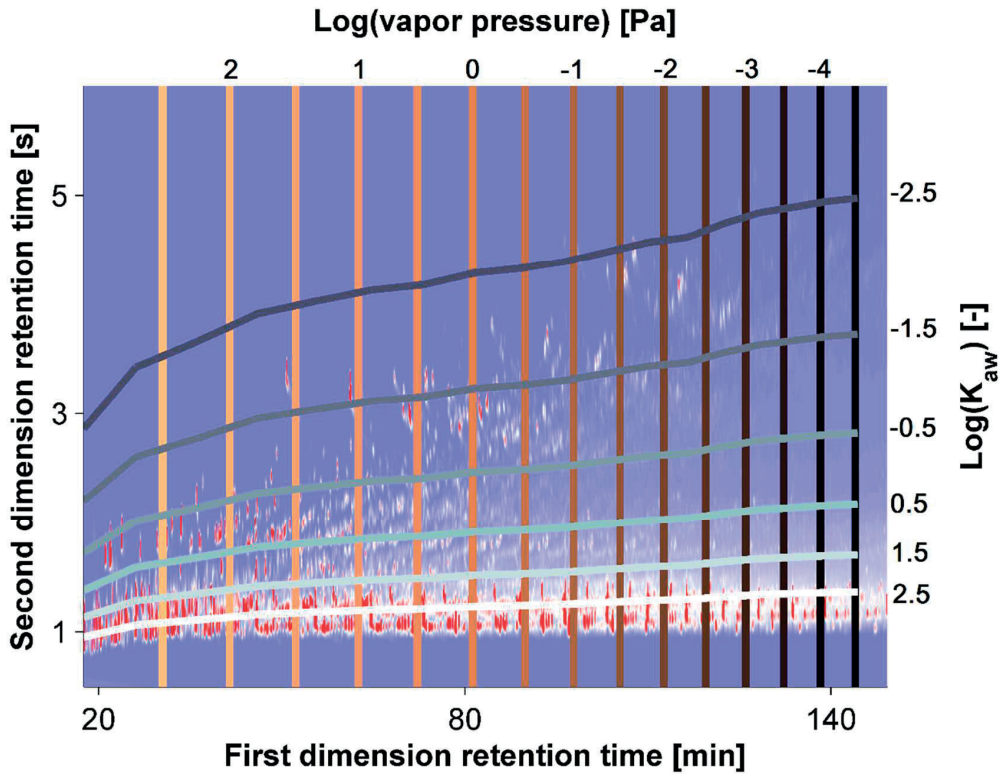


Figure 1-4. GCxGC-FID chromatogram of an oil sample overlaid with estimated contours of the base 10 logarithm of decreasing vapor pressure (from left to right) and base 10 logarithm of increasing air-water partition coefficient, K_{aw} (from top to bottom). These lines were drawn by use of the Matlab algorithms of Nabi et al.⁷² K_{aw} is expressed here in units of $(\text{mol m}^{-3}) (\text{mol m}^{-3})^{-1}$, i.e. concentration in gas phase divided by concentration in aqueous phase.

Compared to more well-studied sea-surface petroleum releases, the behavior of petroleum fluids released in deep waters is poorly understood, in spite of the recent development of deep-water offshore drilling. Processes resulting from the high pressure and low temperature conditions, especially the largely increased extent of aqueous dissolution, lead to a fractionation of petroleum compounds that differ profoundly from what is observed for a sea-surface release. Here we seek to explain the measured concentrations in the deep water column near the broken Macondo riser stub in terms of the physical processes that were relevant in the deep waters of the Gulf of Mexico, including buoyant plume dynamic, aqueous dissolution, and effect of hydrates. In particular, we took into account the effect of composition, pressure, temperature and salinity on these processes. Available data^{8,75} indicate that aqueous dissolution played a major role, but a modeling study was lacking to quantitatively support this claim and to enable predictions for possible future deep-water releases of petroleum fluids. Also, there was a debate on whether tiny droplets having low rise velocities remained in deep waters for prolonged periods, and model predictions are able to provide insights in this debate.

Finally, the modeling study conducted in this thesis allows us to validate the predicted droplet and bubble size distributions based on the measured compositional data taken in the deep water column and at the sea surface during the event, and this had not been attempted previously. Again, in this study I sought to investigate the behavior of the petroleum fluid using the detailed knowledge of its composition made available by previous reports, an approach unlike that chosen by other teams working on the *Deepwater Horizon* disaster. My work focused on gas-liquid-water partitioning modeling, estimation methods for bulk phase properties, and compilation or estimation of required chemical properties for the different compounds and pseudo-components. My developments have been included in a larger deep-water blowout model, TAMOC, implemented by Scott A. Socolofsky. The model also includes physical aspects developed by other contributors, including plume dynamics and a model of the effect of hydrates on droplet and bubble ascent speeds and mass transfer coefficients.

Biodegradation is a major process affecting petroleum residues after completion of the majority of evaporation and aqueous dissolution. It is usually the dominant process acting on compounds larger than approximately normal eicosane ($n\text{-C}_{20}$). In particular, the degradation of saturated hydrocarbon compounds is usually poorly studied, despite the fact that they typically represent a large fraction of a petroleum fluid emitted into the marine environment. Here we investigate the relative extent of biodegradation of different families of petroleum saturated hydrocarbons, based on samples collected on beaches after the *Deepwater Horizon* blowout.

Chapter 2 A robust algorithm for aligning two-dimensional chromatograms

Published in: Analytical Chemistry 2012, 84, 9033–9040
(<http://pubs.acs.org/doi/abs/10.1021/ac301367s>).

Authors: Jonas Gros, Deedar Nabi, Petros Dimitriou-Christidis, Rebecca Rutler, and J. Samuel Arey.

Contributions: This chapter was prepared principally by me. I wrote the Matlab code of the alignment algorithm and I also led the development of the concept of the algorithm. Deedar Nabi and Samuel Arey participated in the controlled release on the North Sea during which oil spill samples were collected. Deedar Nabi performed extraction and GC×GC analysis of oil spill samples, whereas Petros Dimitriou-Christidis sampled and analyzed the wastewater samples. Rebecca contributed to the lab work. Samuel Arey, finally, provided guidance, participated largely in the conceptual development of the algorithm, and had an important participation in text writing and editing.

Note: An update to the Matlab peak-matching codes of Wardlaw et al.,⁵⁵ used in this study, was made after publication during a later work. The present chapter contains updated statistics using the corrected codes (Table 2-2).

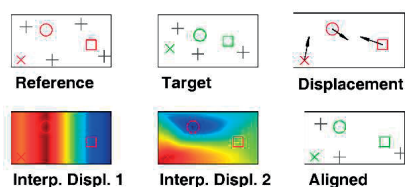


Figure 2-1. Schematic depiction of the principle of the alignment algorithm.

Reproduced/adapted with permission from Analytical Chemistry 2012, 84, 9033–9040. Copyright 2012 American Chemical Society.

2.1 Abstract

Comprehensive two-dimensional gas chromatography (GC×GC) chromatograms typically exhibit run-to-run retention time variability (<1 typical peak width, both in first and second dimension). Chromatogram alignment is often a desirable step prior to further analysis of the data, for example in studies on the weathering or environmental forensics of complex mixtures. We present a new algorithm for aligning whole GC×GC chromatograms. This technique is based on alignment points that have locations indicated by the user both in a target chromatogram and in a reference chromatogram. We applied the algorithm to two sets of samples. First, we aligned the chromatograms of twelve compositionally distinct oil spill samples, all of which we analyzed using the same instrument parameters. Second, we applied the algorithm to two compositionally distinct wastewater extracts that we had analyzed using two different instrument temperature programs, thus involving larger retention time shifts than the first sample set. For both sample sets, the new algorithm performed favorably compared to two other available alignment algorithms: the algorithm of Pierce et al. (2005)⁶⁴ and 2-D COW from Zhang et al. (2008).⁷⁶ The new algorithm achieves the best matches of retention times for test analytes, avoids some artifacts which result from the two other alignment algorithms, and incurs the least modification of quantitative signal information.

2.2 Introduction

Comprehensive two-dimensional gas chromatography (GC×GC) is widely used to analyze complex mixtures based on two sequential separation steps: material eluting from a first chromatographic column is trapped and then released collectively at discrete intervals into a second column. Transport in the (shorter) second column is fast compared with the first column, which allows the compounds to be separated further without significant loss of resolution from the first separation. Compared to one-dimensional gas chromatography, GC×GC improves the signal to noise ratio⁵⁴ and allows the separation of thousands of compounds.⁵⁵ Since its inception two decades ago,⁵⁶ this technique has proven effective in domains involving very complex mixtures, such as petroleum, volatile organic compounds in air, fragrances, plant and animal extracts, food and alcoholic beverages, and pesticides in environmental samples.^{57–59}

Good retention time reproducibility between GC×GC chromatograms (within << 1 typical peak width) is broadly important for practical applications. For example, difference chromatograms,^{55,65} which selectively show only the compositional differences between two samples, require well-aligned chromatograms. Similarly, automated peak-tracking tools have been developed that can quantify abundance changes for thousands of compounds between different samples.⁵⁵ Such data analysis applications require good reproducibility of retention times between chromatograms. However, some uncontrollable processes, such as small pressure and temperature variations and column degradation,⁶⁴ lead to variations of analyte retention times from run to run. This variability complicates the ability to make effective and automated comparisons between samples. Therefore, chromatogram alignment is of interest to diverse scientific fields that apply GC×GC, including metabolomics,^{77,78} and oil weathering and oil spill forensics (as in Chapter 3 and Chapter 6).^{15,39,40,55,62,65,79,80} This is also an interesting step prior

to the application of chemometric techniques,^{81,82} and more widely for any kind of analysis implying comparisons between different samples.^{83–85}

Alignment algorithms have been developed in order to improve the agreement of retention times between whole GC×GC chromatograms of compositionally similar samples. To do this, a *target chromatogram* is modified to improve the similarity of the retention times of its peaks with respect to those in a *reference chromatogram*. Ni et al.⁸⁶ developed an algorithm to correct deformations due to controllable parameters variations, e.g., intended pressure or temperature program modifications, using a global affine transformation which is calibrated by a set of pre-defined alignment points. However, this algorithm is not designed for correcting the shifts resulting from uncontrollable variations. The first published alignment algorithm for the correction of shifts resulting from uncontrollable variations for whole GC×GC chromatograms was developed by Pierce et al.,⁶⁴ extending their previous 1-D GC alignment algorithm.⁸⁷ The principle of their algorithm is to divide the target chromatogram into windows of a user-defined size, to shift each window within limits defined by the user, and to determine the extent of shift that optimizes the correlation with the corresponding window on a reference chromatogram. This shifting is then applied to the center of the window, and the remaining values are interpolated. A second alignment algorithm called two-dimensional correlation optimized warping (2-D COW) was introduced by Zhang et al.,⁷⁶ and it also represents an extension of a 1-D method.⁸⁸ Like the algorithm of Pierce et al., 2-D COW relies on the division of chromatograms into windows, but instead of shifts, warping (i.e. stretching or compression) is applied to the target chromatogram within a certain limit set by the user. Maximum correlation is used to optimize the extent of deformation that is applied. An attempt was also made by Vial et al.^{89,90} to apply dynamic time warping (DTW) to GC×GC chromatograms, but it was limited to the correction of the shifts in the second dimension, because such shifts are normally larger than in the first dimension. Some other tools have also been developed for GC×GC coupled with mass spectrum measurements,^{91–93} but these are not directly applicable to GC×GC coupled with other types of detectors.

As part of the analysis of GC×GC chromatograms acquired from environmental samples in our laboratory, I tried the different alignment algorithms currently available. I experienced the following limitations and shortcomings, depending on the method used: unrealistic distortions of the peaks, unwanted modification of the reference chromatogram, lack of access to the raw code of the alignment tool, and limited possibilities to improve the alignment if results were not satisfactory. Therefore we decided to develop our own alignment algorithm according to the following principles. The user selects a set of alignment points that correspond to compound peaks found in both the reference chromatogram and in the target chromatogram. As long as the user is able to confidently identify the alignment points in both the reference and target chromatograms, knowing their identities (chemical name) is not necessary. These points are aligned, and deformations between these points are interpolated. With this new algorithm, we aimed to satisfy the following criteria: (a) significant improvement in the alignment of a target chromatogram with respect to the reference, (b) ease of use, (c) straightforward strategies to improve unsatisfactory results, (d) avoidance of unrealistic artifacts, (e) robustness to differences of composition between samples, and (f) modification of only the target chromatogram and not the reference. We evaluated the performance of the

new algorithm using several GC×GC chromatograms of environmentally relevant complex mixtures, and we compared this to the performance of other previously developed algorithms. The mixtures used for this evaluation (oil and wastewater) contained different types of compounds (hydrocarbons and halogenated compounds).

2.3 Experimental section

2.3.1 Sample analysis.

The algorithm was tested using two sets of samples. In the first test set, twelve differently weathered, compositionally distinct oil spill samples were analyzed by Deedar Nabi using the same GC×GC instrument parameters, and these chromatograms exhibited some retention time shifting due to normal variations in instrument stability. These samples were obtained by Deedar Nabi and Samuel Arey on September 29-30, 2009 during a marine field experiment on the North Sea, in which 4.3 m³ of Grane crude oil was spilt about 230 km offshore in the North Sea Netherland Exclusive Economic Zone. The experiment was conducted in collaboration with the Royal Netherlands Institute of Sea Research (NIOZ), the Dutch Rijkswaterstaat, and other European institutions. The neat (unweathered) oil was chosen as the reference and eleven weathered oil sample chromatograms were aligned to the chromatogram of this sample. Instrument parameter details (program C) are given in section 2.7.1 of the Appendix. Two types of samples were collected: oil slick and oil sheen samples. Qorpak jars (30 mL) with teflon-lined caps were used to collect the samples. Table 2-4 in section 2.7.1 gives the types of sample collection and inlet injection modes used to analyze the samples. The collected samples were preserved by adding an appropriate amount of dichloromethane (DCM) in a laboratory on the main ship and stored in a refrigerator. A neat (unspilt) oil sample was also taken. All samples were transported in cold storage to our laboratory, then liquid-liquid extracted using 2x50 mL of DCM and rotary evaporated to a final volume of ~ 1 mL.

In the second test set, two compositionally distinct wastewater sample extracts (obtained and analyzed by Petros Dimitriou-Christidis) were both analyzed twice using two different temperature programs, thereby inducing more significant retention time shifts compared to those of the first test set. One temperature program (program A, 3.5 °C/min) was arbitrarily chosen as the reference, and the two chromatograms resulting from analysis of the two samples with the second temperature program (program B, 4 °C/min) were aligned to the chromatograms acquired with the first temperature program. Two different cases were then studied. In the first case, a chromatogram of each sample was aligned to the chromatogram of the same sample analyzed with the other temperature program. In the second and more challenging case, the chromatogram of one sample was aligned to a chromatogram of the other sample, each analyzed using different temperature programs. See Appendix for complete instrument and analysis details (section 2.7.1). Sample WW1 is the particle-phase extract of a 24-hour flow-averaged liquid water sample collected from the inlet of the Vidy wastewater treatment plant (WWTP) in Lausanne, Switzerland. Similarly, WW2 is the particle-phase extract of a 24-hour flow-averaged liquid sample collected at the same time from the outlet of the primary clarifiers of the Vidy WWTP. After collecting the liquid samples from the wastewater, Petros Dimitriou-Christidis obtained the particle phase through filtration. He

then spiked the dry filters with a solution of decafluorobiphenyl (as the surrogate) and extracted them in a Dionex Accelerated Solvent Extractor (ASE) using equal volumes of acetone and hexane. Extraction also involved in-cell extract cleanup in a bed of Florisil.⁹⁴ Finally, extracts were rotary evaporated to a final volume of 1.0 mL.

2.3.2 Data pretreatment.

Prior to alignment, all chromatograms were baseline-corrected using GC Image with default parameters.⁷⁰ After baseline correction, a chemical surrogate which had been added to the oil spill samples was found to produce a disproportionately large peak for some chromatograms; the surrogate peak was deleted in these chromatograms (corresponding pixels set to zero) to avoid biasing the results. Additionally, the signal in each oil spill chromatogram was normalized (rescaled) such that the sum of the five integrated *n*-alkanes peaks, octacosane (*n*-C₂₈) to dotriacontane (*n*-C₃₂), was same as in the neat oil, for all samples (see Chapter 3 for more details on the rationale). Wastewater extract chromatograms were normalized such that the total signal was the same in the target and reference chromatograms for the cases where a chromatogram was aligned to a chromatogram of the same sample analyzed using a different temperature program. These data pretreatment steps represent typical protocols that would be used in the analysis of real samples. Although not required for application of any of the alignment algorithms, we considered these steps likely to improve the realism of the results.

2.3.3 Alignment algorithm.

Our alignment algorithm is designed to improve the similarity of peak retention times in a target chromatogram with respect to those in a reference chromatogram. The algorithm alters the target chromatogram, whereas the reference chromatogram remains unchanged. Chromatogram alignment is conducted in three steps. First, alignment points selected by the user are assigned on both the target chromatogram and the reference chromatogram. Second, a shift, or displacement, is estimated for each pixel in the reference chromatogram with respect to the target chromatogram, based on information gained from the alignment points. Third, the signal values of shifted points are re-interpolated based on nearby points and corrected for stretching or compression. These steps are described in detail below.

An alignment point is the pixel with the maximal signal value of a peak which is believed to have the same chemical identity in both the reference chromatogram and the target chromatogram. The positions of each alignment point, both in the target and reference chromatograms, are supplied by the user. In the first step of the algorithm, these points are perfectly aligned. In other words, the location of the alignment point in the aligned chromatogram is made identical to its location in the reference chromatogram.

In the second step of the algorithm, the displacement of each reference chromatogram pixel is estimated on the basis of the displacements of nearby alignment points. First dimension displacements and second dimension displacements were computed differently. First dimension displacements are independent of second dimension elution time, and therefore they

are linearly interpolated between alignment points. This was considered physically reasonable; for example, a linear temperature ramp produces a nearly linear sequence of retention times for a homologous set of compounds.⁹⁵ Hence, in the case where two different linear temperature ramp programs would be used, the discrepancies in first dimension retention times from one chromatogram to the other would be approximately linear with respect to retention time. First dimension displacements outside of the region of the chromatogram bounded by alignment points are estimated using a linear extrapolation based on the first and last alignment points in the first dimension.

To calculate displacements in the second dimension, the two-dimensionality of shift variation must be taken into account. The second dimension displacement is estimated using a Sibson natural-neighbor interpolation, which is based on Voronoi diagrams,⁹⁶ as explained in Figure 2-2. This interpolation is applicable only within the convex hull of the alignment points. In order to apply the algorithm to the whole chromatogram, an additional alignment point is imposed at each corner of a rectangle 10% bigger than the reference chromatogram. The displacements assigned to these four added alignment points are extrapolated from a weighted average of displacements of the interior set of alignment points, each weighted by the square of the inverse of the distance from the corner point.⁹⁷ The displacements of these four additional alignment points are extrapolated based on the following formula:

$$D(AP_i) = \frac{\sum_{k=1}^N \left(\frac{1}{(\delta_{P_k, AP_i})^2} \cdot D(P_k) \right)}{\sum_{k=1}^N \frac{1}{(\delta_{P_k, AP_i})^2}} \quad \text{for } i = 1, 2, 3, 4$$

Equation 2-1

Where D is the displacement, $\{P_1, P_2, \dots, P_N\}$ are the initial alignment points, and $\{AP_1, AP_2, AP_3, AP_4\}$ are the four added alignment points. δ_{P_k, AP_i} is the distance between the alignment point P_k and the additional alignment point AP_i , i.e.:

$$\delta_{P_k, AP_i} = \sqrt{(\pi_1(P_k) - \pi_1(AP_i))^2 + (\pi_2(P_k) - \pi_2(AP_i))^2}$$

Equation 2-2

Where π_1 is the first dimension position and π_2 is the second dimension position (using the distance unit chosen, i.e. *typical peak width* (tpw) for our algorithm, as explained below in the text).

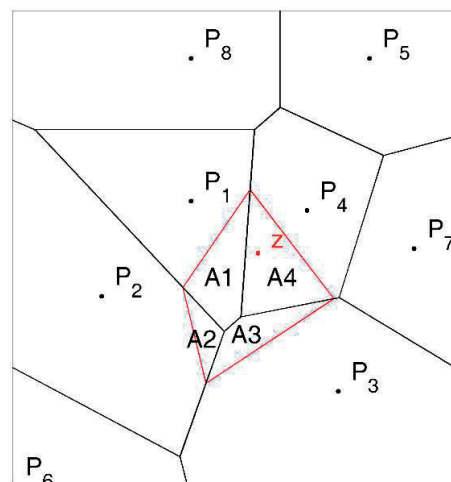


Figure 2-2. Explanation of the Sibson natural neighbor interpolation. In the example schematic above, a Voronoi decomposition of a GC×GC chromatogram space is shown, based on the positions of a hypothetical set of alignment points, P_1 to P_8 . In the example above, the Voronoi diagram segregates the plane into a set of 8 convex polygons, where each associated polygon is defined as the region of space that is nearer to point P_k than to any other alignment point. We denote this set *basis polygons* (black solid lines). Now consider any pixel z . The appropriate second dimension shift for pixel z is calculated based on a weighted average of second dimension shifts from nearby alignment points. For each pixel z , a new polygon is temporarily constructed, which is given by the Voronoi diagram of the combined set of points $\{P_1, P_2, \dots, P_8, z\}$. The new polygon adopts some area (A_1, A_2, A_3, A_4 in the example above) from the set of basis polygons. The second dimension shift for pixel z is computed as the weighted average of second dimension shifts of nearby alignment points (P_1, P_2, P_3, P_4) according to weights A_1, A_2, A_3, A_4 (see Appendix section 2.7.2 for formula).

The second dimension interpolation scheme could, in principle, depend upon the way that the distances are computed. Distances expressed in pixels are dependent on the modulation period and sampling rate, and this may lead to arbitrary bias in the interpolation. In order to ensure a consistent treatment across different chromatograms obtained using different instrument parameters, interpeak distances are renormalized with respect to a single typical peak width (tpw) value in both the first and second dimension. In other words, distances in first and second dimensions were defined so that a typical peak has a width equal to approximately one in both dimensions. The tpw parameter, defined as the number of pixels corresponding to approximately two standard deviations of a typical peak signal (assumed Gaussian-shaped), is supplied by the user for each dimension. We chose values which correspond to a typical peak eluting close to the middle of the run. Although this definition is somewhat subjective, in practice we found that algorithm results are insensitive to the tpw parameter. See Figure 2-3 for an example of the pixel displacements generated for sample OS1.

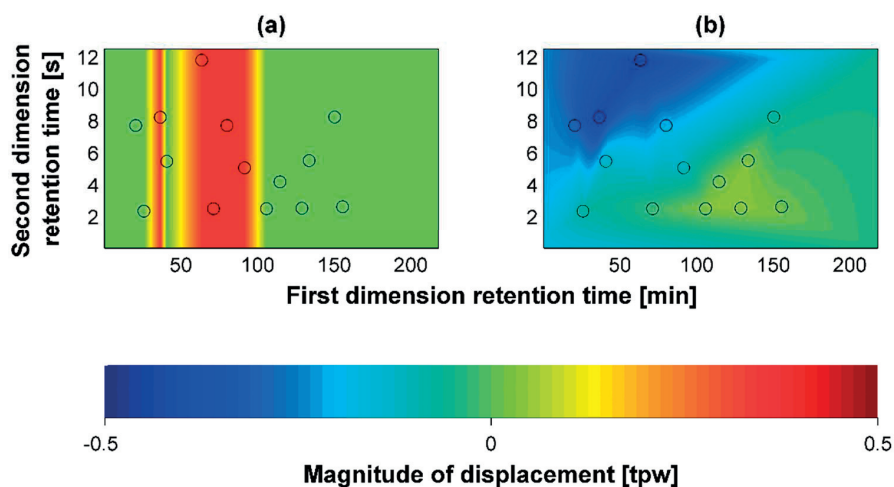


Figure 2-3. Pixel displacements generated for OS1 in (a) first dimension and (b) second dimension, in units of typical peak width (tpw). The black circles show the positions of the alignment points.

In the third step of the algorithm, the signal values of all pixels are reinterpolated. Displacements are not applied directly to the pixels of the target chromatogram because it would be inconvenient to work with a pixel grid having irregular spacings. Instead, to account for the displacement, the pixel grid in the aligned chromatogram remains identical to that in the target chromatogram, but each pixel signal value is reinterpolated using a bicubic convolution interpolation of the sixteen pixels surrounding that pixel (see section 2.7.3 of the Appendix for more details).⁹⁸ Transfer of a pixel to the next or previous modulation is allowed if required by the displacement estimate (wrapped-around peak). Finally, peak volumes (i.e., the sum of pixel signal values for a peak) should not be modified by the alignment. Hence, pixel signal values are corrected for the extent of deformation resulting from alignment: the signal value at each pixel after alignment is divided by one plus the fraction change in the adjacent inter-pixel spacing through alignment. This correction is applied in both dimensions. Our alignment technique is the first to correct chromatogram signals for the extent of deformation incurred. (It should be noted that by principle this correction assumes no remaining baseline; therefore, baseline-correction using a Reichenbach-type or an Eilers-type algorithm prior to alignment with our algorithm is strongly advocated.)

The alignment algorithm was implemented in Matlab,⁹⁹ using its implementation of the Sibson natural-neighbor and bicubic convolution interpolations. To aid the identification of alignment points, we also developed a tool which proposes alignment point positions in target chromatograms based on their positions in the reference chromatogram. This algorithm searches the target chromatogram for the maximum pixel value in a window (having size defined by the user) around the position corresponding to the peak in the reference chromatogram, and then verifies that the value found is a true local maximum (i.e. a maximum pixel of a peak). Proposed matching points can be accepted, modified, or rejected, upon inspection by the user. The success of the tool is not guaranteed for every case, and it is dependent upon the severity of shifting present in the target chromatogram as well as the proximity of alignment points to other prominent peaks.

This tool functioned well for oil spill chromatograms: in 11 target chromatograms, only one alignment point's position was wrongly estimated, whereas the 107 other alignment points' positions were correctly determined. The user is advised to always verify the results. This tool is not adapted for the severe shifts created by a change of temperature program, and was therefore not applied for the analysis of wastewater samples.

I have updated the Matlab codes several times after publication, not changing the algorithm applied, but making the codes more robust, including allowing the code to be used with other, more recent Matlab versions, and allowing different input data formats to be provided. I developed a user-friendly package, provided with a detailed user guide. The Matlab codes are freely available at <https://github.com/jsarey/GCxGC-alignment>.¹⁰⁰

2.3.4 Parameters used for the different alignment algorithms.

The new alignment algorithm was applied using 7 to 14 alignment points for chromatograms of oil spill samples (among which the normal alkanes *n*-C₁₂, *n*-C₁₈, *n*-C₂₄, *n*-C₂₉, *n*-C₃₆, naphthalene, biphenyl, and 17 α (H),21 β (H) hopane) and 10 alignment points for wastewater sample chromatograms (the positions of all alignment points for all chromatograms are shown in Appendix section 2.7.4). Alignment points were chosen according to the following criteria: (a) they correspond to analyte peaks having confirmed presence in both the target and reference chromatograms; (b) they bound the interesting sample region of the chromatogram, where possible; and (c) they remain sufficiently few in number as to be easily managed by the user.

Parameter values chosen with the Pierce et al. (access to the raw code was not given) and 2-D COW (Matlab code freely available for academic purposes) alignment codes were those which appeared to give the best results after testing different sets of model input parameters. For oil spill chromatograms the following values were applied: maximum warping (2-D COW) or shifting (Pierce et al.) of 75 pixels in second dimension and 5 pixels in first dimension; and window size of 100 pixels in the second dimension and 50 pixels in the first dimension. Larger values were also tested, because these parameter values did not allow sufficient shifting correction for two of the alignment points used with our code for the sample OS7. However, using larger values did not globally improve alignment for all the samples. For wastewater chromatograms, the values of the four parameters listed above were: 115 pixels, 35 pixels, 150 pixels, and 50 pixels, respectively.

2.4 Results and discussion

2.4.1 Extent of misalignment observed in the original, unaligned chromatograms.

To evaluate the extent of misalignment in target chromatograms prior to application of any alignment algorithm, we evaluated the retention time shifts of test points (alignment points for unaligned chromatograms, see section 2.4.3 for details) identified in both target and reference chromatograms (the positions of all alignment points for all chromatograms are shown in Appendix section 2.7.4). For oil spill chromatograms the mean deviations were 0.19 and

0.17 typical-peak-widths (tpw) in the first and second dimensions, respectively (Table 2-1). The shifts exhibited by wastewater chromatograms acquired using two different temperature programs were much larger, with mean retention time deviations of 18.75 and 0.98 tpw in the first and second dimensions, respectively (Table 2-1). For both oil spill and wastewater samples, retention time shifts were not systematic throughout each chromatogram. Some regions were much more prone to deformations than others, as indicated by the observed “spread” and maximum value statistics (Table 2-1).

Table 2-1. Statistics of retention time deviations^a of test points, before and after alignment, using different algorithms, in units of typical peak width (tpw)^b

		Mean		Median		Spread ^c		Maximum value	
		I	II	I	II	I	II	I	II
		weathered oil	Unaligned	0.19	0.17	0.03	0.10	0.27	0.19
2-D COW	0.19		0.19	0.00	0.03	0.36	0.40	4.33	1.80
Pierce et al.	0.13		0.11	0.05	0.04	0.19	0.17	1.33	2.14
Gros et al.	0.11		0.11	0.06	0.05	0.15	0.14	1.00	1.72
wastewater, same samples	Unaligned	18.75	0.98	18.50	0.89	10.65	0.71	34.00	2.83
	2-D COW	2.50	0.49	0.00	0.12	6.14	0.92	20.00	2.95
	Pierce et al.	2.89	1.33	1.80	1.11	4.06	1.18	14.00	3.55
	Gros et al.	0.75	0.48	0.75	0.24	0.95	0.57	4.00	1.63
wastewater, different samples	Unaligned	18.75	0.98	18.50	0.83	10.66	0.72	34.00	2.60
	2-D COW	5.28	0.71	3.25	0.18	6.80	1.08	20.00	3.18
	Pierce et al.	3.40	1.34	2.00	1.21	4.04	1.12	14.00	3.25
	Gros et al.	0.80	0.50	0.75	0.24	0.97	0.58	4.00	1.63

^a Values for first (I) and second (II) dimension are presented separately. In some cases of application of the 2-D COW and Pierce et al. codes, a peak was so distorted by alignment that it was no longer recognizable as a test point. These test points are not considered in the statistics above, except for the median statistic, in which case the value for the affected peak was considered as a very large number. Such distortions eliminated four points on oil spill chromatograms aligned using 2-D COW, three points on wastewater chromatograms aligned using the Pierce et al. code, and one point on a wastewater chromatogram aligned using 2-D COW. ^b A typical peak width (tpw) is equal to 37.5 s and 0.6 s in first and second dimension, respectively, for oil spill chromatograms, and to 15 s and 0.8 s in first and second dimension, respectively, for wastewater chromatograms. ^c The spread is defined as the square root of the variance of mean-subtracted retention time deviations.

2.4.2 Visual comparison of alignment results using different algorithms

The alignment algorithm proposed here was compared with the two other available alignment algorithms for whole two-dimensional chromatograms: 2-D COW developed by Zhang et al.⁷⁶ and the alignment algorithm developed by Pierce et al.⁶⁴ For oil spill samples, all chromatograms were aligned to the neat oil chromatogram, because the latter represents the native state of the spilled oil. On visual inspection, the Pierce et al.⁶⁴ algorithm produces slightly improved alignment of the target chromatograms and the reference chromatogram. The version of the code that we obtained also modifies the reference chromatogram, and for some chromatograms, this led to excessive and unrealistic distortions in the second dimension (Fig-

ure 2-4c,f and Appendix Figure 2-8c,f). Results obtained with 2-D COW were better for chromatograms that are highly similar to the reference chromatogram, but unrealistic distortions nonetheless appear in some regions where only a few compounds eluted (Appendix Figure 2-6c).

Additionally, when the target chromatogram contains peaks not present in the reference chromatogram, 2-D COW leads to unrealistic peak distortions (Appendix Figure 2-7c). Our algorithm avoids these artifactual distortions and visibly improves the alignment in every case, regardless of the degree of signal similarity of the samples (Appendix Figure 2-6b and Figure 2-7b). In other words, our algorithm is robust against composition differences between the reference and target chromatograms, assuming that at least some common analytes can be identified and employed as alignment points.

Similar conclusions are reached for the wastewater chromatograms (Figure 2-4 and Appendix Figure 2-8). Our code leads to significant improvement without apparent unrealistic distortions of peaks. 2-D COW gives good results when it is used to align together two chromatograms of the same sample (Appendix Figure 2-8e), but considerable artifacts arise when it is applied to aligning different samples analyzed with different temperature programs; some peaks of the aligned chromatograms exhibit zigzag-shaped deformations (Figure 2-4e, especially the peaks with peak tailing). The Pierce et al.⁶⁴ code behaves poorly by unrealistically modifying both peak shapes and positions, even when applied to alignment of two chromatograms of the same sample analyzed using different temperature programs (Figure 2-4c,f and Appendix Figure 2-8c,f).

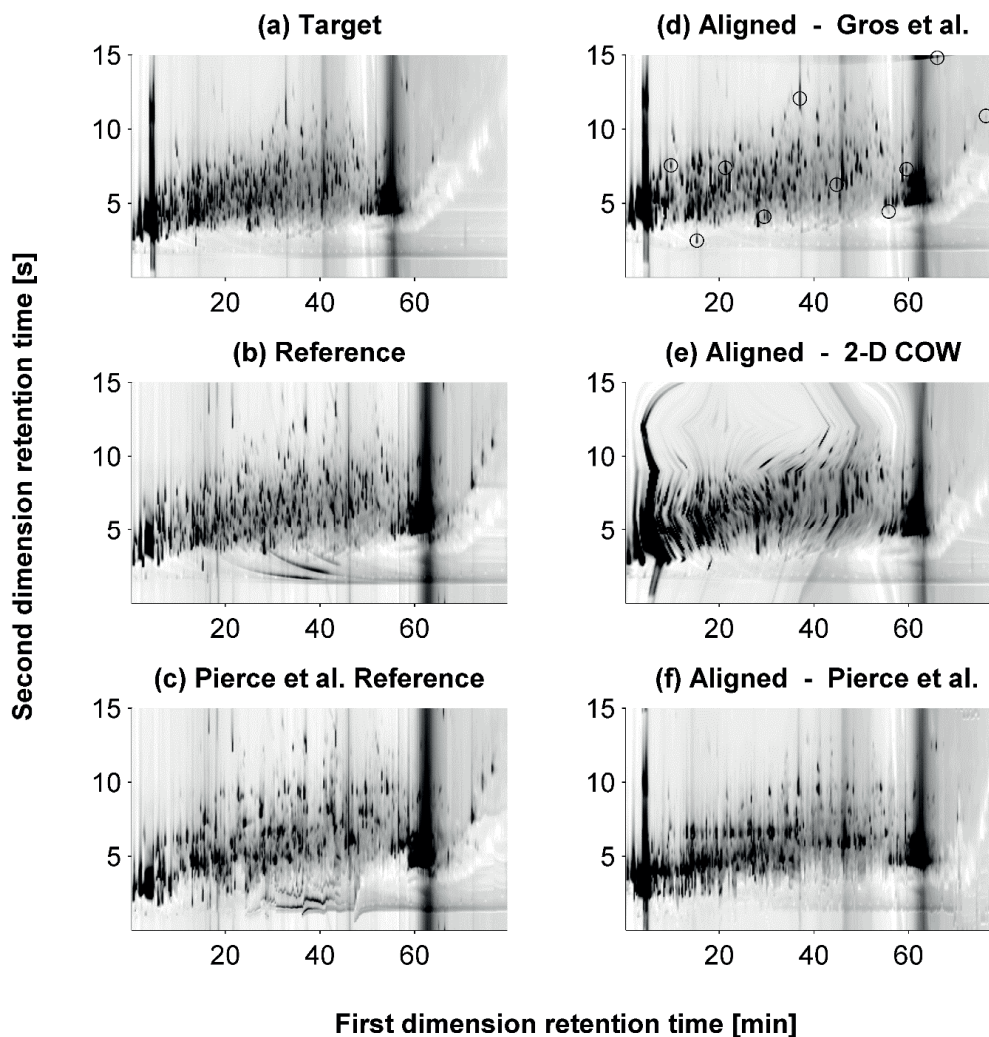


Figure 2-4. (a) The chromatogram of wastewater sample WW2B (target) is aligned to (b) the chromatogram of the sample WW1A (reference), which is a compositionally distinct sample analyzed using a different temperature program, or (c) to a modified version of this chromatogram for the Pierce et al. code. This leads to different results, depending on the alignment code used: (d) our code; (e) 2-D COW; (f) the Pierce et al. code. The ten black circles indicate the positions of the alignment points used with our algorithm.

2.4.3 Improvement in peak retention time deviations after alignment, using different algorithms.

In order to assess quantitatively the performance of the different alignment codes, we conducted several tests. In the first test, we measured the deviations of test points both before and after alignment. To evaluate our own code, we performed a leave-one-out test of the alignment points. In other words, for each chromatogram, we applied our alignment code using all alignment points except one, which we treated as a test point. We repeated this procedure, each time leaving out a different alignment point, until we had tested all alignment points. This reflects a conservative estimate of the performance of our code compared to what it actually achieves. To conduct comparable tests of the Pierce et al.⁶⁴ and 2-DCOW codes, we evaluated their abilities to properly align the set of points that we had used as alignment points. Although the data-withholding procedure applied to our code gives it a slight disadvantage, this approach enables a direct comparison of the three codes for the same set of test points (Table 2-1).

The new alignment code obtains the best global results. Our code successfully improves both first dimension deviations and second dimension deviations, on average, for both oil spill chromatograms and wastewater chromatograms (Table 2-1). By comparison, the Pierce et al. code worsens mean second dimension retention time shifts for both sets of wastewater chromatograms. 2-D COW improves the mean retention time deviation in both dimensions for wastewater chromatograms, but it does not significantly improve mean retention time deviation for oil spill chromatograms. As shown by the median retention time deviation (Table 2-1), 2-D COW is able to achieve good alignment for most of the test points in oil spill chromatograms. However, misalignments for some test points remain significant, as shown by the spread and maximum value statistics. Our code has higher median deviation values for oil spill chromatograms in comparison to the two other codes, but it is the most successful at limiting the most egregious shifts, as shown by low values for both the spread and maximum value statistics.

The code by Pierce et al.⁶⁴ sometimes suffers from inconsistent treatment of first and second dimension deviations: in cases where it brings improvement in the first dimension, it often worsens the situation in the second dimension. In such cases, peak shapes are badly distorted by alignment, leading to difficulties in identifying the peaks studied. 2-D COW works well for very similar chromatograms, but often performs poorly for samples having significant compositional differences, and this is frequently associated with distortions of the aligned chromatogram. By construction, our code avoids unrealistic distortion of the aligned chromatogram, and the test points are always easily identifiable.

In additional tests of our code, we evaluated the dependence of alignment quality on the number of alignment points used (section 2.7.7 in Appendix). For the samples considered here, the use of eight or more alignment points gave reliably improved alignments.

2.4.4 Improvement in quality of difference chromatograms after alignment, using different algorithms.

In a second quantitative test, we compared the evolution of the sum of the absolute values of the pixel intensities of the difference chromatograms. A “difference chromatogram” represents the difference, pixel by pixel, between two chromatograms (Appendix section 2.7.5).⁶⁵ In principle, chromatogram alignment should decrease the total sum of pixel absolute values of the difference chromatogram of the reference minus the target. This test gives greater weight to large-valued pixels. Therefore, we excluded column bleed and solvent signal, because this signal would obscure that of the relevant sample region. Using our algorithm, the sum of the absolute values of the pixel intensities of the difference chromatograms shows improvement for all samples except one (sample OS5) (Appendix Table 2-5). Of the three algorithms, ours results in the lowest absolute values for difference chromatograms, overall. 2-D COW obtains globally better results for the oil spill chromatograms; in principle this should correspond to the best alignment, in contradiction to results shown in Table 2-1. The apparent success of 2-D COW for difference chromatograms may result partly from unrealistic peak distortions which apparently maximize correlation and thereby also decrease the total signal of the corresponding difference chromatogram. The code of Pierce et al. did not give better global results than the other two codes for this test. Finally, in cases where samples are most dissimilar, our new code obtains favorable results compared to the other two.

2.4.5 Peak volumes alterations induced by alignment, using different algorithms.

In a third quantitative test of the alignment codes, we evaluated peak volumes bias arising from alignment. Ideally, the alignment should leave the peak volumes unchanged, so that the aligned chromatograms can be used in subsequent analysis without undue bias in chromatogram information. To conduct this test, we employed a peak-tracking code developed by Wardlaw et al. (2008)⁵⁵ as updated in a later work, which identifies matching peaks in different chromatograms, based on an analysis of the respective “blob tables” (i.e., tabulated lists of integrated peak retention times). The peak-tracking match criteria were parameterized very conservatively, so as to minimize or eliminate the possibility of wrongly assigned matches. We studied two oil spill samples: OS5 and OS8. For each sample, we used the peak-tracking code to identify peaks that could be matched in all four of the following chromatograms: the unaligned target chromatogram and the three aligned chromatograms obtained with the three alignment codes. Using this set of matched peaks, we computed peak volume changes induced by alignment, for each sample (Table 2-2). It was not possible to apply the peak tracking code to the severely shifted wastewater chromatograms; therefore, we evaluated peak volume changes observed in the 10 alignment points for the case of sample WW2B aligned to WW1A. Because integrated peak volumes are sensitive to the baseline delineation method, we decided to report results for chromatograms baseline-corrected using the relatively conservative delineation method of Reichenbach et al.⁷⁰ and also using a more aggressive delineation method developed by Eilers⁶⁸ that we extended to two-dimensional data by applying the one-dimensional code independently to each second dimension modulation

(Matlab codes freely available at: <https://github.com/jsarey/GCxGC-baseline-correction>).⁶⁹ As stated in section 1.3.1, the second method is more appropriate for the quantification of individual analytes.^{40,62,66} Peak footprint areas were delineated and integrated using the inverted watershed algorithm implemented in GC Image.^{71,101}

Among the three alignment codes, our code globally induced the smallest changes in integrated peak volumes (Table 2-2). Use of the Eilers baseline delineation, which we believe to be more appropriate for the quantification of peak volumes for individual analytes,^{40,62,66} usually leads to the smallest peak volume alterations, for our code. Our alignment code induced <11% average change in peak volume, except for OS8 aligned to neat oil with the baseline of Reichenbach et al. This peak volume bias is sufficiently small to allow further quantitative analysis of the data. By comparison, 2-D COW and the Pierce et al.⁶⁴ code both led to >19% average change in peak volume in 2/3 of the cases, which limits the usefulness of these aligned samples for further quantitative analysis. Unlike the other two algorithms, our code incorporates a correction for the local deformation applied during the reinterpolation step, and this limits the peak volume bias induced by alignment. Additional analysis of total chromatogram signal bias (Appendix section 2.7.9) further corroborated these results.

All three alignment procedures led to modest increases in the total number of apparent chromatogram peaks that were detectable using the GC Image¹⁰¹ peak delineation tool. Additional analysis revealed that all three alignment procedures also caused increases in the footprint area of delineated peaks, on average. We think these artifacts arise from the effective smoothing caused by signal reinterpolation during alignment. Subsequent changes in integrated peak volumes should thus depend on the way that the baseline is delineated. When used with our alignment method, the (more aggressive) Eilers baseline correction led to lower peak volume bias than did the (more conservative) Reichenbach baseline correction. To minimize peak volume bias caused by alignment, we recommend the use of our alignment procedure in combination with the baseline correction of Eilers.

Table 2-2. Peak volumes bias brought by alignment, for different codes

Sample name	Baseline Method (number of peaks) ^a	Alignment code	Mean absolute deviation ^b	Mean absolute percent deviation
OS5	GC Image (79 peaks)	Gros et al.	2.0	10.6%
		2-D COW	1.4	7.8%
		Pierce et al.	4.3	25.9%
	Eilers (208 peaks)	Gros et al.	0.6	2.1%
		2-D COW	1.1	10.9%
		Pierce et al.	4.8	30.7%
OS8	GC Image (34 peaks)	Gros et al.	4.2	33.7%
		2-D COW	2.3	25.1%
		Pierce et al.	7.9	41.9%
	Eilers (104 peaks)	Gros et al.	0.4	3.8%
		2-D COW	4.5	22.4%
		Pierce et al.	4.9	21.9%
WW2B aligned to WW1A	GC Image	Gros et al.	2.9	8.6%
		2-D COW ^c	8.0	28.8%
		Pierce et al. ^d	5.3	20.0%
	Eilers	Gros et al.	2.8	8.6%
		2-D COW ^c	10.5	29.0%
		Pierce et al. ^d	5.0	19.9%

^a Shown in parentheses is the number of peaks that were successfully matched across all four alignment cases: unaligned, using our algorithm, 2-D COW, and Pierce et al.⁶⁴ ^b Values given in arbitrary units. ^c One alignment point not detected by GC Image, statistics computed with the 9 remaining values. ^d One alignment point not recognizable, statistics computed with the 9 remaining values.

2.5 Conclusions

We present a new alignment algorithm for 2-D chromatograms. In this study, the algorithm is applied to real samples analyzed using GC×GC, but in principle it could also be applied to other types of 2-D chromatograms (e.g. LC×LC). In comparison to other available algorithms, our algorithm performs the best overall in terms of decreased retention time deviations of matching analytes. Additionally, the new alignment algorithm performs better than the two previously published algorithms according to three more criteria: it is insensitive to differences in composition between the target and reference chromatograms; it avoids unrealistic distortions of the aligned chromatograms; and it leads to only limited modification of the peak volumes. This makes it particularly suited for the study of samples showing important differences in composition. Moreover, our tests with wastewater chromatograms demonstrate the usefulness of our algorithm for aligning chromatograms acquired under different chromatographic conditions. The algorithm modifies only the target chromatogram, perfectly aligns designated alignment points, and uses displacement interpolation for aligning the other pixels, thereby avoiding distortion artifacts which arise with the other two algorithms. Unlike previous algorithms, we apply a correction of pixel intensity values to account for the applied alignment deformation, and this limits the extent of modification of peak volumes induced by

alignment. This enables further quantitative analysis to be applied to aligned chromatograms, whereas previously developed algorithms result in large peak volumes bias in certain cases. Although not discussed in this article, our algorithm can also be applied directly to the alignment of peak tables, comparable to a previously developed method.¹⁰²

Unlike the other two algorithms considered, our algorithm requires the *a priori* knowledge of alignment points. This may be viewed as a limitation. However, user-assigned alignment points confer important advantages in terms of flexibility and control, compared to the other two codes. Our code enables the user to choose appropriate points leading to proper alignment of two chromatograms, whereas the previous two codes determine points considered similar in an automated way. The previously developed codes thus leave the user blind to occasional false assignments of corresponding information between chromatograms. This leads to inferior performance of the previous codes compared to our algorithm, despite that our approach employs significantly less alignment information.

How can the user ensure that alignment points are properly assigned? In cases where sample compositions are similar or where retention time shifts are small, matching peak positions are often identifiable by visual inspection, because peak patterns remain similar.¹⁰³ This depends partly on the user's familiarity with the samples' compositions. If in doubt, a user could also add or ascertain alignment points using added internal standards. To help support the identification of alignment points, we developed a tool which proposes matches of alignment point positions in the target chromatograms based on their positions in the reference chromatogram (see section 2.3.3).

The algorithm presented here is systematically improvable. Alignment points are intuitive to use, and the improvement of the alignment is straightforwardly achievable by changing the number and positions of alignment points. We recommend that alignment points are chosen in each part of the chromatogram that exhibits shifting trends different from neighboring regions and that the most interesting sample information of the chromatogram is situated within the convex hull of the alignment points retained. The use of 8 to 10 well-distributed alignment points appears sufficient to produce reliable improvements in alignment. In cases where the choice of reference sample is not dictated by the study aim, the reference chromatogram should be selected as that which contains the largest number of well-distributed analytes employable as alignment points. Finally, we note that the positions of peaks can be altered for severely overloaded peaks; we advise to avoid such peaks in the set of alignment points.

In practice, the algorithm could be applied to large sample sets. Once alignment points have been assigned in a reference chromatogram, an experienced practitioner typically can locate alignment points and perform alignment of a target chromatogram in 15 min or less, using a typical desktop computer.

The new algorithm is expected to increase the possibilities available for scientists to use more deeply and quantitatively the information contained in two-dimensional chromatograms. The alignment algorithm is used in Chapter 3 and in Chapter 6. Upon request, our Matlab codes

have been shared with several scientific teams, and these codes have also been used by colleagues at EPFL (Saer Samanipour and Bobby Hamwey). We have been actively collaborating with Yasuyuki Zushi and Shunji Hashimoto to extend the algorithm to multivariate detectors (mass spectrum data). The algorithm described here together with the extended algorithm for MS data (the latter being currently not deeply validated) have been implemented as a plug-in into one of the leading softwares for GC×GC data handling, GC Image.

2.6 Acknowledgment

We thank Dabao Zhang, Robert E. Synovec and Jeremy S. Nadeau for sharing their respective alignment algorithms with us, as well as Qingping Tao and Stephen E. Reichenbach at GC Image for technical support. We are also grateful to Paul H. C. Eilers for allowing free access to his baseline correction code. We acknowledge Jan van der Meer (UNIL), Corina Brussaard (NIOZ), Sjon Huisman (Dutch Rijkswaterstaat) and the crew of the R/V *Arca* for their organization of the North Sea expedition during which our oil samples were taken. We also thank Dustin Baum for valuable comments on the manuscript.

2.7 Appendix

2.7.1 GC×GC analysis methods

Three different GC×GC analysis methods were used. Methods A and B were applied to wastewater samples, and method C was applied to oil spill samples. Samples analyzed with method A are referred to as WW1A and WW2A, whereas samples analyzed with method B are referred to as WW1B and WW2B. The GC×GC analysis methods are described in Table 2-3 below. All chromatography measurements were performed on a Leco GC×GC instrument comprising: an Agilent 7890A chromatograph with a split/splitless autoinjector; a Leco quadruple-jet, dual-stage thermal modulator; and a Leco secondary oven. Descriptions of the samples are given in Table 2-4.

Table 2-3. Description of GC×GC methods

Parameter	Value / material used	Method
Detector	Agilent micro-electron capture detector (μ ECD)	A, B
	Flame ionization detector (FID)	C
First-dimension column inside the main oven	Restek Rxi-1ms column: 100% dimethyl polysiloxane phase, 30 m length, 0.25 mm inner diameter, 0.25 μ m film thickness	A, B
	Restek Rtx-1, 6.6 m length, 0.1 mm inner diameter, 0.4 μ m film thickness	C
Second-dimension column inside the secondary oven: SGE BPX50 (50% Phenyl Polysilphenylene-siloxane) 0.10-mm-inner diameter, 0.10- μ m film thickness	1.8 m length	A, B
	0.70 m length	C
Modulation	Modulation was done on the initial part of secondary column	A, B
	Modulation was done on 0.17 m length, 0.10 mm inner diameter Restek IP Deactivated Guard Column	C
Deactivated column joining the second-dimension column to the detector: Restek IP Deactivated Guard Column, 0.10-mm-inner diameter	0.3 m length	A, B
	0.21 m length	C
Sample injections	Splitless mode at an inlet temperature of 260 °C	A, B
	Split/splitless mode (see Table 2-4 for details) at an inlet temperature of 300 °C	C
Carrier gas (helium) at a constant flow rate	1.5 mL/min	A, B
	1 mL/min	C
Thermal modulator	Dry nitrogen gas, chilled by liquid nitrogen, for the cold jets, and dry air for the hot jets	A, B, C
Temperature of the modulator	25 °C higher than that of the main oven	A, B
	50 °C higher than that of the main oven	C
Modulation period	15 s, comprising two hot pulse periods of 1.0 s each and two cool periods of 6.5 s each	A, B
	12.5 s, comprising two hot pulse periods of 0.6 s each and two cool periods of 5.65 s each	C
Detector temperature	350 °C	A, B, C
Detector rate	50 Hz	A, B
	200 Hz	C
Main oven temperature	40 °C for 2 minutes, then ramped at 3.5 °C/min to 300 °C, whence it was maintained for 10 minutes	A
	40 °C for 2 minutes, then ramped at 4.0 °C/min to 300 °C, whence it was maintained for 19.3 minutes	B
	37 °C for 5 minutes, then ramped up to 307 °C at 1.5 °C/min, whence it was maintained for 30 minutes	C
Second oven temperature	Kept 15 °C higher than that of the main oven throughout a run	A, B
	Kept 33 °C higher than that of the main oven throughout a run	C
Data acquisition delay	400 s	A, B
	210 s	C

Table 2-4. Description of samples

Sample name	Sample description	GC×GC Injection mode	GC×GC analysis method
OS0	Neat oil	Splitless	C
OS1	Oil blob	Split ratio: 1:25	C
OS2	Oil blob	Split ratio: 1:25	C
OS3	Tarball + Water	Splitless	C
OS4	Tarballs	Split ratio: 1:25	C
OS5	Tarballs	Split ratio: 1:25	C
OS6	Tarballs	Split ratio: 1:25	C
OS7	Sheen + water	Splitless	C
OS8	Sheen on glass wool	Splitless	C
OS9	Sheen on glass wool	Splitless	C
OS10	Sheen on glass wool	Splitless	C
OS11	Sheen on glass wool	Splitless	C
WW1	Inlet of the WWTP	Splitless	A (WW1A), B (WW1B)
WW2	Outlet of the primary clarifiers of the WWTP	Splitless	A (WW2A), B (WW2B)

2.7.2 Weighted average used in Sibson's natural-neighbor interpolation

We define S the subset of m alignment points P corresponding to basis polygons which contribute some area to the new polygon introduced in the Voronoi diagram defined by $\{P_1, \dots, P_N, z\}$. In the example shown in Figure 2-2, $S = \{P_1, P_2, P_3, P_4\}$.

The weighted average used by Sibson's natural neighbor interpolation is then computed according to:

$$D(z) = \frac{\sum_{j=1}^m A_j \cdot D(S_j)}{\sum_{j=1}^m A_j}$$

Equation 2-3

where D refers to second dimension shifts, z is the pixel for which the interpolated second dimension shift (or displacement) is calculated, and A_j is the area contribution to the new polygon by the basis polygon corresponding to the alignment point S_j .

2.7.3 Bicubic convolution interpolation

Bicubic convolution interpolation is used in order to determine the new signal value of a displaced pixel in the aligned chromatogram. The signal value of the displaced pixel (in the aligned chromatogram) is determined based on the signal values of the sixteen pixels (in the unaligned target chromatogram) nearest to the estimated position of that pixel before alignment. The bicubic convolution interpolation, introduced by Keys,⁹⁸ is a third-order approximation of the unknown function f of the data.

For a 1-D case, the interpolating function is expressed as:

$$g(x_j) = \sum_k c_k u(j-k)$$

Equation 2-4

where the c_k are the data point values, k takes the values of the indices of the data points used for interpolation, j is the index of the location at which an interpolated value is desired, and $u(s)$ is the interpolation kernel, defined as:

$$u(s) = \begin{cases} \frac{3}{2}|s|^3 - \frac{5}{2}|s|^2 + 1 & 0 < |s| < 1 \\ -\frac{1}{2}|s|^3 + \frac{5}{2}|s|^2 - 4|s| + 2 & 1 < |s| < 2 \\ 0 & 2 < |s| \end{cases}$$

Equation 2-5

Two-dimensional interpolation is achieved by performing one-dimensional interpolation in each dimension.

2.7.4 Alignment points used for each chromatogram

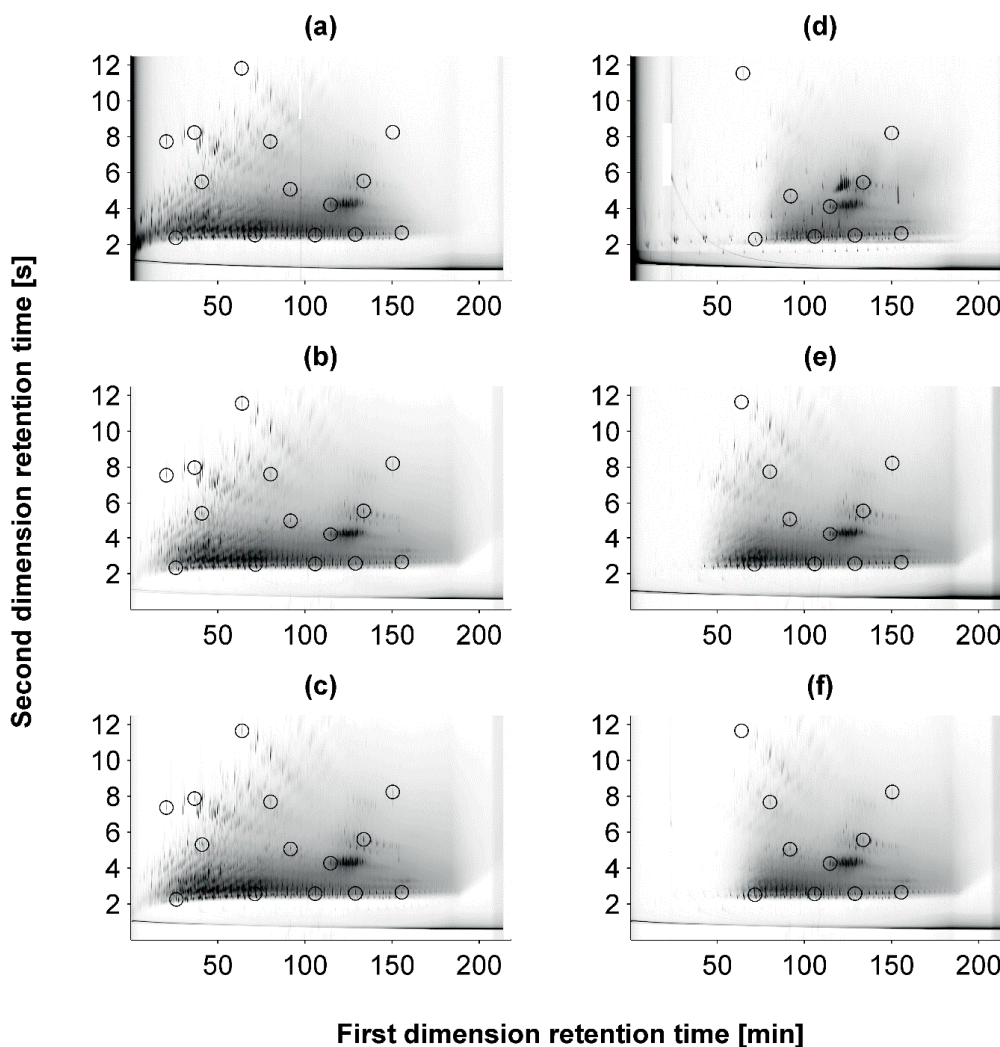


Figure 2-5. Chromatograms showing the positions of alignment points. These are also the test points used to evaluate the extent of misalignment of target chromatograms both prior to alignment and after alignment, for all algorithms. In order to evaluate misalignments after application of the algorithm reported here, a leave-one-out test of alignment points was performed, as described in the main text. The panels show chromatograms for (a) neat oil (OS0), (b) OS1, (c) OS2, (d) OS3, (e) OS4, (f) OS5, (g) OS6, (h) OS7, (i) OS8, (j) OS9, (k) OS10, (l) OS11, (m) WW2A (reference), (n) WW1A (reference), (o) WW2B (target), (p) WW1B (target).

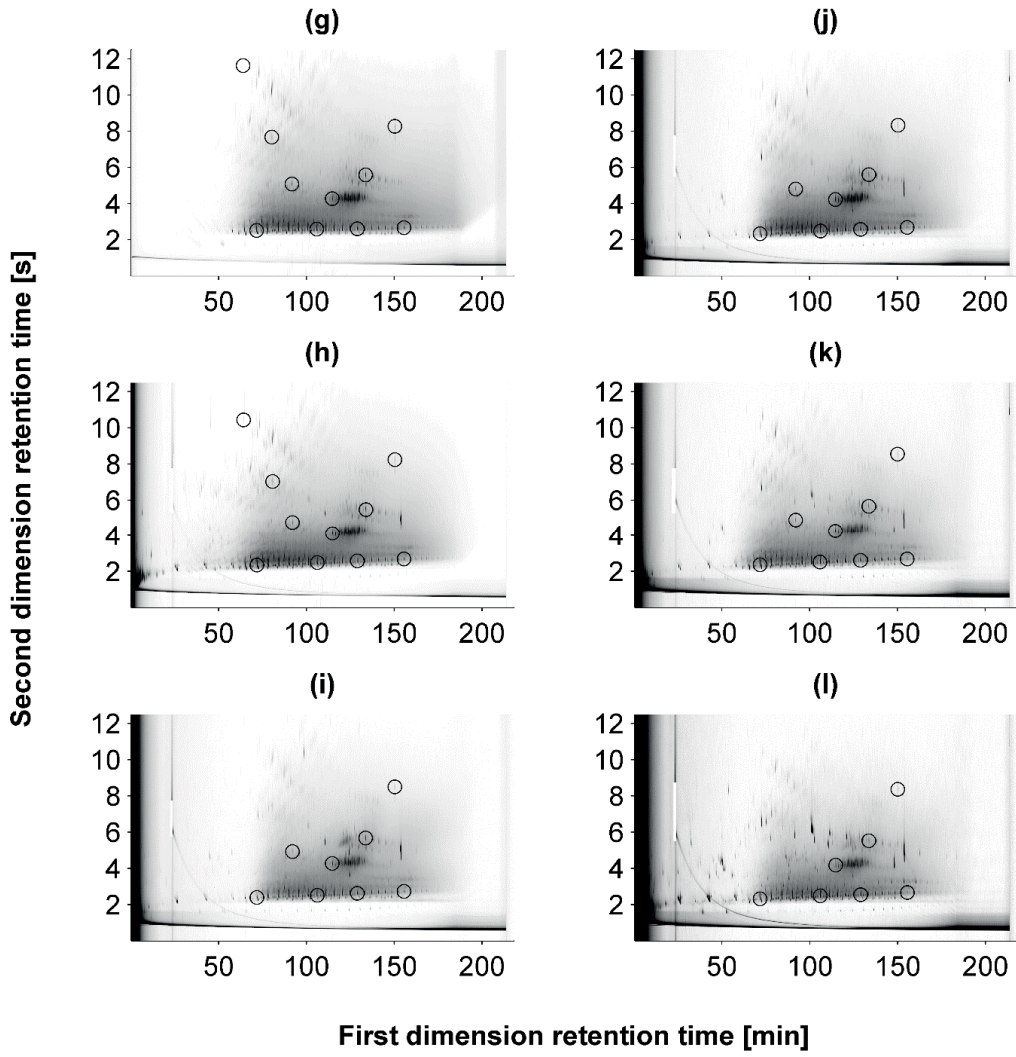


Figure 2-5 (continued)

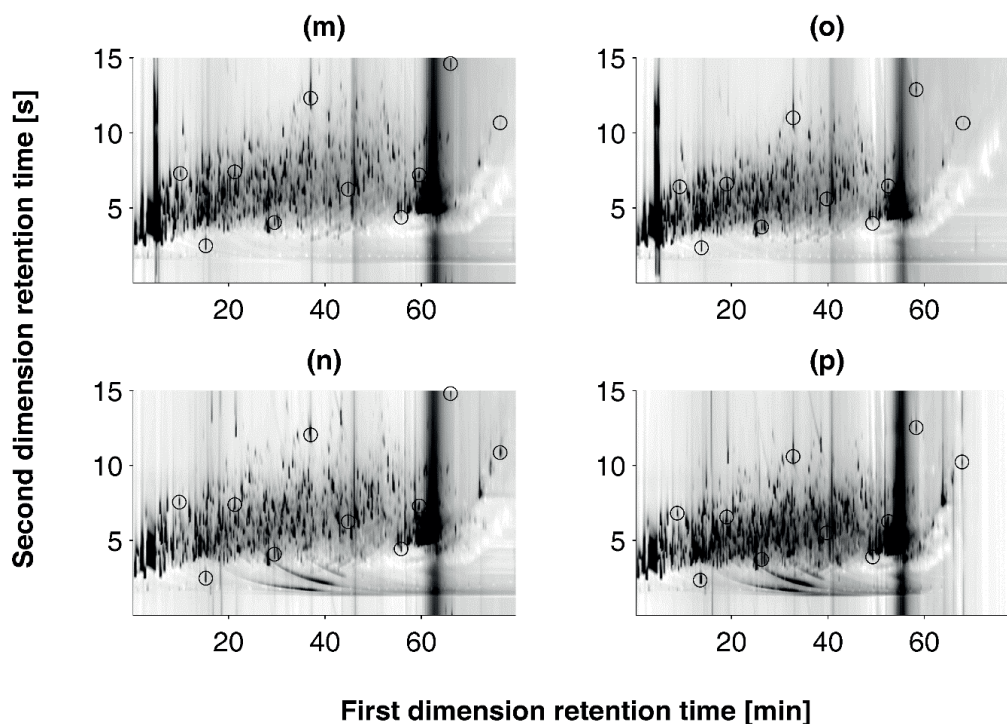


Figure 2-5 (continued)

2.7.5 Visual comparison of difference chromatograms, after alignment

Difference chromatograms are depicted for: neat oil minus a sample of slightly weathered oil from the oil slick (Figure 2-6); and for neat oil minus a highly weathered oil sheen sample (Figure 2-7). Difference chromatograms were introduced by Nelson et al.⁶⁵ and consist of the difference, pixel by pixel, between two chromatograms. A white color signifies that the intensity value of the pixel is the same in both chromatograms, whereas a red (blue) color indicates a larger (smaller) value in the weathered chromatogram relative to the neat oil. Thus, misaligned peaks in the real chromatograms appear as two neighboring peaks in the difference chromatogram, one red and the other blue.

Although sample OS2 exhibits a composition similar to that of the neat oil, the corresponding difference chromatogram shows significant signal of early analytes (those eluting between 20 and 70 minutes), indicating misalignment in this region (Figure 2-6a). Our alignment code and 2-D COW both effectively improve the alignment in this part of the difference chromatogram (Figure 2-6b,c) whereas the Pierce et al. code performs less well (Figure 2-6d).

The composition of sample OS11 differs significantly from that of the neat oil, thus the corresponding difference chromatogram would necessarily exhibit significant signal even in a perfectly aligned case. Our code and the code of Pierce et al. show improved difference chromatograms compared to that of the unaligned samples (Figure 2-7a,b,d). Alignment using

2-D COW leads to artifactual distortions of the target (OS11) and this appears as unrealistic zigzag distortions in the difference chromatogram (Figure 2-7c).

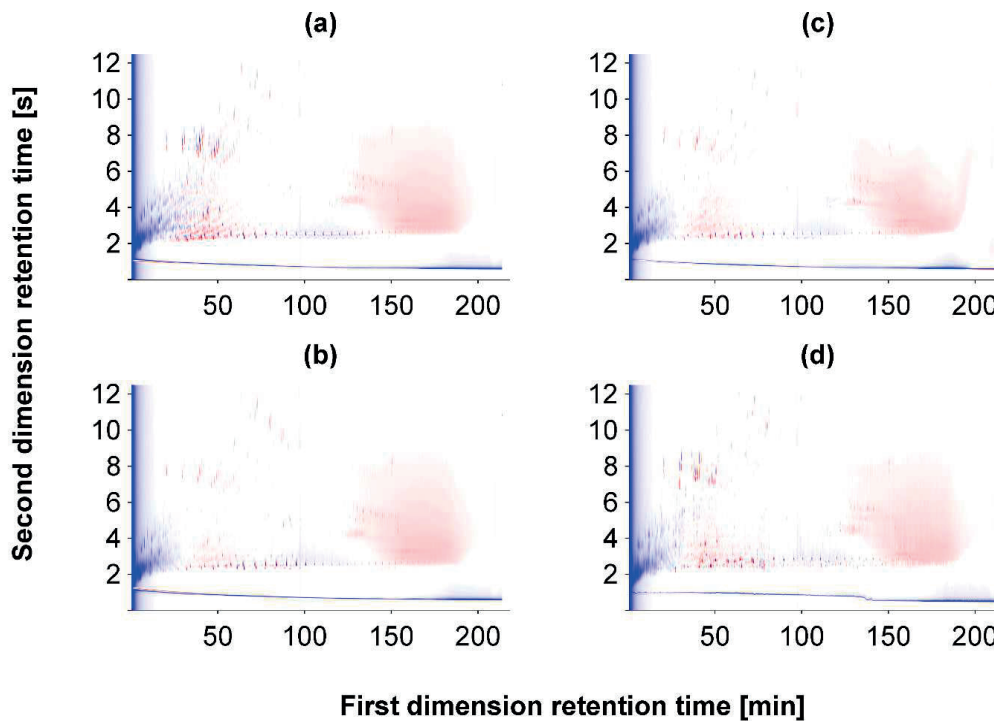


Figure 2-6. Difference chromatograms between neat oil (reference) and sample OS2 (target), a slightly weathered slick sample, for four cases: (a) the target chromatogram unaligned, (b) the target chromatogram aligned using our code, (c) the target chromatogram aligned using 2-D COW, and (d) the reference and target chromatograms aligned using the Pierce et al. code.

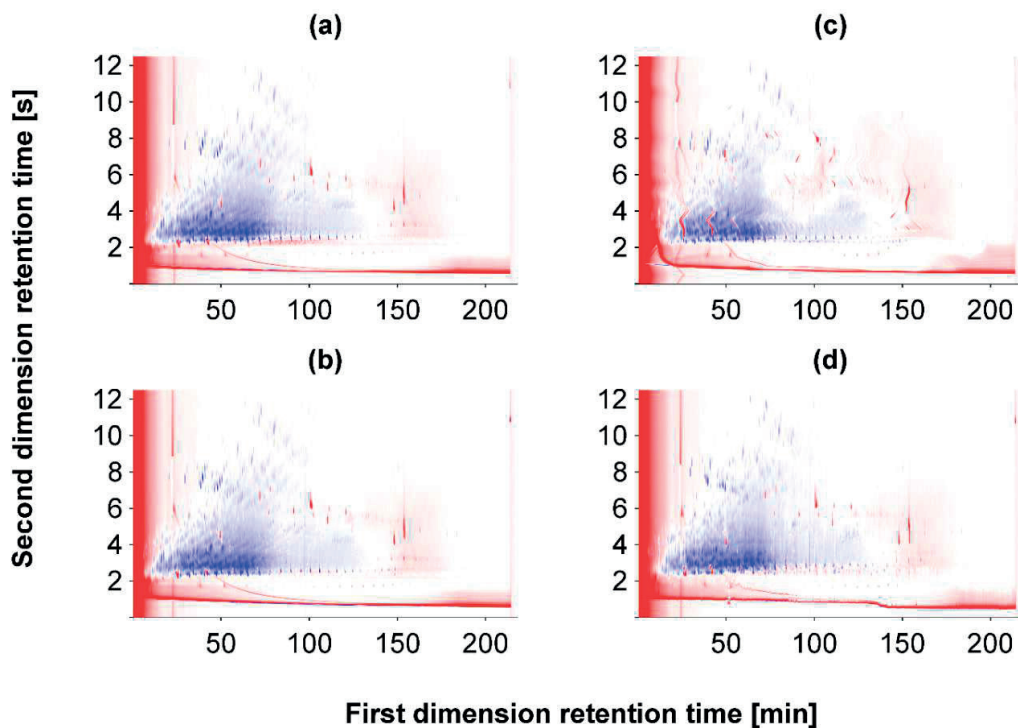


Figure 2-7. Difference chromatograms between neat oil (reference) and the oil sheen sample OS11 (target). Four cases are shown: (a) the target chromatogram unaligned, (b) the target chromatogram aligned using our code, (c) the target chromatogram aligned using 2-D COW, and (d) the reference and target chromatogram aligned using the Pierce et al. code.

2.7.6 Visual comparison of alignment results for chromatograms resulting from the analysis of the same wastewater sample with different temperature programs

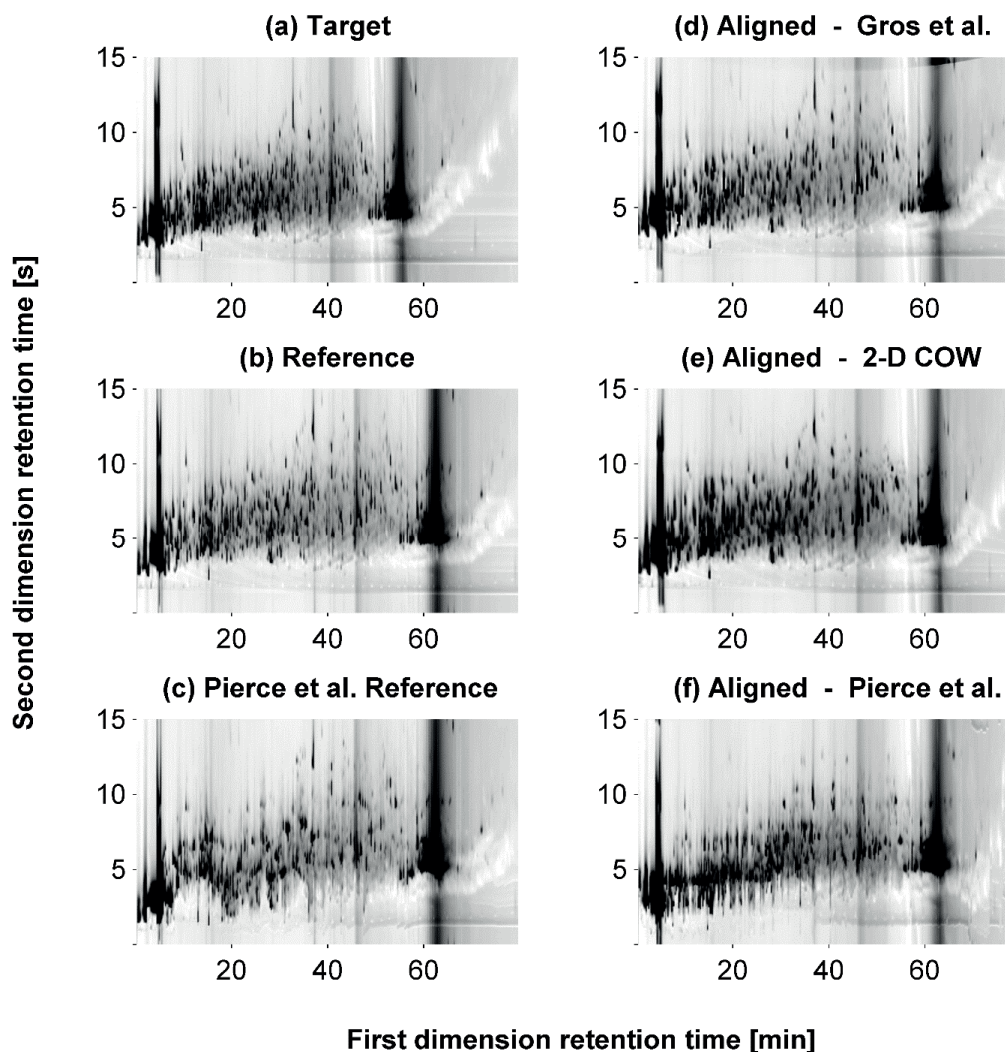


Figure 2-8. (a) The chromatogram of wastewater sample WW2B (target) is aligned to (b) the chromatogram of the sample WW2A (reference), which is the same sample analyzed using a different temperature program, or (c) to a modified version of this chromatogram for the Pierce et al. code. This leads to different results, depending on the alignment code used: (d) our code; (e) 2-D COW; (f) the Pierce et al. code.

2.7.7 Dependence of alignment quality on the number of alignment points used

In order to evaluate the influence of the number of alignment points on the quality of alignment, we computed retention time deviations in the second dimension using different numbers of alignment points. For each chromatogram containing up to N possible alignment

points (as shown in Figure 2-5), we report alignment results ranging from the use of 0 alignment points (i.e. unaligned) to up to $N-1$ alignment points. For each subset of n alignment points, the superset of all N alignment points was evaluated as test points. This was achieved by successively assigning each (superset) alignment point as a test point, and then conducting an alignment employing the “optimal subset” of n points from the remaining $N-1$ alignment points. The optimal subset was defined as the set of n points chosen from the $N-1$ points which maximize the sum of the distances between each subset alignment point and the nearest subset alignment point. For the case where only one alignment point was used in the subset ($n = 1$), we decided to always employ the alignment point nearest to the first moment (center of mass) of the available ($N-1$) alignment points. For each subset of n alignment points, the retention time deviations for all N test points were averaged; results are shown in Figure 2-9 (oil spill chromatograms) and Figure 2-10 (wastewater chromatograms).

Results for oil spill chromatograms show that alignment quality is systematically improved when 7 or more alignment points are used. For these chromatograms, using a low number (1 to 5) of alignment points leads to the possibility of worsened alignment. It remains unclear whether alignment quality would be further improved if more than 13 alignment points would be used. Wastewater chromatograms, which suffer much more severe initial misalignment, exhibit consistently improved alignment regardless of the number of alignment points used. Overall, our results suggest that using 8 or more alignment points likely leads to robust alignment.

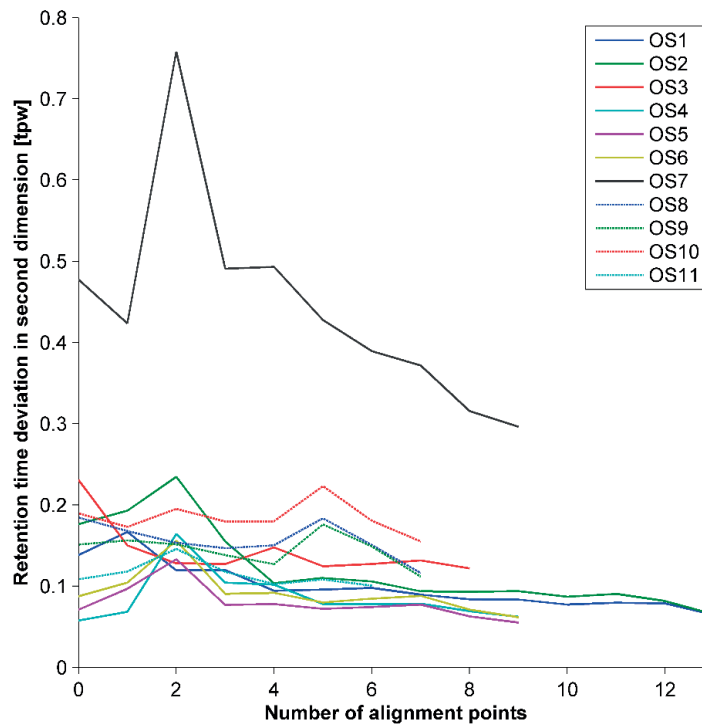


Figure 2-9. Second dimension retention time deviation with respect to the number of alignment points used, for oil spill chromatograms.

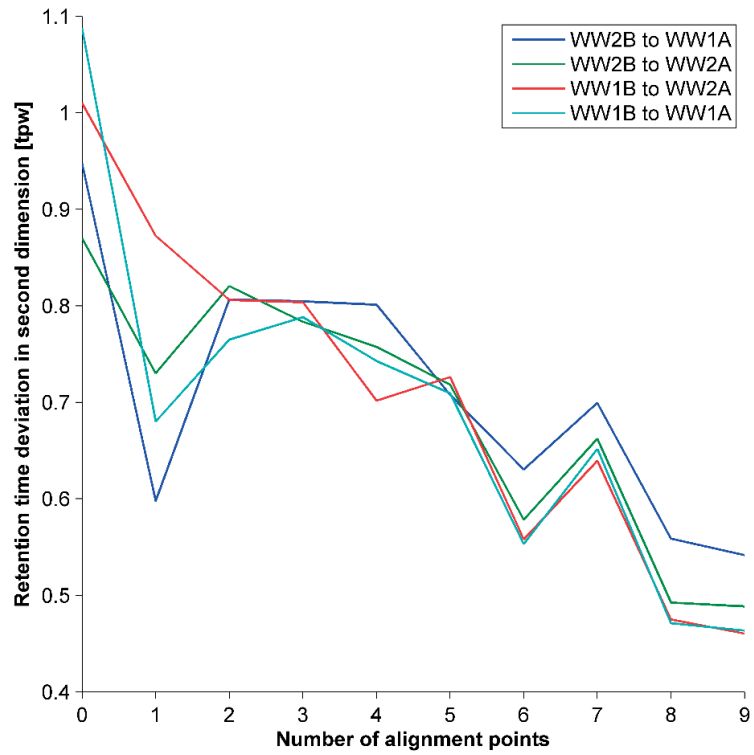


Figure 2-10. Second dimension retention time deviation with respect to the number of alignment points used, for wastewater chromatograms.

2.7.8 Sums of the absolute values of the pixels of the difference chromatograms, after alignment

Table 2-5. Sums of the absolute values of the pixels of the difference chromatograms ^a

Type		Sample name	Un-aligned	Gros et al.	2-D COW	Pierce et al.
oil spill	slick	OS1	1000	947	835	943
		OS2	1000	879	796	878
		OS3	1000	962	923	961
		OS4	1000	996	1003	994
		OS5	1000	1007	946	1006
	sheen	OS6	1000	994	917	994
		OS7	1000	914	796	915
		OS8	1000	965	890	963
		OS9	1000	948	909	946
		OS10	1000	944	996	941
		OS11	1000	938	1035	933
	total		11,000	10,495	10,045	10,476
wastewater	same samples ^b	WW1B	1000	541	472	677
		WW2B	1000	466	481	749
	different samples ^c	WW1B	1000	639	1034	784
		WW2B	1000	712	877	888
		total		4,000	2,359	2,864
overall total			15,000	12,854	12,908	13,574

^a Normalized to a value of 1000 for the unaligned chromatogram. ^b Each chromatogram was aligned to a chromatogram of the same sample analyzed using a different GC×GC program. ^c The chromatogram was aligned to the chromatogram of the other sample, each analyzed using a different GC×GC program.

2.7.9 Changes in total chromatogram signal resulting from alignment

In addition to the peak volumes bias evaluation reported in the main text, we present here total signal volume alteration, i.e. the variation of the total sum of the signal values of all the pixels of the chromatograms, excluding column bleed or solvent signal (Table 2-6). 2-D COW leads to the greatest bias, up to 24.5% for oil spill sheen chromatograms and up to 49.3% for wastewater chromatograms. Signal volume bias from the Pierce et al. code is significantly better than that of 2-D COW. However, for wastewater chromatograms, which are significantly modified through alignment, the bias brought by the Pierce et al. alignment code becomes excessive for one case (29.1%). Overall, our code produces the least signal volume bias, with 0.4% total signal change, on average, for oil spill chromatograms and 3.7%, on average, for wastewater chromatograms. The signal modification brought by the new code always remains below 6%, which makes it suited for further quantitative analysis of the data.

Table 2-6. Total chromatogram signal volume bias ^a induced by alignment

Type		Sample name	Gros et al.	2-D COW	Pierce et al.
oil spill	slick	OS1	-0.02%	-1.65%	-1.04%
		OS2	-0.02%	-1.60%	-1.16%
		OS3	-0.62%	7.13%	-2.42%
		OS4	-0.01%	2.66%	-0.96%
		OS5	-0.03%	-2.23%	-1.41%
	sheen	OS6	-0.05%	-4.34%	-1.76%
		OS7	-0.44%	1.92%	-2.54%
		OS8	-0.68%	6.64%	-1.83%
		OS9	-0.57%	8.58%	-0.12%
		OS10	-0.73%	15.17%	-1.65%
		OS11	-1.14%	24.51%	0.55%
	average of absolute values	0.39%	6.95%	1.40%	
wastewater	same samples	WW1B	-1.70%	22.00%	0.15%
		WW2B	-5.18%	15.24%	5.04%
	different samples	WW1B	-1.49%	49.34%	5.96%
		WW2B	-5.61%	20.02%	29.14%
	average of absolute values	3.50%	26.65%	10.07%	

^a Negative values indicate a global “signal disappearance” induced by alignment, and positive values indicate a global “signal creation”. All values were computed as the percentage change in the total sum of the pixels of the aligned chromatogram relative to the target chromatogram. Signal arising from column bleed and solvent were excluded from the above analysis. Chromatograms were baseline-corrected using the method of Reichenbach et al.⁷⁰

Chapter 3 First day of an oil spill on the open sea: Early mass transfers of hydrocarbons to air and water

Published in: Environmental Science & Technology 2014, 48, 9400–9411
(<http://pubs.acs.org/doi/abs/10.1021/es502437e>).

Authors: Jonas Gros, Deedar Nabi, Birgit Würz, Lukas Y. Wick, Corina P. D. Brussaard, Johannes Huisman, Jan R. van der Meer, Christopher M. Reddy, and J. Samuel Arey.

Contributions: This chapter was prepared principally by me. I wrote the Matlab codes for the transport model. Deedar Nabi and Samuel Arey participated in the North Sea experiment during which oil spill samples were collected. Deedar Nabi performed extraction and GC×GC analysis of oil spill samples. The GC–MS analysis work was performed by Birgit and Lukas. Samuel Arey provided guidance in the original development of the study, participated in the conceptual development of the model, and had a prominent participation in text writing and editing.

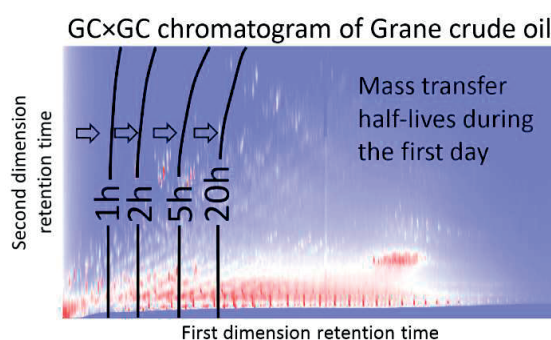


Figure 3-1. Schematic summary of the losses predicted by our transport model.

Reproduced/adapted with permission from Environmental Science & Technology 2014, 48, 9400–9411. Copyright 2014 American Chemical Society.

3.1 Abstract

During the first hours after release of petroleum at sea surface, crude oil hydrocarbons partition rapidly into air and water. However limited information is available about very early evaporation and dissolution processes. We report on the composition of the oil slick during the first day after a permitted, unrestrained 4.3 m³ oil release conducted on the North Sea. Rapid mass transfers of volatile and soluble hydrocarbons were observed, with >50% of $\leq C_{17}$ hydrocarbons disappearing within 25 hours from this oil slick of <10 km² area and <10 μ m thickness. For oil sheen, >50% losses of $\leq C_{16}$ hydrocarbons were observed after 1 hour. We developed a mass transfer model to describe the evolution of oil slick chemical composition and water column hydrocarbon concentrations. The model was parameterized based on environmental conditions and hydrocarbon partitioning properties estimated from comprehensive two-dimensional gas chromatography (GC \times GC) retention data. The model correctly predicted the observed fractionation of petroleum hydrocarbons in the oil slick resulting from evaporation and dissolution. This is the first report on the broad-spectrum compositional changes in oil during the first day of a spill at the sea surface. Expected outcomes under other environmental conditions are discussed, as well as comparisons to other models.

3.2 Introduction

After an oil spill at the sea surface, many petroleum hydrocarbon compounds fractionate rapidly into the atmosphere and water column.⁷ The early behavior of oil spilt at sea thus controls the initial exposures of marine organisms to oil components: high concentrations of dissolved aromatic hydrocarbons in the water underlying oil slicks are considered especially likely during the first hours and days after a spill.^{13,104,105}

However compositional data describing early evaporation and dissolution processes in the field are limited. Environmental sampling does not begin until several days after an accidental sea-surface oil spill, because logistical challenges preclude early sampling of an unanticipated release. Data describing early fractionations have been reported for long-lasting releases resulting from offshore oil well blowouts^{8,37,106,107} and natural sea floor oil seeps.⁵⁵ However oil and gas hydrocarbons emitted from the deep sea floor experience prolonged exposure to the water column before reaching the atmosphere at the sea surface. Consequently a sea floor release likely undergoes a much greater extent of dissolution compared to a sea surface release. Some experimental data relevant to sea surface releases have been obtained through meso-scale laboratory experiments.^{108,109} Additionally, several controlled oil release experiments of up to 100 metric tons have been conducted at sea (off Norway, the United States, Canada, the United Kingdom, and the Netherlands), as early as 1930.^{13,43,110–134} Among these, several studied early evaporation of the slick and/or dispersion/dissolution into the underlying water column,^{13,111,114,116,120–124,126,127,129,134} using techniques including: evaluation of distillation data for collected oil slick samples; gas chromatography (GC) analysis of slick and water column samples; and in-situ fluorimetry, light-scattering, and radioactive tracer tracking of the water column. These field data were used for the development and validation of oil spill models such as the OSCAR model, developed by SINTEF, and its oil weathering model (OWM) component.^{112,124,128,130,135} However limited data are available describing the concentrations

of individual hydrocarbons, except a few reports of trends for *n*-alkanes in oil slicks during the initial hours after the release.^{13,114,122}

After the release of oil on the sea, several physical processes simultaneously modify oil composition and properties, including evaporation, aqueous dissolution, sorption, emulsification, and dispersion.⁷ Evaporation usually dominates the early fractionation of petroleum compounds after a spill, typically affecting compounds with boiling points lower than *n*-pentadecane (*n*-C₁₅).¹¹ Evaporation can remove up to 75% of the oil volume within a few days for light crude oils, up to 40% for medium crude oils, and about 5% for heavy or residual oils.¹² Under turbulent sea surface conditions, some oils rapidly form water-in-oil emulsions, and this is expected to decrease mass transfer rates.^{11,136,137} In this chapter the term *mass transfer* has units of mass; the terms *mass transfer rate* or *mass loss rate* have units of mass time⁻¹; and *mass transfer flux* has units of mass time⁻¹ area⁻¹.

Compared to evaporation, aqueous dissolution removes less mass from the oil phase during early weathering of a sea-surface oil slick.^{13–16} However dissolution is important in terms of aquatic ecotoxicological impact, because several individual soluble hydrocarbon compounds as well as hydrocarbon mixtures are toxic to aquatic species.^{7,17–20} For example, total polycyclic aromatic hydrocarbons (PAHs) levels of up to 115 and 42 µg L⁻¹ were detected in the water column a few days to months after the *North Cape* and *Exxon Valdez* oil spills, respectively.^{24,138} Higher concentrations of total PAHs of up to 100 mg L⁻¹ were recorded in the water column during the *Deepwater Horizon* oil spill,¹⁰⁷ where ascending liquid petroleum and gas were subjected to prolonged exposure to the water column before having the opportunity to ventilate into the atmosphere.⁷⁵

It is challenging to apportion mass transfers of hydrocarbons resulting from evaporation and dissolution out of the oil phase, because both processes act simultaneously on many of the same compounds.¹⁵ Different models have been developed to predict the evaporation and dissolution of hydrocarbons at sea.^{12–16,25,41,42,74,112,139–151} Several of these models consider oil as a single component,^{139–141} unable to capture the independent behaviors of the thousands of compounds that constitute oils.¹⁵² However models applicable to the partitioning behavior of individual compounds or to pseudo-components have also been developed.^{13,14,25,41,42,74,112,142–151} Additionally, some models consider dispersion, or entrainment of oil into the water column, plus oil dissolution and evaporation.^{25,41,112,113,147,153} The processes of evaporation and dispersion have received more extensive field testing,^{112,113,116,118,121–123,126,129,134} whereas dissolution has received less evaluation in the field.¹¹⁰

Two field studies have evaluated compound-by-compound modeling of evaporation and dissolution for a broad range of petroleum hydrocarbon compounds in beached oils.^{14,74} In both studies, comprehensive two-dimensional gas chromatography (GC×GC) retention information was used to estimate the vapor pressures and aqueous solubilities of measured oil hydrocarbons in the *n*-C₁₀ to *n*-C₂₄ elution range, or 174 to 391 °C boiling point range.³⁹ Resulting estimates of partitioning properties were then used to parameterize simulations of evaporation and dissolution mass transfers for all GC×GC-determined hydrocarbon analytes eluting in this boiling point window. Using this approach, mass transfer model predictions were successfully compared to measured field sample data for oil beached near Cape Cod, MA, after the 2003

Bouchard 120 oil spill¹⁴ and also for oil beached in San Francisco Bay after the 2007 *Cosco Busan* oil spill.⁷⁴ However neither of these studies evaluated the very early period (<7 days) of mass transfers to air and water.

Here, we report results from a controlled oil release experiment conducted in open waters on the North Sea during September 29-30, 2009. With this study, we aim to bridge the knowledge gap that exists due to the lack of early oil composition data, and specifically to shed light on the initial evaporation and dissolution processes during the first day of an oil spill. We present detailed hydrocarbon compositional analysis of collected oil slick and oil sheen samples during the first day after release. These field measurements are compared to a transport model that we developed to describe early mass transfer processes during the field experiment.

3.3 Experimental and computational methods

3.3.1 Open sea oil spill experiment

A permitted, controlled oil release experiment was conducted jointly by several European research institutes during September 29-30, 2009, approximately 200 km offshore in the North Sea Netherlands Exclusive Economic Zone (Figure 3-2). Starting at 12:10 UTC, 4.3 m³ of Norwegian Grane crude oil was released from the deck of the *Arca*, a hydrographic survey and pollution response vessel, over a 1.15 hour period. The resulting unrestrained sea-surface slick was monitored during a 26 h period. The oil had a density of 940 kg m⁻³, a Reid vapor pressure of 3.4 kPa, and a kinematic viscosity of 373 mm² s⁻¹ at 20 °C. These and other measured properties of the oil compared favorably with values reported previously by Statoil¹⁵⁴ for Grane crude (Appendix section 3.5.1). Due to weather and logistical constraints, oil slick, oil sheen, and water column samples were taken at irregular time intervals. Oil slick and sheen samples were taken from the sea surface, from a small rubber motorboat deployed from the *Arca*, at several time points after the end of the oil release: 0.58; 0.88; 3.70; 18.07; 19.62; 19.82; 22.53; and 25.23 h. Four water column samples were taken 20 h after the end of the oil release, in three locations, at depth of ~1.5 m, using a custom-built grab sampler (Appendix section 3.5.2). Sampling procedures are described in detail in Appendix section 3.5.2. Recorded slick surface area and wind speed measurements during the experiment are given in Table 3-1.

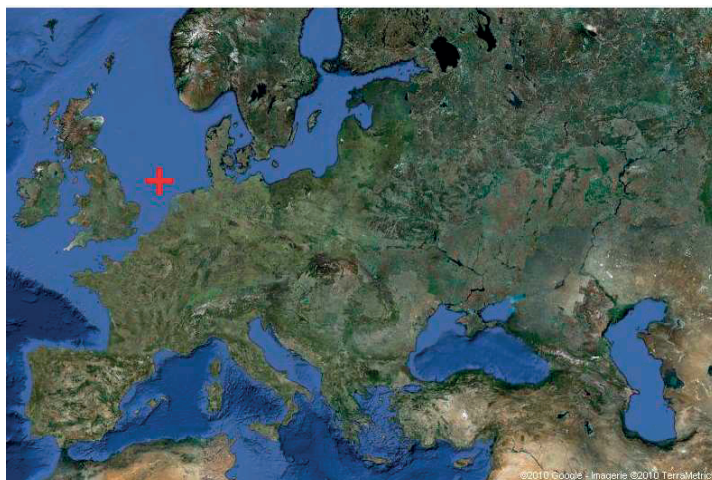


Figure 3-2. Location where the oil was discharged (red cross). The map is from google maps.

Table 3-1. Position, slick extent,^a and wind measurements during the experiment

Date	Time (UTC)	Latitude (North)	Longitude (East)	Length of slick [km]	Width of slick [km]	Wind (Beaufort scale)
September 29 th 2009	12:20	54°10'	3°30'	0.815	0.26	3
September 29 th 2009	13:26	54°9'30"	3°31'	1	0.9	3
September 29 th 2009	14:15	54°9'	3°31'	3.1	0.9	4
September 29 th 2009	15:05	54°9'30"	3°31'54"	1.8	1.8	4
September 29 th 2009	16:37	54°9'12"	3°32'18"	2.5	1.4	3
September 29 th 2009	19:41	54°7'59"	3°32'37"	4.5	1.3	3
September 30 th 2009	07:35	54°8'54"	3°32'12"	5.2	1.4	3

^a Maximum length and width of the oil slick based on measurements by SeadarQ radar from the Arca and aerial over-flight. The shape of the slick was approximately rectangular.

3.3.2 Analysis of oil slick and oil sheen samples

Oil slick and oil sheen samples were analyzed by GC×GC coupled to a flame ionization detector (GC×GC–FID); details of the analysis method are provided in Chapter 2 (section 2.7.1). GC×GC–FID chromatograms were baseline-corrected with the method of Reichenbach and co-workers⁷⁰ using GC Image⁷¹ with the following parameters: 200 deadband pixels per modulation; filter window size of 3 pixels; 3.5 for the expected value of baseline plus noise to the estimated standard deviation of the noise; and one baseline value per modulation. The conservative baseline correction of Reichenbach et al. is appropriate for quantification of the total (resolved plus unresolved) signal (section 1.3.1).⁶² FID response factors of hydrocarbons have been shown to be similar (within ±12% of central value) for 22 PAHs and 16 *n*-alkanes analyzed by GC–FID.⁶¹ Therefore the GC×GC–FID instrument response factor was assumed to be the same for all hydrocarbon compounds.^{62,63,155} This allowed quantitative comparisons of mass changes of both resolved and unresolved GC×GC-amenable hydrocarbon material between chromatograms of different samples. Collected oil sample chromatograms were then aligned to the neat oil chromatogram using the algorithm presented in Chapter 2.⁶⁷

GC×GC chromatograms were finally normalized so that the total peak volumes of five consecutive *n*-alkanes, octacosane (*n*-C₂₈) to dotriacontane (*n*-C₃₂), were of the same magnitude in all chromatograms. These *n*-alkanes were considered unlikely to undergo significant fractionation (Chapter 6)⁶² and they exhibited relative changes in concentration of ≤15% during the experiment. In order to quantify the peak volumes for these and other individual compounds, we applied the GC Image implementation of the inverted watershed algorithm⁷¹ to the (unaligned) chromatograms, after baseline-correction with the algorithm of Eilers (using $\lambda = 10^4$ for *n*-alkanes and $10^{6.5}$ for PAHs).^{62,66,68,69}

Not all petroleum compounds are GC×GC-amenable. Non-GC-amenable compounds include those with very high and very low boiling points that lie outside of the volatility range separated by the instrument, as well as compounds that are thermally unstable or that adhere to active sites within the chromatographic system. The mass contributions of the non-GC-amenable high boiling and low boiling fractions were estimated from true boiling point distillation data for Grane crude provided by Statoil¹⁵⁴ (Appendix section 3.5.1). The GC×GC analysis separated an elution range of *n*-C₉ to *n*-C₄₅, which corresponds to a simulated distillation boiling point interval of 150 °C to 550 °C. True boiling point distillation data show that 68.9% of the Grane crude oil mass falls within this boiling point window. Consequently we infer that 31.1% of the oil mass was not measured by GC×GC, having boiling point >550 °C or <150 °C. In this chapter we will always refer to percentages of the whole oil including the non-GC-amenable fraction. This assumes that the very low-volatility (boiling point >550 °C) compounds remained in the oil phase throughout the duration of the experiment. Several high-volatility compounds, including BTEX (benzene, toluene, ethylbenzene, and xylenes) and *n*-C₇ to *n*-C₉ *n*-alkanes, were modeled separately based on their concentrations in neat oil as measured by GC–FID and GC–MS (Appendix Table 3-4). The remaining 5.6% of oil mass in the <174 °C boiling point range was assumed immediately evaporated upon release, in our model calculations.

3.3.3 Analysis of water column samples

Water column samples were analyzed by Lukas Wick and Birgit Würz for several PAHs and *n*-alkanes (*n*-C₈ – *n*-C₄₀) by gas chromatography coupled to a mass spectrometer (GC–MS), and by headspace GC with a flame ionization detector (GC–FID) for benzene, toluene, ethylbenzene, and xylenes (BTEX). Detailed analysis method descriptions are given in Appendix section 3.5.4.

3.3.4 Mass transfer model

A transport model was developed to describe mass transfer fluxes of hydrocarbons from floating oil into air and water, as well as downward turbulent mixing of dissolved hydrocarbons in the water column. The model was parameterized based on temperature, wind, and wave conditions observed during the experiment, as well as the observed lateral spreading of the slick detected by SeadarQ radar from the *Arca* and aerial over-flight (Table 3-1). The model was tailored to individual analyzed hydrocarbon compounds based on their known or estimated

physical properties, as explained in detail below. None of the model parameters were calibrated based on the observed evolution of hydrocarbon concentration data in either the oil slick or the water column.

The model assumes a well-mixed, uniform layer of oil slick at the sea surface. Oil input to the sea surface was assumed a constant rate during the 1.15 h release period. In the model, the surface area of the oil slick was assumed to grow continuously such that its extent matched the footprint observed at several time points throughout the experiment (0.98 h before the end of the oil release; and 0.12; 0.93; 1.77; 3.30; 6.37; and 18.27 h after the end of the oil release). The modeled oil slick thickness varied with time and was updated iteratively based on the modeled quantity of total oil slick mass and the observed surface area of the oil slick footprint, assuming a constant oil density. Additionally, the oil slick formed during the field experiment was observed to be patchy, partly interspersed with a visible sheen (thinner oil layer) at the air-water interface. Hence, in the model, oil slick was assumed to cover only half of the footprint, or total sea surface area, explored by the oil spill. Emulsification of the oil in the slick was not visibly noticed during the experiment.

Hydrocarbon mass transfer fluxes (mass time⁻¹ area⁻¹) from the liquid oil phase into air and water were computed with a boundary layer model:¹⁵⁶

$$F_{i,oil}|_{evap} = - \frac{C_{i,oil}}{\frac{\delta_{oil}}{D_{i,oil}} + \frac{\delta_{air}}{D_{i,air} \cdot K_{i,air/oil}}}$$

Equation 3-1

$$F_{i,oil}|_{diss} = \frac{\frac{C_{i,water}}{K_{i,water/oil}} - C_{i,oil}}{\frac{\delta_{oil}}{D_{i,oil}} + \frac{\delta_{water}}{D_{i,water} \cdot K_{i,water/oil}}}$$

Equation 3-2

where δ_j refers to the boundary layer thickness of phase j , D_{ij} is the diffusion coefficient of compound i in phase j , $K_{i,j/k}$ is the partition coefficient of compound i between phases j and k , $C_{i,oil}$ is the concentration present in the oil layer, and $C_{i,water}$ is the concentration in the uppermost water layer (1 m thickness). Equation 3-1 and Equation 3-2 are comparable to expressions used previously to describe evaporation and dissolution of individual compounds from a liquid oil phase,^{13,14,16,41,42,142,143,148–151,153} and the correspondences between several of these models are explained in detail in section 3.5.5. Air and water boundary layer thicknesses (δ_{oil} and δ_{water}) were estimated from wind speed according to the following set of formulas:¹⁵⁶

$$v_{CO_2,water} = \frac{4 \cdot 10^{-5} \cdot u_{10}^2 + 4 \cdot 10^{-4}}{100}$$

Equation 3-3

where $v_{CO_2,water}$ is the mass transfer velocity of CO₂ in water in m s⁻¹ and u_{10} is the wind speed at 10 m altitude in m s⁻¹.

$$\delta_{water} = \frac{D_{CO_2,water}}{v_{CO_2,water}}$$

Equation 3-4

where $D_{CO_2,water}$ is the diffusion coefficient of CO₂ in water (2·10⁻⁹ m² s⁻¹).

$$v_{water,air} = \frac{0.2 \cdot u_{10} + 0.3}{100}$$

Equation 3-5

where $v_{water,air}$ is the mass transfer velocity of water in air in m s⁻¹ and u_{10} is the wind speed at 10 m altitude in m s⁻¹.

$$\delta_{air} = \frac{D_{water,air}}{v_{water,air}}$$

Equation 3-6

where $D_{water,air}$ is the diffusion coefficient of water in air (3·10⁻⁵ m² s⁻¹).

Observed wind speeds ranged from 3 to 4 degrees Beaufort (3.4–7.9 m s⁻¹), and wind speed values used by the model correspond to the middle of the measured Beaufort intervals, with linear interpolation between measurements. Owing to the wind conditions and limited lateral extent of the oil slick, the air phase concentration of hydrocarbons was assumed negligible (zero) for the purpose of estimating evaporative mass transfer fluxes (Equation 3-1).

Vertical turbulent mixing in the water column was modeled with a finite difference formulation, where downward transport was assumed to follow Fick's first law:^{156–159}

$$F_{i,water}(z)|_{mix} = -E \cdot \frac{\Delta C_{i,water}(z)}{\Delta z_{water}}$$

Equation 3-7

where $\Delta C_{i,water}$ is the concentration difference between two water layers for compound i , E is the vertical turbulent mixing coefficient of the water column, and Δz_w is the thickness of the water layers (1 m each). A Neumann boundary condition or wall boundary (vertical concentration gradient equal to zero)¹⁶⁰ was imposed at the sea floor, which had ~42 m depth.¹⁶¹ Transport in the water column was assumed to have a vertical gradient only; i.e., dissolved hydrocarbons were assumed to be laterally well-mixed under the oil slick footprint but not extend laterally outside of the slick footprint. Based on an estimated lateral turbulent mixing coefficient of 50–250 m² s⁻¹,^{156,159} the water mass below the slick was expected to mix 3–7 km laterally over the duration of the experiment. This is similar to the observed oil slick spreading extent of 1.4 km width and 5.2 km length. Therefore the assumption that hydrocarbons were

laterally well-mixed below the oil slick was assumed valid for this early phase of the oil spill. Volatilization of dissolved compounds from the “slick free” water surface (where sheen might be observed) was modeled using previously developed expressions for air-water mass transfer fluxes.¹⁵⁶

Methods to estimate the vertical turbulent mixing coefficient of the water column based on wind speed have been reported, some of them in an oil spill modeling context.^{162–165} However, these formulas neglect convective mixing, which may be dominant at night or in autumn and winter. Therefore we estimated the air-sea heat flux balance during the experiment, based on wind speed, relative humidity, and air and water temperatures at K13 platform obtained from the Royal Netherlands Meteorological Institute (KNMI).^{159,166–168} From these data, we interpreted that convection was the dominant mixing process in the water column throughout the entire duration of the experiment (Appendix section 3.5.6). Consistent with a convective mixing situation, we assumed a single mixed layer throughout the entire 42 m depth water column, based on literature reports describing the absence of pycnocline for nearby locations around this time of year.^{169,170} Based on the net heat flux, we thus estimated the vertical turbulent mixing coefficient, E , to be $0.22 \text{ m}^2 \text{ s}^{-1}$ throughout the water column during the entire period of the experiment (Appendix section 3.5.6), using the expression:¹⁵⁹

$$E = k \cdot \left(\frac{\alpha \cdot g \cdot h \cdot H}{C_p \cdot \rho_w} \right)^{1/3} \cdot h$$

Equation 3-8

where α is the thermal expansivity of water, g is the gravitational acceleration, h is the water depth (~42 m), H is the net heat flux (Appendix Figure 3-12), C_p is the specific heat capacity of water at constant pressure, ρ_w is the water density, and k is a factor approximately equal to 0.5.¹⁷¹

Mass transfer fluxes of oil hydrocarbon compounds more volatile than *n*-decane were modeled individually. For these compounds, partitioning from oil to air and water were estimated based on Raoult’s law¹⁵⁶ using experimental vapor pressure and aqueous solubility data.^{156,172} Aqueous solubilities were corrected for salinity by dividing them by a factor of 1.36 (a more accurate correction factor can be obtained as in Chapter 4 if the compound or pseudo-component structure is known).¹⁷³ Molecular diffusion constants in air and water were estimated from molar mass and corrected for temperature:¹⁵⁶

$$D_{i,air}(T_{ref}) = \frac{1.74 \cdot 10^{-6}}{(M_i)^{0.65}}$$

Equation 3-9

$$D_{i,water}(T_{ref}) = \frac{2 \cdot 10^{-10}}{(M_i)^{0.71}}$$

Equation 3-10

where $D_{i,j}$ is the diffusion coefficient of component i in phase j at a reference temperature, T_{ref} , of 298.15 K, in $m^2 s^{-1}$, and M_i is the molecular weight, in $kg mol^{-1}$. The formulas used for temperature corrections from the reference temperature (298.15 K) to another temperature (T , in K) are:¹⁵⁶

$$D_{i,air}(T) = D_{i,air}(T_{ref}) \cdot \left(\frac{T}{T_{ref}} \right)^{1.5}$$

Equation 3-11

$$D_{i,water}(T) = D_{i,water}(T_{ref}) \cdot \left(\frac{\eta_{water}(T_{ref})}{\eta_{water}(T)} \right)^{1.14}$$

Equation 3-12

where η_{water} is the dynamic viscosity of water, which was estimated using the the Matlab code of Sharqawy et al.¹⁷⁴ Equation 3-12 is based on the Hayduk-Laudie formula, assuming a constant molar volume.

Partitioning properties and molar masses for hydrocarbons eluting between n -C₁₀ and n -C₂₄ were estimated from GC×GC retention time information (Appendix section 3.5.7).^{14,39} This includes intervening n -alkanes and other substituted aliphatic and aromatic hydrocarbons in the n -C₁₀– n -C₂₄ elution window, or boiling point range of 174 to 391 °C. For both individually modeled compounds and GC×GC-analyzed hydrocarbons, estimated or experimental vapor pressure data at 25 °C were temperature-corrected to the surface water temperature of the field site, using enthalpy of vaporization estimates^{39,156} or data:^{39,172}

$$p_{i,L}(T) = p_{i,L}(T_{ref}) \cdot e^{\frac{\Delta H_{i,vap}}{R} \left(\frac{1}{T_{ref}} - \frac{1}{T} \right)}$$

Equation 3-13

where $p_{i,L}$ is the (hypothetical) pure liquid vapor pressure of compound i , $\Delta H_{i,vap}$ is the enthalpy change of phase transfer from pure liquid phase to gas phase, and R is the molar gas constant.

Surface water temperature was estimated to be 16.1 °C based on measurements at nearby locations (K13 platform and Europlatform). GC×GC-based estimates of aqueous solubility may or may not be valid for n -alkanes longer than n -C₁₁, due to possible folding of straight-chained n -alkanes in aqueous solution,¹⁷⁵ an interpretation that is challenged by recent modeling results.¹⁷⁶ The oil molar volume ($0.25 L mol^{-1}$) was estimated from the mass-weighted average of the molar mass divided by the measured oil density:

$$\bar{V}_{oil} = \frac{\sum_{i=1}^N (m_{i,oil} \cdot M_i)}{\sum_{i=1}^N (m_{i,oil}) \cdot \rho_{oil}}$$

Equation 3-14

where \bar{V}_{oil} is the estimated oil molar volume, $m_{i,oil}$ is the mass of component i in the oil, M_i is the molar weight, and ρ_{oil} is the density of the oil (assumed constant).

Compounds with boiling points >391 °C (corresponding to $>n$ -C₂₄) were assumed unaffected by either dissolution or evaporation during the time frame of this experiment.

According to our model, mass transfer fluxes were not limited by molecular diffusion within the oil slick layer, but this process was nevertheless included in the model. Oil-side diffusion limitation of mass transfer fluxes is likely to be important for water-in-oil emulsions,^{11,136,137} which were not observed during our experiment. $D_{i,oil}$ was estimated from molecular radius, oil viscosity and temperature according to the Stokes-Einstein relation:^{14,156}

$$D_{i,oil} = \frac{k_B \cdot T}{6 \cdot \pi \cdot \eta_{oil} \cdot r_i}$$

Equation 3-15

where k_B is the Boltzman constant, T is the temperature, η_{oil} is the oil dynamic viscosity, and r_i is the effective compound molar radius. Effective compound molecular radii were estimated from molar volume, assuming spherical molecule shape:⁷⁴

$$r_i = \left(\frac{3 \cdot \bar{V}_i}{4 \cdot \pi \cdot N_A} \right)^{1/3}$$

Equation 3-16

where $\bar{V}_i \cong M_i / \rho_{oil}$ is the molar volume of component i , and N_A is the Avogadro constant ($\sim 6.022 \cdot 10^{23}$).

Oil viscosity was adjusted as a function of temperature:¹⁷⁷

$$\eta_{oil}(T) = \frac{10^{C \cdot 10^{-0.5644 \cdot \log\left(\frac{9}{5}T - 459.67\right)}} - 1}{1000}$$

Equation 3-17

where η_{oil} is the dynamic viscosity of the oil. The oil-specific constant C can be determined from one viscosity measurement (at $T_{meas} = 293.15$ K in our case):

$$C = \frac{\log(\eta_{oil}(T_{meas}) \cdot 1000 + 1)}{10^{-0.5644 \left(\frac{9}{5} T_{meas} - 459.67 \right)}}$$

Equation 3-18

where $\eta_{oil}(T_{meas})$ was 0.35 Pa s for the Grane crude oil used during the experiment.

Oil viscosity was also adjusted as a function of the fraction evaporated, F_E ,¹⁷⁸ using a value of 5 for the “prefactor” ζ ; this value lies in between the value of 1 suggested for gasoline and the value of 10 used by Arey et al. for heavy fuel oil:¹⁴

$$\eta_{oil}(t) = \eta_{oil}(t_0) \cdot e^{\zeta \cdot F_E(t)}$$

Equation 3-19

Dispersion, or oil-in-water emulsion, is the process of entrainment of oil droplets within the water column. Dispersed droplets reduce the amount of oil present within the oil slick and also enhance the rate of hydrocarbon dissolution. Most oil entrainment models are based on the work by Delvigne and Sweeney,¹⁷⁹ which is designed for entrainment by breaking waves.¹⁸⁰ The ADIOS model,²⁵ which is based on Delvigne and Sweeney’s oil entrainment model, predicted 0.7% dispersion during the experiment (Appendix section 3.5.8). We estimated that 0.7% dispersion would increase truly dissolved concentrations of the most soluble PAHs by <20%, therefore we chose not to include this process explicitly in the mass transfer model of our experiment.

We did not conduct a formal error propagation analysis based on model input parameter variability, because we judged that the most important uncertainties arose from the treatment of oil entrainment into the water column, the associated oil-water interactions, and water mass mixing controlled by water column stability. We briefly discuss the sensitivity of the model to these and other uncertainties in the Results and discussion.

3.4 Results and discussion

3.4.1 Compositional changes in oil slick and oil sheen samples

Analysis of collected oil slick samples shows that volatile and/or soluble hydrocarbon compounds are removed rapidly from the floating oil during the first day of the oil spill, including several light *n*-alkanes and PAHs (Figure 3-3). Oil slick samples OS1 and OS2, taken 0.58 h after the end of the oil release, exhibit 55% ± 9% loss of undecane (*n*-C₁₁) and 41% ± 10% loss of naphthalene, based on quantification of analyte peak volumes in GC×GC–FID chromatograms (Appendix Table 3-6). Samples OS5 and OS6, taken 25.23 h after the release, exhibited partial to total losses of two- to three-ring PAHs and >50% loss of *n*-alkanes up to *n*-C₁₇ (Table 3-6). We did not detect naphthalene in oil slick samples taken after 18 hours, in agreement with the transport model and consistent with previous estimates¹³ suggesting that naphthalene would disappear from a small sea-surface oil slick within 3 to 8 hours after release. Two-ring PAHs are of particular concern for early exposures of organisms in the water column.⁷ Normal

alkanes and PAHs represent hydrocarbons that are typically evaluated during oil weathering studies. However *n*-alkanes and parent PAHs in the *n*-C₇–*n*-C₄₀ boiling range represent only <2% of the oil mass of Grane crude.

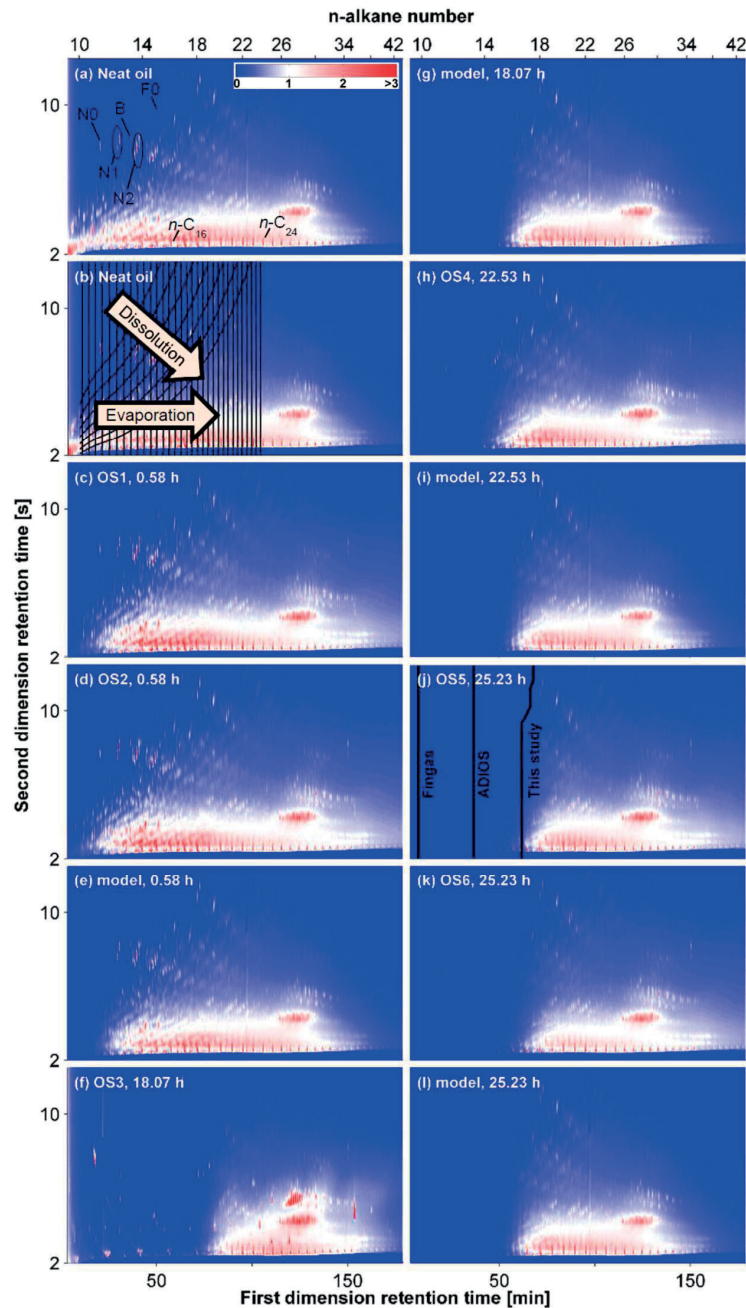


Figure 3-3. GCxGC–FID chromatograms of oil slick samples, and transport model-generated chromatograms at corresponding times, for: (a) neat oil overlaid with positions of selected compounds, including naphthalene (N₀), C₁-naphthalenes (N₁), C₂-naphthalenes (N₂), biphenyl (B), fluorene (F₀), hexadecane (*n*-C₁₆), and tetracosane (*n*-C₂₄); (b) neat oil overlaid with solubility and vapor pressure contours; these contours define discrete cells that were used to construct mass loss tables (MLTs); (c) sample OS1; (d) OS2; (e) model (0.58 h); (f) OS3; (g) model (18.07 h); (h) OS4; (i) model (22.53 h); (j) OS5 overlaid with removal extent predictions inferred from Fingas Equation 3-35 and the ADIOS model, and the half-life

contour predicted by our model; (k) OS6; and (l) model (25.23 h). GC×GC chromatograms are normalized such that the total peak volumes of the five *n*-alkanes *n*-C₂₈ to *n*-C₃₂ are the same in all chromatograms. Listed time points correspond to time after the end of the oil release. The color scale on the upper right of the neat oil chromatogram indicates FID signal response (arbitrary units).

It is more instructive to study the systematic fractionation patterns that arise in GC×GC chromatograms of collected oil slick samples (Figure 3-3). GC×GC–FID chromatograms allow the visualization and quantification of mass changes affecting all resolved and unresolved hydrocarbon material eluting between *n*-C₉ and *n*-C₄₅, corresponding to the 150 to 550 °C boiling point range, which represents 68.9% of the total oil mass. In the oil slick samples, we observe a progressive removal of hydrocarbons that appears initially in the upper left region of the GC×GC chromatogram in early samples and encroaches toward the lower right region of the GC×GC chromatogram with increasing sample age (Figure 3-3). The observed hydrocarbon fractionation pattern aligns well with plotted contours of estimated liquid vapor pressures of the analyzed hydrocarbons, which decrease progressively from left to right in the GC×GC chromatogram, and plotted contours of estimated aqueous solubilities, which decrease monotonically from upper left to lower right (Figure 3-3b). The observed removal of both resolved and unresolved hydrocarbon mass from oil slick samples is thus consistent with the expected combined effects of evaporation and dissolution, manifest as a disappearance of hydrocarbons systematically from the upper left to the lower right of the GC×GC chromatogram.

Mass transfer model simulations of oil slick evolution can be projected directly on the GC×GC chromatogram of the neat oil,¹⁴ enabling the visualization of simulated oil slick sample chromatograms throughout the duration of the field experiment (Figure 3-3). The mass transfer model predicts that hydrocarbon material removal corresponds to a progressive disappearance of compounds from upper left to lower right in the GC×GC chromatogram. On visual inspection, the mass transfer model agrees remarkably well with the six oil slick samples, correctly describing the pattern of mass removal in the GC×GC chromatogram as well as the progression of hydrocarbon removal with increasing sample age. A more quantitative analysis of the observed and simulated removal patterns is reported in the next section.

These measurement and modeling results imply fast evaporation and dissolution rates of oil hydrocarbons, when compared to other field studies. >50% losses of *n*-alkanes up to *n*-C₁₂ within 4.1¹²² to 6 hours¹¹⁴ have been reported in two oil spill field experiments during which ≤2 m³ of oil was spilled. Ezra et al.¹⁸¹ reported removal of volatile compounds up to *n*-C₁₅ after three weeks for a beached residual fuel oil on the southeastern Mediterranean coast. Similarly, based on mass transfer calculations and field measurements at Nyes Neck beach, MA, Arey et al.¹⁴ proposed a half-life of about one week for *n*-C₁₅ in a ~0.04 mm thick coating of heavy fuel oil on beach cobbles. Early weathering rates at those field sites were also comparable to early weathering observed in Prince William Sound after the 1989 *Exxon Valdez* spill.¹⁰⁵ Compared to these previous field studies, our oil slick samples exhibited relatively fast losses of light (≤*n*-C₁₇) hydrocarbons.

Oil sheen samples exhibited yet faster fractionation rates than oil slick samples. We observed >50% losses for compounds more volatile than *n*-C₁₇ after only 1 h, and up to *n*-C₁₉ after 4 h. GC×GC chromatograms of oil sheen samples show dramatically accelerated removal of resolved and unresolved hydrocarbon mass, when compared to oil slick samples of the same

age (Figure 3-3, Figure 3-4). Colloidal structures, which include films, water-in-oil emulsions, and dispersions,¹⁸² play a major role in determining oil fractionation rate.^{13,55,183–185} A very thin oil layer can fractionate very quickly: for example, while investigating ascending oil droplets from Santa Barbara natural offshore oil seep, Wardlaw and coworkers⁵⁵ estimated that a thin oil film of 0.3 μm thickness on the sea would exhibit significant evaporative losses of compounds in the C_{12} – C_{15} volatility range within minutes. Similarly, samples taken in 2012 from sheens appearing at the sea surface above the site of the *Deepwater Horizon* disaster were depleted of compounds more volatile than $n\text{-C}_{15}$.¹⁸⁶ We did not attempt to make meaningful comparisons between the mass transfer model results and oil sheen samples, since the model was parameterized for the oil slick. Sheen samples have unknown histories and were assumed to have departed from or remixed with slick material at unknown times.

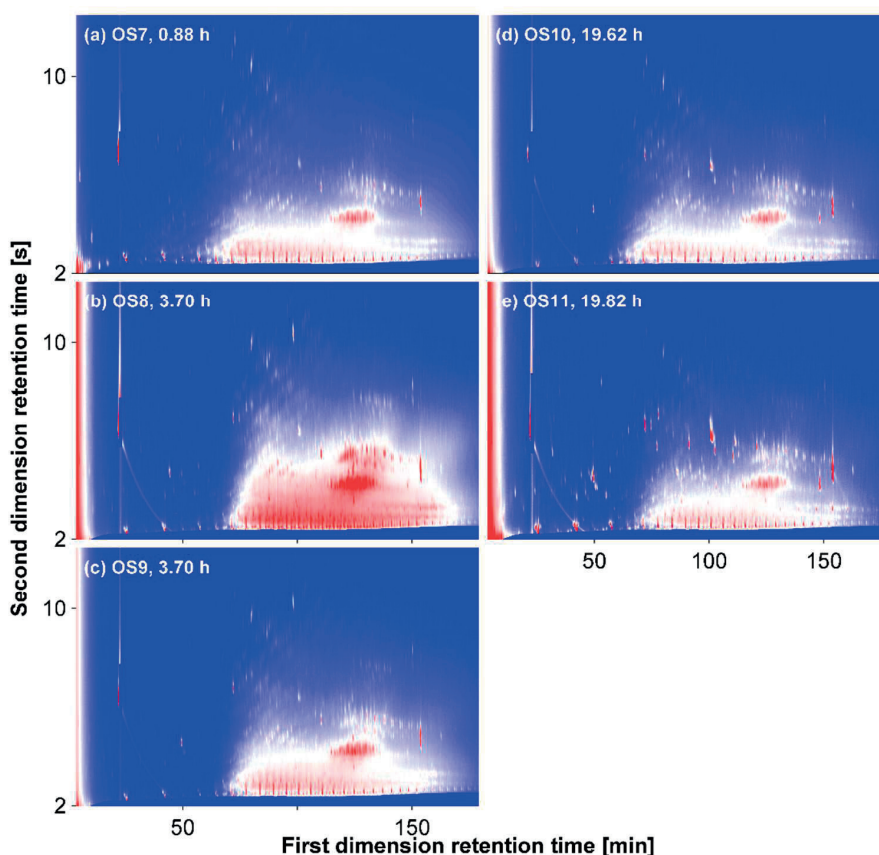


Figure 3-4. Oil sheen sample GCxGC–FID chromatograms for: (a) OS7, (b) OS8, (c) OS9, (d) OS10, and (e) OS11. Listed time points correspond to time after the end of the oil release. Sheen samples also exhibit some uptake of ambient biogenic compounds.

GCxGC–FID brings several important advantages to the present field study, complementing to the GC–FID and GC–MS techniques conventionally employed for analysis of oil mixtures in the environment. GCxGC retention time information enables the estimation of environmental partitioning properties of all resolved and unresolved hydrocarbon material in the $n\text{-C}_9$ to $n\text{-C}_{25}$ elution range.^{39,72} By comparison, conventional GC retention times do not enable estimates of environmental partitioning properties other than vapor pressure and boiling point,

and thus they convey limited information about the environmental fate of the unresolved hydrocarbon mass. Additionally, the FID instrument response factor can be assumed similar ($\pm 12\%$) for different analyzed hydrocarbon compounds.^{61–63,155} Thus it is possible to measure and also model the quantitative mass changes in the complete resolved and unresolved GC×GC-amenable hydrocarbon material that arises in different samples. By comparison, the 52 individual compounds that we quantified by GC–FID and GC–MS in the neat oil account for only 1.6% of the mass of this particular crude oil (Table 3-4). The GC–FID chromatogram of this oil presents a prominent unresolved complex mixture, likely arising from biodegradation in the Grane crude oil field that is characterized by at least two phases of oil reservoir charge.¹⁸⁷

3.4.2 Diagnosing evaporation and dissolution of hydrocarbons using Mass Loss Tables (MLTs)

To differentiate signatures of evaporation and dissolution in a quantitative way, we converted GC×GC chromatogram data into mass loss tables (MLTs).¹⁵ MLTs are generated from finite element cells delineated by contours of estimated hydrocarbon vapor pressure and estimated aqueous solubility overlaid onto the GC×GC retention time space¹⁵ (Figure 3-3b). MLTs show the mass losses of individual cells in a weathered sample relative to the neat oil, organized in volatility-vs-aqueous solubility space (Figure 3-5). This allows a straightforward visualization of the dominant physical processes leading to fractionation of the oil slick samples: aqueous dissolution leads to disappearance of hydrocarbon mass progressively from top rows to bottom rows of the MLT, whereas evaporation removes mass from leftmost columns progressively toward columns on the right. The MLTs also provide a basis for quantitative comparisons between mass transfer model predictions and observed fractionation patterns in oil slick samples from the field.

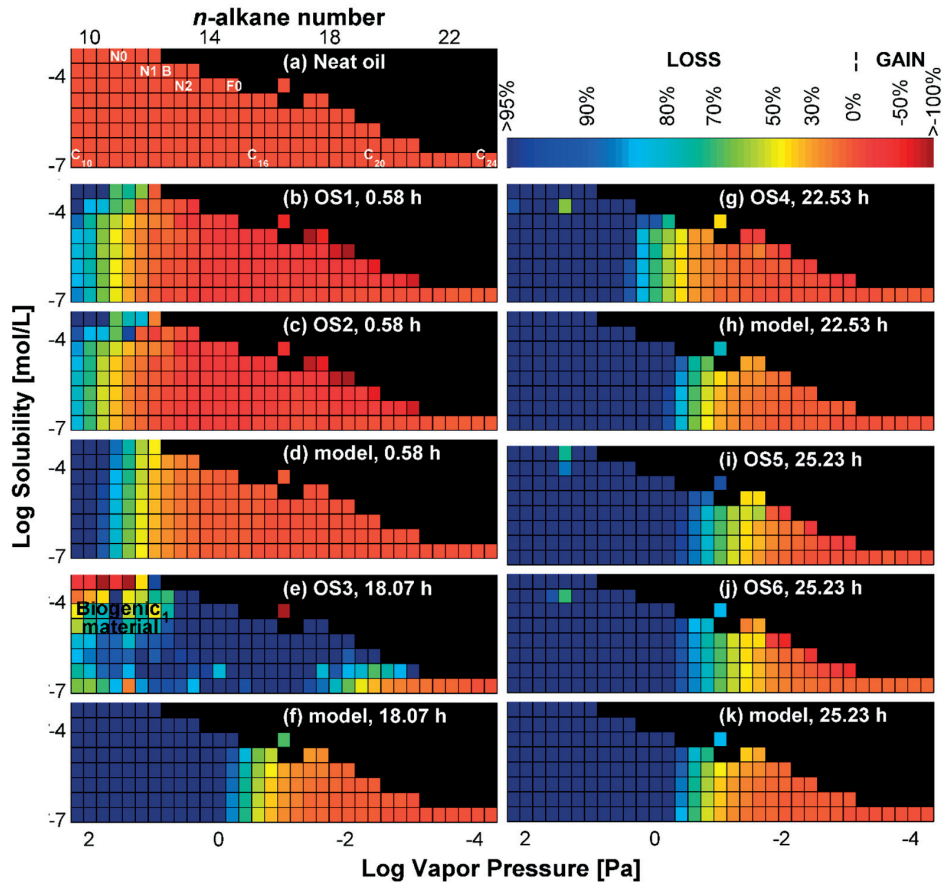


Figure 3-5. Mass loss tables (MLTs) showing fractionation of petroleum hydrocarbon mass removed from oil slick samples, organized as cells of compound groups in volatility versus solubility space. The color bar indicates the percentage of mass lost from a sample cell relative to the neat oil reference; negative values represent mass gains. Positions of the cells on the neat oil chromatogram are given in Figure 3-3b. Black cells correspond to property values not explored by compounds in the oil mixture or to cells containing mostly noise, defined as those containing less than 0.02% of the total signal contained in the part of the chromatogram covered by the MLTs, for neat oil. (a) The neat oil reference with labeled positions of selected compounds in the MLT space (refer to Figure 3-3 for abbreviations); (b-k) modeled MLTs and observed sample MLTs for oil slick samples OS1 to OS6. The time after the end of the oil release is indicated for each MLT.

¹ Signal arising in the upper left region of the MLT for sample OS3 is thought to be biogenic material arising from the sea water incidentally included in this sample.

In agreement with the mass transfer model predictions, MLTs of collected oil slick samples exhibited an evaporation front progressing through time according to a decelerating trend (Figure 3-5 and Figure 3-6). Evaporation is the dominant fractionation process, based on inspection of the MLTs. With the exception of sample OS3, the position of the evaporation front predicted by the model agrees with collected oil slick samples to within 1 log vapor pressure unit (Figure 3-6). Overall, the root-mean-squared-deviation (rmsd) of model-predicted MLTs with respect to sample MLTs was 0.38 in the $\log M_i(t)/M_i(t_0)$ over the 155 MLT cells considered

in each of the six oil slick field samples, thus entailing a comparison of model versus observations for 930 cells in total. This implies, for example, that if 80% mass loss was observed for a particular MLT cell, the model typically predicted a mass loss ranging from 52 to 92% for this cell. We interpret that the model captured the dominant evaporative weathering trend correctly (Figure 3-5).

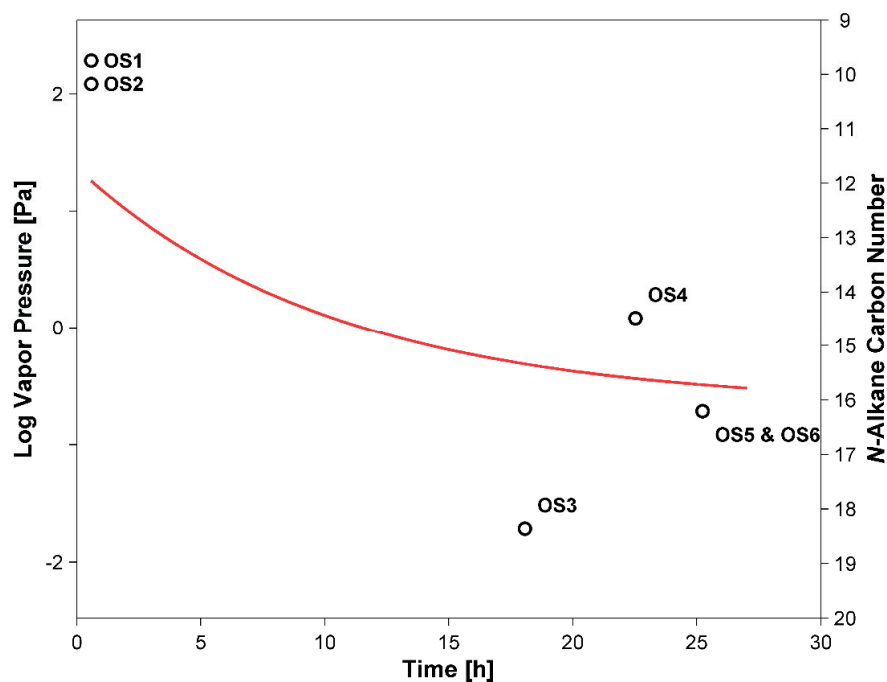


Figure 3-6. Observed and modeled evaporation front plotted versus time, expressed both in log vapor pressure (left axis) and *n*-alkane carbon number (right axis). We defined the position of the evaporation front as the volatility value where the three lowest-solubility regions of the MLT all exceed 80% mass loss. Black circles represent evaporation front values observed for oil slick samples and the red line represents the evaporation front predicted by the mass transfer model.

Subtle dissolution signatures are also evident in the MLT data of several oil slick samples, distinct from evaporation trends. Samples OS1 and OS2, taken 0.58 h after the end of the oil release, both show signs of dissolution. For both of these samples, the uppermost rows of the MLT exhibit mass removal that is superimposed onto the evaporation signature (Figure 3-5). Samples OS4 and OS5, taken at 22.53 and 25.23 h, also exhibit a possible dissolution signature. By comparison, mass transfer simulations appear to under-predict dissolution extent at 0.58 h but are in closer agreement with compositional data for samples taken >20 h after the release.

Our analysis of hydrocarbon evaporation and dissolution processes takes a fundamental departure from conventional techniques that focus on the environmental behaviors of selected individual hydrocarbons that constitute a small fraction of the oil. Here, we compare model simulations and field observations of mass transfer fractionations affecting all resolved and unresolved hydrocarbon material in the 174 to 391 °C boiling point range. This elution window

contains 44% of the total oil mass and it comprises most of the hydrocarbon components that are affected by mass transfer during the initial 24 h after an oil release in the environment. Some other approaches model evaporation using pseudo-components based on oil distillation curves;^{25,153} however this cannot capture the dissolution process.

3.4.3 Hydrocarbon contamination of the water column at 1.5 m depth

Four water column samples taken at 1.5 m depth from three sampling locations, 20 h after the oil release, were analyzed for several individual hydrocarbon compounds (Appendix Table 3-4). For nine compounds having measured sample concentration values that exceeded the field blank value, we found that water column levels of extractable hydrocarbons implied mass apportionments to the water column that far exceeded the total hydrocarbon mass released during the spill (Appendix Table 3-7). Our confounded results may plausibly have arisen from: cross-contamination of water column samples from the oil slick during sampling; other analytical error; field sampling variability; contamination from boats used during the experiment; or high background levels of hydrocarbons arising from resuspension of sediments due to the convective mixing regime of the water column. We thus concluded that the water column data were unreliable, and we omit further consideration of these results from the study.

3.4.4 Simulated hydrocarbon mass apportionments to air and water

The mass transfer model allows the simulation of time-dependent apportionments of hydrocarbon mass transferred to air and water (Figure 3-7). According to the model, 74.0% of the whole oil remained in the slick, 25.7% was evaporated, and 0.3% was dissolved, 25 h after the oil release. Predictions after two days (71.1%, 28.4%, and 0.5% respectively) suggest that mass transfer rates decelerated rapidly after the first day (see also the animation available online at <http://pubs.acs.org/doi/suppl/10.1021/es502437e>). Dispersion was estimated to be 0.7% based on the ADIOS model, 25 h after the oil release; this process was not considered in our mass transfer model.

Compound-specific mass apportionments were also calculated. Simulations predicted that 10% of naphthalene became dissolved and 90% was evaporated during the course of the experiment. According to the model, naphthalene was predicted to be already 52% depleted from the oil slick at the end of the oil release period, and 99% depleted 1 h later. Compound-specific mass apportionment predictions for BTEX, naphthalene, phenanthrene, anthracene, and *n*-C₇ to *n*-C₁₈ *n*-alkanes are shown in Table 3-2. BTEX compounds were predicted to disappear very rapidly from the oil slick. Benzene became 13% dissolved and 87% evaporated, whereas toluene was 5% dissolved and 95% evaporated, according to our model.

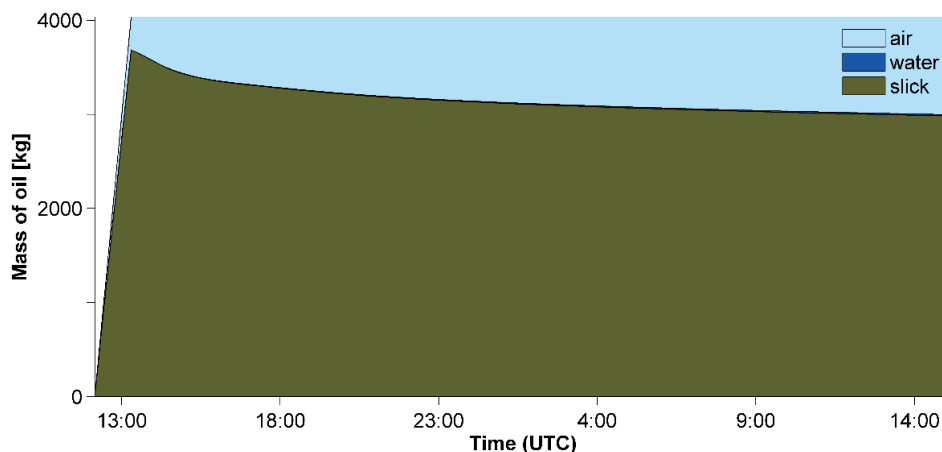


Figure 3-7. Modeled whole oil repartition in the three compartments air, water, and oil slick (does not include dispersion).

Table 3-2. Percentage of mass apportioned to air, water, and remaining in the oil slick for individual compounds, according to model predictions, 26 h after the end of the oil release. Aqueous solubilities of naphthalene, phenanthrene, and anthracene were corrected for temperature as explained in Appendix section 3.5.11. Aqueous solubilities of other compounds were assumed independent of temperature. Ventilation of the water column after dissolution was found to be a very minor contribution on the time frame of the field experiment.

Compound	air	water	oil
benzene	87%	13%	<0.5%
toluene	95%	5%	<0.5%
<i>p+m</i> -xylenes	98%	2%	<0.5%
ethylbenzene	98%	2%	<0.5%
<i>o</i> -xylene	98%	2%	<0.5%
naphthalene	90%	10%	<0.5%
phenanthrene	41%	40%	20%
anthracene	19%	18%	63%
<i>n</i> -C ₇	100%	<0.5%	<0.5%
<i>n</i> -C ₈	100%	<0.5%	<0.5%
<i>n</i> -C ₉	100%	<0.5%	<0.5%
<i>n</i> -C ₁₀	100%	<0.5%	<0.5%
<i>n</i> -C ₁₂	100%	<0.5%	<0.5%
<i>n</i> -C ₁₄	100%	<0.5%	<0.5%
<i>n</i> -C ₁₆	67%	<0.5%	33%
<i>n</i> -C ₁₈	29%	<0.5%	71%

Studying a thicker slick of emulsified Grane crude oil in ice-cold seawater, others have observed slower evaporation rates, reporting 10–18% evaporative mass loss after 2 days.¹⁰⁹ Compared to our experiment, decelerated evaporation rate would be expected under colder temperatures, increased oil slick thickness, and water-in-oil emulsification. For example, our model would predict ~17% evaporative mass loss if our experiment had taken place at 0 °C

(Appendix Figure 3-15). For comparison, Wolfe et al. estimated that ~10% of *Exxon Valdez* oil mass had evaporated within 1–2 days and that 3.5% was dispersed into the water column within the first 3 days of the 1989 oil spill in Prince William Sound, Alaska.¹⁰⁵ At these different sites, the mass transfer rates to air and water were dependent on oil composition, ambient temperature, turbulence-induced emulsification, and other environmental conditions.

3.4.5 Hydrocarbon evaporation predicted by the expressions of Fingas and by the ADIOS model

We briefly evaluated the evaporation extent predicted by two empirical equations developed by Fingas¹⁸⁸ and also by the ADIOS oil spill model²⁵ (Appendix section 3.5.8). Both models underestimated early evaporation rates for the end of the present experiment. The Fingas equations predict an evaporation extent that would be equivalent to the loss of hydrocarbons up to only *n*-C₁₀ after 25.23 h, assuming that volatilization progressively removes hydrocarbons from the oil according to decreasing boiling point (Figure 3-3j). By similar reasoning, the ADIOS model would predict evaporative removal up to *n*-C₁₃ (section 3.5.8). By comparison, the mass transfer model of the present study predicted >50% evaporative removal up to *n*-C₁₆ after 25.23 h, in closer agreement with collected oil slick samples that exhibited >50% removal up to *n*-C₁₇ (Figure 3-3j, Appendix Table 3-6). Oil slick thickness is not considered in the Fingas equations, however the thickness plays an influential role in mass transfer rate of hydrocarbons during an oil spill.^{13,14,74,146} The thickness of an oil slick of a given volume is expected to influence the total mass loss rate by evaporation. This arises from the physics of interfaces, where the rate of mass loss depends on area of the interface (Appendix section 3.5.5). This interpretation is supported by reports from other field studies,^{55,186} as well as by the fact that collected oil sheens exhibited accelerated evaporative losses compared to thicker oil slick samples during our experiment (Figure 3-3, Figure 3-4, Figure 3-5, Appendix Figure 3-16). Nonetheless oil slick thickness is not included in some models used to describe mass loss rates from oil.¹⁸⁹

3.4.6 Implications for early mass transfer processes and resulting ecological exposures during oil spills

To our knowledge, this is the first study to report on the broad-spectrum compositional evolution of an oil slick undergoing simultaneous evaporation and dissolution during the initial day of a sea-surface oil spill. Early fluxes of evaporated hydrocarbons are relevant for anticipating the inhalation exposure levels of downwind populations or personnel involved in emergency response.¹⁹⁰ Dissolution and dispersion of hydrocarbons into the water column control the exposures of marine organisms, and these exposures may be the most elevated during the initial hours or days after a release. However, for many light hydrocarbons, the kinetics of evaporation compete directly with kinetics of dissolution, and these two processes are thus difficult to disentangle in the field.

Ambient environmental conditions regulated the oil slick behavior and early mass transfer processes during this oil spill. With the aid of the mass transfer model, we can infer outcomes

that may be expected under other temperature conditions, wind conditions, and water column stability conditions, and these are each discussed in turn below.

Evaporation flux and dissolution flux are both expected to be decelerated at low temperatures compared to higher temperatures. However vapor pressure decreases with decreasing temperature more steeply than does aqueous solubility, for hydrocarbons.¹⁵⁶ Additionally, with decreasing temperature, diffusion coefficients in air and water both decrease, leading to decreased mass transfer velocities (length time⁻¹) through the air and water boundary layers. Among these competing temperature effects, the temperature dependence of vapor pressure is expected to dominate. Thus cold weather conditions are expected to produce increased mass apportionments to water relative to air, for the compounds that we studied. For example, according to the mass transfer model, a spill of Grane crude oil in cold sea water (3 °C) would experience dissolution extent increased by 60% and evaporation extent decreased by 40% compared to the same spill in warm sea water (33 °C) (Figure 3-15). In interpreting these predictions, the reader should bear in mind that our model includes a temperature correction to vapor pressure but not to aqueous solubility. The solubility correction may be significant for PAHs: aqueous solubility is decreased by 40% for naphthalene and 86% for phenanthrene at 3 °C compared to 33 °C.¹⁵⁶ This is discussed further in Appendix section 3.5.11.

Wind speed strongly influences early mass transfer rates of hydrocarbons. Air and water boundary layer thicknesses are both decreased by increasing wind speed, and therefore increasing wind speed will lead to increased mass transfer rates to both air and water (Figure 3-17). Additionally, the entrainment of oil droplets into the water column would become important at wind speeds higher than those encountered during the experiment.^{25,179} Thus, under higher wind speed conditions, substantially higher quantities of hydrocarbons would become dispersed and would thereby lead to increased aqueous dissolution.

For this field experiment, the modeled vertical turbulent mixing coefficient, E , had little impact on total mass of hydrocarbons dissolved into the water column. However E largely dictates the volume of water into which the hydrocarbons are diluted and thus the depth to which marine organisms are exposed. Our experiment took place in a shallow shelf sea during autumnal convection. This led to a high vertical turbulent mixing coefficient and no water column stratification, with dissolved hydrocarbons predicted to reach the sea bottom (42 m depth) within hours. For a stratified water column, the turbulent mixing coefficient near the sea surface usually will depend on the wind speed. Water column stability is also relevant to deep water oil releases. For example, during the *Deepwater Horizon* oil spill, ~1100 m depth intrusions of dissolved hydrocarbons into the highly stable Gulf of Mexico water column exhibited narrow vertical variability as far as 16.5 km downstream from emission point.⁸

The thickness of the oil layer affects the fractionation rates of highly toxic and soluble compounds such as naphthalene or phenanthrene. For example, the very rapid hydrocarbon fractionation exhibited by sheen samples, relative to slick samples, are related to the oil sheen thickness, which was estimated to lie near 0.1-0.3 μm according to its color.¹⁹¹ By comparison, the oil slick thickness was an estimated 10 μm after the first hour of the experiment and decreased to an estimated thickness of <1 μm by the end of the experiment (Figure 3-18). A

thinner slick would lead to more rapid fractionation of oil hydrocarbons arising from evaporation and dissolution. However, beneath a larger and thicker slick, higher concentrations within the water column would be expected, due to the larger load of oil mass per area of sea surface (calculations not shown).

Finally, the present study points to a key area where further insight is needed. Reliable water column composition data would prove an invaluable complement to oil slick composition data during the very early stages of an oil spill. This would provide a basis for closing the mass balance on estimated mass transfers to the water column. This includes the evaluation of accelerated hydrocarbon mass transfer rates resulting from entrainment of whole oil droplets in the water column,¹⁸⁴ addition of dispersants,¹⁹² and DOC-enhanced mass transfer of hydrocarbons to the aqueous phase.¹⁹³ Additionally, under more energetic sea surface conditions than those reported here, early hydrocarbon mass transfers to the water column may be more difficult to estimate, due to turbulent entrainment of oil into the water column. A better understanding of these mechanisms and additional early field sample data are needed in order to properly assess ecological exposures during the initial hours and days of a sea-surface oil spill.

3.4.7 Funding sources

This research was supported by grants from the NSF (OCE-0960841 and EAR-0950600), the BP/the Gulf of Mexico Research Initiative (GoMRI-015), the DEEP-C consortium, and the European Framework programs *FACEIT* (FP6, contract 018391) and *BACSIN* (FP7, contract KBBE-211684). It contributes to the 'Chemicals in the Environment' research program of the Helmholtz Association.

3.4.8 Acknowledgments

We thank Karin L. Lemkau (UCSB), Rob Modini (EPFL), Damien Bouffard (EPFL), Johnny Wüest (EPFL), Oliver C. Mullins (Schlumberger), and Per Daling (SINTEF) for conversations about data interpretation and modeling. We gratefully acknowledge Louis Peperzak (NIOZ) and the crew of the *Arca* for field logistics. We also thank Rebecca Rutler for assistance with sample analysis and Flavio Comino for construction of the water column grab sampler.

3.5 Appendix

3.5.1 Grane crude oil properties

Available properties determined for the Grane crude oil used during the experiment are found to compare reasonably with literature data for Grane crude oil (Table 3-3, Figure 3-8). Based on this comparison, distillation data from Statoil¹⁵⁴ were considered valid for the oil used during the experiment (Figure 3-9).

Table 3-3. Properties of the Grane crude oil used during the experiment and comparison to literature data

Property	Oil used during the experiment	Statoil analysis		Fritt-Rasmussen et al. (2012) ¹⁹⁴	Ross et al. (2010) ¹⁹⁵
		2003 ¹⁵⁴	2012 ¹⁹⁶		
API gravity (° API)	19.1	19	18.7		
gases ≤ C4 (weight percent)	0.15	0.38	0.42		
pour point [°C]	-30	<-33	-36	-26	-26
kinematic viscosity at 20°C [mm ² /s]	373	354	308		
Reid Vapor Pressure (RVP) [kPa]	3.4	11.6	17.9		
<i>n</i> -heptane (weight percent)	0.02	<0.01	0.02		
<i>n</i> -octane (weight percent)	0.02	0.03	0.04		
<i>n</i> -nonane (weight percent)	0.01	<0.01	0.04		
benzene (weight percent)	0.05	<0.01	0.01		
toluene (weight percent)	0.03	0.07	0.09		
ethylbenzene (weight percent)	0.03	0.05	0.04		
<i>p+m</i> xylenes (weight percent)	0.01	0.13	0.12		
<i>o</i> -xylene (weight percent)	0.01	0.06	0.07		
pristane/ <i>n</i> -C ₁₇ ratio	0.69				0.72 to 0.82

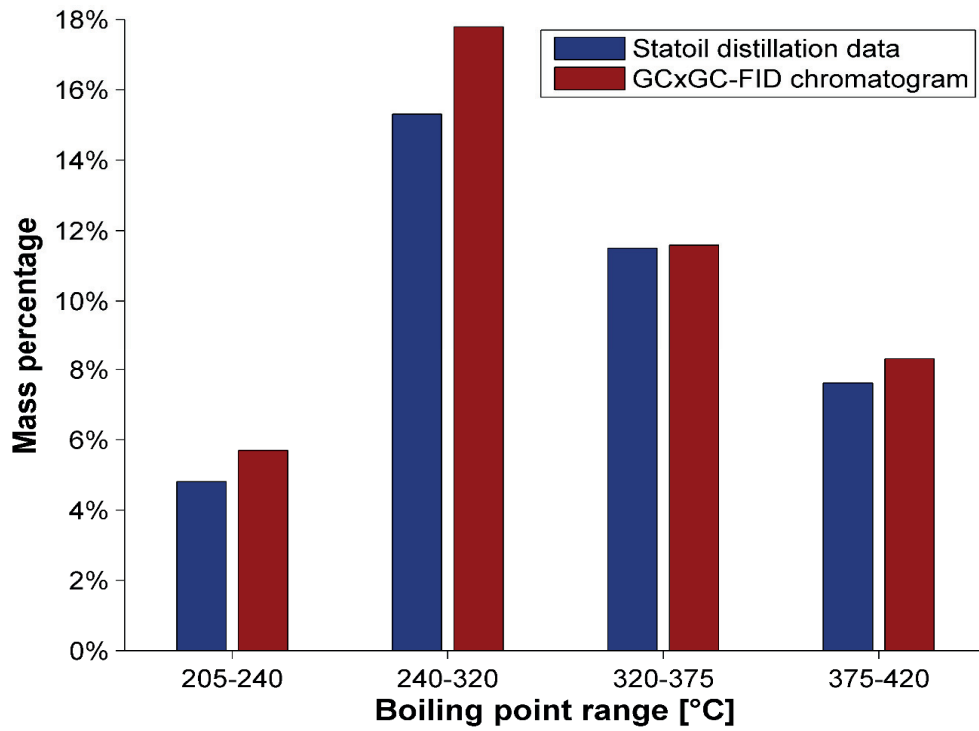


Figure 3-8. Comparison of mass percentage of the total oil with respect to boiling point range, based on Statoil distillation data (Figure 3-9; blue)¹⁵⁴ and based on the GC×GC–FID chromatogram of the neat oil used during the experiment, after normalization as described in main text (red). Boiling point estimates were assigned to the boiling point range 205–420 °C, corresponding to approximately the *n*-C₁₁–*n*-C₂₅ elution range of the GC×GC–FID chromatogram, based on the first dimension retention index (section 3.5.7).

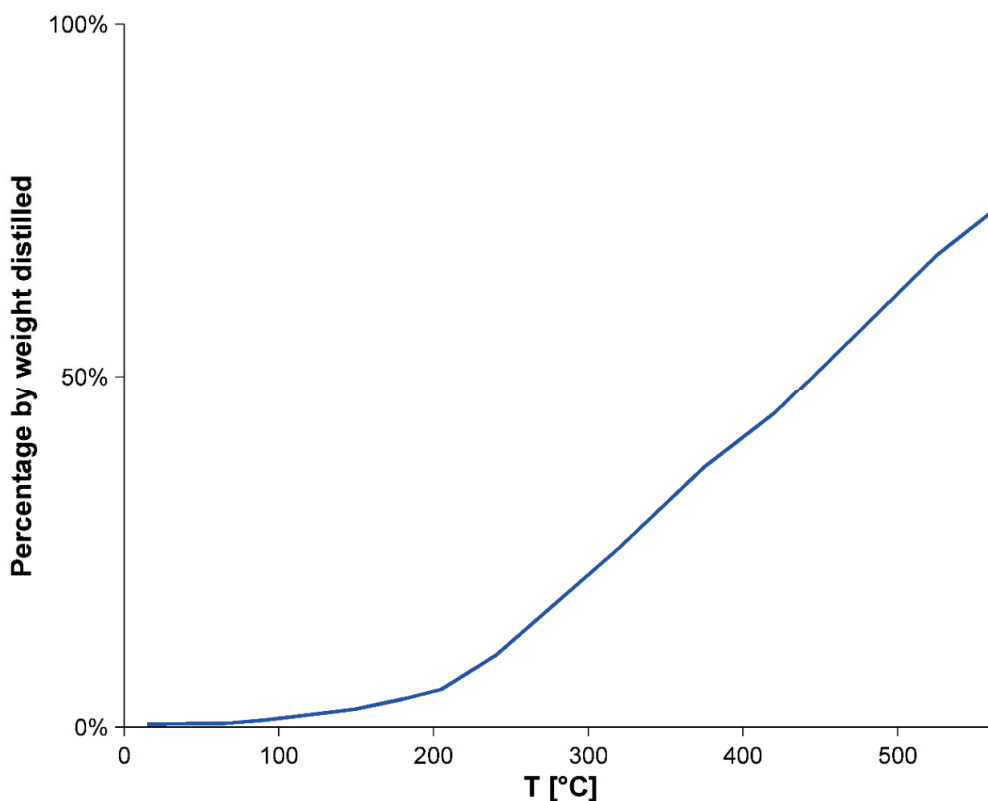


Figure 3-9. Distillation curve of Grane crude oil based on Statoil data.¹⁵⁴

3.5.2 Field sample collection

Oil slick samples (OS1, OS2, OS3, OS4, OS5, and OS6) were collected directly from the sea surface with 30 mL glass jars. One sheen sample was collected following the same protocol (sample OS7), whereas all other sheen samples were taken by sweeping glass wool on the sea surface (samples OS8, OS9, OS10, and OS11). Oil slick and oil sheen samples were preserved by the addition of 5 mL of dichloromethane (DCM) within 30 to 45 min after collection. They were then refrigerated in the dark until extractions, which were performed within 40 days at EPFL (Switzerland). Details about the analysis of slick and sheen samples by comprehensive two-dimensional gas chromatography coupled to a flame ionization detector (GC×GC–FID) are provided in Chapter 2.

Water column samples were taken using a grab sampler custom-built for this experiment (Figure 3-10). The grab sampler allows lowering of a closed 1 L bottle to ~1.5 m depth, opening of the bottle while at this depth in the water, and again closing of the bottle at the same depth. In this way, contamination by water at other depths or from the surface slick is avoided. This device for water column sampling below oil slicks is similar to a device used during oil spill field experiments about thirty years ago.¹²¹ Two samples were taken below the edge of the oil slick, and two samples were taken below the “middle” of the slick, ~20 h after the end of the oil release. 50 mL of DCM was added to water column samples within 30-45

min of collection. For field blanks, a different device was used: water was pumped through a plastic tube lowered in the water column at the desired depth (1.5 m or 8 m). The blanks reported were taken ~15 min after the end of the oil release at some distance from the oil slick.

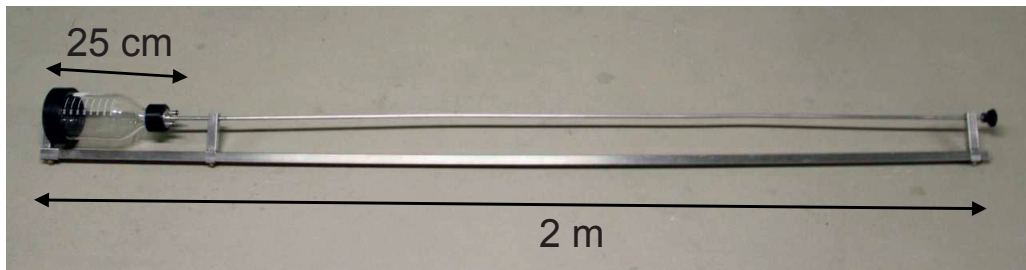


Figure 3-10. Grab sampler used for water column sample collection. About 25 cm of the top of the device (right of the figure) was held outside of the water during sampling, resulting in collection of water from ~1.5 m depth.

3.5.3 Concentrations of individual analyzed hydrocarbons in the water column and neat oil

Table 3-4. Concentrations for individual compounds in neat oil ($\mu\text{g g}^{-1}$), water column samples ($\mu\text{g L}^{-1}$), and field blanks ($\mu\text{g L}^{-1}$), as measured by GC-MS and GC-FID. Limit of quantification (LOQ) for water samples is also given ($\mu\text{g L}^{-1}$). Shown in bold face are the water column sample values considered significantly larger than field blank values; comparisons with model predictions are available for a selection of these compounds in Table 3-7. Some corrupted measurements (superimposition with unidentified signal) are not reported and are indicated by the letter "a". Values below LOQs are not reported and are indicated as "n.d."

Concentration	Neat oil (OSO)	"Middle" of slick footprint		"Edge" of slick footprint		Field blank 1.5 m	Field blank 8 m	LOQ
		WC1	WC2	WC3	WC4			
Benzene	470.41	n.d.	n.d.	n.d.	1.302	n.d.	n.d.	0.81
Toluene	344.68	<47.54	<27.87	<35.35	<97.75	n.d.	n.d.	6.9
<i>p + m</i> Xylene	87.66	n.d.	n.d.	n.d.	n.d.	n.d.	n.d.	1.667
Ethylbenzene	252.02	n.d.	n.d.	n.d.	n.d.	n.d.	n.d.	5.676
<i>o</i> - Xylene	87.98	n.d.	n.d.	n.d.	n.d.	n.d.	n.d.	11.007
Naphthalene	832.20	0.369	0.544	0.534	0.316	0.062	0.058	0.001
2-Methylnaphthalene	1184.27	0.105	a	0.353	0.109	n.d.	n.d.	0.001
1-Methylnaphthalene	834.41	0.070	a	0.222	0.072	n.d.	n.d.	0.001
2,6 Dimethylnaphthalene	1026.97	0.019	0.014	0.021	0.018	n.d.	n.d.	0.001
1,6 Dimethylnaphthalene	732.05	0.012	0.010	0.011	0.016	n.d.	n.d.	0.001
1,2 Dimethylnaphthalene	276.01	n.d.	n.d.	n.d.	n.d.	n.d.	n.d.	0.001
Acenaphthylene	5.26	0.002	0.003	0.005	0.004	n.d.	n.d.	0.001
Acenaphthene	16.60	0.006	0.004	0.033	0.004	n.d.	n.d.	0.001
Phenanthrene	338.18	0.059	0.109	0.109	0.063	n.d.	n.d.	0.001
2-Methylphenanthrene	295.11	n.d.	n.d.	n.d.	n.d.	n.d.	n.d.	0.002
1-Methylphenanthrene	232.16	n.d.	n.d.	n.d.	n.d.	n.d.	n.d.	0.001
Anthracene	13.07	n.d.	n.d.	n.d.	n.d.	n.d.	n.d.	0.002
2-Methylanthracene	8.54	n.d.	n.d.	n.d.	n.d.	n.d.	n.d.	0.003
Fluoranthene	8.91	n.d.	n.d.	n.d.	n.d.	n.d.	n.d.	0.004
Pyrene	16.81	n.d.	n.d.	n.d.	n.d.	n.d.	n.d.	0.004
Chrysene	10.49	n.d.	n.d.	n.d.	n.d.	n.d.	n.d.	0.009
6-Methylchrysene	17.13	n.d.	n.d.	n.d.	n.d.	n.d.	n.d.	0.009
Benzo[a]anthracene	126.65	n.d.	n.d.	n.d.	n.d.	n.d.	n.d.	0.007
Benzo[b]fluoranthene	25.89	n.d.	n.d.	n.d.	n.d.	n.d.	n.d.	0.018
Benzo[k]fluoranthene	0.00	n.d.	n.d.	n.d.	n.d.	n.d.	n.d.	0.007
Benzo[a]pyrene	35.93	n.d.	n.d.	n.d.	n.d.	n.d.	n.d.	0.016
Indeno[1,2,3,cd]pyrene	0.00	n.d.	n.d.	n.d.	n.d.	n.d.	n.d.	0.022
Dibenzo[a,h]anthracene	0.00	n.d.	n.d.	n.d.	n.d.	n.d.	n.d.	0.025
Benzo[g,h,i]perylene	8.91	n.d.	n.d.	n.d.	n.d.	n.d.	n.d.	0.017
<i>n</i> -Heptane	244.13	n.d.	n.d.	n.d.	n.d.	n.d.	n.d.	unknown
<i>n</i> -Octane	225.20	n.d.	1.052	0.436	1.131	0.710	n.d.	unknown
<i>n</i> -Nonane	76.16	n.d.	n.d.	0.034	0.088	n.d.	0.558	unknown
<i>n</i> -Decane	30.84	4.528	4.617	2.715	5.820	3.287	4.772	0.001
<i>n</i> -Undecane	74.16	0.752	2.141	1.375	1.326	1.283	1.106	0.001
<i>n</i> -Dodecane	311.62	1.961	1.426	0.927	1.716	1.117	2.170	0.002
<i>n</i> -Tetradecane	847.55	3.824	3.644	1.337	3.510	0.289	0.210	0.004
<i>n</i> -Hexadecane	905.23	1.166	2.348	1.942	0.411	n.d.	n.d.	0.015

<i>n</i> -Heptadecane	905.59	0.424	n.d.	1.251	n.d.	n.d.	n.d.	0.022
Pristane	623.80	0.206	n.d.	n.d.	n.d.	n.d.	n.d.	0.017
<i>n</i> -Octadecane	760.40	n.d.	n.d.	n.d.	n.d.	n.d.	n.d.	0.022
Phytane	463.88	n.d.	n.d.	n.d.	n.d.	n.d.	n.d.	0.023
<i>n</i> -Eicosane	628.99	0.108	0.080	0.084	n.d.	n.d.	n.d.	0.021
<i>n</i> -Docosane	513.99	1.956	3.659	0.643	0.989	n.d.	n.d.	0.025
<i>n</i> -Tetracosane	453.71	2.519	a	2.061	0.787	n.d.	n.d.	0.036
<i>n</i> -Hexacosane	398.47	0.934	2.874	0.526	0.486	n.d.	n.d.	0.047
<i>n</i> -Octacosane	283.32	0.741	n.d.	n.d.	n.d.	n.d.	n.d.	0.049
<i>n</i> -Triacontane	194.16	0.904	n.d.	n.d.	n.d.	n.d.	n.d.	0.038
<i>n</i> -Dotriacontane	99.08	0.712	n.d.	n.d.	n.d.	n.d.	n.d.	0.050
<i>n</i> -Tetratriacontane	113.46	0.319	n.d.	n.d.	n.d.	n.d.	n.d.	0.051
<i>n</i> -Hexatriacontane	47.61	n.d.	n.d.	n.d.	n.d.	n.d.	n.d.	0.070
<i>n</i> -Octatriacontane	33.50	n.d.	n.d.	n.d.	n.d.	n.d.	n.d.	0.104
<i>n</i> -Tetracontane	26.37	n.d.	n.d.	n.d.	n.d.	n.d.	n.d.	0.186

3.5.4 GC–FID and GC–MS analysis of water column samples and neat oil (by Birgit Würz and Lukas Wick)

3.5.4.1 Sample preparation

Polycyclic aromatic hydrocarbons (PAHs), n-C₈–n-C₁₀ and n-C₁₂–n-C₄₀. 50 mL of seawater sample were filled into pre-cleaned 70 mL bottles and spiked with 3 µL of a perdeuterated PAH-standard mix, consisting of: naphthalene-*d*₈ (36.61 mg L⁻¹), acenaphthalene-*d*₁₀ (34.62 mg L⁻¹), fluorene-*d*₁₀ (34.82 mg L⁻¹), phenanthrene-*d*₁₀ (31.61 mg L⁻¹), anthracene-*d*₁₀ (28.56 mg L⁻¹), fluoranthene-*d*₁₀ (27.59 mg L⁻¹), pyrene-*d*₁₀ (27.78 mg L⁻¹), chrysene-*d*₁₀ (2.12 mg L⁻¹), benzo[*a*]anthracene-*d*₁₂ (4.56 mg L⁻¹); the individual products were obtained from Dr. Ehrensdoerfer GmbH, Augsburg, Germany. 10 µL of HgCl₂ solution were also added, to reach a final concentration of 132 mg L⁻¹. The seawater samples were extracted with 1 mL of hexane (Lichrosolv, Merk Darmstadt Germany) for six hours on a horizontal shaker, the extract was dried with pre-cleaned, dry sodium sulfate, and acenaphthylene-*d*₈ was added as injection standard.

n-C₈–n-C₉. Immediately after sampling 10 mL of seawater sample was filled into pre-cleaned 20 mL bottles and directly afterwards spiked with 5 µL of a perdeuterated nonane-*d*₂₀ standard mixture (91.2 mg L⁻¹; Aldrich Chem. Co, USA, Milwaukee) and 2 µL of HgCl₂ solution to reach a final concentration of 132 mg L⁻¹. The seawater samples were extracted with 1 mL of hexane (Lichrosolv, Merk Darmstadt Germany) for 6 hours on a horizontal shaker, the extract was dried with pre-cleaned, dry sodium sulfate, and acenaphthylene-*d*₈ was added as injection standard.

Benzene, toluene, ethylbenzene, xylenes (BTEX), and n-C₇. 10 mL of seawater sample were filled into pre-cleaned 20 mL bottles and directly afterwards spiked with 2 µL of HgCl₂ solution to reach a final concentration of 132 mg L⁻¹.

3.5.4.2 Instrumental analysis

Headspace gas chromatography with flame ionization detector (GC–FID). The concentrations of the BTEX compounds and *n-C₇* were determined by headspace GC–FID (Hewlett Packard

6890 Series). The injection was automated using a headspace autosampler (Hewlett Packard 7694) with an oven temperature of 95 °C and an injection volume of 1 mL. A fused silica capillary column was used (Optima δ-3, 60 m length, 0.25 mm internal diameter (i.d.), 0.35 µm film thickness; Macherey-Nagel, Düren, Germany). The following temperature sequence was applied: 60 °C for 2 min, heat to 120 °C at a rate of 4 °C min⁻¹, followed by a second gradient up to 280 °C at a rate of 20 °C min⁻¹, and a subsequent cooling down to 60 °C. The FID was operated at 280 °C and helium was used as carrier gas under constant flow mode at 2.0 mL min⁻¹.

Gas chromatography with mass spectrum (GC-MS) analyses for PAHs and n-C₁₀-n-C₄₀ were performed using an HP 6890 Series GC (Palo Alto, California, USA), with a 20 m HP5MS capillary column (0.18 mm i.d. and 0.18 µm film thickness) and 1 m uncoated and deactivated HP retention gap (0.18 mm i.d.). This was connected to an Agilent 5973 MSD (Palo Alto, California, USA) operating in selected ion monitoring mode (SIM). Splitless injection of 1 µL sample was performed using an automatic HP 7683 Series injector (Palo Alto, California, USA) and a HP septumless PTV injector (Palo Alto, California, USA). The injector program was 80 °C for 0.02 min, followed by a ramp of 600 °C min⁻¹ to 300 °C which was held for 10 min. The oven temperature program was 50 °C for 2 min, followed by a ramp of 15 °C min⁻¹ to 300 °C which was held for 6.3 min. The analysis was run under constant flow mode at 1.0 mL min⁻¹, with helium as the carrier gas.

GC-MS analyses for n-C₈-n-C₉ were performed using an HP 6890 Series GC (Palo Alto, California, USA), with a 60 m Optima delta-3 capillary column (0.25 mm i.d. and 0.25 µm film thickness, Macherey-Nagel). This was connected to an Agilent 5973 MSD (Palo Alto, California, USA) operating in selected ion monitoring mode (SIM). Splitless injection of 0.5 µL sample was performed using an automatic HP 7683 Series injector (Palo Alto, California, USA) and a HP septumless PTV injector (Palo Alto, California, USA). The injector program was 70 °C for 0.01 min, 600 °C min⁻¹ to 250 °C which was held for 10 min. The oven temperature program was 70 °C for 2 min, 10 °C min⁻¹ to 180 °C and then 30 °C min⁻¹ to 250 °C which was held for 2 min. The analysis was run under constant flow mode at 1.0 mL min⁻¹, with helium as the carrier gas.

3.5.5 Mass transfers at interfaces: basis of Equation 3-1 and Equation 3-2 and similarity to other equations used in oil spill modeling

The mass flux $F_{A \rightarrow B}$ of a compound from phase *A* to phase *B* through an interface, which has units of mass time⁻¹ length⁻², may be approximated as:¹⁹⁷

$$F_{A \rightarrow B} = -v_{tot} \cdot \left(\frac{C_B}{K_{B/A}} - C_A \right)$$

Equation 3-20

where C_A and C_B are concentrations of the compound in the bulk phases A and B , respectively, $K_{B/A}$ is the equilibrium partition coefficient between phases B and A , and v_{tot} is the overall mass transfer velocity. v_{tot} can be separated into two contributions:

$$\frac{1}{v_{tot}} = \frac{1}{v_A} + \frac{1}{v_B \cdot K_{B/A}}$$

Equation 3-21

There are different interpretations of mass transfer velocities v_A and v_B .

Mass transfer at an interface between two phases is often described according to the “two-resistance” or “two-film” theory, initially presented by Lewis and Whitman ninety years ago.^{197,198} The underlying assumptions are that the transfer across the interface is fast (no resistance to phase transfer), and that diffusion through boundary layers (“films”) adjacent to the interface controls the rate of mass transfer.

For the two-film theory, which is used to derive Equation 3-1 and Equation 3-2, v_A can be described as:

$$v_A = \frac{D_A}{\delta_A}$$

Equation 3-22

where δ_A is the thickness of the film (boundary layer) in phase A , and D_A is the diffusion coefficient in phase A . An analogous relation holds for phase B .

If equation Equation 3-22 is introduced in Equation 3-20 (using Equation 3-21), one obtains the general form of Equation 3-1 and Equation 3-2:

$$F_{A \rightarrow B} = - \frac{1}{\left(\frac{\delta_A}{D_A} + \frac{\delta_B}{D_B K_{B/A}} \right)} \left(\frac{C_B}{K_{B/A}} - C_A \right)$$

Equation 3-23

The net mass transfer rate (mass time⁻¹) through the interface is given by:

$$\frac{dM}{dt} = S \cdot F_{A \rightarrow B}$$

Equation 3-24

where S is the surface area of the interface (length²).

It is worth noting that, regardless of the interpretation of v_{tot} , it is not inversely proportional to the surface of the interface. Therefore, contrary to the theory presented by Fingas,¹⁸⁹ the surface area (or alternatively, the thickness) of an oil slick (assumed a fixed volume) must play

a role in the mass loss rate of oil compounds due to evaporation. This arises from the basic structure of mass transfer fluxes and is independent of a diffusion limitation in either of the phases.

Equations used in the literature to describe the net mass rate of aqueous dissolution of hydrocarbons from oil slicks are either analogous to Equation 3-2^{148,149} or are variants of Equation 3-25:^{13,41,145,146,150,180}

$$\frac{dM_i}{dt} = S \cdot v_{i,diss} \cdot (e_i \cdot x_i \cdot C_{i,w}^{sat} - C_{i,w}) = S \cdot v_{i,diss} \cdot \left(e_i \cdot \frac{C_{i,oil}}{K_{i,oil/water}} - C_{i,w} \right)$$

Equation 3-25

where *diss* stands for “dissolution”, x_i is the mole fraction of compound *i* in the oil phase, $C_{i,w}^{sat}$ is the concentration of compound *i* in water at saturation, and e_i is the so called “solubility enhancement factor”. Values of e_i are compound class specific, reported to be 1.4 for alkanes and cycloalkanes and 2.2 for single-ring aromatic compounds.^{42,150} Neglecting this solubility enhancement factor, the formula we used to describe the net mass transfer rate of aqueous dissolution at the oil-water interface (Equation 3-2) is fully equivalent to Equation 3-25, provided that:

$$v_{i,diss} = \frac{1}{\frac{\delta_{oil}}{D_{i,oil}} + \frac{\delta_{water}}{D_{i,water} \cdot K_{i,water/oil}}}$$

Equation 3-26

Mackay and Leinonen^{42,150} reported a value of $2.36 \cdot 10^{-6} \text{ m s}^{-1}$ for $v_{i,diss}$ based on experimental data for toluene. $v_{i,diss}$ can alternatively be estimated with an empirical formula proposed by Riazi and Edalat:¹⁶

$$v_{i,diss} = \frac{4.18 \cdot 10^{-9} \cdot T^{0.67}}{V^{0.4} \cdot (S_0)^{0.1}}$$

Equation 3-27

where V is the molar volume of the oil at its normal boiling point in $\text{m}^3 \text{ mol}^{-1}$, $v_{i,diss}$ is in m s^{-1} , T is the temperature in kelvins, and S_0 is the initial surface area in m^2 .

We compared the overall mass transfer velocities given by Equation 3-27 to those given by equation Equation 3-26 for the conditions of our field experiment. For Equation 3-27, we estimated the molar volume at the boiling point using the Rackett equation as described by Bandara et al.,¹⁹⁹ using tabulated estimated or experimental critical properties and boiling point data.²⁰⁰ We interpreted the “initial surface area” as the oil slick surface area at the end of the oil release period (0.83 km^2). The values of $v_{i,diss}$ given by Equation 3-27 are in reasonable agreement with the ones of Equation 3-26 used in our model (Figure 3-11).

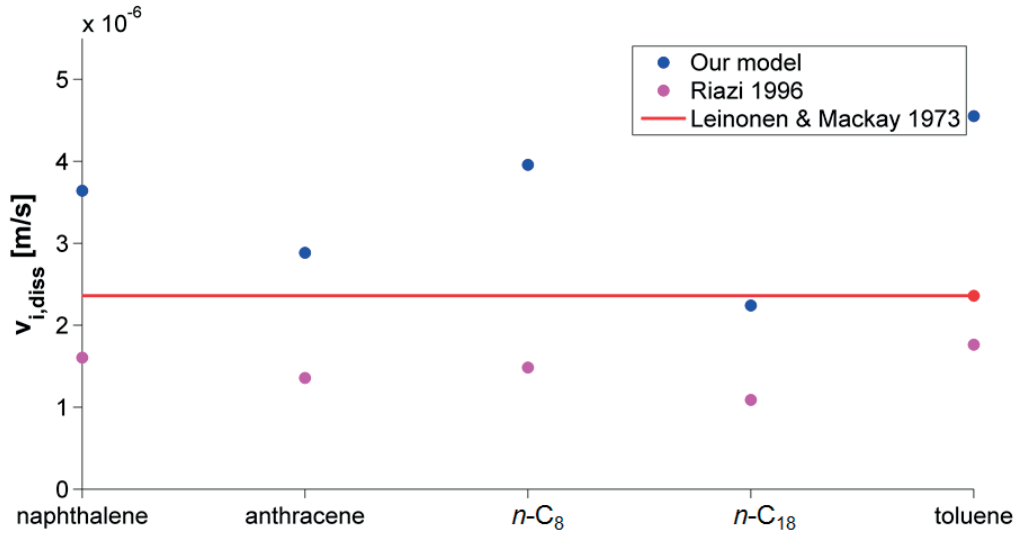


Figure 3-11. Overall mass transfer velocities for dissolution as used in our model compared to values used previously in the literature. Values for our model are shown for the time point 26 hours after the oil release, with wind speed = 4.4 m/s.

Several empirical formulas for the modeling of oil evaporation have been developed.¹⁸⁹ More physically grounded relations have also been presented, including formulas analogous to Equation 3-1¹⁴⁸ or to the following relation:^{41,42,151,153}

$$F_{i,oil}|_{evap} = v_{i,evap} \cdot \frac{(p_i - p_{i,air})}{R \cdot T} \cdot (\bar{V}_{oil} \cdot \rho)$$

Equation 3-28

where $F_{i,oil}|_{evap}$ is the mass flux of compound i lost through evaporation (mass time⁻¹ length⁻²), p_i is the vapor pressure of compound i , $p_{i,air}$ is the partial pressure of compound i in the bulk air phase, R is the molar gas constant, and T is the temperature in kelvins. The multiplication by the molar weight (i.e. the product of the density ρ_i and the molar volume \bar{V}_{oil}) allows the flux to be expressed in mass units instead of mole units. The atmosphere does not contain appreciable amounts of >C₅ hydrocarbon vapors, and we assumed a rapid air renewal, thus we dropped the $p_{i,air}$ term in Equation 3-28:

$$F_{i,oil}|_{evap} = v_{i,evap} \cdot \frac{p_i}{R \cdot T} \cdot (\bar{V}_{oil} \cdot \rho_i)$$

Equation 3-29

or:

$$F_{i,oil} \Big|_{evap} = v_{i,evap} \cdot (x_i \cdot \rho_i) \cdot \left(\frac{p_i^* \cdot \bar{V}_{oil}}{R \cdot T} \right)$$

Equation 3-30

where p_i^* is the pure compound vapor pressure. This can be rewritten as:

$$F_{i,oil} \Big|_{evap} = v_{i,evap} \cdot (C_i) \cdot (K_{i,air/oil})$$

Equation 3-31

Equation 3-31 is equivalent to Equation 3-1, where $v_{i,evap}$ was interpreted as:

$$v_{i,evap} = \frac{\frac{1}{K_{i,air/oil}}}{\frac{\delta_{oil}}{D_{i,oil}} + \frac{\delta_{air}}{D_{i,air} \cdot K_{i,air/oil}}}$$

Equation 3-32

3.5.6 Estimation of the vertical turbulent mixing coefficient in the water column, E .

The vertical turbulent mixing coefficient, E , used in Equation 3-8 was estimated as follows. We first estimated the heat budget balance as a function of time from hourly wind speed, relative humidity, and air and water temperature data obtained from the Royal Netherlands Meteorological Institute (KNMI) for the nearby K13 platform. In these calculations, we assumed a 100% cloudy situation, consistent with conditions observed. The net heat flux (H) can be written as:

$$H = H_S + H_A + H_W + H_E + H_C$$

Equation 3-33

where H_S is the shortwave absorption (light from the sun), H_A is the longwave absorption (gray body emission from atmosphere to water), H_W is the longwave emission (gray body emission from water), H_E is the heat flux through evaporation/condensation, and H_C is the convection heat.

We estimated the different terms of Equation 3-33 from textbook formulas,^{159,166,167} using tabulated data for properties of dry air, seawater,^{156,201} and a Matlab code by Felix Hebelers that implements a published procedure to estimate solar shortwave radiation as a function of latitude, date, and time.¹⁶⁸ To avoid lengthy presentation, the reader is referred to the cited literature for details. The estimated magnitudes of the different contributions to H are illustrated in Figure 3-12.

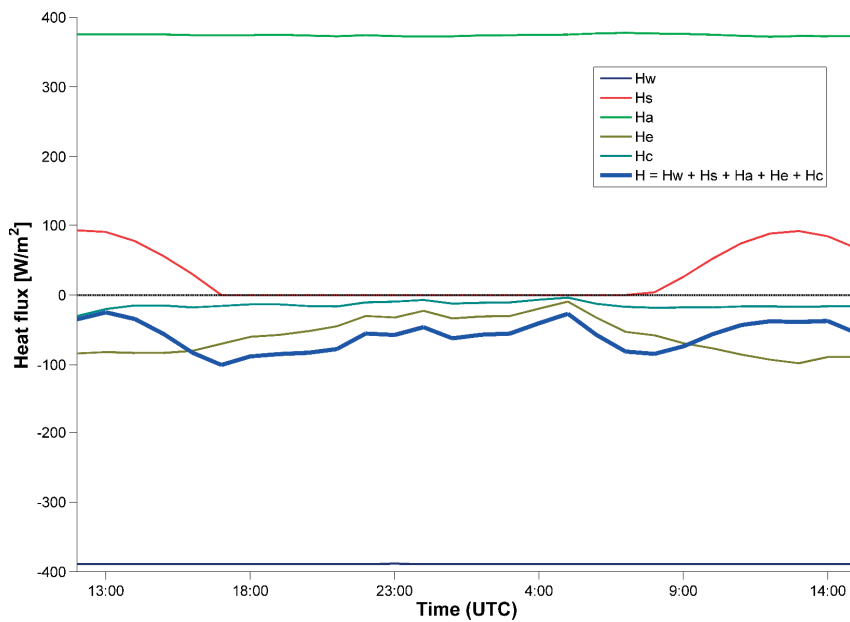


Figure 3-12. Heat fluxes as a function of time during the experiment, as estimated from data at K13 platform (53° 13' 4'' N, 3° 13' 13'' E). H_s is the shortwave absorption, H_A is the longwave absorption, H_W is the longwave emission, H_E is the heat flux through evaporation/condensation, H_C is the heat convection, and H is the net heat flux.

The estimated net heat flux was found to be from sea to atmosphere throughout the entire duration of the experiment (negative value of H in Figure 3-12). Therefore the water column (assumed as one single mixed layer) was always under a convection situation. In such a case, the turbulent mixing coefficient can be estimated with Equation 3-8, given in main text.¹⁵⁹

The estimated vertical turbulent mixing coefficient varied little throughout the experiment and we assumed a constant value of $0.22 \text{ m}^2 \text{ s}^{-1}$ (Figure 3-13).

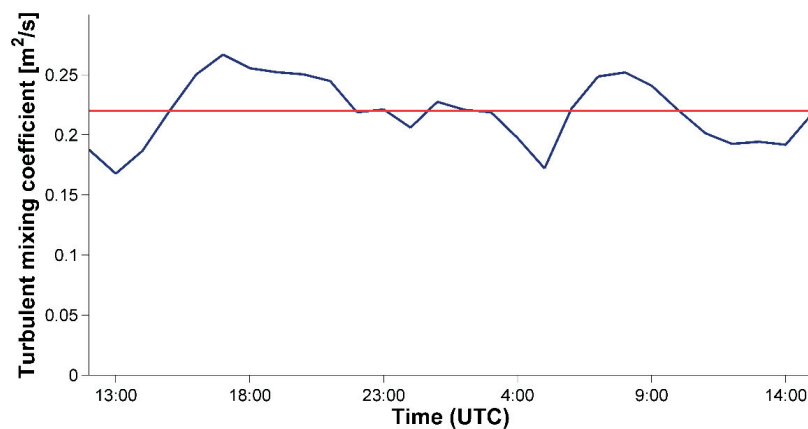


Figure 3-13. Estimated vertical turbulent mixing coefficient, E , as a function of time (blue line), and constant value assumed throughout the experiment (red line).

3.5.7 Estimation of hydrocarbon partitioning properties from GC×GC retention time information

Environmental partitioning properties were estimated for all hydrocarbons eluting in the $n\text{-C}_{10}\text{-}n\text{-C}_{24}$ range of the GC×GC chromatogram, based on GC×GC retention indices. The reader is referred to previous work for a complete description of the method.³⁹ In short, GC×GC retention times were transformed into two-dimensional retention indices. Then, different partitioning properties can be estimated from the calculated retention indices using formulas of the type:

$$P_{xy,i} = a_{xy} \cdot I_{1,i} + b_{xy} \cdot I_{2,i} + c_{xy}$$

Equation 3-34

where $I_{1,i}$ is the GC×GC first dimension retention index of solute i , $I_{2,i}$ is the GC×GC second dimension retention index of solute i , and a_{xy} , b_{xy} , and c_{xy} are fitted coefficients that are specific to the property estimated, P_{xy} . Values of the coefficients a_{xy} , b_{xy} , and c_{xy} corresponding to the GC×GC method used in this study are given in Table 3-5. Values for the coefficients for the boiling point temperature were obtained in the same way as for other properties,³⁹ based on a calibration set of literature data.²⁰⁰ For the 25 compounds used to calibrate the coefficients for boiling point prediction, the mean absolute error in the regression according to Equation 3-34 was found to be 11.2 °C.

Table 3-5. Coefficients to Equation 3-34.¹

Property (units)	a_{xy}	b_{xy}	c_{xy}
$\log C_w$ (mol L ⁻¹)	-0.0177	0.0135	-2.28
$\log K_{aw}$ (-)	0.0135	-0.0138	2.58
$\log p_L$ (Pa)	-0.00458	–	6.74
ΔH_{vap} (kJ mol ⁻¹)	0.0664	-0.0253	12.9
MW (g mol ⁻¹)	0.299	-0.174	30.5
T_b (K)	0.157	–	305

¹ C_w is the aqueous solubility in fresh water, K_{aw} is the air-water partition coefficient, p_L is the (hypothetical) pure component liquid vapor pressure, ΔH_{vap} is the enthalpy of vaporization, MW is the molar mass, T_b is the (atmospheric) boiling point. All reported properties (except T_b) are estimated at 25 °C and 1 atmosphere.

3.5.8 Comparisons of different models for the evaporation mass loss of the oil slick during the field experiment

Fingas (2004) developed two empirical formulas to predict the percentage of mass lost due to evaporation for whole oil:¹⁸⁸

$$\% \text{ evaporated} = (0.165 \cdot (\% D) + 0.045 \cdot (T - 15)) \cdot \ln(t)$$

Equation 3-35

$$\% \text{ evaporated} = (0.0254 \cdot (\% D) + 0.01 \cdot (T - 15)) \cdot \sqrt{t}$$

Equation 3-36

where the percentage evaporated is a function of time t , in minutes, $\%D$ is the percentage of oil mass distilled at 180 °C (here, 3.96%),¹⁵⁴ and T is temperature in °C. The natural logarithm dependence (Equation 3-35) applied for the majority of the oils for which results are reported in Fingas's article, whereas the square root dependence (Equation 3-36) was found to apply only to a limited number of oils, including diesel and Bunker C Light.

We also downloaded the ADIOS oil spill weathering model from the US National Oceanic and Atmospheric Administration (NOAA) web site (version 2.0.1).²⁵ ADIOS includes consideration of the influence of oil slick thickness on evaporation mass loss rate. In the ADIOS model, we could not provide an input of oil slick surface area, therefore all computations were performed with the oil slick spreading and surface area as estimated within ADIOS. Figure 3-14 shows the ADIOS prediction for percentage of Grane crude oil evaporated during the field experiment.

Equation 3-35 and Equation 3-36 predict that 5.2 and 4.4% of the Grane crude oil would be evaporated at the end of our field experiment. ADIOS predicts 13.7% (Figure 3-14). Our model predicts 25.7%.

Under the assumption that evaporation removes hydrocarbons from the oil progressively in order of increasing vapor pressure,^{15,39,79} we can estimate the portion of the GC×GC–FID chromatogram of the neat oil that is predicted to be removed by the Fingas and ADIOS models, thus enabling a comparison to our model and also to the observed sample data (Figure 3-3j in main text).

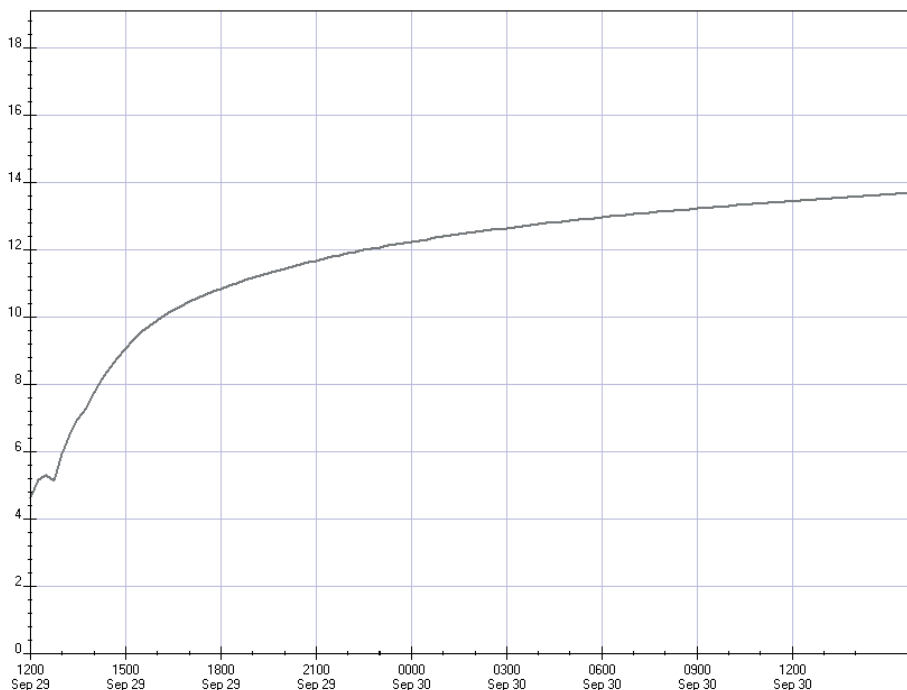


Figure 3-14. Evaporated mass percentage of Grane crude oil predicted by the ADIOS model for our field experiment.

3.5.9 Measured mass losses of individual compounds based on GC×GC–FID data for oil slick and oil sheen samples

Table 3-6. Percentage mass losses for individual compounds, determined based on GC×GC–FID chromatograms, according to the procedure described in the main text. Sheen samples and one oil slick sample (OS3) exhibited *n*-alkane peaks at early first dimension elution times. These peaks are supposed of biogenic origin, as suspected from the predominance of *n*-alkanes with even carbon number compared to odd-carbon-numbered *n*-alkanes,²⁰² which is not consistent with Grane crude oil composition. The peaks suspected to be mostly of biogenic origin are displayed in gray in the table, but some impact of biogenic material on other *n*-alkane peaks is probable, inferred from oscillations of mass loss estimates from odd to even carbon numbers. Cells labeled “>95%” correspond to peaks not detected by GC Image inverted watershed algorithm (peaks not present in most cases, or at very low residual concentrations).

Compound	OS1	OS2	OS3	OS4	OS5	OS6	OS7	OS8	OS9	OS10	OS11
naphthalene	31%	51%	>95%	>95%	>95%	>95%	96%	>95%	>95%	>95%	>95%
2-methylnaphthalene	-15%	-21%	>95%	>95%	>95%	>95%	93%	>95%	>95%	>95%	>95%
1-methylnaphthalene	-11%	-19%	>95%	>95%	>95%	>95%	92%	>95%	>95%	>95%	>95%
biphenyl	-5%	-21%	>95%	>95%	>95%	>95%	93%	>95%	>95%	>95%	>95%
fluorene	-27%	-33%	>95%	60%	>95%	>95%	84%	>95%	>95%	>95%	>95%
<i>n</i> -C ₁₀	90%	74%	-101%	>95%	98%	>95%	-82%	>95%	19%	1%	>95%
<i>n</i> -C ₁₁	64%	46%	43%	>95%	>95%	>95%	28%	43%	71%	69%	-121%
<i>n</i> -C ₁₂	12%	-4%	-28%	97%	95%	99%	-61%	-28%	-16%	-62%	-1048%
<i>n</i> -C ₁₃	-21%	-25%	85%	97%	98%	99%	89%	85%	97%	97%	78%
<i>n</i> -C ₁₄	-23%	-28%	72%	86%	98%	99%	61%	72%	75%	65%	-138%
<i>n</i> -C ₁₅	-16%	-16%	97%	57%	97%	96%	85%	97%	98%	97%	94%
<i>n</i> -C ₁₆	-20%	-16%	91%	21%	84%	84%	63%	91%	93%	73%	44%
<i>n</i> -C ₁₇	-10%	-8%	97%	6%	55%	57%	43%	97%	84%	52%	77%
<i>n</i> -C ₁₈	-8%	-4%	85%	-4%	22%	30%	19%	85%	43%	25%	30%
<i>n</i> -C ₁₉	-3%	-1%	61%	-4%	2%	16%	7%	61%	13%	21%	33%
<i>n</i> -C ₂₀	-8%	2%	26%	-1%	-5%	8%	1%	26%	-4%	13%	8%
<i>n</i> -C ₂₁	19%	12%	36%	-2%	17%	29%	6%	36%	22%	37%	35%
<i>n</i> -C ₂₂	-2%	8%	9%	1%	-3%	10%	2%	9%	-8%	14%	19%
<i>n</i> -C ₂₃	10%	9%	11%	5%	-3%	18%	6%	11%	4%	20%	10%
<i>n</i> -C ₂₄	6%	12%	9%	9%	5%	14%	8%	9%	2%	15%	10%
<i>n</i> -C ₂₅	1%	12%	13%	10%	7%	8%	-1%	13%	2%	26%	15%
<i>n</i> -C ₂₆	10%	12%	17%	9%	8%	6%	2%	17%	12%	26%	18%
<i>n</i> -C ₂₇	4%	10%	12%	10%	7%	6%	7%	12%	6%	13%	12%
<i>n</i> -C ₂₈	16%	14%	9%	13%	15%	14%	14%	9%	13%	11%	11%
<i>n</i> -C ₂₉	-5%	-3%	-3%	-2%	0%	-1%	-5%	-3%	-4%	-9%	-1%
<i>n</i> -C ₃₀	-2%	-3%	-2%	0%	-5%	-2%	0%	-2%	-1%	-4%	-2%
<i>n</i> -C ₃₁	-9%	-8%	-4%	-9%	-11%	-8%	-6%	-4%	-7%	-2%	-8%
<i>n</i> -C ₃₂	-13%	-13%	-7%	-12%	-12%	-17%	-14%	-7%	-10%	0%	-10%

3.5.10 Comparison of model predictions and measured hydrocarbon concentrations in the water column

Table 3-7. Model-predicted and mean observed water column concentrations 20 h after the end of the oil release, and implied mass fraction apportioned to the water column, for several compounds. Mass fraction apportioned for samples corresponds to the roughly estimated fraction of the total contaminant mass that has been transferred to the water column under the hypothesis of a constant concentration profile throughout the 42 m water depth. Mean composition of blanks taken outside of the oil slick footprint 15 min after the end of the oil release is shown for comparison. Concentrations below limit of quantification (LOQ) are indicated by “n.d.”, and LOQs are also reported.

Compound name		Model	Observed water column (mean value) ^d	Field blanks (mean value)	Limit of Quantification (LOQ)
Toluene ^a	Concentration, µg/L	0.00019	52	n.d.	6.9
	Fraction apportioned	0.04	11000		
Naphthalene ^a	Concentration, µg/L	0.0012	0.44	0.060	0.0006
	Fraction apportioned	0.11	35		
2-Methylnaphthalene ^a	Concentration, µg/L	0.0017	0.19	n.d.	0.0009
	Fraction apportioned	0.11	12		
1-Methylnaphthalene ^a	Concentration, µg/L	0.0015	0.12	n.d.	0.0010
	Fraction apportioned	0.14	11		
2,6-Dimethylnaphthalene ^b	Concentration, µg/L	0.00067	0.018	n.d.	0.0013
	Fraction apportioned	0.05	1.3		
1,6-Dimethylnaphthalene ^c	Concentration, µg/L	0.00040	0.012	n.d.	0.0014
	Fraction apportioned	0.04	1.1		
Acenaphthylene ^a	Concentration, µg/L	0.000013	0.0034	n.d.	0.0009
	Fraction apportioned	0.19	42		
Acenaphthene ^a	Concentration, µg/L	0.000076	0.012	n.d.	0.0013
	Fraction apportioned	0.35	52		
Phenanthrene ^a	Concentration, µg/L	0.0023	0.085	n.d.	0.0011
	Fraction apportioned	0.51	19		

^a Partitioning properties from Schwarzenbach et al.¹⁵⁶

^b Partitioning properties from Mackay et al.¹⁷²

^c Properties of 1,6-dimethylnaphthalene assumed identical to that of 2,6-dimethylnaphthalene

^d Observed water column concentrations are lower than solubility at saturation for all compounds listed in the Table.

3.5.11 Effect of temperature on oil mass fractions apportioned to air and water

Enthalpy change of phase transfer from liquid (oil) phase to gas phase ($\Delta H_{i,vap}$) is higher than the enthalpy change of phase transfer from pure liquid phase to water ($\Delta H_{i,oil \rightarrow water}$) for most compounds (Table 3-8).

Table 3-8. Enthalpy change for phase transfer from the pure liquid phase to gas phase ($\Delta H_{i,vap}$) and for phase transfer from pure liquid phase to water ($\Delta H_{i,oil \rightarrow water}$), based on literature data^{39,156}

Compound	$\Delta H_{i,vap}$ [kJ mol ⁻¹]	$\Delta H_{i,oil \rightarrow water}$ [kJ mol ⁻¹]
naphthalene	56.0	12
phenanthrene	74.4	46
anthracene	83.1 ^a	43
<i>n</i> -C ₆	28.9	~0
benzene	30.7	4

^a estimated from the hypothetical pure liquid vapor pressure.¹⁵⁶

The formulas used in the model for temperature corrections from a reference temperature (T_{ref} , 298.15 K) to another temperature (T , in K) have been listed in the main text. All other variables used in the model were assumed independent of temperature.

Solubility may also be corrected for temperature according to:

$$C_{i,w}^{sat}(T) = C_{i,w}^{sat}(T_{ref}) \cdot e^{\frac{\Delta H_{i,oil \rightarrow water}}{R} \left(\frac{1}{T_{ref}} - \frac{1}{T} \right)}$$

Equation 3-37

where $C_{i,w}^{sat}$ is the solubility, and $\Delta H_{i,oil \rightarrow water}$ is the enthalpy change of phase transfer from pure liquid phase to water.

The temperature dependence of mass apportionment to air and water can be evaluated (Figure 3-15). Evaporation extent is found to be highly dependent on temperature. Conclusions regarding effect of temperature on dissolution extent should be considered as approximate, as explained below.

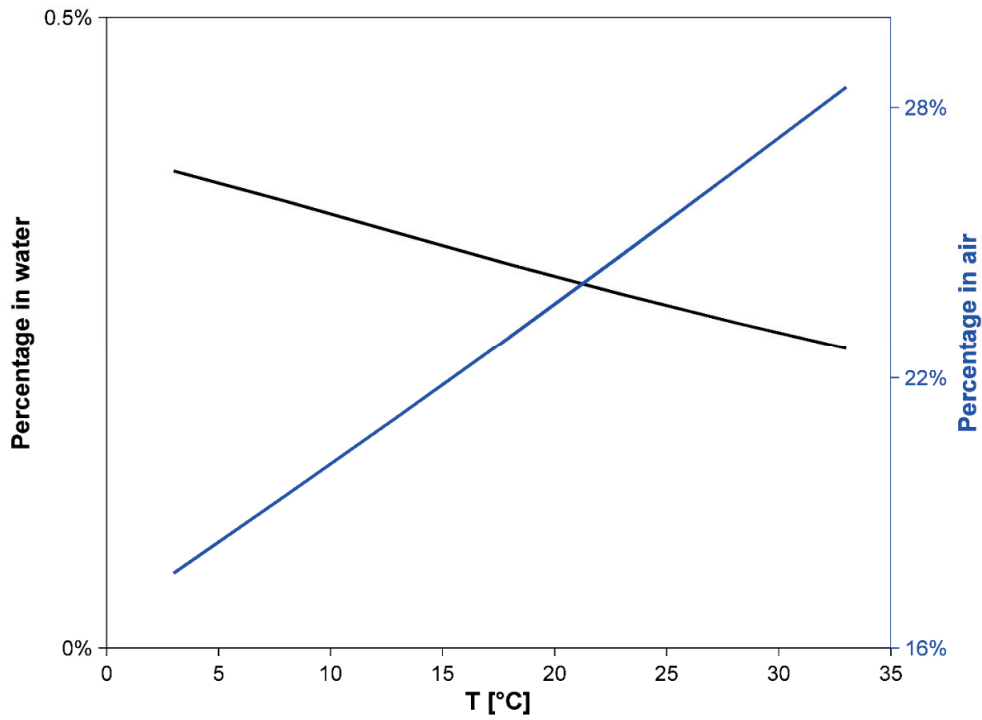


Figure 3-15. Fraction of total oil mass apportioned to air (blue line, right axis) and water (black line, left axis) as a function of water temperature, according to the model.

The temperature-dependence of aqueous solubility was not included in the mass transfer model. The impact of temperature on mass transfer to air and water can be evaluated by considering the quantities $v_{i, \text{evap}} \cdot K_{i, \text{air}/\text{oil}}$ and $v_{i, \text{diss}} \cdot K_{i, \text{water}/\text{oil}}$ (as defined in section 3.5.5, Equation 3-26 and Equation 3-32). The ratio of these two quantities is indicative of the relative importance of evaporation and dissolution, neglecting the build-up of non-zero concentrations in water or air. Results highlight the importance of including a temperature correction for aqueous solubility for PAHs (Table 3-9).

Table 3-9. Model ratio $\frac{v_{i, \text{evap}} \cdot K_{i, \text{air} / \text{oil}}}{v_{i, \text{diss}} \cdot K_{i, \text{water} / \text{oil}}}$ at several different temperatures, both with and without the

inclusion of a temperature correction for aqueous solubility ($C_w^{\text{sat}}(T)$ versus $C_w^{\text{sat}}(25\text{ °C})$). Enthalpies of phase transfer to water (dilute) were taken as 12 kJ/mol (naphthalene), 46 kJ/mol (phenanthrene), and 43 kJ/mol (anthracene).¹⁵⁶

T [°C]	$\frac{v_{i, \text{evap}} \cdot K_{i, \text{air} / \text{oil}}}{v_{i, \text{diss}} \cdot K_{i, \text{water} / \text{oil}}}$					
	naphthalene		phenanthrene		anthracene	
	variable $C_w^{\text{sat}}(T)$	constant $C_w^{\text{sat}}(25\text{ °C})$	variable $C_w^{\text{sat}}(T)$	constant $C_w^{\text{sat}}(25\text{ °C})$	variable $C_w^{\text{sat}}(T)$	constant $C_w^{\text{sat}}(25\text{ °C})$
3	6.23	4.24	0.82	0.19	0.63	0.16
8	7.44	5.55	0.87	0.28	0.73	0.26
13	8.89	7.26	0.92	0.42	0.85	0.41
18	10.65	9.48	0.98	0.63	0.99	0.65
23	12.74	12.33	1.06	0.93	1.15	1.02
28	15.23	15.98	1.14	1.37	1.34	1.59
33	18.17	20.62	1.22	1.99	1.55	2.45

3.5.12 Mass loss tables for oil sheen samples

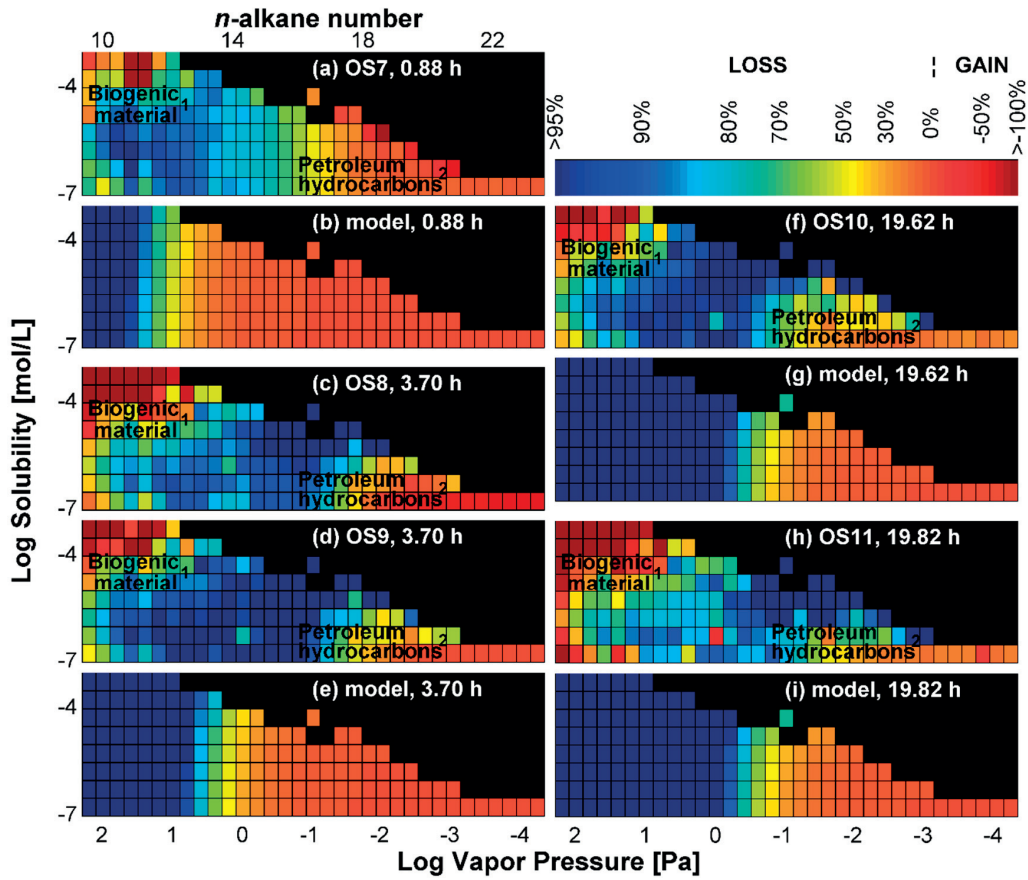


Figure 3-16. Oil sheen sample MLTs compared to modeled oil slick MLTs at corresponding times. Time after the end of the oil release is indicated for each MLT. Dark cells correspond to properties not covered by the chromatogram or to cells containing mostly noise, defined as those containing less than 0.02% of total signal contained in the part of the chromatogram covered by the MLTs, for neat oil. The color bar indicates the mass loss scale (as % mass loss); negative values represent mass gains.

¹ Material in the upper left region of sheen sample MLTs is thought to be of biogenic origin.

² Signal in the lower right region corresponds to petroleum hydrocarbons.

3.5.13 Effect of wind speed on oil mass fractions apportioned to air and water

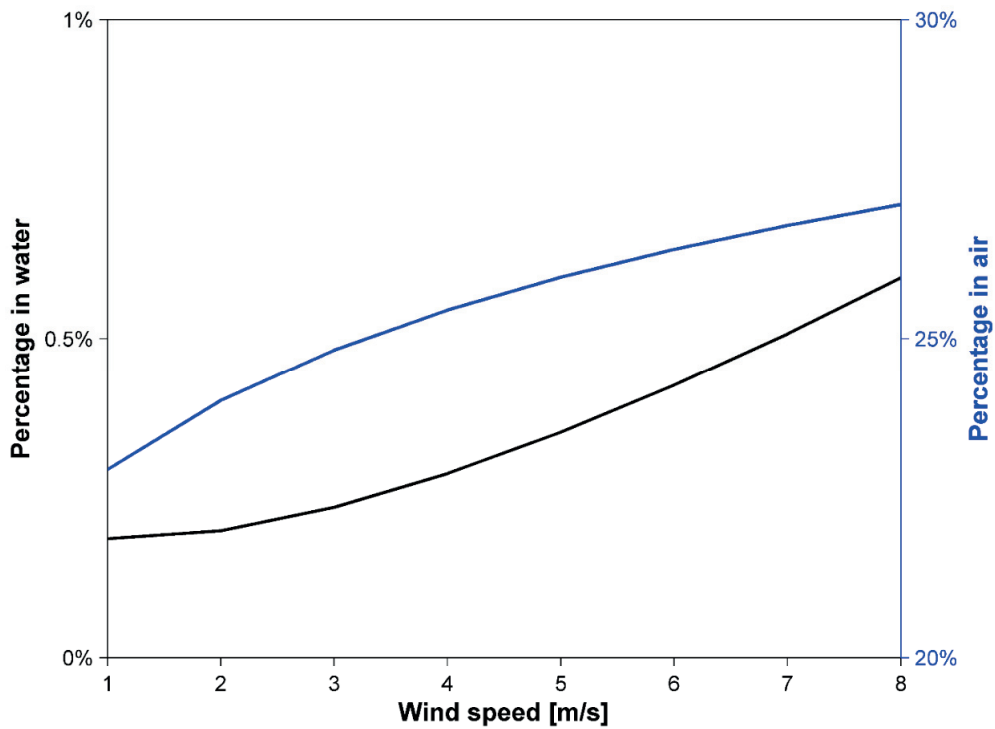


Figure 3-17. Fraction of total oil mass apportioned to air (blue line, right axis) and water (black line, left axis) as a function of wind speed, according to the model. This assumes a constant turbulent vertical mixing coefficient of the water column, representative of the convection situation during the experiment. The wind speed was thus assumed to impact only air and water boundary layer thicknesses for this experiment. At wind speed above 8 m s^{-1} , oil dispersion in the water column is expected to become important, and this process was not considered explicitly in the model.

3.5.14 Modeled evolution of oil slick thickness during the experiment

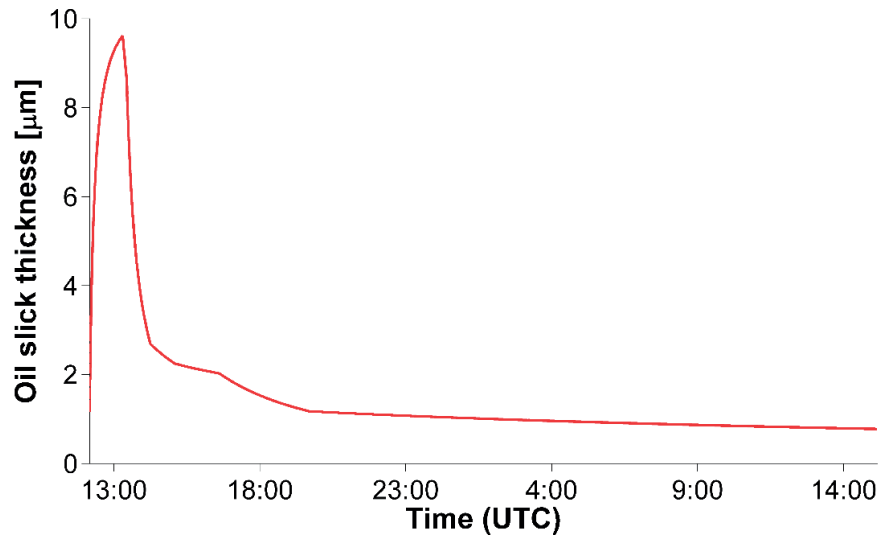


Figure 3-18. Evolution of oil slick thickness as predicted by the model.

Chapter 4 Gas-liquid-water partitioning and fluid properties of petroleum mixtures under pressure: Implications for deep-sea blowouts

Submitted to: Environmental Science & Technology on September 21, 2015.

Authors: Jonas Gros, Christopher M. Reddy, Robert K. Nelson, Scott A. Socolofsky, and J. Samuel Arey.

Contributions: This chapter was prepared principally by me. I wrote the Matlab codes used for all modeling calculations. Experimental and laboratory data come from previous work by others (especially Christopher Reddy, Bob Nelson, and co-workers), except for the GC×GC analysis, specially performed by Bob Nelson. Samuel Arey provided guidance to me, and had a prominent participation in text writing and editing.

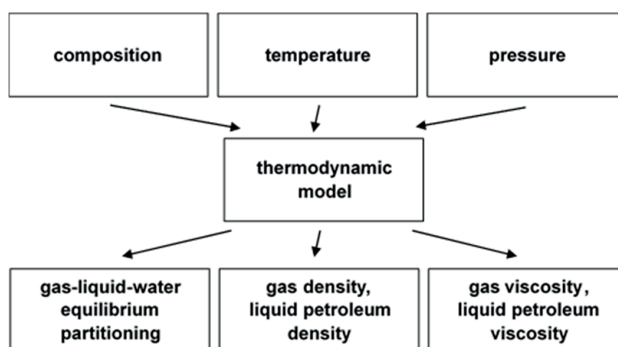


Figure 4-1. Schematic depiction of the thermodynamic model.

Reproduced/adapted with permission from Environmental Science & Technology, submitted for publication. Unpublished work copyright 2015 American Chemical Society.

4.1 Abstract

With the expansion of offshore petroleum exploration and extraction activities, validated models are needed to simulate the behaviors of petroleum compounds released in deep (>100 m) waters. We present a thermodynamic model of the gas-liquid-water partitioning, densities, and viscosities of petroleum mixtures with varying composition, pressure, and temperature, based on the Peng-Robinson equation-of-state and the modified Henry's law (Krychevsky-Kasarnovsky equation). We define pseudo-components based on comprehensive two-dimensional gas chromatography (GC×GC) measurements, which enable the modeling of aqueous partitioning for >*n*-C₈ compound fractions not quantified individually. The resulting thermodynamic model is tested against available laboratory data on petroleum liquid densities, gas/liquid volume fractions, and liquid viscosities. The model is applied to the Macondo reservoir fluid released during the *Deepwater Horizon* disaster, represented with 279–280 components including 131–132 individual compounds. We find that the emitted petroleum mixture was ~29–44% gas and ~56–71% liquid, after cooling to local conditions near the Macondo well (~153 atm and 4.3 °C). These high pressure conditions dramatically increase the aqueous dissolution of petroleum hydrocarbons and also modifies the buoyancies of gas bubbles and liquid droplets. The gas-liquid partitioning predicted by our thermodynamic model also affects published flow rate estimates of dead oil from the broken Macondo well stub, with some uncertainty arising from the uncertainty regarding the composition of the Macondo reservoir fluid.

4.2 Introduction

In Chapter 3 we evaluated the partitioning of petroleum hydrocarbons following a sea-surface release. In this chapter and in Chapter 5, we will investigate how specific conditions, especially the tremendous pressure, affect petroleum compound partitioning during a deep-water release.

The 2010 *Deepwater Horizon* disaster revealed the limits of pre-existing knowledge on the behavior of petroleum fluids under extreme, deep-sea conditions. *Deepwater Horizon* was likely the largest accidental marine oil spill in history, emitting over a three-month period more than half a million tonnes of total petroleum-compound mass^{8–10} from the *Macondo* well into the Gulf of Mexico at 1524 m depth²⁰³ (emission depth once the remains of the riser had been cut). During this event, water column measurements revealed the presence at ~1100 m depth of a plume of mostly dissolved⁸ hydrocarbons that extended up to 27 km horizontally from the emission point.^{31,32} This deep-water hydrocarbon plume contained reported total BTEX (benzene, toluene, ethylbenzene, *o*-, *m*-, and *p*-xylenes) concentrations of up to 77.2 μg L⁻¹.⁸ By comparison, during a sea-surface oil spill, evaporation processes compete with aqueous dissolution to remove light hydrocarbon compounds, such as these toxic aromatic hydrocarbons, from the floating oil (Chapter 3).^{13,39–42} However, during the *Deepwater Horizon* release, evaporation was suppressed during ascent of petroleum fluids in the water column, and this dramatically increased the fraction of soluble hydrocarbon mass that was transferred to the water column, relative to a sea-surface spill.^{8,40,75} As a result, the deep

marine ecosystem experienced substantially heightened toxic hydrocarbon exposures.⁸ Finally, 0.5–14.4%^{204,205} of the Macondo dead oil emitted in the environment was discovered to have deposited on the deep sea floor (900–1600 m depth).²⁰⁵ Here, we use the terms *dead oil* to refer to the liquid petroleum phase at atmospheric conditions, and *live oil* or simply *liquid* to refer to the liquid petroleum phase under local, higher pressure conditions.²⁰⁶ The unusual phenomena described above were controlled by changes in the pressure- and temperature-dependent mechanical properties (density, viscosity) of the ascending Macondo reservoir fluid (MRF), as well as chemical repartitioning among the associated gas-liquid-water phases, under deep-sea conditions.

Unlike a sea-surface spill, the *Deepwater Horizon* disaster also generated hydrates, which can usually occur at water depths of >500 m. Hydrates are buoyant solid materials composed of light compounds ($\leq C_5$ hydrocarbons, CO_2) entrapped in crystal-like structures of water molecules. Hydrate formation contributed to early failures to contain the release.³⁸ Thin⁴⁶ hydrate shells can also form around petroleum gas bubbles or liquid droplets,^{47–51} and this influences mass transfer rates of hydrocarbons dissolving into the water column.

As offshore petroleum exploration and extraction activities expand,^{1,38,207,208} validated models are needed to simulate the unusual phenomena affecting petroleum mixtures released under deep-sea (>100 m depth) conditions. Equation-of-state (EOS) models are used widely to estimate the gas-liquid equilibrium phase distribution of petroleum mixtures with respect to varying pressure, temperature, and composition.^{177,206} In practice, petroleum compounds usually are grouped into approximately 10 (pseudo-)components, conventionally based on distillation cut data.^{177,206} An EOS model has been developed and tuned for the MRF by Aaron A. Zick, an independent petroleum engineer summoned by the United States Department of Justice.²⁰⁹ However the 11 components of the Zick model are not designed to distinguish differences in aqueous solubility. For example, benzene is grouped with *n*-hexane, yet these compounds have aqueous solubilities that differ by a factor of 151.¹⁵⁶ Due to this large difference in solubilities, benzene and *n*-hexane experienced very different trajectories during the *Deepwater Horizon* release.^{8,75} This illustrates how conventional EOS models for petroleum mixtures are inappropriate and inaccurate for modeling aqueous dissolution of hydrocarbons in the deep sea.

To investigate this problem, de Hemptinne and coworkers^{210–213} studied the aqueous dissolution of hydrocarbons under oil reservoir conditions. They determined experimentally the equilibrium partitioning between a live oil and water at 25 MPa and 100 °C, and they modeled this system using 19 components (including several saturated and aromatic hydrocarbons, N_2 , and CO_2) defined so as to capture differences in both volatilities and aqueous solubilities of the mixture components.²¹⁰ They showed that the *modified Henry's law* (Krychevsky-Kasarnovsky equation)^{214,215} can accurately model aqueous dissolution at high pressures, in conjunction with use of the Peng-Robinson EOS²¹⁶ (PR EOS) to describe the hydrocarbon-rich phases.²¹¹ However their model considered only highly water-soluble components ($\leq C_6$ alkanes, single-ring aromatics, CO_2 , and N_2) for which Henry's law constant data are available.

In particular, the moderately water-soluble hydrocarbons in the $n\text{-C}_8\text{--}n\text{-C}_{20}$ range are challenging to simulate, since this oil fraction cannot be fully characterized on an individual-compound basis.

Comprehensive two-dimensional gas chromatography (GC×GC) can fill this data gap. GC×GC uses two serially-joined columns to separate thousands of hydrocarbons in the $n\text{-C}_8\text{--}n\text{-C}_{45}$ range of dead oils.^{55,217} Structurally related compounds are grouped together in different regions of the GC×GC chromatogram (Figure 4-2a,b).^{65,217–221} Additionally, GC×GC can separate compounds approximately according to vapor pressure and air-water partition coefficient (Figure 4-3),^{39,72} which makes it a natural approach for defining pseudo-components for gas-liquid-water equilibrium calculations.^{15,40,55,73,74} Consequently, GC×GC has been used previously to define pseudo-components that were successfully applied to the modeling of simultaneous evaporation and aqueous dissolution of hydrocarbons from sea-surface oil slicks (as in Chapter 3).^{14,40,74}

In the present work, we present a thermodynamic model that is designed to simulate MRF properties and gas-liquid-water equilibrium partitioning in the deep sea, based on extensively detailed compositional data made available in previous reports. We also introduce a new method to generate pseudo-components suitable for aqueous dissolution modeling of water-soluble hydrocarbons in the $n\text{-C}_8\text{--}n\text{-C}_{26}$ range, based on GC×GC–FID data. For compounds for which model input properties are unavailable, validated estimation methods are applied. The proposed thermodynamic model is then further validated with several experimental and model data sets, including data recently made public through court documents from *United States of America versus BP Exploration & Production, Inc., et al.*²²² Finally, we explore the influence of pressure, composition, and temperature on the partitioning and fluid properties that controlled the transport and redistribution of petroleum compounds emitted from the Macondo well during the 2010 *Deepwater Horizon* disaster.

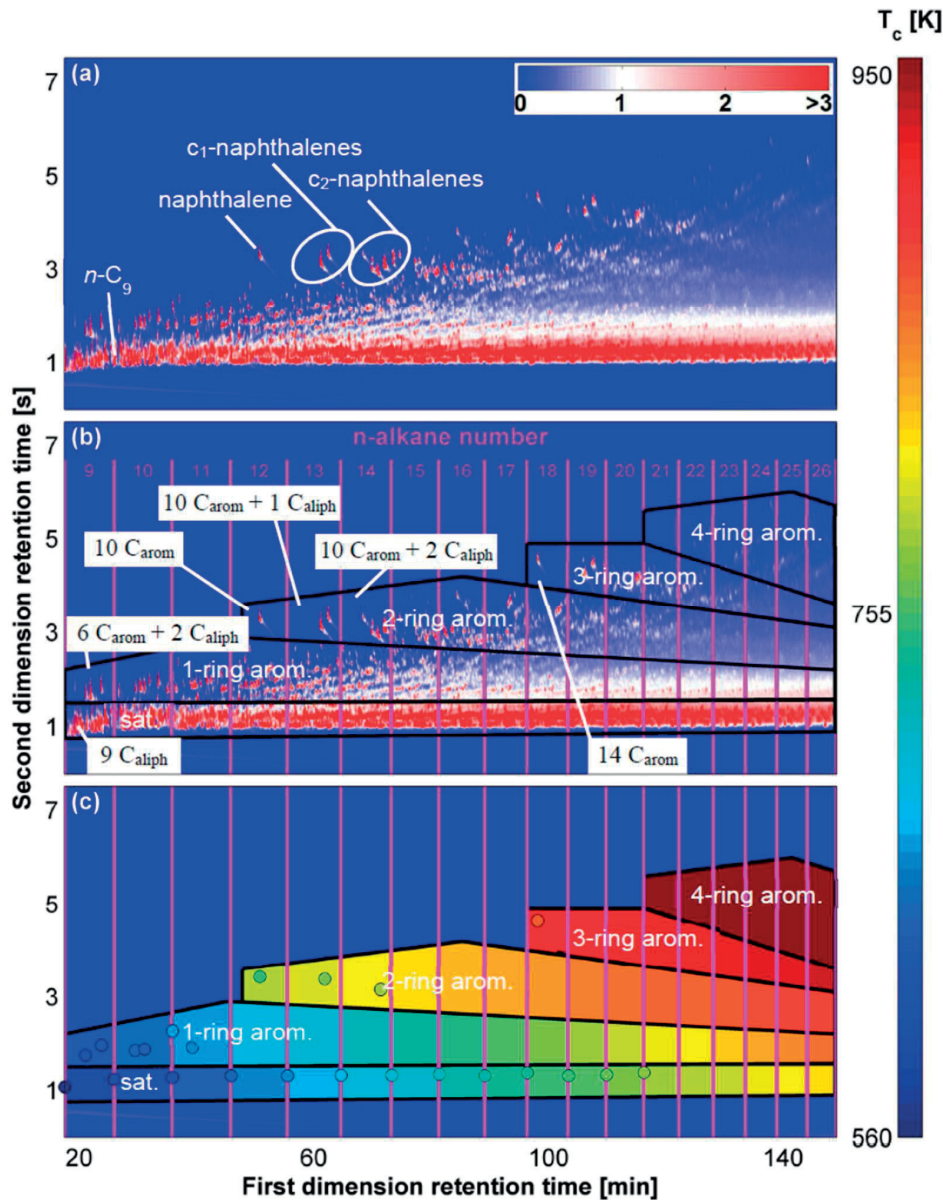


Figure 4-2. (a) GCxGC–FID chromatogram of the dead oil fraction of *Deepwater Horizon* sample MW-1, overlaid with the elution positions of a few compounds. (b) Same chromatogram overlaid with polygons that delineate distillation cuts by n -alkane carbon number along the 1st dimension, and five separated hydrocarbon groups along the 2nd dimension, including saturated hydrocarbons (sat.) and 1-ring to 4-ring aromatics (arom.). Examples of assigned pseudo-component structures are also displayed, expressed as a number of aromatic (C_{arom}) and aliphatic carbon atoms (C_{aliph}) (a complete list of assigned approximate structures is provided in Appendix section 4.9.5). (c) Same chromatogram overlaid with estimates of the critical temperature (T_c). Each polygon is colored according to the estimated T_c of the corresponding pseudo-component. Circles correspond to the elution positions of individual compounds, with the interior part of the circles colored according to the T_c from literature data.²⁰⁰ The color scale on the upper right of panel (a) indicates FID signal response (arbitrary units).

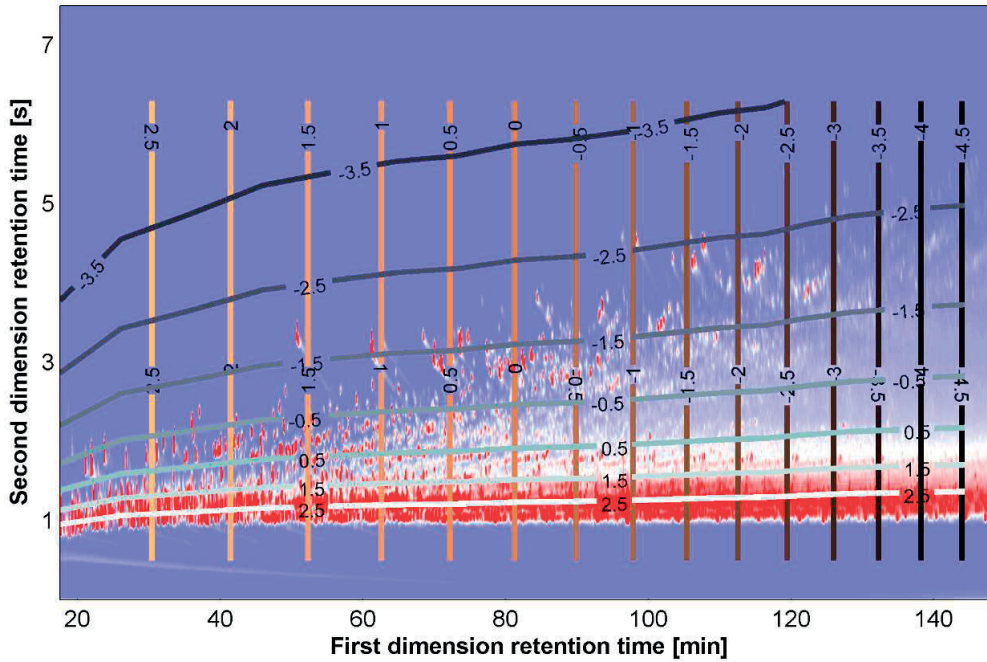


Figure 4-3. GCxGC-FID chromatogram of MW-1 dead oil overlaid with estimated contours of the base 10 logarithm of decreasing vapor pressure (from left to right) and base 10 logarithm of increasing air-water partition coefficient, K_{ow} (from top to bottom). These lines were drawn by use of the Matlab algorithms of Nabi et al.⁷² K_{ow} is expressed here in units of $(\text{mol m}^{-3}) / (\text{mol m}^{-3})^{-1}$, i.e. concentration in gas phase divided by concentration in aqueous phase. The relation between K_{ow} and the Henry's law constant $K_{H,i}$, here defined as in $\text{kg m}^{-3} \text{Pa}^{-1}$, is: $K_{H,i} = (M_i / R \cdot T) \cdot (K_{ow,i})^{-1}$, where M_i is the molar weight of compound i in kg mol^{-1} , R is the gas constant ($8.314510 \text{ J mol}^{-1} \text{ K}^{-1}$), and T is the temperature in K.

4.3 Modeling Approach

To model the pressure-dependent, temperature-dependent equilibrium distribution of a petroleum mixture between a gas phase and a liquid petroleum phase, we employed the PR EOS with the 1978 modification:^{206,216,223}

$$P = \frac{R \cdot T}{\bar{V} - b} - \frac{a(T)}{\bar{V} \cdot (\bar{V} + b) + b \cdot (\bar{V} - b)}$$

Equation 4-1

where P refers to the (total system) pressure, T is the temperature, R the molar gas constant, \bar{V} the molar volume, a is a parameter interpreted as an average measure of the attraction between molecules, and b represents the average volume occupied by the molecules. Fugacities of individual components in the two phases, f_i , are computed from:²¹⁶

$$\ln(f_i) = \ln(x_i \cdot P) + \frac{b_i}{b} \cdot (Z - 1) - \ln(Z - B) - \frac{A}{2 \cdot \sqrt{2} \cdot B} \cdot \left(\frac{2 \cdot \sum_j (x_j \cdot a_{i,j})}{a} - \frac{b_i}{b} \right) \cdot \ln \left(\frac{Z + 2.414 \cdot B}{Z - 0.414 \cdot B} \right)$$

Equation 4-2

where the new terms appearing in equation 2 are defined below:

Equation 4-1 can be rewritten as a 3rd degree polynomial of the compressibility factor, Z :

$$Z^3 - (1 - B) \cdot Z^2 + (A - 3 \cdot B^2 - 2 \cdot B) \cdot Z - (A \cdot B - B^2 - B^3) = 0$$

Equation 4-3

where:

$$Z = \frac{P \cdot \bar{V}}{R \cdot T}$$

Equation 4-4

$$A = \frac{a \cdot P}{R^2 \cdot T^2}$$

Equation 4-5

$$B = \frac{b \cdot P}{R \cdot T}$$

Equation 4-6

where P refers to the (total system) pressure, T is the temperature, R is the molar gas constant, \bar{V} is the molar volume, and a and b are defined by Equation 4-7 to Equation 4-13 below.

$$b_i(T) = b_i(T_{c,i}) = 0.07780 \cdot \frac{R \cdot T_{c,i}}{P_{c,i}}$$

Equation 4-7

where $P_{c,i}$ refers to the critical pressure of component i , and $T_{c,i}$ is the critical temperature of component i .

$$a_i(T) = a_i(T_c) \cdot \alpha_i(T_{r,i}, \omega_i) = 0.45724 \cdot \frac{R^2 \cdot T_{c,i}^2}{P_{c,i}} \cdot \alpha(T_{r,i}, \omega_i)$$

Equation 4-8

where T_r refers to the reduced temperature $\left(T_{r,i} = \frac{T}{T_{c,i}}\right)$, and ω is the acentric factor.

$$\alpha_i(T_{r,i}, \omega_i) = \left(1 + \kappa_i(\omega_i) \cdot (1 - T_{r,i}^{0.5})\right)^2$$

Equation 4-9

$$\kappa_i(\omega_i) = \begin{cases} 0.37464 + 1.54226 \cdot \omega_i - 0.26992 \cdot \omega_i^2 & (\omega_i \leq 0.49) \\ 0.379642 + 1.48503 \cdot \omega_i - 0.164423 \cdot \omega_i^2 + 0.016666 \cdot \omega_i^3 & (\omega_i > 0.49) \end{cases}$$

Equation 4-10

$$a_{i,j}(T) = (1 - \delta_{i,j}) \cdot a_i(T)^{0.5} \cdot a_j(T)^{0.5}$$

Equation 4-11

where $\delta_{i,j}$ refers to the binary interaction parameter between components i and j .

$$a = \sum_i \sum_j (x_i \cdot x_j \cdot a_{i,j}(T))$$

Equation 4-12

where x refers to mole fractions in the mixture, and i and j refer to components i and j in the mixture.

$$b = \sum_i (x_i \cdot b_i)$$

Equation 4-13

Depending on the number of phases present, Equation 4-3 has one to three roots in terms of Z . In the two-phase region, the smallest positive root corresponds to the compressibility factor of the liquid, and the largest root corresponds to that of the gas phase.

To solve numerically the PR EOS for a petroleum fluid (a gas-liquid system), we use a combination of successive substitution, stability analysis, and second-order minimization techniques.²²⁴ These procedures are described further in Appendix section 4.9.1.

Once the compressibility factor has been determined from Equation 4-3, the molar volume of a petroleum phase can be computed from Equation 4-4, and the density ρ is given by:²⁰⁶

$$\rho = \frac{\sum x_i \cdot M_i}{\bar{V}}$$

Equation 4-14

where x_i is the mole fraction of component i in the phase of interest, and M_i is the molar weight of component i . However, the PR EOS underpredicts the densities of liquid phases,²⁰⁶ which can be improved by the volume translation introduced by Pénéloux et al..²²⁵

$$\bar{V}_{VT} = \bar{V}_{PREOS} - c$$

Equation 4-15

where the corrected molar volume, \bar{V}_{VT} , is obtained by adjusting the molar volume predicted by the equation of state, \bar{V}_{PREOS} , with the volume translation parameter, c .

This correction modifies only the predicted densities and does not affect gas-liquid equilibrium. We estimated the volume translation parameter (Equation 4-15) based on measured or estimated critical properties of the individual mixture components and their acentric factors.²²⁶

Additionally, we assumed that the low mole fractions of water encountered in petroleum phases at environmentally relevant temperatures^{212,227} do not affect substantially the fugacities of petroleum compounds in either the liquid or gas phases, therefore water was not included as a component in the gas-liquid PR EOS calculations. Finally, Macondo dead oil had a reportedly low asphaltene content (0.9–1% by weight),²²⁸ and therefore we did not consider EOS models that account for asphaltenes.²²⁹

We now consider the coupled equilibrium partitioning between the gas-liquid petroleum phases and water, in order to complete our description of the three-phase system. We described the partitioning of a compound between water and gas phase using the modified Henry's law,^{211,214,215} which is valid up to pressures of ~100 MPa, corresponding to water depths of ~10,000 meters:^{211,215}

$$K_{H,i}(P) = K_{H,i}(P^*) \cdot e^{\frac{(P^* - P)\bar{v}_i^L}{R \cdot T}}$$

Equation 4-16

where K_H is the Henry's law constant in units of $\text{kg m}^{-3} \text{Pa}^{-1}$, P^* is the reference pressure at which the Henry's law constant is known (here atmospheric pressure, or 101325 Pa), and \bar{v}^L is the partial molar volume at infinite dilution of the compound in water, assumed independent of pressure and temperature. The Henry's law constant was also corrected for temperature:^{156,230}

$$K_{H,i}(T) = K_{H,i}(T^*) \cdot e^{-\frac{\Delta H_{\text{gas} \rightarrow \text{H}_2\text{O},i}}{R} \left(\frac{1}{T} - \frac{1}{T^*} \right)}$$

Equation 4-17

where T^* is a reference temperature (298.15 K), and $\Delta H_{\text{gas} \rightarrow \text{H}_2\text{O}}$ is the enthalpy of transfer from gas phase to aqueous phase. Finally, the Henry's law constant was also corrected for salinity, according to the Setschenow equation:¹⁵⁶

$$K_{H,i}(S) = K_{H,i}(S = 0) \cdot 10^{-C_{\text{salt}} \cdot K_{\text{salt},i}}$$

Equation 4-18

where S is the salinity, K_{salt} is the Setschenow constant, and C_{salt} is the concentration of salt in seawater (~0.5 M).¹⁵⁶

4.4 Results

We first discuss the formulation of pseudo-components suitable for the three-phase partitioning modeling of the MRF. In the subsequent two sections, we report on the validation of the input properties required to solve the thermodynamic model (Equation 4-1 to Equation 4-18). Model simulation results and output properties are then validated with available experimental data for the MRF. Finally we discuss the implications of our simulations for interpreting subsurface events during the *Deepwater Horizon* disaster.

4.4.1 Model compositions of MRF

We conducted thermodynamic simulations for three different reported compositions of MRF,^{8,231,232} here represented by model compositions denoted MC₁, MC₂, and MC₃. The procedures used to define these model compositions are described below.

Discrepancies exist among different reports of the composition of MRF. During the release event, a sample (MW-1) of the emitted reservoir fluid was taken directly from the broken Macondo well stub using an isobaric gas-tight sampler (June 21, 2010).⁸ MW-1 was composed of >95% petroleum compounds and <5% seawater (percentages by volume for dead oil and seawater, excluding the gas phase separated through a single-stage separation at atmospheric conditions). Based on the sampling procedure,⁸ this sample is considered representative of the single-phase reservoir fluid. The measured gas-to-oil ratio (GOR), defined as the ratio of the volume of gas to that of dead oil at atmospheric conditions, was 1600 standard cubic feet per barrel for MW-1 (single-stage separation).⁸ Because it was taken directly from within the broken Macondo well stub, we believe that MW-1 is probably the most representative sample of the emitted petroleum mixture taken during the event, compared to the other available samples taken from collection vessels at the sea surface (further discussion was presented by Reddy et al.⁸). However, the MW-1 GOR differs from the GOR values reported for pre-spill downhole single-phase MRF samples (2441–2747, four-stage separation; 2819–2945, single-stage separation).⁵ Compared to pre-spill downhole samples, MW-1 did not exhibit a systematic fractionation among the volatile components (Appendix section 4.9.2), thus we infer that this sample was not biased towards the liquid petroleum phase at emission depth. The apparent discrepancy in composition among MW-1 and pre-spill downhole samples remains unexplained, and we therefore chose to construct model compositions for the MW-1 sample (MC₁) and also for two different pre-spill downhole samples (MC₂ and MC₃).

MC₁ is based on the analysis of MW-1, as follows:

(a) We modeled 131 individual compounds that were quantified previously by gas chromatography – mass spectrometry (GC–MS), including 74 saturated hydrocarbons ranging from methane to *n*-C₂₆, 56 aromatic hydrocarbons ranging from benzene to C₂-benz[*a*]anthracenes and chrysenes, and CO₂. (In Table S2 of ref. ⁸ fluoranthene was incorrectly listed and the actual mass fraction of $4.6 \cdot 10^{-6} \text{ g g}^{-1}$ in the reconstituted reservoir fluid was used here.⁸) We excluded alkanes $>n\text{-C}_{26}$, which were considered unlikely to partition substantially into the aqueous phase; no sign of aqueous dissolution during ascent was observed for *n*-alkanes larger than heptane.⁷⁵ These 131 individual compounds represent 48.3% of the MW-1 mass. By comparing quantified individual compounds with simulated distillation⁵³ data (Appendix section 4.9.3),^{8,233} we concluded that the emitted mixture composition is approximately known on an individual-compound basis up to *n*-C₈, and the mass fraction of unknown composition increases with increasing carbon number after *n*-C₈ (Figure 4-7).

(b) For MC₁, we used GC×GC–FID data to define pseudo-components for hydrocarbons in the *n*-C₈–*n*-C₂₆ range, excluding individually quantified compounds. Instrument settings and chromatogram pre-processing methods^{62,66,70,71} are given in Appendix section 4.9.4. For simplicity, we delineated the chromatogram by *n*-alkane elution intervals (i.e., simulated distillation elution intervals or approximate boiling points) along the first dimension, and we further segregated the chromatogram space into five hydrocarbon groups along the second dimension, including: saturated hydrocarbons, single-ring aromatics, two-ring aromatics, three-ring aromatics, and four-ring aromatics, based on known elution patterns of these compounds²¹⁷ (Figure 4-2). The resulting grid of polygons effectively separates the GC×GC chromatogram mass into a set of pseudo-components that are suited to model gas-liquid-water partitioning. This is analogous to previously reported approaches to separate the GC×GC chromatogram space into pseudo-components along contours of volatility and aqueous solubility (Figure 4-3),^{15,40,55,72–74} as was done in Chapter 3. The mass assigned to each pseudo-component is proportional to the total GC×GC–FID signal in the corresponding polygon, minus the mass attributed to individually quantified compounds (described below). This is possible because the FID detector signal is approximately proportional to hydrocarbon mass,^{61–63} enabling the grouping and quantification of structurally related compounds.^{73,218,220}

An approximate chemical structure can be assigned to each pseudo-component represented by the polygons in Figure 4-2b (Appendix section 4.9.5). Compounds grouped within a given pseudo-component are expected to have similar chemical structures and therefore exhibit similar properties (Figure 4-2c). Consequently each pseudo-component can be modeled using empirical fragment structure contribution methods (next section). Additionally, the 131 individually quantified compounds represented by category *a* (above) each were attributed to appropriate polygons, and their mass was removed to avoid double-counting. Using this procedure, 66 pseudo-components were defined based on the *n*-C₈–*n*-C₂₆ elution range of the GC×GC–FID chromatogram, representing 29.1% of the MW-1 mass.

(c) Lastly, for MC₁ we defined 82 pseudo-components corresponding to single carbon number intervals from *n*-C₂₇ to *n*-C₁₀₈ defined from simulated distillation data^{8,233} which represent 22.1% of the MW-1 mass (Appendix section 4.9.6). >99% of the MW-1 dead oil mass was

eluted at n -C₁₀₈, and resins are considered included in the GC-amenable simulated distillation mass up to n -C₁₀₈.

We also constructed MC_{1,do}, defined as the dead oil composition of MW-1, based on reported compositional data⁸ (Appendix section 4.9.7).

Model compositions MC₂ and MC₃ are based on previously reported compositional analysis by Schlumberger (sample 1.18)²³¹ and Pencor (sample 53),²³² respectively, for two pre-spill downhole MRF samples, both collected on April 12, 2010, at a depth of 5529.7 m. In brief, we renormalized the detailed composition of the MW-1 fluid, based on the reported simulated distillation data of the Schlumberger and Pencor samples, in order to construct MC₂ and MC₃ (see Appendix section 4.9.8 for the detailed procedure). MC₁ includes 279 components (no nitrogen quantified) whereas MC₂ and MC₃ include 280 components (including nitrogen at <0.25 mass percent).

4.4.2 Estimation of input parameters for the thermodynamic model

To simulate gas-liquid-water partitioning for the whole petroleum mixture according to the thermodynamic model described by Equation 4-1–Equation 4-18, several properties must be known or estimated for each component, including the acentric factor, critical temperature, critical pressure, critical volume, K_h , $\Delta H_{gas \rightarrow H_2O}$, \bar{v}^L , and K_{salt} . For compounds quantified individually, data for some or all of these properties were found in existing compilations.^{173,200,215,230,234–239} For the remaining cases, component properties were estimated using group contribution or property correlation methods, as described below. For pseudo-components defined based on the GC×GC–FID chromatogram, properties were estimated using the approximate structure assigned to each pseudo-component.

For hydrocarbon compounds $\leq n$ -C₂₆, the group-contribution methods^{240–243} that we selected were found to exhibit root-mean-squared-relative-error (RMSRE) values of <11% for 5 out of 8 of the needed input parameters, based on our comparisons to available experimental data (Table 4-1). Estimation methods for the acentric factor, K_h , and $\Delta H_{gas \rightarrow H_2O}$ had RMSRE of 280%, 45%, and 18%, respectively. However, these errors drop to 6.4% and 6.6% for the acentric factor and $\Delta H_{gas \rightarrow H_2O}$, respectively, when light compounds ($\leq n$ -C₅) are excluded (Appendix Figure 4-9 to Figure 4-14). For the purposes of our thermodynamic simulations, these property estimates were not needed for light compounds, since literature data were available in these cases. Finally, uncertainty exists regarding the correct Henry's law constants for $>n$ -C₁₃ normal alkanes.¹⁷⁶ This uncertainty is not expected to influence modeling of aqueous dissolution during the blowout, since normal alkanes $>n$ -C₇ were reported to have not dissolved noticeably during ascent to the sea surface.⁷⁵

For the $>n$ -C₂₆ pseudo-components, which were assumed effectively insoluble in water, we estimated only the properties required for gas-liquid modeling with the PR EOS, namely the

critical properties and the acentric factor, using the Twu and Kesler-Lee correlations (Appendix section 4.9.6).^{244–248} The properties of our 279 components are listed in Appendix Table 4-12.

Finally, the temperature-dependent binary interaction parameters (for the PR EOS) were estimated based on the group-contribution method by Jaubert and co-workers.²⁴⁹ This method is parameterized for all pairwise interactions between aromatic hydrocarbons, non-aromatic hydrocarbons, CO₂, and nitrogen. For the purpose of estimating binary interaction parameters, each $>n$ -C₂₆ pseudo-component was assumed to have the structure of a normal alkane; this was preferred to a more recent method²⁵⁰ that was not retained due to unphysical predicted carbon numbers for large molecules.

Table 4-1. Validation of property estimation methods with available experimental data for hydrocarbons.

Property	Available literature experimental data	Estimation method	Number of tested compounds ^a (out of 147 ^b)	RMSE (RMSRE) ^c
Critical pressure ^d	Poling et al. ²⁰⁰	Group contribution ^{240,241}	69	0.77 bar (3.7%)
Critical temperature ^d	Poling et al. ²⁰⁰	Group contribution ^{240,241}	73	15 K (3.9%)
Critical volume ^d	Poling et al. ²⁰⁰	Group contribution ^{240,241}	62	17 cm ³ mol ⁻¹ (9.4%)
Acentric factor ^d	Poling et al. ²⁰⁰	Group contribution ^{240,241}	64	0.064 (280%) ^e
Henry's law constant	Sander ^{230,f}	Group contribution ²⁴²	60	13 mol dm ⁻³ atm ⁻¹ (45%)
Enthalpy of phase transfer from gas to water	Plyasunov and Shock ²³⁴	Group contribution ²⁴³	26	3.2 kJ mol ⁻¹ (18%) ^g
Partial molar volume at infinite dilution in water	Liu and Ruckenstein, ²³⁵ Graziano (CH ₄ and C ₂ H ₆), ²³⁶ King (CO ₂) ²¹⁵	Equation 4-19	18 ^h	3.2 cm ³ mol ⁻¹ (4.8%)
Setschenow constant	Ni and Yalkowsky ²³⁷ Xie et al., ¹⁷³ Schwarzenbach et al., ¹⁵⁶ Weiss ²³⁸	Equation 4-20	29 ^h	0.026 L mol ⁻¹ (10.9%)

^a Compounds for which literature data were available for a given property.

^b All the compounds quantified in MW-1 by Reddy et al., excluding CO₂.⁸

^c Root mean squared error (RMSE) and root mean squared relative error (RMSRE), where the relative error is defined as (estimated – experimental) / experimental.

^d The Aवालlee et al. estimation method was used only for PAHs.²⁴⁰

^e The large reported RMSRE value arises due to inaccurate predictions for compounds smaller than n -C₅. However, property estimates were not necessary for these compounds, since literature data were available. See Appendix section 4.9.10 for more details. Exclusion of small compounds ($\leq n$ -C₅) yields RMSE (RMSRE) values of 0.023 (6.4%).

^f Here we retained only the measurement and literature review values from reference²³⁰ (Appendix section 4.9.9).

^g Excluding small compounds yields RMSE (RMSRE) values of 0.30 kJ mol⁻¹ (6.6%).

^h Includes CO₂.

4.4.3 New proposed correlations for prediction of \bar{v}^L and K_{salt} for hydrocarbons

For \bar{v}^L and K_{salt} , no satisfactory prediction methods were found that could be applied to all components up to n -C₂₆. Hence we developed and validated new correlations for these two properties.

To adjust the Henry's law constant for changes in pressure (Equation 4-16), we must estimate the partial molar volume at infinite dilution in water (\bar{v}^L). Based on data for CO₂, 4 aromatic compounds, 2 cycloalkanes, 2 branched alkanes, and 9 normal alkanes (Appendix section 4.9.11),^{215,235,236} we obtained the following correlation (Figure 4-15a; $r^2 = 0.995$; root-mean-squared error (RMSE) = 3.2 cm³ mol⁻¹):

$$\bar{v}_i^L = 1.132 \cdot \bar{V}_{MG,i} + 3.333 \cdot 10^{-6}$$

Equation 4-19

where $\bar{V}_{MG,i}$ is the McGowan molecular volume, which is determined with a group contribution method.¹⁵⁶ Both \bar{v}_i^L and $\bar{V}_{MG,i}$ have units of m³ mol⁻¹. A previous correlation by Lyckman et al.,^{213,251} developed only with data for gases, was found to provide less good predictions for compounds other than methane, ethane, propane and CO₂ (RMSE = 27.0 cm³ mol⁻¹).

Since K_{salt} depends principally on molecular size and molecular polarity,²⁵² we surmised that a simple two-parameter correlation could be developed for hydrocarbons. Based on reported data for 28 hydrocarbons plus CO₂ (Appendix section 4.9.11),^{156,173,237,238} we obtained the following correlation (Figure 4-15b; $r^2 = 0.83$; RMSE = 0.026 L mol⁻¹):

$$K_{salt,i} = -1.345 \cdot M_i + 2799 \cdot \bar{v}_i^L + 0.08356$$

Equation 4-20

where $K_{salt,i}$ is in L mol⁻¹, M_i in kg mol⁻¹, and \bar{v}_i^L in m³ mol. These correlation statistics are comparable to a previously reported correlation based on the Abraham solvation model.²⁵²

4.4.4 Validation of gas-liquid predictions of the thermodynamic model for MRF

We compared our thermodynamic model predictions for petroleum compositions MC_{1,do}, MC₂, and MC₃ to 88 previously measured property data on (a) density (8 data), (b) gas-liquid partitioning (19 data), and (c) viscosity (61 data) under a broad range of pressure and temperature conditions. We also compared our model predictions to those made by a tuned EOS model reported previously by A. Zick.²⁰⁹ These three different sets of validation tests are discussed in turn below.

(a) The predicted density of the dead oil at surface conditions (atmospheric pressure, 22 °C) is 819.5 kg m⁻³ for the mixture MC_{1,do}. This agrees well with the measured value of 820 kg m⁻³ for MW-1 dead oil.⁸ The predicted extent of change of the dead oil density as a function of pressure, up to 15 MPa, is within 6 kg m⁻³ of the experimental data by Abdelrahim, obtained with a different dead oil sample (Appendix Figure 4-16).²⁵³ For the Schlumberger pre-spill downhole sample,²³¹ our model and the Zick model both match satisfactorily high-pressure experimental densities, with maximum deviations of 6 and 5 kg m⁻³ (~1%), respectively (Appendix sections 4.9.12 and 4.9.13).

(b) For the Schlumberger sample, the experimental volume fraction of liquid hydrocarbons²³¹ at 7.6–34.7 MPa and ~117 °C agrees with our thermodynamic model predictions for mixture MC₂ to within 16% (Appendix section 4.9.13). Our model also agrees well with the Zick model for pressures ≤25 MPa (≤2500 meters depth) and a temperature range of -2 to 30 °C (Appendix sections 4.9.12 and 4.9.13). For example, at emission depth (15.5 MPa and 4.3 °C), the two models give very similar predictions for the Schlumberger pre-spill downhole sample: simulated gas volume fractions are 39% versus 44%, predicted gas-phase densities are 200 versus 194 kg m⁻³, and predicted liquid-phase densities are 696 versus 699 kg m⁻³. Our thermodynamic model fails to predict the correct gas-liquid volume fractions at much higher pressures (>25 MPa and -2–30 °C) and also the dew point (transition from one phase to two phases through drop formation) at 43–47 MPa for -2–40 °C (Appendix Figure 4-17 and Appendix Figure 4-18). This is discussed further in Appendix section 4.9.13.

(c) We compared the estimated viscosity predicted by our model for MC_{1,do} (3.9 mPa s, or centipoise, at 15 °C; 2.5 mPa s at 35 °C) to that measured on a Macondo dead oil sample called “ENT-052210-178” (4.1 mPa s at 15 °C; 1.4 mPa s at 35 °C)²⁵⁴ and find good correspondence between them (Appendix section 4.9.13). Finally, our attempts to make comparisons with high-pressure viscosity data for the Pencor pre-spill downhole sample were confounded by the failure of our model to correctly predict the dew point (Appendix Figure 4-17 and Appendix Figure 4-18), which occurs at very high pressures (46 MPa at 4.3 °C).²³² Additional discussion is given in Appendix section 4.9.13.

4.4.5 Domain of applicability of the thermodynamic model

The formulas and approximations used in the model are usually considered valid for typical conditions found anywhere in the global ocean (depths down to ~10,000 m, seawater salinity of ~35‰, and seawater temperatures of -2–30 °C).^{156,173,177,211,215,216} However, based on the comparisons discussed above, we interpret that the predictions of our model of the MRF are valid for gas-liquid partitioning, densities, and fluid viscosities at conditions ranging from the sea surface to ≤2500 m depth (0.1–25 MPa and -2–30 °C). Additionally, the presented model is not considered validated for brines under oil reservoir conditions (explained further in Appendix section 4.9.14), and further EOS modifications may be required for heavier petroleum fluids.

4.5 Implications for deep-sea petroleum fluid releases

4.5.1 Estimated state of the MRF at the Macondo well stub

Compared to a conventional sea-surface spill, the high pressure conditions of the *Deepwater Horizon* release profoundly modified the state of the emitted petroleum mixture. Based on the estimated conditions in the Macondo well pipe below the blowout preventer (~24 MPa and 38 °C),²⁵⁵ the mixture was in the two-phase region before its emission into the sea (Appendix Figure 4-17 and Appendix Figure 4-18). The emitted mixture is predicted to have been 29–44% gas (by volume) and 56–71% liquid hydrocarbons at emission depth (15.5 MPa and 4.3 °C, Table 4-2), based on the compositions of samples taken both at the broken well stub (MC₁) and downhole before the spill (MC₂, MC₃). By comparison, the petroleum mixture is 99.7% gaseous by volume at the sea surface.⁸ Relative to surface conditions, the small value of the gas volume fraction at 1524 m depth is due largely to the compression of the gas and to a lesser extent also due to the increased partitioning of light compounds into the liquid hydrocarbon phase (Table 4-3). For example, 36–51% of the methane, the lightest and most abundant compound in the reservoir fluid, is predicted to have partitioned into the liquid petroleum phase at emission depth, which decreases both the density and the viscosity of the liquid phase. By comparison, 99.8% of methane would reside in the gas phase under surface conditions (Table 4-3).

Table 4-2. Predicted properties of emitted fluids at 1524 m depth (15.5 MPa and 4.3 °C) and surface conditions (0.101325 MPa and 15.6 °C) according to the thermodynamic model.

Property	1524 m depth (15.5 MPa and 4.3 °C)	Surface conditions (0.101325 MPa and 15.6 °C)
	Values for model compositions MC ₁ (MC ₂ , and MC ₃)	Values for model composition MC ₁
density of gas (kg m ⁻³)	181 (194, 194)	0.94
density of liquid (kg m ⁻³)	707 (699, 690)	824
percent gas (by volume)	29% (44%, 42%)	99.7%
viscosity of gas (mPa s)	0.020 (0.022, 0.022)	0.011
viscosity of liquid (mPa s)	0.74 (0.69, 0.65)	4.1

Table 4-3. Predicted percentage in gas and liquid hydrocarbon phases, for selected compounds at 1524 m water depth (15.5 MPa and 4.3 °C) and surface conditions (0.101325 MPa and 15.6 °C) according to the thermodynamic model.

Compound	1524 m water depth (15.5 MPa and 4.3 °C)		Surface conditions (0.101325 MPa and 15.6 °C)	
	Percent in liquid phase for MC ₁ (MC ₂ , MC ₃)	Percent in gas phase for MC ₁ (MC ₂ , MC ₃)	Percent in liquid phase for MC ₁	Percent in gas phase for MC ₁
methane	51% (36%, 38%)	49% (64%, 62%)	0.2%	99.8%
ethane	74% (59%, 61%)	26% (41%, 39%)	1.1%	98.9%
propane	83% (70%, 72%)	17% (30%, 28%)	3.7%	96.3%
<i>n</i> -butane	90% (82%, 83%)	10% (18%, 17%)	14.3%	85.7%
benzene	98.4% (96.3%, 96.5%)	1.6% (3.7%, 3.5%)	76.3%	23.7%
CO ₂	70% (54%, 56%)	30% (46%, 44%)	0.5%	99.5%

4.5.2 Gas-liquid-water partitioning equilibrium in the deep sea

We simulated the equilibrium partitioning of the MRF between water, gas, and liquid petroleum phases, at varying depths (Figure 4-4). Whereas the aqueous solubilities of hydrocarbons in liquid state are approximately independent of depth,^{8,256–258} the aqueous solubilities of gaseous compounds increase rapidly with increasing depth (Figure 4-4). Thermodynamically, this favors profound dissolution of light hydrocarbons into water in the deep sea, far exceeding that observed for a conventional sea surface oil spill (Figure 4-4). For example, when the MRF has equilibrated with 100 mass equivalents of water at 1500 m depth (which can happen rapidly for small bubbles and droplets), 15% of the MRF mass will have dissolved into the aqueous phase, mostly comprised of light compounds. By comparison, near the sea surface, a 1:100 mass ratio of MRF:water would lead to equilibrium partitioning of only 0.6% of MRF into the aqueous phase (Figure 4-4). This illustrates how deep-sea conditions dramatically increase the thermodynamic driving force for aqueous dissolution of light hydrocarbons, compared to a release at the sea surface.

In deep waters, hydrates also form, which can decrease mass transfer speeds and also modify the hydrodynamics of bubbles and droplets, leading to drastically increased bubble lifetimes.⁴⁷ Dispersants injected at emission depth may have lowered interfacial tension of gas/water and liquid/water interfaces, which would influence kinetics of aqueous dissolution. However, dispersants are not expected to alter equilibrium partitioning of hydrocarbons into water unless the critical micelle concentration (CMC) in water is exceeded.¹⁸² The key water-soluble component of the dispersant injected near the broken Macondo well stub was dioctyl sodium sulfocinate (DOSS), which was measured in the deep-water hydrocarbon plume at concentrations up to $12 \mu\text{g L}^{-1}$.²⁵⁹ This level is about four orders of magnitude lower than the CMC for DOSS,²⁵⁹ suggesting that DOSS did not influence the thermodynamics of partitioning of hydrocarbons into water.

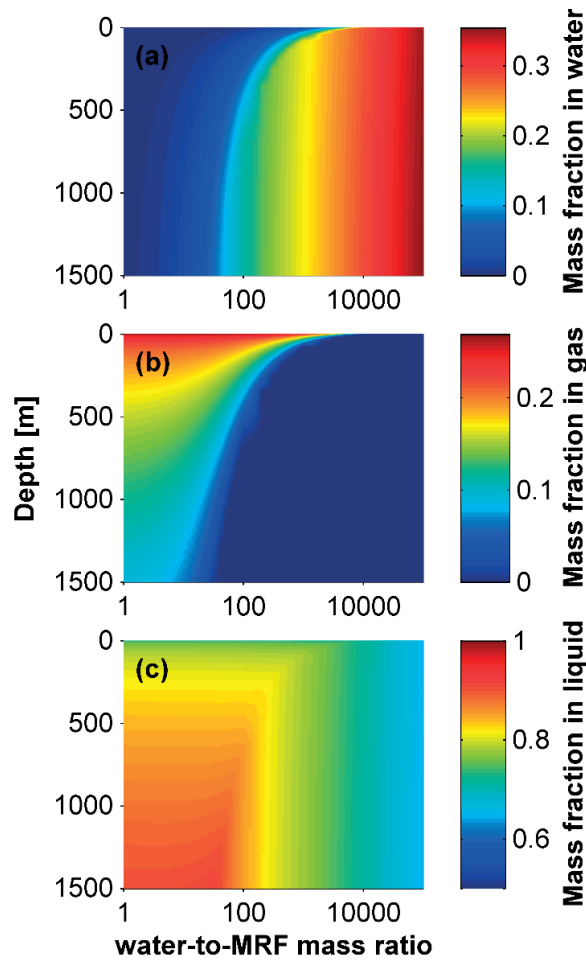


Figure 4-4. Simulated gas-liquid-water equilibrium partitioning of complete MRF with varying volumes of seawater (expressed as seawater-to-MRF mass ratio), shown with varying depth. The color scale represents the simulated mass fraction of total hydrocarbons in (a) seawater, (b) gas, and (c) liquid petroleum phase. The plots should not be interpreted as showing the compositional evolution of liquid droplets or gas bubbles that undergo kinetically controlled aqueous dissolution of selected hydrocarbons during buoyant ascent. To generate the plots, we assumed a temperature profile based on observed mean annual conditions in the Gulf of Mexico as a function of depth,²⁵³ and we assumed a salinity of 35 g kg^{-1} throughout the water column.

4.5.3 Expected changes in liquid and gas densities due to pressure and aqueous dissolution

According to our model, predicted densities at Macondo well emission conditions (15.5 MPa and $4.3 \text{ }^\circ\text{C}$) are $181\text{--}194 \text{ kg m}^{-3}$ for the gaseous petroleum phase and $690\text{--}707 \text{ kg m}^{-3}$ for the liquid petroleum phase (Table 4-2). The densities of these fluids directly influence the velocities of ascent for gas bubbles and liquid droplets at local pressure and temperature conditions, both due to changes in buoyancy force and changes in shear stress (friction) associated with changing bubble/droplet size.²⁶⁰ Associated changes in bubble or droplet surface area and ascent speed also affect mass transfer rates from the petroleum phases into water.²⁶⁰

Aqueous dissolution selectively removes light compounds from an ascending liquid droplet (or gas bubble), and this also influences the densities of both gaseous and liquid petroleum phases. In the aftermath of *Deepwater Horizon*, a portion (1.8–14.4%^{204,205} or 0.5–9.1%²⁰⁴) of the dead oil emitted in the environment was found to have ended up in the deep sea floor (900–1600 m depth).²⁰⁵ The transport mechanism of these compounds to the sediments remains unclear.²⁰⁴ Valentine et al. proposed deposition of liquid petroleum dispersed in deep waters,²⁰⁵ whereas others proposed sinking of surfaced petroleum mixture through marine snow as a potential mechanism.^{261–263} Here, we used equilibrium partitioning simulations to investigate whether aqueous dissolution and/or evaporation might sufficiently alter the density of the liquid petroleum to cause this material to lose buoyancy and therefore sink. We find that the simulated effect of aqueous dissolution on density is insufficient to generate a loss of buoyancy (Appendix section 4.9.15). According to the model, extensive evaporation of the oil (>50% mass removal, including all hydrocarbons lighter than *n*-C₂₂) would produce a loss of buoyancy of the liquid oil (Appendix section 4.9.15). However this hypothesis is not supported by the composition of the petroleum residues found in the deep-sea sediments, which occasionally contained the light compounds *n*-C₁₁ and *n*-C₁₆.²⁰⁵ In conclusion, aqueous dissolution and evaporation processes alone cannot explain a buoyancy change that would have led to the observed broad deposition of petroleum compounds on the seafloor. However, our simulations show that evaporation and aqueous dissolution processes both increase the density of the liquid petroleum phase, and this process may cause buoyancy loss for heavier petroleum mixtures or under other conditions.

4.5.4 Implications for Macondo well flow rate estimates

The uncertainty in the MRF composition (MC₁ versus MC₂ or MC₃) leads to an uncertainty in the gas and liquid volume fractions at emission depth, and this in turn affects several existing estimates of the MRF flow rate from broken Macondo well stub. Some published flow rate estimates are based on (1) measurement of a volume flux of emitted fluids at depth, and (2) conversion of this value into an estimated volume flux of dead oil at surface conditions.^{45,255,264} However, converting the measured volume flux to a (surface) dead oil volume flux depends on the assumptions about the gas and liquid volume fractions at depth. Our thermodynamic model is designed to provide this information. According to the model, 1 m³ of (gas + liquid) fluids at depth (15.5 MPa and 4.3 °C) are equivalent to 154 m³ of gas and 0.500 m³ of dead oil at surface conditions (0.101325 MPa and 15.56 °C), assuming a single-stage flash of model composition MC₁ and assuming negligible influence of hydrates on bulk properties of the petroleum fluid phases. However if we assume composition MC₂, then 1 m³ of (gas + liquid) fluids at depth produce 182 m³ of gas and 0.363 m³ of dead oil at surface conditions. This uncertainty in the MRF composition (MC₁ versus MC₂) therefore leads to a 32% uncertainty in the estimated flow rate of dead oil. By comparison, previous reports have assumed a value of ~0.4 m³ dead oil per m³ of fluids at depth,^{9,255} or ~0.8 m³ when methane was assumed 100% in hydrate form.⁴⁵

Other flow rate estimates are available based on reservoir modeling, using measured pressures after the well was capped.^{265–268} In this case, the estimated flow of barrels of dead oil (at surface conditions) is obtained by dividing the estimated flow rate of single-phase MRF by

the so-called *formation volume factor*, which depends on the MRF composition.²⁶⁵ Our model estimates of this parameter are either 1.73 (MC₁) or 2.22–2.19 (MC₂, MC₃) for a single-stage flash from reservoir conditions²⁶⁵ to surface, which imply dead oil flow rates that differ by 25%. By comparison, Paul Hsieh used a value of 2.35, provided to him by BP personnel.²⁶⁵ Further complicating matters, these two estimates depend upon the exact process by which the single-phase MRF or the liquid and gas phases at depth (15.5 MPa and 4.3 °C) are brought to surface conditions. For example, a four-stage flash separation would yield ~11% more dead oil at surface conditions than the single-stage flash.⁵

These uncertainties illustrate that dead oil flow rates are a problematic metric for imposing legal penalties on deep-water petroleum fluid releases, unless a clear thermodynamic definition is introduced and used consistently. In contrast, total mass fluxes of emitted petroleum fluids would be a more broadly useful metric, being independent of both pressure and temperature conditions. However under the current legal framework in the United States, penalties are imposed based on the emitted volume of (dead) oil.

4.6 Outlook

The compositionally detailed thermodynamic model presented here can be viewed as a “benchmark”, useful for validating chemically simplified, less computationally intensive models of petroleum fluid thermodynamics and properties of MRF in the deep sea. In Chapter 5, simulated gas-liquid-water equilibria and associated fluid properties will be combined with detailed modeling of plume dynamics,²⁶⁹ aqueous dissolution kinetics, and hydrate formation.²⁷⁰ These combined simulation approaches can be used to improve our fundamental understanding of deep-sea petroleum fluid releases, further constrain hydrocarbon transfers to the water column during such events, and improve response planning for future deep-sea releases in other regions. This is a necessary step to allow the prediction of phase partitioning during a real deep-water release of petroleum fluids.

4.7 Acknowledgement

We are indebted to Marcia McNutt, Paul Hsieh and Rich Camilli for helpful discussions on flow rate estimates, to Jeff Seewald for discussions on MW-1 sample analysis procedure, and to Inok Jun for discussions on gas hydrates. We thank Aniela Burant and Deedar Nabi for fruitful discussions on property estimation methods, and we express gratitude to Aaron A. Zick for discussions about his EOS modeling. GRIDDC doi: <http://dx.doi.org/10.7266/N7PZ56RH>.

4.8 Funding Sources

This research was supported by grants from the NSF (OCE-0960841, OCE-1043976, and EAR-0950600), the BP/the Gulf of Mexico Research Initiative (GoMRI-015), C-IMAGE and DEEP-C consortia.

4.9 Appendix

4.9.1 Procedure for gas-liquid-water equilibrium calculation

The general procedure of our gas-liquid-water equilibrium calculation is described in Figure 4-5. Each step is detailed further below.

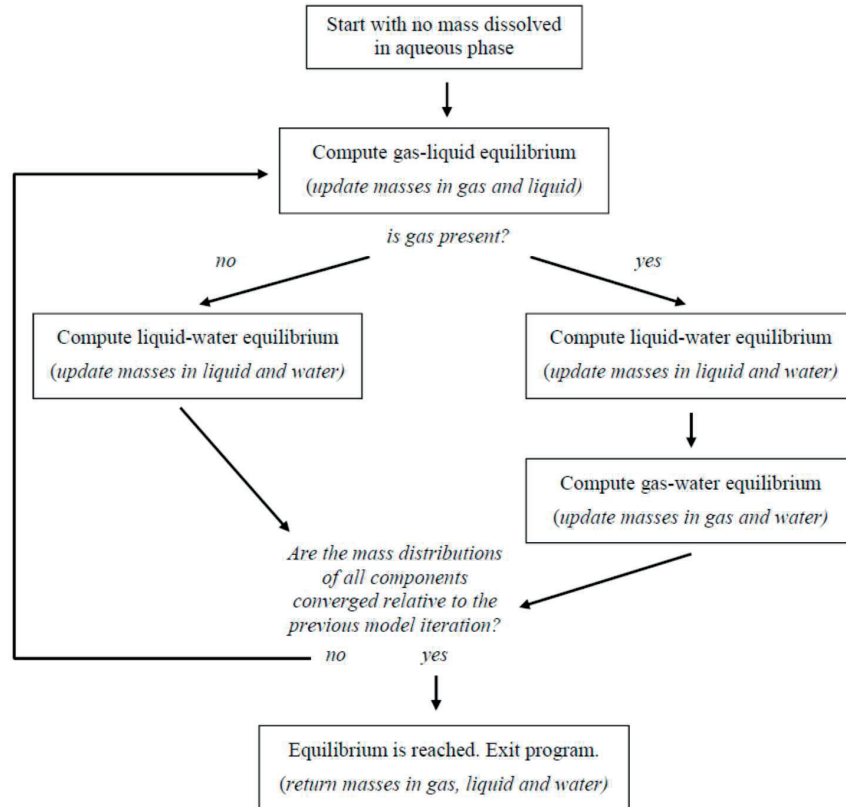


Figure 4-5. Schematic representation of our gas-liquid-water equilibrium calculation procedure.

4.9.1.1 Convergence of gas-liquid equilibrium computations

The gas-liquid equilibrium calculation is performed using a combination of successive substitution, stability analysis, and second order minimization techniques.²²⁴ We follow the overall procedure outlined on pages 266–267 of reference 224.

Successive substitution relies on so-called “K-factors”, defined as:

$$K_i = \frac{y_i}{x_i} = \frac{\phi_{liq,i}}{\phi_{gas,i}}$$

Equation 4-21

where K_i is the K-factor of component i , x_i and y_i are mole fractions in the liquid and gas phase, respectively, and $\phi_{liq,i}$ and $\phi_{gas,i}$ are fugacity coefficients in the liquid and gas phase, respectively.

An initial guess for K-factors is obtained from the Wilson correlation (page 259 of reference 224). Successive substitution consists in using the current K-factor estimates to determine the new x_i and y_i values (procedure at pages 253–254 of reference 224, where we chose the tolerance value for convergence to be 10^{-6}). Fugacity coefficients are then computed from x_i and y_i , using the PR EOS, which allows the determination of an updated K-factor estimate ($K_i = \phi_{liq,i} / \phi_{gas,i}$). The procedure is repeated iteratively.

Initially, three steps of successive substitution are performed, after which the difference in Gibbs energy of the resulting vapor and liquid compared to the single-phase mixture is evaluated. Different procedures are followed depending on the outcome of this evaluation (cases a–c on page 266 of reference 224). In favorable cases, the equilibrium calculation can be converged rapidly with additional steps of successive substitution (convergence was evaluated using the error function defined by equation 15-31 at page 430 of reference 177 with a convergence criterion set to $1.49012 \cdot 10^{-8}$). In other cases, the so-called tangent plane stability analysis is performed, which is a procedure to verify whether two phases are thermodynamically stable, or whether only one phase is present (pages 267–270 of reference 224); convergence for stability analysis is evaluated by verifying that the sum of the absolute values of the left-hand side of equation 46 on page 267 of reference 224 becomes smaller than 10^{-6} . When the rate of convergence becomes too low (which we defined by a number of iterations larger than $40 \cdot n_c$, where n_c is the number of components in the mixture), we switch to second order minimization techniques (pages 262–263 and 269 of reference 224).

Finally, after the three initial steps of successive substitution, any time that successive substitution reaches a stage where the current K-factor estimate indicates a single-phase mixture (i.e. that the fraction of the total moles in the gas phase obtained from the procedure at pages 253–254 of reference 224 is 0 or 1), a stability analysis is conducted to confirm this outcome or provide an improved estimate for the K-factors (page 267 of reference 224).

Any phase with $<10^{-5}$ times the total number of moles in the mixture is assumed negligible (i.e. in such cases the mixture is assumed single-phase).

4.9.1.2 Convergence of liquid-water and gas-water equilibrium computations

Initially, Henry's law constants are corrected for pressure, temperature, and salinity (Equation 4-16–Equation 4-18 in main text). Then, an iterative procedure is started. Fugacities in the petroleum phase (gas or liquid) can be computed from the PR EOS (Equation 4-2 in main text), and the aqueous solubilities, $C_{s,i}$, are simply obtained as:

$$C_{s,i} = f_i \cdot K_{H,i}$$

Equation 4-22

where f_i is the fugacity of component i in the hydrocarbon phase, and $K_{H,i}$ is the Henry's law constant (corrected for pressure, temperature and salinity). The mass dissolved at each iteration is obtained as $\Delta m_{diss,i} = (C_{s,i} - C_{water,i}) \cdot V_{water} \cdot \lambda$. $C_{water,i}$ is the concentration already in the water, V_{water} is the volume of water, and λ is a parameter that has a value of 1 at first iteration, and its value is divided by two when the iterative decrease in the change in composition is <1% for any of the total mass dissolved in water, methane, ethane, or propane (the minimal value of λ is set to 1/128). The amount of mass obtained for each compound is transferred to the aqueous phase, and the masses in the petroleum phase are updated accordingly. This procedure is repeated for at least 10 iterations and at maximum $1/\lambda$ iterations.

4.9.1.3 Convergence criterion for the gas-liquid-water equilibrium calculation

Convergence of the gas-liquid-water equilibrium is assumed to be reached when the total mass dissolved in water changes by <0.5% between two consecutive iterations, and the individual masses dissolved in water for methane, ethane, and propane are changed by <0.05% between two consecutive iterations.

4.9.2 Comparison of the composition of light compounds in MW-1 versus pre-spill downhole single-phase Macondo reservoir fluid (MRF) samples

We investigated whether biased sampling could explain the reportedly lower value of the gas-to-oil ratio (GOR) of the MW-1 sample, relative to the pre-spill downhole samples. In this section, we will demonstrate that the available data does not support this hypothesis. The pre-spill downhole samples were taken at pressure and temperature conditions (81.7 MPa and 386 K) indicating a single-phase mixture. However for MW-1 sample, the local conditions indicated that the mixture was partitioned into two phases. At the MW-1 sampling conditions, lighter compounds will tend to partition to the gas phase in larger proportion compared to heavier compounds. As a result, a hypothetical sampling bias towards the liquid-petroleum phase in the MW-1 sample would produce a lower relative concentration of the lowest molecular weight compounds compared to the higher molecular weight compounds, especially for C_1 – C_5 . However, the measured C_1 – C_5 data do not appear to exhibit any systematic fractionation pattern in one sample compared to the other (Figure 4-6), which suggests that sampling bias towards the liquid phase is not a likely explanation of the overall compositional discrepancy. As a result, we consider the two different sources of compositional information (MW-1 and pre-spill downhole samples) as equally valid.

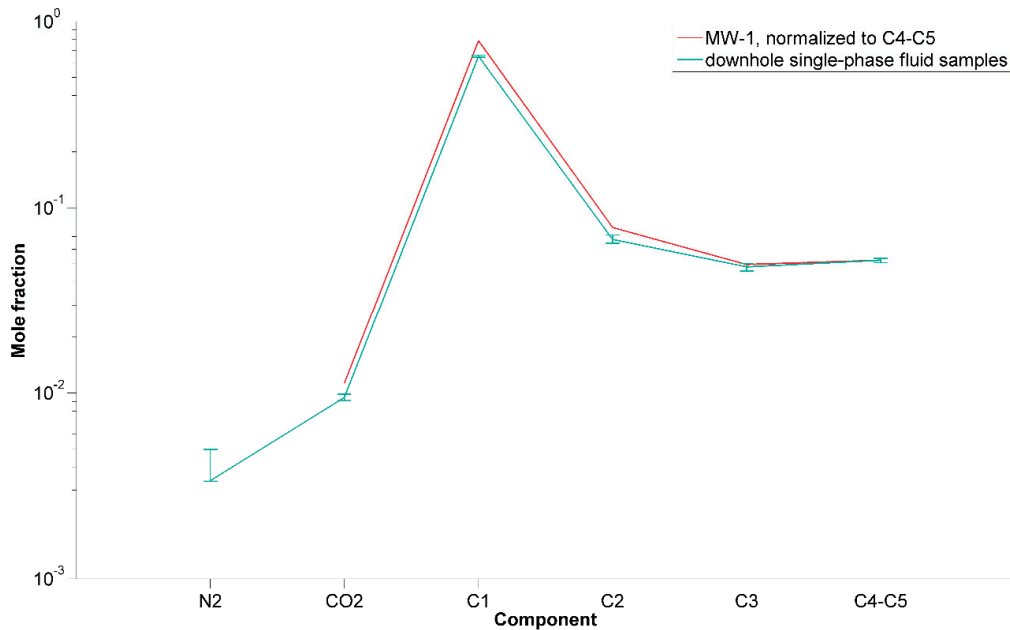


Figure 4-6. Comparison of reported N₂, CO₂, and C₁–C₅ hydrocarbon content between different reservoir fluid samples. The “average” pre-spill downhole sample composition is defined by Zick as the average of the heaviest and lightest pre-spill downhole samples,²⁰⁹ with error bars showing the range of values for the four sample compositions provided in his Table 2. The composition of the MW-1 sample is normalized so that the C₄–C₅ mole fraction matches the average of the lightest and heaviest pre-spill downhole single-phase fluid samples.

4.9.3 Combining light hydrocarbon and dead oil composition data

To obtain the mass fractions of single carbon number intervals from C₁ to C₁₀₈, results from the compositional analysis of the gas phase and dead oil must be combined. To construct the model mixture MC₁, we used the listed mass fractions in Macondo reservoir fluid (MRF) from Table S2 in Reddy et al. for the C₁–C₅ hydrocarbon compounds and CO₂.⁸ We used the simulated distillation data (mass fraction in dead oil for each single carbon number interval) in the C₆–C₁₀₈ range. The mass fraction of C₆–C₁₀₈ dead oil to mass fraction of MRF was assumed to have a ratio of 0.757:1.⁸ The mass fraction for each single carbon number interval from C₁ to C₁₀₈ are provided in Table 4-4. The mass fractions of single carbon number intervals for the pre-spill downhole single-phase MRF samples were obtained as described in section 4.9.8.

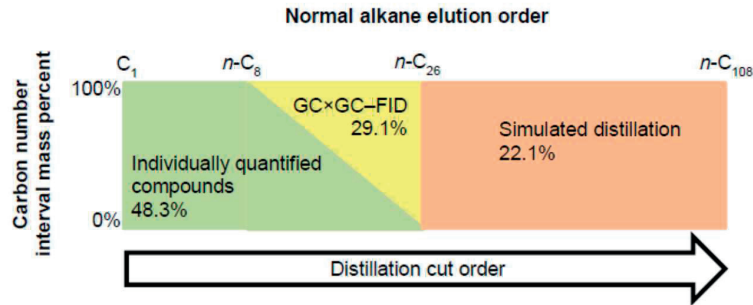


Figure 4-7. Schematic summary of existing knowledge about the composition of MRF. Nearly 100% of the mass of C_1 – n - C_8 hydrocarbons is characterized by the measured mass fractions of individually quantified known compounds (green). With increasing carbon number beyond n - C_8 , individually quantified compounds represent a decreasing fraction of the mixture, and GCxGC-FID data (yellow) is used to provide pseudo-components for compounds not quantified individually. Finally, compounds larger than n - C_{26} are characterized based on simulated distillation data (salmon color). Mass percentage in MW-1 for each category are displayed on the figure.

Table 4-4. Mass fraction in MW-1 sample for each single carbon number interval. Estimated properties of each single carbon number interval are also listed (see section 4.9.6 for explanations on estimation methods).

Carbon number interval	Pc [MPa]	Tc [K]	Vc [cm ³ mol ⁻¹]	omega [-]	Molar mass [g mol ⁻¹]	Mass fraction in MW-1 [-]
C ₁	4.599	190.6	98.6	0.011	16.043	1.50E-01
C ₂	4.872	305.3	145.5	0.099	30.07	2.80E-02
C ₃	4.248	369.8	200.0	0.152	44.097	2.60E-02
<i>i</i> -C ₄	3.640	407.8	262.7	0.186	58.123	6.70E-03
<i>n</i> -C ₄	3.796	425.1	255.0	0.200	58.123	1.50E-02
<i>i</i> -C ₅	3.381	460.4	308.3	0.229	72.15	7.90E-03
<i>n</i> -C ₅	3.370	469.7	311.0	0.252	72.15	1.00E-02
C ₆	3.025	507.6	368.0	0.300	84	2.73E-02
C ₇	2.948	550.2	407.9	0.299	96	3.32E-02
C ₈	2.725	581.8	459.1	0.337	107	4.10E-02
C ₉	2.539	608.4	508.3	0.374	121	3.86E-02
C ₁₀	2.361	632.7	560.1	0.413	134	3.90E-02
C ₁₁	2.196	654.8	614.6	0.454	147	3.25E-02
C ₁₂	2.068	674.7	664.3	0.490	161	2.90E-02
C ₁₃	1.962	693.6	711.6	0.524	175	2.98E-02
C ₁₄	1.865	712.3	759.9	0.558	190	2.85E-02
C ₁₅	1.784	729.2	804.6	0.590	206	2.79E-02
C ₁₆	1.700	744.1	852.0	0.624	222	2.32E-02
C ₁₇	1.636	758.4	893.5	0.654	237	2.26E-02
C ₁₈	1.566	770.7	938.2	0.686	251	2.28E-02
C ₁₉	1.504	782.4	981.6	0.717	263	1.86E-02
C ₂₀	1.437	794.9	1030.5	0.751	275	2.02E-02
C ₂₁	1.382	806.6	1075.2	0.782	291	1.89E-02
C ₂₂	1.339	816.9	1112.8	0.810	305	1.51E-02

Carbon number interval	Pc [MPa]	Tc [K]	Vc [cm ³ mol ⁻¹]	omega [-]	Molar mass [g mol ⁻¹]	Mass fraction in MW-1 [-]
C ₂₃	1.302	826.9	1147.8	0.836	318	1.39E-02
C ₂₄	1.261	836.4	1186.5	0.863	331	1.37E-02
C ₂₅	1.225	845.5	1222.7	0.890	345	1.34E-02
C ₂₆	1.191	854.6	1259.0	0.916	359	1.34E-02
C ₂₇	1.163	862.9	1289.9	0.940	374	1.17E-02
C ₂₈	1.132	870.8	1324.9	0.965	388	1.14E-02
C ₂₉	1.104	878.3	1357.2	0.989	402	1.01E-02
C ₃₀	1.077	885.7	1389.6	1.013	416	9.77E-03
C ₃₁	1.056	893.6	1417.4	1.035	430	9.46E-03
C ₃₂	1.034	900.7	1446.8	1.057	444	8.48E-03
C ₃₃	1.014	907.4	1473.2	1.078	458	8.18E-03
C ₃₄	0.993	913.2	1501.6	1.099	472	7.42E-03
C ₃₅	0.974	919.9	1528.0	1.119	486	7.87E-03
C ₃₆	0.954	925.7	1556.4	1.140	500	7.04E-03
C ₃₇	0.941	931.7	1576.6	1.157	514	6.44E-03
C ₃₈	0.926	936.8	1599.0	1.175	528	5.68E-03
C ₃₉	0.907	942.6	1627.4	1.196	542	6.44E-03
C ₄₀	0.893	947.7	1649.8	1.213	556	5.22E-03
C ₄₁	0.881	952.4	1669.1	1.228	570	4.62E-03
C ₄₂	0.863	957	1697.1	1.247	584	5.00E-03
C ₄₃	0.850	962.1	1719.4	1.265	598	4.77E-03
C ₄₄	0.841	966.5	1735.5	1.278	612	3.79E-03
C ₄₅	0.832	970.8	1751.4	1.292	626	3.71E-03
C ₄₆	0.819	975.9	1774.1	1.309	640	4.39E-03
C ₄₇	0.810	980.2	1790.7	1.323	654	3.63E-03
C ₄₈	0.800	984.5	1807.4	1.336	668	3.48E-03
C ₄₉	0.795	988	1818.1	1.346	682	2.65E-03
C ₅₀	0.786	992.3	1835.2	1.360	696	3.33E-03
C ₅₁	0.780	995.8	1846.2	1.370	710	2.57E-03
C ₅₂	0.771	1000	1863.6	1.384	724	3.26E-03
C ₅₃	0.766	1003.5	1874.8	1.394	738	2.42E-03
C ₅₄	0.758	1007.3	1889.4	1.406	752	2.65E-03
C ₅₅	0.752	1010.7	1900.9	1.416	766	2.27E-03
C ₅₆	0.747	1014.2	1912.6	1.426	780	2.27E-03
C ₅₇	0.741	1017.6	1924.4	1.436	794	2.20E-03
C ₅₈	0.735	1021	1936.3	1.446	808	2.12E-03
C ₅₉	0.727	1024.8	1951.5	1.459	822	2.42E-03
C ₆₀	0.725	1027.4	1957.4	1.465	836	1.44E-03
C ₆₁	0.719	1030.8	1969.7	1.475	850	2.04E-03
C ₆₂	0.715	1033.8	1978.9	1.483	864	1.67E-03
C ₆₃	0.712	1036.4	1985.1	1.489	878	1.36E-03
C ₆₄	0.706	1039.8	1997.8	1.500	892	1.89E-03
C ₆₅	0.701	1042.8	2007.3	1.508	906	1.59E-03

Carbon number interval	Pc [MPa]	Tc [K]	Vc [cm ³ mol ⁻¹]	omega [-]	Molar mass [g mol ⁻¹]	Mass fraction in MW-1 [-]
C ₆₆	0.699	1045.3	2013.9	1.514	920	1.29E-03
C ₆₇	0.696	1047.9	2020.5	1.520	934	1.29E-03
C ₆₈	0.691	1050.9	2030.4	1.529	948	1.51E-03
C ₆₉	0.688	1053.4	2037.2	1.535	962	1.29E-03
C ₇₀	0.683	1056.4	2047.3	1.543	976	1.51E-03
C ₇₁	0.680	1058.9	2054.3	1.549	990	1.21E-03
C ₇₂	0.677	1061.5	2061.5	1.556	1004	1.14E-03
C ₇₃	0.676	1063.6	2065.6	1.560	1018	9.09E-04
C ₇₄	0.672	1066.2	2072.9	1.566	1032	1.14E-03
C ₇₅	0.668	1069.1	2083.4	1.574	1046	1.29E-03
C ₇₆	0.664	1071.6	2090.8	1.581	1060	1.06E-03
C ₇₇	0.659	1074.5	2101.5	1.589	1074	1.21E-03
C ₇₈	0.656	1077	2109.1	1.595	1088	9.84E-04
C ₇₉	0.653	1079.5	2116.8	1.601	1102	9.84E-04
C ₈₀	0.651	1081.6	2121.5	1.605	1116	7.57E-04
C ₈₁	0.647	1084.1	2129.3	1.612	1130	9.09E-04
C ₈₂	0.642	1087	2140.3	1.619	1144	1.06E-03
C ₈₃	0.642	1088.7	2142.1	1.622	1158	5.30E-04
C ₈₄	0.637	1091.5	2153.3	1.630	1172	1.06E-03
C ₈₅	0.636	1093.3	2155.2	1.632	1186	5.30E-04
C ₈₆	0.631	1096.1	2166.5	1.640	1200	1.06E-03
C ₈₇	0.630	1097.8	2168.6	1.642	1214	5.30E-04
C ₈₈	0.628	1099.9	2173.8	1.647	1228	7.57E-04
C ₈₉	0.626	1102	2179.1	1.651	1242	7.57E-04
C ₉₀	0.622	1104.4	2187.6	1.657	1256	9.09E-04
C ₉₁	0.620	1106.5	2193.0	1.661	1270	7.57E-04
C ₉₂	0.619	1108.2	2195.4	1.663	1284	5.30E-04
C ₉₃	0.617	1110.2	2200.9	1.667	1298	6.81E-04
C ₉₄	0.616	1111.9	2203.5	1.670	1312	5.30E-04
C ₉₅	0.613	1113.9	2209.2	1.674	1326	6.81E-04
C ₉₆	0.611	1116	2214.9	1.678	1340	6.81E-04
C ₉₇	0.610	1117.6	2217.6	1.681	1354	4.54E-04
C ₉₈	0.608	1119.7	2223.4	1.685	1368	6.06E-04
C ₉₉	0.606	1121.3	2226.2	1.687	1382	4.54E-04
C ₁₀₀	0.604	1123.3	2232.2	1.691	1396	5.30E-04
C ₁₀₁	0.603	1125	2235.1	1.693	1410	4.54E-04
C ₁₀₂	0.602	1126.6	2238.1	1.696	1424	3.79E-04
C ₁₀₃	0.600	1128.3	2241.2	1.698	1438	3.79E-04
C ₁₀₄	0.599	1129.9	2244.3	1.700	1452	3.79E-04
C ₁₀₅	0.598	1131.5	2247.4	1.703	1466	3.79E-04
C ₁₀₆	0.597	1133.1	2250.6	1.705	1480	3.79E-04
C ₁₀₇	0.596	1134.8	2253.9	1.707	1494	3.03E-04
C ₁₀₈	0.596	1136	2254.2	1.708	1508	2.27E-04

4.9.4 Comprehensive two-dimensional gas chromatography (GC×GC) analysis method

An aliquot of the dead oil separated from the MW-1 sample⁸ was analyzed by GC×GC coupled to a flame ionization detector (GC×GC–FID).

The sample was injected splitless on a GC×GC–FID (Agilent 7890) having an Rxi-ms first-dimension column (60 m length, 0.25 mm internal diameter (I.D.), 0.25 μm film thickness) and a BPX-50 second-dimension column (1.5 m length, 0.10 mm I.D., 0.10 μm film thickness). The carrier gas was dihydrogen at a constant flow rate of 1.00 mL min⁻¹. The inlet temperature was held at 310 °C. The first oven was programmed as follows: hold at 45 °C for 10 min, ramp from 45 to 330 °C at 1.50 °C min⁻¹ (held 0.50 min). The second oven was programmed so as to remain 5 °C warmer than the first oven throughout the run. The modulation period was 7.50 s. The modulator was maintained 10 °C warmer than the second oven, with a hot pulse time of 0.75 s and cool time of 3.00 s. The FID was at 330 °C, and the detector acquisition rate was 100 Hz, with a 1000 s acquisition delay.

For the quantification of the total (resolved plus unresolved) signal,⁶⁶ we have shown previously that it is appropriate to baseline-correct the chromatogram^{62,66} with the deadband method of Reichenbach and co-workers (section 1.3.1).⁷⁰ We used GC Image (version 2.2b4)⁷¹ with the following parameters: 10 deadband pixels per modulation; filter window size of 3 pixels, 3.5 for the expected value of baseline plus noise to the estimated standard deviation of the noise; and one baseline value per modulation.

4.9.5 Approximate structures assigned to pseudo-components derived from GC×GC–FID

The rules employed to assign approximate structures to pseudo-components are the following:

- **Saturated hydrocarbons** are modeled as a normal alkane with varying chain length, from *n*-C₉ to *n*-C₂₆.
- **1-ring aromatic hydrocarbons** are modeled as a linear alkyl benzene with varying alkyl chain length, from ethylbenzene to nonadecylbenzene.
- **2-ring aromatic hydrocarbons** are modeled as a naphthalene structure with different degrees of methylation. The smallest 2-ring structure assigned is that of naphthalene, and each increase of one carbon atom corresponds to the addition of a methyl group. When no more methyl groups can be added, one of the methyl chain is converted to an ethyl group and subsequently to longer linear chain groups (propyl, butyl, ...) for each carbon number increase.

- **3-ring aromatic hydrocarbons** are modeled as a phenanthrene structure with different degrees of methylation. The smallest 3-ring structure assigned is that of phenanthrene, and each increase of one carbon atom corresponds to the addition of a methyl group.
- **4-ring aromatic hydrocarbons** are modeled as a pyrene structure with different degrees of methylation. The smallest 4-ring structure assigned is that of pyrene, and each increase of one carbon atom corresponds to the addition of a methyl group.

The reader is referred to Figure 4-2b (main text) for a few examples of the assigned approximate structures. A key indicating the assumed structure of each pseudo-component obtained from the GC×GC–FID chromatogram is provided by Figure 4-8 and Table 4-5.

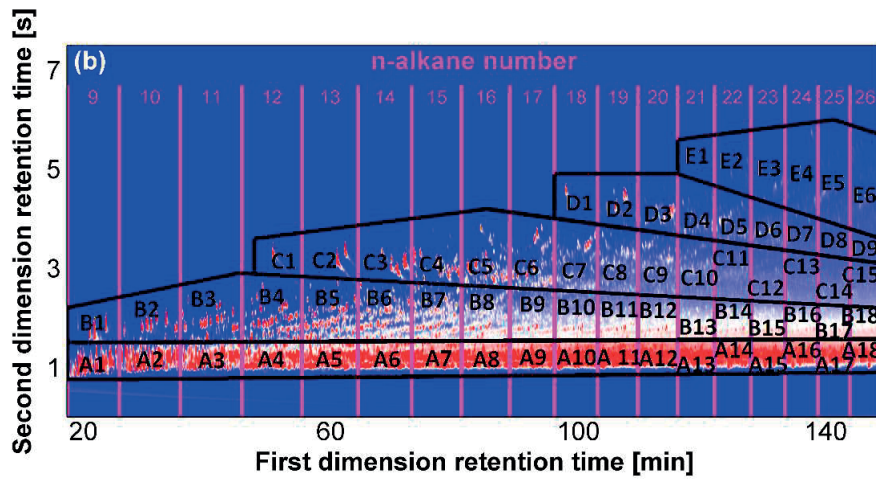


Figure 4-8. Names of the pseudo-components obtained from the GC×GC–FID chromatogram as used in Table 4-5, which provides the corresponding chemical names of the approximate structures. Acenaphthene and fluorene (each of which contain 2 aromatic rings and one non-aromatic ring) are included in the 2-ring aromatics group.

Table 4-5. Chemical names for the approximate structure of the pseudo-components obtained from the GC×GC–FID chromatogram (see Figure 4-8 for the pseudo-component names).

Pseudo-component name	Chemical name	Number of carbon atoms
A1	<i>n</i> -C ₉	9
A2	<i>n</i> -C ₁₀	10
A3	<i>n</i> -C ₁₁	11
A4	<i>n</i> -C ₁₂	12
A5	<i>n</i> -C ₁₃	13
A6	<i>n</i> -C ₁₄	14
A7	<i>n</i> -C ₁₅	15
A8	<i>n</i> -C ₁₆	16
A9	<i>n</i> -C ₁₇	17
A10	<i>n</i> -C ₁₈	18
A11	<i>n</i> -C ₁₉	19
A12	<i>n</i> -C ₂₀	20
A13	<i>n</i> -C ₂₁	21
A14	<i>n</i> -C ₂₂	22
A15	<i>n</i> -C ₂₃	23

Pseudo-component name	Chemical name	Number of carbon atoms
A16	<i>n</i> -C ₂₄	24
A17	<i>n</i> -C ₂₅	25
A18	<i>n</i> -C ₂₆	26
B1	linear ethylbenzene	8
B2	linear propylbenzene	9
B3	linear butylbenzene	10
B4	linear pentylbenzene	11
B5	linear hexylbenzene	12
B6	linear heptylbenzene	13
B7	linear octylbenzene	14
B8	linear nonylbenzene	15
B9	linear decylbenzene	16
B10	linear undecylbenzene	17
B11	linear dodecylbenzene	18
B12	linear tridecylbenzene	19
B13	linear tetradecylbenzene	20
B14	linear pentadecylbenzene	21
B15	linear hexadecylbenzene	22
B16	linear heptadecylbenzene	23
B17	linear octadecylbenzene	24
B18	linear nonadecylbenzene	25
C1	naphthalene	10
C2	methylnaphthalene	11
C3	dimethylnaphthalene	12
C4	trimethylnaphthalene	13
C5	tetramethylnaphthalene	14
C6	pentamethylnaphthalene	15
C7	hexamethylnaphthalene	16
C8	heptamethylnaphthalene	17
C9	octamethylnaphthalene	18
C10	(ethyl,heptamethyl)naphthalene	19
C11	(propyl,heptamethyl)naphthalene	20
C12	(butyl,heptamethyl)naphthalene	21
C13	(pentyl,heptamethyl)naphthalene	22
C14	(hexyl,heptamethyl)naphthalene	23
C15	(heptyl,heptamethyl)naphthalene	24
D1	phenanthrene	14
D2	methylphenanthrene	15
D3	dimethylphenanthrene	16
D4	trimethylphenanthrene	17
D5	tetramethylphenanthrene	18
D6	pentamethylphenanthrene	19
D7	hexamethylphenanthrene	20
D8	heptamethylphenanthrene	21
D9	octamethylphenanthrene	22
E1	pyrene	16
E2	methylpyrene	17
E3	dimethylpyrene	18
E4	trimethylpyrene	19
E5	tetramethylpyrene	20
E6	pentamethylpyrene	21

4.9.6 Definition of pseudo-components for single carbon number intervals $\geq n$ -C₂₆ based on simulated distillation data

For chromatographic elution intervals after n -C₂₆, we used mass fractions provided by simulated distillation (section 4.9.3) and we used a classical procedure to define pseudo-component critical properties and acentric factors. For each carbon number elution interval from C₂₆ to C₁₀₈, correlations were used to estimate the critical properties (T_{wu})²⁴⁴ and the acentric factor (Kesler-Lee).²⁴⁵ In these computations, we assigned molecular weights and specific gravities of carbon number intervals from C₂₆ to C₄₅ using the values published by Katz and Firoozabadi.²⁴⁸ This estimation method is often used, bearing in mind that the specific gravities of individual distillation fractions depend slightly on the composition of the oil.^{246,247} We followed the procedure of Zuo et al.²⁴⁶ to extrapolate these data to elution intervals in the C₄₆–C₁₀₈ range:

$$M_i = 14 \cdot N_i - 4$$

Equation 4-23

where the molar weight M_i in g mol^{-1} is estimated from the number of carbon atoms N_i for each carbon number elution interval i after C₄₅ ($N_i \geq 46$), and:

$$SG_i = D_1 \cdot \ln(M_i) + D_2$$

Equation 4-24

where SG_i is the specific gravity, and D_1 and D_2 are two fitted constants. We fitted the two constants to the Katz and Firoozabadi values for C₄₂ and C₄₅.

The estimated properties for each pseudo-component $\geq n$ -C₂₆ are provided in Table 4-4.

4.9.7 Definition of model composition of MW-1 dead oil, MC_{1,do}

Model dead oil composition of MW-1, MC_{1,do}, was defined based on dead oil analysis. MC_{1,do} is identical to MC₁, except that the mass fractions of CO₂ and C₁–C₆ hydrocarbons have been reassigned to values measured in the dead oil,⁸ and the concentrations of all other compounds have been divided by 0.757, taken as the ratio of mass of dead oil to mass of MRF.⁸

4.9.8 Definitions of model compositions MC₂ and MC₃

Model compositions MC₂ and MC₃ are based on compositional analysis of pre-spill downhole MRF samples by Schlumberger (sample 1.18)²³¹ and Pencor (sample 53),²³² respectively. These analyses used different gas chromatography devices to quantify mass fractions of N₂, CO₂, and carbon number elution intervals from C₁ to C₃₅ (Schlumberger) or to C₄₉ (Pencor).

We used the mass fractions reported by these laboratories for N₂, CO₂, and the C₁–C₅ hydrocarbons. The concentrations of all other compounds individually quantified in MW-1 were

assumed present in the dead oil fractions of MC₂ and MC₃ at the same concentrations as for MW-1, and their concentrations in MC₂ and MC₃ were therefore normalized according to:

$$m_i(MC_x) = m_i(MC_1) \cdot \frac{m_{C_{6+}}(MC_x)}{m_{C_{6+}}(MC_1)}$$

Equation 4-25

where m stands for mass fraction, i for any individual compound $>n$ -C₅, x is 2 or 3, and $m_{C_{6+}}$ is the mass fraction of C₆₊ compounds.

We used the mass fractions reported by Schlumberger (MC₂) and Pencor (MC₃) for single carbon number elution intervals up to C₃₅ (MC₂) or C₄₉ (MC₃) as simulated distillation data. In other words, we used these values to generate the pseudo-components of MC₂ and MC₃ based on the GC×GC–FID chromatogram of MW-1 dead oil. This means that the mass fraction eluting between two consecutive normal alkanes was taken as that measured in the original (Schlumberger or Pencor) sample, whereas the relative contributions of different hydrocarbon compounds in this mass fraction were assumed the same as found in MW-1.

For MC₂ and MC₃, the assignment of mass fractions for $\geq n$ -C₂₆ pseudo-components are described in section 4.9.6. The remaining fraction (C₃₆₊ or C₅₀₊) was separated into single carbon number intervals up to C₁₀₈, assuming that the relative concentrations were identical to that of MW-1.

MC₂ and MC₃ are very similar to one another, and these model compositions were used to validate the thermodynamic model against laboratory density and gas-liquid equilibrium data (MC₂), and viscosity data (MC₃). The principal difference between MC₁ and the two other model compositions arises from the value of the $m_{C_{6+}}$ fraction (assigned as 0.75 for MC₁ and as 0.65 for MC₂ and MC₃). A more minor difference is that MC₁ does not include nitrogen, therefore MC₁ includes 279 components, whereas MC₂ and MC₃ each include nitrogen and therefore each comprise of 280 components.

4.9.9 Procedure for selection of Henry's law constant values from Sander²³⁰

To select literature data²³⁰ values of the Henry's law constant for individual compounds, we followed the procedure summarized below. We use the abbreviations "L", "M", "Q", "E", and "?" as defined by Sander,²³⁰ each defined below after their first occurrence. (Note that in order to validate the group-contribution estimation method (Table 4-1 and section 4.9.10) we retained only a subset of these data, corresponding to values coming from literature reviews or measurements.)

- Take the values considered by the author to be the most reliable²³⁰ (category denoted "L" by Sander,²³⁰ from literature reviews), and average them;
- If no value of the "L" type is listed, take the second best type of values ("M", from original publication of a measurement), and average them;

- Otherwise, take all values of any other type that are listed and average them, excluding values with type "Q" (estimate obtained with the quantitative structure property relationship (QSPR)), "E" (estimate), and "?" (the cited reference does not state clearly how the value was obtained).
- As a last resort, take the "Q", "E" and "?" values.

In doing this, we considered only references from 1950 onward unless no other data were available.

We discarded some obvious outliers among conflicting reported data, as reported below, and we made a few exceptions to the procedure above, also listed below:

- Isopropylbenzene: among the "L" values, we selected the value of $1.2 \cdot 10^{-3}$, and we discarded the value of $7.7 \cdot 10^{-3}$, which is an outlier with respect to the other "L" and "M" values.
- Fluoranthene: the oldest value ($4.5 \cdot 10^{-3}$, two orders of magnitude lower than other reported values) was discarded.
- C₁-naphthalenes, C₂-naphthalenes, C₃-naphthalenes, C₁-phenanthrenes: we took a mean of values for compounds for which an "L" value was reported (obtain a value by structural isomer, average if needed, and then perform an average over all isomers). For example, C₁-naphthalenes corresponds to the grouping of all isomers formed of naphthalene to which one methyl substituent is added. To get a value for C₁-naphthalenes, we considered the two isomers for which "L" data were available,²³⁰ 1-methylnaphthalene and 2-methylnaphthalene. The average of "L" values for 1-methylnaphthalene is $2.2 \cdot 10^{-2} \text{ mol m}^{-3} \text{ Pa}^{-1}$, and the only "L" value for 2-methylnaphthalene is $1.8 \cdot 10^{-2} \text{ mol m}^{-3} \text{ Pa}^{-1}$. Hence, the value retained for C₁-naphthalenes is $2.0 \cdot 10^{-2} \text{ mol m}^{-3} \text{ Pa}^{-1}$.
- Normal alkanes from *n*-C₁₃ to *n*-C₂₀: considerable discrepancies exist in reported values between different references. We retained data from the only reference that provides data for all of these compounds (Yaws and Yang, 1992). Data for normal alkanes >*n*-C₂₀ were discarded. We note that the large discrepancy among available literature data for normal alkanes^{176,230} will not affect predictions of the model for dissolution extents to be expected in the environment (Figure 4-21).
- N₂: the value from the oldest reference was discarded (obtained at a different temperature, 310 K, than the reference temperature chosen, 298.15 K).

4.9.10 Validation of group-contribution methods used for estimation of the chemical properties

In the thermodynamic model, we used estimated input properties only when literature data were unavailable. However, here we consider the cases where literature measurement data were available, and we compute the corresponding estimated values. We compare the resulting sets of measured and estimated values as a validation exercise for the estimation methods.

Figure 4-9 to Figure 4-14 show results of this brief evaluation of the validity of the property-estimation methods. In this series of figures, we compare the literature measurement data to estimates obtained from the selected group-contribution methods, for compounds quantified in MW-1 for which literature measurement data could be found (excluding CO₂). For several methods, the predictions are the least accurate for small compounds ($\leq n\text{-C}_5$). However, for these small compounds, group-contribution methods were not used, since literature data were always available.

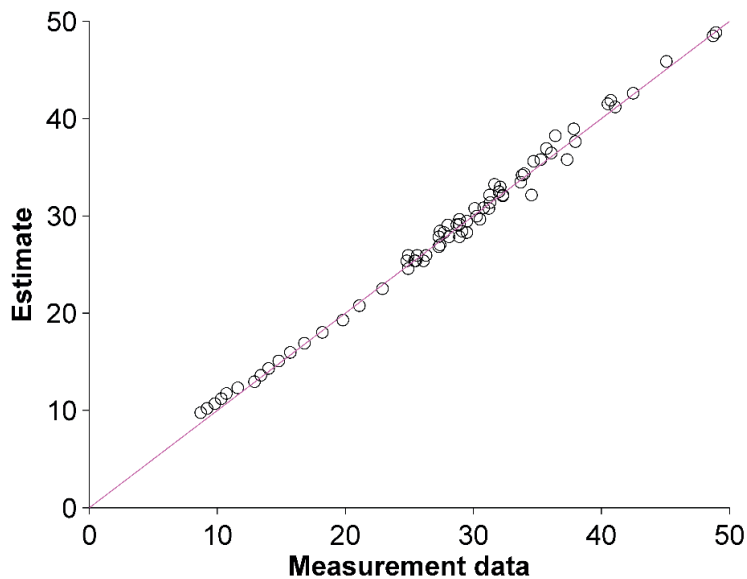


Figure 4-9. Comparison of literature measurement data and group-contribution estimates for the critical pressure, in bar. (See Table 4-1 in main text for references and statistics.)

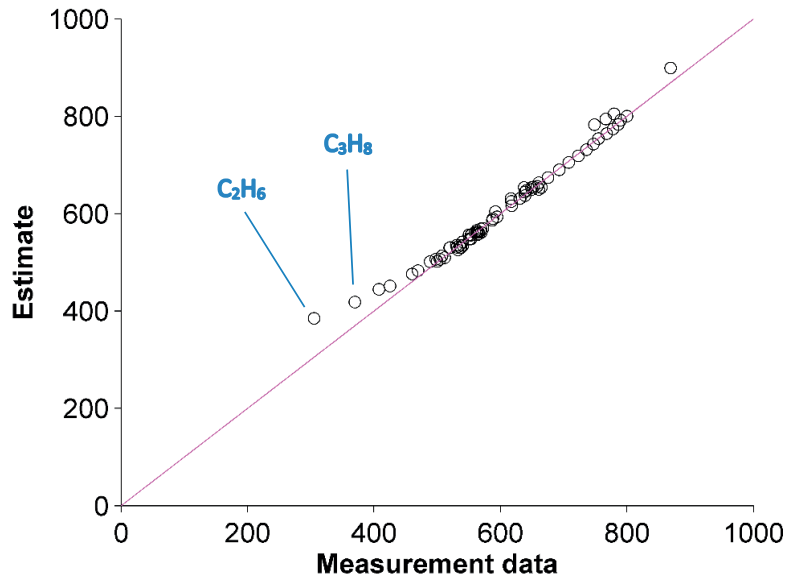


Figure 4-10. Comparison of literature measurement data and group-contribution estimates for the critical temperature, in K. (See Table 4-1 in main text for references and statistics.)

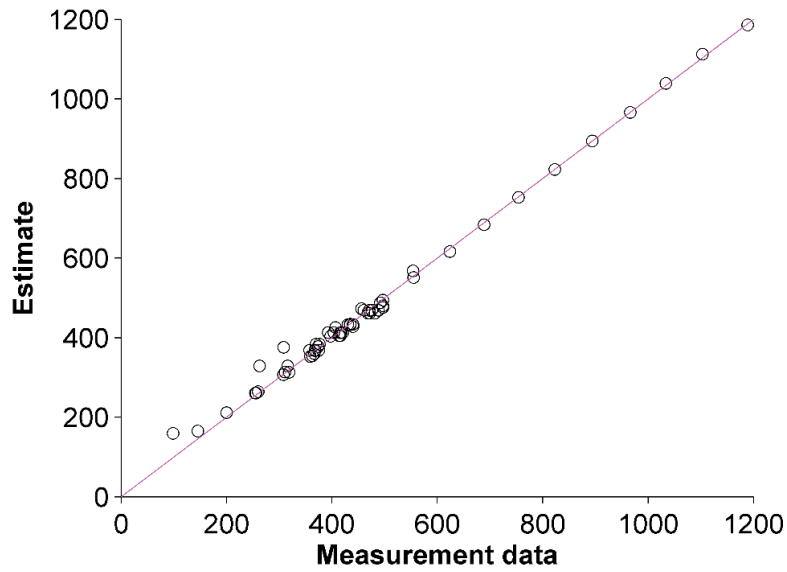


Figure 4-11. Comparison of literature measurement data and group-contribution estimates for the critical volume, in $\text{cm}^3 \text{mol}^{-1}$. (See Table 4-1 in main text for references and statistics.)

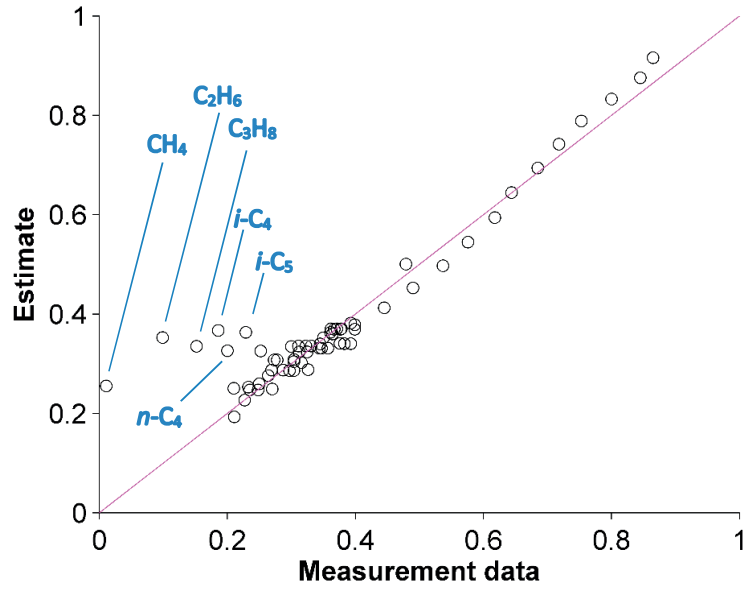


Figure 4-12. Comparison of literature measurement data and group-contribution estimates for the acentric factor. (See Table 4-1 in main text for references and statistics.)

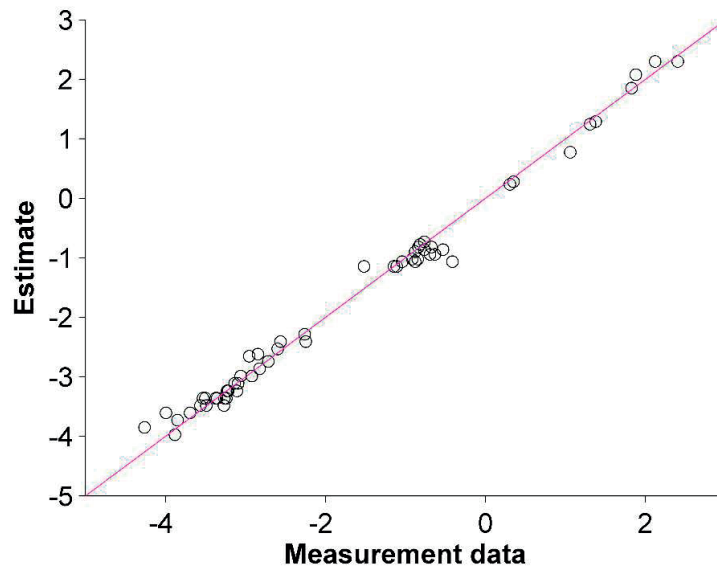


Figure 4-13. Comparison of literature measurement data and group-contribution estimates for the (base 10) logarithm of the Henry's law constant, in $\text{mol L}^{-1} \text{atm}^{-1}$. (See Table 4-1 in main text for references and statistics.)

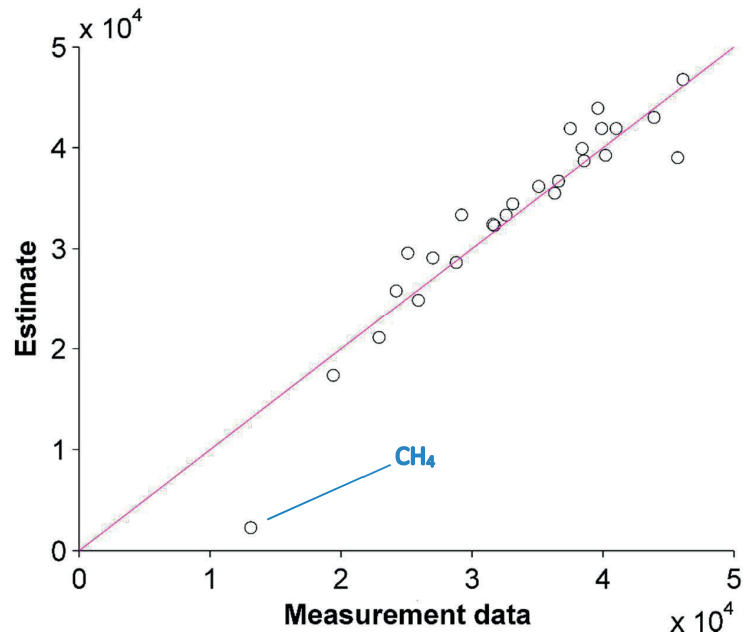


Figure 4-14. Comparison of literature measurement data and group-contribution estimates for the negative of the enthalpy of transfer from gas phase to water, in J mol^{-1} . (See Table 4-1 in main text for references and statistics.)

4.9.11 Literature measurement data used to derive the correlations of Equation 4-19 and Equation 4-20

Table 4-6. Literature measurement data (\bar{V}_{meas}^L) used to derive the correlation for estimating the partial molar volume at infinite dilution in water (Equation 4-19). The absolute value of the relative error

is defined as $\left| \frac{\bar{V}_{meas}^L - \bar{V}_{equation\ 4-19}^L}{\bar{V}_{meas}^L} \right|$. The McGowan volume, \bar{V}_{MG} , is also provided.

Compound	Reference for \bar{V}_{meas}^L	\bar{V}_{meas}^L cm ³ mol ⁻¹	$\bar{V}_{equation\ 4-19}^L$ cm ³ mol ⁻¹	\bar{V}_{MG} cm ³ mol ⁻¹	Absolute relative error
methane	Graziano ²³⁶	34.7	31.6	24.95	9.0%
ethane	Graziano ²³⁶	50.4	47.5	39.04	5.7%
propane	Liu and Ruckenstein ²³⁵	70.7	63.5	53.13	10.2%
<i>i</i> -C ₄	Liu and Ruckenstein ²³⁵	81.3	79.4	67.22	2.3%
<i>n</i> -C ₄	Liu and Ruckenstein ²³⁵	76.6	79.4	67.22	3.7%
<i>n</i> -C ₅	Liu and Ruckenstein ²³⁵	92.3	95.4	81.31	3.3%
CO ₂	King ²¹⁵	32	35.1	28.09	9.8%
cyclopentane	Liu and Ruckenstein ²³⁵	84.5	83.1	70.45	1.7%
2,3-dimethylbutane	Liu and Ruckenstein ²³⁵	106.8	111.3	95.40	4.2%
<i>n</i> -C ₆	Liu and Ruckenstein ²³⁵	110	111.3	95.40	1.2%
benzene	Liu and Ruckenstein ²³⁵	82.5	84.4	71.64	2.3%
cyclohexane	Liu and Ruckenstein ²³⁵	98.8	99.0	84.54	0.2%
<i>n</i> -C ₇	Liu and Ruckenstein ²³⁵	129.4	127.3	109.49	1.7%
toluene	Liu and Ruckenstein ²³⁵	97.7	100.4	85.73	2.7%
<i>n</i> -C ₈	Liu and Ruckenstein ²³⁵	145.2	143.2	123.58	1.4%
ethylbenzene	Liu and Ruckenstein ²³⁵	111.1	116.3	99.82	4.7%
<i>n</i> -C ₁₀	Liu and Ruckenstein ²³⁵	176.8	175.1	151.76	1.0%
1,2,3,4 tetramethylbenzene	Liu and Ruckenstein ²³⁵	209.5	207.0	179.94	1.2%

K_{salt} measured in seawater or NaCl solutions usually agree within experimental errors.¹⁵⁶ Therefore, although we preferred data for seawater or artificial seawater whenever available, we included values obtained with NaCl when this was the only information available. The salts used to obtain the experimental values are listed in Table 4-7.

Table 4-7. Literature measurement data ($K_{salt,meas}$) used to derive the correlation for estimating the Setschenow constant (Equation 4-20). The absolute value of the relative error is defined as

$$\frac{K_{salt,meas} - K_{salt,equation\ 4-20}}{K_{salt,meas}}$$

Compound	Reference for $K_{salt,meas}$	Salt	$K_{salt,meas}$ L mol ⁻¹	$K_{salt,equation\ 4-20}$ L mol ⁻¹	Absolute relative error
methane	Ni and Yalkowsky ²³⁷	NaCl	0.127	0.159	25.3%
ethane	Ni and Yalkowsky ²³⁷	NaCl	0.162	0.184	13.7%
propane	Ni and Yalkowsky ²³⁷	NaCl	0.194	0.222	14.5%
<i>n</i> -C ₄	Ni and Yalkowsky ²³⁷	NaCl	0.217	0.220	1.3%
<i>n</i> -C ₅	Xie et al. ¹⁷³	"artificial, NaCl"	0.221	0.245	10.8%
CO ₂	Weiss ²³⁸	seawater	0.132	0.114	13.9%
cyclopentane	Xie et al. ¹⁷³	NaCl	0.182	0.226	24.1%
<i>n</i> -C ₆	Xie et al. ¹⁷³	NaCl	0.276	0.276	0.2%
methylcyclopentane	Xie et al. ¹⁷³	"artificial, NaCl"	0.273	0.248	9.3%
benzene	Schwarzenbach et al. ¹⁵⁶	seawater	0.200	0.209	4.7%
cyclohexane	Xie et al. ¹⁷³	NaCl	0.277	0.247	10.9%
methylcyclohexane	Xie et al. ¹⁷³	NaCl	0.274	0.273	0.2%
toluene	Schwarzenbach et al. ¹⁵⁶	seawater	0.240	0.233	2.9%
ethylbenzene	Schwarzenbach et al. ¹⁵⁶	seawater	0.290	0.252	13.2%
<i>p/m</i> -xylenes	Schwarzenbach et al. ¹⁵⁶	seawater	0.295	0.266	9.7%
<i>o</i> -xylene	Schwarzenbach et al. ¹⁵⁶	seawater	0.300	0.266	11.2%
isopropylbenzene	Xie et al. ¹⁷³	artificial seawater	0.316	0.292	7.5%
1,3,5-trimethylbenzene	Xie et al. ¹⁷³	artificial seawater	0.318	0.292	8.1%
1,2,4-trimethylbenzene	Xie et al. ¹⁷³	artificial seawater	0.293	0.292	0.3%
sec-butylbenzene	Xie et al. ¹⁷³	artificial seawater	0.288	0.318	10.4%
1,2,3-trimethylbenzene	Xie et al. ¹⁷³	artificial seawater	0.321	0.344	7.2%
<i>n</i> -butylbenzene	Xie et al. ¹⁷³	artificial seawater	0.375	0.318	15.2%
naphthalene	Schwarzenbach et al. ¹⁵⁶	seawater	0.280	0.264	5.6%
fluorene	Xie et al. ¹⁷³	NaCl	0.267	0.299	12.0%
phenanthrene	Schwarzenbach et al. ¹⁵⁶	seawater	0.300	0.314	4.7%
fluoranthene	Xie et al. ¹⁷³	NaCl	0.339	0.323	4.7%
pyrene	Schwarzenbach et al. ¹⁵⁶	seawater	0.300	0.323	7.6%
benz[a]anthracene	Xie et al. ¹⁷³	NaCl	0.354	0.364	2.7%
chrysene	Xie et al. ¹⁷³	NaCl	0.336	0.364	8.2%

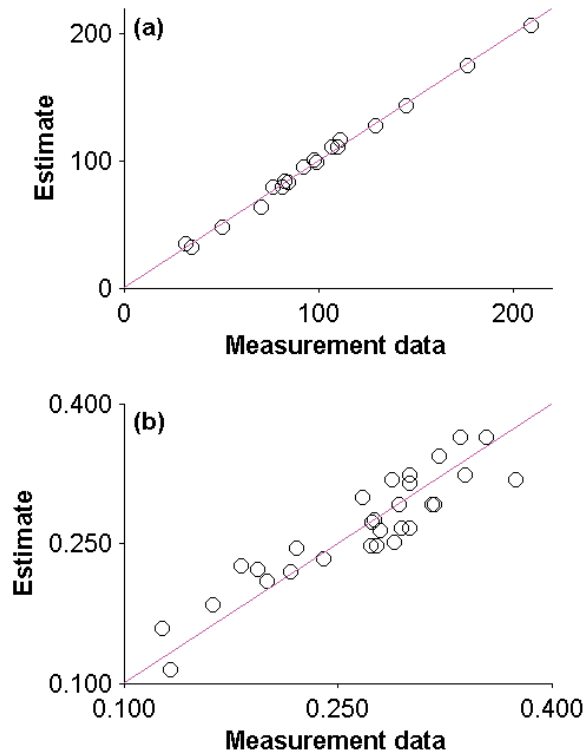


Figure 4-15. (a) Comparison of measured \bar{v}_i^L data (from literature) to estimates according to Equation 4-19, and (b) comparison of measured K_{salt} data (literature) to estimates according to Equation 4-20 (see Table 4-6 and Table 4-7 for the lists of compounds and the numerical values). The 1-1 line is shown in pink.

4.9.12 Methodological differences between the thermodynamic model of the present study and the Zick model

In this section we specifically discuss the differences between the gas-liquid equilibrium calculations of our thermodynamic model and those of the Zick model. The Zick model relies on the same EOS as used by us (1978 Peng-Robinson EOS). The thermodynamic model of the present study assumes that, based on the detailed compositional information available (~280 components), valid predictions can be obtained without requiring any tuning of either the EOS parameters or the modeled composition. In contrast, the model developed by Aaron A. Zick employed only 11 components and was tuned to match approximately 1000 individual measurements. EOS tuning is a frequently used procedure that usually implies careful modification of the values of some properties of the components (e.g. binary interaction parameters) in order to improve the correspondence between EOS predictions and laboratory data acquired with reservoir fluid samples. The detailed tuning procedure can be found in his report,²⁰⁹ we will only mention here that the Zick model tuning also included the adjustment of the composition of the sample 1.18 of Schlumberger. However, MC₂ (as defined in the current study) is based on the untuned composition. (Using the tuned composition instead was found

to provide less satisfactory predictions with our thermodynamic model.) The final component properties that Zick obtained are listed in Table 4-8 and Table 4-9.

Three differences between the Zick model and our model should be mentioned:

(1) Volume translation. In the Zick model, a fixed volume shift parameter, VS , was assigned for each component as listed in Table 4-8. VS is related to the volume translation parameter, c , through:

$$c_i = VS_i \cdot 0.07780 \cdot R \cdot \frac{T_{c,i}}{P_{c,i}}$$

Equation 4-26

$$c = \sum z_i \cdot c_i$$

Equation 4-27

where z_i is the mole fraction of component i in the phase of interest, T_c is the critical temperature, P_c the critical pressure, and R the molar gas constant.

By contrast, in the thermodynamic model of the present study, we used the Lin-Duan method to estimate the volume translation parameter from critical properties and acentric factors.²²⁶

(2) Viscosity. Zick used the Lohrenz-Bray-Clark viscosity model,²⁷¹ whereas we preferred the Pedersen et al. viscosity model, which has better predictive capabilities without tuning.²⁴⁷ We slightly modified the Pedersen et al. procedure to use our (volume-translated) EOS for estimating the reference compound (methane) density; Lin and Duan obtained a mean absolute error of 0.61% for the saturated liquid density of methane (in a reduced temperature range of 0.483–0.997).²²⁶ We did not include the modification of the Pedersen et al. procedure for heavy oils,²⁴⁷ because our oil was relatively light and also because the original model proved to provide more robust predictions.

(3) Binary interaction parameters. Finally, the Zick model used temperature-independent, constant binary interaction parameters (Table 4-9), whereas in the present study we estimated temperature-dependent binary interaction parameters from a group-contribution method.²⁴⁹

All predictions from the Zick model presented here were obtained by use of our own Matlab implementation of his model. Except for the differences mentioned above, our implementation of the Zick model corresponds to the same algorithms as our thermodynamic model applied to MC₂ and MC₃. The values obtained with our Matlab implementation for the Zick model compared favorably with the values originally obtained by Zick with his EOS software PhaseComp (based on figures in his report²⁰⁹ and personal communication on 26th May 2015).

Regarding the implementation of our model, we successfully validated the implementation of the EOS gas-liquid equilibrium calculations against the software provided as supplementary material to the book by Michelsen and Mollerup,²²⁴ available at: <http://www.tie->

tech.com/products/publications/more.php?id=32_0_1_0_M13 (accessed on 29th May 2015). Thus we conclude that our computational procedure has a correct technical implementation. (This procedure is used for gas-liquid equilibrium calculations in both our thermodynamic model and the Zick model.)

Table 4-8. List of the properties of the 11 components of the Zick model.²⁰⁹ These properties include the molar weight, M ; the critical temperature, T_c ; the critical pressure, P_c ; the acentric factor, ω ; the volume shift parameter, VS ; the critical volume, V_c ; the mass fraction in Schlumberger sample 1.18, $MC_{z,2}$; and the mass fraction in Pencor sample 53, $MC_{z,3}$.²⁰⁹

Component	M (g/mol)	T_c (K)	P_c (MPa)	ω (-)	VS (-)	V_c (cm ³ mol ⁻¹)	$MC_{z,2}$ (-)	$MC_{z,3}$ (-)
N ₂	28.014	126.20	3.3980	0.037	-0.16758	90.10	0.00175562	0.00237483
CO ₂	44.01	304.12	7.3740	0.225	0.00191	94.07	0.00813986	0.00771591
C ₁	16.043	190.56	4.5990	0.011	-0.14996	98.60	0.1926728	0.2003477
C ₂	30.07	305.32	4.8720	0.099	-0.0628	145.50	0.0398621	0.03681465
C ₃	44.097	369.83	4.2480	0.152	-0.06381	200.00	0.04141159	0.03845829
C ₄ -C ₅	63.37	437.51	3.5949	0.21328	-0.05005	273.70	0.06351786	0.06161619
C ₆ -C ₇	89.779	523.09	3.0992	0.27691	0.00117	371.30	0.05626886	0.05887051
C ₈ -C ₉	113.271	578.88	2.7419	0.33414	0.0283	463.30	0.0757595	0.07900799
C ₁₀ -C ₁₂	151.237	650.89	2.3257	0.42755	0.05886	612.92	0.08579121	0.0835788
C ₁₃ -C ₁₉	215.517	739.12	1.8630	0.57931	0.0893	857.67	0.1502443	0.1527663
C ₂₀₊	441.107	892.62	1.2566	1.09027	0.00389	1669.51	0.2845762	0.2784489

Table 4-9. Binary interaction parameter values for the Zick model.²⁰⁹

	N ₂	CO ₂	C ₁	C ₂	C ₃	C ₄ -C ₅	C ₆ -C ₇	C ₈ -C ₉	C ₁₀ -C ₁₂	C ₁₃ -C ₁₉	C ₂₀₊
N ₂	0	0	0.025	0.01	0.09	0.09943	0.11	0.11	0.11	0.11	0.09453
CO ₂	0	0	0.105	0.13	0.125	0.11587	0.115	0.115	0.115	0.115	0.09962
C ₁	0.025	0.105	0	0.00097	0.00319	0.00689	0.01123	0.01478	0.01981	0.0269	0.06074
C ₂	0.01	0.13	0.00097	0	0	0	0	0	0	0	0.02106
C ₃	0.09	0.125	0.00319	0	0	0	0	0	0	0	0.02106
C ₄ -C ₅	0.09943	0.11587	0.00689	0	0	0	0	0	0	0	0.02106
C ₆ -C ₇	0.11	0.115	0.01123	0	0	0	0	0	0	0	0.02106
C ₈ -C ₉	0.11	0.115	0.01478	0	0	0	0	0	0	0	0.02106
C ₁₀ -C ₁₂	0.11	0.115	0.01981	0	0	0	0	0	0	0	0.02106
C ₁₃ -C ₁₉	0.11	0.115	0.0269	0	0	0	0	0	0	0	0.02106
C ₂₀₊	0.09453	0.09962	0.06074	0.02106	0.02106	0.02106	0.02106	0.02106	0.02106	0.02106	0

4.9.13 Thermodynamic model validation against laboratory data and comparison with the Zick model

To validate our thermodynamic model, we made comparisons to both measured laboratory data and also to the Zick model predictions. We considered three different types of data: (a) the density of the single-phase fluid at high pressures; (b) the volume fraction of liquid at lower pressures; and (c) the predicted viscosities of the single-phase fluid or liquid phase. Each of these tests is described in turn below.

(a) Density of the single-phase fluid.

Both our thermodynamic model and the Zick model perform well at predicting the density of the single-phase fluid, with maximum deviations of 6 and 5 kg m⁻³, respectively, or ~1% error (Table 4-10). Our model slightly underpredicts the bubble point pressure at ~390 K, whereas the Zick model slightly overpredicts the bubble point pressure (Table 4-10).

To evaluate model prediction skill for fluid density, we selected laboratory data from Schlumberger,²³¹ obtained with their sample 1.18 at 243°F (~390.37 K). Therefore, for the purpose of evaluating model predictive capabilities for fluid density, the model composition MC₂ used for our thermodynamic model and the model composition MC_{z,2} (as tuned by Zick) was used for the Zick model. As discussed by Zick,²⁰⁹ there is some disagreement among the available laboratory data regarding the phase envelope, with incompatible dew points and bubble points obtained by Pencor²³² and Schlumberger,²³¹ respectively, in the 310–390 K temperature range (and pressures around 40 MPa). Zick concludes that this inconsistency cannot be explained, and he managed to match his EOS predictions to the experimental bubble points in the 310–390 K temperature range and also to the experimental dew points at lower temperatures, by tuning both the component properties and the model fluid composition MC_{z,2}. However, we bring attention to the fact that some uncertainty remains regarding the real behavior of the MRF at pressures of 40 MPa and temperatures <310 K,²⁰⁹ which are conditions that exceed substantially the pressures and temperatures encountered during the release in the Gulf of Mexico at ~1524 m depth (~15.5 MPa and ~278 K).

Table 4-10. Single-phase fluid density at 243°F (~390.37 K).

Pressure (psia)	Pressure (MPa)	Density from laboratory ^{231,a} (kg m ⁻³)	Density predicted by our thermodynamic model, using model composition MC ₂ (kg m ⁻³)	Density predicted by the Zick model, using model composition MC _{z,2} (kg m ⁻³)
15015	103.5	610–613	613	615
14015	96.6	601–607	607	609
13015	89.7	598–598	600	603
11871	81.8	590–591	591	595
10015	69.1	575–576	575	579
9015	62.2	562–568	565	569
8015	55.3	555–556	553	558
7015	48.4	543–544	539	544
6370	43.9	535–536	529	two phases: 419 and 569
6348	43.8	535–536	529	two phases: 417 and 570

^a The two density values reported by Schlumberger were described as follows in their report: “liquid densities were measured using two methods at 15000 psia, 14000 psia, 10000 psia, and 9000 psia at 243°F, known volume displacement into pre-weighted cylinder and a direct read from an Anton Parr densitometer. Densities at all other points are calculated from the values at 10000 psia.”²³¹

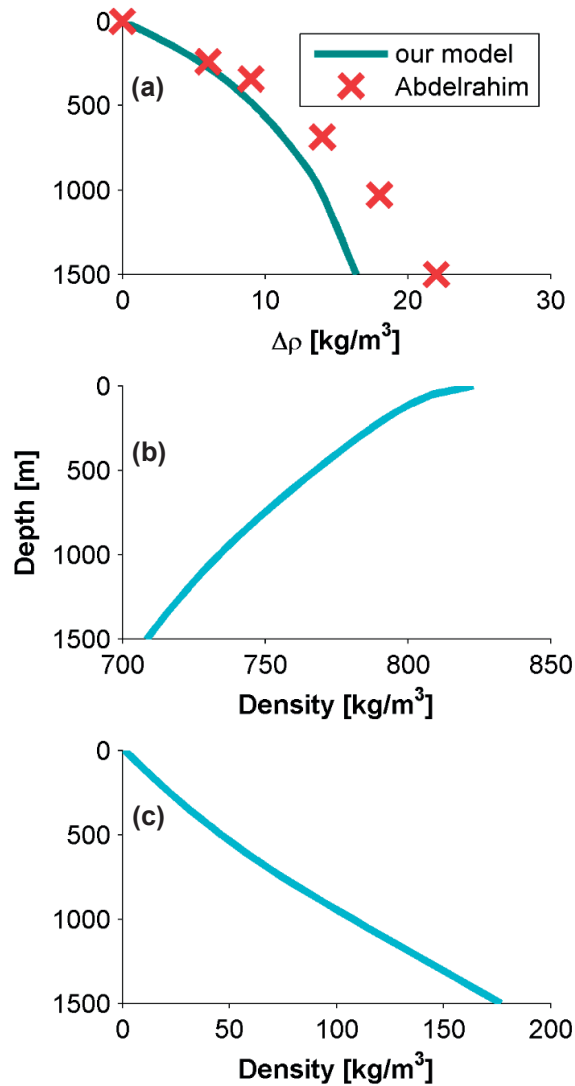


Figure 4-16. (a) Predicted and measured density change, $\Delta\rho$, as a function of depth for Macondo dead oil, where $\Delta\rho = \rho(P, T) - \rho(P_{surface}, T_{surface})$; (b) predicted live oil density as a function of depth; and (c) the predicted density as a function of depth, for the gas phase at equilibrium with the live oil. The measured pressure and temperature conditions as a function of depth were interpolated from the values reported by Abdelrahim.²⁵³ The blue line shows the predictions of our thermodynamic model for model compositions MC₁ (light blue) and MC_{1,do} (dark blue), whereas the red crosses are laboratory measurements by Abdelrahim. Abdelrahim used a different sample of *Deepwater Horizon* dead oil, which has a reported density at surface conditions ($\sim 847 \text{ kg m}^{-3}$) that differs slightly from the density of MW-1 dead oil (820 kg m^{-3}). Values of $\Delta\rho$ from Abdelrahim were obtained from his Figure 32. The reported density predictions shown above assume that the (dead or live) oil composition has not been altered by fractionation processes such as aqueous dissolution and evaporation. Therefore these results should not be construed to convey the predicted fluid densities of oil droplets or gas bubbles ascending the water column after emission from the Macondo well.

(b) Percent of liquid for the two-phase region.

At 243°F (~390.37 K), the partitioning of the MRF into a liquid phase and a gas phase is predicted within 16% of measured value at pressures ≤50 MPa by both our thermodynamic model and the Zick model (Table 4-11).

Table 4-11. Predicted and measured volume fraction^a of liquid for the two-phase region at 243°F (~390.37 K).^b

Pressure (psia)	Pressure (MPa)	Experimental liquid volume fraction ²³¹ (-)	Liquid volume fraction predicted by our thermodynamic model, using model composition MC ₂ (-)	Liquid volume fraction predicted by the Zick model, using model composition MC _{z,2} (-)
5039	34.7	0.608	0.674	0.585
4537	31.3	0.579	0.602	0.544
4037	27.8	0.541	0.537	0.501
3536	24.4	0.496	0.474	0.453
3025	20.9	0.445	0.408	0.398
2530	17.4	0.386	0.343	0.338
2027	14.0	0.315	0.273	0.272
1525	10.5	0.239	0.201	0.201
1098	7.6	0.164	0.140	0.140

^a E.g. a liquid volume fraction value of "0.99" means 99% liquid and 1% gas, by volume. ^b Data between the bubble point pressure (6348 psia) and 5039 psia were not considered here, since large discrepancies between laboratory data from Pencor (dew point) and Schlumberger (bubble point) were noticed in this pressure range.²⁰⁹ Therefore it was chosen to perform EOS validation only based on the unambiguous data reported for the 5039 to 1098 psia range.

For conditions from emission depth (~15.5 MPa and ~278 K) to sea surface (~0.1 MPa and ~300 K), our thermodynamic model and the Zick model are in good agreement with each other. However, at substantially higher pressures (~40 MPa), our model predicts a bubble point <310 K, whereas the Zick model predicts a dew point in agreement with available experimental data (Figure 4-17 and Figure 4-18). Significant discrepancies in the two models would arise for water depths of >2500 m.

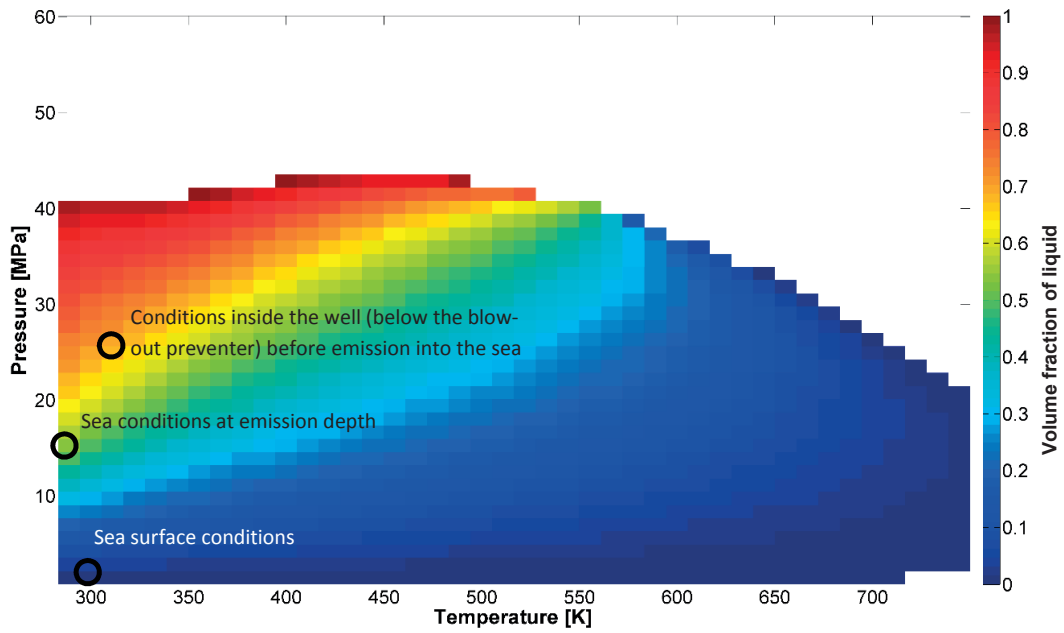


Figure 4-17. Phase envelope of MRF as predicted by our model using model composition MC_3 . The colored pixels are predicted to be within the two-phase region, where the color shade represents the volume fraction of liquid, ranging from 0 (100% gas) to 1 (100% liquid). The single-phase region is displayed in white.

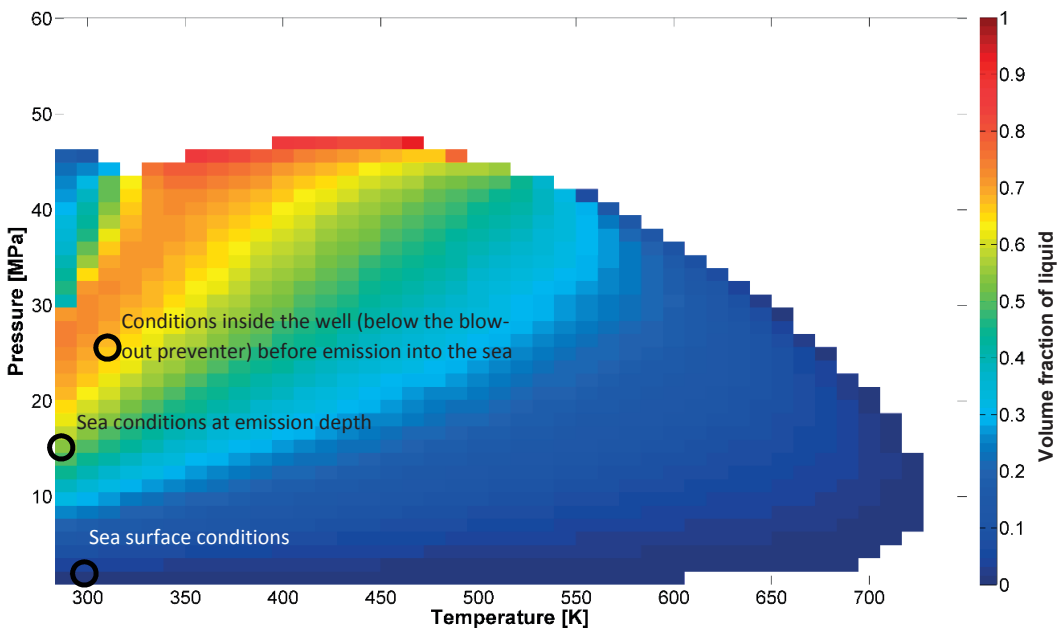


Figure 4-18. Phase envelope of MRF as predicted by the Zick model using model composition $MC_{z,3}$. The colored pixels are predicted to be within the two-phase region, where the color shade represents the volume fraction of liquid, ranging from 0 (100% gas) to 1 (100% liquid). The single-phase region is displayed in white.

(c) Viscosity for the single-phase fluid or liquid phase.

High-pressure experimental viscosity data were reported previously for Pencor sample 53,²³² and therefore the corresponding model compositions MC_3 and $MC_{z,3}$ were used. First, it should be explained how viscosity data were obtained (according to a usual procedure, with which some readers may be unfamiliar). The test begins at high pressure with a single-phase fluid. The temperature is maintained constant, and the pressure is decreased in a step-wise fashion. At each step, if the fluid is single phase, its viscosity is measured; if there are two phases present, the gas phase is discarded, and the viscosity is measured for the liquid phase; then the experiment continues with the liquid phase. Petroleum engineers call this procedure, where the generated gas phase is discarded at each step, a *differential liberation experiment*. This same procedure is also what was modeled with our thermodynamic model and with the Zick model. However, errors in phase partitioning predictions, especially close to dew points, will tend to alter the quality of the viscosity predictions (which will be based on an inaccurate composition of the liquid phase), independently of the predictive abilities of the chosen viscosity model. This explains why poorer predictions arise for our model at 40°F (~277.59 K) and <46 MPa for the two-phase region (Figure 4-19), where our thermodynamic model fails to correctly predict the experimental dew point. For the pressure and temperature conditions under which our model predicts the gas-liquid partitioning correctly, the predicted viscosities of our model and the Zick model exhibit similar extent of agreement with the laboratory data (Figure 4-19 and Figure 4-20). We interpret that the predictive viscosity model used in our thermodynamic model is representative of the viscosity of the Macondo fluids within a factor of 2 to 10. We infer that predictions of viscosity at deep-water conditions (<2500 m depth) by our model would be similar to that of the Zick model, because the gas-liquid partitioning predicted by our model and the Zick model are very similar at these conditions (Figure 4-17 and Figure 4-18).

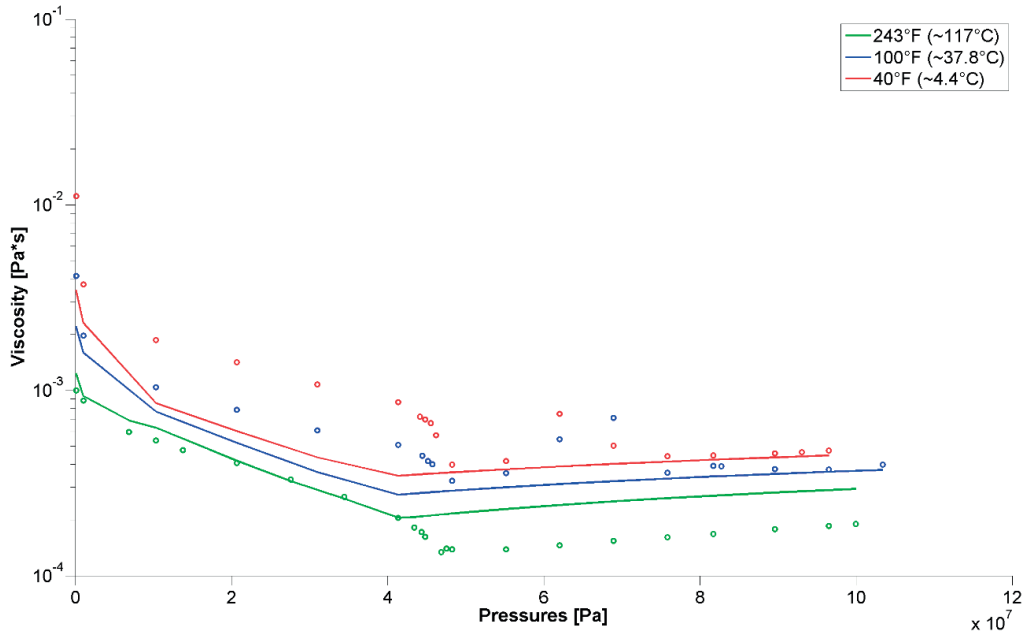


Figure 4-19. Comparison of measured (circles) and predicted (lines) viscosities of the single-phase fluid or liquid phase. Predictions are shown for our thermodynamic model using model composition MC₃ and the Pedersen et al. viscosity model.

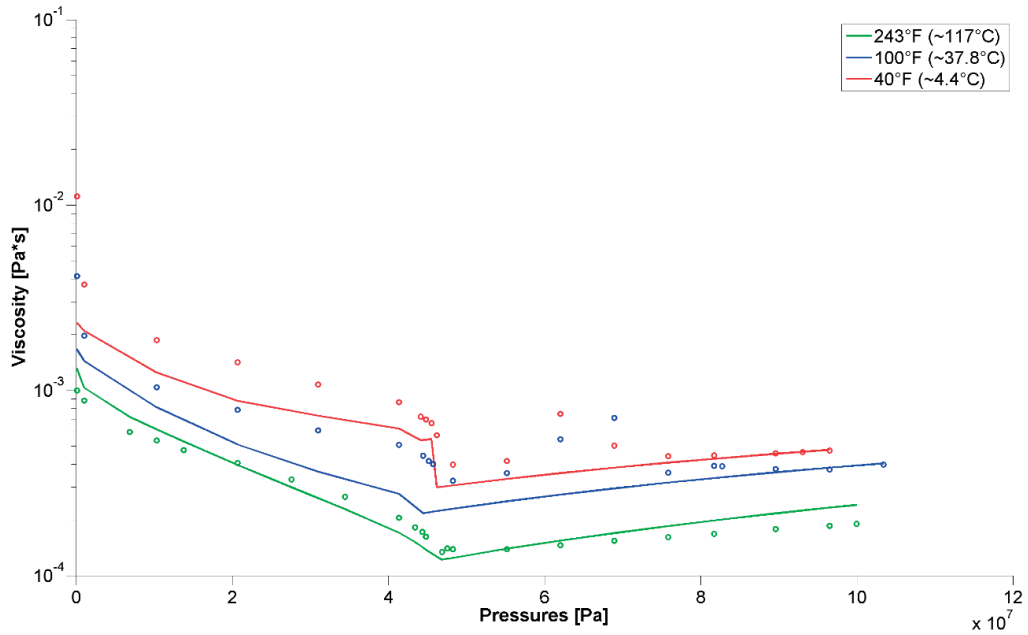


Figure 4-20. Comparison of measured (circles) and predicted (lines) viscosities of the single-phase fluid or liquid phase. Predictions are shown for the Zick model using model composition MC_{2,3} and the Lohrenz-Bray-Clark viscosity model.

4.9.14 Model domain of validity (extended discussion)

The thermodynamic model presented here is not validated for brines under oil reservoir conditions, because: (i) the equation of state calculations neglect the influence of water^{212,227} on the fugacities in the hydrocarbon-rich phase(s), and this approximation will become increasingly inappropriate as pressure and temperature are raised; (ii) we are unaware of datasets used to validate the combined adjustment of Henry's law constant to oil reservoir pressure and temperature conditions; (iii) the adjustment for the effect of salt is valid up to a concentration of 2–5 M,²⁷² whereas salt concentrations in reservoir brines can be much higher.¹⁷⁷

4.9.15 Predicted density of Macondo dead oil and live oil as a function of dissolution and evaporation extent

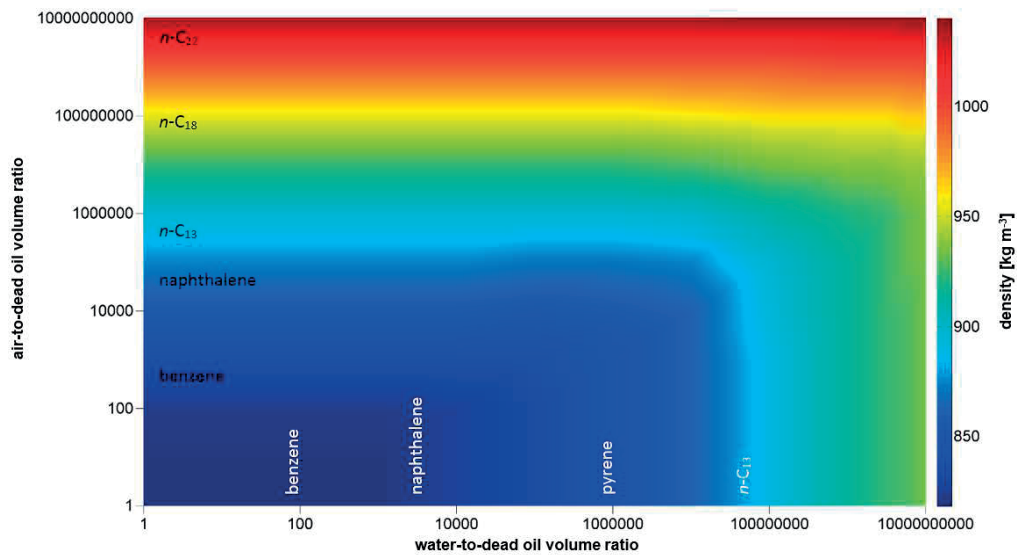


Figure 4-21. Density (kg m^{-3}) of $\text{MC}_{1,\text{do}}$ as a function of extent of dissolution and evaporation (expressed as water-to-dead oil ratio and air-to-dead oil ratio, by volume), as predicted by our thermodynamic model at 101325 Pa (1 atm) and 25 °C. Labeled compound names indicate the location on the plot where 50% depletion from the oil by evaporation (black font) or dissolution (white font) would be expected, according to equilibrium partitioning calculations.

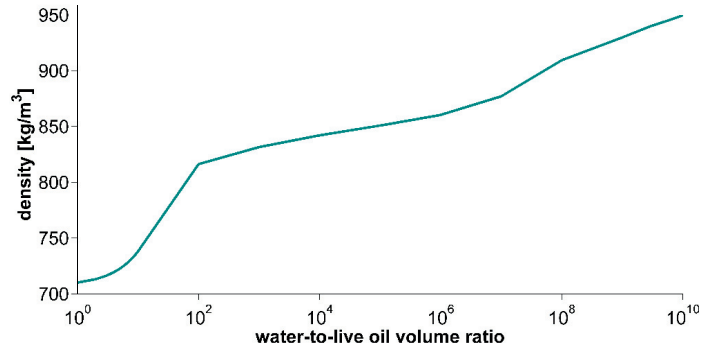


Figure 4-22. Predicted density (kg m^{-3}) of MC_1 liquid phase at emission depth (15.5 MPa and 4.3 °C) as a function of dissolution extent (expressed as water-to-live oil volume ratio).

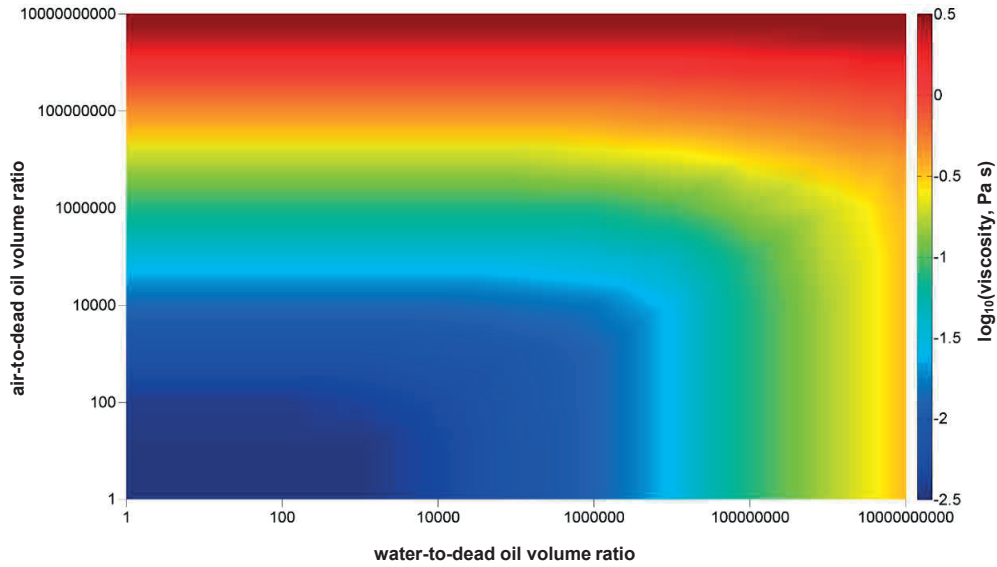


Figure 4-23. Base 10 logarithm of the viscosity (Pa s) of $\text{MC}_{1,\text{do}}$ as a function of extent of dissolution and evaporation (expressed as water-to-dead oil ratio and air-to-dead oil ratio, by volume), as predicted by our thermodynamic model at 101325 Pa and 25 °C.

4.9.16 Component properties

Table 4-12. Component properties. Estimated values are italicized, our estimates being underlined (see main text for references and description of estimation methods). Single carbon number intervals are named SCN followed by their carbon number. Pseudo-components derived from GCxGC are called A (saturated hydrocarbons), B, C, D, and E (1-, 2-, 3-, and 4-ring aromatic hydrocarbons) followed by their carbon number. Compositions MC₁–MC₃ are given as mass fractions.

Compound	M	P _c	T _c	V _c	T _b	V _b	ω	K _H (T [*])	$\Delta H_{\text{gas} \rightarrow \text{H}_2\text{O}}$	$\frac{L}{V}$	K _{est}	MC ₁	MC ₂	MC ₃
	g mol ⁻¹	MPa	K	cm ³ mol ⁻¹	K	cm ³ mol ⁻¹	–	mol atm ⁻¹ L ⁻¹	J mol ⁻¹	cm ³ mol ⁻¹	L mol ⁻¹	–	–	–
nitrogen	28.01	3.400	126.20	90.10	77.35	34.70	0.0372	6.52E-04	10947	41.00	0.183	0	2.3E-04	2.3E-04
oxygen	32.00	5.043	154.58	73.37	90.17	27.90	0.0216	1.30E-03	12611	31.00	0.169	0	0	0
methane	16.04	4.599	190.56	98.60	111.66	37.70	0.0110	1.43E-03	13100	34.70	0.127	1.5E-01	2.1E-01	2.0E-01
ethane	30.07	4.872	305.32	145.50	184.55	53.50	0.0990	1.93E-03	19400	50.40	0.162	2.8E-02	3.7E-02	3.7E-02
propane	44.10	4.248	369.83	200.00	231.02	74.50	0.1520	1.50E-03	22900	70.70	0.194	2.6E-02	3.9E-02	3.8E-02
<i>i</i> -C ₄	58.12	3.640	407.85	262.70	261.34	<u>97.82</u>	0.1860	8.74E-04	24200	81.30	<u>0.233</u>	6.7E-03	1.1E-02	1.1E-02
<i>n</i> -C ₄	58.12	3.796	425.12	255.00	272.66	96.60	0.2000	1.20E-03	25900	76.60	0.217	1.5E-02	2.4E-02	2.4E-02
<i>i</i> -C ₅	72.15	3.381	460.39	308.30	300.99	<u>115.69</u>	0.2290	7.30E-04	25100	<u>95.37</u>	<u>0.253</u>	7.9E-03	1.2E-02	1.2E-02
<i>n</i> -C ₅	72.15	3.370	469.70	311.00	309.22	118.00	0.2520	8.11E-04	28800	92.30	0.221	1.0E-02	1.4E-02	1.5E-02
CO ₂	44.01	7.374	304.12	94.07	194.65	37.30	0.2250	3.39E-02	<u>19697</u>	32.00	0.132	5.9E-03	7.6E-03	7.7E-03
2,2-dimethylbutane	86.18	3.080	488.70	359.10	322.87	<u>135.74</u>	0.2330	5.88E-04	<u>32264</u>	<u>111.31</u>	<u>0.279</u>	1.9E-04	<u>1.6E-04</u>	<u>1.7E-04</u>
cyclopentane	70.13	4.508	511.60	260.00	322.38	97.90	<u>0.1780</u>	5.47E-03	27000	84.50	0.182	1.0E-03	<u>8.7E-04</u>	<u>8.7E-04</u>
2,3-dimethylbutane	86.18	3.130	499.90	357.60	331.12	<u>135.15</u>	0.2480	7.80E-04	29200	106.80	<u>0.267</u>	6.3E-04	<u>5.5E-04</u>	<u>5.5E-04</u>
2-methylpentane	86.18	3.010	497.50	366.70	333.40	<u>138.75</u>	0.2780	5.98E-04	32600	<u>111.31</u>	<u>0.279</u>	4.7E-03	<u>4.1E-03</u>	<u>4.1E-03</u>
3-methylpentane	86.18	3.120	504.40	366.70	336.40	<u>138.75</u>	0.2730	5.88E-04	<u>33326</u>	<u>111.31</u>	<u>0.279</u>	3.0E-03	<u>2.6E-03</u>	<u>2.6E-03</u>

Compound	M	P _c	T _c	V _c	T _b	V _b	ω	K _H (T*)	$\Delta H_{\text{vap}}^{\text{pure}} \rightarrow \text{H}_2\text{O}$	$\frac{L}{V}$	K _{airH}	MC ₁	MC ₂	MC ₃
	g mol ⁻¹	MPa	K	cm ³ mol ⁻¹	K	cm ³ mol ⁻¹	-	$\frac{\text{mol}}{\text{atm} \cdot \text{L}^{-1}}$	J mol ⁻¹	cm ³ mol ⁻¹	L mol ⁻¹	-	-	-
n-C ₆	86.18	3.025	507.60	368.00	341.88	<u>139.27</u>	0.3000	6.08E-04	31600	110.00	0.276	1.4E-02	<u>1.2E-02</u>	<u>1.2E-02</u>
2,2-dimethylpentane	100.20	2.770	520.40	415.80	352.32	<u>158.28</u>	0.2870	3.14E-04	<u>36025</u>	<u>127.26</u>	<u>0.305</u>	2.3E-04	<u>2.0E-04</u>	<u>2.0E-04</u>
methylcyclopentane	84.16	3.784	532.79	319.00	344.98	120.00	0.2270	2.74E-03	<u>33667</u>	<u>99.02</u>	0.273	5.3E-03	<u>4.6E-03</u>	<u>4.6E-03</u>
2,4-dimethylpentane	100.20	2.740	519.70	417.50	353.62	<u>158.96</u>	0.3040	3.34E-04	<u>38002</u>	<u>127.26</u>	<u>0.305</u>	6.0E-04	<u>5.2E-04</u>	<u>5.2E-04</u>
2,2,3-trimethylbutane	100.20	2.950	531.10	397.60	354.01	<u>151.03</u>	0.2500	3.28E-04	<u>36940</u>	<u>127.26</u>	<u>0.305</u>	4.6E-05	<u>4.0E-05</u>	<u>4.0E-05</u>
benzene	78.11	4.895	562.05	256.00	353.24	96.50	0.2100	1.72E-01	31700	82.50	0.200	2.3E-03	<u>2.0E-03</u>	<u>2.0E-03</u>
3,3-dimethylpentane	100.20	2.950	536.30	414.10	359.19	<u>157.61</u>	0.2690	5.47E-04	<u>36025</u>	<u>127.26</u>	<u>0.305</u>	1.3E-04	<u>1.1E-04</u>	<u>1.1E-04</u>
cyclohexane	84.16	4.073	553.50	308.00	353.93	117.00	0.2110	5.67E-03	33100	98.80	0.277	5.7E-03	<u>4.9E-03</u>	<u>5.0E-03</u>
2-methylhexane	100.20	2.730	530.10	421.00	363.18	<u>160.36</u>	0.3310	2.94E-04	<u>37087</u>	<u>127.26</u>	<u>0.305</u>	3.7E-03	<u>3.2E-03</u>	<u>3.2E-03</u>
2,3-dimethylpentane	100.20	2.910	537.30	393.00	362.91	<u>149.20</u>	0.2970	5.78E-04	<u>38002</u>	<u>127.26</u>	<u>0.305</u>	1.2E-03	<u>1.0E-03</u>	<u>1.0E-03</u>
1,1-dimethylcyclopentane	98.19	3.358	<u>546.98</u>	<u>373.02</u>	360.90	<u>141.26</u>	0.2559	2.95E-03	<u>38248</u>	<u>114.97</u>	0.273	6.7E-04	<u>5.8E-04</u>	<u>5.8E-04</u>
3-methylhexane	100.20	2.810	535.20	404.00	365.00	<u>153.58</u>	0.3230	4.26E-04	<u>37087</u>	<u>127.26</u>	<u>0.305</u>	4.0E-03	<u>3.5E-03</u>	<u>3.5E-03</u>
1,3-dimethylcyclopentane (cis)	98.19	3.400	551.00	363.30	364.71	<u>137.41</u>	0.2760	2.95E-03	<u>38248</u>	<u>114.97</u>	0.273	1.4E-03	<u>1.2E-03</u>	<u>1.2E-03</u>
1,3-dimethylcyclopentane (trans)	98.19	3.400	553.00	363.30	363.90	<u>137.41</u>	0.2530	2.95E-03	<u>38248</u>	<u>114.97</u>	0.273	1.4E-03	<u>1.2E-03</u>	<u>1.2E-03</u>
3-ethylpentane	100.20	2.890	540.50	415.80	366.63	<u>158.28</u>	0.3110	4.66E-04	<u>37087</u>	<u>127.26</u>	<u>0.305</u>	2.9E-04	<u>2.5E-04</u>	<u>2.5E-04</u>
1,2-dimethylcyclopentane (trans)	98.19	3.591	<u>548.21</u>	<u>354.52</u>	365.00	<u>133.93</u>	0.2818	2.95E-03	<u>38248</u>	<u>114.97</u>	0.273	2.3E-03	<u>2.0E-03</u>	<u>2.0E-03</u>
n-C ₇	100.20	2.740	540.20	428.00	371.57	<u>163.15</u>	0.3500	4.41E-04	35100	129.40	0.311	1.0E-02	<u>8.7E-03</u>	<u>8.7E-03</u>
methylcyclohexane	98.19	3.471	572.19	368.00	374.09	<u>139.27</u>	0.2350	2.53E-03	<u>45700</u>	<u>114.97</u>	0.274	1.3E-02	<u>1.1E-02</u>	<u>1.1E-02</u>
2,5-dimethylhexane	114.23	2.490	550.00	482.00	382.26	<u>184.79</u>	0.3570	2.74E-04	<u>41763</u>	<u>143.21</u>	0.331	5.0E-04	<u>4.3E-04</u>	<u>4.4E-04</u>
2,4-dimethylhexane	114.23	2.560	553.50	472.00	382.58	<u>180.77</u>	0.3440	2.38E-04	<u>41763</u>	<u>143.21</u>	0.331	6.6E-04	<u>5.7E-04</u>	<u>5.7E-04</u>
ethylcyclopentane	98.19	3.397	569.50	375.00	376.59	<u>142.05</u>	0.2700	2.95E-03	<u>37428</u>	<u>114.97</u>	0.273	7.7E-04	<u>6.7E-04</u>	<u>6.7E-04</u>

Gas-liquid-water partitioning and fluid properties of petroleum mixtures under pressure: Implications for deep-sea blowouts

Compound	M	P _c	T _c	V _c	T _b	V _b	ω	K _{HL} (T*)	$\Delta H_{\text{vap}}^{\text{pure}} + R_2 \cdot 0$	$\frac{L}{V}$	K _{airH}	MC ₁	MC ₂	MC ₃
	g mol ⁻¹	MPa	K	cm ³ mol ⁻¹	K	cm ³ mol ⁻¹	–	$\frac{\text{mol}}{\text{atm} \cdot \text{L}^{-1}}$	J mol ⁻¹	cm ³ mol ⁻¹	L mol ⁻¹	–	–	–
1,2,3-trimethylcyclopentane (etc)	112.21	3.327	577.84	395.20	0.00	150.08	0.3001	2.22E-03	42828	130.92	0.299	7.1E-04	6.2E-04	6.2E-04
2,3,4-trimethylpentane	114.23	2.730	566.30	456.20	386.62	174.44	0.3160	5.37E-04	42678	143.21	0.331	1.1E-04	9.5E-05	9.6E-05
2,3-dimethylhexane	114.23	2.630	563.40	468.20	388.76	179.25	0.3470	3.04E-04	41763	143.21	0.331	4.4E-04	3.8E-04	3.8E-04
2-methylheptane	114.23	2.480	559.60	488.20	390.80	187.28	0.3780	2.94E-04	40848	143.21	0.331	4.0E-03	3.5E-03	3.5E-03
4-methylheptane	114.23	2.540	561.70	476.00	390.86	182.38	0.3710	2.89E-04	40848	143.21	0.331	1.1E-03	9.5E-04	9.6E-04
3-methylheptane	114.23	2.550	563.60	471.10	392.08	180.41	0.3710	2.74E-04	40848	143.21	0.331	2.4E-03	2.1E-03	2.1E-03
3-ethylhexane	114.23	2.610	565.40	460.50	391.69	176.16	0.3620	3.19E-04	40848	143.21	0.331	2.6E-04	2.3E-04	2.3E-04
toluene	92.14	4.108	591.75	316.00	383.79	118.00	0.2640	1.52E-01	36300	97.70	0.240	6.5E-03	5.6E-03	5.7E-03
1,4-dimethylcyclohexane (trans)	112.22	3.279	587.70	420.61	429.75	160.20	0.3224	1.11E-03	43607	130.92	0.299	1.1E-04	9.5E-05	9.6E-05
n-C ₈	114.23	2.490	568.70	492.00	398.82	188.81	0.3990	3.24E-04	38400	145.20	0.336	1.0E-02	8.7E-03	8.7E-03
1,2-dimethylcyclohexane	112.21	3.279	589.71	420.61	402.95	160.20	0.3224	2.84E-03	43607	130.92	0.299	1.5E-03	1.3E-03	1.3E-03
4-methyloctane	128.26	2.329	586.60	528.79	415.55	203.63	0.4111	1.01E-04	44609	159.16	0.357	1.2E-03	1.0E-03	1.0E-03
2-methyloctane	128.26	2.310	587.00	529.00	416.44	203.72	0.4230	2.03E-04	44609	159.16	0.357	1.6E-03	1.4E-03	1.4E-03
ethylbenzene	106.17	3.609	617.15	374.00	409.36	140.00	0.3040	1.32E-01	40200	111.10	0.290	9.5E-04	8.2E-04	8.3E-04
3-methyloctane	128.26	2.329	586.60	528.79	417.00	203.63	0.4111	2.18E-04	44609	159.16	0.357	1.6E-03	1.4E-03	1.4E-03
p/m-xylenes	106.17	3.526	616.60	376.50	411.94	142.64	0.3245	1.45E-01	38550	116.32	0.295	5.1E-03	4.4E-03	4.4E-03
o-xylene	106.17	3.732	630.30	370.00	417.59	140.06	0.3120	2.10E-01	36600	116.32	0.300	1.9E-03	1.6E-03	1.7E-03
n-C ₉	128.26	2.290	594.60	555.00	423.97	214.22	0.4450	2.03E-04	43694	159.16	0.357	9.4E-03	8.1E-03	8.2E-03
isopropylcyclohexane	126.24	2.846	637.93	472.65	426.00	181.04	0.3402	1.67E-03	47464	146.87	0.325	4.4E-04	3.8E-04	3.8E-04
isopropylbenzene	120.19	3.209	631.00	434.70	425.52	165.83	0.3260	1.22E-01	39600	132.26	0.316	2.6E-04	2.3E-04	2.3E-04
3,3-dimethyloctane	142.28	2.244	605.74	580.33	433.31	224.48	0.4177	1.62E-04	47309	175.11	0.382	1.5E-04	1.3E-04	1.3E-04

Gas-liquid-water partitioning and fluid properties of petroleum mixtures under pressure: Implications for deep-sea blowouts

Compound	M	P _c	T _c	V _c	T _b	V _b	ω	K _{HL} (T*)	$\Delta H_{\text{vap}}^{\text{pure}} - \Delta H_{2,0}$	$\frac{L}{V}$	K _{airK}	MC ₁	MC ₂	MC ₃
	g mol ⁻¹	MPa	K	cm ³ mol ⁻¹	K	cm ³ mol ⁻¹	–	$\frac{\text{mol}}{\text{atm} \cdot \text{L}^{-1}}$	J mol ⁻¹	cm ³ mol ⁻¹	L mol ⁻¹	–	–	–
<i>n</i> -propylbenzene	120.19	3.200	638.35	440.00	432.35	167.95	0.3450	1.42E-01	43900	132.26	0.292	4.4E-04	3.8E-04	3.8E-04
2-methylnonane	142.28	2.148	609.73	591.78	440.15	229.12	0.4558	1.62E-04	48370	175.11	0.382	9.5E-04	8.2E-04	8.3E-04
3-methylnonane	142.28	2.148	613.60	591.78	440.90	229.12	0.4558	1.72E-04	48370	175.11	0.382	7.9E-04	6.8E-04	6.9E-04
1-methyl-3-ethylbenzene	120.19	3.205	647.56	433.72	434.50	165.44	0.3598	1.32E-01	42465	132.26	0.292	1.2E-03	1.0E-03	1.0E-03
1-methyl-4-ethylbenzene	120.19	3.230	640.20	440.00	435.13	167.95	0.3640	2.03E-01	42465	132.26	0.292	4.9E-04	4.2E-04	4.3E-04
1,3,5-trimethylbenzene	120.19	3.127	637.30	430.00	437.90	163.95	0.3990	1.72E-01	41000	132.26	0.318	9.2E-04	8.0E-04	8.0E-04
1-methyl-2-ethylbenzene	120.19	3.205	647.56	433.72	438.30	165.44	0.3598	2.33E-01	40463	132.26	0.292	5.3E-04	4.6E-04	4.6E-04
<i>n</i> -C ₁₀	142.29	2.110	617.70	624.00	447.30	242.21	0.4900	1.42E-04	47456	176.80	0.387	8.7E-03	7.5E-03	7.6E-03
1,2,4-trimethylbenzene	120.19	3.232	649.10	435.00	442.49	165.95	0.3770	1.72E-01	39900	132.26	0.293	2.3E-03	2.0E-03	2.0E-03
isobutylbenzene	134.22	3.050	650.00	480.00	445.90	183.99	0.3830	3.04E-02	47695	148.21	0.318	8.4E-05	7.3E-05	7.3E-05
sec-butylbenzene	134.22	2.890	660.50	497.00	456.42	190.82	0.3930	7.19E-02	47695	148.21	0.288	1.5E-04	1.3E-04	1.3E-04
1-methyl-3-isopropylbenzene	134.22	2.908	654.94	494.33	448.00	189.75	0.3410	9.12E-02	47141	148.21	0.318	2.8E-04	2.4E-04	2.4E-04
1-methyl-4-isopropylbenzene	134.22	2.800	652.00	497.00	450.26	190.82	0.3760	1.32E-01	47141	148.21	0.318	1.5E-04	1.3E-04	1.3E-04
1,2,3-trimethylbenzene	120.19	3.454	664.50	435.00	449.23	165.95	0.3670	2.94E-01	37500	150.77	0.321	7.6E-04	6.6E-04	6.6E-04
1,3-diethylbenzene	134.22	2.881	663.27	486.49	454.00	186.59	0.4008	3.85E-01	46226	148.21	0.318	1.2E-04	1.0E-04	1.0E-04
1-methyl-3-propylbenzene	134.22	2.881	663.27	486.49	454.00	186.59	0.4008	9.12E-02	46226	148.21	0.318	5.6E-04	4.9E-04	4.9E-04
1-methyl-4-propylbenzene	134.22	2.881	663.27	486.49	456.50	186.59	0.4008	1.32E-01	46226	148.21	0.318	2.3E-04	2.0E-04	2.0E-04
<i>n</i> -butylbenzene	134.22	2.890	660.50	497.00	456.42	190.82	0.3930	7.80E-02	46100	148.21	0.375	2.1E-04	1.8E-04	1.8E-04
1,2-dimethyl-4-ethylbenzene	134.22	2.899	665.76	412.17	462.00	156.83	0.2462	1.04E-01	45672	148.21	0.318	4.0E-04	3.5E-04	3.5E-04
1-methyl-2-propylbenzene	134.22	2.881	663.27	486.49	457.00	186.59	0.4008	1.22E-01	44225	148.21	0.318	3.0E-04	2.6E-04	2.6E-04
1,4-dimethyl-2-ethylbenzene	134.22	2.899	665.76	412.17	460.00	156.83	0.2462	1.04E-01	45672	148.21	0.318	2.8E-04	2.4E-04	2.4E-04

Compound	M	P _c	T _c	V _c	T _b	V _b	ω	K _H (T*)	$\Delta H_{\text{vap}}^{\text{pure}} + R_2 \cdot 0$	$\frac{L}{V}$	K _{airH}	MC ₁	MC ₂	MC ₃
	g mol ⁻¹	MPa	K	cm ³ mol ⁻¹	K	cm ³ mol ⁻¹	-	mol atm ⁻¹ L ⁻¹	J mol ⁻¹	cm ³ mol ⁻¹	L mol ⁻¹	-	-	-
<i>n</i> -C ₁₁	156.31	1.980	639.00	689.00	469.08	268.72	0.5370	5.47E-05	51217	191.05	0.408	8.1E-03	7.0E-03	7.0E-03
1,3-dimethyl-4-ethylbenzene	134.22	2.899	665.76	412.17	461.50	156.83	0.2462	1.04E-01	45672	148.21	0.318	2.9E-04	2.5E-04	2.5E-04
1,3-dimethyl-5-ethylbenzene	134.22	2.899	665.76	412.17	456.80	156.83	0.2462	1.04E-01	45672	148.21	0.318	3.8E-04	3.3E-04	3.3E-04
naphthalene	128.17	4.050	748.40	407.00	491.16	154.77	0.3040	2.23E+00	43626	126.19	0.280	8.2E-04	7.1E-04	7.1E-04
C ₁ -naphthalenes	142.20	3.570	766.50	462.00	516.02	176.76	0.3610	2.03E+00	46834	142.13	0.290	1.8E-03	1.6E-03	1.6E-03
C ₂ -naphthalenes	156.23	3.165	779.50	517.00	537.25	198.88	0.4175	1.93E+00	50041	158.08	0.316	2.2E-03	1.9E-03	1.9E-03
C ₃ -naphthalenes	170.25	3.022	814.83	593.50	558.15	229.82	0.4709	3.09E+00	53248	174.03	0.342	1.6E-03	1.4E-03	1.4E-03
C ₄ -naphthalenes	184.28	2.769	824.01	649.25	0.00	252.49	0.5229	1.28E+00	56456	189.98	0.367	6.9E-04	6.0E-04	6.0E-04
1,2,3,4-tetramethylbenzene	134.22	2.709	699.12	509.98	478.15	196.05	0.4163	2.81E-02	45118	177.91	0.401	3.3E-04	2.9E-04	2.9E-04
<i>n</i> -C ₁₂	170.34	1.820	658.00	754.00	489.48	295.35	0.5760	1.32E-04	54978	209.50	0.441	7.2E-03	6.2E-03	6.3E-03
<i>i</i> -C ₁₃	184.36	1.735	668.59	881.70	0.00	347.97	0.5871	8.04E-05	55893	222.95	0.460	1.8E-03	1.6E-03	1.6E-03
<i>i</i> -C ₁₄	198.39	1.628	685.08	957.42	0.00	379.35	0.6309	6.06E-05	59654	238.90	0.485	1.3E-03	1.1E-03	1.1E-03
<i>n</i> -C ₁₃	184.37	1.680	675.00	823.00	508.63	323.73	0.6180	4.36E-04	58739	222.95	0.460	6.3E-03	5.5E-03	5.5E-03
<i>i</i> -C ₁₅	212.41	1.532	700.21	1034.88	0.00	411.57	0.6741	4.56E-05	63415	254.85	0.511	1.3E-03	1.1E-03	1.1E-03
<i>n</i> -C ₁₄	198.39	1.570	693.00	894.00	526.76	353.06	0.6440	8.82E-04	62500	238.90	0.485	5.8E-03	5.0E-03	5.0E-03
<i>i</i> -C ₁₆	226.44	1.445	714.12	1113.74	0.00	444.50	0.7159	3.44E-05	70938	270.79	0.537	2.2E-03	1.9E-03	1.9E-03
<i>n</i> -C ₁₅	212.42	1.480	708.00	966.00	543.83	382.91	0.6850	2.13E-03	66262	254.85	0.511	5.5E-03	4.8E-03	4.8E-03
fluorene	166.22	3.112	802.73	546.21	568.15	210.67	0.4382	1.14E+01	45862	156.87	0.267	1.3E-04	1.1E-04	1.1E-04
C ₁ -fluorenes	180.25	2.772	811.36	597.36	591.15	231.39	0.4918	5.41E+00	49070	172.82	0.325	3.4E-04	2.9E-04	3.0E-04
C ₂ -fluorenes	194.27	2.476	819.54	648.41	0.00	252.15	0.5440	4.90E+00	52277	188.77	0.351	5.0E-04	4.3E-04	4.4E-04
C ₃ -fluorenes	208.30	2.217	827.34	699.38	0.00	272.96	0.5944	4.44E+00	55484	204.72	0.376	4.4E-04	3.8E-04	3.8E-04

Compound	M	P _c	T _c	V _c	T _b	V _b	ω	K _{HL} (T*)	$\Delta H_{\text{gas} \rightarrow \text{H}_2\text{O}}$	$\frac{L}{V}$	K _{airK}	MC ₁	MC ₂	MC ₃
	g mol ⁻¹	MPa	K	cm ³ mol ⁻¹	K	cm ³ mol ⁻¹	–	$\frac{\text{mol}}{\text{atm} \cdot \text{L}^{-1}}$	J mol ⁻¹	cm ³ mol ⁻¹	L mol ⁻¹	–	–	–
<i>n</i> -C ₁₆	226.45	1.400	723.00	1034.00	559.98	411.21	0.7180	4.36E+03	70023	270.79	0.537	4.6E-03	4.0E-03	4.0E-03
<i>i</i> -C ₁₈	254.49	1.292	738.76	1274.36	0.00	511.91	0.7938	1.95E+05	78460	302.69	0.588	1.5E-03	1.3E-03	1.3E-03
<i>n</i> -C ₁₇	240.47	1.340	736.00	1103.00	574.56	440.01	0.7530	1.82E+02	73784	286.74	0.563	4.1E-03	3.6E-03	3.6E-03
pristane	268.52	1.231	752.68	1074.14	0.00	427.95	0.9011	1.47E+05	84966	318.64	0.614	2.4E-03	2.1E-03	2.1E-03
dibenzothiophene	184.26	3.217	851.32	559.19	605.70	215.92	0.4641	2.33E+00	44964	159.43	0.282	7.6E-05	6.6E-05	6.6E-05
C ₁ -dibenzothiophenes	198.28	2.858	856.52	610.17	0.00	236.59	0.5171	2.11E+00	48171	175.38	0.308	2.6E-04	2.3E-04	2.3E-04
C ₂ -dibenzothiophenes	212.31	2.547	861.68	661.07	0.00	257.32	0.5684	1.91E+00	51378	191.33	0.334	3.7E-04	3.2E-04	3.2E-04
C ₃ -dibenzothiophenes	226.34	2.275	866.82	711.91	0.00	278.09	0.6180	1.73E+00	54586	207.27	0.359	3.0E-04	2.6E-04	2.6E-04
C ₄ -dibenzothiophenes	240.36	2.037	871.91	762.68	0.00	298.91	0.6658	1.57E+00	57793	223.22	0.385	1.8E-04	1.6E-04	1.6E-04
phenanthrene	178.23	2.870	869.00	554.00	611.55	213.82	0.4790	2.38E+01	54964	167.95	0.300	3.1E-04	2.7E-04	2.7E-04
C ₁ -phenanthrenes	192.26	2.627	903.50	623.39	627.15	241.96	0.5520	2.03E+01	58171	183.90	0.340	7.6E-04	6.6E-04	6.6E-04
C ₂ -phenanthrenes	206.28	2.389	907.65	678.76	0.00	264.54	0.6015	1.60E+01	61379	199.85	0.365	8.2E-04	7.1E-04	7.1E-04
C ₃ -phenanthrenes	220.31	2.188	911.76	734.09	0.00	287.18	0.6493	1.45E+01	64586	215.80	0.391	5.8E-04	5.0E-04	5.0E-04
C ₄ -phenanthrenes	234.34	2.014	915.83	789.37	0.00	309.88	0.6953	1.31E+01	67793	231.74	0.417	2.8E-04	2.4E-04	2.4E-04
<i>n</i> -C ₁₈	254.50	1.290	747.00	1189.00	588.30	476.03	0.8000	1.11E+01	77545	302.69	0.588	3.3E-03	2.9E-03	2.9E-03
phytane	282.55	1.171	762.18	1144.22	0.00	457.26	0.9046	1.11E+05	88727	334.59	0.640	1.4E-03	1.2E-03	1.2E-03
<i>n</i> -C ₁₉	268.53	1.160	755.00	1260.08	602.34	505.90	0.8450	3.45E+01	81306	318.64	0.614	2.9E-03	2.5E-03	2.5E-03
<i>n</i> -C ₂₀	282.55	1.070	768.00	1334.25	616.84	537.15	0.8650	3.04E+00	85068	334.59	0.640	2.6E-03	2.3E-03	2.3E-03
fluoranthene	202.25	2.277	895.39	632.75	657.15	245.78	0.5763	6.69E+01	56301	182.69	0.339	4.6E-06	4.0E-06	4.0E-06
pyrene	202.25	2.773	950.51	655.73	677.15	255.14	0.5473	7.58E+01	56301	182.69	0.300	1.5E-05	1.3E-05	1.3E-05
C ₁ -fluoranthenes/pyrenes	216.28	2.528	951.97	711.00	0.00	277.72	0.5970	1.09E+02	59509	198.64	0.349	1.2E-04	1.0E-04	1.0E-04

Gas-liquid-water partitioning and fluid properties of petroleum mixtures under pressure: Implications for deep-sea blowouts

Compound	M	P _c	T _c	V _c	T _b	V _b	ω	K _{HL} (T*)	$\Delta H_{\text{gas} \rightarrow \text{H}_2\text{O}}$	$\frac{L}{V}$	K _{airH}	MC ₁	MC ₂	MC ₃
	g mol ⁻¹	MPa	K	cm ³ mol ⁻¹	K	cm ³ mol ⁻¹	–	mol atm ⁻¹ L ⁻¹	J mol ⁻¹	cm ³ mol ⁻¹	L mol ⁻¹	–	–	–
C ₂ -fluoranthenes/pyrenes	230.30	2.318	953.64	766.22	0.00	300.36	0.6449	1.81E+02	62716	207.16	0.354	1.9E-04	1.6E-04	1.7E-04
C ₃ -fluoranthenes/pyrenes	244.33	2.137	955.47	821.41	0.00	323.08	0.6912	3.02E+02	65923	215.68	0.359	2.1E-04	1.8E-04	1.8E-04
C ₄ -fluoranthenes/pyrenes	258.36	1.979	957.43	876.56	0.00	345.84	0.7357	5.02E+02	69131	224.21	0.364	1.5E-04	1.3E-04	1.3E-04
n-C ₂₁	296.58	1.030	778.00	1408.58	629.65	568.55	0.9556	8.33E-06	88829	350.53	0.666	2.1E-03	1.8E-03	1.8E-03
n-C ₂₂	310.61	0.980	786.00	1483.04	641.75	600.09	0.9937	6.27E-06	92590	366.48	0.692	1.8E-03	1.6E-03	1.6E-03
n-C ₂₃	324.63	0.920	790.00	1557.62	653.35	631.75	1.0309	4.73E-06	96351	382.43	0.717	1.6E-03	1.4E-03	1.4E-03
n-C ₂₄	338.66	0.870	800.00	1632.30	664.45	663.53	1.0677	3.56E-06	100112	398.38	0.743	1.4E-03	1.2E-03	1.2E-03
benz[<i>a</i>]anthracene	228.29	2.327	964.31	719.64	711.15	281.26	0.6055	1.32E+02	66301	209.72	0.354	1.5E-05	1.3E-05	1.3E-05
chrysene	228.29	2.327	964.31	719.64	721.20	281.26	0.6055	2.53E+02	66301	209.72	0.336	8.4E-05	7.3E-05	7.3E-05
C ₁ -benz[<i>a</i>]anthracenes/chrysenes	242.31	2.133	965.63	774.80	0.00	303.89	0.6531	1.81E+02	69509	225.67	0.389	1.8E-04	1.6E-04	1.6E-04
C ₂ -benz[<i>a</i>]anthracenes/chrysenes	256.34	1.965	967.11	829.92	0.00	326.58	0.6990	1.64E+02	72716	241.61	0.415	2.2E-04	1.9E-04	1.9E-04
n-C ₂₅	352.68	0.938	808.26	1707.09	675.10	695.42	1.1044	2.68E-06	103873	414.33	0.769	1.1E-03	9.5E-04	9.6E-04
n-C ₂₆	366.71	0.901	815.94	1781.98	0.00	727.43	1.1411	2.02E-06	107635	430.27	0.795	1.0E-03	8.7E-04	8.7E-04
A9	128.26	2.251	593.55	551.40	423.71	212.77	0.4126	2.50E-04	43694	159.16	0.357	1.5E-02	1.2E-02	1.4E-02
A10	142.28	2.077	616.33	616.80	447.04	239.29	0.4525	1.88E-04	47456	175.11	0.382	2.1E-02	1.6E-02	1.7E-02
A11	156.31	1.930	637.26	684.06	469.26	266.70	0.4972	1.42E-04	51217	191.05	0.408	1.7E-02	1.3E-02	1.3E-02
A12	170.33	1.803	656.46	752.89	489.26	294.89	0.5450	1.07E-04	54978	207.00	0.434	1.4E-02	1.1E-02	1.2E-02
A13	184.36	1.693	674.06	823.05	508.15	323.75	0.5945	8.04E-05	58739	222.95	0.460	1.3E-02	1.0E-02	1.1E-02
A14	198.39	1.596	690.21	894.29	527.04	353.18	0.6445	6.06E-05	62500	238.90	0.485	1.3E-02	9.2E-03	1.1E-02
A15	212.41	1.510	705.06	966.39	544.26	383.08	0.6940	4.56E-05	66262	254.85	0.511	1.2E-02	9.9E-03	9.2E-03
A16	226.44	1.433	718.75	1039.16	560.37	413.36	0.7421	3.44E-05	70023	270.79	0.537	8.4E-03	7.5E-03	9.3E-03

Gas-liquid-water partitioning and fluid properties of petroleum mixtures under pressure: Implications for deep-sea blowouts

Compound	M	P _c	T _c	V _c	T _b	V _b	ω	K _{HL} (T*)	$\Delta H_{\text{vap}}^{\text{H}_2\text{O}}$	$\frac{L}{V}$	K _{airH}	MC ₁	MC ₂	MC ₃
	g mol ⁻¹	MPa	K	cm ³ mol ⁻¹	K	cm ³ mol ⁻¹	–	$\frac{\text{mol}}{\text{atm} \cdot \text{L}^{-1}}$	J mol ⁻¹	cm ³ mol ⁻¹	L mol ⁻¹	–	–	–
A17	240.47	1.361	731.42	1112.45	575.37	443.96	0.7885	2.59E-05	73784	286.74	0.563	1.1E-02	8.6E-03	9.4E-03
A18	254.49	1.296	743.18	1186.12	589.26	474.82	0.8330	1.95E-05	77545	302.69	0.588	8.3E-03	6.2E-03	7.5E-03
A19	268.52	1.234	754.15	1260.08	602.59	505.90	0.8755	1.47E-05	81306	318.64	0.614	7.2E-03	6.6E-03	7.4E-03
A20	282.55	1.176	764.43	1334.25	617.04	537.15	0.9163	1.11E-05	85068	334.59	0.640	9.5E-03	6.7E-03	7.5E-03
A21	296.57	1.122	774.11	1408.58	630.37	568.55	0.9556	8.33E-06	88829	350.53	0.666	9.1E-03	6.6E-03	6.5E-03
A22	310.60	1.071	783.27	1483.04	642.04	600.09	0.9937	6.27E-06	92590	366.48	0.692	6.8E-03	5.9E-03	5.9E-03
A23	324.63	1.023	791.98	1557.62	653.15	631.75	1.0309	4.73E-06	96351	382.43	0.717	6.1E-03	5.3E-03	5.4E-03
A24	338.65	0.979	800.29	1632.30	664.26	663.53	1.0677	3.56E-06	100112	398.38	0.743	6.1E-03	5.0E-03	5.1E-03
A25	352.68	0.938	808.26	1707.09	674.82	695.42	1.1044	2.68E-06	103873	414.33	0.769	5.9E-03	4.5E-03	4.1E-03
A26	366.71	0.901	815.94	1781.98	685.37	727.43	1.1411	2.02E-06	107635	430.27	0.795	5.8E-03	4.3E-03	3.8E-03
B8	106.17	3.647	625.04	377.59	399.26	143.08	0.3046	1.27E-01	39257	116.32	0.266	3.2E-04	3.2E-06	5.5E-04
B9	120.19	3.249	644.79	428.04	423.71	163.17	0.3402	9.54E-02	43018	132.26	0.292	3.5E-03	2.6E-03	2.8E-03
B10	134.22	2.915	663.38	480.20	447.04	184.07	0.3819	7.18E-02	46780	148.21	0.318	1.5E-03	8.4E-04	8.9E-04
B11	148.24	2.635	680.76	533.89	469.26	205.69	0.4281	5.41E-02	50541	164.16	0.344	5.7E-03	4.7E-03	4.7E-03
B12	162.27	2.399	696.97	588.84	489.26	227.93	0.4770	4.07E-02	54302	180.11	0.369	6.0E-03	4.8E-03	5.0E-03
B13	176.30	2.200	712.09	644.79	508.15	250.68	0.5269	3.07E-02	58063	196.06	0.395	5.7E-03	4.5E-03	4.9E-03
B14	190.32	2.032	726.23	701.41	527.04	273.79	0.5765	2.31E-02	61824	212.00	0.421	5.9E-03	4.9E-03	4.7E-03
B15	204.35	1.888	739.53	758.40	544.26	297.15	0.6245	1.74E-02	65586	227.95	0.447	5.0E-03	4.4E-03	5.0E-03
B16	218.38	1.764	752.14	815.44	560.37	320.62	0.6704	1.31E-02	69347	243.90	0.473	4.9E-03	4.0E-03	4.2E-03
B17	232.40	1.657	764.20	872.23	575.37	344.06	0.7136	9.88E-03	73108	259.85	0.498	4.6E-03	3.7E-03	4.1E-03
B18	246.43	1.561	775.87	928.51	589.26	367.35	0.7540	7.44E-03	76869	275.80	0.524	4.0E-03	3.6E-03	3.9E-03

Compound	M	P _c	T _c	V _c	T _b	V _b	ω	K _{HL} (T*)	$\Delta H_{\text{gas} \rightarrow \text{H}_2\text{O}}$	$\frac{L}{V}$	K _{airH}	MC ₁	MC ₂	MC ₃
	g mol ⁻¹	MPa	K	cm ³ mol ⁻¹	K	cm ³ mol ⁻¹	-	$\frac{\text{mol}}{\text{atm} \cdot \text{L}^{-1}}$	J mol ⁻¹	cm ³ mol ⁻¹	L mol ⁻¹	-	-	-
B19	260.46	1.476	787.26	984.05	602.59	390.42	0.7917	5.60E-03	80630	291.75	0.550	4.4E-03	3.2E-03	3.5E-03
B20	274.48	1.400	798.50	1038.69	617.04	413.16	0.8270	4.22E-03	84392	307.69	0.576	4.2E-03	3.1E-03	3.1E-03
B21	288.51	1.329	809.68	1092.31	630.37	435.54	0.8603	3.18E-03	88153	323.64	0.601	3.3E-03	2.9E-03	2.9E-03
B22	302.54	1.265	820.88	1144.89	642.04	457.54	0.8917	2.39E-03	91914	339.59	0.627	3.2E-03	2.8E-03	2.8E-03
B23	316.56	1.204	832.18	1196.43	653.15	479.15	0.9218	1.80E-03	95675	355.54	0.653	3.1E-03	2.5E-03	2.6E-03
B24	330.59	1.148	843.62	1247.03	664.26	500.41	0.9509	1.36E-03	99436	371.49	0.679	3.0E-03	2.4E-03	2.2E-03
B25	344.62	1.096	855.25	1296.82	674.82	521.37	0.9791	1.02E-03	103198	387.43	0.704	3.0E-03	2.3E-03	2.1E-03
C10	128.17	4.152	782.98	425.68	447.04	162.23	0.3085	1.90E+00	43626	126.19	0.264	0	0	0
C11	142.20	3.693	794.47	481.73	469.26	184.68	0.3632	1.72E+00	46834	142.13	0.290	5.3E-04	3.0E-04	4.0E-04
C12	156.22	3.325	805.02	537.67	489.26	207.22	0.4175	1.56E+00	50041	158.08	0.316	8.9E-04	5.0E-04	7.3E-04
C13	170.25	3.022	814.83	593.50	508.15	229.82	0.4709	1.41E+00	53248	174.03	0.342	1.3E-03	9.8E-04	8.8E-04
C14	184.28	2.769	824.01	649.25	527.04	252.49	0.5229	1.28E+00	56456	189.98	0.367	2.1E-03	1.9E-03	2.2E-03
C15	198.30	2.553	832.67	704.91	544.26	275.23	0.5734	1.16E+00	59663	205.93	0.393	2.5E-03	2.0E-03	2.1E-03
C16	212.33	2.366	840.86	760.50	560.37	298.01	0.6222	1.05E+00	62871	221.87	0.419	1.9E-03	1.5E-03	1.7E-03
C17	226.36	2.203	848.64	816.03	575.37	320.86	0.6692	9.52E-01	66078	237.82	0.445	1.6E-03	1.5E-03	1.6E-03
C18	240.38	2.059	856.06	871.49	589.26	343.75	0.7146	8.62E-01	69286	253.77	0.471	2.2E-03	1.6E-03	1.8E-03
C19	254.41	1.896	861.06	925.59	602.59	366.15	0.7522	6.49E-01	73047	269.72	0.496	2.2E-03	1.6E-03	1.6E-03
C20	268.44	1.748	865.99	979.65	617.04	388.59	0.7886	4.89E-01	76808	285.67	0.522	1.7E-03	1.5E-03	1.5E-03
C21	282.46	1.613	870.85	1033.66	630.37	411.07	0.8239	3.68E-01	80569	301.62	0.548	1.8E-03	1.6E-03	1.6E-03
C22	296.49	1.490	875.63	1087.63	642.04	433.59	0.8581	2.77E-01	84330	317.56	0.574	1.8E-03	1.5E-03	1.5E-03
C23	310.52	1.377	880.33	1141.56	653.15	456.14	0.8912	2.09E-01	88092	333.51	0.599	1.8E-03	1.4E-03	1.3E-03

Compound	M	P _c	T _c	V _c	T _b	V _b	ω	K _{HL} (T*)	$\Delta H_{\text{vap}}^{\text{pure}} - R_2 \cdot 0$	$\frac{L}{V}$	K _{airH}	MC ₁	MC ₂	MC ₃
	g mol ⁻¹	MPa	K	cm ³ mol ⁻¹	K	cm ³ mol ⁻¹	-	$\frac{\text{mol}}{\text{atm} \cdot \text{L}^{-1}}$	J mol ⁻¹	cm ³ mol ⁻¹	L mol ⁻¹	-	-	-
C24	324.54	1.273	884.93	1195.45	664.26	478.74	0.9233	1.57E+01	91853	349.46	0.625	1.8E-03	1.3E-03	1.2E-03
D14	178.23	2.910	899.33	567.96	527.04	219.47	0.5008	1.95E+01	54964	167.95	0.314	0	0	0
D15	192.26	2.627	903.50	623.39	544.26	241.96	0.5520	1.76E+01	58171	183.90	0.340	5.5E-05	7.7E-05	1.3E-04
D16	206.28	2.389	907.65	678.76	560.37	264.54	0.6015	1.60E+01	61379	199.85	0.365	3.6E-04	1.7E-04	2.4E-04
D17	220.31	2.188	911.76	734.09	575.37	287.18	0.6493	1.45E+01	64586	215.80	0.391	4.5E-04	2.7E-04	2.6E-04
D18	234.34	2.014	915.83	789.37	589.26	309.88	0.6953	1.31E+01	67793	231.74	0.417	8.0E-04	6.9E-04	6.9E-04
D19	248.36	1.863	919.84	844.61	602.59	332.65	0.7397	1.19E+01	71001	247.69	0.443	9.5E-04	8.3E-04	8.4E-04
D20	262.39	1.730	923.79	899.81	617.04	355.47	0.7824	1.08E+01	74208	263.64	0.469	8.5E-04	7.0E-04	7.1E-04
D21	276.42	1.613	927.67	954.98	630.37	378.34	0.8235	9.75E+00	77416	279.59	0.494	7.9E-04	6.2E-04	5.7E-04
D22	290.44	1.508	931.46	1010.11	642.04	401.26	0.8632	8.83E+00	80623	295.54	0.520	6.8E-04	5.1E-04	4.6E-04
E16	202.25	2.773	950.51	655.73	560.37	255.14	0.5473	1.20E+02	56301	182.69	0.323	1.5E-05	9.5E-06	9.1E-06
E17	216.28	2.528	951.97	711.00	575.37	277.72	0.5970	1.09E+02	59509	198.64	0.349	2.3E-06	1.5E-06	1.6E-06
E18	230.30	2.318	953.64	766.22	589.26	300.36	0.6449	9.88E+01	62716	214.59	0.374	6.0E-05	5.1E-05	5.6E-05
E19	244.33	2.137	955.47	821.41	602.59	323.08	0.6912	8.95E+01	65923	230.53	0.400	2.0E-04	1.5E-04	1.6E-04
E20	258.36	1.979	957.43	876.56	617.04	345.84	0.7357	8.11E+01	69131	246.48	0.426	5.0E-04	3.7E-04	3.2E-04
E21	272.38	1.840	959.49	931.68	630.37	368.67	0.7785	7.35E+01	72338	262.43	0.452	9.7E-04	7.1E-04	6.2E-04
SCN27	374.00	1.163	862.93	1289.87	694.82	518.44	0.9398					1.2E-02	9.6E-03	1.0E-02
SCN28	388.00	1.132	870.79	1324.85	704.26	533.18	0.9650					1.1E-02	9.2E-03	9.2E-03
SCN29	402.00	1.104	878.26	1357.17	713.15	546.82	0.9887					1.0E-02	9.1E-03	8.5E-03
SCN30	416.00	1.077	885.71	1389.56	722.04	560.50	1.0125					9.8E-03	8.7E-03	8.0E-03
SCN31	430.00	1.056	893.61	1417.36	730.93	572.26	1.0349					9.5E-03	8.2E-03	7.9E-03

Compound	M	P _c	T _c	V _c	T _b	V _b	ω	K _H (T [*])	ΔH _{gas → #2,0}	$\frac{L}{V}$	K _{airk}	MC ₁	MC ₂	MC ₃
	g mol ⁻¹	MPa	K	cm ³ mol ⁻¹	K	cm ³ mol ⁻¹	–	mol atm ⁻¹ L ⁻¹	J mol ⁻¹	cm ³ mol ⁻¹	L mol ⁻¹	–	–	–
SCN32	444.00	1.034	900.68	1446.78	739.26	584.72	1.0572					8.5E-03	7.7E-03	7.3E-03
SCN33	458.00	1.014	907.37	1473.23	747.04	595.92	1.0779					8.2E-03	7.4E-03	6.5E-03
SCN34	472.00	0.993	913.21	1501.63	754.26	607.97	1.0985					7.4E-03	7.1E-03	6.5E-03
SCN35	486.00	0.974	919.90	1527.97	762.04	619.15	1.1193					7.9E-03	7.4E-03	5.6E-03
SCN36	500.00	0.954	925.74	1556.43	769.26	631.24	1.1401					7.0E-03	7.2E-03	5.2E-03
SCN37	514.00	0.941	931.68	1576.60	775.93	639.82	1.1573					6.4E-03	6.6E-03	5.2E-03
SCN38	528.00	0.926	936.77	1599.00	782.04	649.35	1.1745					5.7E-03	5.8E-03	5.0E-03
SCN39	542.00	0.907	942.61	1627.44	789.26	661.46	1.1955					6.4E-03	6.6E-03	4.5E-03
SCN40	556.00	0.893	947.70	1649.80	795.37	670.98	1.2127					5.2E-03	5.3E-03	4.5E-03
SCN41	570.00	0.881	952.42	1669.06	800.93	679.19	1.2281					4.6E-03	4.7E-03	3.3E-03
SCN42	584.00	0.863	957.03	1697.13	807.04	691.17	1.2473					5.0E-03	5.1E-03	3.8E-03
SCN43	598.00	0.850	962.13	1719.44	813.15	700.70	1.2646					4.8E-03	4.9E-03	3.5E-03
SCN44	612.00	0.841	966.48	1735.48	818.15	707.55	1.2781					3.8E-03	3.9E-03	3.4E-03
SCN45	626.00	0.832	970.84	1751.43	823.15	714.37	1.2915					3.7E-03	3.8E-03	3.2E-03
SCN46	640.00	0.819	975.90	1774.08	829.26	724.05	1.3090					4.4E-03	4.5E-03	2.8E-03
SCN47	654.00	0.810	980.21	1790.67	834.26	731.15	1.3227					3.6E-03	3.7E-03	3.2E-03
SCN48	668.00	0.800	984.49	1807.44	839.26	738.33	1.3364					3.5E-03	3.6E-03	2.7E-03
SCN49	682.00	0.795	988.01	1818.11	843.15	742.89	1.3463					2.7E-03	2.7E-03	2.5E-03
SCN50	696.00	0.786	992.27	1835.20	848.15	750.21	1.3601					3.3E-03	3.4E-03	3.4E-03
SCN51	710.00	0.780	995.76	1846.18	852.04	754.92	1.3701					2.6E-03	2.6E-03	2.6E-03
SCN52	724.00	0.771	999.99	1863.57	857.04	762.37	1.3840					3.3E-03	3.3E-03	3.3E-03

Compound	M	P _c	T _c	V _c	T _b	V _b	ω	K _{HL} (T*)	$\Delta H_{\text{gas} \rightarrow \text{#2,0}}$	$\frac{L}{V}$	K _{airk}	MC ₁	MC ₂	MC ₃
	g mol ⁻¹	MPa	K	cm ³ mol ⁻¹	K	cm ³ mol ⁻¹	-	mol atm ⁻¹ L ⁻¹	J mol ⁻¹	cm ³ mol ⁻¹	L mol ⁻¹	-	-	-
SCN53	738.00	0.766	1003.46	1874.84	860.93	767.20	1.3940					2.4E-03	2.5E-03	2.5E-03
SCN54	752.00	0.758	1007.29	1889.38	865.37	773.44	1.4060					2.7E-03	2.7E-03	2.7E-03
SCN55	766.00	0.752	1010.74	1900.92	869.26	778.39	1.4161					2.3E-03	2.3E-03	2.3E-03
SCN56	780.00	0.747	1014.17	1912.59	873.15	783.40	1.4262					2.3E-03	2.3E-03	2.3E-03
SCN57	794.00	0.741	1017.59	1924.39	877.04	788.47	1.4363					2.2E-03	2.2E-03	2.2E-03
SCN58	808.00	0.735	1021.01	1936.32	880.93	793.59	1.4464					2.1E-03	2.2E-03	2.2E-03
SCN59	822.00	0.727	1024.78	1951.51	885.37	800.12	1.4585					2.4E-03	2.5E-03	2.5E-03
SCN60	836.00	0.725	1027.43	1957.39	888.15	802.64	1.4648					1.4E-03	1.5E-03	1.5E-03
SCN61	850.00	0.719	1030.81	1969.67	892.04	807.92	1.4749					2.0E-03	2.1E-03	2.1E-03
SCN62	864.00	0.715	1033.81	1978.92	895.37	811.90	1.4831					1.7E-03	1.7E-03	1.7E-03
SCN63	878.00	0.712	1036.42	1985.14	898.15	814.57	1.4894					1.4E-03	1.4E-03	1.4E-03
SCN64	892.00	0.706	1039.78	1997.75	902.04	820.00	1.4995					1.9E-03	1.9E-03	1.9E-03
SCN65	906.00	0.701	1042.75	2007.33	905.37	824.12	1.5077					1.6E-03	1.6E-03	1.6E-03
SCN66	920.00	0.699	1045.34	2013.87	908.15	826.93	1.5141					1.3E-03	1.3E-03	1.3E-03
SCN67	934.00	0.696	1047.92	2020.52	910.93	829.79	1.5204					1.3E-03	1.3E-03	1.3E-03
SCN68	948.00	0.691	1050.87	2030.40	914.26	834.05	1.5286					1.5E-03	1.5E-03	1.5E-03
SCN69	962.00	0.688	1053.44	2037.24	917.04	836.99	1.5349					1.3E-03	1.3E-03	1.3E-03
SCN70	976.00	0.683	1056.37	2047.31	920.37	841.33	1.5431					1.5E-03	1.5E-03	1.5E-03
SCN71	990.00	0.680	1058.93	2054.34	923.15	844.36	1.5494					1.2E-03	1.2E-03	1.2E-03
SCN72	1004.00	0.677	1061.47	2061.46	925.93	847.42	1.5556					1.1E-03	1.2E-03	1.2E-03
SCN73	1018.00	0.676	1063.63	2065.56	928.15	849.19	1.5601					9.1E-04	9.3E-04	9.2E-04

Compound	M	P _c	T _c	V _c	T _b	V _b	ω	K _H (T [*])	$\Delta H_{\text{gas} \rightarrow \text{#2,0}}$	$\frac{L}{V}$	K _{airK}	MC ₁	MC ₂	MC ₃
	g mol ⁻¹	MPa	K	cm ³ mol ⁻¹	K	cm ³ mol ⁻¹	-	mol atm ⁻¹ L ⁻¹	J mol ⁻¹	cm ³ mol ⁻¹	L mol ⁻¹	-	-	-
SCN74	1032.00	0.672	1066.16	2072.86	930.93	852.34	1.5664					1.1E-03	1.2E-03	1.2E-03
SCN75	1046.00	0.667	1069.06	2083.36	934.26	856.86	1.5744					1.3E-03	1.3E-03	1.3E-03
SCN76	1060.00	0.664	1071.58	2090.83	937.04	860.08	1.5807					1.1E-03	1.1E-03	1.1E-03
SCN77	1074.00	0.659	1074.48	2101.48	940.37	864.67	1.5886					1.2E-03	1.2E-03	1.2E-03
SCN78	1088.00	0.656	1076.99	2109.11	943.15	867.96	1.5948					9.8E-04	1.0E-03	1.0E-03
SCN79	1102.00	0.652	1079.49	2116.81	945.93	871.28	1.6010					9.8E-04	1.0E-03	1.0E-03
SCN80	1116.00	0.651	1081.61	2121.48	948.15	873.30	1.6054					7.6E-04	7.7E-04	7.7E-04
SCN81	1130.00	0.647	1084.10	2129.33	950.93	876.68	1.6115					9.1E-04	9.3E-04	9.2E-04
SCN82	1144.00	0.642	1086.97	2140.35	954.26	881.44	1.6193					1.1E-03	1.1E-03	1.1E-03
SCN83	1158.00	0.642	1088.69	2142.14	955.93	882.21	1.6219					5.3E-04	5.4E-04	5.4E-04
SCN84	1172.00	0.637	1091.55	2153.29	959.26	887.03	1.6296					1.1E-03	1.1E-03	1.1E-03
SCN85	1186.00	0.636	1093.26	2155.24	960.93	887.87	1.6322					5.3E-04	5.4E-04	5.4E-04
SCN86	1200.00	0.631	1096.11	2166.51	964.26	892.74	1.6398					1.1E-03	1.1E-03	1.1E-03
SCN87	1214.00	0.630	1097.81	2168.59	965.93	893.63	1.6424					5.3E-04	5.4E-04	5.4E-04
SCN88	1228.00	0.628	1099.89	2173.83	968.15	895.90	1.6466					7.6E-04	7.7E-04	7.7E-04
SCN89	1242.00	0.626	1101.96	2179.13	970.37	898.19	1.6508					7.6E-04	7.7E-04	7.7E-04
SCN90	1256.00	0.622	1104.41	2187.57	973.15	901.83	1.6566					9.1E-04	9.3E-04	9.2E-04
SCN91	1270.00	0.620	1106.48	2192.99	975.37	904.17	1.6608					7.6E-04	7.7E-04	7.7E-04
SCN92	1284.00	0.619	1108.16	2195.41	977.04	905.22	1.6633					5.3E-04	5.4E-04	5.4E-04
SCN93	1298.00	0.617	1110.21	2200.95	979.26	907.61	1.6674					6.8E-04	7.0E-04	6.9E-04
SCN94	1312.00	0.616	1111.88	2203.49	980.93	908.71	1.6699					5.3E-04	5.4E-04	5.4E-04

Compound	M	P _c	T _c	V _c	T _b	V _b	ω	K _H (T [*])	$\Delta H_{\text{gas} \rightarrow \text{H}_2\text{O}}$	$\frac{L}{V}$	K _{oilR}	MC ₁	MC ₂	MC ₃
	g mol ⁻¹	MPa	K	cm ³ mol ⁻¹	K	cm ³ mol ⁻¹	-	mol atm ⁻¹ L ⁻¹	J mol ⁻¹	cm ³ mol ⁻¹	L mol ⁻¹	-	-	-
SCN95	1326.00	0.613	1113.93	2209.15	983.15	911.16	1.6740					6.8E-04	7.0E-04	6.9E-04
SCN96	1340.00	0.611	1115.97	2214.87	985.37	913.63	1.6780					6.8E-04	7.0E-04	6.9E-04
SCN97	1354.00	0.610	1117.63	2217.59	987.04	914.80	1.6805					4.5E-04	4.6E-04	4.6E-04
SCN98	1368.00	0.607	1119.67	2223.41	989.26	917.32	1.6845					6.1E-04	6.2E-04	6.2E-04
SCN99	1382.00	0.606	1121.32	2226.25	990.93	918.55	1.6869					4.5E-04	4.6E-04	4.6E-04
SCN100	1396.00	0.604	1123.35	2232.17	993.15	921.11	1.6909					5.3E-04	5.4E-04	5.4E-04
SCN101	1410.00	0.603	1124.99	2235.11	994.82	922.38	1.6933					4.5E-04	4.6E-04	4.6E-04
SCN102	1424.00	0.602	1126.63	2238.11	996.48	923.68	1.6956					3.8E-04	3.9E-04	3.8E-04
SCN103	1438.00	0.600	1128.26	2241.16	998.15	925.00	1.6980					3.8E-04	3.9E-04	3.8E-04
SCN104	1452.00	0.599	1129.89	2244.26	999.82	926.34	1.7004					3.8E-04	3.9E-04	3.8E-04
SCN105	1466.00	0.598	1131.51	2247.41	1001.48	927.70	1.7027					3.8E-04	3.9E-04	3.8E-04
SCN106	1480.00	0.597	1133.14	2250.61	1003.15	929.09	1.7051					3.8E-04	3.9E-04	3.8E-04
SCN107	1494.00	0.595	1134.76	2253.86	1004.82	930.49	1.7074					3.0E-04	3.1E-04	3.1E-04
SCN108	1508.00	0.596	1135.98	2254.16	1005.93	930.62	1.7083					2.3E-04	2.3E-04	2.3E-04

Chapter 5 Controls on the aqueous dissolution of petroleum emitted into the Gulf of Mexico during the *Deep-water Horizon* disaster

Not published

Authors: Jonas Gros, Scott A. Socolofsky, Anusha L. Dissanayake, Inok Jun, Lin Zhao, Michel C. Boufadel, Robert K. Nelson, Christopher M. Reddy, and J. Samuel Arey. (Authors for version to be sent to a journal)

Contributions: This chapter was prepared principally by me. For modeling I used a customized version of the Texas A&M oil spill calculator (TAMOC, version 0.1.17; <https://github.com/socolofs/tamoc>); TAMOC was implemented by Scott Socolofsky. The thermodynamic model in TAMOC is based largely on my contributions (Chapter 4), whereas I did not contribute to some other features of TAMOC including the bent plume model and the hydrate model. Other persons working with Scott Socolofsky contributed to the development of TAMOC, especially Inok Jun and Anusha Dissanayake. Anusha Dissanayake gave me helpful advice on how to use the bent plume model and we had fruitful interactions on modeling assumptions. I also obtained ocean model predictions through Anusha Dissanayake (crcm from Chuan-Yuan Hsu and Ping Chang; sabgom; and hycom). Lin Zhao ran her model to predict droplet and bubble size distributions based on my property estimates of Chapter 4. Samuel Arey provided guidance to me and also contributed to the project conception, data interpretation, and writing of the chapter. Christopher Reddy also provided guidance and

contributed to the writing of the chapter.

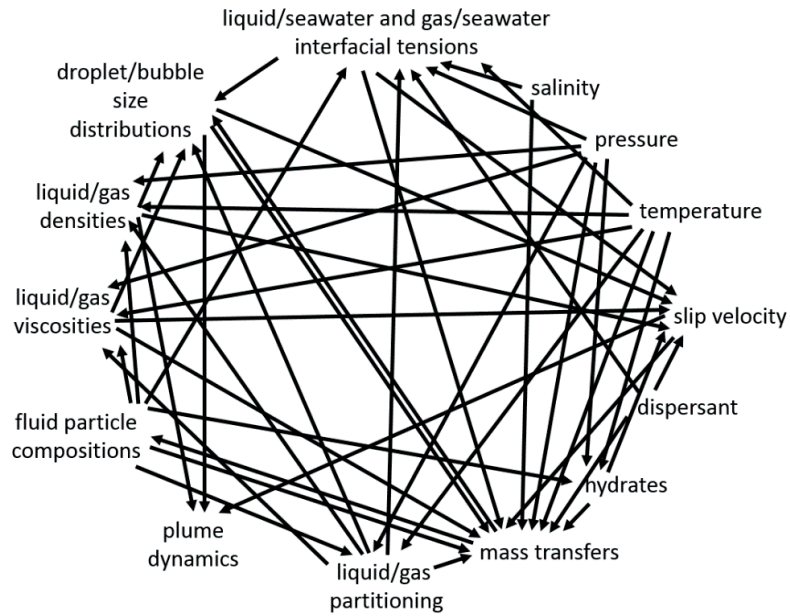


Figure 5-1. Schematic representation of the interdependences among the modeled processes leading to aqueous dissolution during the *Deepwater Horizon* disaster, at ~1500 meters depth.

5.1 Abstract

Compared to conventional sea-surface spills, the *Deepwater Horizon* disaster led to dramatically increased aqueous dissolution of several petroleum compounds in the ocean water column, due to elevated pressures in deep waters, the presence of added dispersants, and the long exposure time to the water column during the ascent of petroleum fluids to the sea surface. For example, methane, ethane, and benzene were reported as becoming >99% aqueously dissolved in the water column during the *Deepwater Horizon* disaster.⁷⁵ However, we lack quantitative models to describe in detail the processes leading to the apparently massive aqueous dissolution of petroleum compounds during a deep-sea release. In the present chapter, we introduce the TAMOC-c model (customized version of the Texas A&M oil spill calculator model), which describes buoyant plume dynamics, ascent of fluid particles, detailed aqueous dissolution kinetics (131 individual compounds modeled), and relevant deep-water effects including composition-dependent, pressure-dependent and temperature-dependent densities and viscosities of fluid particles; composition-dependent, pressure-dependent, temperature-dependent, and salinity-dependent liquid-seawater and gas-seawater interfacial tensions; composition-dependent, pressure-dependent and temperature-dependent liquid-gas partitioning; composition-dependent, pressure-dependent, temperature-dependent, and salinity-dependent aqueous solubilities of petroleum compounds; and the effect of hydrates on aqueous dissolution kinetics and on droplet and bubble slip velocities. We successfully validate predictions of the TAMOC-c model using several previously reported field observations made in the deep water column and at the sea surface during the *Deepwater Horizon* disaster. For June 8, 2010, the TAMOC-c model predicts that 27% of the mass flow rate of petroleum fluids emitted at 1524 m depth in the Gulf of Mexico became aqueously dissolved during ascent, demonstrating the important role of aqueous dissolution for this deep-sea release of petroleum fluids. The TAMOC-c model predicts that, in the absence of dispersant injection, 22% (rather than 27%) of the mass flow rate of emitted petroleum fluids would have become aqueously dissolved. We predict that <1% of the emitted petroleum fluids became dispersed as small droplets for prolonged times (>60 hours) before reaching the sea surface (June 8, 2010), indicating that this process was less important than has been suggested in some other studies. The TAMOC-c model provides detailed insights into these and other processes that controlled the aqueous dissolution of petroleum compounds in the deep sea during the *Deepwater Horizon* disaster. The highly mechanistic model also enables prognostic, quantitative predictions of ascent times, extent of dissolution in the water column, and influence of dispersant addition for hypothetical future releases of other petroleum fluids, at other emission depths, and under other environmental conditions. This tool could prove helpful in damage assessment studies, and it can also improve the understanding of the processes in play during such an event which is needed to guide response action for a potential future accident in deep waters.

5.2 Introduction

After the blowout at the *Deepwater Horizon* platform on April 20, 2010, petroleum fluids were emitted initially from two leak sources: a kink in the riser tube and the open end of the broken riser. Once the remains of the riser tube had been severed on 3rd June, petroleum fluids were

emitted continuously into the deep sea from a single emission source at the broken Macondo riser stub at 1524 m depth.^{9,203} This deep-sea release, which lasted 87 days, favored extensive dissolution of petroleum compounds into the deep water column, making this event totally unlike any previously documented accidental oil spill. It was found that >99% of the emitted mass of several highly water-soluble compounds did not reach the sea surface, including methane, ethane, and benzene.⁷⁵ These light compounds were largely trapped in a deep-water hydrocarbon plume that formed at a depth of 1000–1200 m.³¹ The composition of this hydrocarbon-rich water mass⁸ indicated that it had been formed chiefly by aqueous dissolution processes, a sign that most of the emitted liquid droplets and gas bubbles (by mass) were not trapped at this location and probably continued ascent towards the sea surface. Until the present study, no model has been proposed that provides a mechanistic explanation of these field observations and that enables predictions of the extent of aqueous dissolution of petroleum compounds in the water column. This situation reflects our lack of understanding of the processes controlling the fate of petroleum fluids emitted during the *Deepwater Horizon* disaster, and it leaves us without tools to predict the expected outcome of another potential future deep-water release of petroleum fluids. Such tools would help in guiding response actions during a future accidental release of petroleum fluids in deep waters. Model predictions of the fractionation of the different petroleum compounds into the water column could aid assessments of damage to aquatic wildlife, as well as exposures to volatile compounds endured by human emergency response workers at the sea surface.

The sizes of liquid droplets and gas bubbles play a crucial role in determining times of arrival of emitted petroleum fluids at the sea surface,⁷⁵ as well as extent of aqueous dissolution of petroleum compounds into the water column. In this chapter, we use the term *fluid particles*²⁶⁰ to refer collectively to liquid petroleum droplets, gas (or supercritical fluid) bubbles, and mixed entities composed of both petroleum liquid and gas. The (single-phase) Macondo reservoir fluid spontaneously separated into liquid and gas petroleum phases at the emission source boundary,^{9,45,255} considered here to be the broken Macondo riser stub at 1524 m depth. When liquid and gas petroleum fluids are emitted into seawater, they will usually break up into droplets and bubbles, with size distributions that are controlled largely by interfacial tension between liquid petroleum and seawater, interfacial tension between gaseous petroleum and seawater, the densities and viscosities of the liquid and gas phases, the shape of the emission opening, and the velocities of the emitted fluids.²⁷³ Measurements obtained *in situ* using a digital holographic camera (Holocam) during the event²⁷⁴ did not explore the principal path taken by fluid particles on their way to the sea surface and therefore can only provide information about fluid particles that remained trapped in the water column for prolonged times. Other measurements of droplet or bubble sizes using laser in-situ scattering and transmissometry system (LISST) during the *Deepwater Horizon* disaster were also conducted^{254,275} and provide additional evidence of the presence of some small droplets in the water column. However the LISST measurements were of limited relevance, because the range of sizes studied (2.5–500 μm)²⁵⁴ does not encompass the millimeter-scale droplets thought to have brought most of the mass of emitted petroleum fluids to the sea surface.^{75,276} Additional complications arise from the fact that LISST measurements were performed at sea surface conditions after recovering samples taken at different depths in the water column, and this prevented the measurement of liquid droplets having size >70 μm that would have ascended to

the surface of the sampling container by measurement time.²⁵⁴ As a consequence, very indirect data remain the most reliable information available to infer the size distributions of droplets and bubbles at the emission source boundary. Such indirect observations data include the timing and location of arrival of petroleum fluids at the sea surface,⁷⁵ and the observed fractionations of hydrocarbons in the water column and in the atmosphere at the sea surface.^{8,75} A few models have been proposed to predict size distributions of liquid droplets and gas bubbles at the emission source boundary for deep-water releases of petroleum fluids.^{273,277,278} For example, Zhao et al.²⁷⁶ have predicted a median diameter for droplets ($d_{50,droplets}$, 50% of the emitted volume present as smaller droplets) of 3.9 mm without dispersant and 0.9 mm with dispersant addition. Predicted $d_{50,bubbles}$ were 8.1 mm without dispersant, and 1.4 mm with dispersant addition. These predicted size distributions were in reasonable agreement with the estimate that millimeter-scale droplets brought most of the mass of emitted petroleum fluids to the sea surface.^{75,276} However these models have not been tested for their ability to predict the observed fractionations of hydrocarbons in the deep water column and at the sea surface during the *Deepwater Horizon* disaster, due to the lack of a detailed mechanistic model that couples the relevant processes.

Buoyant plume ascent and related plume dynamics are major processes that partly control the fractionation of petroleum compounds between the liquid, gas, and seawater phases.³³ These coupled processes are particularly important in the formation of the deep-water hydrocarbon plume. In the case of a massive release of petroleum in the deep sea, a *buoyant plume* is formed, consisting of dispersed petroleum fluid particles that ascend through the water column together with an envelope of entrained seawater (Figure 5-2).^{33,44,279,280} Ambient cross flows tend to promote the separation of the dispersed phases from the bulk of the entrained seawater, with fluid particles situated in the upstream part of the buoyant plume due to their slip velocities, leading to export of the largest fluid particles outside of the plume under extreme circumstances.²⁸¹ In case of a stratified ambient water column (typical in the ocean anywhere except in case of convective mixing), the water in the buoyant plume is denser than the ambient seawater, the buoyancy being brought by the petroleum fluid particles. After the ascending entrained seawater and petroleum fluid particles arrive a depth such that the buoyancy of the petroleum fluid particles is not sufficient to carry the negatively-buoyant entrained water within the ascending plume, the largest fluid particles will separate from the entrained water at a depth called *peel height*: while the large fluid particles continue to ascend towards the sea surface where they will form surface slicks, the entrained seawater detrains, forming a *descending plume*, and sinks back to a depth where its buoyancy matches that of the ambient water where it forms a *deep-water hydrocarbon plume* (Figure 5-2).³³ The detrained seawater contains aqueously dissolved hydrocarbons, and possibly also small fluid particles that are not buoyant enough to rise against the detraining seawater and thus become trapped (initially) in the deep-water hydrocarbon plume. The fate of fluid particles after separation from the entrained water is not well-known, but it has been proposed that these petroleum fluid particles ascend toward the sea surface as individual entities without group buoyancy effects.²⁸² Similarly, small fluid particles that may initially be carried by the detrained seawater could later escape from the deep-water hydrocarbon plume and continue their journey towards the sea surface where they will mix with surface slicks. These fluid particles rise in the water column with a velocity equal to the resultant of their buoyant velocities

and the ambient seawater current velocities. Several deep-water blowout models have been developed,^{44,270,279,283,284} and here we use a customized version of the Texas A&M oil spill model calculator (TAMOC)^{270,283,284} which enables the simulation of the processes described above.

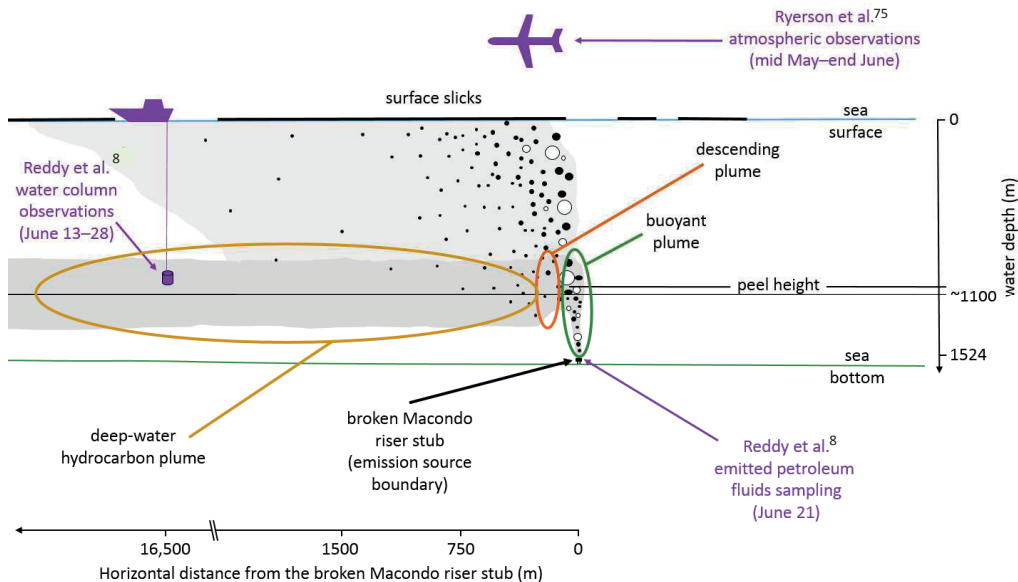


Figure 5-2. Conceptual representation of plume dynamics and resulting trajectories of petroleum fluids during the *Deepwater Horizon* disaster, after the remains of the riser had been severed immediately above the blowout preventer, on June 3, 2010.⁹ Liquid and gas phase petroleum fluids were emitted from the broken Macondo riser stub. Immediately above the broken Macondo riser stub, fluid particles entrain ambient water, generating a *buoyant plume*.³³ At the *peel height*, which was previously estimated to be located at 900–1000 m depth for the *Deepwater Horizon* disaster,³³ the water in the buoyant plume detrain forming a *descending plume*. The descending plume will reach a depth where its density matches that of the ambient seawater, where it will generate a *deep-water hydrocarbon plume* containing water, dissolved petroleum compounds, and possibly a few small fluid particles.³³ Fluid particles that separated from the buoyant plume, the descending plume, or from the deep-water hydrocarbon plume ascend to the sea surface at velocities that depend on their individual buoyancies.²⁸² Depicted sizes of fluid particle are magnified $\sim 20,000\times$. (Before June 3, two emission sources were present, ~ 100 meters apart from each other, at depths of ~ 1500 m.²⁵⁵)

To simulate buoyant plume ascent and related plume dynamics, as well as aqueous dissolution kinetics for individual petroleum compounds, we must also account for the slip velocities of fluid particles and the coefficients of mass transfer to the seawater for individual compounds.^{44,270,279,283,284} Slip velocities impact both mass transfer coefficients and buoyant plume dynamics, where mass transfer coefficients play a major role in determining the rate of aqueous dissolution of petroleum compounds. Several investigators have proposed equations to predict slip velocity^{260,285} and mass transfer coefficients^{260,286,287} for individual circulating or non-circulating droplets or bubbles. Such formulas have been used to model the fate of individual methane bubbles rising in seawater,^{35,47} and to model dissolution of petroleum hydrocarbons from gas bubbles.^{44,279} TAMOC applies such formulas to both gas and liquid petroleum fluids.^{270,283,284} Finally, in the presence of a hydrate shell (which can form spontaneously at >500 m depth in the oceans), methane bubbles exhibit an apparent decrease in aqueous dissolution rate corresponding to a change in mass transfer coefficient.⁴⁷

The TAMOC model^{270,283,284} includes a near-field integral plume model, and a far-field single particle tracking model to simulate and investigate the fate of the emitted fluids during the *Deepwater Horizon* disaster. The TAMOC model also takes into account the hydrodynamic processes and thermodynamic properties of petroleum fluid particles that are needed to predict mass transfers of petroleum compounds to the aqueous phase, heat transfers to the aqueous phase, and slip velocities of fluid particles. The behaviors of fluid particles depend on their size and estimated shape. The coupled thermodynamic model enables the prediction of properties of fluid particles, including density, viscosity, interfacial tension with seawater, volume, and aqueous solubility of individual compounds/pseudo-components. These predictions depend on the local conditions of pressure, temperature, fluid particle composition, and seawater salinity (Chapter 4 and section 5.3.7).

In this chapter, we aim to propose a mechanistic explanation to the large extent of aqueous dissolution reported during the *Deepwater Horizon* disaster. For this purpose, we developed a mechanistic model named TAMOC-c which describes the coupled processes of buoyant plume dynamics, fluid particle ascent, and aqueous dissolution of petroleum compounds from ascending fluid particles. The emitted petroleum mixture is represented with unprecedented detail by using 279 components, including 131 individual compounds (Chapter 4), therefore enabling detailed investigation of aqueous dissolution of individual compounds and also the cumulative reservoir fluid mixture. The TAMOC-c model is a modified version of TAMOC^{270,283,284} that also includes a simplified model of the deep-water hydrocarbon plume (section 5.3.8), and that enables two-phase fluid particles (section 5.3.6). Here we report predictions of the TAMOC-c model when parameterized for boundary conditions on June 8, 2010, which we chose as a representative day of the period after the remains of the riser tube had been cut. This choice was based on the net flow rate in the environment and on the mass flow rate of dispersant injected at the broken Macondo riser stub. We performed validation of the TAMOC-c model with several independent field observations. Our simulations enables us to constrain the fractionation of compounds between the deep-water hydrocarbon plume, the upper water column, and sea surface slicks. We were also able to investigate the effect of deep-water dispersant application during the *Deepwater Horizon* disaster: deep-water dispersant application was predicted to have led to increased fractionation to the water column, therefore leading to decreased exposure of response workers to toxic volatile compounds.

5.3 Computational methods

5.3.1 Overview of TAMOC-c: a model for deep-water releases of petroleum fluids

The TAMOC-c model is a customization of the version 0.1.17 of the TAMOC model. The custom modifications are described in sections 5.3.6 and 5.3.8, whereas the aqueous dissolution modeling for petroleum compounds in TAMOC^{270,283,284} version 0.1.17 is described in section 5.3.7. The TAMOC model, version 0.1.17, was implemented by Scott Socolofsky, and it includes my contributions from Chapter 4. TAMOC is a freely available software (<http://github.com/socolofs/tamoc>) coded in Python and Fortran.^{270,283,284} I implemented the custom modifications described in sections 5.3.6 and 5.3.8 to obtain TAMOC-c.

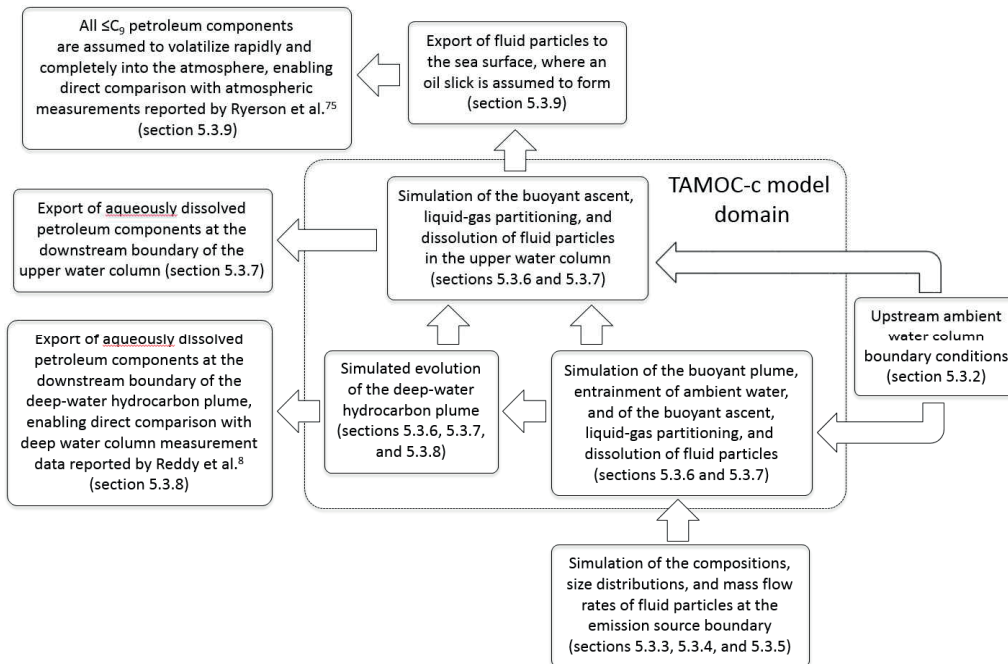


Figure 5-3. Schematic representation of the organization of the TAMOC-c model. This diagram shows the flows of material from upstream boundaries, through the different parts of the model, up to emission at the downstream boundaries. Each part of this diagram is described in more detail in section 5.3.1.

At the upstream ambient water column boundary, the version 0.1.17 of the TAMOC model handles data describing ambient water column conditions, including currents, temperature, salinity, and concentrations of dissolved compounds (Figure 5-3 and section 5.3.2).

At the emission source boundary, the version 0.1.17 of the TAMOC model has to be provided with simulations of the compositions, (initial) size distributions, and mass flow rates of fluid particles (Figure 5-3 and sections 5.3.3, 5.3.4, and 5.3.5).

TAMOC version 0.1.17 includes two near-field plume models to simulate the buoyant plumes formed in either stagnant, stratification-dominated (stratified plume model) or ambient current-dominated (bent plume model) environments (Figure 5-3).^{270,283,284} The simulations conducted in this work employed the bent plume model,^{270,283,284} which neglects any re-entrainment of detrained seawater within the buoyant plume. The bent plume model describes the dynamics of both the buoyant plume and the descending plume (Figure 5-2), including the entrainment of ambient seawater. The bent plume model has been validated previously with available laboratory and field data by Anusha Dissanayake (manuscript in preparation).^{283,284} The version 0.1.17 of the TAMOC model estimates the points in time and space where individual fluid particles separate from the buoyant plume or from the descending plume. TAMOC version 0.1.17 predicts ascent velocities of fluid particles which depend on a combination of their slip velocities and the velocity of the plume in which these particles are situated. TAMOC version 0.1.17 also includes the thermodynamic model described in Chapter 4, which simulates liquid-gas partitioning of petroleum compounds and the associated bulk phase properties of density and viscosity of the petroleum liquid and gas phases. The TAMOC-c model allows the existence of two-phase fluid particles (section 5.3.6). Thanks to the inclusion of this

thermodynamic model, the sizes of fluid particles in the model evolve as a function of local composition, pressure, and temperature. TAMOC version 0.1.17 predicts mass transfer coefficients of the petroleum compounds within a fluid particle, which enables to predict aqueous dissolution kinetics, as described in section 5.3.7. The effect of the presence of a hydrate rim on slip velocities of fluid particles and mass transfer coefficients is simulated. The simulation of the effect of hydrates in the version 0.1.17 of the TAMOC model has been validated previously with available laboratory and field data by Inok Jun.^{283,284,288}

Also implemented into TAMOC-c is a model description of the deep-water hydrocarbon plume (Figure 5-3, Figure 5-4, and section 5.3.8). The TAMOC-c model simulates the aqueous dissolution from fluid particles present in the deep-water hydrocarbon plume, as well as the progressive ascent of fluid particles towards the upper limit of the deep-water hydrocarbon plume, due to their slip velocities. The TAMOC-c model estimates the points in time and space where individual fluid particles separate from the deep-water hydrocarbon plume.

The TAMOC-c model simulate the ascent to the sea surface of fluid particles that separated from the buoyant plume, the descending plume, or the deep-water hydrocarbon plume (Figure 5-3). This includes the estimation of the slip velocities of fluid particles, their liquid-gas partitioning, and aqueous dissolution in the upper water column (sections 5.3.6 and 5.3.7).

The TAMOC-c simulations are terminated when fluid particles reach the sea surface (Figure 5-3). Outside of the TAMOC-c model domain, these fluid particles that reached the sea surface are assumed to form an oil slick at the sea surface. We assumed that all $\leq C_9$ petroleum components volatilize rapidly and completely from sea surface slicks into the atmosphere. This enabled us to compare the predictions of the TAMOC-c model with observations made by Ryerson et al.,⁷⁵ as explained in section 5.3.9.

Petroleum compounds aqueously dissolved in the upper water column are assumed rapidly exported at the downstream boundary of the upper water column (Figure 5-3), and therefore the concentrations of dissolved petroleum compounds in the upper water column are assumed to be zero when modeling the aqueous dissolution of individual fluid particles during ascent in the upper water column (section 5.3.7).

Petroleum compounds aqueously dissolved in the deep-water hydrocarbon plume are exported at the downstream boundary of the deep-water hydrocarbon plume (Figure 5-3). The concentrations of aqueously dissolved petroleum compounds at this downstream boundary were compared in this Chapter to observations of the composition of the deep-water hydrocarbon plume reported previously by Reddy et al.⁸

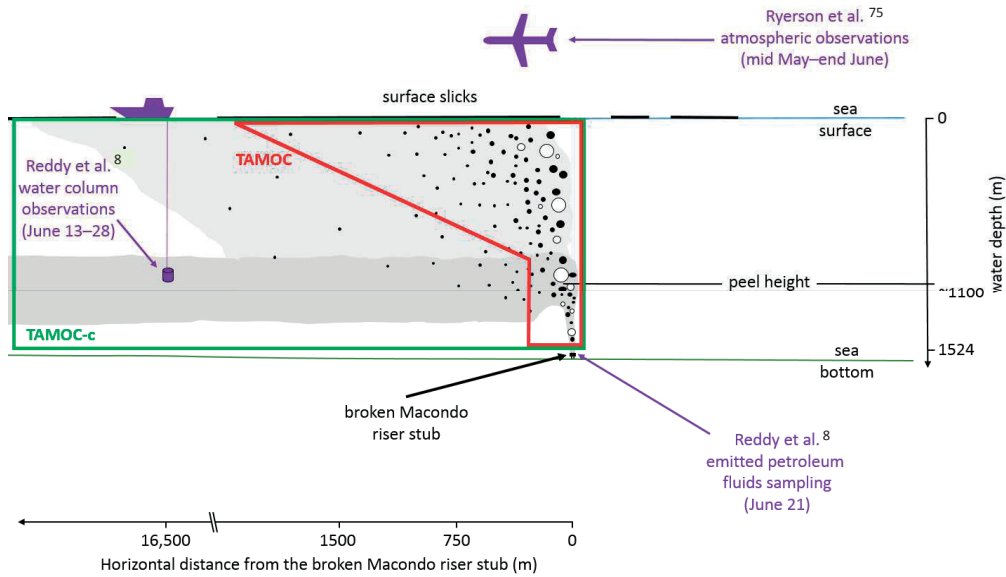


Figure 5-4. Schematic depiction of the domains included in TAMOC and TAMOC-c. TAMOC-c includes consideration of the deep-water hydrocarbon plume. Refer to the legend of Figure 5-2 for a description of the remainder of the figure.

5.3.2 Boundary conditions of the ambient water column: current velocity, temperature, and salinity profiles

The ambient conditions (current velocity profile and density profile) should in principle dictate the type of model regime that is employed (bent plume model or stratified plume model). Here, we use the bent plume model regardless of the low currents in the lower water column which would indicate that the stratified plume model is the most representative of the situation. Between the peel height and the depth of the deep-water hydrocarbon plume, the stratified plume model simulates an inner buoyant plume surrounded by an outer descending plume: this results in computationally expensive simulations if we simulate the possibility for fluid particles to be re-entrained several times from the outer plume into the inner plume. The bent plume model is used here as a simplification of the reality that enables less computationally expensive simulations, by neglecting this re-entrainment of fluid particles. Ambient current velocities also provide the upstream boundary for the seawater that becomes entrained in the buoyant plume. Additionally, the ambient density profile (given by temperature and salinity) influences the buoyancies of fluid particles with respect to depth. Finally, the pressure and temperature profiles influence the liquid-gas partitioning and the densities of fluid particles with respect to composition and depth.

Profiles of ambient horizontal current velocities in the water column measured at 28.73° North and 88.36° West were taken from www.ndbc.noaa.gov/download_data.php?file-name=42916b2010.txt.gz&dir=data/historical/adcp2/ (the position of the broken Macondo riser stub was 28.74° North and 88.39° W). Here, we assumed that the water current velocity profile was constant in time, where values from 64 to 1184 m depth (at a 32 m measurement grid interval) correspond to the mean measured profile of horizontal velocities with respect

to depth, as recorded on June 8, 2010. We assumed a single velocity value of 1.6 cm s^{-1} between 1185 m depth and the depth of the emission source (broken Macondo riser stub at 1524 m depth²⁰³) equal to the mean of the velocity measurements taken below 600 m depth (i.e. the depth below which the salinity has approximately a constant value), for that day. Physical ocean models^{289–291} exhibited disagreements with reported measurements of the water column current velocity profile, and therefore the ocean model estimates were not used to estimate the ambient current profile in TAMOC-c (Appendix section 5.6.2). Other ambient seawater conditions in the model, including temperature, salinity, and oxygen concentration profiles, are parameterized from data collected at station B54 from the R/V *Brooks McCall* on May 30, 2010 at 28.73° North and 88.38° West. We used temperature, salinity, and oxygen data recorded on May 30 to model the situation on June 8, because we expect these parameters to vary only on time scales of weeks to months, whereas water currents (parameterized in the TAMOC-c simulations based on data from June 8) can vary on a daily or hourly time scale.

5.3.3 The detailed model composition of the Macondo reservoir fluid (279 components)

To be able to run TAMOC-c simulations, we need to use a completely defined model composition of the Macondo reservoir fluid. Here, we used a model composition, termed MC_1 , which is defined in detail in Chapter 4. The composition of MC_1 is based on analysis results from the MW-1 sample, which was taken from the broken Macondo riser stub using an isobaric gas-tight sampler on June 21, 2010.⁸ MC_1 uses 279 components to represent the Macondo reservoir fluid. Properties of the 279 components were estimated as explained in Chapter 4 and in section 5.3.7. MC_1 includes 131 individually quantified compounds and 148 pseudo-components determined using comprehensive two-dimensional gas chromatography (GC×GC) and simulated distillation. MC_1 enables us to simulate aqueous dissolution of components $<n-C_{27}$, including all compounds that were reportedly fractionated by aqueous dissolution during the *Deepwater Horizon* disaster.⁷⁵

5.3.4 The simplified model composition of the Macondo reservoir fluid (14 components)

The TAMOC-c model requires several days of simulation time on a computer with Intel X5650 CPU (1 core, 4 GB of RAM) when using model petroleum fluid composition MC_1 . For model development and in order to investigate the sensitivities of some parameters on predictions of the TAMOC-c model, we used a simplified representation of the reservoir fluid having 14 components, which is able to predict dissolution of compounds $\leq n-C_5$ (Appendix section 5.6.1). However, the results reported in this chapter are based on the model petroleum fluid composition MC_1 , not the 14-component model, unless stated otherwise.

5.3.5 Boundary conditions at the emission source: size distributions, compositions, and volumetric flow rates of droplets and bubbles

Three different approaches were tested to model the size distributions of droplets and bubbles at the emission source boundary: the VDROD-J model,²⁷³ which considers coalescence and breakup, the Johansen et al. correlation (Rosin-Rammler distributions),²⁷⁷ and finally a simplified custom distribution (droplets all having 1.5 mm diameters and bubbles all having 3.75 mm diameters). All available models to predict fluid particle size distributions during *Deepwater Horizon* assume complete separation of the liquid and gas phases at the emission source boundary, and therefore predict size distributions at the source boundary for pure droplets and pure bubbles, without any two-phase fluid particle. To predict size distributions at the emission source boundary, the composition of the emitted petroleum fluids, the volumetric flow rate, and the liquid/seawater and gas/seawater interfacial tensions (with or without dispersant) need to be estimated. The assumptions retained for these three properties are described first, and after that we discuss the three size distributions in more detail.

The compositions of liquid droplets and gas bubbles at the emission source boundary were obtained through a liquid-gas equilibrium calculation of the Macondo reservoir fluid model composition MC₁ at 15.5 MPa and 4.3 °C (Chapter 4). This assumes that emitted fluids rapidly cool from their initial temperature of 105 °C⁸ to the local ambient temperature of 4.3 °C. We assumed that this cooling is faster than the time needed for initial size distributions to stabilize.²⁷³ Indeed, cooling to ambient temperature is likely to have happened faster than the stabilized formation of petroleum droplets and bubbles within the entrained seawater: Reddy et al.⁸ measured a temperature of 105 °C at the emission source boundary (broken Macondo riser stub) and only 37 °C a few meters above, within the ascending buoyant plume. However, for completeness, we separately evaluated the influence of the temperature at the emission source boundary on predicted compound fractionations, and this is discussed in Appendix section 5.6.3.

To parameterize the model for the effective volumetric flow rate of emitted petroleum fluids at the emission source boundary, we relied on previous estimates of the rate at which petroleum was emitted into the deep-sea on June 8, 2010. On that day, the remains of the riser tube had already been severed immediately above the blowout preventer, and the *top hat #4* collection device was in place,⁸ recovering a portion of the fluids emitted from the broken Macondo riser stub.²⁵⁴ Here we neglect the effect of the *top hat #4* collection device on the geometry of the emission source boundary, and we assume a circular emission source boundary having a 0.5 m diameter, consistent with the broken Macondo riser pipe diameter.²⁵⁵ Acknowledging that volumetric flow rate estimates have uncertainties,²²² we report here predictions obtained using the estimates provided in the *Oil Budget Calculator*,²⁵⁴ viewed as the U.S. government estimate of the volumetric flow rate of dead oil out of the broken Macondo riser stub. On June 8, the estimated daily volumetric flow rate of dead oil emitted from the broken Macondo riser stub was 59400 barrels day⁻¹, from which we subtracted the amount collected on that day through the *top hat #4* (15006 barrels day⁻¹), thereby obtaining a net volumetric flow rate of dead oil into the deep ocean of 44394 barrels day⁻¹ for June 8.²⁵⁴ This

estimated net volumetric flow rate of dead oil into the ocean is converted into a volumetric flow rate of total petroleum fluids based on the Macondo reservoir fluid model composition MC₁ (Chapter 4), assuming a single-stage flash for liquid-gas separation of the petroleum mixture and assuming non-preferential capture of both liquid and gaseous phases by the *top hat #4* device. A thermodynamic model (Chapter 4) is used to estimate the corresponding volumetric flow rates of liquid petroleum phase (0.12 m³ s⁻¹) and gas (0.047 m³ s⁻¹) under local conditions at the emission source boundary (15.5 MPa and 4.3 °C). Estimated properties of the emitted liquid and gas phases at the conditions prevailing at the emission source boundary are provided in Table 5-1.

Table 5-1. Estimated properties of the liquid and gas phases at the emission source boundary (15.5 MPa and 4.3 °C), predicted by the thermodynamic model (Chapter 4), used as input for the VDROD-J model.

Volumetric flow rate of liquid (m ³ s ⁻¹)	0.12
Volumetric flow rate of gas (m ³ s ⁻¹)	0.047
Density of liquid (kg m ⁻³)	707
Density of gas (kg m ⁻³)	181
Interfacial tension between liquid and seawater, no dispersant (N m ⁻¹)	0.024
Interfacial tension between gas and seawater, no dispersant (N m ⁻¹)	0.065
Interfacial tension between liquid and seawater, dispersant (N m ⁻¹)	0.0045
Interfacial tension between gas and seawater, dispersant (N m ⁻¹)	0.012
Viscosity of liquid (Pa s)	7.4·10 ⁻⁴
Viscosity of gas (Pa s)	2.0·10 ⁻⁵

On the 8th of June, 327.7 barrels of Corexit EC9500A dispersant²⁵⁴ were injected at the emission source boundary by a jet emplaced in the jet of emitted petroleum fluids.²⁵⁹ This would produce a concentration of dispersant in live oil of ~5,300 ppm (by mass), assuming that 100% of the dispersant was mixed with 100% of the liquid petroleum mixture at 15.5 MPa and 4.3 °C. For simplicity, I assumed that the dispersant was evenly mixed with the emitted liquid petroleum. Based on reported measurements conducted in the deep-water hydrocarbon plume, we found that dioctyl sodium sulfosuccinate (DOSS), the most water-soluble component of Corexit EC9500,^{292,293} exhibited an extent of fractionation that exceeded that observed for toluene and was less than that observed for benzene (section 5.4.4). Consistent with its observed fractionation in the deep sea, the aqueous solubility of DOSS falls between the solubilities of toluene and benzene, which indicates that DOSS experienced dissolution kinetics that were similar to these two compounds. Our model predicts that only 2.5% of the toluene and 8.8% of the benzene had dissolved during the first 100 m of ascent, which corresponds to the distance to stabilize droplet and bubble size distributions as predicted by the VDROD-J model. Based on these observations and simulation results, we conclude that >91.2% of the DOSS remained partitioned to the liquid petroleum phase during the initial 100 m of ascent from the emission source, and therefore the other surfactant components of Corexit EC9500A also were assumed to remain predominantly associated with the liquid petroleum phase during this interval of ascent. Based on these considerations, we interpret that a negligible amount of dispersant was lost to the water column from petroleum fluids during the first 100 m of ascent. This assumption allowed us to evaluate the influence of Corexit EC9500A on the interfacial tensions between petroleum phases and water during the first 100 m of ascent,

and thus we were able to assign values for the interfacial tension parameters employed in VDROP-J simulations, as explained below.

Experimental data on the influence of Corexit EC9500A on the interfacial tension between seawater and the live petroleum phase at emission depth are not available. The closest proxy is experimental data obtained for Macondo dead oil under pressure and temperature conditions similar to that at the emission source boundary (25 g kg⁻¹ seawater salinity, 15.3 MPa, and 4.4 °C) and a dispersant concentration in dead oil of 5,000 ppm.²⁵³ Under these conditions, the liquid/seawater interfacial tension was reduced by a factor of ~5.4, from 22.5 mN m⁻¹ for untreated dead oil to ~4.2 mN m⁻¹ for dead oil amended with 5,000 ppm of Corexit EC9500A.²⁵³ Lacking knowledge of the interaction between dispersant and pressurized gas, I estimated that the gas-seawater interfacial tension was decreased by the same factor as that predicted for the liquid-seawater interface. Consequently, we assumed that dispersant reduced the interfacial tension by a factor 5.4 for both the liquid/seawater interface and the gas/seawater interface. We assumed that the reduction of interfacial tension induced by the dispersant is independent of the droplet size, in agreement with previous experimental evidence.²⁹³ The concentration of DOSS, a key water-soluble component of the dispersant injected near the broken Macondo riser stub, is estimated to have remained far below the critical micelle concentration (CMC) in water (Chapter 4).²⁵⁹ Therefore we assumed that DOSS did not influence the thermodynamics of partitioning of petroleum compounds into seawater.

We conducted three separate sets of TAMOC-c simulations, using different assumptions about the size distributions of droplets and bubbles at the emission source boundary. All these simulations assumed that the petroleum fluid was separated into purely liquid droplets and purely gaseous bubbles at the emission source boundary. In the first set of TAMOC-c simulations, we used size distributions predicted by the VDROP-J model, as follows. The VDROP-J model predicts size distributions of liquid droplets and gas bubbles, neglecting any possible interaction between droplets and bubbles. The VDROP-J model predicts that size distributions of droplets and bubbles are converged after 100 m of ascent from the emission source boundary. We assumed that the well-stabilized size distributions predicted after 200 m by the VDROP-J model can be employed at the emission source boundary in TAMOC-c simulations. This means that the TAMOC-c model does not include the initial phase of coalescence and breakup that is simulated explicitly by VDROP-J. For computational efficiency, we re-sampled the distributions predicted by the VDROP-J model using 10 equally-spaced diameters chosen from $d_{0.01}$ (1% of the mass is comprised of fluid particles with a diameter smaller than $d_{0.01}$) to $d_{0.99}$ (Figure 5-6). These re-sampled distributions were then assigned as the size distributions of droplets and bubbles at the emission source boundary. In the second set of TAMOC-c simulations, we employed size distributions predicted by the correlation of Johansen et al.,²⁷⁷ which predicts Rosin-Rammler (RR) size distributions, as follows. The RR size distributions were obtained from the Johansen et al. correlation, using $A = 15$ and $B = 0.8$ for the values of the empirical coefficients.²⁷⁷ However, portions of the RR size distributions were predicted to exceed the maximum stable diameters²⁶⁰ of droplets and bubbles (4.7 and 4.8 mm, respectively, with dispersant addition) at local conditions (15.5 MPa and 4.3 °C) at the emission source boundary. These unphysical mass fractions of the RR size distributions were therefore re-attributed to the population of droplets and bubbles having diameters of 4.7 and 4.8 mm, respectively (Figure 5-7b,d). Finally, the third set of TAMOC-c simulations was conducted with

customized size distributions comprised of droplets all having 1.5 mm diameters and bubbles all having 3.75 mm diameters at the emission source boundary. The custom size distributions were selected because they produced the minimized sum of the root mean squared errors (RMSEs) of model predictions with respect to the observed fractionation of C₁–C₃ hydrocarbons in the deep-water hydrocarbon plume⁸ and the observed fractionation of C₁–C₅ hydrocarbons at the sea surface,⁷⁵ using the 14-component representation of the reservoir fluid and assuming that dispersant was present. The 14-component model mixture was used to identify the custom size distributions leading to the lowest RMSEs for these two datasets, but the results reported here are based on the 279-component model mixture, MC₁.

5.3.6 Modeling two-phase fluid particles in TAMOC-c

In ascending fluid particles, liquid-gas transfers of petroleum compounds were assumed instantaneous, controlled entirely by the thermodynamics of liquid-gas partitioning, which is dependent on chemical composition, pressure, and temperature. Although TAMOC-c assumes initially separated populations of liquid droplets and gas bubbles (section 5.3.5), we found that two-phase fluid particles spontaneously evolved during simulations. According to preliminary TAMOC-c model predictions for single bubbles (i.e., without the simulation of buoyant plume dynamics) with initial composition as defined in section 5.3.5, we concluded that a liquid phase would condense spontaneously during the ascent of gas bubbles that contained initially a pure gas phase. This occurs because aqueous dissolution removes preferentially the lightest compounds during ascent, consequently the resulting remaining mixture within this fluid particle will have larger mole fractions of heavier compounds, therefore making this mixture more prone to generating a liquid petroleum phase. Single bubbles having initial diameters of 4 mm are predicted to transition to 100% liquid at 1324 m depth, from which a gas phase is subsequently re-generated after ascent to 14 m depth (schematically depicted on Figure 5-5). Smaller bubbles having ≤ 1 mm diameters are predicted to transition to 100% liquid within ≤ 4 m from the emission source and to remain 100% liquid until the sea surface. Similarly, large single droplets that are 100% liquid at the emission source boundary (with initial composition as defined in section 5.3.5) are predicted to generate a gas phase by spontaneous ebullition at a depth of < 20 m. These examples illustrate the importance of simulating the changes in the liquid-gas partitioning of the petroleum fluids as controlled by varying composition, pressure, and temperature.

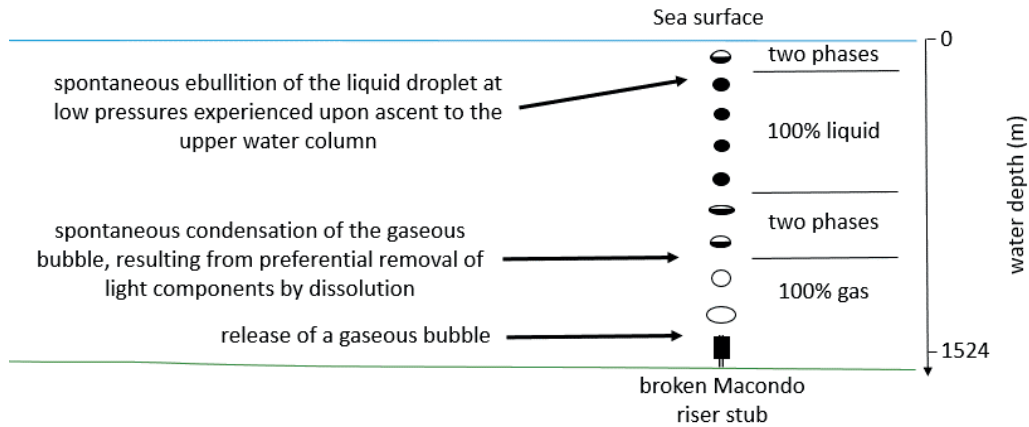


Figure 5-5. Schematic depiction of an initially 100% gaseous bubble exhibiting phase transition to a 100% liquid droplet (through a two-phase region), followed by regeneration of a gas phase as it nears the sea surface.

We define a *two-phase fluid particle* as a fluid particle that contains both a liquid phase and a gas phase. Here we assumed that when a two-phase fluid particle is present, liquid and gas petroleum phases remain attached together as a single fluid particle, and we assumed that thermodynamic equilibrium is maintained between these two phases. We considered a non-circulating interface for two-phase fluid particles, and we estimated the effective interfacial tension between a two-phase fluid particle and seawater as a weighted average of the liquid-phase and gas-phase interfacial tensions with seawater, using the equivalent spherical surface area as the weighting factor. The effective density of a two-phase fluid particle is given by:

$$\rho_p = \frac{m_{gas} + m_{liq}}{V_{gas} + V_{liq}}$$

Equation 5-1

where ρ_p is the effective density of the two-phase fluid particle, m_{liq} and m_{gas} are the masses of liquid and gas phases, respectively, and V_{liq} and V_{gas} are the corresponding volumes (as predicted by the thermodynamic model).

5.3.7 Simulation of aqueous dissolution kinetics for petroleum compounds in TAMOC version 0.1.17

A kinetics expression is used to describe the rates of mass transfer of individual petroleum compounds and pseudo-components from single petroleum fluid particles to seawater:³⁵

$$\frac{dm_i}{dt} = -A \cdot \beta_i \cdot (C_{w,i}^{eq} - C_{w,i})$$

Equation 5-2

where m_i is the total mass of component i in the fluid particle; A is the surface area of the fluid particle; β_i is the mass transfer coefficient (units: length time⁻¹) of component i at the particle-water interface; $C_{w,i}^{eq}$ is the hypothetical aqueous concentration of component i based on partitioning equilibrium with the fluid particle phase, estimated from the pressure-dependent, temperature-dependent, and salinity-dependent Henry's law constant^{156,211,215,230} and petroleum phase fugacities computed from the Peng-Robinson equation of state (PR EOS) with the 1978 modification^{206,216,223} (Chapter 4); and $C_{w,i}$ is the aqueous concentration of component i in the seawater. Values of C_w in the buoyant plume, descending plume, and deep-water hydrocarbon plume are computed from the volume of water present in the corresponding plume at a given location and the simulated dissolved mass at the corresponding location. Concentrations of petroleum compounds in the seawater are assumed to be zero outside of the buoyant plume, descending plume, and deep-water hydrocarbon plume. Properties of fluid particles—including shape, surface area, ascent speed—and mass transfer coefficients are estimated based on formulas by Clift et al.,²⁶⁰ with the exception of the mass transfer coefficients for compounds in liquid droplets²⁸⁷ and circulating bubbles.²⁸⁶ In the computations of the slip velocities of fluid particles and mass transfer coefficients,^{260,286,287} we used estimates of the liquid and gas dynamic viscosities (Chapter 4),²⁴⁷ and liquid-seawater and gas-seawater interfacial tensions,^{294,295} which are in turn described as a function of fluid particle composition and pressure and temperature conditions. The predicted liquid-seawater interfacial tension was forced to match a measured value of 25.69 mN m⁻¹ at 1 atm and 24.4 °C.²⁵³

The temperature-dependent diffusion coefficient of each solute dissolved in water, D_i , is required in the computation of the mass transfer coefficient for the particle-water interface. D_i can be predicted from the Hayduk-Laudie formula:²⁹⁶

$$D_i(T) = \frac{13.26 \cdot 10^{-9}}{(\eta(T) \cdot 10^3)^{1.14} \cdot (\bar{V}_{bp,i} \cdot 10^6)^{0.589}}$$

Equation 5-3

where D_i has units of m s⁻²; η is the temperature-dependent dynamic viscosity of seawater,¹⁷⁴ in Pa s; and $\bar{V}_{bp,i}$ is the molar volume of the solute at its normal boiling point, in m³ mol⁻¹. Equations 5-3 and 5-4 include some modified coefficients compared to the traditional way of writing them that may be unfamiliar to some readers; these coefficients arise purely from the arithmetic needed to convert the relations to base units of the International Unit System. When unknown,²⁹⁶ we estimated $\bar{V}_{bp,i}$ from the critical volume according to the Tyn and Calus formula:²⁰⁰

$$\bar{V}_{bp,i} = 0.285 \cdot (V_{c,i} \cdot 10^6)^{1.048} \cdot 10^{-6}$$

Equation 5-4

where both $\bar{V}_{bp,i}$ and the critical volume, $V_{c,i}$, are expressed in $\text{m}^3 \text{mol}^{-1}$. For the 279 components included in the model composition of the Macondo reservoir fluid, $V_{c,i}$ is obtained from literature data²⁰⁰ or estimated,^{240,241,244} as explained in Chapter 4. Equation 5-4 was viewed to be more accurate than the Le Bas method used by Hayduk and Laudie.²⁰⁰

Hydrate shells are expected to form around liquid droplets and gas bubbles in deep-water conditions (>500 m depth)⁴⁷ (Chapter 4), and this will affect their behaviors during ascent.⁴⁷ TAMOC uses a model developed by Inok Jun and Scott Socolofsky²⁸⁸ that assumes that droplets and bubbles initially exhibit circulating behavior and subsequently, after a hydrate initiation time, become non-circulating. In this interpretation, the presence of a hydrate skin is considered as equivalent to the presence of a surfactant layer, except that interfacial tensions are assumed unaffected by the hydrate skin. Once the fluid particle transitions to a non-circulating state, both the mass transfer coefficients and the ascent speed are modified from their values in the circulating fluid particle. Circulating droplets and bubbles are assumed to have a clean interface and manifest an internal fluid mixing that non-circulating droplets and bubbles don't exhibit.²⁶⁰ TAMOC enables the prediction of the mass transfers and ascent speeds for droplets and bubbles, using existing formulas for circulating or non-circulating droplets and bubbles depending on the absence or presence of hydrate.^{260,286,287} The parameters of the hydrate model were fitted previously²⁸⁸ to available experimental data.⁴⁷

The presence of surfactant has been shown to promote faster and more extensive hydrate formation on water drops in methane.²⁹⁷ These experimental results were obtained using dioctyl sodium sulfosuccinate (DOSS) at 100 ppmv in water.²⁹⁷ DOSS was present at 10% (by mass)²⁵⁹ in the Corexit EC9500A dispersant mixture injected at the broken Macondo riser stub (Table 5-2). However, the effect of dispersant on hydrate formation remains poorly characterized and is dependent on the gas phase composition (e.g. CO_2 vs CH_4).²⁹⁷ It is therefore unclear how to model this phenomenon for fluid particles of varied compositions in seawater. Because sufficient data to model this process are lacking, the TAMOC-c model neglects any potential effect of surfactant on the extent of hydrate growth. However TAMOC-c does account for the effect of surfactant on the particle-seawater interfacial tension, and this in turn influences the size distributions of droplets and bubbles at the emission source boundary, as discussed above in section 5.3.5.

Table 5-2. Composition of the Corexit EC9500A dispersant.²⁹²

Name	CAS number
Sorbitan, mono-(9Z)-9-octadecanoate	1338-43-8
Sorbitan, mono-(9Z)-9-octadecanoate, poly(oxy-1,2-ethanediyl) derivs	9005-65-6
Sorbitan, tri-(9Z)-9-octadecanoate, poly(oxy-1,2-ethanediyl) derivs	9005-70-3
Dioctyl sodium sulfosuccinate (DOSS) (contains 2-propanediol)	577-11-7
Propanol, 1-(2-butoxy-1-methylethoxy)	29911-28-2
Distillates (petroleum), hydrotreated light	64742-47-8

5.3.8 Model of the deep-water hydrocarbon plume in TAMOC-c

The bent plume model describes the dynamics of the buoyant plume and the descending plume (Figure 5-2). In TAMOC-c, the formation of the deep-water hydrocarbon plume is defined as the location where the descending plume reaches neutral buoyancy. For the deep-water hydrocarbon plume, we assumed a horizontal structure of constant depth, constant lateral width, and constant vertical thickness that did not mix with (entrain) adjacent water masses. The deep-water hydrocarbon plume is carried by the ambient water current. These assumptions are in reasonable agreement with available information indicating little change in the depth of the deep-water hydrocarbon plume and constant aqueous concentrations of total benzene, toluene, ethylbenzene, and xylenes (BTEX) up to 27 km from the broken Macondo riser stub.⁸ However, we note that isopycnal spreading, neglected here, may explain why observations³¹ indicate that the vertical thickness of the deep-water hydrocarbon plume was likely less than predicted by our simulations. Buoyant fluid particles that had been carried into the deep-water hydrocarbon plume (from the descending plume) were allowed to depart from the plume by ascent, according to their slip velocities. Aqueous dissolution of fluid particles within the deep-water hydrocarbon plume participates in determining the predicted composition of the water at the downstream boundary of the deep-water hydrocarbon plume. The downstream boundary of the deep-water hydrocarbon plume is fixed at 7500 m along an axis starting at the broken Macondo riser stub and going through the center line of the buoyant plume, the descending plume, and the deep-water hydrocarbon plume.

5.3.9 Modelling the sea surface boundary and processes happening at the sea surface outside of the TAMOC-c model boundary

The TAMOC-c simulations are terminated when fluid particles reach the sea surface (Figure 5-3), i.e. that only ascent within the water column is included in the TAMOC-c simulations. Outside of the TAMOC-c model domain, these fluid particles that reached the sea surface are assumed to form an oil slick at the sea surface. We assumed that all $\leq C_9$ petroleum components volatilize rapidly and completely into the atmosphere. This enabled us to compare the predictions of the TAMOC-c model with observations made by Ryerson et al.⁷⁵ Ryerson et al.⁷⁵ used measurements of the concentrations of volatile hydrocarbons in the atmosphere above the fresh sea surface oil slick to infer the fraction of these compounds that were predicted to have been fractionated to the water column. To perform this estimate, Ryerson et al.⁷⁵ compared the relative concentrations of these compounds within the atmosphere above the oil slicks with their relative concentrations in the Macondo reservoir fluid that were determined previously by Reddy et al.⁸ Ryerson et al.⁷⁵ confirmed the rapid evaporation of compounds up to $n-C_9$, as the atmospheric concentrations of $n-C_6$ – $n-C_9$ alkanes were linearly related despite of these compounds having different volatilities.

5.4 Results and implications

5.4.1 Size distributions of droplets and bubbles emitted at the emission source boundary

The size distributions of droplets and bubbles emitted from the broken Macondo riser stub, viewed here as the emission source boundary, represent a crucial and little-known boundary condition that would be needed in any model of aqueous dissolution of petroleum compounds during the *Deepwater Horizon* disaster. We viewed that the VDROD-J model²⁷³ would likely predict the most reliable size distributions for liquid droplets and gas bubbles at the emission source boundary, based on the fact that VDROD-J predicts physical processes (coalescence and breakup of droplets and bubbles) and has been validated previously against 25 datasets of laboratory and field observations.²⁷³ The VDROD-J size distributions (Figure 5-6) were parameterized with the estimated liquid and gas properties at the emission source boundary (Table 5-1), which had been obtained by the TAMOC-c implementation of the thermodynamic model of Chapter 4. These properties include viscosities, volumetric flow rates, densities, and interfacial tensions with seawater for both the liquid and gas phases. Dispersant addition lowers interfacial tensions with seawater, which results in decreased sizes of fluid particles at the emission source boundary.²⁷⁶ The predicted d_{50} values of the size distributions are 1.3 mm for droplets and 2.6 mm for bubbles, when dispersants are added. These values represent a decrease in d_{50} by a factor of 3.2 and 3.4, respectively, when compared to VDROD-J simulation results without dispersant addition (Figure 5-6). Our estimates of the d_{50} for liquid droplets and gas bubbles with dispersant addition are, respectively, 50% and 80% larger than a previous estimate obtained also using the VDROD-J model but using different estimates of liquid and gas properties.²⁷⁶ We think that the updated estimates are more representative of the prevailing situation on June 8, 2010.

For purposes of comparison with the VDROD-J results, we additionally report RR size distributions (Figure 5-7) obtained from a recently proposed correlation,²⁷⁷ using the same liquid and gas property values as for the VDROD-J model. Globally, the RR size distributions give larger droplets and bubbles than the VDROD-J size distributions, and this discrepancy is larger for liquid droplets. Finally, we also considered custom-fitted droplet and bubble size distributions at the emission source boundary comprised of droplets all having 1.5 mm diameters and bubbles all having 3.75 mm diameters, obtained by a best fit of the model predictions with respect to observed fractionation data (see Methods section 5.3.5). We find that the custom size distribution for droplets correspond approximately to the center of the corresponding VDROD-J size distribution with dispersant. We used these three different size distributions at the emission source boundary (VDROD-J, RR, and custom fit) to conduct simulations of aqueous dissolution of petroleum fluids in the water column, employing the TAMOC-c model. Notably, these size distributions are used at the emission source boundary, but the sizes of droplets and bubbles evolve in the TAMOC-c simulations during ascent of fluid particles as a function of local composition, pressure, and temperature. The results of our simulations of aqueous dissolution are presented in section 5.4.4, and they validate our assumption that the VDROD-J size distributions are probably the most representative of the situation during the release event.

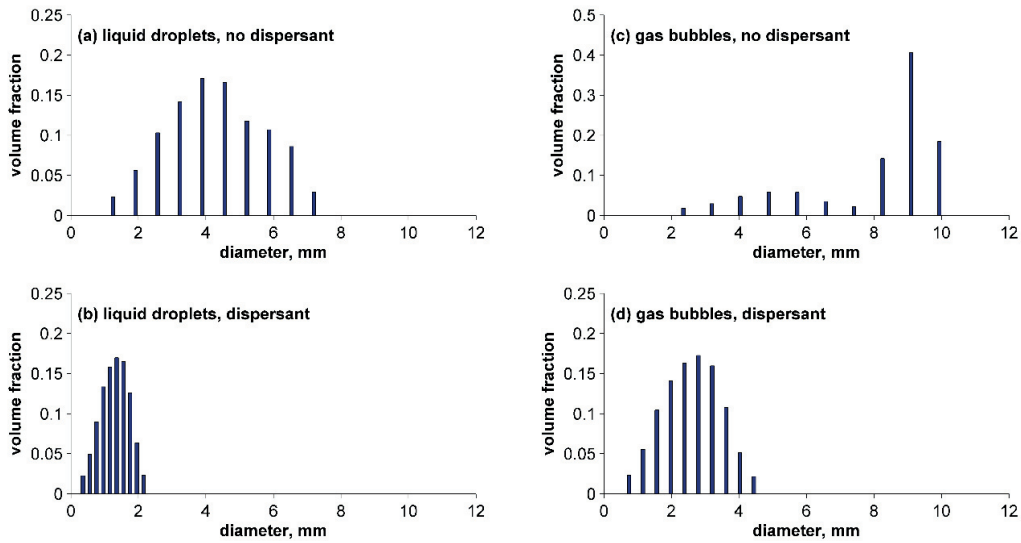


Figure 5-6. Size distributions of liquid droplets and gas bubbles predicted by the VDROP-J model,²⁷³ at the emission source boundary, for June 8, 2010. (a) Liquid droplets without dispersant; (b) liquid droplets with dispersant; (c) gas bubbles without dispersant; (d) gas bubbles with dispersant.

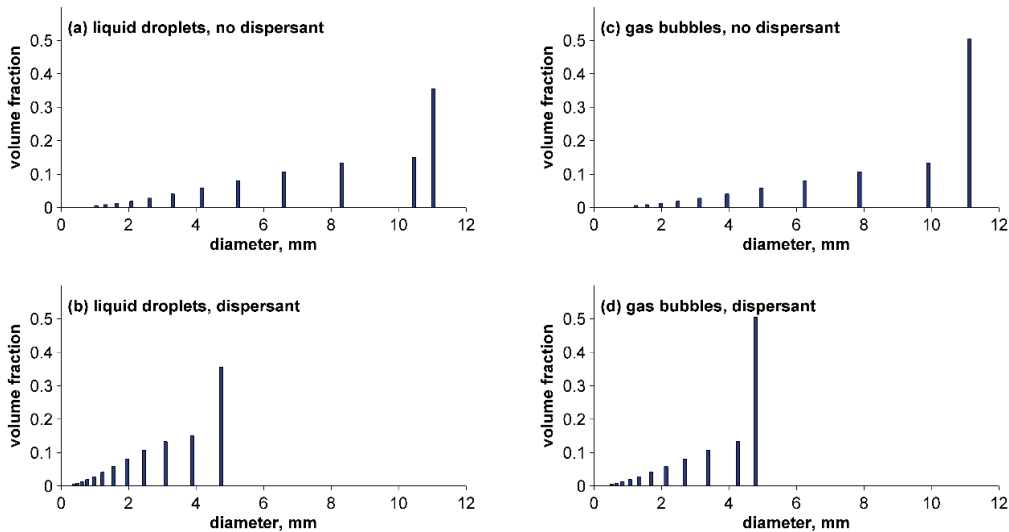


Figure 5-7. RR size distributions of liquid droplets and gas bubbles predicted by the Johansen et al. correlation,²⁷⁷ at the emission source boundary, for June 8, 2010. (a) Liquid droplets without dispersant; (b) liquid droplets with dispersant; (c) gas bubbles without dispersant; (d) gas bubbles with dispersant.

5.4.2 Time and location of arrival at the sea surface for fluid particles emitted from the broken Macondo riser stub

The TAMOC-c model predicts that on June 8, 2010, with deep-water dispersant injection, 96% of the mass flow rate of fluid particles contributing to the surface slicks would arrive at the sea surface at a location having 0.3–1.7 km horizontal distance from the broken Macondo riser stub. These predictions are consistent with observations. A small area of arrival of fluid

particles at the sea surface, of ~ 1.6 km diameter laterally offset by 0.5–1.5 km from the broken Macondo riser stub, was deduced by Ryerson et al., based on aerial hydrocarbon concentration measurements on June 8 and 10, 2010, concomitant with dispersant injection.⁷⁵ The predictions of the TAMOC-c model are in reasonable agreement with these observations, regardless of the choice of model size distribution for droplets and bubbles at the emission source boundary (Figure 5-8b).

The TAMOC-c model predicts that on June 8, 2010, with deep-water dispersant injection, 50% of the mass flow rate of fluid particles contributing to the surface slicks would arrive at the sea surface within 6 h from their emission at the broken Macondo riser stub. These predictions are not in agreement with field observations indicative of the time of arrival of fluid particles at the sea surface without dispersant addition. Ryerson et al. reported an ascent time of ~ 3 h, based on the time to see a change in the fresh surface slick during dispersant application tests.⁷⁵ It was observed that ~ 3 h were necessary to see a change in the fresh surface slick after the start of dispersion addition at the emission source. Approximately the same time was needed to see a change in the fresh surface slick after the dispersant addition was stopped at the end of the test. The time required for the arrival at the sea surface of 50% of the mass flow rate of fluid particles, as predicted by TAMOC-c without dispersant addition, are in good agreement with this estimate, for both the VDROD-J and RR size distributions (Figure 5-8a). The time required for the arrival at the sea surface of 50% of the mass flow rate of fluid particles with dispersant addition, as predicted by TAMOC-c simulations, are the double of the 3 h observation by Ryerson et al.⁷⁵ for the VDROD-J size distributions, with $<1\%$ of the mass flux of petroleum fluids predicted to have reached the sea surface within 3 h. Predictions of the TAMOC-c model using VDROD-J size distributions at the emission source boundary indicate a clear change in times of arrival of fluid particles at the sea surface at the onset of dispersant injection (Figure 5-8a), which rationalizes the visual observations of a modification in the fresh surface slick following the start of dispersion injection (Appendix Figure 5-12).^{75,298} To the contrary, the predicted change in the times of arrival of fluid particles at the sea surface with RR distributions, ~ 1 hour, would lead to a less large predicted modification in the fresh surface slick following the start of dispersant injection (Figure 5-12). This analysis supports our conclusion that the VDROD-J distributions are more representative of the situation during the *Deepwater Horizon* disaster.

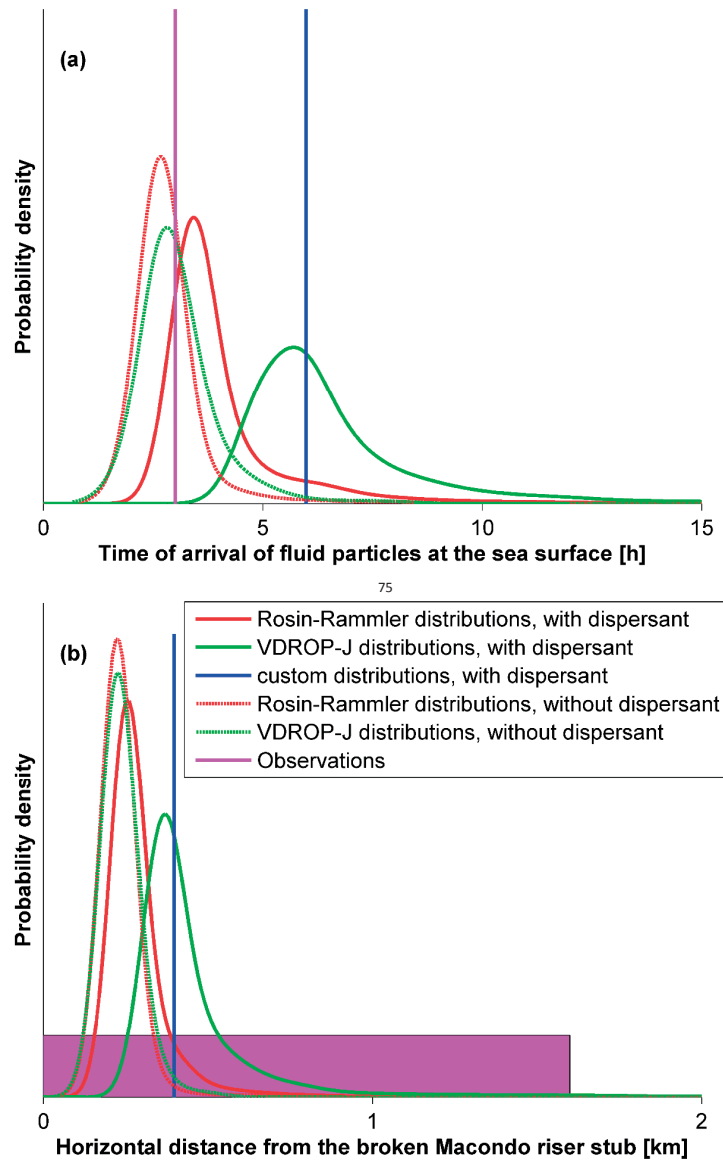


Figure 5-8. (a) Time of arrival of fluid particles at the sea surface, according to field observations and according to predictions of the TAMOC-c model. The pink line corresponds to the observation (3 h) reported by Ryerson et al.⁷⁵ Other lines correspond to predictions of the TAMOC-c model for the VDROP-J (green), RR (red), and custom (blue) droplet and bubble size distributions, with (solid lines) or without (dashed lines) dispersant injection. The time of arrival of fluid particles for the custom distribution is reported as an individual line, because a single droplet diameter is considered at the emission source boundary, and bubbles are predicted to bring only negligible mass to the sea surface. The other lines were determined by applying the Matlab implementation^{299,300} of kernel density estimation to TAMOC-c simulation results. (b) Horizontal distance from the broken Macondo riser stub at which fluid particles arrived at the sea surface, according to field observations and predictions of the TAMOC-c model. Ryerson et al.⁷⁵ reported a 1.6 km-diameter area of arrival of fluid particles at the sea surface, laterally offset from the broken Macondo riser stub by 0.5–1.5 km. This 1.6 km distance is displayed as a pink rectangle, centered at 0.8 km from the broken Macondo riser stub on this figure. Other lines correspond to model predictions for the different droplet and bubble size distributions considered, with the same color code as for panel a.

5.4.3 Apportionment of total mass flow rates of petroleum fluids to the deep water column, the upper water column, and the sea surface

Based on TAMOC-c model simulations with the VDROD-J size distributions for droplets and bubbles at the emission source boundary, we estimate that 27% of the emitted mass flow rate of total petroleum fluids became aqueously dissolved in the Gulf of Mexico and did not arrive at the sea surface, on June 8, 2010 (Table 5-3 and Figure 5-9). Simulations show that aqueously dissolved petroleum compounds were channeled predominantly (23%) into the deep-water hydrocarbon plume (900–1300 m depth), with a smaller percentage (4%) becoming aqueously dissolved in the upper water column (0–900 m depth). The estimated extent of aqueous dissolution (23–27%) is found to be insensitive to the choice of the three models (VDROD-J, RR, or custom-fit) used to describe the droplet and bubble size distributions at the emission source boundary (Table 5-3). This result is consistent with the previous estimates of Ryerson et al., who deduced that ~25% of the emitted mass flow rate became aqueously dissolved.⁷⁵ Ryerson et al.⁷⁵ conducted measurements in the atmosphere above the sea-surface oil slick and reported concentrations of several soluble and volatile compounds $<n\text{-C}_8$. Their measurements indicated that these compounds $<n\text{-C}_8$ were rapidly fractionated out of the sea surface slicks. Ryerson et al. then calculated the extent of depletion of these compounds in the atmosphere relative to their concentrations in the reservoir fluid,⁸ allowing these authors to estimate the fraction of these compounds that were lost due to aqueous dissolution (mostly) during ascent.⁷⁵ However, unlike the field observations that were published previously, the TAMOC-c model provides us with a detailed understanding of the physical-chemical processes that led to this unprecedented extent of aqueous dissolution during the *Deepwater Horizon* disaster. Consequently, the TAMOC-c model is able to simulate quantitative apportionments based on the trajectories of petroleum components in the water column (Table 5-3).

The apportionments reported in the paragraph above are expressed as percentages of the mass flow rate of total petroleum fluids (i.e. as a percentage of the sum of live oil and live gas mass flow rates). The *Oil Budget Calculator* has previously estimated the fraction of dead oil that became aqueously dissolved during ascent as 5–10%,²⁵⁴ i.e. that only the compounds that would partition to the liquid petroleum phase at sea-surface conditions of pressure and temperature are included in this estimate. TAMOC-c prediction of the percentage of the mass flow rate of the dead oil that aqueously dissolved during ascent with dispersion addition (5.4%) agrees with their estimate.

Table 5-3. Predicted apportionment of emitted petroleum fluids on June 8, 2010 according to the TAMOC-c model, assuming VDROD-J size distributions at the emission source boundary. Shown in parentheses are TAMOC-c model results computed with RR size distributions and custom size distributions, respectively, for droplets and bubbles at the emission source boundary.

Compartment	Estimated percentage of the total mass flow rate of petroleum fluids
fluid particles predicted to reach the sea surface	73% (77%, 74%)
deep-water hydrocarbon plume, 900–1300 m depth (aqueously dissolved)	23% (19%, 22%)
deep-water hydrocarbon plume, 900–1300 m depth (as fluid particles)	<1%*
water column 0–900 m (aqueously dissolved)	4% (4%, 4%)

*fluid particles predicted to remain within the deep-water hydrocarbon plume at the downstream boundary of the deep-water hydrocarbon plume.

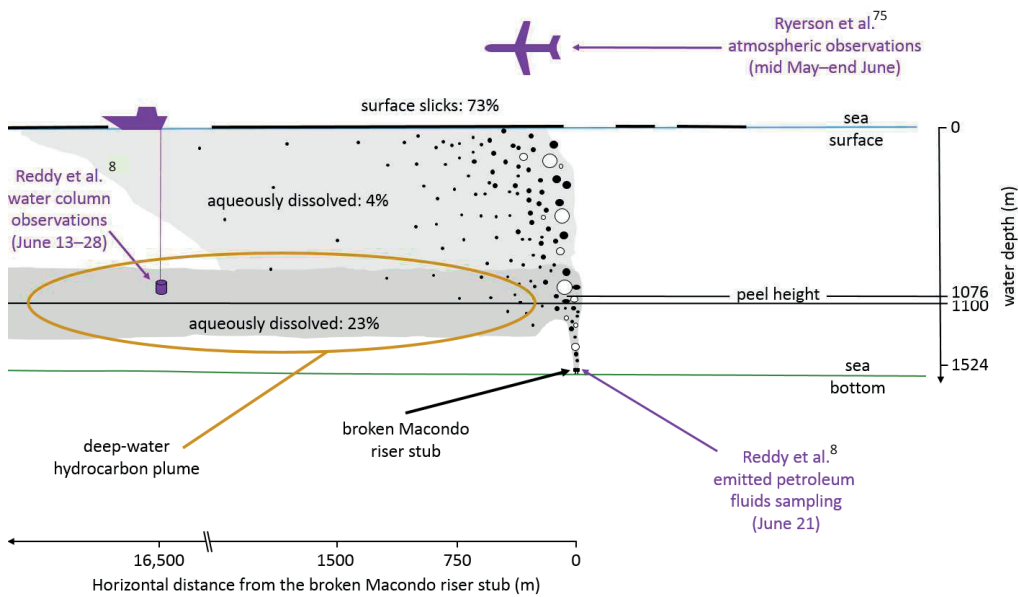


Figure 5-9. Predicted apportionment of emitted petroleum fluids on June 8, 2010 according to the TAMOC-c model, assuming VDROD-J size distributions at the emission source boundary. The figure displays the percentages of the total mass flow rate of petroleum fluids predicted to be aqueously dissolved in the deep-water hydrocarbon plume (23%), to be aqueously dissolved at shallower depths (4%), or to have reached the sea surface (73%). The peel height and the depth of the deep-water hydrocarbon plume, as predicted by our TAMOC-c simulations, are also displayed on the figure. Refer to the legend of Figure 5-2 for a description of the remainder of the figure.

5.4.4 Apportionments of the mass flow rates of individual petroleum compounds to the deep water column, the upper water column, and the sea surface

Predicted apportionments of individual compounds would greatly aid studies or assessments that investigate the quantitative exposures of marine organisms to toxic compounds at different zones in the water column. According to TAMOC-c simulations, C₁–C₄ hydrocarbons constitute 82% of the mass of petroleum compounds predicted to have become aqueously dissolved in the water column. This agrees closely with the estimates of Ryerson et al., who deduced that 89% of the aqueously dissolved mass was constituted of C₁–C₄ hydrocarbons and that the remaining 11% were saturated hydrocarbons and one to two-ring aromatic hydrocarbons having a solubility lower than that of 2-methylheptane.⁷⁵ TAMOC-c simulations predict mass apportionments to the water column that are much larger than that observed or predicted during sea-surface spills, in particular for single-ring aromatic hydrocarbons, which are highly toxic to aquatic organisms (Table 5-4). For example, benzene is predicted to have been >99% apportioned to the water column during the *Deepwater Horizon* disaster (Table 5-4). By comparison, we predicted that for a thin slick of Grane crude oil spilled on the surface of the North Sea, 87% of the benzene was evaporated and only 13% became aqueously dissolved (Chapter 3). This example highlights how the depth of the release profoundly modified the exposures of water column organisms and the risks for emergency response workers, because most of this aqueously dissolved mass would have been rapidly transferred to the atmosphere in case of a release at or near the sea surface.^{11,40}

However, the apportionment of petroleum compounds is not uniform within the water column. According to TAMOC-c simulations, different compositions of aqueously dissolved petroleum compounds are expected at different depths. For example, C₁–C₃ hydrocarbons are predicted to be >99% dissolved (Table 5-4), in agreement with the >98.9% reported by Ryerson et al.⁷⁵ (Figure 5-10 and Appendix Table 5-19). The TAMOC-c simulations enable us to predict that 100%, 99%, and 86% of methane, ethane, and propane, respectively, became trapped in the deep-water hydrocarbon plume (900–1300 m depth), and the remaining mass of these three compounds (0%, 1%, and 14%, respectively) became trapped in the upper water column (Table 5-4). Similarly, we find that the most aqueously-soluble aromatic compound, benzene, became 93% trapped in the deep-water hydrocarbon plume (900–1300 m depth). A less aqueously-soluble aromatic compound, ethylbenzene is predicted to have become 42% trapped in the upper water column at 0–900 m depth (Table 5-4). We find that the aqueously dissolved fractions of C₂-naphthalenes and petroleum compounds with lower solubilities (e.g. fluorene, phenanthrene) were trapped approximately ¼ in the deep-water hydrocarbon plume, and ¾ in the upper water column. In summary, we find that in order to investigate the exposure of marine organisms, one would need to consider the different mix of dissolved toxic compounds to be expected at different depths in the water column, now made available by our TAMOC-c model results.

The compound-specific apportionments described above are supported by existing field data. We tested TAMOC-c for its ability to correctly predict the relative concentrations of dissolved

petroleum components in the water column, since this provides a direct test of the fractionation processes that we aimed to evaluate. We did not attempt to evaluate TAMOC-c for its ability to predict absolute concentrations of hydrocarbons in the water column, which is highly dependent on spurious mixing of water masses and on sampling location. TAMOC-c model predictions are in agreement with observations of the deep-water hydrocarbon plume composition reported by Reddy et al.⁸ (Figure 5-10 and Appendix Table 5-18). Reddy et al. defined the fractionation indices relative to methane and benzene as:⁸

$$F_{i,methane} = \frac{\left(\frac{C_{i, deep-water hydrocarbon plume}}{C_{methane, deep-water hydrocarbon plume}} \right)}{\left(\frac{C_{i, reservoir fluid}}{C_{methane, reservoir fluid}} \right)}$$

Equation 5-5

$$F_{i,benzene} = \frac{\left(\frac{C_{i, deep-water hydrocarbon plume}}{C_{benzene, deep-water hydrocarbon plume}} \right)}{\left(\frac{C_{i, reservoir fluid}}{C_{benzene, reservoir fluid}} \right)}$$

Equation 5-6

where $F_{i,methane}$ is the fractionation index of component i relative to methane (used by Reddy et al.⁸ for ethane and propane), $F_{i,benzene}$ is the fractionation index of component i relative to benzene (used by Reddy et al.⁸ for compounds $>C_6$), $C_{i,deep-water hydrocarbon plume}$ is the concentration of compound i measured in the deep-water hydrocarbon plume, and $C_{i,reservoir fluid}$ is the concentration of compound i measured in the (Macondo) reservoir fluid. The observed fractionation index values reported by Reddy et al.⁸ indicate the differences in relative extent of dissolution experienced by different compounds in the deep sea, as measured in the deep-water hydrocarbon plume at 1065–1221 m depth during that June 2010 field campaign. The values of the fractionation indices predicted by the TAMOC-c model are based on mass fractions predicted to be aqueously dissolved in the deep-water hydrocarbon plume. In agreement with the $F_{toluene,benzene}$ value of 0.505 observed by Reddy et al.,⁸ TAMOC-c predicts an $F_{toluene,benzene}$ value of 0.657 (Figure 5-10 and Appendix Table 5-18). We find similar agreements between TAMOC-c predictions and the Reddy et al. observations for compounds having predicted $F_{i,benzene}$ values as low as ~ 0.01 (Appendix Table 5-18). Observed $F_{i,benzene}$ values for the compounds having predicted $F_{i,benzene}$ values < 0.01 are up to three orders of magnitude larger than predicted by our TAMOC-c simulations. This can be rationalized if we assume that small droplets having slow rise velocities were present within the samples taken by Reddy et al.⁸ Reddy et al.⁸ did not report the presence of such droplets in their samples, however such small droplets may not be visible to the naked eye. The concentration of small droplets in the samples reported by Reddy et al.⁸ that could explain this discrepancy would imply that 1.2% of the total mass flow rate of sparingly-soluble petroleum compounds became trapped in the deep-water hydrocarbon plume as small droplets having slow rise velocities (Appendix section 5.6.10). As 24% of the mass flow rate of

petroleum fluids were predicted to have become aqueously dissolved in the deep-water hydrocarbon plume according to our TAMOC-c simulations, this would imply that the petroleum compounds within the deep-water hydrocarbon plume were at ~4% present within fluid particles, and ~96% as aqueously dissolved compounds.

As discussed in the two paragraphs above, we validated our TAMOC-c predictions by comparing them with two datasets^{8,75} representative of the two main compartments to which petroleum compounds were channeled during the *Deepwater Horizon* disaster (the deep-water hydrocarbon plume and sea surface slicks). We are aware that other similar datasets exist that might have been used alternatively.^{31,301–303}

It has remained unclear whether the concentrations of DOSS reported in the deep-water hydrocarbon plume were due to aqueous dissolution of this compound or to the presence of small liquid petroleum droplets in this plume.²⁵⁹ DOSS is a component of the surfactant injected at the broken Macondo riser stub (Table 5-2).²⁹² We are able to provide a likely answer to the question of whether DOSS was present in aqueously dissolved form or within small droplets, even if we did not explicitly modeled the kinetics of aqueous dissolution of DOSS in our TAMOC-c simulations. The solubility of DOSS in pure water at 4.3 °C and 101325 Pa, 0.016 mol L⁻¹,³⁰⁴ lies in between that of benzene (0.022) and that of toluene (0.0058). Therefore we infer that DOSS became aqueously dissolved in the water column to an extent similar to benzene (100%) or toluene (96%). This implies that only <4% of the injected mass of DOSS reached the sea surface (Table 5-4 and Appendix Table 5-19), >61% of DOSS remained trapped in the deep-water hydrocarbon plume, and <35% became dissolved in the upper water column (Table 5-4). This interpretation is further corroborated by determining the fractionation index of DOSS with respect to methane, based on the relation between the DOSS concentration in the deep-water hydrocarbon plume and that of methane as reported by Kujawinski et al.²⁵⁹ Kujawinski et al.²⁵⁹ reported only the relation between the concentration of DOSS and that of methane, this is why we used the fractionation index with respect to methane in this analysis. The $F_{DOSS,methane}$ determined from the field observations reported by Kujawinski et al.²⁵⁹ is 0.70, which falls in between the $F_{toluene,methane}$ value of 0.61 and the $F_{benzene,methane}$ value of 0.93 predicted by our TAMOC-c simulations (Appendix Table 5-18). Taken together, these results suggest that the concentrations of DOSS detected in the deep-water hydrocarbon plume²⁵⁹ were mostly present in aqueous solution and not associated with small droplets.

Finally, as explained in Chapter 4, there is some uncertainty about the reservoir fluid composition. Here we report TAMOC-c predictions for the reservoir fluid model composition MC₁, derived from the MW-1 sample (Chapter 4). However, TAMOC-c simulations with the 14-component model compositions of the pre-spill samples (MC_{2,14c} or MC_{3,14c}, section 5.6.1) in place of MC_{1,14c} (section 5.6.1) produced similar results for the extent of aqueous dissolution for C₁–C₅ compounds. The total mass flow rate of C₁–C₅ compounds predicted to become aqueously dissolved according to TAMOC-c simulations is larger for MC_{2,14c} and MC_{3,14c} reservoir fluid model compositions than for MC_{1,14c} (section 5.6.5) as expected from the larger content of compounds ≤C₅ in MC_{2,14c} and MC_{3,14c} (Chapter 4).

Table 5-4. Predicted mass apportionments of methane, ethane, propane, CO₂, *n*-C₆, cyclohexane, single-ring aromatic compounds, and multi-ring aromatic compounds in the water column, based on the model composition MC₁ of the Macondo reservoir fluid that was emitted from the broken Macondo riser stub at 1524 m depth. Predictions are reported for June 8, 2010 using the TAMOC-c model, based on the VDROp-J, RR, and custom initial size distributions of droplets and bubbles.

Compound	mass percent aqueously dissolved in the deep-water hydrocarbon plume, 900–1300 m depth			mass percent aqueously dissolved in the upper water column, 0–900 m depth			mass percent predicted to reach the sea surface as fluid particles		
	VDROp-J	RR	Custom	VDROp-J	RR	Custom	VDROp-J	RR	Custom
methane	100%	95%	99%	0%	5%	1%	0%	0%	0%
ethane	99%	80%	95%	1%	20%	5%	0%	0%	0%
propane	86%	42%	75%	14%	43%	25%	0%	15%	0%
CO ₂	100%	100%	100%	0%	0%	0%	0%	0%	0%
<i>n</i> -C ₆	3%	1%	1%	10%	3%	4%	87%	96%	95%
cyclohexane	13%	5%	6%	30%	10%	23%	57%	85%	72%
benzene	93%	49%	90%	7%	40%	10%	0%	10%	0%
toluene	61%	24%	46%	35%	33%	51%	4%	44%	3%
<i>p/m</i> -xylenes	28%	10%	15%	42%	18%	44%	30%	73%	41%
<i>o</i> -xylene	28%	10%	15%	43%	18%	45%	29%	72%	39%
ethylbenzene	28%	10%	15%	42%	18%	45%	30%	72%	40%
naphthalene	18%	6%	9%	36%	13%	32%	45%	80%	59%
C ₁ -naphthalenes	6%	2%	2%	16%	5%	9%	78%	93%	89%
C ₂ -naphthalenes	2%	1%	1%	7%	2%	3%	92%	97%	97%
C ₃ -naphthalenes	0%	0%	0%	2%	1%	1%	98%	99%	99%
C ₄ -naphthalenes	0%	0%	0%	0%	0%	0%	100%	100%	100%
fluorene	4%	1%	1%	12%	4%	6%	84%	95%	92%
phenanthrene	1%	0%	0%	3%	1%	1%	97%	99%	99%
C ₁ -phenanthrenes	0%	0%	0%	0%	0%	0%	100%	100%	100%
C ₂ -phenanthrenes	0%	0%	0%	0%	0%	0%	100%	100%	100%
C ₃ -phenanthrenes	0%	0%	0%	0%	0%	0%	100%	100%	100%
C ₄ -phenanthrenes	0%	0%	0%	0%	0%	0%	100%	100%	100%
fluoranthene	0%	0%	0%	1%	0%	0%	99%	100%	100%
pyrene	0%	0%	0%	0%	0%	0%	100%	100%	100%

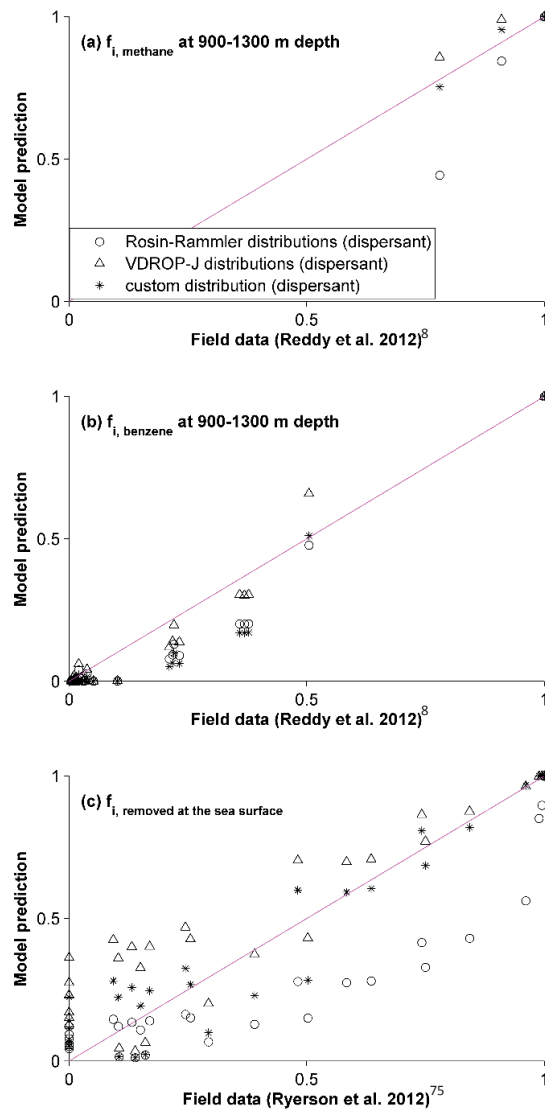


Figure 5-10. Comparison of the TAMOC-c predictions with field observations for fractionation indices of several hydrocarbon compounds, evaluated in the deep-water hydrocarbon plume and at the sea surface. (a) Fractionation of C_1 – C_3 hydrocarbons in the deep-water hydrocarbon plume (900–1300 m depth); (b) fractionation of $\geq C_6$ hydrocarbons in the deep-water hydrocarbon plume (900–1300 m depth); and (c) extent of fractionation for volatile compounds at the sea surface. Displayed simulation results are based on the VDROP-J, RR, and custom initial size distributions of droplets and bubbles, with dispersant. (Compound names and corresponding tabulated values are available in Appendix section 5.6.8, and a similar figure for predictions of the TAMOC-c model without dispersant is provided in Appendix section 5.6.9.)

5.4.5 Stripping of aqueously dissolved nitrogen and oxygen from ambient seawater by ascending petroleum fluids

Dissolved gases in the ambient ocean water can enter ascending droplets and bubbles emitted from the broken Macondo riser stub, possibly leading to changes in their properties and trajectories. Owing to their high concentrations in ambient ocean water, the gases predominately stripped from the ocean water are oxygen and nitrogen.³⁵ Decreased levels of aqueously dissolved oxygen content were observed in the deep-water hydrocarbon plume at 1000–1300 m depth.^{34,301} It remains unclear what was the contribution of oxygen stripping to the depletion of oxygen from the water column. Our model predictions enable an independent investigation of this question.

According to TAMOC-c simulations, the predicted decrease in dissolved oxygen (O_2) content in the deep-water hydrocarbon plume resulting from gas stripping by fluid particles amount to $\sim 6.5 \text{ mg m}^{-3}$, or $<1\%$ of the oxygen anomaly reported in this plume ($\sim 900 \text{ mg m}^{-3}$).³⁴ This confirms previous conclusions that hydrocarbon biodegradation is probably the primary contribution to the deep-water oxygen depletion.³⁴ To estimate the extent of gas stripping in the water column, we used a measured oxygen profile (section 5.3.2), and an estimated nitrogen (N_2) profile, because nitrogen profiles in the ocean are generally within a few percent of concentration at equilibrium with the atmosphere,³⁰⁵ allowing easy estimation of the nitrogen profile.^{35,305,306} To include oxygen in our thermodynamic model, we assumed that the binary interaction parameters between any petroleum compound and oxygen are the same as for this petroleum compound and nitrogen (Appendix section 5.6.7). Based on simulations of the ascent of individual gas bubbles and live oil droplets (i.e., without the simulation of buoyant plume dynamics), we find that oxygen constitutes $\sim 0.01\%$ of the mass of liquid droplets and $\sim 0.2\%$ of the mass of gas bubbles, at the peel height. Simulated gas bubbles already had lost a significant fraction of their mass to aqueous dissolution when they departed from the buoyant plume, the descending plume, or the deep-water hydrocarbon plume. At this stage, the mass flow rate of gaseous bubbles represented only 7% of the initial gas mass flow rate. We estimate that at peel height the oxygen stripped by droplets and bubbles represented $\sim 0.01\%$ of the mass flow rate of total petroleum fluids emitted. Assuming a total mass flow rate of petroleum fluids released of $\sim 110 \text{ kg s}^{-1}$ (neglecting any collection at the broken Macondo riser stub),⁴⁵ an estimated 0.011 kg s^{-1} of oxygen was stripped out of the volumetric flow rate of $\sim 1,700 \text{ m}^3 \text{ s}^{-1}$ of entrained ocean water³³ flowing into deep-water hydrocarbon plume. The decrease in oxygen-content in the deep-water hydrocarbon plume resulting from gas stripping would therefore amount to $\sim 6.5 \text{ mg m}^{-3}$.

We find that oxygen and nitrogen stripping has negligible impacts on predicted ascent times of individual droplets and bubbles, which differ by <4 min with and without the explicit inclusion of oxygen and nitrogen in simulations (excluding the simulation of buoyant plume dynamics). Therefore we decided to remove oxygen and nitrogen from all other TAMOC-c simulations reported in the present chapter, which allowed those simulations to be conducted with decreased computational cost.

5.4.6 Predicted influence of subsurface dispersant injection on the trajectories and aqueous dissolution of petroleum fluids in the sea

Dispersants are frequently applied on liquid petroleum slicks at the sea surface, in order to decrease the interfacial tension between petroleum and seawater. The aim is to allow waves to disperse the liquid petroleum into the water column as droplets having very low rise velocities, thanks to their diameters $<70\ \mu\text{m}$.³⁰⁷ Large scale deep-water dispersant injection was attempted for the first time during the *Deepwater Horizon* disaster.^{259,308} According to the updated predictions of the VDRO-P-J model reported here, the doses of dispersant applied during this event did not generate significant mass fractions of $<70\ \mu\text{m}$ fluid particles at the emission source boundary (Figure 5-6). Previously published, earlier predictions of the VDRO-P-J model also did not predict significant mass fractions of $<70\ \mu\text{m}$ fluid particles at the emission source boundary.²⁷⁶

According to TAMOC-c simulations conducted both with and without dispersant addition, we find that the $0.57\ \text{kg s}^{-1}$ of dispersants injected at the broken Macondo riser stub on June 8, 2010 resulted in the additional aqueous dissolution of $5.0\ \text{kg s}^{-1}$ of petroleum compounds, based on VDRO-P-J model size distributions of droplets and bubbles at the emission source boundary. In other words, according to TAMOC-c simulations, 27% of the mass flow rate of total petroleum fluids became trapped in the water column when dispersants were added, whereas only 22% of the petroleum fluid mass would have become trapped in the water column if dispersants were not added (Table 5-5). Therefore our TAMOC-c simulations indicate that dispersant addition led to substantially increased aqueous dissolution of hydrocarbons into the deep water column. Dispersant injection leads to the formation of smaller droplets and bubbles at the emission source (discussed in section 5.4.1, above), which in turn increases the extent of aqueous dissolution during the ascent of petroleum fluids toward the sea surface. Notably, the 5% of the total petroleum fluids that were prevented from reaching the sea surface by dispersant addition are volatile compounds that would otherwise have rapidly evaporated. Consequently, the dispersant addition is not predicted to have significantly reduced the amount of petroleum fluids present in sea surface slicks, but rather to have improved air quality above the broken Macondo well. According to simulations, dispersant injection increased the total extent of aqueous dissolution of toxic compounds in the water column. For example, benzene became 100% aqueously dissolved with dispersant addition, versus 80% aqueously dissolved without dispersant, and toluene was 96% aqueously dissolved with dispersant addition instead of 41% aqueously dissolved without dispersant. Predicted apportionments within the water column are also affected. For example, in the absence of dispersant addition, only 36% of the benzene mass is predicted to have been retained in the deep-water hydrocarbon plume at 900–1300 m depth, compared to 93% with dispersant addition (Table 5-5). It is predicted that the percentage of total petroleum fluids dissolved into the upper water column has been lowered by dispersant injection from 7% without dispersant to 4% with dispersant. The predicted percentage of total petroleum fluids dissolved into the deep-water hydrocarbon plume exhibits an opposite trend, going from 15% without

dispersant to 23% with dispersant. In summary, subsurface dispersant injection is predicted to have principally changed the environmental compartments to which toxic compounds were transferred, with only minimal impact on the predicted mass flow rate in surface slicks (discussed further below). Our discussion is based on simulations for June 8, 2010, with the TAMOC-c model. However, we note that in terms of the relative flow rates of dispersant and live oil, predictions for June 8, 2010 are probably representative for at least ~62% of the days after the riser was cut (on June 3, 2010, Appendix section 5.6.11).

The TAMOC-c model predicts that on June 8, 2010, with deep-water dispersant injection, >99% of the non-dissolved fraction of the emitted flux of petroleum compounds would surface within <60 h, arriving at a location of <4 km horizontal distance from the broken Macondo riser stub location, with <1% of non-dissolved material retained in the deep-water hydrocarbon plume. Therefore, we find that the application of dispersant at the broken Macondo riser stub probably did not result in a large fraction of the petroleum compound mass flow rate being trapped in the water column as small droplets having slow rise velocities, contrary to what has been suggested in the past.²⁹⁸ We think that this previous suggestion is partly due to a misinterpretation of altered time and location of arrival of fluid particles at the sea surface in presence of dispersant (section 5.4.2). Field observations indicate clearly that the deep-water hydrocarbon plume was composed principally of aqueously dissolved compounds.⁸ Our model predicts <1% of the mass flow rate of sparingly-soluble compounds were retained in the deep-water hydrocarbon plume at the downstream boundary of the deep-water hydrocarbon plume model, whereas that we estimated that field observations reported by Reddy et al.⁸ would indicate that 1.2% of the mass flow rate of sparingly-soluble compounds became trapped in the deep-water hydrocarbon plume (Appendix section 5.6.10). Thus, both field observations and simulation results demonstrate that most of the mass of sparingly-soluble compounds ascended rapidly to the sea surface. A previous attempt to model a deep-water hydrocarbon plume composed of finely dispersed droplets³⁰⁹ would have a composition that is incompatible with available field observations.⁸ This previous study³⁰⁹ used an extremely simplified model that neglected aqueous dissolution and any change in fluid particle properties (e.g. density) that a fluid particle would experience in reality as its composition, pressure, and temperature evolve during ascent. Finally, we note that our TAMOC-c model does not provide an explanation for the fact that 0.5–14.4%^{204,205} of the Macondo dead oil emitted in the environment was found to have deposited on the seafloor. This is discussed further in Chapter 4.

Table 5-5. Predicted mass apportionments of methane, ethane, propane, CO₂, *n*-C₆, cyclohexane, single-ring aromatic compounds, and multi-ring aromatic compounds in the water column, based on the MC₁ representation of the composition of the petroleum fluids that were emitted from the broken Macondo riser stub at 1524 m depth. Predictions are reported for June 8, 2010 using the TAMOC-c model, based on the VDROD-J initial size distributions of droplets and bubbles, with and without dispersant addition.

Compound	mass percent aqueously dissolved in the deep-water hydrocarbon plume, 900–1300 m depth		mass percent aqueously dissolved in the upper water column, 0–900 m depth			mass percent predicted to reach the sea surface as fluid particles	
	VDROP-J, with dispersant	VDROP-J, no dispersant	VDROP-J, with dispersant	VDROP-J, no dispersant	VDROP-J, with dispersant	VDROP-J, no dispersant	
total petroleum fluids	23%	15%	4%	7%	73%	78%	
methane	100%	77%	0%	22%	0%	1%	
ethane	99%	62%	1%	36%	0%	2%	
propane	86%	26%	14%	46%	0%	28%	
CO ₂	100%	100%	0%	0%	0%	0%	
<i>n</i> -C ₆	3%	0%	10%	1%	87%	99%	
cyclohexane	13%	1%	30%	5%	57%	93%	
benzene	93%	36%	7%	44%	0%	20%	
toluene	61%	13%	35%	28%	4%	59%	
<i>p/m</i> -xylenes	28%	4%	42%	11%	30%	85%	
<i>o</i> -xylene	28%	4%	43%	12%	29%	84%	
ethylbenzene	28%	4%	42%	12%	30%	84%	
naphthalene	18%	2%	36%	7%	45%	90%	
C ₁ -naphthalenes	6%	1%	16%	2%	78%	98%	
C ₂ -naphthalenes	2%	0%	7%	1%	92%	99%	
C ₃ -naphthalenes	0%	0%	2%	0%	98%	100%	
C ₄ -naphthalenes	0%	0%	0%	0%	100%	100%	
fluorene	4%	0%	12%	1%	84%	98%	
phenanthrene	1%	0%	3%	0%	97%	100%	
C ₁ -phenanthrenes	0%	0%	0%	0%	100%	100%	
C ₂ -phenanthrenes	0%	0%	0%	0%	100%	100%	
C ₃ -phenanthrenes	0%	0%	0%	0%	100%	100%	
C ₄ -phenanthrenes	0%	0%	0%	0%	100%	100%	
fluoranthene	0%	0%	1%	0%	99%	100%	
pyrene	0%	0%	0%	0%	100%	100%	

5.4.7 Implications for deep-water petroleum fluid releases

In this chapter, we showed that predictions of the TAMOC-c model enabled a better understanding of the states and trajectories of petroleum compounds ascending the water column during the *Deepwater Horizon* disaster. TAMOC-c simulation results were also validated, exhibiting reasonable agreement with several sets of field observations. Here we briefly discuss the principal processes that explain the unusual apportionments of petroleum compounds during this event, in order to provide improved intuition about the behavior of this release of petroleum fluids under deep-water conditions. Three principal factors explain the unprecedented extent of aqueous dissolution of ~27% of the mass flow rate of the reservoir fluid in the water column: the large surface-to-volume ratio produced by the formation of small (0.5–4 mm) droplets and bubbles in the deep water column; the 3-fold to 125-fold increased aqueous solubilities of light (C_1 – C_4) hydrocarbons at elevated deep-sea pressures; and the long (4–15 hour) ascent in the water column, during which evaporation processes were suppressed. Other factors that also participated in determining the extent of aqueous dissolution of petroleum compounds include dispersant addition, temperature, hydrate shells at depths >500 m, buoyant plume dynamics, and salinity. It is by considering these interwoven effects that predictions can be made about the trajectories and impacts of petroleum compounds in the marine environment during a deep-sea release.

The TAMOC-c model could provide prognostic insight into the outcomes that may be expected for deep-water releases of other petroleum fluids, under different conditions, at other locations. In particular, the high pressures of the deep water column have a preponderant role in determining the effective aqueous solubilities of light compounds (Chapter 4), determining the buoyancy of the emitted fluid particles, and determining the duration of time in which fluid particles are exposed to aqueous dissolution. Size distributions of droplets and bubbles at the emission source boundary also play an influential role on the rate of aqueous dissolution of petroleum compounds, therefore the emission context (orifice size, volumetric flow rate) could impact size distributions and lead to different outcomes. Dispersant injection also has a large influence on the fate of petroleum compounds, by decreasing the size distributions of droplets and bubbles at the emission source boundary, thereby leading to increased extent of aqueous dissolution of petroleum compounds in the deep sea (section 5.4.6). Additionally, the composition of the emitted fluids will participate in determining the concentrations of individual compounds to be expected during a deep-water release. In particular, the content of light (< C_5) hydrocarbons, which varies among petroleum reservoirs, will play an influential role in both the fraction of mass that becomes aqueously dissolved and the available buoyancy within the buoyant plume stage. Finally, water currents can influence the buoyant plume behavior.³³ We found that moderate changes in current velocity had little influence on predicted mass flow rate apportionment to the deep-water hydrocarbon plume (Appendix section 5.6.6). The TAMOC-c model offers an opportunity to study the behaviors of potential future releases of petroleum fluids in deep waters under other conditions, based on physical-chemical simulations of the predominant processes of importance.

5.4.8 Acknowledgements

I thank Peter Brewer and Peter Walz for sharing data on their experimental work with carbon dioxide droplets and methane-saturated decane in deep waters, which improved my understanding of some physical processes that are relevant in deep waters. I am also grateful to Tom Ryerson for discussions on his published estimates. Finally, we acknowledge Chuan-Yuan Hsu and Ping Chang for providing us with CRCM model predictions,²⁸⁹ and Ruoying He for providing us with SABGOM model predictions.^{290,291}

5.5 Funding Sources

This research was supported by grants from the NSF (OCE-0960841, OCE-1043976, and EAR-0950600), the BP/the Gulf of Mexico Research Initiative (GoMRI-015), C-IMAGE and DEEP-C consortia.

5.6 Appendix

5.6.1 The 14-component model compositions: $MC_{1,14c}$, $MC_{2,14c}$, and $MC_{3,14c}$

TAMOC-c simulation results reported in the main text are based on a detailed model composition of the reservoir fluid using 279 components (Chapter 4), MC_1 . This reservoir fluid model composition allows detailed simulation of aqueous dissolution but requires long simulation times (~1–2 weeks on our computer having Intel X5650 CPU, 1 core, 4 GB of RAM). This time constraint limited our ability to use this detailed model composition in early development stages of the project and to evaluate different sets of conditions. Therefore, I developed a simplified model composition of the reservoir fluid that was used to test some assumptions and investigate the importance of some parameters (sections 5.6.3, 5.6.5, and 5.6.6).

In the simplified model composition, $MC_{1,14c}$, 14 components are defined (Table 5-6). These include individual small hydrocarbons, a C_6 pseudo-component, and five pseudo-components regrouping carbon-number intervals from C_7 to C_{108} . Therefore, $MC_{1,14c}$ only allows modeling of aqueous dissolution up to hydrocarbons having ≤ 6 atoms of carbon. The modeling of aqueous dissolution for the C_6 pseudo-component is only approximate, as it is based on the aqueous solubility of *n*- C_6 . $MC_{1,14c}$ is similar to traditional pseudo-component groupings used for equation-of-state liquid-gas equilibrium calculations for petroleum fluids.²⁰⁹ Properties of components up to C_6 were determined as explained in Chapter 4. Properties of single carbon number intervals from C_7 to C_{108} were estimated from the Twu and Kesler-Lee correlations (section 4.9.6), and these are listed in Table 4-4.^{244–248} Pseudo-components were then constructed by grouping single-carbon number intervals, and properties of the pseudo-components were estimated from the properties of the grouped single carbon number intervals using Lee's mixing rule (weighted average using mole fractions as weights).^{310,311}

$$Prop_L = \frac{\sum_L z_i \cdot Prop_i}{\sum_L z_i}$$

Equation 5-7

where a property $Prop_L$ (for example, critical pressure) of a pseudo-component (e.g. C_7 - C_9) is estimated from the properties of the single carbon number intervals (e.g. C_7 , C_8 , and C_9), $Prop_i$, using a weighted average, with mole fractions, z_i , as weights.

Fixed binary interaction parameters were taken from previous literature,²⁹⁴ as listed in Table 5-7. We find a reasonable agreement between the fluid properties estimated using $MC_{1,14c}$, and MC_1 , when compared to available experimental data (Table 5-8). Model compositions $MC_{2,14c}$ and $MC_{3,14c}$ (Table 5-6) were obtained similarly based on the compositions of two pre-spill reservoir fluid samples (Chapter 4).^{231,232}

Table 5-6. Estimated or literature properties for $MC_{1,14c}$ components. Arising from the use of Equation 5-7, the properties of the pseudo-components larger than C_6 are dependent on the mole fractions of the different single carbon number intervals and therefore the values are specific for the reservoir fluid studied here ($MC_{1,14c}$). The Table lists the critical temperature, T_c , the critical pressure, P_c , the critical volume, V_c , the acentric factor, ω , the molar weight, M , and the mass fractions in the Macondo reservoir fluid based on the sample reported by Reddy et al.,⁸ and two pre-spill reservoir fluid samples,^{231,232} $MC_{1,14c}$, $MC_{2,14c}$ and $MC_{3,14c}$, respectively.

Pseudo-component	T_c [K]	P_c [MPa]	V_c [cm ³ mol ⁻¹]	ω [-]	M [g mol ⁻¹]	$MC_{1,14c}$ [-]	$MC_{2,14c}$ [-]	$MC_{3,14c}$ [-]
C_1	190.56	4.599	98.6	0.011	16.043	0.1500	0.2046	0.1999
C_2	305.32	4.872	145.5	0.099	30.070	0.0280	0.0373	0.0367
C_3	369.83	4.248	200.0	0.152	44.097	0.0260	0.0388	0.0384
$i-C_4$	407.85	3.640	262.7	0.186	58.123	0.0067	0.0105	0.0105
$n-C_4$	425.12	3.796	255.0	0.200	58.123	0.0150	0.0236	0.0241
$i-C_5$	460.39	3.381	308.3	0.229	72.150	0.0079	0.0115	0.0122
$n-C_5$	469.70	3.370	311.0	0.252	72.150	0.0100	0.0139	0.0148
C_6	507.60	3.025	368.0	0.300	86.177	0.0273	0.0210	0.0231
C_7-C_9	579.47	2.742	457.2	0.336	107.637	0.1128	0.1042	0.1144
$C_{10}-C_{12}$	650.68	2.232	604.6	0.446	145.178	0.1005	0.0817	0.0834
$C_{13}-C_{15}$	710.35	1.877	755.2	0.555	189.151	0.0861	0.0691	0.0716
$C_{16}-C_{21}$	772.68	1.556	949.2	0.693	252.704	0.1264	0.1032	0.1114
C_{22+}	901.20	1.059	1449.4	1.064	481.373	0.2907	0.2790	0.2570
CO_2	304.12	7.374	94.1	0.225	44.010	0.0059	0.0076	0.0077

Table 5-7. Binary interaction parameters used for $MC_{1,14c}$, $MC_{2,14c}$, and $MC_{3,14c}$.²⁹⁴

Pseudo-component	C_1	C_2	C_3	$i-C_4$	$n-C_4$	$i-C_5$	$n-C_5$	C_6	C_7-C_9	$C_{10}-C_{12}$	$C_{13}-C_{15}$	$C_{16}-C_{21}$	C_{22+}	CO_2
C_1	0	0.0026	0.014	0.0256	0.0133	0.0056	0.0236	0.0422	0.0432	0.05	0.0533	0.0633	0.07	0.107
C_2	0.0026	0	0.0011	0.0067	0.0096	0.008	0.0078	0.014	0.0167	0.03	0.0333	0.0433	0.05	0.1322
C_3	0.014	0.0011	0	0.0078	0.0033	0.0111	0.012	0.0267	0.0467	0.02	0.0217	0.0267	0.03	0.1241
$i-C_4$	0.0256	0.0067	0.0078	0	0	0.004	0.002	0.024	0.0223	0.01	0.0117	0.0167	0.02	0.14
$n-C_4$	0.0133	0.0096	0.0033	0	0	0.017	0.017	0.0174	0.0137	0.001	0.001	0.0012	0.0015	0.1333
$i-C_5$	0.0056	0.008	0.0111	0.004	0.017	0	0	0	0	0	0	0	0	0.14
$n-C_5$	0.0236	0.0078	0.012	0.002	0.017	0	0	0	0	0	0	0	0	0.14
C_6	0.0422	0.014	0.0267	0.024	0.0174	0	0	0	0	0	0	0	0	0.145
C_7-C_9	0.0432	0.0167	0.0467	0.0223	0.0137	0	0	0	0	0	0	0	0	0.0998
$C_{10}-C_{12}$	0.05	0.03	0.02	0.01	0.001	0	0	0	0	0	0	0	0	0.0145
$C_{13}-C_{15}$	0.0533	0.0333	0.0217	0.0117	0.001	0	0	0	0	0	0	0	0	0.0145
$C_{16}-C_{21}$	0.0633	0.0433	0.0267	0.0167	0.0012	0	0	0	0	0	0	0	0	0.0145
C_{22+}	0.07	0.05	0.03	0.02	0.0015	0	0	0	0	0	0	0	0	0.0145
CO_2	0.107	0.1322	0.1241	0.14	0.1333	0.14	0.14	0.145	0.0998	0.0145	0.0145	0.0145	0.0145	0

Table 5-8. Predictions of the thermodynamic model using the reservoir fluid model compositions MC_{1,14c} and MC₁.

property	predicted value, MC _{1,14c}	predicted value, MC ₁	measured value from literature
dead oil viscosity (mPa s), 0.101325 MPa and 15 °C	3.7	4.2	4.1 ²⁵⁴
dead oil viscosity (mPa s), 0.101325 MPa and 35 °C	2.7	3.1	1.4 ²⁵⁴
dead oil density, 0.101325 MPa and 22 °C	865	823	820 ⁸
gas density (kg m ⁻³), 15.5 MPa and 4.3 °C	182	181	–
liquid density (kg m ⁻³), 15.5 MPa and 4.3 °C	739	707	–
volume percent of gas (-), 15.5 MPa and 4.3 °C	31%	29%	–

5.6.2 Comparison of measured and predicted velocities of currents in the water column near the Macondo well

The available measured profiles of water current velocities (one profile each 10 min) spanned only the 64–1184 m depth range (section 5.3.2). Therefore we sought to obtain a reasonable estimate of water column velocities for water depths between 1524 m and 1184 m. In this process, we investigated whether three different ocean models could bridge this data gap. We find relatively poor agreement between reported measurements at 64–1184 m depth and the predictions of the three models studied. Additionally, model predictions at >1184 m depth span a large range of predicted velocities, and they do not extend to >1400 m depth (Figure 5-11). Consequently, we preferred to use a simplified water velocity at >1184 m depth, assumed constant in time and space, estimated as the mean of the measured water velocities at depths >600 m. I found that the extent of aqueous dissolution is not sensitive to the value assumed for the water current velocity at >1184 m depth, due to rapid ascent of petroleum fluids to shallower depths during the buoyant plume phase (section 5.6.6).

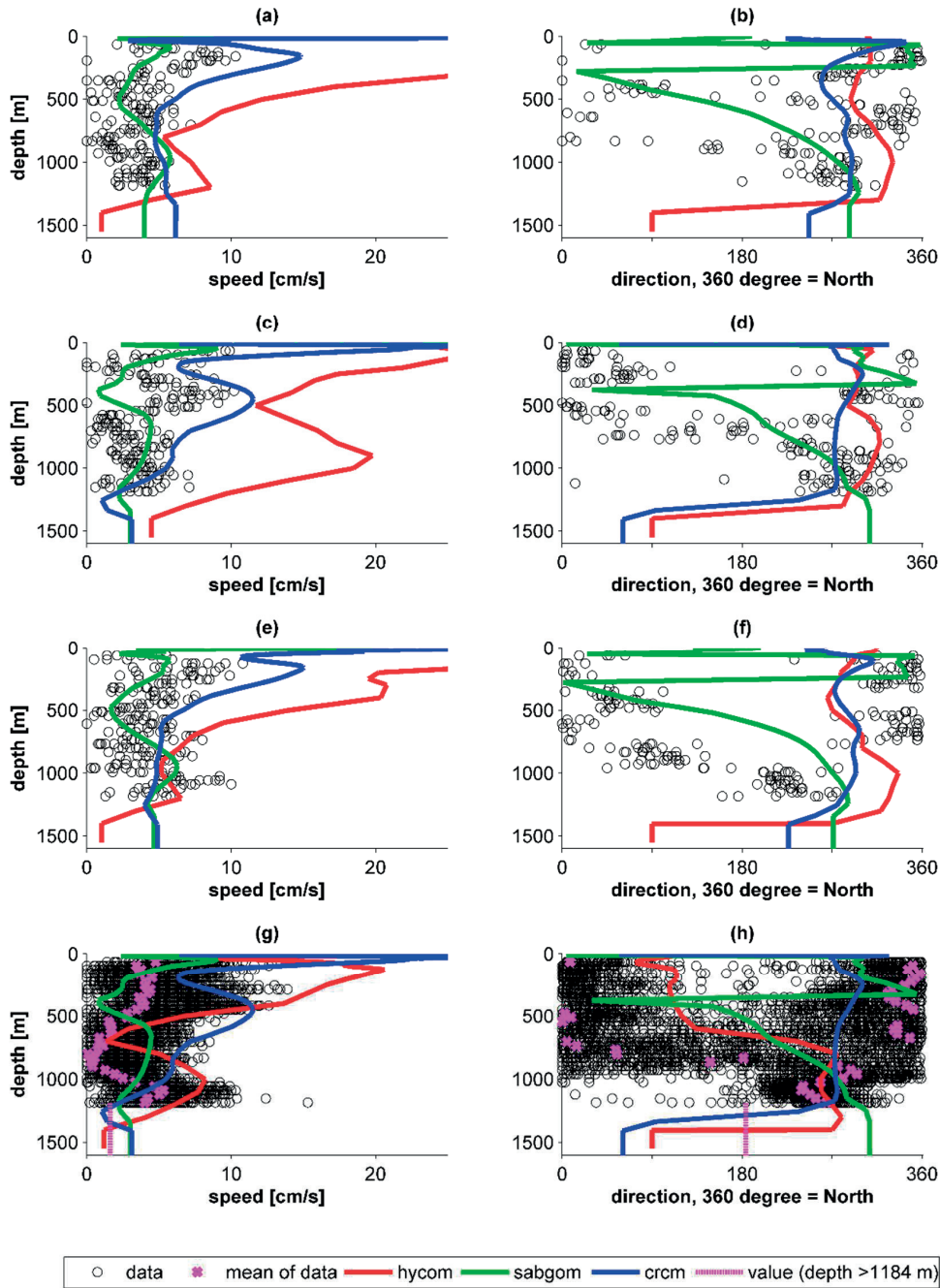


Figure 5-11. Water velocity magnitudes and directions measured by the American National Oceanic and Atmospheric Administration, NOAA, (black circles) compared to the predictions of three different ocean models (hycom, red; sabgom, green; crcm, blue). Values are reported at different time points on June 8, 2010: (a-b) 0–1 am, (c-d) 11–12 am, (e-f) 23–24 pm, (g-h) all values measured on June 8, 2010. The axis describing velocity magnitude (speed) is truncated at 25 cm s^{-1} , but predictions of the hycom model go up to 90 cm s^{-1} in some cases. Model predictions are extended beyond 1400 m depth by assuming a spatially and temporally constant value at these depths. (Hycom model data were downloaded from <http://hycom.org/data/goml0pt04/expt-31pt0>)

5.6.3 Influence of temperature at the emission source boundary on predicted aqueous dissolution extent of petroleum compounds based on MC_{1,14C}

The mass flow rates of liquid and gas petroleum at the emission source boundary are dependent on the assumed temperature at which liquid-gas partitioning occurs. Based on petroleum fluid composition MC₁, the mass flow rate of gas is predicted to be 8.5 kg s⁻¹ at 4.3 °C, which was the temperature of ambient seawater. By contrast, the mass flow rate of gas would be 14.8 kg s⁻¹ if a temperature of 105 °C is assumed, which was the maximum temperature measured by Reddy et al. when collecting sample MW-1.⁸ The emitted fluid is 54% gas by volume at 105 °C versus 29% at 4.3 °C. The initial liquid-gas partitioning of the lightest compounds can affect aqueous dissolution kinetics. For example 71% of the methane is partitioned into the gas phase at 105 °C versus 49% at 4.3 °C, and 41% of the propane is partitioned into the gas phase at 105 °C versus 17% at 4.3 °C. The uncertainty in the liquid-gas partitioning processes at the emission source boundary therefore impacts the predicted extent of aqueous dissolution of petroleum compounds (Table 5-9 and Table 5-10).

Table 5-9. TAMOC-c predictions of the fractionation indices with respect to methane for two different assumed temperatures at the emission source boundary, T₀, using the reservoir fluid model composition MC_{1,14C}. We assumed that added dispersant led to a decrease in the liquid/seawater and gas/seawater interfacial tensions by a factor 5.4. The Johansen et al. correlation²⁷⁷ was used to determine the resulting RR size distributions* of droplets and bubbles at the emission source boundary.

compound	field observations (Reddy et al., ⁸ table S-3)	TAMOC-c predictions** (T ₀ = 4.3 °C)	TAMOC-c predictions** (T ₀ = 105 °C)
methane	1	1	1
ethane	0.91	0.84	0.92
propane	0.78	0.43	0.56
<i>i</i> -C ₄	-	0.16	0.24
<i>n</i> -C ₄	-	0.15	0.23
<i>i</i> -C ₅	-	0.043	0.077
<i>n</i> -C ₅	-	0.040	0.073
CO ₂	-	1.06	1.00

* RR size distributions were used at the emission source in this test because the TAMOC implementation of the correlation of Johansen et al.²⁷⁷ could be used to determine the size distributions. Using the VDRO-P-J size distributions would have required to obtain VDRO-P-J simulation results from Lin Zhao for each tested case, which was impractical in the time frame of this work.

** With the RR size distributions, <<1% of the mass flux of petroleum fluids was predicted to be trapped in the deep-water hydrocarbon plume at the downstream boundary of the deep-water hydrocarbon plume model. Therefore we report the simulated fractionation indices based on aqueously dissolved compounds only.

Table 5-10. TAMOC-c predicted fractions of petroleum compounds that became aqueously dissolved during ascent for two different assumed temperatures at the emission source boundary, T_0 , using the reservoir fluid model composition $MC_{1,14C}$. We assumed that added dispersant led to a decrease in the liquid/seawater and gas/seawater interfacial tensions by a factor 5.4. The Johansen et al. correlation²⁷⁷ was used to determine the resulting RR size distributions* of droplets and bubbles at the emission source boundary.

compound	field observations (Ryerson et al., ⁷⁵ table S01)	TAMOC-c predictions ($T_0 = 4.3$ °C)	TAMOC-c predictions ($T_0 = 105$ °C)
methane	1.00	1.00	1.00
ethane	1.00	1.00	1.00
propane	0.99	0.83	0.94
<i>i</i> -C ₄	0.84	0.42	0.60
<i>n</i> -C ₄	0.74	0.38	0.56
<i>i</i> -C ₅	0.26	0.14	0.23
<i>n</i> -C ₅	0.17	0.13	0.21
CO ₂	-	1.00	1.00

* RR size distributions were used at the emission source in this test because the TAMOC implementation of the correlation of Johansen et al.²⁷⁷ could be used to determine the size distributions. Using the VDROD-J size distributions would have required to obtain VDROD-J simulation results from Lin Zhao for each tested case, which was impractical in the time frame of this work.

5.6.4 Effect of the start/end of dispersant injection on the fraction of mass surfacing

According to TAMOC-c simulation results for a simulated dispersant application test (Figure 5-12), a steady flow rate of petroleum residues reach the sea surface before dispersant application (time zero), corresponding to 78% of the mass flow rate at the emission source. At the onset of dispersant addition, smaller fluid particles are generated at the emission source boundary, resulting in decreased ascent speeds of droplets and bubbles. This causes a temporary period of substantially decreased flow rate of liquid petroleum reaching the sea surface, which becomes apparent starting at approximately 2 hours after the onset of dispersant addition. Within approximately 20 hours after dispersant addition, simulations achieve a new steady state in which the mass flow rate of petroleum residues arriving at the sea surface is equivalent to 73% of the mass flow rate of petroleum fluids at the emission source boundary. At time = 88 hours, the dispersant addition is stopped, and larger and faster fluid particles emitted at the source boundary now catch up with the slower fluid particles generated during the previous period of dispersant addition. This leads to a temporarily increased mass flow rate of liquid petroleum fluids arriving at the sea surface, followed by a return to the original steady state without dispersant addition (i.e., the mass flow rate at the sea surface is equivalent to 78% of the mass flow rate at the emission source).

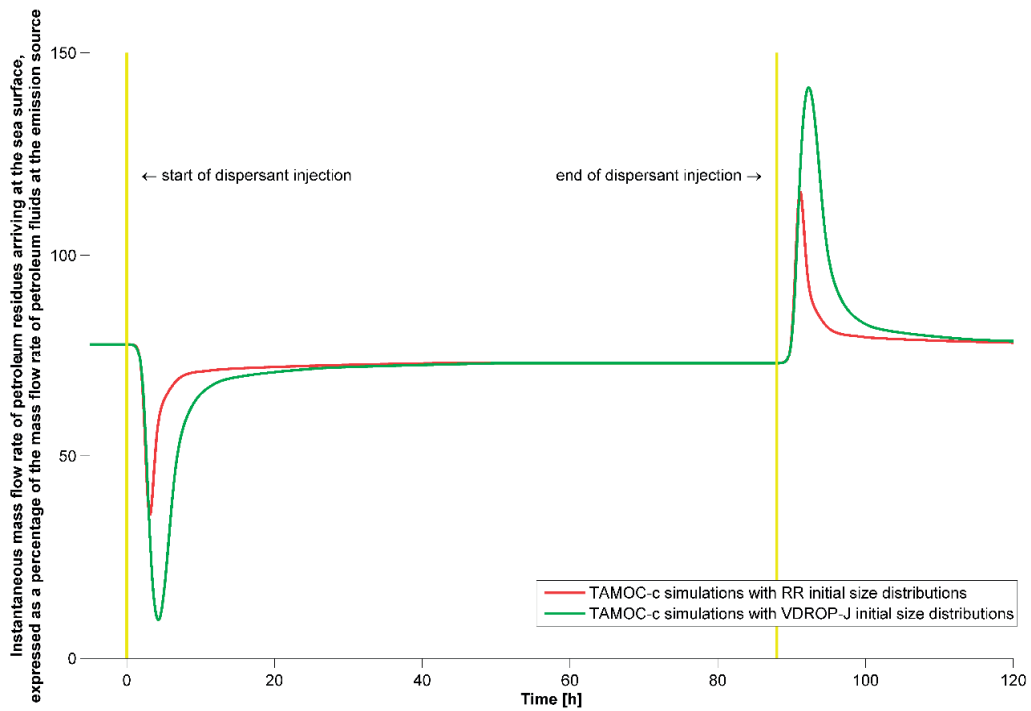


Figure 5-12. TAMOC-c simulations of the time-dependent mass flow rate of petroleum residues arriving at the sea surface during a dispersant application test. In the simulation results shown above, a situation of steady state flow has been achieved before time zero, during which dispersant is not applied. At time = 0, dispersant application begins, continuing for a duration of 88 h, as shown by the time window delimited by the two vertical yellow lines. The simulated dispersant application ends at time = 88 h. The resulting dynamical mass flow rate of petroleum residues arriving at the sea surface is expressed as a percentage of the total mass flow rate of petroleum fluids emitted from the broken Macondo riser stub, which is assumed constant with time. Results are shown for TAMOC-c simulations with both the VDROD-J model (green line) and the Johansen et al.²⁷⁷ correlation (red line) used to describe size distributions of droplets and bubbles at the emission source boundary.

5.6.5 Effect of reservoir fluid composition on predicted aqueous dissolution extent of petroleum compounds based on MC_{1,14C}, MC_{2,14C}, and MC_{3,14C}

The predicted relative extents of aqueous dissolution (Table 5-11 and Table 5-12) are insensitive to the model reservoir fluid composition used (MC_{1,14C}, MC_{2,14C}, or MC_{3,14C}, see Chapter 4). The main difference in TAMOC-c predictions depending on the reservoir fluid model composition used resides in the total mass flow rate of petroleum compounds predicted to partition to the water column (Table 5-13), as expected from the larger content of C₁–C₅ compound in MC_{2,14C} and MC_{3,14C} compared to MC_{1,14C}.

Table 5-11. TAMOC-c predicted fractionation indices with respect to methane for three different assumed reservoir fluid model compositions (MC_{1,14C}, MC_{2,14C}, or MC_{3,14C}). We assumed that added dispersant led to a decrease in the liquid/seawater and gas/seawater interfacial tensions by a factor 5.4. The Johansen et al. correlation²⁷⁷ was used to determine the resulting RR size distributions* of droplets and bubbles at the emission source boundary.

compound	field observations (Reddy et al., ⁸ table S-3)	TAMOC-c predictions** (MC _{1,14C})	TAMOC-c predictions** (MC _{2,14C})	TAMOC-c predictions** (MC _{3,14C})
methane	1	1	1	1
ethane	0.91	0.84	0.84	0.84
propane	0.78	0.43	0.46	0.46
<i>i</i> -C ₄	-	0.16	0.19	0.19
<i>n</i> -C ₄	-	0.15	0.17	0.17
<i>i</i> -C ₅	-	0.043	0.055	0.055
<i>n</i> -C ₅	-	0.040	0.052	0.052
CO ₂	-	1.06	1.08	1.07

* RR size distributions were used at the emission source in this test because the TAMOC implementation of the correlation of Johansen et al.²⁷⁷ could be used to determine the size distributions. Using the VDROD-J size distributions would have required to obtain VDROD-J simulation results from Lin Zhao for each tested case, which was impractical in the time frame of this work.

** With the RR size distributions, <<1% of the mass flux of petroleum fluids was predicted to be trapped in the deep-water hydrocarbon plume at the downstream boundary of the deep-water hydrocarbon plume model. Therefore we report the simulated fractionation indices based on aqueously dissolved compounds only.

Table 5-12. TAMOC-c predicted fractions of petroleum compounds aqueously dissolved during ascent for three different assumed reservoir fluid model compositions (MC_{1,14C}, MC_{2,14C}, or MC_{3,14C}). We assumed that added dispersant led to a decrease in the liquid/seawater and gas/seawater interfacial tensions by a factor 5.4. The Johansen et al. correlation²⁷⁷ was used to determine the resulting RR size distributions* of droplets and bubbles at the emission source boundary.

compound	field observations (Ryerson et al., ⁷⁵ table S01)	TAMOC-c predictions (MC _{1,14C})	TAMOC-c predictions (MC _{2,14C})	TAMOC-c predictions (MC _{3,14C})
methane	1.00	1.00	1.00	1.00
ethane	1.00	1.00	1.00	1.00
propane	0.99	0.83	0.84	0.84
<i>i</i> -C ₄	0.84	0.42	0.43	0.43
<i>n</i> -C ₄	0.74	0.38	0.41	0.41
<i>i</i> -C ₅	0.26	0.14	0.16	0.15
<i>n</i> -C ₅	0.17	0.13	0.15	0.14
CO ₂	-	1.00	1.00	1.00

* RR size distributions were used at the emission source in this test because the TAMOC implementation of the correlation of Johansen et al.²⁷⁷ could be used to determine the size distributions. Using the VDROD-J size distributions would have required to obtain VDROD-J simulation results from Lin Zhao for each tested case, which was impractical in the time frame of this work.

Table 5-13. Predicted mass flow rate apportionment for three different assumed reservoir fluid model compositions (MC_{1,14C}, MC_{2,14C}, or MC_{3,14C}). We assumed that added dispersant led to a decrease in the liquid/seawater and gas/seawater interfacial tensions by a factor 5.4. The Johansen et al. correlation²⁷⁷ was used to determine the resulting RR size distributions* of droplets and bubbles at the emission source boundary. (Note: the 14-component model compositions of the reservoir fluid underestimate the total aqueous dissolution, because compounds >C₆ are assumed insoluble.)

estimated mass flow rate of petroleum compound (kg s ⁻¹)	TAMOC-c predictions (MC _{1,14C})	TAMOC-c predictions (MC _{2,14C})	TAMOC-c predictions (MC _{3,14C})
fluid particles predicted to reach the sea surface	74.0	76.9	76.1
deep-water hydrocarbon plume, 900–1300 m depth (aqueously dissolved)	17.5	27.2	26.5
upper water column, 0–900 m depth (aqueously dissolved)	3.0	5.6	5.2

* RR size distributions were used at the emission source in this test because the TAMOC implementation of the correlation of Johansen et al.²⁷⁷ could be used to determine the size distributions. Using the VDROD-J size distributions would have required to obtain VDROD-J simulation results from Lin Zhao for each tested case, which was impractical in the time frame of this work.

5.6.6 Effect of estimated water current velocity at >1184 m depth on predicted aqueous dissolution extent of petroleum compounds based on MC_{1,14C}

Recognizing that some uncertainty exists regarding the magnitude of water current velocities at >1184 m depth, we tested how the assumed velocity value at >1184 m depth affected the TAMOC-c model predictions. In these tests, we considered only the influence of varying magnitude of the water current velocity, assuming a constant current heading (direction). We find that the predicted extent of relative aqueous dissolution for petroleum compounds are insensitive to the assumed magnitude of the water current velocity (Table 5-14 and Table 5-15), whereas the total water flow into the intrusion layer is more sensitive to the magnitude of the water current velocity (Table 5-16).

Table 5-14. TAMOC-c predictions of fractionation indices with respect to methane for four different assumed water current velocities at >1184 m depth, using the reservoir fluid model composition MC_{1,14C}. We assumed that added dispersant led to a decrease in the liquid/seawater and gas/seawater interfacial tensions by a factor 5.4. The Johansen et al. correlation²⁷⁷ was used to determine the resulting RR size distributions of droplets and bubbles at the emission source boundary.

compound	field observations (Reddy et al., ⁸ table S-3)	TAMOC-c predictions* (base case: 1.6 cm s ⁻¹ below 1184 m)	TAMOC-c predictions* (doubled velocity below 1184 m)	TAMOC-c predictions* (tripled velocity below 1184 m)	TAMOC-c predictions* (quadrupled velocity below 1184 m)
methane	1	1	1	1	1
ethane	0.91	0.84	0.81	0.79	0.79
propane	0.78	0.43	0.40	0.38	0.38
<i>i</i> -C ₄	-	0.16	0.15	0.14	0.14
<i>n</i> -C ₄	-	0.15	0.14	0.13	0.13
<i>i</i> -C ₅	-	0.043	0.038	0.034	0.034
<i>n</i> -C ₅	-	0.040	0.036	0.032	0.032
CO ₂	-	1.06	1.08	1.10	1.10

* With the RR size distributions, <<1% of the mass flux of petroleum fluids was predicted to be trapped in the deep-water hydrocarbon plume at the downstream boundary of the deep-water hydrocarbon plume model. Therefore we report the simulated fractionation indices based on aqueously dissolved compounds only.

Table 5-15. TAMOC-c predictions of the fractions of petroleum compounds that became aqueously dissolved during ascent for four different assumed water current velocities at >1184 m depth, using the reservoir fluid model composition MC_{1,14C}. We assumed that added dispersant led to a decrease in the liquid/seawater and gas/seawater interfacial tensions by a factor 5.4. The Johansen et al. correlation²⁷⁷ was used to determine the resulting RR size distributions of droplets and bubbles at the emission source boundary.

compound	field observations (Ryerson et al., ⁷⁵ table S01)	predictions (base case: 1.6 cm s ⁻¹ at >1184 m depth)	predictions (doubled velocity at >1184 m depth)	predictions (tripled velocity at >1184 m depth)	predictions (quadrupled velocity at >1184 m depth)
methane	1.00	1.00	1.00	1.00	1.00
ethane	1.00	1.00	1.00	1.00	1.00
propane	0.99	0.83	0.83	0.83	0.83
<i>i</i> -C ₄	0.84	0.42	0.41	0.41	0.41
<i>n</i> -C ₄	0.74	0.38	0.38	0.38	0.38
<i>i</i> -C ₅	0.26	0.14	0.14	0.14	0.14
<i>n</i> -C ₅	0.17	0.13	0.13	0.13	0.13
CO ₂	-	1.00	1.00	1.00	1.00

Table 5-16. TAMOC-c predictions of: the total mass flow rate of aqueously dissolved petroleum compounds into the deep-water hydrocarbon plume; the volumetric flow rate of seawater into the deep-water hydrocarbon plume; and the depth of the center line of the deep-water hydrocarbon plume for four different assumed water current velocities at >1184 m depth, using the reservoir fluid model composition MC_{1,14C}. We assumed that added dispersant led to a decrease in the liquid/seawater and gas/seawater interfacial tensions by a factor 5.4. The Johansen et al. correlation²⁷⁷ was used to determine the resulting RR size distributions of droplets and bubbles at the emission source boundary. (Note: MC_{1,14C} underestimates the total aqueous dissolution, because compounds >C₆ are assumed insoluble.)

	predictions (base case: 1.6 cm s ⁻¹ at >1184 m depth)	predictions (doubled velocity at >1184 m depth)	predictions (tripled velocity at >1184 m depth)	predictions (quadrupled velocity at >1184 m depth)
mass flow rate of petroleum compounds aqueously dissolved in the deep-water hydrocarbon plume (kg s ⁻¹)	17.5	16.9	16.5	16.5
water flow in the deep-water hydrocarbon plume (m ³ s ⁻¹)	4544	3600	2880	2810
depth of the center line of the deep-water hydrocarbon plume (m)	1092	1113	1144	1145

5.6.7 Binary interaction parameters used to describe oxygen interactions with petroleum compounds

The group-contribution method²⁴⁹ used to estimate binary interaction parameters (Chapter 4) has not been parameterized for oxygen. Here we propose that the binary interaction parameter between oxygen and a hydrocarbon can be assumed as the same as the binary interaction parameter between nitrogen and this hydrocarbon. This assumption is made based on the fact that dioxygen (O₂) and dinitrogen (N₂) are both of similar size and shape, and both molecules are nonpolar.³¹²

To validate this assumption, we used previously reported data on the equilibrium mole fractions of oxygen dissolved into different liquid hydrocarbons at atmospheric pressure (101325 Pa), including *n*-C₅, *n*-C₆, *n*-C₇, *n*-C₈, *n*-C₉, *n*-C₁₀, 2,2,4-trimethylpentane, cyclohexane, methylcyclohexane, cyclooctane, benzene, toluene, 1,2-dimethylbenzene, 1,3-dimethylbenzene, 1,4-dimethylbenzene, ethylbenzene, *n*-propylbenzene, isopropylbenzene (cumene), and butylbenzene.³¹³ These data span a temperature range of 243.15 K to 353.15 K. 70% of these data span a temperature range of 0 to 30 °C. We compared experimentally observed equilibrium mole fractions to predictions of our thermodynamic model, using two different assumptions for the binary interaction parameters with oxygen. The first assumption was to treat the binary interaction parameter between oxygen and a hydrocarbon as the same as the binary interaction parameter between nitrogen and this hydrocarbon. The second assumption was to treat the binary interaction parameter between oxygen and a hydrocarbon as equal to zero. The former assumption performs better than the latter (Figure 5-13 and Table 5-17).

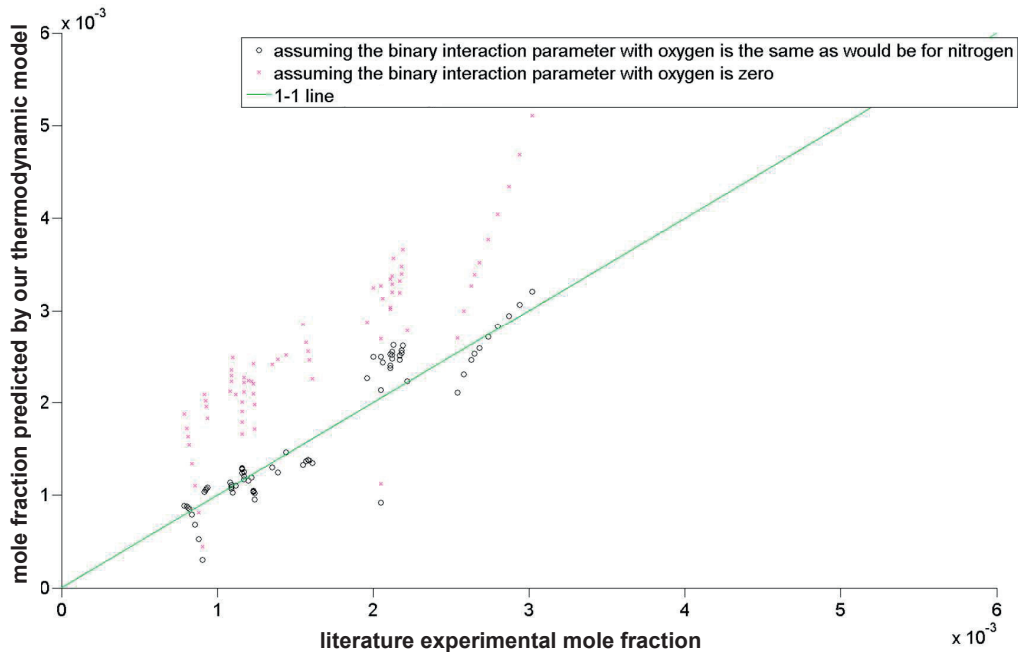


Figure 5-13. Comparison of our thermodynamic model with literature experimental data on the equilibrium mole fractions of oxygen in liquid hydrocarbons.³¹³ We tested two assumptions: the oxygen-hydrocarbon binary interaction parameter is equal to zero, or the oxygen-hydrocarbon binary interaction parameter is equal to that describing the nitrogen-hydrocarbon interaction.²⁴⁹ (Refer to the text above for the list of compound names.)

Table 5-17. Error statistics describing the agreement between experimental observations and thermodynamic model predictions for the equilibrium mole fractions of oxygen dissolved into liquid hydrocarbons. Results are shown for two sets of assumptions for the binary interaction parameter between oxygen and hydrocarbon liquids.

	assuming the binary interaction parameter with oxygen is zero	assuming the binary interaction parameter with oxygen is the same as would be for nitrogen
average relative error	0.4916	-0.0615
average relative absolute error	0.5310	0.2320

5.6.8 Numerical values of the predicted fractionation indices and fraction of aqueously dissolved mass for petroleum compounds during ascent of petroleum fluids to the sea surface

Table 5-18. Fractionation indices for several petroleum compounds predicted by the TAMOC-c model, and comparison to available field observations.⁸ Results are shown based on size distributions of droplets and bubbles given by three different models: VDRO-P-J, RR, and a custom distribution.

Compound	$F_{i, \text{methane}}$				$F_{i, \text{benzene}}$			
	field observations (Reddy et al. ⁷⁵)	VDRO-P-J initial size distributions	Custom initial size distributions	RR initial size distributions	field observations (Reddy et al. ⁷⁵)	VDRO-P-J initial size distributions	Custom initial size distributions	RR initial size distributions
methane	1	1	1	1		1.07E+0	1.10E+0	1.92E+0
ethane	9.10E-1	9.89E-1	9.54E-1	8.44E-1		1.06E+0	1.05E+0	1.62E+0
propane	7.80E-1	8.58E-1	7.53E-1	4.44E-1		9.22E-1	8.29E-1	8.53E-1
benzene		9.30E-1	9.09E-1	5.20E-1	1	1	1	1
toluene		6.13E-1	4.64E-1	2.48E-1	5.05E-1	6.59E-1	5.11E-1	4.78E-1
<i>o</i> -xylene		2.84E-1	1.56E-1	1.05E-1	3.78E-1	3.05E-1	1.72E-1	2.02E-1
ethylbenzene		2.81E-1	1.54E-1	1.04E-1	3.69E-1	3.02E-1	1.70E-1	2.00E-1
<i>p/m</i> -xylenes		2.83E-1	1.55E-1	1.05E-1	3.59E-1	3.04E-1	1.71E-1	2.01E-1
naphthalene		1.84E-1	8.97E-2	6.76E-2	2.21E-1	1.98E-1	9.87E-2	1.30E-1
1,2,4-trimethylbenzene		1.11E-1	4.71E-2	4.07E-2	2.11E-1	1.19E-1	5.19E-2	7.82E-2
<i>n</i> -propylbenzene		1.30E-1	5.80E-2	4.81E-2	2.18E-1	1.40E-1	6.38E-2	9.25E-2
1,3,5-trimethylbenzene		1.29E-1	5.62E-2	4.71E-2	2.32E-1	1.38E-1	6.19E-2	9.06E-2
C ₁ -naphthalenes		5.66E-2	2.21E-2	2.06E-2	2.04E-2	6.08E-2	2.43E-2	3.96E-2
dibenzothiophene		1.06E-3	3.70E-4	3.81E-4	1.38E-2	1.14E-3	4.08E-4	7.33E-4
fluorene		3.89E-2	1.47E-2	1.41E-2	3.83E-2	4.18E-2	1.62E-2	2.71E-2
C ₂ -naphthalenes		1.78E-2	6.34E-3	6.40E-3	1.04E-2	1.92E-2	6.98E-3	1.23E-2
C ₁ -dibenzothiophenes		2.98E-4	1.02E-4	1.07E-4	1.05E-2	3.20E-4	1.13E-4	2.05E-4
phenanthrene		6.56E-3	2.30E-3	2.35E-3	1.12E-2	7.05E-3	2.53E-3	4.52E-3
C ₁ -fluorenes		5.86E-3	2.04E-3	2.10E-3	3.35E-2	6.30E-3	2.25E-3	4.04E-3
C ₃ -naphthalenes		3.91E-3	1.34E-3	1.40E-3	1.42E-2	4.20E-3	1.48E-3	2.69E-3
C ₂ -dibenzothiophenes		9.24E-5	3.13E-5	3.29E-5	8.50E-3	9.93E-5	3.44E-5	6.33E-5
C ₂ -fluorenes		1.77E-3	6.02E-4	6.29E-4	1.29E-2	1.90E-3	6.62E-4	1.21E-3
C ₄ -naphthalenes		5.21E-4	1.76E-4	1.85E-4	1.74E-2	5.60E-4	1.93E-4	3.56E-4
fluoranthene		1.53E-3	5.21E-4	5.46E-4	1.02E-1	1.65E-3	5.73E-4	1.05E-3
pyrene		2.53E-4	8.81E-5	9.09E-5	3.19E-2	2.72E-4	9.70E-5	1.75E-4
C ₃ -dibenzothiophenes		3.06E-5	1.02E-5	1.08E-5	4.30E-3	3.29E-5	1.12E-5	2.08E-5
C ₂ -phenanthrenes		8.82E-5	2.99E-5	3.14E-5	5.15E-2	9.48E-5	3.29E-5	6.05E-5
C ₃ -fluorenes		5.60E-4	1.87E-4	1.98E-4	1.38E-2	6.02E-4	2.06E-4	3.82E-4
C ₁ -fluoranthenes/pyrenes		1.11E-4	3.84E-5	3.99E-5	1.32E-2	1.20E-4	4.22E-5	7.68E-5
C ₄ -dibenzothiophenes		1.08E-5	3.52E-6	3.82E-6	4.40E-3	1.16E-5	3.88E-6	7.34E-6
C ₃ -phenanthrenes		2.72E-5	9.08E-6	9.66E-6	5.90E-3	2.93E-5	1.00E-5	1.86E-5
benz[<i>a</i>]anthracene		1.04E-4	3.58E-5	3.73E-5	2.95E-2	1.12E-4	3.94E-5	7.17E-5
C ₂ -fluoranthenes/pyrenes		6.53E-5	2.22E-5	2.33E-5	1.26E-2	7.02E-5	2.44E-5	4.49E-5
C ₄ -phenanthrenes		8.87E-6	2.91E-6	3.13E-6	5.90E-3	9.54E-6	3.20E-6	6.03E-6
C ₃ -fluoranthenes/pyrenes		4.04E-5	1.35E-5	1.44E-5	1.07E-2	4.34E-5	1.49E-5	2.76E-5
C ₄ -fluoranthenes/pyrenes		2.63E-5	8.67E-6	9.32E-6	1.01E-2	2.83E-5	9.54E-6	1.79E-5

Table 5-19. Predicted fraction of aqueously dissolved mass during ascent to the sea surface for several petroleum compounds according to the TAMOC-c model, and comparison to available field observations.⁷⁵

Compound	field observations (Ryerson et al. ⁷⁵)	TAMOC-c with VDROF-J initial size distributions	TAMOC-c with custom initial size distributions	TAMOC-c with RR initial size distributions
methane	1.00	1.00	1.00	1.00
ethane	1.00	1.00	1.00	1.00
propane	0.99	1.00	1.00	0.85
benzene	1.00	1.00	1.00	0.90
toluene	0.96	0.96	0.97	0.56
<i>i</i> -C ₄	0.84	0.88	0.82	0.43
<i>n</i> -C ₄	0.74	0.87	0.81	0.42
cyclopentane	0.75	0.77	0.69	0.33
<i>o</i> -xylene	0.64	0.71	0.61	0.28
<i>p/m</i> -xylenes	0.58	0.70	0.59	0.28
cyclohexane	0.50	0.43	0.28	0.15
ethylbenzene	0.48	0.70	0.60	0.28
methylcyclopentane	0.39	0.37	0.23	0.13
methylcyclohexane	0.29	0.20	0.099	0.067
1-methyl,4-ethylbenzene	0.24	0.47	0.33	0.16
<i>i</i> -C ₅	0.26	0.43	0.27	0.15
<i>n</i> -C ₅	0.17	0.40	0.25	0.14
2,3-dimethylpentane	0.16	0.064	0.023	0.021
1-methyl,3-ethylbenzene	0.15	0.33	0.19	0.11
2-methylhexane	0.14	0.034	0.011	0.012
1,3,5-trimethylbenzene	0.13	0.40	0.26	0.14
3-methylhexane	0.11	0.045	0.015	0.015
1,2,4-trimethylbenzene	0.1039	0.3616	0.2231	0.1216
<i>n</i> -propylbenzene	0.0932	0.4255	0.2818	0.1465
1,2,3-trimethylbenzene	0.0000	0.3632	0.2241	0.1223
2,2-dimethylbutane	0.0000	0.2312	0.1127	0.0787
2,3-dimethylbutane	0.0000	0.2748	0.1419	0.0937
2-methylpentane	0.0000	0.1706	0.0754	0.0577
3-methylpentane	0.0000	0.1521	0.0652	0.0513
<i>n</i> -C ₆	0.0000	0.1287	0.0527	0.0433

5.6.9 Comparison of TAMOC-c model predictions (assuming no dispersant addition) with field observations for the fraction of aqueously dissolved mass during ascent and fractionation indices of several individual petroleum compounds

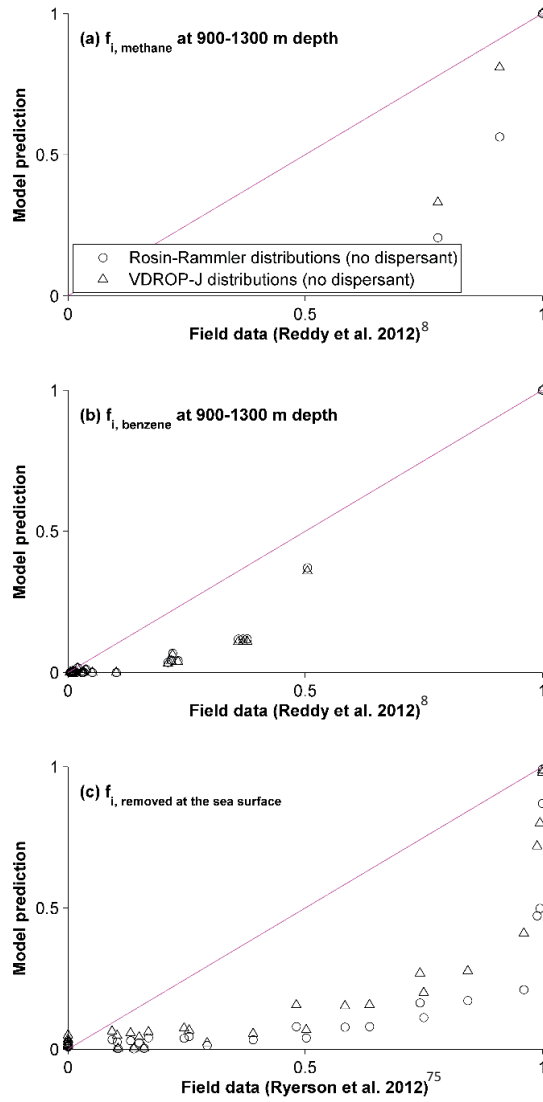


Figure 5-14. Comparison of TAMOC-c predictions with field observations for fractionation indices of several hydrocarbon compounds, evaluated at 900–1300 m depth and also at the sea surface. (a) Fractionation of C_1 – C_3 hydrocarbons in the deep-water hydrocarbon plume at 900–1300 m depth; (b) fractionation of $\geq C_6$ hydrocarbons in the deep-water hydrocarbon plume; and (c) extent of fractionation for volatile compounds at the sea surface. Displayed simulation results are based on the VDROF-J, RR, and custom initial size distributions of droplets and bubbles, without dispersant addition.

5.6.10 Estimation of the fraction of the mass flow rate of petroleum fluids trapped in the deep-water hydrocarbon plume as small droplets having slow rise velocities

We compared the composition of the deep-water hydrocarbon plume predicted by TAMOC-c simulations with that observed by Reddy et al.⁸ Based on this comparison, we infer that 1.2% of the mass flow rate of sparingly soluble petroleum compounds became trapped in the deep-water hydrocarbon plume as small droplets having slow rise velocities. This estimate is discussed in detail below.

$F_{i,\text{benzene}}$ values predicted by TAMOC-c simulations agree with observed $F_{i,\text{benzene}}$ values for predicted $F_{i,\text{benzene}}$ values ≥ 0.01 (Table 5-18). Discrepancies between predicted and observed $F_{i,\text{benzene}}$ values of up to three orders of magnitudes are noticed for compounds with predicted $F_{i,\text{benzene}}$ values < 0.01 (Table 5-18). We postulated that this could be explained by the presence of small droplets of liquid petroleum. Based on a previous approach,³¹⁴ we assumed that the following relation holds for the deep-water hydrocarbon plume:

$$C_{\text{observed},i} = C_{\text{dissolved predicted},i} + m_{\text{dead oil},i} \cdot C_{\text{droplets}}$$

Equation 5-8

where $C_{\text{observed},i}$ is the concentration of the compound i observed in the deep-water hydrocarbon plume, $C_{\text{dissolved predicted},i}$ is the concentration of the compound i predicted by TAMOC-c simulations to be aqueously dissolved in the deep-water hydrocarbon plume, C_{droplets} is the concentration of droplets estimated to be trapped in the deep-water hydrocarbon plume, and $m_{\text{dead oil},i}$ is the mass fraction of compound i in the Macondo dead oil. $m_{\text{dead oil},i}$ is chosen here as a proxy for the composition of small droplets trapped in the deep-water hydrocarbon plume. In this computation, we normalized $C_{\text{observed},i}$ so that $C_{\text{observed,benzene}} = C_{\text{dissolved predicted,benzene}}$.

We fitted the C_{droplets} value that minimizes the difference between the left hand side and right hand side of Equation 5-8. We then use this fitted C_{droplets} value to compute the fractionation index of droplets with respect to methane, $F_{\text{droplets,methane}}$, and we obtain a value of 0.012. In other words, we conclude that 1.2% of the mass flow rate of sparingly-soluble petroleum compounds became trapped in the deep-water hydrocarbon plume as small droplets having slow rise velocities. When this contribution of small droplets having slow rise velocities is added to the TAMOC-c model predictions, a good agreement with the Reddy et al.⁸ field observations is obtained for all of the compounds studied by these authors (Figure 5-15).

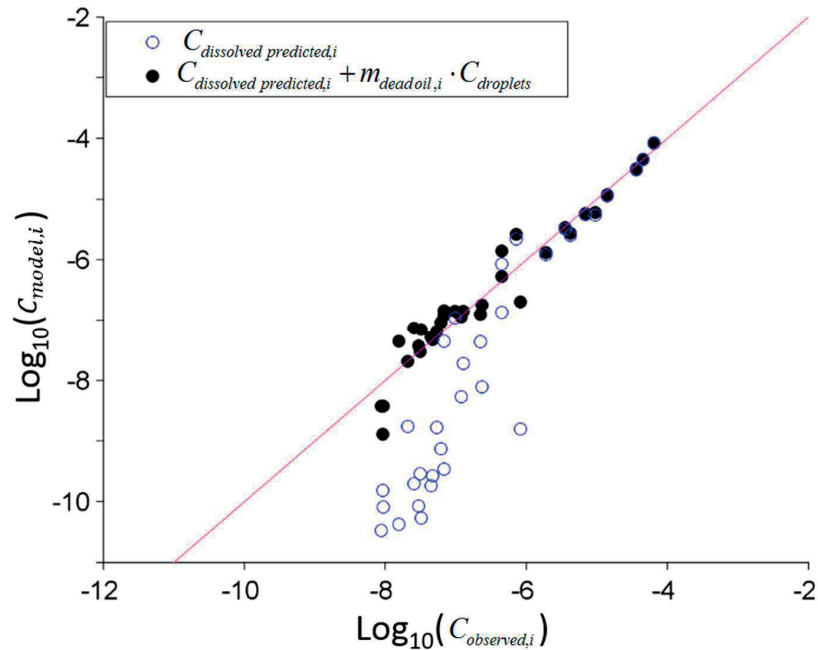


Figure 5-15. Comparison of predictions with field observations⁸ for the composition of the deep-water hydrocarbon plume. Comparisons are shown both for the case when no droplets are assumed to be present in the deep-water hydrocarbon plume ($C_{dissolved\ predicted,i}$), and for the case when 1.2% of the mass flow rate of sparingly-soluble petroleum compounds is assumed to have become trapped in the deep-water hydrocarbon plume as small droplets having slow rise velocities ($C_{dissolved\ predicted,i} + m_{dead\ oil,i} \cdot C_{droplets}$).

5.6.11 Estimated concentration of dispersant in live oil at the emission source boundary (15.5 MPa and 4.3 °C) on different days during the *Deepwater Horizon* disaster

We find that estimated concentrations of dispersant in live oil at the emission source boundary during the period after the riser was cut (June 4 to July 14) are between 2,500 and 5,300 ppm on 62% of the days (Figure 5-16). Dispersant dosages in this range (2,500–5,300 ppm) likely led to small variations in initial droplet and bubble size distributions, and therefore our TAMOC-c simulations for June 8 are likely representative of $\geq 62\%$ of the days after the riser was cut (\geq June 4). This arises because the interfacial tension of dead oil with water is 5.05 mN m^{-1} for dead oil with 2,500 ppm of Corexit EC9500A, and this interfacial tension is 4.2 mN m^{-1} for dead oil with 5,000 ppm of Corexit EC9500A. (These data, reported previously by Abdelrahim, were acquired at 25 g kg^{-1} salinity, 15.3 MPa, and $4.4\text{ }^{\circ}\text{C}$.²⁵³) Predicted droplet and bubble size distributions are not sensitive to such small variations of interfacial tension between liquid petroleum and seawater.

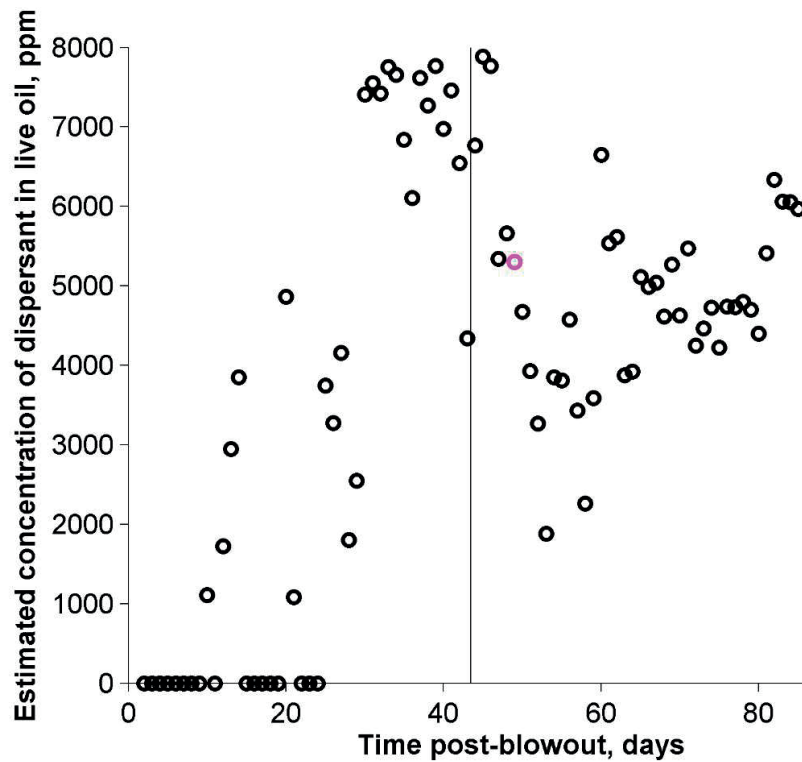


Figure 5-16. Estimated concentrations of dispersant in live oil at the emission source boundary. These estimates are based on previously reported volumetric flow rates from Appendix 3 of the *Oil Budget Calculator*.²⁵⁴ We estimated the concentration of dispersant in live oil at the emission source boundary (15.5 MPa and 4.3 °C), assuming that 100% of the injected dispersant was mixed with 100% of the live oil exiting the broken Macondo riser stub, on each day after the riser was cut (44th day, vertical line). Before the riser was cut, we computed the concentration of dispersant in live oil at the open end of the broken riser (assumed 74% of the flow based on estimates reported previously by Camilli et al.⁴⁵); no dispersant was injected at the riser kink emission location, not reported on this graph (before riser was cut, estimated to 26% of the flow⁴⁵). The pink circle represents June 8, 2010.

Chapter 6 Resolving biodegradation patterns of persistent saturated hydrocarbons in weathered oil samples from the *Deepwater Horizon* disaster

Published in: Environmental Science & Technology 2014, 48, 1628–1637
(<http://pubs.acs.org/doi/abs/10.1021/es4042836>).

Authors: Jonas Gros, Christopher M. Reddy, Christoph Aeppli, Robert K. Nelson, Catherine A. Carmichael, and J. Samuel Arey.

Contributions: This chapter was prepared principally by me. I wrote the Matlab codes for the data analysis. Christoph Aeppli, Catherine Carmichael, Christopher Reddy, and Bob Nelson conducted field sampling and laboratory analysis. Some previously published results from Christoph Aeppli are used to draw conclusions regarding the fraction of originally spilled material that remains in the environment. Christopher Reddy and Samuel Arey provided guidance to me and participated prominently in text writing and editing.

Note: An error in the Matlab built-in function `interp2` resulted in a slightly altered performance of our alignment algorithm in the published version. This chapter was updated using a version of the alignment algorithm compatible with both the bugged and non-bugged Matlab versions.

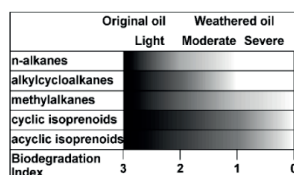


Figure 6-1. Schematic depiction of our biodegradation index.

Reproduced/adapted with permission from Environmental Science & Technology 2014, 48, 1628–1637. Copyright 2014 American Chemical Society.

6.1 Abstract

Biodegradation plays a major role in the natural attenuation of oil spills. However, limited information is available about biodegradation of different saturated hydrocarbon classes in surface environments, despite that oils are composed mostly of saturates, due to the limited ability of conventional gas chromatography (GC) to resolve this compound group. We studied eight weathered oil samples collected from four Gulf of Mexico beaches 12–19 months after the *Deepwater Horizon* disaster. Using comprehensive two-dimensional gas chromatography (GC×GC), we successfully separated, identified, and quantified several distinct saturates classes in these samples. We find that saturated hydrocarbons eluting after *n*-C₂₂ dominate the GC-amenable fraction of these weathered samples. This compound group represented 8–10%, or 38–68 thousand metric tons, of the oil originally released from Macondo well. Saturates in the *n*-C₂₂ to *n*-C₂₉ elution range were found to be partly biodegraded, but to different relative extents, with ease of biodegradation decreasing in the following order: *n*-alkanes > methylalkanes and alkylcyclopentanes+alkylcyclohexanes > cyclic and acyclic isoprenoids. We developed a new quantitative index designed to characterize biodegradation of >*n*-C₂₂ saturates. These results shed new light onto the environmental fate of these persistent, hydrophobic, and mostly overlooked compounds in the unresolved complex mixtures (UCM) of weathered oils.

6.2 Introduction

In previous chapters, we considered mass transfer processes which are dominant during the early hours to days after release of petroleum fluids. In this chapter we will focus on the longer-term fate, by considering biodegradation.

Biodegradation is a major transformation process for petroleum hydrocarbons in both surface and subsurface environments.^{105,315,316} However, it is not uniform, varying in extent, compound specificity, and relative rates for different compounds, depending on environmental conditions.^{7,316} Oil residues can persist for years in the environment without exhibiting any significant sign of biodegradation,¹⁸³ whereas under other conditions 40% of the oil can be degraded within one month.³¹⁵ Additionally, biodegradability depends on oil composition, because different compounds exhibit different susceptibilities to biodegradation.^{55,316,317} In order to understand the spectrum of fates of spilled hydrocarbons, it is therefore essential to account for the rate, extent, and possible cessation of biodegradation in relevant environmental contexts. In this chapter, we assess the biodegradation of several classes of saturated hydrocarbons (“saturates”) that are difficult to resolve and that can persist in weathered oils in surface environments.

Saturates often dominate the gas chromatography (GC)-amenable fraction of moderately weathered oils in surface environments,^{318,28,319,320} typically described as an “unresolved complex mixture” (UCM) of compounds that are difficult or impossible to separate using conventional GC-based techniques.³²¹ Early stages of weathering are typified by the loss of light compounds (<15-20 carbons) from the oil mixture through evaporation (Chapter 3),¹¹ as well as loss of two- to four-ring polycyclic aromatic hydrocarbons (PAHs) by evaporation, aqueous dissolution, and photodegradation.^{105,317,14,79} The remaining compounds in the weathered oil,

which are subject to removal principally by biodegradation,^{7,317} are usually mostly saturates.^{318,28,319,320} This oil fraction includes easily biodegradable *n*-alkanes and more resistant branched and cyclic compounds,^{6,316} as well as some highly recalcitrant biomarkers such as hopanoids or steranes³²² that biodegrade only under extreme conditions.³²³ Indirect photo-degradation can also affect saturates,^{324–326} although the time frame of this process under relevant environmental conditions remains unclear.

Despite the prominence of saturates in weathered oils,³²⁰ presently available approaches to diagnose biodegradation are centered mostly on PAHs and highly recalcitrant biomarkers.^{6,316} Several different biodegradation indices, formulated as compound concentration ratios,^{315,327} have been proposed to diagnose biodegradation in weathered oil; however most of these ratios involve PAHs and/or biomarkers (see reference¹⁵ for a compilation). In a recent review, biodegradability rankings for the “>C₁₅ category” included 10 PAH groups, 7 biomarker groups, and only 2 saturates groups (*n*-alkanes+isoalkanes group and isoprenoids group).³¹⁶ These biases partly reflect the wide use of conventional GC, which effectively separates and quantifies PAHs in weathered petroleum mixtures, but which is less effective at separating structural isomers of saturates,^{221,328} thus giving rise to the “unresolved” fraction of weathered oil, or UCM.³²¹

Compared to PAHs, limited information is available about biodegradation of different saturates classes in surface environments. Both laboratory^{329–331} and field^{332,333} studies have reported preferential biodegradation of *n*-alkanes versus acyclic isoprenoids and cycloalkanes in surface environments. However most knowledge about hydrocarbons biodegradation comes from subsurface reservoir studies.^{6,316,334} In subsurface environments, decreasing susceptibility to biodegradation is observed in the order: *n*-alkanes > 2-methyl- and 3-methylalkanes > alkylcyclohexanes and methylalkylcyclopentanes > acyclic isoprenoids.³³⁵ It remains unclear whether these trends are transferable to surface environments, where oil mixtures experience very different conditions and residence times compared to subsurface environments.

Studies on oil toxicity have largely focused on aromatic components that have important acute and chronic toxicity.^{7,28} However few studies have addressed the toxicity arising from saturates-dominated UCMs.²⁸ Narcotic-based toxicity of UCMs^{19,319} cannot be explained by resolved compounds only,²⁰ and Scarlett et al. demonstrated toxicity of the aliphatic fraction of UCMs that had been previously regarded as non-toxic.²⁹

How can we gain better insight into the composition and behavior of saturates-dominated UCMs in the environment? Comprehensive two-dimensional gas chromatography (GC×GC) provides well-resolved compositional information for weathered oil UCMs, including separation of saturates.^{65,79,217,219} This technique uses two serially joined columns to separate thousands of compounds in complex mixtures of petroleum hydrocarbons (Chapter 1). GC×GC produces a distinct elution pattern for each hydrocarbon compound class, providing an elementary means to differentiate compound classes as well as individual compounds within a class. This enables detailed knowledge about the state of biodegradation of oil. For example, Wardlaw et al. used GC×GC coupled to a flame ionization detector (FID) to study the compositional evolution of oil that was biodegraded during subsurface ascent from a reservoir to the sea

floor.⁵⁵ More recently, Mao et al. drew hydrocarbon-group windows on GC×GC-FID chromatograms to study accelerated hydrocarbons biodegradation occurring in aerobic “biopiles”.²²⁰ Mao et al successfully separated different saturates classes, observing the decreasing biodegradability preference: *n*-alkanes > branched alkanes > cyclic alkanes.

In the present study, we sought to expand information available about the biodegradation of saturated hydrocarbons occurring in the UCMs of weathered oils in surface environments. We used beached oil samples from the *Deepwater Horizon* disaster that exhibited typical signs of moderate saturates biodegradation. The *Deepwater Horizon* disaster was likely the largest accidental marine dead oil release in history³³⁶ and emitted 470-690 thousand tonnes of dead oil into the marine environment.^{8,9} This included 62³²⁰ to 74%⁸, or 291-511 thousand tonnes, of saturated oil hydrocarbons. Despite massive clean-up and countermeasure efforts, oil-soaked sand patties continued to wash ashore³²⁰ more than three years after the release. We studied saturates biodegradation in beached oil samples that were taken at four different locations at several time points 12-19 months after the release event. Relative to the original Macondo well (MW) oil, these samples had lost the most volatile (<*n*-C₁₈) and soluble compounds, providing an excellent example in which traditional GC-based techniques did not resolve meaningful compositional differences in the UCM. Using GC×GC, we observed systematic patterns in the ordering and relative extent of biodegradation among different classes of saturates compounds in these samples. The presented data improve our understanding of the compositional changes in the UCM arising from biodegradation in surface environments. This could inform future assessments of the toxicity and environmental impact of the persistent and poorly understood hydrocarbon UCM fraction of weathered oil.

6.3 Methods

6.3.1 Sample collection

Oil-soaked sand patties were collected from April to November 2011, 12 to 19 months after the beginning of the *Deepwater Horizon* oil release (Figure 6-2). Samples were composed of either a single patty or a composite of several patties collected within a few meters of each other. They were obtained from sites as far away as 200 km from the MW site, including: Perdido Beach, FL (PB), Gulf Shores, AL (GS), Chandeleur Islands, LA (CI), and Grand Isle, LA (GI). Eight samples in total were studied: B60; B92, B10, B61, and B93; B94 and B48; and B86, at PB, GS, CI, and GI, respectively. This labeling scheme was used by Aeppli et al., who confirmed that all of these samples were MW oil residues using hopane and sterane biomarkers.³²⁰ Detailed information about the weathered samples is available in the Appendix (section 6.5.1). Original, neat MW oil has been fully characterized elsewhere.⁸ Samples were taken from both “dry” locations, high above the usual shoreline (B48, B86, B92), and “wet” locations, from within the surf zone (<0.5 m depth) or intertidal zone (B10, B60, B61, B93, B94). Detailed sampling environment descriptions are provided for each sample (Table 6-1).

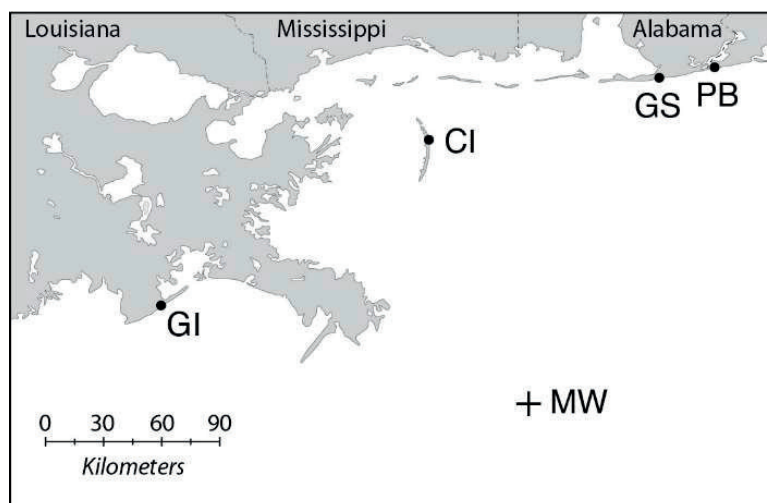


Figure 6-2. Sampling locations. The cross (+) indicates the position of the Macondo well (MW). Samples B60 and B92 were collected at Perdido Beach (PB). B10, B61, B93 and B94 were collected at Gulf Shores (GS). B48 and B86 were collected at Chandeleur Islands (CI) and Grand Isle (GI), respectively.

6.3.2 Sample extraction

Approximately 50 grams of each sample was Soxhlet extracted in dichloromethane/methanol (90/10) for 24 hours. For sub-samples, the solvent was removed via rotary evaporation and a total extractable mass was obtained. Extracts dissolved in dichloromethane/methanol were stored at room temperature until analysis.

6.3.3 Chemicals

Standards included normal alkanes, methylalkanes, farnesane, norpristane, pristane, and phytane that were obtained from Sigma-Aldrich. Alkylcyclohexanes, (4,8-dimethylnonyl)benzene, (4,8-dimethylnonyl)cyclohexane, 1,3-dimethyl-2-(3,7-dimethyloctyl)benzene, and 1,3-dimethyl-2-(3,7-dimethyloctyl)cyclohexane were bought from Chiron (Norway). Linear alkylbenzenes and PAHs were supplied by Sigma-Aldrich and Alltech. C_{30} $17\alpha(H),21\beta(H)$ -hopane and other biomarker standards were obtained from Chiron and the National Institute of Standards and Technology. Professor Roger Summons (MIT) kindly provided us alkylcyclopentanes synthesized in his laboratory.

6.3.4 GC-FID

GC-FID analysis of sample extracts was performed on a Hewlett-103 Packard 5890 Series II GC. Samples were injected splitless and separated on a Restek Rtx-1 capillary column (30 m, 0.25 mm inner diameter (I.D.), 0.25 μm film thickness) with $5 \text{ mL min}^{-1} \text{ H}_2$ as the carrier gas. The temperature program was 7 min at $35 \text{ }^\circ\text{C}$, followed by ramp to $315 \text{ }^\circ\text{C}$ at $6 \text{ }^\circ\text{C min}^{-1}$ and then to $320 \text{ }^\circ\text{C}$ at $20 \text{ }^\circ\text{C min}^{-1}$ (held 15 min).

6.3.5 GC×GC–FID

Sample extracts were injected splitless on a GC×GC–FID (Leco, St. Joseph, MI) having an Rtx-1 first-dimension column (60 m, 0.25 mm I.D., 0.25 μm film) and an SGE BPX-50 second-dimension column (1.25 m, 0.10 mm I.D., 0.10 μm film). The carrier gas was H_2 at a constant flow rate of 0.95 mL min^{-1} . The inlet temperature was held at 300 $^\circ\text{C}$. The first oven was programmed as follows: hold at 40 $^\circ\text{C}$ for 10 min, ramp from 40 to 340 $^\circ\text{C}$ at 1.00 $^\circ\text{C min}^{-1}$ (held 5 min). The second oven was programmed as follows: hold at 45 $^\circ\text{C}$ for 10 min, ramp from 45 to 345 $^\circ\text{C}$ at 1.00 $^\circ\text{C min}^{-1}$ (held 5 min). The modulation period was 15 s. The modulation was carried out using a two-stage modulator, cooled with liquid nitrogen.

Using a series of calibration solutions of standards, co-authors from Woods Hole Oceanographic Institution determined that the relative response factors of petroleum hydrocarbons in our samples were all near unity (root mean squared deviation of $\sim 10\%$ for saturates in the $n\text{-C}_{25}$ region), for both GC–FID and GC×GC–FID analysis. This implies that total FID signal recorded is proportional to mass present in the samples, which allowed quantification of aggregated compound groups as well as comparisons of mass changes in the entire saturate elution region between different GC×GC chromatograms. To aid in the identification and confirmation of some compounds, samples were also analyzed by GC×GC–TOF-MS, described in Appendix section 6.5.2.

6.3.6 Data analysis of GC×GC–FID chromatograms

Several operations were performed on the GC×GC–FID data (except where stated otherwise, “GC×GC” refers to GC×GC–FID). First, the baseline was corrected^{68–70} and the chromatograms were normalized.¹⁵ Second, retention times were aligned using our alignment algorithm (Chapter 2) to allow pixel-by-pixel comparisons between chromatograms,⁶⁷ and signal cutoff was defined in order to remove poorly resolved background signal. These tasks were conducted using a combination of pre-packaged algorithms and elementary Matlab operations.^{67–70,100} The techniques are relatively straightforward to apply, and the different steps are described in detail below. Several applied Matlab protocols are freely available at <https://github.com/jsarey/>.^{69,100}

Although GC×GC separates petroleum hydrocarbons more effectively than GC, some areas of the GC×GC chromatogram exhibit a locally elevated baseline, indicative of material that remains unresolved (Figure 6-3). This occurs especially in the saturates region of GC×GC chromatograms (Figure 6-4); hence the choice of baseline treatment may affect quantification of the saturated hydrocarbons (section 1.3.1). Two different baseline correction methods were applied, reflecting different aims: the method of Reichenbach et al.,⁷⁰ in which the baseline is defined conservatively using a white-noise criterion; and the polynomial-fitting baseline estimation code of Eilers.^{68,69} The method of Reichenbach et al., which allows depiction of coeluting material in areas of locally elevated signal, was used for visual comparisons between chromatograms and estimates of total resolved+unresolved mass in the saturates sub-region of the chromatograms. Default parameters were used (five deadband pixels per modulation; filter window size of seven pixels; ratio of 3.5 for the expected value of baseline plus noise to

the estimated standard deviation of the noise; one baseline value per modulation). However, for the quantification of individual resolved compounds, Eilers' baseline correction was applied, in order to minimize interference from unresolved material. With appropriate parameters, Eilers' method is designed to follow the base of the resolved peaks, whereas Reichenbach's method preserves unresolved signal. For Eilers' method, we chose parameter values of 10^4 for λ , 0.02 for p , and 2 for d . We refer to the signal retained after Eilers' baseline correction as the *resolved* signal.

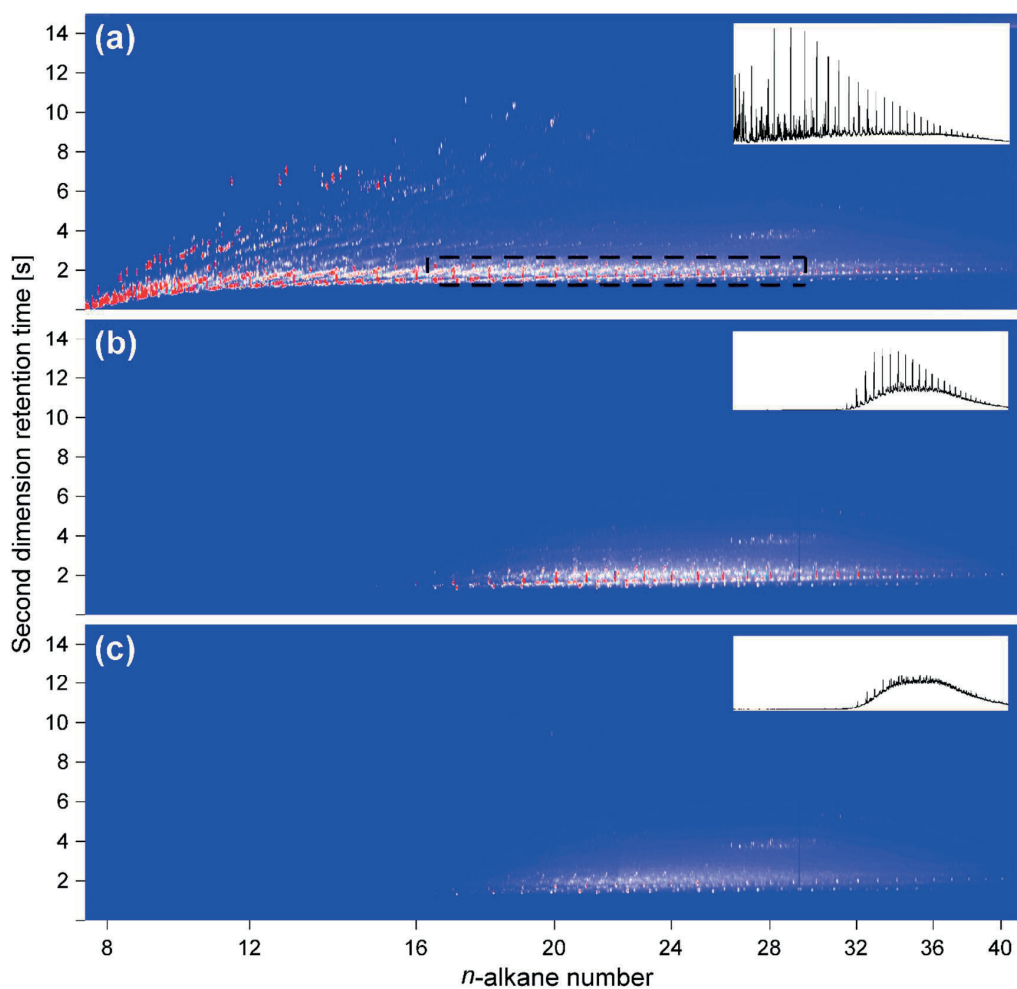


Figure 6-3. GCxGC-FID chromatograms of (a) original MW oil, (b) weathered sample B86, and (c) B92. The black rectangle shows the sub-region that was studied in detail. This area contains most of the resolved compound mass of the weathered sample chromatograms (72% for B86 and 59% for B92). Insets: corresponding GC-FID chromatograms (n -C₈ to n -C₄₁) are displayed for comparison.

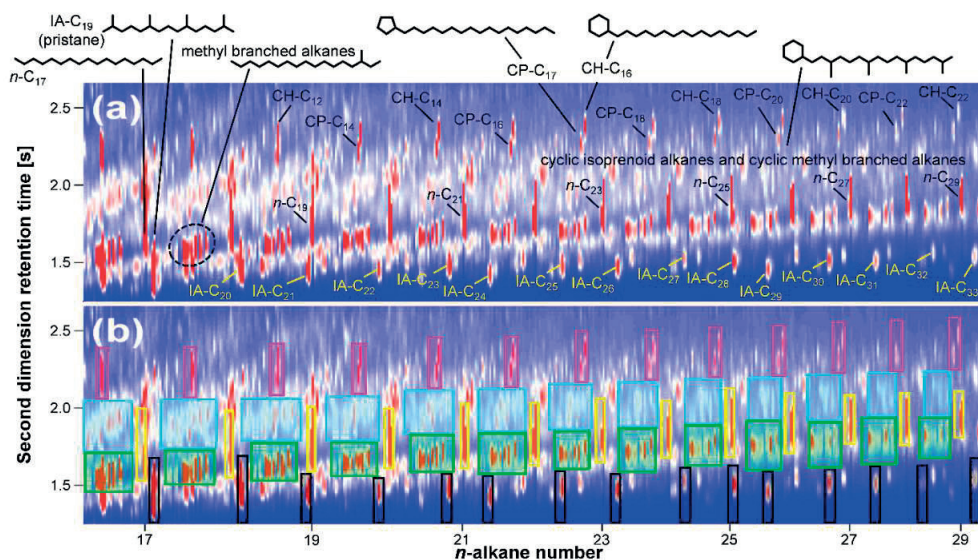


Figure 6-4. (a) Zoom on the GCxGC–FID sub-region studied (demarcated in Figure 6-3a) for the original MW oil chromatogram. (b) Same sub-region overlaid with the integration boxes used: acyclic isoprenoids (black rectangle); methylalkanes (green rectangle); *n*-alkanes (yellow rectangle); cyclic isoprenoids (blue rectangle); and alkylcyclopentanes and alkylcyclohexanes (pink rectangle).

After baseline correction, chromatograms were normalized such that the peak volume of C_{30} 17 α (H),21 β (H)-hopane is the same in all chromatograms. This conserved biomarker is often used to normalize GCxGC chromatograms, because it has been found to biodegrade only under extreme conditions.^{14,15,55,65,322} Volumes of the C_{30} 17 α (H),21 β (H)-hopane peaks were computed with the Arey et al. Gaussian-peak fit code.¹⁵

Our analysis focused on the saturates region eluting from *n*-C₁₇ to *n*-C₂₉ (Figure 6-3a), since this represented the dominant GC-amenable fraction of material in collected samples. Retention time reproducibility between chromatograms was improved within this sub-region by aligning all the weathered oil chromatograms to the original MW oil chromatogram, using the algorithm described in Chapter 2.⁶⁷ This method relies on user-selected alignment points that represent identical analytes identified by the user in both the reference (original oil) and target (weathered sample) chromatograms. Twenty-one alignment points were chosen in the sub-region studied (Figure 6-10). Finally, pixels with low remaining signal (<10⁴ in FID signal units) were considered to represent noise and poorly resolved background, and these were set to zero. This noise cutoff value corresponded to ~15% of the apex value of the smallest peak of interest in this study.

For quantification of individual resolved compounds or compound groups, we delineated rectangular borders around each compound or group of compounds. These “boxes” were drawn to include the desired peak or group of peaks, while excluding other compounds or excessive baseline area, in all the chromatograms studied (Figure 6-4b). This approach was considered likely to give consistent results for quantifying signal changes in this very information-dense region of the chromatogram, compared to algorithms^{71,337} that attempt to delineate individual analyte peaks in an automated way. The baseline correction method of Eilers is designed to eliminate low frequency signal arising from poorly resolved material, which enables the

estimation of peak volumes by the sum of the pixels included in the boxes. A remaining fraction of <15% (<5% for *n*-alkanes) in a given box, relative to MW oil, was considered as background and set to zero. Our signal integration procedure is analogous to methods used by Mao and coworkers^{73,220} and Frysinger et al.²¹⁸

To estimate the uncertainty of our quantification method, we analyzed our most weathered sample (B93) in triplicate, with three GC×GC injections over three days. The subsequent numerical treatment was applied separately to each of the three chromatograms produced. We obtained standard deviations of 8.8 and 6.1% for quantification of cyclic isoprenoids and acyclic isoprenoids, respectively, relative to C₃₀ 17α(H),21β(H)-hopane. Other compound classes were mostly degraded in this sample. We thus estimated the overall uncertainties in reported analyte relative abundances to be ≤10%.

6.4 Results and Discussion

6.4.1 GC–FID and GC–MS chromatograms of weathered samples

The GC–FID chromatograms of weathered samples exhibit a poorly separated UCM (insets in Figure 6-3b,c and Appendix Figure 6-9). This is typical for a GC–FID chromatogram of a weathered crude oil, resulting from ineffective separation of the mixture that remains after the preferential removal of abundant compounds such as *n*-alkanes.^{219,338} In response to a suggestion of one reviewer we also briefly investigated whether GC–MS would be effective for the quantification of the compounds studied here. In short, it would be difficult to quantify individual analytes from the resulting mass spectrum data, because individual saturate compounds co-elute severely and give rise to highly fragmented and very similar spectra (Appendix section 6.5.5). Compounds in UCMs, which can arise from samples having different compositions, are estimated to number more than 100,000.^{219,339} Beyond a certain extent of biodegradation, all UCMs appear similar (Appendix Figure 6-9c to Figure 6-9h); consequently further compositional changes from biodegradation are not discernible.³¹⁶ Increased instrument separation capacity is needed to investigate further these apparently compositionally similar UCMs, and to determine whether this similarity is real and whether the biodegraded oil eventually reaches a terminal composition.²¹⁹

6.4.2 GC×GC chromatograms of weathered samples

Compared to GC, GC×GC provides improved separation of petroleum-derived UCMs.^{79,328} In the GC×GC chromatogram of original MW oil (Figure 6-3a), *n*-alkanes elute early in the second dimension, forming regularly spaced prominent peaks. Other saturate compounds elute shortly afterwards in the second dimension. The biomarkers steranes and hopanes elute between *n*-C₂₆ and *n*-C₃₅ in the first dimension and between 3.5 and 5.5 s in the second dimension. PAHs elute earlier than *n*-C₂₃ in the first dimension and later than 3 s in the second dimension, differentiating them clearly from the saturate region. These elution patterns are typical for petroleum mixtures, as expected from a separation according to volatility in the first dimension and according to polarity in the second dimension.^{39,79,219}

GC×GC chromatograms of the weathered samples contained mostly low-volatility saturates. Relative to the neat MW oil, our weathered samples exhibit total loss of two-ring PAHs and >65% loss of three-ring PAHs, as well as losses of compounds eluting in the n -C₈ to n -C₁₈ region (Figure 6-3). These loss patterns correspond to removal due to aqueous dissolution (which proceeds roughly from the top left corner in the direction of the bottom right corner of the GC×GC chromatograms, Figure 3-3b) and to evaporation (which removes compounds from left to right in the chromatograms), as was discussed in Chapter 3.^{14,39} These processes have left behind a mixture of which the GC-amenable fraction is mainly saturates having >18 carbons. Due to their low volatilities and low aqueous solubilities,¹⁵⁶ these saturates are not expected to appreciably evaporate or dissolve further. We focused our analysis on the saturates sub-region eluting between n -C₁₆ and n -C₂₉ (black rectangle in Figure 6-3a). This area contains ~60 and ~70% of the resolved GC×GC signal of the weathered samples B92 and B86, respectively. Saturates compounds eluting after n -C₂₂ are most likely acted upon only by biodegradation.³¹⁷ The loss patterns of > n -C₂₂ saturates are not consistent with either evaporation or dissolution signatures that are usually observed for lighter compounds (Chapter 3),^{181,317,11,14} although we note that unusual environmental conditions exceptionally can cause fractionation of >C₂₂ hydrocarbons.³⁴⁰ Additionally, saturates are not expected to photodegrade easily, based on their molecular structure¹⁵⁶ and results from photooxidation experiments.^{317,341}

The GC×GC sub-region depicted in Figure 6-4 contains five principal saturates classes, annotated on the chromatograms, including: n -alkanes, methylalkanes, alkylcyclopentanes+alkylcyclohexanes, acyclic isoprenoids, and cyclic isoprenoids. Methylalkanes elute in the order 3-methyl, 2-methyl, 4-methyl, 5-methyl, 6-methyl (decreasing first dimension retention times). Among alkylcycloalkanes, the alkylcyclohexane always elutes slightly later in the second dimension compared to the alkylcyclopentane structural isomer, and also elutes later in the first dimension for the >C₁₈ carbon isomers. Each compound or compound class was identified with pure standards and using GC×GC-TOF-MS (Appendix Figure 6-14).

In order to visualize trends of compound mass losses, we applied algebraic operations directly to the chromatographic data and thus constructed pixel-by-pixel percent mass loss chromatograms (PMLCs; Figure 6-5). PMLCs correspond to the percent of signal lost from the weathered sample chromatogram relative to the original MW oil chromatogram, computed for each pixel (normalized to C₃₀ 17 α (H),21 β (H)-hopane). These operations were enabled by low retention time variability between chromatograms, further improved by chromatogram alignment. The root mean squared deviation (rmsd) values of the positions of the alignment points used were 0.9 and 5.4 pixels in first and second dimension, respectively, before alignment. After alignment, rmsd values were reduced to 0.5 and 2.4 pixels, according to the leave-one-out test described in Chapter 2,⁶⁷ indicating good retention time matching between chromatograms. On PMLCs, the position of the evaporation front, corresponding to a systematic removal of compounds along the first dimension,¹⁵ can be identified easily (e.g., near n -C₁₈ for sample B86; near n -C₁₉ for sample B92). PMLCs allow comparisons within compound classes: on visual inspection, there appear to be no preferential degradation among different methylalkane isomers, and alkylcyclohexanes and alkylcyclopentanes also appear degraded to similar extents (Figure 6-5).

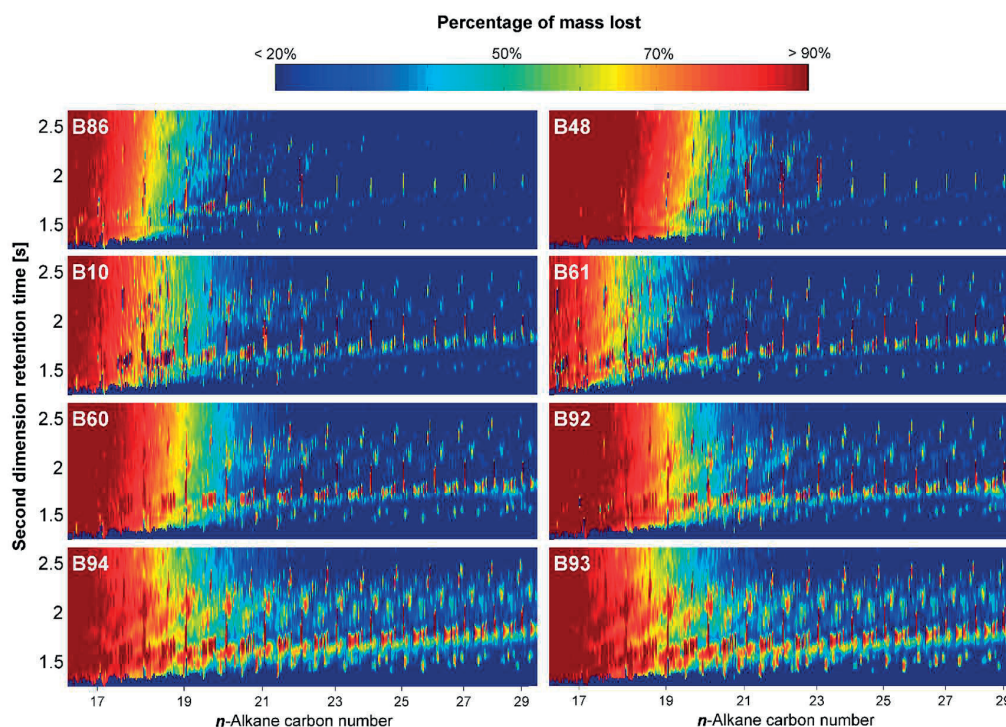


Figure 6-5. Percentage of mass lost, computed pixel by pixel for the GCxGC sub-region studied (Figure 6-3a) relative to original MW oil, for all the samples studied. To limit noise in the figure, pixels with signal $<10^5$ (FID signal units) in MW oil were shaded dark blue. Refer to Figure 6-4 for the positions of saturates compound classes.

6.4.3 Percent mass losses of saturates compound classes

In order to quantify degradation extent for saturates eluting in the $n\text{-C}_{17}\text{--}n\text{-C}_{29}$ window, we computed peak volumes inside designated rectangular borders: rectangular boxes were drawn on the GCxGC chromatograms (Figure 6-4b), and the volumes of the resolved peaks situated within each box were estimated by the sum of the pixels contained in the box after applying Eilers' baseline correction (see section 6.3.6).

Several distinct degradation patterns are visible (Figure 6-6, Appendix Figure 6-15). Normal alkanes are initially preferentially lost (Figure 6-5, Figure 6-6, Appendix Figure 6-15), consistent with their known high susceptibility to biodegradation.^{6,316} In the original MW oil, n -alkanes represent 40-50% of the total resolved mass of the saturates in the GCxGC sub-region studied, but these compounds are >95% depleted from the most weathered samples (Figure 6-6). Methylalkanes and alkylcyclopentanes+alkylcyclohexanes are degraded to similar extents throughout the sample set, independently of the position of the methyl group. They are degraded concomitantly with n -alkanes but to a lesser extent than n -alkanes. For all but the least weathered samples (B86 and B48, <20% n -alkanes depletion), acyclic and cyclic isoprenoid saturates exhibit the lowest extent of degradation compared to the other saturates classes. In the most weathered samples, the resolved signal in the sub-region studied is dominated by isoprenoid saturates (27-33%; Appendix Figure 6-15).

We think that biodegradation is the principal transformation process affecting $>C_{22}$ saturates in the samples studied here, rather than photodegradation. The biodegradability of saturated hydrocarbons is widely established.^{6,7,316,335} Indirect photodegradation of saturates has been observed in both laboratory and field studies.^{324,326} However, compared to other petroleum hydrocarbons, saturates are the least susceptible to indirect photodegradation,^{156,317,341} and the relevant time frames for photo-oxidation of saturates under environmental conditions are not well established. Among the five saturates families that we studied, extent of mass loss is found to decrease in the order: *n*-alkanes > methylalkanes and alkylcyclopentanes+alkylcyclohexanes > cyclic and acyclic isoprenoids. This depletion pattern is consistent with previous findings that biodegradation rates of aliphatic compounds decrease progressively with increased branching of the molecular structure.^{316,335,342} In contrast, we expect photo-generated oxidants to attack aliphatic compounds with rates decreasing in the order: highly-branched > less-branched > non-branched.^{343,344} Hence, in our samples, the observed loss patterns for saturates are consistent with a biodegradation process, which is expected to transform less-branched saturates more quickly than more-branched saturates, whereas abiotic oxidation processes would be expected to produce the opposite mass loss pattern.

6.4.4 A new biodegradation index for oil weathering in surface environments

Aware of the biases in traditional indices for biodegradation (see Introduction), we propose a new diagnostic for saturates biodegradation in moderately weathered oils in surface environments. We developed an index that incorporates information about the observed losses of the five different saturates classes considered here. The “saturates biodegradation index”, I_s , was defined as:

$$I_s = F_n + F_b + F_i$$

Equation 6-1

where F_n is the fraction of *n*-C₂₂ to *n*-C₂₉ *n*-alkanes remaining in the weathered sample relative to original MW oil; F_b is the fraction remaining for alkylcyclopentanes+alkylcyclohexanes and methylalkanes in the *n*-C₂₂ to *n*-C₂₉ elution window; and F_i is the fraction remaining for acyclic and cyclic isoprenoid compounds in this window. For the terms where two compound classes are grouped together (for example, F_i groups cyclic isoprenoids and acyclic isoprenoids), the term corresponds to the mean value of the two fractions remaining for the two classes. For each compound class, the fraction remaining is computed with respect to the original MW oil content normalized to C₃₀ 17 α (H),21 β (H)-hopane. The index definition is independent of the quantification procedure, and alternative quantification procedures could be used, assuming they are reliable for the compounds incorporated into Equation 6-1. By excluding compounds eluting before *n*-C₂₂, the index is designed to be unaffected by evaporation processes relevant to surface environments. The new biodegradation index may vary between a value of 3 (corresponding to the saturates composition of the original oil) and a value of 0 (corresponding to complete degradation of the five classes of saturates considered by the index). We defined index values of $3 > I_s > 2$ as “light” biodegradation, $2 > I_s > 1$ as “moderate” biodegradation, and $1 > I_s > 0$ as “severe” biodegradation.

Ordering our samples by weathering extent according to I_s (Figure 6-6), we obtain a sequence similar to that inferred from n -C₁₈/phytane ratios computed for the same samples by Aeppli et al.³²⁰ In fact, I_s was found to correlate well with the n -C₁₈/phytane ratio ($r^2=0.95$; Appendix Figure 6-17), for this sample set, corroborating previous evidence that the n -C₁₈/phytane ratio is a good indicator of saturates biodegradation.^{6,316,333} However, removal by evaporation appeared to be important for compounds eluting up to n -C₁₈ or n -C₁₉, depending on the sample (Figure 6-5); consequently some evaporation impact on the n -C₁₈/phytane ratio cannot be ruled out, since n -C₁₈ and phytane likely have slightly different vapor pressures. (n -C₁₈ and phytane exhibit slightly different GC×GC 1st dimension elution times, indicative of a difference in vapor pressures.³⁹) We consider the new saturates index, I_s , to be more robust than previously proposed biodegradation indices for saturates. Equation 6-1 incorporates information about five major classes of saturates that span a broad range of susceptibility to biodegradation.

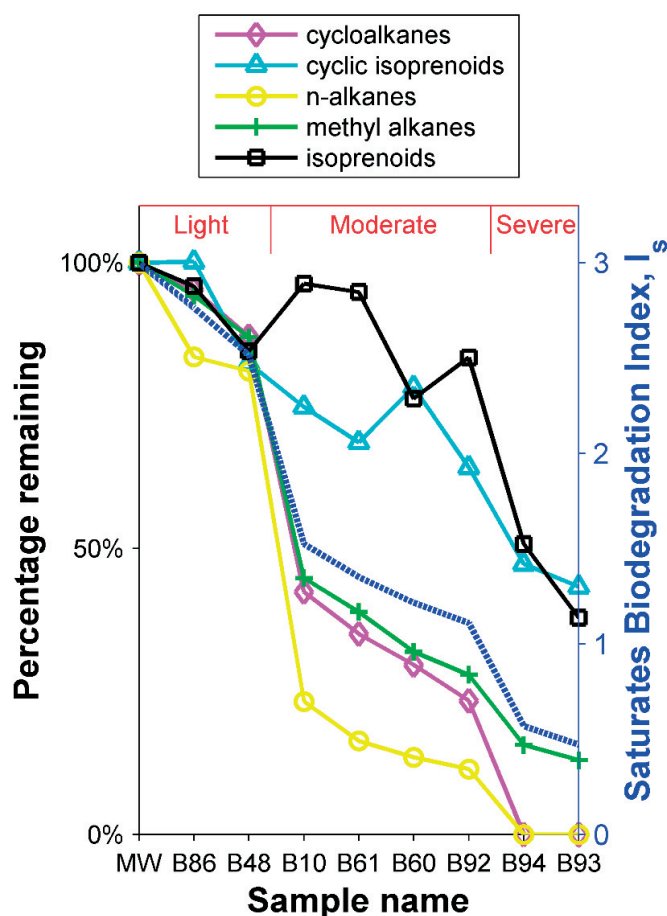


Figure 6-6. Percentage remaining for different classes of saturates eluting in the n -C₂₂ to n -C₂₉ elution range, relative to the original MW oil, after normalisation to C₃₀ 17 α (H),21 β (H)-hopane (left axis). Samples are ordered from least to most biodegraded (bottom axis). Saturates biodegradation index values as given by Equation 6-1, I_s (blue dashed line), are shown for each sample (right axis), and corresponding biodegradation classifications (light, moderate, severe) are displayed (top axis).

According to the new index, biodegradation extent is correlated to time of environmental exposure: ordering our samples by I_5 value corresponds roughly to ordering them by sampling time (Appendix Figure 6-16). Some discrepancies exist between samples taken at similar times, reflecting differences in the individual histories of the investigated sand patties. Three samples were taken in relatively dry beach locations, away from the shoreline (B86, B48, and B92), whereas the other samples were taken from within or near the surf zone and were considered as wet locations (Table 6-1). The samples from dry locations all exhibit higher I_5 values than samples collected from wet locations at the same period. Samples taken from wet locations exhibited low sample-to-sample variability at each sampling time point, and these samples display a consistent trend of decreasing I_5 value with increasing time (Appendix Figure 6-16). The quantitative differentiation of biodegradation extent in wet versus dry beach environments provides direct information about exposures faced by organisms in these different habitats. Additionally, the observed disparities in I_5 values in wet environments versus dry environments support the interpretation that depletion of $>C_{22}$ saturates resulted primarily from biodegradation rather than from indirect photodegradation.

6.4.5 Implications for oil weathering in the environment

GC×GC elucidates compositional differences in UCMs that appear otherwise similar with conventional GC analysis. This allowed us to quantify differences in biodegradation extent among five classes of saturates in weathered oil samples taken from several field sites. For these compound classes, we find that biodegradation is not a simple stepwise process. Rather, different classes are consumed simultaneously but to different extents, implying different biodegradation rates for these compounds. These results are based on the unprecedented quantification of relative abundances of several saturates classes achieved by the GC×GC techniques applied here. Our results are consistent with previous indications that increased aliphatic branching is associated with decreased biodegradation rate,³⁴² as well as previous evidence for the preferential biodegradation of *n*-alkanes versus isoprenoids.³¹⁶

Based on the characteristic degradation patterns of saturates identified in weathered oil samples, we propose a new quantitative biodegradation index that allows the classification and ordering of samples having different biodegradation extent. The proposed biodegradation index succinctly and quantitatively conveys the time-dependent compositional evolution of $>C_{22}$ saturates, analogous to the traditional *n*-C₁₇/pristane and *n*-C₁₈/phytane ratios.^{333,345–348} Observed index variability among different samples is explained by residence time in the surface environment and by the suitability of local conditions for biodegradation. The index is a transferable metric to quantify these differences in biodegradation extent among different samples. The $>C_{22}$ saturates represent a large fraction of the persistent oil residues. Thus the proposed index could inform overall mass balance estimates of weathered oil persisting from the *Deepwater Horizon* release, and it may also be a useful indicator in toxicity assessments of this long-lived material.

What did our samples reveal about the fate of MW oil in Gulf of Mexico coastal environments? Example mass apportionment calculations are shown here for our most weathered sample,

B93, collected 19 months after the beginning of the oil release. Compounds lighter than n -C₁₆ were totally absent from sample B93, with partial mass losses observed in the n -C₁₆– n -C₂₂ elution region. For this sample, observed $\leq n$ -C₂₂ losses correspond to 59% of the original MW oil mass (Appendix section 6.5.10), based on GC×GC chromatogram data and simulated distillation data.^{8,233} This loss pattern is consistent with removal by evaporation and dissolution, but photodegradation and biodegradation also probably participated in the mass depletion of the $\leq n$ -C₂₂ fraction. In this same sample, mass losses in the $>n$ -C₂₂ elution region correspond to a disappearance of 9% of the original oil mass, and this is attributed primarily to biodegradation (Appendix Figure 6-18). Additionally, based on simulated distillation data, 14% of the original MW oil mass is not GC×GC-amenable and its fate cannot be assessed with this technique.^{8,233} After accounting for these different apportionments for sample B93, 18% of the original MW oil mass was estimated to remain in the GC×GC chromatogram (Appendix Figure 6-18). The original MW oil contained 8-10% $>n$ -C₂₂ saturates (our estimate), and sample B93 still contained more than half (56%) of this original $>n$ -C₂₂ saturates load. These example calculations are relevant to the 38-68 thousand metric tons of $>C_{22}$ saturates material released into the marine environment during the *Deepwater Horizon* disaster.

Consideration of both GC-amenable and non-GC-amenable fractions of weathered sample B93 leads to a more global understanding of the fate of MW oil (Figure 6-7). According to silica-gel flash column chromatography analysis, $\frac{2}{3}$ of sample B93 was constituted of mostly non-GC-amenable oxygenated compounds, and the bulk sample contained 9.8% oxygen (compared to the oxygen content of 0.4% in MW oil).³²⁰ Hence 31% of the initial oil mass remained in the most weathered sample as oxygenated residues, invisible to GC-based analysis (Appendix section 6.5.10). Therefore disappearance of compounds from the GC×GC chromatogram should not be regarded as synonymous with removal from the weathered sample, because a significant fraction of the weathered oil cannot be measured with this technique and may remain in the residue as transformation products. Formation of oxygenated products (carboxylic acids) during oil aerobic biodegradation has been previously reported.³⁴⁶ Recent analysis shows that disappearance of some saturates correlates with the formation of (mostly non-GC-amenable) oxygenated weathering products.³⁴⁹ Straight-chained carboxylic acids, attributed to degradation products of saturated hydrocarbons, were also recently identified in these samples.³²⁰ Carboxylic acid-substituted degradation products of these saturated hydrocarbons may have direct environmental impact: terminal carboxylic acid derivatives of several saturates classes have been found toxic to aquatic organisms.³⁵⁰

In summary, in the warm climate of the Gulf of Mexico, which favors rapid weathering, mass transfer and mineralization processes are estimated to have removed only 51% of the original oil load from our most weathered oil-soaked sand patty (B93), 19 months after the explosion of the *Deepwater Horizon* platform (Figure 6-7b, section 6.5.10). The remaining 49% manifests as a mixture of persistent and partly degraded compounds, consisting of aromatics (4%), saturated hydrocarbons (14%), and non-GC-amenable oxygenated compounds (31%), in sample B93 (Figure 6-7b).

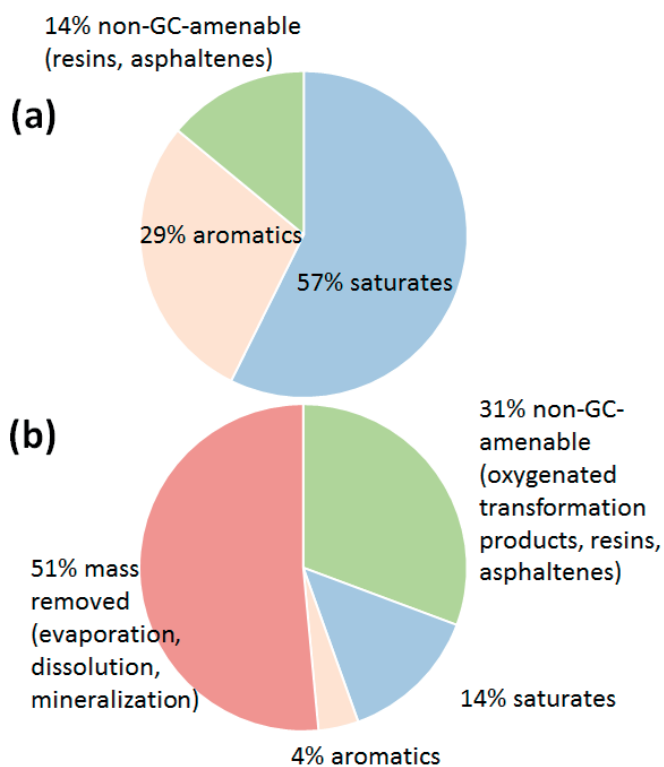


Figure 6-7. (a) Composition of the original MW oil, based on simulated distillation data (non-GC-amenable percentage)^{8,233} and silica-gel flash column chromatography analysis.³²⁰ (b) Apportionment of the oil that led to sample B93, including compounds removed through mass transfer or mineralization, and remaining mass, further divided into aromatics, saturates and oxygenated compounds based on silica-gel flash column chromatography data.³²⁰

6.4.6 Acknowledgement

This research was supported by grants from the NSF (OCE-0960841 and EAR-0950600), the BP/the Gulf of Mexico Research Initiative (GoMRI-015), and the DEEP-C consortium. We thank Paul H. C. Eilers for allowing free access to his baseline correction code.

6.5 Appendix

6.5.1 Samples information

Table 6-1. Sample list, with sampling date and location.¹

label	date	location	lat. (°N)	long. (°W)	Local sampling environment
B10	04/05/11	Gulf Shores, AL (GS)	30.24	87.74	>1" sand patties taken in surf zone along entrance to inlet at lifeguard stand #6.
B48	04/06/11	Chandeleur Islands, LA (CI)	29.95	88.82	Thick sand patty mats 1-2" thick collected high on beach (50 yards from the usual shoreline). Samples were dry and partially covered with new sand.
B60	07/17/11	Perdido Beach, FL (PB)	30.29	87.48	Round <1" sand patties, collected in knee-deep water in the surf zone.
B61	07/17/11	GS	30.24	87.74	Collected in ankle-deep water at mouth of inlet during incoming tide.
B86	07/19/11	Grand Isle, LA (GI)	29.17	90.08	Large, flattened, dry sand patty embedded in the surrounding sand collected high on beach near beach grass. Sample was dug out of the sand.
B92	11/27/11	PB	30.29	87.48	~1 cm flat sand patties found high on the beach, near grass dunes. Sand patties were covered with a layer of loose sand that was brushed away for sampling.
B93	11/27/11	GS	30.25	87.69	Large and small samples collected from the intertidal zone. Samples had recently been deposited on beach by surf, still wet. Most samples were found at the same height on the beach.
B94	11/28/11	GS	30.24	87.74	Large and small samples collected from the intertidal zone. Samples had recently been deposited on beach by surf, still wet. Most samples were found at the same height on the beach.

¹ A typographical error (i.e., the use of the "-" sign) in the longitudinal data reported by Aeppli et al. (2012)³²⁰ was corrected here.



Figure 6-8. Photographic images of samples B48 (top) and B10 (bottom). Sample B48 was taken at Chandeleur Islands, LA, on April 6, 2011. Sample B10 was taken at Gulf Shores, AL, on April 5, 2011.

6.5.2 GC×GC coupled to time-of-flight mass spectrometry (GC×GC–TOF-MS)

Weathered oil sample extracts were analyzed by GC×GC–TOF-MS (Leco) with the following instrument settings. The first-dimension was an Rtx-1 column (30 m, 0.25 mm I.D., 0.25 μm film). The second-dimension was an SGE BPX-50 column (1.25 m, 0.10 mm I.D., 0.10 μm film). Inlet temperature was 300 $^{\circ}\text{C}$. The injection mode was splitless and the carrier gas was He at a constant flow rate of 1 mL min^{-1} . The first oven was programmed as follows: hold at 100 $^{\circ}\text{C}$ for 0.50 min, ramp from 100 to 150 $^{\circ}\text{C}$ at 10 $^{\circ}\text{C min}^{-1}$, and 150 to 320 $^{\circ}\text{C}$ at 0.75 $^{\circ}\text{C min}^{-1}$. The second oven was programmed as follows: hold at 110 $^{\circ}\text{C}$ for 0.25 min, ramp from 110 to 160 $^{\circ}\text{C}$ at 10 $^{\circ}\text{C min}^{-1}$, and 160 to 330 $^{\circ}\text{C}$ at 0.66 $^{\circ}\text{C min}^{-1}$. The modulation period was 15 s. The TOF source temperature was 225 $^{\circ}\text{C}$ and the detector voltage was 1525 Volts. The TOF detector signal was sampled at 50 spectra per second. The mass spectrometer employs 70 eV electron ionization energy and operates at a push pulse rate of 5 kHz.

6.5.3 GC-FID chromatograms

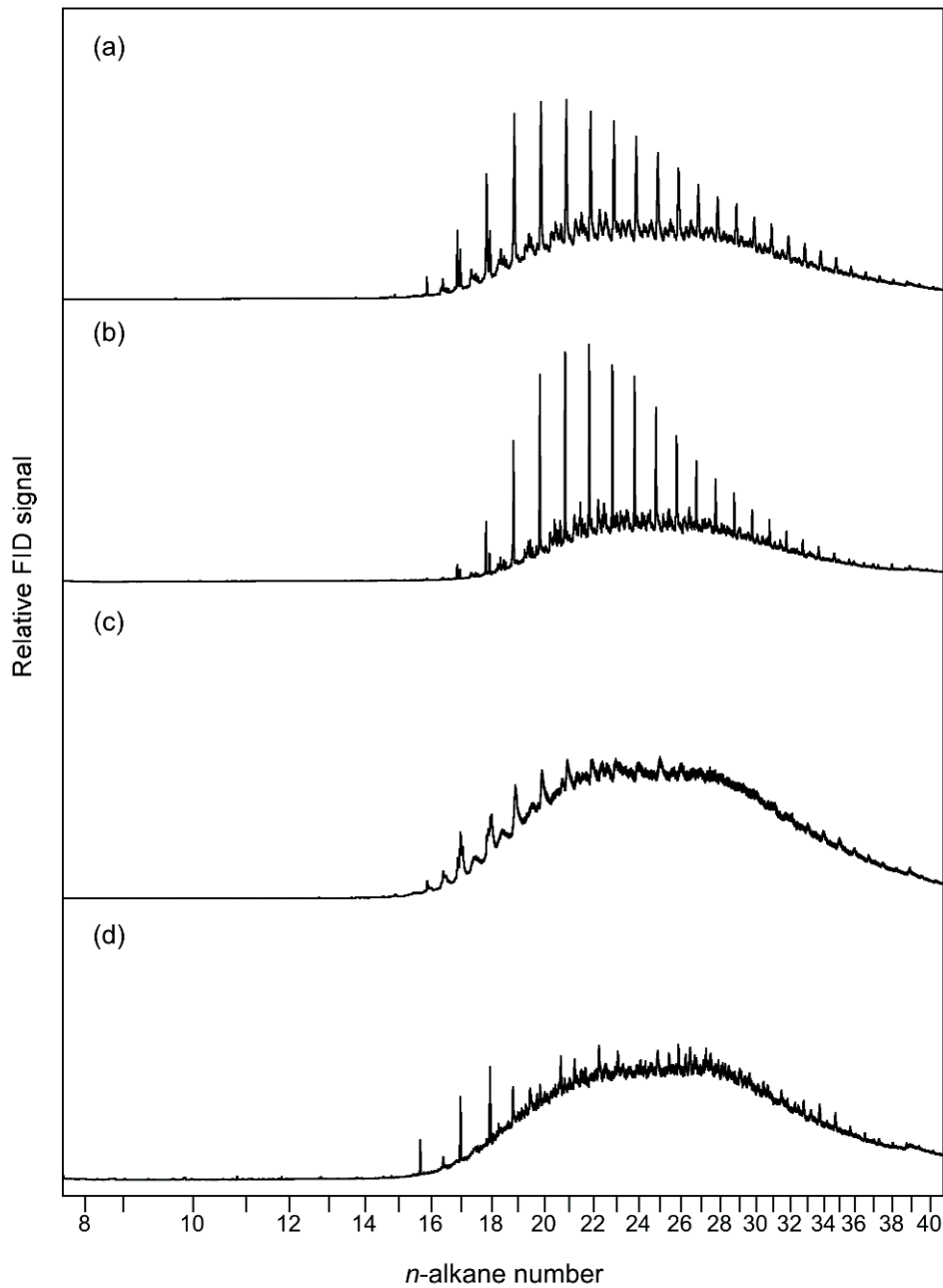


Figure 6-9. GC-FID chromatograms of sample extracts (a) B86, (b) B48, (c) B10, and (d) B61. See Table 6-1 for sampling locations and dates.

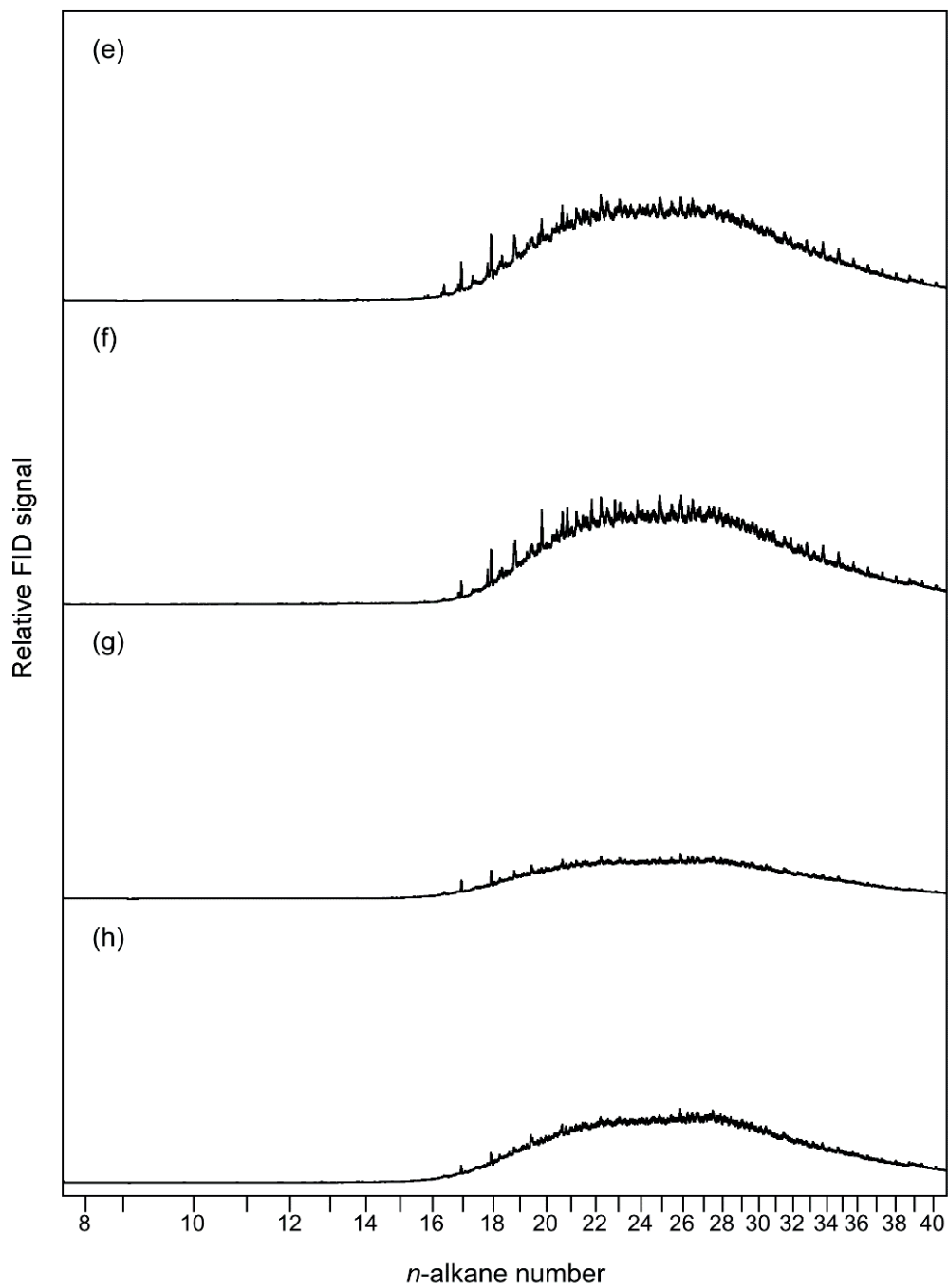


Figure 6-9 (continued). GC-FID chromatograms of sample extracts (e) B60, (f) B92, (g) B94, and (h) B93. See Table 6-1 for sampling locations and dates.

6.5.4 Alignment points

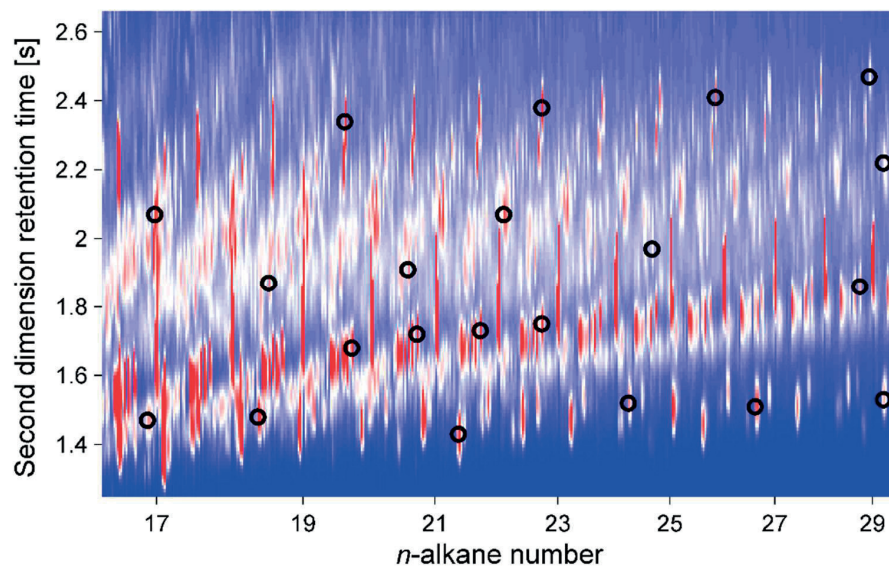


Figure 6-10. GCxGC subregion studied (demarcated in Figure 6-3a), shown here for the original MW oil chromatogram. Black circles indicate positions of the alignment points used for chromatogram alignment.⁶⁷ Only alignment points corresponding to compounds still present in a weathered sample were used to align it to the MW oil chromatogram.

6.5.5 Investigation of GC-MS ability to separate the compounds studied

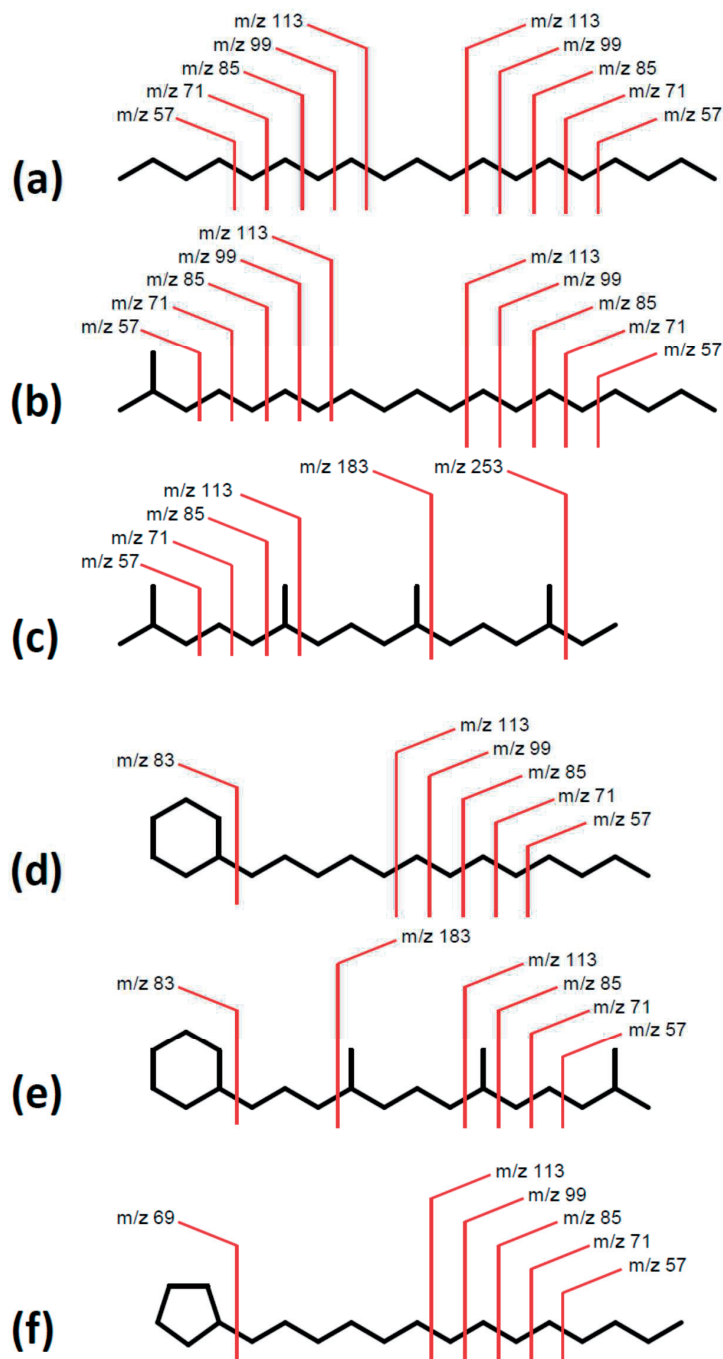


Figure 6-11. Ions generated by the different compounds investigated in our study. (a) An *n*-alkane, (b) a methylalkane, (c) an acyclic isoprenoid, (d) an alkylcyclohexane, (e) a cyclic isoprenoid, and (f) an alkylcyclopentane. These compounds generate similar mass spectra, which is problematic for separation based on mass spectrum only (Figure 6-12).

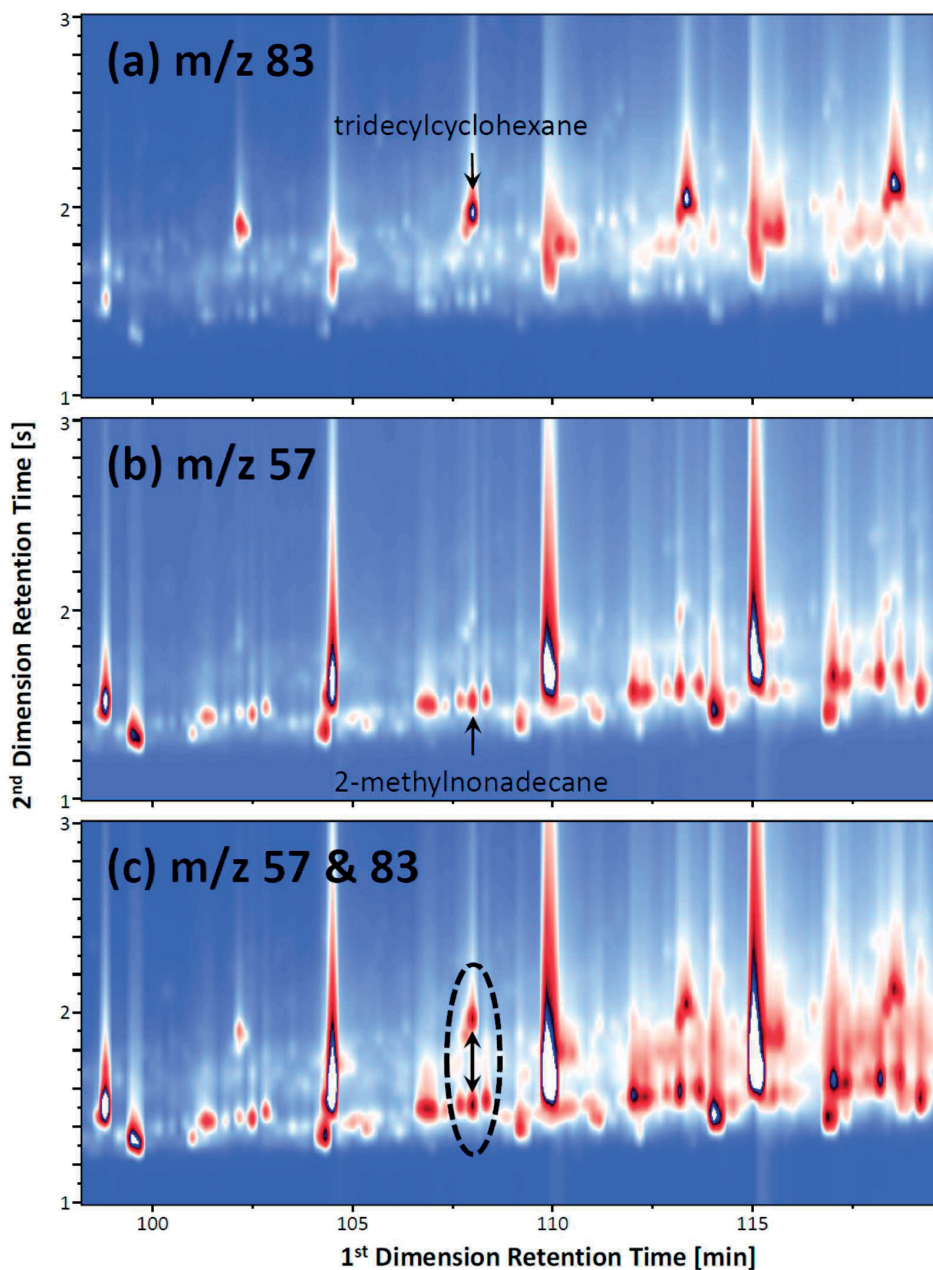


Figure 6-12. Zoom on GCxGC-TOF-MS chromatograms of sample B48 for selected usual diagnostic ions^{2,6} for two compounds investigated in this study (tridecylcyclohexane and 2-methylnonadecane); (a) m/z 83, (b) m/z 57, (c) both m/z 57 and 83. These two compounds have the same first dimension retention time (c), hence they would co-elute in GC-MS. Additionally, both compounds generate both ions 57 and 83, which impairs accurate separation based on mass spectrum only (the similarity of the mass spectra of the two compounds is further detailed in Figure 6-13). In general, the selection of one or two ions for specific hydrocarbons is difficult due to the lack of authentic standards and to the fact that these ions represent only a trace of the total ion signal when ionized in the MS (Table 6-2).

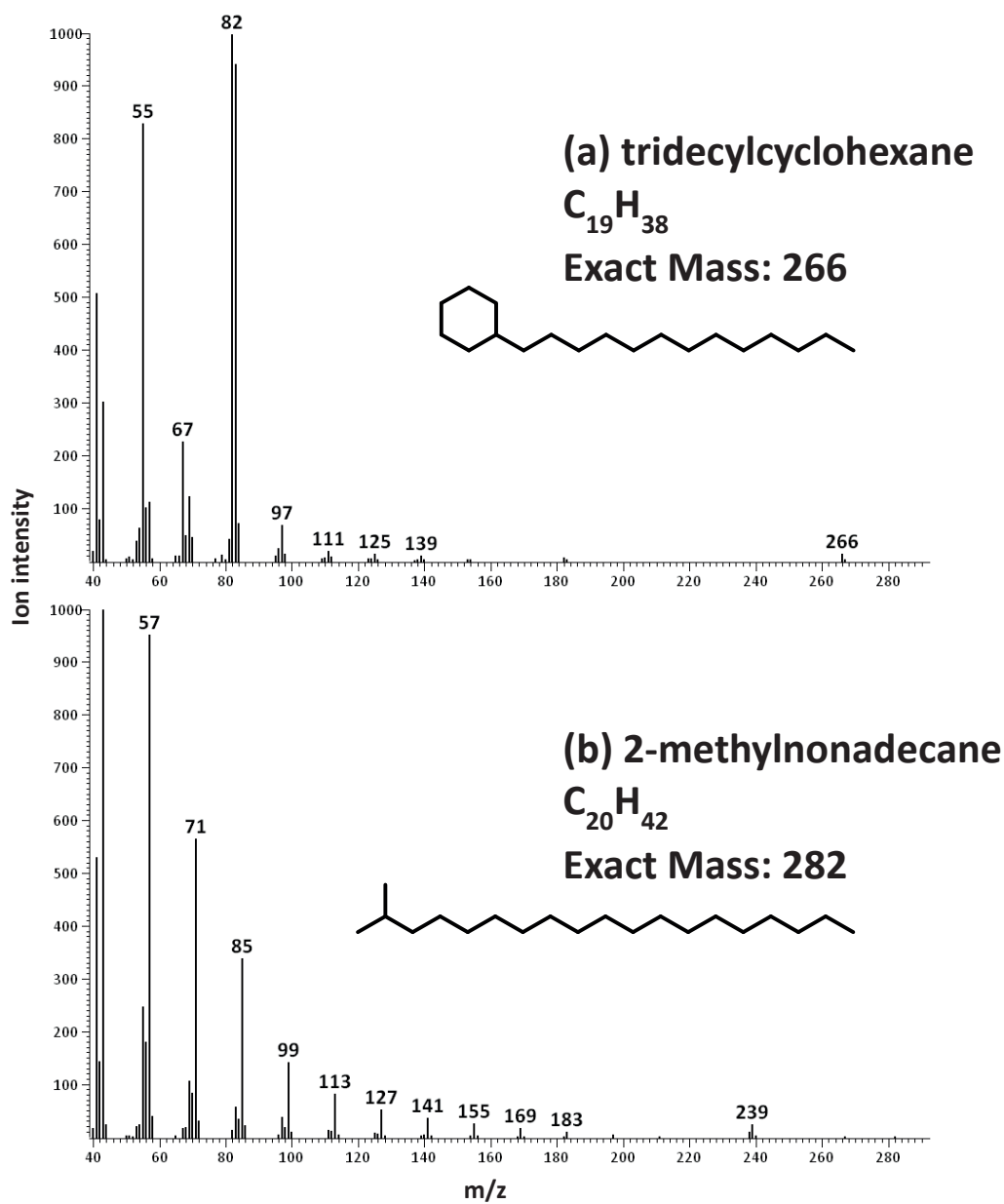


Figure 6-13. Mass spectra of (a) tridecylcyclohexane and (b) 2-methylnonadecane.

Table 6-2. Fraction of total ion signal represented by the diagnostic ions 57 and 83 for tridecylcyclohexane and 2-methylnonadecane.

	m/z 57	m/z 83
tridecylcyclohexane	3.39%	17.91%
2-methylnonadecane	18.50%	1.25%

6.5.6 GC×GC–TOF-MS chromatogram

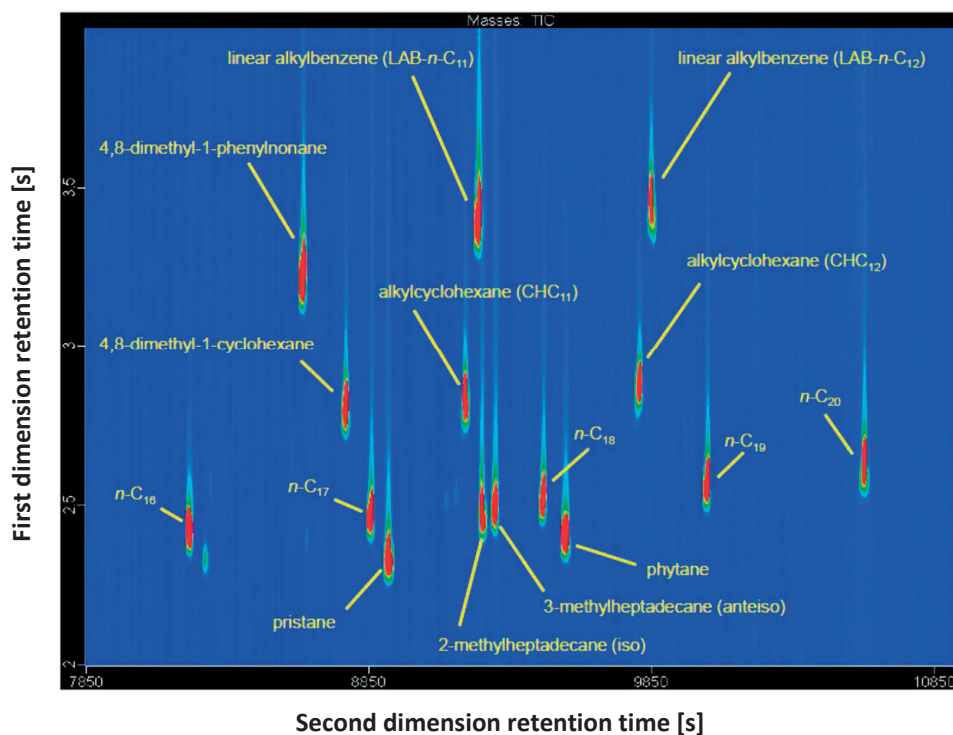


Figure 6-14. GC×GC–TOF-MS total ion current (TIC) chromatogram of standards for a selected window with the elution pattern of several compound classes indicated. This includes *n*-alkanes (*n*-C₁₆, *n*-C₁₇, *n*-C₁₈, *n*-C₁₉, *n*-C₂₀), methylalkanes (3-methylheptadecane and 2-methylheptadecane), acyclic isoprenoids (pristane, phytane), cyclic isoprenoids (alkylcyclohexanes) and a dimethyl-alkylcyclohexane (4,8-dimethyl-1-cyclohexane).

6.5.7 Percentage of each saturate class in the samples studied

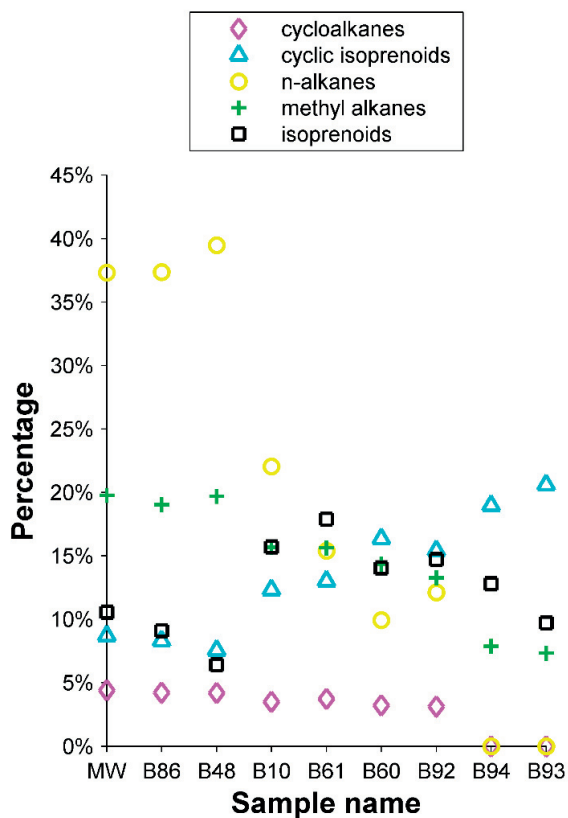


Figure 6-15. Percentage of the mass of each class of saturates compounds for each sample, in the GC×GC subregion studied (Figure 6-3a).

6.5.8 Evolution of the saturates biodegradation index with respect to sampling time

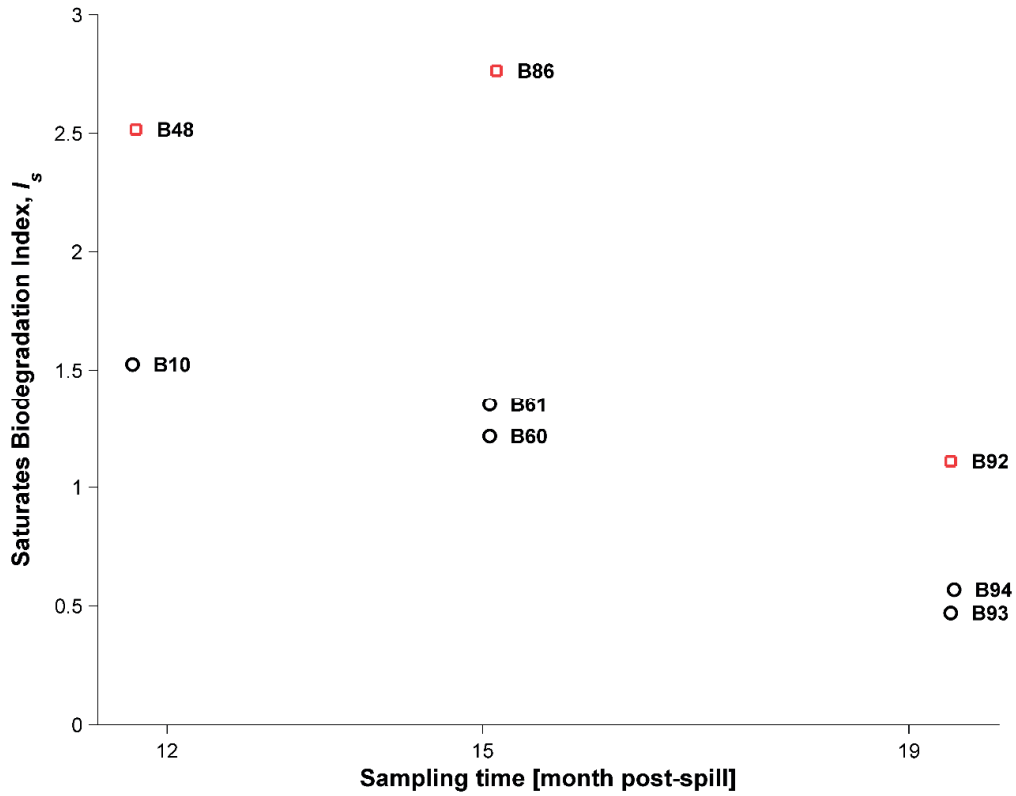


Figure 6-16. Biodegradation index values of the collected samples, plotted with respect to sampling date. Red squares represent samples taken in relatively dry beach locations (B48, B86, and B92); black circles represent samples taken in wet environments, within the surf zone or intertidal zone (B10, B60, B61, B93, B94). Refer to Table 6-1 for precise sampling dates and detailed descriptions of sampling environment.

6.5.9 Comparison of the saturates biodegradation index with the $n\text{-C}_{18}$ /phytane ratio

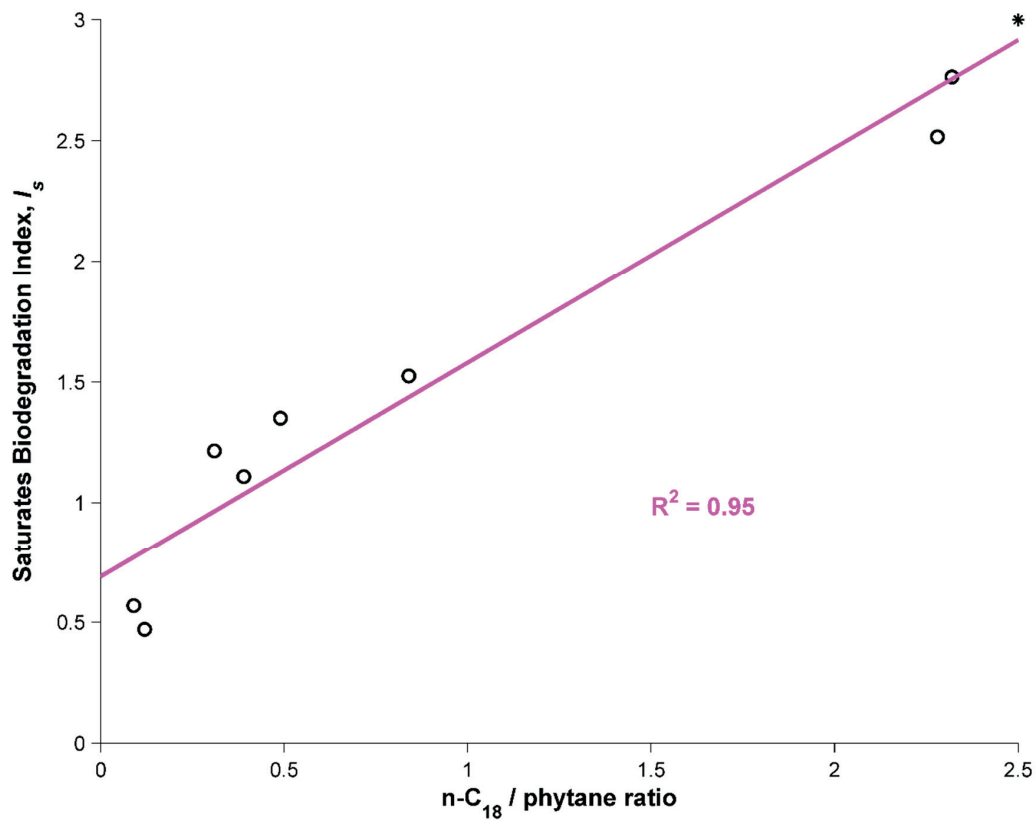


Figure 6-17. Saturates biodegradation index value versus $n\text{-C}_{18}$ /phytane ratio. Circles (o) represent weathered samples, and the star (*) represents neat MW oil.

6.5.10 Estimation of the fraction of the original oil load remaining in sample B93

A preliminary assessment of the fate of the original “dead” oil can be obtained from GC×GC and simulated distillation data (Figure 6-18). For example, simulated distillation analysis showed that 47.0% of the dead oil was lighter than $n\text{-C}_{16}$, corresponding to compounds totally removed from sample B93. As chromatograms were aligned and normalized to C_{30} 17 α (H),21 β (H)-hopane, whole regions of GC×GC chromatograms can be compared. By integrating the part of the GC×GC chromatograms between $n\text{-C}_{16}$ and $n\text{-C}_{22}$, it is found that 74.1% of the oil mass in this range has been removed from sample B93 with respect to the original oil. As 15.6% of the original oil mass is comprised of compounds in this range according to pseudo-distillation data, the percentage of original oil mass removed or transformed $\leq n\text{-C}_{22}$ is equal to 59% (47.0% + (74.1% · 15.6%)).

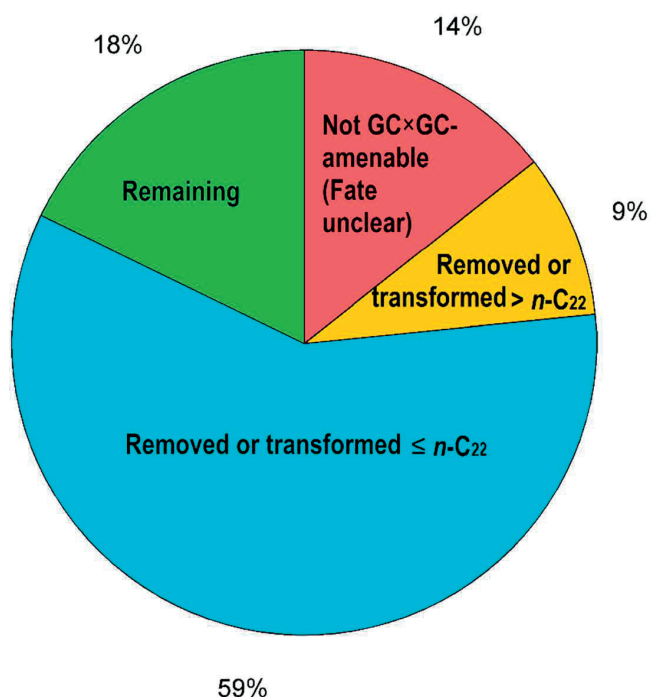


Figure 6-18. Preliminary apportionment of the original MW oil mass that led to sample B93.

Additionally, $\frac{2}{3}$ of sample B93 was composed of non-GC-amenable weathering products. We assumed that the saturates and aromatics fraction of B93, previously determined to constitute 33% of the sample,³²⁰ are totally GC-amenable, and that the remaining oxygenated compounds are not. Then, Figure 6-18 indicates that:

$$\frac{1}{3} M_{B93} = 0.18 \cdot M_{MW, initial}$$

Equation 6-2

where M_{B93} is the total mass of sample B93, and $M_{MW,initial}$ is the initial mass of MW oil that led to sample B93. It follows that:

$$M_{B93} = 0.54 \cdot M_{MW,initial}$$

Equation 6-3

However, sample B93 contained 9.8% oxygen, whereas the original oil contained only 0.4% oxygen. This mass was not originally present in the oil, and it should be deducted to obtain the mass of original oil remaining in sample B93, $M_{MW,remaining}$.

$$M_{MW,remaining} = 0.54 \cdot M_{MW,initial} \cdot (1 - 0.094) \cong 0.49 \cdot M_{MW,initial}$$

Equation 6-4

Therefore 49% of the original MW oil mass remains in sample B93, which includes 18% GC-amenable compounds (Figure 6-18) and 31% transformed, oxygenated compounds. The 18% can be categorized as aromatics and saturates, based on the composition of sample B93 (26% saturates, 7% aromatics):³²⁰

$$M_{aro,remaining} = \frac{0.18 \cdot M_{MW,initial} \cdot 7}{7 + 26} = 0.04 \cdot M_{MW,initial}$$

$$M_{sat,remaining} = \frac{0.18 \cdot M_{MW,initial} \cdot 26}{7 + 26} = 0.14 \cdot M_{MW,initial}$$

Equation 6-5

Therefore, 4% of the original MW oil mass that led to sample B93 is remaining as aromatic compounds ($M_{aro,remaining}$), and 14% as saturates ($M_{sat,remaining}$).

Similar computations can be conducted for the whole sample set (Table 6-3).

Table 6-3. Fate of the set of samples studied, expressed as percentage of initial mass of MW oil that led to the sample (analogous to Figure 6-7b).

Sample name	Mass re-moved	Non GC-amenable	Saturates	Aromatics	Total GC-amenable
B86	50%	23%	22%	5%	27%
B48	- ¹	-	16%	6%	22%
B10	55%	23%	18%	4%	22%
B61	-	-	18%	6%	24%
B60	52%	28%	17%	3%	20%
B92	53%	28%	15%	4%	19%
B94	60%	22%	13%	5%	18%
B93	51%	31%	14%	4%	18%

¹ For two samples, oxygen content was not measured. Therefore the non-GC-amenable fraction cannot be expressed as a fraction of the initial mass of MW oil that led to the sample.

Chapter 7 Conclusions

Petroleum compounds in marine environments have both acute and long-term toxic effects, and it is consequently crucial to understand the exposures of marine organisms, both from an emergency response point of view and from a damage assessment point of view. These exposures can be better understood if detailed, measured or predicted, compositional data are available. However, for several stages of petroleum weathering in the environment, we usually lack such data. Especially, the first hours after release of petroleum fluids at the sea surface have been poorly studied, in spite of the fact that it is during this time window that the highest concentrations of toxic compounds are to be expected within the water column below oil slicks. There was also a lack of knowledge regarding the behavior of petroleum fluids when they are released in deep waters. In particular, models able to explain the underlying processes and provide detailed predictions of compound apportionments were lacking. For example, no compositionally detailed modeling of aqueous dissolution had been conducted for the *Deepwater Horizon* disaster, despite the fact that aqueous dissolution had been estimated to have transferred ~25% of the mass of emitted petroleum fluids to the water column.⁷⁵ Finally, we found limited available information on the biodegradation of saturated hydrocarbons in surface environments, despite the fact that they represent a dominant fraction of petroleum fluids. In this chapter, I summarize the main achievements obtained for these different topics, and discuss several remaining open questions.

7.1 Main findings

GC×GC–FID is a powerful tool to quantify the mass of thousands of hydrocarbon compounds and to estimate properties of compounds/components. However, the technical capabilities of GC×GC–FID instruments have outpaced the ability of existing algorithms to handle the very rich datasets that are encoded in GC×GC–FID chromatograms. One of the achievements of this work was to suggest means for improved quantitative handling of GC×GC–FID data. Together with parallel work pursued by colleagues,⁶⁶ I brought some insights about the respective advantages of different baseline-correction techniques to produce quantitative results. We find that a Reichenbach-type baseline is appropriate for quantification of total compound mass (resolved + unresolved), whereas an Eilers-type baseline proved helpful for the quantification of individual resolved analytes. The Gaussian-peak fit code developed by Arey et al.¹⁵ represents an alternative for quantification of individual resolved analytes, but is not as automated and intuitive to use.

A big challenge is the ability to make direct comparisons of the chromatographic data between different samples that have been analyzed by GC×GC–FID, which requires high correspondence of analyte retention times in chromatograms from different samples. This is hampered by the presence of uncontrolled run-to-run retention time shifts. Here we proposed a

new method that performs favorably compared to two earlier algorithms, in terms of decreased retention time variations of matching analytes, when tested with more than a dozen real complex samples taken from the environment. In particular, the new method appears as the one that leads to the smallest alteration of peak volumes, hence allowing meaningful quantitative conclusions to be drawn from aligned chromatograms. Additionally, the algorithm has also the advantage of being insensitive to compositional differences among the target and reference chromatograms, and of being able to avoid the generation of some artificial distortions. The success of the new alignment algorithm has widely important implications for GC×GC–FID, including: the reliable ability to evaluate and visualize direct differences between whole chromatograms of different samples; the improved ability to automatically track the quantitative changes in up to thousands of individual analytes in different samples; and other quantitative applications. The Matlab codes written to apply the Eilers baseline correction algorithm to GC×GC–FID data and the alignment algorithm have been made available on internet, together with user manuals (<https://github.com/jsarey/>), enabling their free use by the scientific community. Our alignment algorithm has also been implemented in GC Image, one of the most widely used software for the handling of GC×GC–FID data.

One aspect considered in the different case studies presented in this thesis is the importance of what is not visible within the GC×GC–FID chromatographic space. GC×GC–FID is a very useful tool as it analyzes for most of the compounds that will be subjected to rapid partitioning processes, except for very volatile compounds. However, crude oils usually contain a significant fraction of heavy compounds that are not eluted during GC×GC–FID analysis. A live oil mixture, like the liquid petroleum fluid that was emitted during the *Deepwater Horizon* disaster, contains usually also an important fraction of light compounds that are too volatile to appear in GC×GC–FID chromatograms. As boiling point increases approximately³⁵¹ linearly along the first dimension of the GC×GC–FID chromatogram, true boiling point distillation (Chapter 3) or simulated distillation (Chapter 4) data are natural candidates to estimate the mass that lies outside of the GC×GC window. Similarly, when studying biodegraded oil residues, it is important to consider that a large part of the mass of these residues can reside outside of the GC×GC window as oxygenated degradation products (Chapter 6).

After crude oil is accidentally spilt at the sea surface, very rapid fractionation to air and water of several light hydrocarbons will happen, usually before the start of any environmental sampling. In this sense, the analysis presented in Chapter 3 of the experimental data from the oil spill experiment on the North Sea bridges a gap in available information on the early period of oil spills at sea. Also, it allows a validation of the early period (<1 day) of predictions by the oil spill modeling framework developed previously, based on GC×GC–FID which is used to define pseudo-components and estimate their partitioning properties.^{14,39} In particular, we highlighted a good capacity to predict the slick composition, and consequently the dominant mass transfer process, evaporation. Our results further demonstrate the importance of oil slick thickness in the speed of mass transfers from oil slicks, a fact which, despite being accepted by many authors, is nonetheless confused in the literature. Our model also allows us to clarify the expected effects of wind speed and temperature on apportionments to air and water.

In stark contrast to sea-surface oil spills such as the one addressed in Chapter 3, the 2010 *Deepwater Horizon* disaster revealed several shortcomings in our conceptual understanding

and quantitative ability to model petroleum releases in deep sea environments. Releases of petroleum fluids in deep waters are challenging to model owing to the specific pressure conditions that make such an event very special. In Chapter 4, we proposed a new thermodynamic model able to provide unprecedentedly detailed estimates of the gas-liquid-water partitioning of petroleum compounds and to estimate several properties of petroleum phases, and this at high pressures (up to 250 atmospheres) and typical temperatures (-2 to 30 °C) that could be encountered in the deep sea. We used this thermodynamic model to investigate the phase partitioning behavior of the Macondo reservoir fluid released during the *Deepwater Horizon* disaster, using an unprecedentedly detailed model composition of this fluid (279 components, more than an order of magnitude more than previous models). We successfully validated the predictions of our thermodynamic model against previously reported measurement data for gas/liquid volume fractions, dead oil density, and liquid viscosity of Macondo reservoir fluid.

Our thermodynamic simulations indicate that the high pressures encountered in the deep sea enormously increase the tendency of light hydrocarbons to partition into the aqueous phase. This finding reveals that high pressure conditions played a central role in dramatically increasing the dissolution of small hydrocarbons into the deep sea during the *Deepwater Horizon* disaster. The thermodynamic model also provides a quantitative basis to simulate the densities, and therefore buoyancies, of liquid droplets and gas bubbles in the deep sea, while also accounting for detailed (and continually changing) chemical composition of the fluid mixture. This is a crucial requirement for building a fully consistent, quantitative transport model of the coupled ascent and compositional evolution of petroleum fluids and entrained water (Chapter 5) in an ocean water column exceeding 100 m depth, because the ascent velocities and mass transfer rates of fluid particles are directly dependent on their densities, viscosities, and chemical compositions. Chapter 4 also allowed us to provide estimates at emission (ambient) conditions which have implications for flow rate estimates and could be used in Chapter 5 to update predictions of initial droplet and bubble size distributions.

A detailed modeling of aqueous dissolution during the *Deepwater Horizon* disaster had not been attempted prior to this thesis, despite the fact that field observations during the event indicated that this process played a major role in determining compound apportionments.^{8,75} We modeled buoyant plume dynamics and aqueous dissolution for the *Deepwater Horizon* disaster using TAMOC-c, a customized version of the TAMOC model. TAMOC-c includes a thermodynamic model, allowing to update the predicted properties of petroleum fluids as a function of local composition, pressure, and temperature (Chapter 4). This modeling showed reasonable agreement with respect to three major independent field data: location where droplets and bubbles reached the sea surface, fractions of petroleum compounds emitted that were aqueously dissolved in the water column, and relative concentrations in the deep-water hydrocarbon plume. This allowed us to demonstrate that aqueous dissolution was the dominant driving force for the apportionment of petroleum compounds to the water column during the *Deepwater Horizon* disaster. Our simulations provide quantitative information on the fractionation of petroleum compounds as a function of depth, which is a relevant information to assessments of ecological exposures for organisms that may occupy different depth ranges in the water column. TAMOC-c simulation results also provide a rigorous mechanistic basis for estimates of the quantity of nitrogen and oxygen stripped from the water column by rising

gas bubbles and liquid droplets. Taken together with existing published measurement data on dissolved oxygen anomalies in the deep water hydrocarbon plume, this simulation result supplies critical support for the interpretation that *in-situ* microbiological activity increased rapidly in response to elevated hydrocarbon levels in the water column, leading to fast oxygen depletion and concomitant oxidation of highly labile hydrocarbons such as ethane and propane. TAMOC-c results also provide insight into a widely debated question, namely the quantitative influence of applied dispersants on the behaviors of petroleum fluids in the water column. Our TAMOC-c simulation results illustrate clearly the influence of dispersant addition, by way of comparisons between simulation predictions with and without dispersant. The findings indicate that dispersant addition played a major role in the outcome of the *Deepwater Horizon* disaster, by accelerating the dissolution of light hydrocarbons into the deep water column, and thereby decreasing the exposure of emergency response workers at the sea surface.

On longer time frames (months to years) biodegradation is the most important process that contributes to the natural attenuation of oil spills. In this study, we clarified the relative rates of biodegradation among different saturated hydrocarbon classes for oil residues collected on beaches 12–19 months after the beginning of the *Deepwater Horizon* disaster. These results are pertinent regarding the fate of saturated hydrocarbons, which are usually given little attention in biodegradation studies, notwithstanding that they represent a major fraction of oils. Saturates in the *n*-C₂₂ to *n*-C₂₉ elution range were found to be partly biodegraded, but to different relative extents, with ease of biodegradation decreasing in the following order: *n*-alkanes > methylalkanes and alkylcyclopentanes+alkylcyclohexanes > cyclic and acyclic isoprenoids.

7.2 Open questions

Further development of softwares for quantitative handling of GC×GC–FID data is possible. In particular, the automatic peak quantification tools available in existing commercial softwares (GC Image, ChromaTOF) remain unsatisfactory for analytes eluting on top of a locally raised baseline. This is principally due to the inability of these softwares to isolate analyte signal (which could be achieved through an Eilers-type baseline correction). Other problematic aspects in the ChromaTOF software include a willingness to hide the underlying algorithms and the impossibility of importing pre-processed chromatograms. For these reasons, users often resolve to "manual integration", where the position of the baseline is manually corrected by the user (ChromaTOF), introducing the risk of errors and inconsistencies among users. Development of a freely available code for automatic peak quantification could allow users to perform most of the usual processing of GC×GC–FID data outside of these specialized commercial softwares (Matlab functions written during this thesis allow chromatogram import, visualization, peak selection, baseline-correction, and chromatogram alignment). These codes have been made freely available online: <https://github.com/jsarey/GCxGC-baseline-correction> and <https://github.com/jsarey/GCxGC-alignment>.

Regarding the alignment of GC×GC chromatograms, the ideal evolution would be a reduction of the analyte retention time shifts at the measurement stage. However, chromatogram align-

ment will remain a needed feature in the near future, due to the necessity to compare chromatograms acquired over long time periods (retention times change with aging columns³⁵²) or slightly different instrument programs. Further improvements in alignment algorithms are limited by the very coarse resolution in the first dimension where peaks are frequently 1 to 3 pixels wide, limiting the ability to identify finer shifts. Additionally, signal re-sampling (or interpolation) is a necessary step for any alignment algorithm. A very interesting open question is how this inherent data smoothing alters the behavior of tools used to extract quantitative information from GC×GC–FID chromatograms. For example, we noticed that the peak footprints determined by GC Image were globally increased after alignment, a result that we tentatively attributed to this smoothing and that certainly participated in the peak volume alterations upon alignment as we determined them. Finally, an extension to the handling of mass-spectrum data is under development in collaboration with Yasuyuki Zushi.

The model of hydrocarbons apportionment for the North Sea experiment showed good prediction skill for the oil slick composition. This implies that evaporation kinetics are accurately predicted, because this is largely the dominant mass loss process in the early period of an oil slick. An aspect that was not included in our study is the dispersion and migration of evaporated compounds in the atmosphere, and the concentrations of possibly toxic hydrocarbons to which oil spill emergency response workers may be exposed. Considering these aspects could improve the ability to take informed measures to avoid health damage for emergency response workers, especially for large-volume releases. Another aspect that could be further evaluated is whether the detailed oil slick composition predicted by the model could be used to estimate oil properties that could guide response actions (for example skimming or in-situ burning). Properties of interest include for example the viscosity of the oil or its density. Finally, the puzzling water column data collected during this experiment highlighted the need of new, better constrained data to validate the aqueous dissolution part of the oil spill model. Such model validation may be performed first within a simpler, better constrained model system, and later further validated against field data at sea. Suggestions of improved sampling strategies for potential future oil spill experiments would include: (a) ensuring that sea-water blanks are taken before the oil release is started, (b) considering options to enable the differentiation of aqueously dissolved hydrocarbons versus dispersed droplets, (c) better monitoring parameters to allow estimation of the mixing in the water column, including wind speed, water temperature and salinity profiles, and information on incoming solar radiation.

We showed that aqueous dissolution is a major process that can explain the transfer of hydrocarbons to the water column that was documented during the *Deepwater Horizon* disaster. However, some uncertainty remains regarding this event. Beyond the uncertainty on flow rate itself, the uncertainty on the composition of the emitted fluid, and especially regarding the quantity of C₁–C₅ hydrocarbons emitted, result in imprecisely constrained mass flow rates of petroleum compounds transferred to the water column during the event. Another incompletely characterized aspect is the predicted droplet and bubble size distributions, which are based on imperfect assumptions. The VDROD-J model, which considers breakup and coalescence, does not include a thermodynamic model, nor does it consider aqueous dissolution. Consequently, it is unable to take into consideration the evolution of the properties of droplets and bubbles over the first 100 m of ascent during which the size distributions are predicted to stabilize. Based on the predicted evolution of the relevant properties during these

first 100 m (our model) and the sensitivity of the VDROD-J model (based on discussions with Lin Zhao), gas/liquid/seawater repartitioning processes are expected to have only a small influence on the fluid particle size distribution. This is further supported by the fact that apportionments of petroleum compounds predicted by our model using the size distributions predicted by the VDROD-J model are in agreement with available field observations. Nevertheless, in order to quantitatively account for the evolution of the properties of petroleum fluids over the first 100 m one would require the integration of the VDROD-J model with TAMOC. Finally, all models to date for deep-water blowouts simply assume that gas and liquid petroleum phases are fully separated into distinct entities (droplets and bubbles) at emission point. It would be extremely interesting to investigate this hypothesis further, together with what happens precisely when a droplet or bubble experiences a phase transition, as our modeling showed that this is predicted to happen. Phase transitions within droplets and bubbles in a deep-water context have barely been experimentally investigated, except from some very preliminary work by Peter Brewer, Peter Walz and co-workers.

Biodegradation of oil residues in the environment is an important route for natural attenuation. However, questions remain open regarding the generation and fate of the oxygenated compounds that represent increasingly large fractions of *Deepwater Horizon* oil residues with increasing biodegradation extent. The toxicity of these compounds, when present in the environment as a complex mixture of compounds, remains uncertain.

Chapter 8 References

- (1) *World Energy Outlook 2009*; International Energy Agency, 2009; p. 698.
- (2) Peters, K. E.; Walters, C. C.; Moldowan, J. M. *The Biomarker Guide, Biomarkers and Isotopes in the Environment and Human History*; 2nd ed.; Cambridge University Press: Cambridge, 2005; Vol. 1.
- (3) McKenna, A. M.; Nelson, R. K.; Reddy, C. M.; Savory, J. J.; Kaiser, N. K.; Fitzsimmons, J. E.; Marshall, A. G.; Rodgers, R. P. Expansion of the analytical window for oil spill characterization by ultrahigh resolution mass spectrometry: Beyond gas chromatography. *Environ. Sci. Technol.* **2013**, *47*, 7530–7539.
- (4) Barker, C.; Robbins, W. K.; Hsu, C. S.; Drew, L. J. Petroleum. In *Kirk-Othmer Encyclopedia of Chemical Technology*; Wiley-Blackwell: Hoboken, 2005.
- (5) Zick, A. A. *Expert rebuttal report*; prepared on behalf of the United States TREX-011491R; 2013.
- (6) Peters, K. E.; Walters, C. C.; Moldowan, J. M. *The Biomarker Guide, Biomarkers and Isotopes in Petroleum Exploration and Earth History*; 2nd ed.; Cambridge University Press: Cambridge, 2005; Vol. 2.
- (7) *Oil in the Sea III: Inputs, Fates, and Effects*; The National Academies press: Washington, DC, 2003.
- (8) Reddy, C. M.; Arey, J. S.; Seewald, J. S.; Sylva, S. P.; Lemkau, K. L.; Nelson, R. K.; Carmichael, C. A.; McIntyre, C. P.; Fenwick, J.; Ventura, G. T.; Mooy, B. A. S. V.; Camilli, R. Composition and fate of gas and oil released to the water column during the *Deepwater Horizon* oil spill. *Proc. Natl. Acad. Sci.* **2012**, *109*, 20229–20234.
- (9) McNutt, M. K.; Camilli, R.; Crone, T. J.; Guthrie, G. D.; Hsieh, P. A.; Ryerson, T. B.; Savas, O.; Shaffer, F. Review of flow rate estimates of the *Deepwater Horizon* oil spill. *Proc. Natl. Acad. Sci.* **2012**, *109*, 20260–20267.
- (10) Barbier, C. J. *Findings of fact and conclusions of law; Phase two trial*; 2015; p. 44.
- (11) Stout, S. A.; Wang, Z. Chemical fingerprinting of spilled or discharged petroleum — Methods and factors affecting petroleum fingerprints in the environment. In *Oil Spill Environmental Forensics*; Wang, Z.; Stout, S. A., Eds.; Academic Press: Burlington, 2007; pp. 1–53.
- (12) Fingas, M. F. Studies on the evaporation of crude oil and petroleum products: I. The relationship between evaporation rate and time. *J. Hazard. Mater.* **1997**, *56*, 227–236.
- (13) Harrison, W.; Winnik, M. A.; Kwong, P. T. Y.; Mackay, D. Disappearance of aromatic and aliphatic components from small sea surface slicks. *Environ. Sci. Technol.* **1975**, *9*, 231–234.
- (14) Arey, J. S.; Nelson, R. K.; Plata, D. L.; Reddy, C. M. Disentangling oil weathering using GC×GC. 2. Mass transfer calculations. *Environ. Sci. Technol.* **2007**, *41*, 5747–5755.
- (15) Arey, J. S.; Nelson, R. K.; Reddy, C. M. Disentangling oil weathering using GC×GC. 1. Chromatogram analysis. *Environ. Sci. Technol.* **2007**, *41*, 5738–5746.

-
- (16) Riazi, M. R.; Edalat, M. Prediction of the rate of oil removal from seawater by evaporation and dissolution. *J. Pet. Sci. Eng.* **1996**, *16*, 291–300.
- (17) Incardona, J. P.; Vines, C. A.; Anulacion, B. F.; Baldwin, D. H.; Day, H. L.; French, B. L.; Labenia, J. S.; Linbo, T. L.; Myers, M. S.; Olson, O. P.; Sloan, C. A.; Sol, S.; Griffin, F. J.; Menard, K.; Morgan, S. G.; West, J. E.; Collier, T. K.; Ylitalo, G. M.; Cherr, G. N.; Scholz, N. L. Unexpectedly high mortality in Pacific herring embryos exposed to the 2007 Cosco Busan oil spill in San Francisco Bay. *Proc. Natl. Acad. Sci.* **2012**, *109*, E51–E58.
- (18) Incardona, J. P.; Vines, C. A.; Linbo, T. L.; Myers, M. S.; Sloan, C. A.; Anulacion, B. F.; Boyd, D.; Collier, T. K.; Morgan, S.; Cherr, G. N.; Scholz, N. L. Potent phototoxicity of marine bunker oil to translucent herring embryos after prolonged weathering. *PLoS ONE* **2012**, *7*, e30116.
- (19) Rowland, S.; Donkin, P.; Smith, E.; Wraige, E. Aromatic hydrocarbon “humps” in the marine environment: Unrecognized toxins? *Environ. Sci. Technol.* **2001**, *35*, 2640–2644.
- (20) Neff, J. M.; Ostazeski, S.; Gardiner, W.; Stejskal, I. Effects of weathering on the toxicity of three offshore Australian crude oils and a diesel fuel to marine animals. *Environ. Toxicol. Chem.* **2000**, *19*, 1809–1821.
- (21) Reed, M.; Johansen, Ø.; Brandvik, P. J.; Daling, P.; Lewis, A.; Fiocco, R.; Mackay, D.; Prentki, R. Oil spill modeling towards the close of the 20th century: Overview of the state of the art. *Spill Sci. Technol. Bull.* **1999**, *5*, 3–16.
- (22) Lehr, W. J. Review of modeling procedures for oil spill weathering behavior. In *Oil Spill Modelling and Processes*; Brebbia, C. A., 2001.
- (23) Tkalich, P.; Chan, E. S. Vertical mixing of oil droplets by breaking waves. *Mar. Pollut. Bull.* **2002**, *44*, 1219–1229.
- (24) Reddy, C. M.; Quinn, J. G. The North Cape oil spill: Hydrocarbons in Rhode Island coastal waters and Point Judith Pond. *Mar. Environ. Res.* **2001**, *52*, 445–461.
- (25) Lehr, W.; Jones, R.; Evans, M.; Simecek-Beatty, D.; Overstreet, R. Revisions of the ADIOS oil spill model. *Environ. Model. Softw.* **2002**, *17*, 189–197.
- (26) Payne, J. R.; Phillips, C. R. Photochemistry of petroleum in water. *Environ. Sci. Technol.* **1985**, *19*, 569–579.
- (27) Scholz, D. K.; Kucklick, J. H.; Pond, R.; Walker, A. H.; Bostrom, A.; Fischbeck, P. *Fate of spilled oil in marine environment, Where does it go? What does it do? How do dispersants affect it*; 4691; American Petroleum Institute: Washington, DC, 1999; p. 43.
- (28) Scarlett, A. G. Effect-directed analysis of toxicants in unresolved complex mixtures (UCMs) of hydrocarbons from biodegraded crude oils. Ph.D. Dissertation, University of Plymouth: Plymouth, 2007.
- (29) Scarlett, A.; Galloway, T. S.; Rowland, S. J. Chronic toxicity of unresolved complex mixtures (UCM) of hydrocarbons in marine sediments. *J. Soils Sediments* **2007**, *7*, 200–206.
- (30) Safina, C. *A Sea in Flames, The Deepwater Horizon Blowout*; Crown: New York, 2011.
- (31) Camilli, R.; Reddy, C. M.; Yoerger, D. R.; Mooy, B. A. S. V.; Jakuba, M. V.; Kinsey, J. C.; McIntyre, C. P.; Sylva, S. P.; Maloney, J. V. Tracking hydrocarbon plume transport and biodegradation at Deepwater Horizon. *Science* **2010**, *330*, 201–204.
- (32) Diercks, A.-R.; Highsmith, R. C.; Asper, V. L.; Joung, D.; Zhou, Z.; Guo, L.; Shiller, A. M.; Joye, S. B.; Teske, A. P.; Guinasso, N.; Wade, T. L.; Lohrenz, S. E. Characterization of subsurface polycyclic aromatic hydrocarbons at the Deepwater Horizon site. *Geophys. Res. Lett.* **2010**, *37*, L20602.

- (33) Socolofsky, S. A.; Adams, E. E.; Sherwood, C. R. Formation dynamics of subsurface hydrocarbon intrusions following the *Deepwater Horizon* blowout. *Geophys. Res. Lett.* **2011**, *38*, L09602.
- (34) Valentine, D. L.; Kessler, J. D.; Redmond, M. C.; Mendes, S. D.; Heintz, M. B.; Farwell, C.; Hu, L.; Kinnaman, F. S.; Yvon-Lewis, S.; Du, M.; Chan, E. W.; Tigreros, F. G.; Villanueva, C. J. Propane respiration jump-starts microbial response to a deep oil spill. *Science* **2010**, *330*, 208–211.
- (35) McGinnis, D. F.; Greinert, J.; Artemov, Y.; Beaubien, S. E.; Wüest, A. Fate of rising methane bubbles in stratified waters: How much methane reaches the atmosphere? *J. Geophys. Res. Oceans* **2006**, *111*, C09007.
- (36) Schmale, O.; Haeckel, M.; McGinnis, D. F. Response of the Black Sea methane budget to massive short-term submarine inputs of methane. *Biogeosciences* **2011**, *8*, 911–918.
- (37) Ryerson, T. B.; Aikin, K. C.; Angevine, W. M.; Atlas, E. L.; Blake, D. R.; Brock, C. A.; Fehsenfeld, F. C.; Gao, R.-S.; de Gouw, J. A.; Fahey, D. W.; Holloway, J. S.; Lack, D. A.; Lueb, R. A.; Meinardi, S.; Middlebrook, A. M.; Murphy, D. M.; Neuman, J. A.; Nowak, J. B.; Parrish, D. D.; Peischl, J.; Perring, A. E.; Pollack, I. B.; Ravishankara, A. R.; Roberts, J. M.; Schwarz, J. P.; Spackman, J. R.; Stark, H.; Warneke, C.; Watts, L. A. Atmospheric emissions from the *Deepwater Horizon* spill constrain air-water partitioning, hydrocarbon fate, and leak rate. *Geophys. Res. Lett.* **2011**, *38*, L07803.
- (38) *Deep water. The Gulf oil disaster and the future of offshore drilling*; Report to the President; National Commission on the BP Deepwater Horizon Oil Spill and Offshore Drilling, 2011; p. 381.
- (39) Arey, J. S.; Nelson, R. K.; Xu, L.; Reddy, C. M. Using comprehensive two-dimensional gas chromatography retention indices to estimate environmental partitioning properties for a complete set of diesel fuel hydrocarbons. *Anal. Chem.* **2005**, *77*, 7172–7182.
- (40) Gros, J.; Nabi, D.; Würz, B.; Wick, L. Y.; Brussaard, C. P. D.; Huisman, J.; van der Meer, J. R.; Reddy, C. M.; Arey, J. S. First day of an oil spill on the open sea: Early mass transfers of hydrocarbons to air and water. *Environ. Sci. Technol.* **2014**, *48*, 9400–9411.
- (41) Rye, H. A multicomponent oil spill model for dissolved aromatic concentrations. *Int. Oil Spill Conf. Proc.* **1995**, 49–53.
- (42) Leinonen, P. J. The fate of spilled oil. Ph.D. Dissertation, University of Toronto: Toronto, 1976.
- (43) Johansen, Ø.; Rye, H.; Cooper, C. DeepSpill—Field study of a simulated oil and gas blowout in deep water. *Spill Sci. Technol. Bull.* **2003**, *8*, 433–443.
- (44) Johansen, Ø. DeepBlow – A lagrangian plume model for deep water blowouts. *Spill Sci. Technol. Bull.* **2000**, *6*, 103–111.
- (45) Camilli, R.; Iorio, D. D.; Bowen, A.; Reddy, C. M.; Techet, A. H.; Yoerger, D. R.; Whitcomb, L. L.; Seewald, J. S.; Sylva, S. P.; Fenwick, J. Acoustic measurement of the *Deepwater Horizon* Macondo well flow rate. *Proc. Natl. Acad. Sci.* **2012**, *109*, 20235–20239.
- (46) Li, S.-L.; Sun, C.-Y.; Liu, B.; Feng, X.-J.; Li, F.-G.; Chen, L.-T.; Chen, G.-J. Initial thickness measurements and insights into crystal growth of methane hydrate film. *AIChE J.* **2013**, *59*, 2145–2154.
- (47) Rehder, G.; Leifer, I.; Brewer, P. G.; Friederich, G.; Peltzer, E. T. Controls on methane bubble dissolution inside and outside the hydrate stability field from open ocean field experiments and numerical modeling. *Mar. Chem.* **2009**, *114*, 19–30.

- (48) Sloan, E. D.; Koh, C. A. *Clathrate Hydrates of Natural Gases*; Chemical Industries; 3rd ed.; CRC Press: Boca Raton, 2008.
- (49) Chen, L.; Sloan, E. D.; Koh, C. A.; Sum, A. K. Methane hydrate formation and dissociation on suspended gas bubbles in water. *J. Chem. Eng. Data* **2014**, *59*, 1045–1051.
- (50) Li, S.-L.; Wang, Y.-F.; Sun, C.-Y.; Chen, G.-J.; Liu, B.; Li, Z.-Y.; Ma, Q.-L. Factors controlling hydrate film growth at water/oil interfaces. *Chem. Eng. Sci.* **2015**, *135*, 412–420.
- (51) Sinquin, A.; Arla, D.; Prioux, C.; Peytavy, J. L.; Glenat, P.; Dicharry, C. Gas hydrate formation and transport in an acidic crude oil: Influence of salt and pH. *Energy Fuels* **2008**, *22*, 721–728.
- (52) Stoporev, A. S.; Manakov, A. Y.; Altunina, L. K.; Bogoslovsky, A. V.; Strelets, L. A.; Aladko, E. Y. Unusual self-preservation of methane hydrate in oil suspensions. *Energy Fuels* **2014**, *28*, 794–802.
- (53) Villalanti, D. C.; Raia, J. C.; Maynard, J. B. High-temperature simulated distillation applications in petroleum characterization. In *Encyclopedia of Analytical Chemistry*; John Wiley & Sons, Ltd, 2006.
- (54) Bertsch, W. Two-dimensional gas chromatography. Concepts, instrumentation, and applications - Part 1: Fundamentals, conventional two-dimensional gas chromatography, selected applications. *Hrc-J. High Resolut. Chromatogr.* **1999**, *22*, 647–665.
- (55) Wardlaw, G. D.; Arey, J. S.; Reddy, C. M.; Nelson, R. K.; Ventura, G. T.; Valentine, D. L. Disentangling oil weathering at a marine seep using GC×GC: Broad metabolic specificity accompanies subsurface petroleum biodegradation. *Environ. Sci. Technol.* **2008**, *42*, 7166–7173.
- (56) Liu, Z.; Phillips, J. Comprehensive 2-dimensional gas-chromatography using an on-column thermal modulator interface. *J. Chromatogr. Sci.* **1991**, *29*, 227–231.
- (57) Ramos, L. *Comprehensive Two Dimensional Gas Chromatography*; Wilson & Wilson's comprehensive analytical chemistry; Elsevier: Amsterdam, 2009.
- (58) Adahchour, M.; Beens, J.; Vreuls, R. J. J.; Brinkman, U. A. T. Recent developments in comprehensive two-dimensional gas chromatography (GC × GC): IV. Further applications, conclusions and perspectives. *TrAC Trends Anal. Chem.* **2006**, *25*, 821–840.
- (59) Adahchour, M.; Beens, J.; Vreuls, R. J. J.; Brinkman, U. A. T. Recent developments in comprehensive two-dimensional gas chromatography (GC × GC): III. Applications for petrochemicals and organohalogenes. *TrAC Trends Anal. Chem.* **2006**, *25*, 726–741.
- (60) Nelson, R. K.; Aeppli, C.; Arey, J. S.; Chen, H.; de Oliveira, A.; Eiserbeck, C.; Fryssinger, G. S.; Gaines, R. B.; Grice, K.; Gros, J.; Hall, G. J.; Koolen, H. H. F.; Lemkau, K. L.; McKenna, A.; Reddy, C. M.; Rodgers, R. P.; Swarthout, R. F.; Valentine, D. L.; White, H. K. Applications of comprehensive two-dimensional gas chromatography (GC×GC) in studying the source, transport, and fate of petroleum hydrocarbons in the environment. In *Standard Handbook of Oil Spill Environmental Forensics*; Stout, S. A.; Wang, Z., Eds.; Elsevier, 2016; pp. 339–448.
- (61) Tong, H. Y.; Karasek, F. W. Flame ionization detector response factors for compound classes in quantitative analysis of complex organic mixtures. *Anal. Chem.* **1984**, *56*, 2124–2128.
- (62) Gros, J.; Reddy, C. M.; Aeppli, C.; Nelson, R. K.; Carmichael, C. A.; Arey, J. S. Resolving biodegradation patterns of persistent saturated hydrocarbons in weathered oil samples from the *Deepwater Horizon* disaster. *Environ. Sci. Technol.* **2014**, *48*, 1628–1637.
- (63) Aeppli, C.; Nelson, R. K.; Radović, J. R.; Carmichael, C. A.; Valentine, D. L.; Reddy, C. M. Recalcitrance and degradation of petroleum biomarkers upon abiotic and biotic

- natural weathering of *Deepwater Horizon* oil. *Environ. Sci. Technol.* **2014**, *48*, 6726–6734.
- (64) Pierce, K. M.; Wood, L. F.; Wright, B. W.; Synovec, R. E. A comprehensive two-dimensional retention time alignment algorithm to enhance chemometric analysis of comprehensive two-dimensional separation data. *Anal. Chem.* **2005**, *77*, 7735–7743.
- (65) Nelson, R. K.; Kile, B. M.; Plata, D. L.; Sylva, S. P.; Xu, L.; Reddy, C. M.; Gaines, R. B.; Frysinger, G. S.; Reichenbach, S. E. Tracking the weathering of an oil spill with comprehensive two-dimensional gas chromatography. *Environ. Forensics* **2006**, *7*, 33–44.
- (66) Samanipour, S.; Dimitriou-Christidis, P.; Gros, J.; Grange, A.; Arey, J. S. Analyte quantification with comprehensive two-dimensional gas chromatography: Assessment of methods for baseline correction, peak delineation, and matrix effect elimination for real samples. *J. Chromatogr. A* **2015**, *1375*, 123–139.
- (67) Gros, J.; Nabi, D.; Dimitriou-Christidis, P.; Rutler, R.; Arey, J. S. Robust algorithm for aligning two-dimensional chromatograms. *Anal. Chem.* **2012**, *84*, 9033–9040.
- (68) Eilers, P. H. C. Parametric time warping. *Anal. Chem.* **2004**, *76*, 404–411.
- (69) Gros, J.; Eilers, P. H. C.; Arey, J. S. *Gros-Eilers-Arey code to perform baseline correction of GC×GC chromatograms*; <https://github.com/jsarey/GCxGC-baseline-correction>, 2015.
- (70) Reichenbach, S. E.; Ni, M.; Zhang, D.; Ledford Jr., E. B. Image background removal in comprehensive two-dimensional gas chromatography. *J. Chromatogr. A* **2003**, *985*, 47–56.
- (71) Reichenbach, S. E.; Ni, M.; Kottapalli, V.; Visvanathan, A. Information technologies for comprehensive two-dimensional gas chromatography. *Chemom. Intell. Lab. Syst.* **2004**, *71*, 107–120.
- (72) Nabi, D.; Gros, J.; Dimitriou-Christidis, P.; Arey, J. S. Mapping environmental partitioning properties of nonpolar complex mixtures by use of GC × GC. *Environ. Sci. Technol.* **2014**, *48*, 6814–6826.
- (73) Mao, D.; Lookman, R.; Van De Weghe, H.; Vanermen, G.; De Brucker, N.; Diels, L. Aqueous solubility calculation for petroleum mixtures in soil using comprehensive two-dimensional gas chromatography analysis data. *J. Chromatogr. A* **2009**, *1216*, 2873–2880.
- (74) Lemkau, K. L. Comprehensive study of a heavy fuel oil spill: Modeling and analytical approaches to understanding environmental weathering. Ph.D. Dissertation, Massachusetts Institute of Technology and Woods Hole Oceanographic Institution: MA, USA, 2012.
- (75) Ryerson, T. B.; Camilli, R.; Kessler, J. D.; Kujawinski, E. B.; Reddy, C. M.; Valentine, D. L.; Atlas, E.; Blake, D. R.; de Gouw, J.; Meinardi, S.; Parrish, D. D.; Peischl, J.; Seewald, J. S.; Warneke, C. Chemical data quantify *Deepwater Horizon* hydrocarbon flow rate and environmental distribution. *Proc. Natl. Acad. Sci.* **2012**, *109*, 20246–20253.
- (76) Zhang, D.; Huang, X.; Regnier, F. E.; Zhang, M. Two-dimensional correlation optimized warping algorithm for aligning GC×GC–MS data. *Anal. Chem.* **2008**, *80*, 2664–2671.
- (77) Mohler, R. E.; Dombek, K. M.; Hoggard, J. C.; Young, E. T.; Synovec, R. E. Comprehensive two-dimensional gas chromatography time-of-flight mass spectrometry analysis of metabolites in fermenting and respiring yeast cells. *Anal. Chem.* **2006**, *78*, 2700–2709.
- (78) Welthagen, W.; Shellie, R. A.; Spranger, J.; Ristow, M.; Zimmermann, R.; Fiehn, O. Comprehensive two-dimensional gas chromatography–time-of-flight mass spectrometry (GC × GC-TOF) for high resolution metabolomics: biomarker discovery on

- spleen tissue extracts of obese NZO compared to lean C57BL/6 mice. *Metabolomics* **2005**, *1*, 65–73.
- (79) Reddy, C. M.; Eglinton, T. I.; Hounshell, A.; White, H. K.; Xu, L.; Gaines, R. B.; Frysiner, G. S. The *West Falmouth* oil spill after thirty years: The persistence of petroleum hydrocarbons in marsh sediments. *Environ. Sci. Technol.* **2002**, *36*, 4754–4760.
- (80) Gaines, R. B.; Frysiner, G. S.; Hendrick-Smith, M. S.; Stuart, J. D. Oil spill source identification by comprehensive two-dimensional gas chromatography. *Environ. Sci. Technol.* **1999**, *33*, 2106–2112.
- (81) Adahchour, M.; Beens, J.; Brinkman, U. A. T. Recent developments in the application of comprehensive two-dimensional gas chromatography. *J. Chromatogr. A* **2008**, *1186*, 67–108.
- (82) Adahchour, M.; Beens, J.; Vreuls, R. J. J.; Brinkman, U. A. T. Recent developments in comprehensive two-dimensional gas chromatography (GC × GC): II. Modulation and detection. *TrAC Trends Anal. Chem.* **2006**, *25*, 540–553.
- (83) Shao, Y.; Marriott, P.; Shellie, R.; Hügel, H. Solid-phase micro-extraction—comprehensive two-dimensional gas chromatography of ginger (*Zingiber officinale*) volatiles. *Flavour Fragr. J.* **2003**, *18*, 5–12.
- (84) Mondello, L.; Casilli, A.; Tranchida, P. Q.; Dugo, P.; Costa, R.; Festa, S.; Dugo, G. Comprehensive multidimensional GC for the characterization of roasted coffee beans. *J. Sep. Sci.* **2004**, *27*, 442–450.
- (85) Lewis, A. C.; Carslaw, N.; Marriott, P. J.; Kinghorn, R. M.; Morrison, P.; Lee, A. L.; Bartle, K. D.; Pilling, M. J. A larger pool of ozone-forming carbon compounds in urban atmospheres. *Nature* **2000**, *405*, 778–781.
- (86) Ni, M.; Reichenbach, S. E.; Visvanathan, A.; TerMaat, J.; Ledford Jr., E. B. Peak pattern variations related to comprehensive two-dimensional gas chromatography acquisition. *J. Chromatogr. A* **2005**, *1086*, 165–170.
- (87) Pierce, K. M.; Hope, J. L.; Johnson, K. J.; Wright, B. W.; Synovec, R. E. Classification of gasoline data obtained by gas chromatography using a piecewise alignment algorithm combined with feature selection and principal component analysis. *J. Chromatogr. A* **2005**, *1096*, 101–110.
- (88) Nielsen, N.-P. V.; Carstensen, J. M.; Smedsgaard, J. Aligning of single and multiple wavelength chromatographic profiles for chemometric data analysis using correlation optimised warping. *J. Chromatogr. A* **1998**, *805*, 17–35.
- (89) Vial, J.; Noçairi, H.; Sassiati, P.; Mallipatu, S.; Cognon, G.; Thiébaud, D.; Teillet, B.; Rutledge, D. N. Combination of dynamic time warping and multivariate analysis for the comparison of comprehensive two-dimensional gas chromatograms: Application to plant extracts. *J. Chromatogr. A* **2009**, *1216*, 2866–2872.
- (90) Vial, J.; Pezous, B.; Thiébaud, D.; Sassiati, P.; Teillet, B.; Cahours, X.; Rivals, I. The discriminant pixel approach: A new tool for the rational interpretation of GCxGC-MS chromatograms. *Talanta* **2011**, *83*, 1295–1301.
- (91) Kim, S.; Fang, A.; Wang, B.; Jeong, J.; Zhang, X. An optimal peak alignment for comprehensive two-dimensional gas chromatography mass spectrometry using mixture similarity measure. *Bioinformatics* **2011**, *27*, 1660–1666.
- (92) Wang, B.; Fang, A.; Heim, J.; Bogdanov, B.; Pugh, S.; Libardoni, M.; Zhang, X. DISCO: Distance and spectrum correlation optimization alignment for two-dimensional gas chromatography time-of-flight mass spectrometry-based metabolomics. *Anal. Chem.* **2010**, *82*, 5069–5081.

- (93) Mommers, J.; Knooren, J.; Mengerink, Y.; Wilbers, A.; Vreuls, R.; van der Wal, S. Retention time locking procedure for comprehensive two-dimensional gas chromatography. *J. Chromatogr. A* **2011**, *1218*, 3159–3165.
- (94) Dimitriou-Christidis, P.; Bonvin, A.; Samanipour, S.; Hollender, J.; Rutler, R.; Westphale, J.; Gros, J.; Arey, J. S. GC×GC quantification of priority and emerging nonpolar halogenated micropollutants in all types of wastewater matrices: analysis methodology, chemical occurrence, and partitioning. *Environ. Sci. Technol.* **2015**, *49*, 7914–7925.
- (95) Frysinger, G. S.; Gaines, R. B.; Reddy, C. M. GC × GC—A new analytical tool for environmental forensics. *Environ. Forensics* **2002**, *3*, 27–34.
- (96) Sibson, R. A vector identity for the Dirichlet tessellation. *Math. Proc. Camb. Philos. Soc.* **1980**, *87*, 151–155.
- (97) de Smith, M. J.; Goodchild, M. F.; Longley, P. A. *Geospatial Analysis, A Comprehensive Guide to Principles, Techniques and Software Tools*; Matador.; Leicester, 2007.
- (98) Keys, R. Cubic convolution interpolation for digital image processing. *IEEE Trans. Acoust. Speech Signal Process.* **1981**, *29*, 1153–1160.
- (99) *Matlab*; The MathWorks Inc.: Natick, 2010.
- (100) Gros, J.; Arey, J. S. *Gros-Arey code to align GC×GC chromatograms*; <https://github.com/jsarey/GCxGC-alignment>, 2015.
- (101) *GC Image*; Zoex Corporation: Houston, 2012.
- (102) van Mispelaar, V. G.; Smilde, A. K.; de Noord, O. E.; Blomberg, J.; Schoenmakers, P. J. Classification of highly similar crude oils using data sets from comprehensive two-dimensional gas chromatography and multivariate techniques. *J. Chromatogr. A* **2005**, *1096*, 156–164.
- (103) van Mispelaar, V. G.; Tas, A. C.; Smilde, A. K.; Schoenmakers, P. J.; van Asten, A. C. Quantitative analysis of target components by comprehensive two-dimensional gas chromatography. *J. Chromatogr. A* **2003**, *1019*, 15–29.
- (104) Mackay, D.; Shiu, W. Y. Aqueous solubilities of weathered northern crude oils. *Bull. Environ. Contam. Toxicol.* **1976**, *15*, 101–109.
- (105) Wolfe, D. A.; Hameedi, M. J.; Galt, J. A.; Watabayashi, G.; Short, J.; O’Claire, C.; Rice, S.; Michel, J.; Payne, J. R.; Braddock, J.; Hanna, S.; Sale, D. The fate of the oil spilled from the *Exxon Valdez*. *Environ. Sci. Technol.* **1994**, *28*, 560A–568A.
- (106) *Proceedings of a symposium on preliminary results from the September 1979 Researcher/Pierce Ixtoc-1 cruise*; National Oceanic and Atmospheric Administration, Office of Marine Pollution Assessment: Boulder, USA, 1980.
- (107) Boehm, P. D.; Cook, L. L.; Murray, K. J. Aromatic hydrocarbon concentrations in seawater: *Deepwater Horizon* oil spill. *Int. Oil Spill Conf. Proc.* **2011**, *2011*, abs371.
- (108) Ross, S.; Potter, S.; Belore, R.; Lewis, A. Dispersant testing at Ohmsett: Feasibility study and preliminary testing. *Int. Oil Spill Conf. Proc.* **2001**, 461–466.
- (109) *Meso-scale weathering of oil as a function of ice conditions. Oil properties, dispersability and in-situ burnability of weathered oil as a function of time*; JIP Report; 19; SINTEF Materials and Chemistry, Marine Environmental Technology, 2010.
- (110) Barth, T. Weathering of crude oil in natural marine environments: The concentration of polar degradation products in water under oil as measured in several field studies. *Chemosphere* **1984**, *13*, 67–86.
- (111) Genders, S. In-situ detection and tracking of oil in the water column. *Oil Chem. Pollut.* **1988**, *4*, 113–126.

-
- (112) Daling, P. S.; Strøm, T. Weathering of oils at sea: Model/field data comparisons. *Spill Sci. Technol. Bull.* **1999**, *5*, 63–74.
- (113) Daling, P. S.; Singaas, I.; Reed, M.; Hansen, O. Experiences in dispersant treatment of experimental oil spills. *Spill Sci. Technol. Bull.* **2002**, *7*, 201–213.
- (114) Smith, C. L.; MacIntyre, W. G. Initial aging of fuel oil films of sea water. *Int. Oil Spill Conf. Proc.* **1971**, 457–461.
- (115) Brussaard, C. P. D.; Peperzak, L.; Witte, Y.; Huisman, J. An experimental oil spill at sea. In *Handbook of Hydrocarbon and Lipid Microbiology*; Timmis, K. N., Ed.; Springer Berlin Heidelberg, 2010; pp. 3491–3502.
- (116) Cormack, D.; Nichols, J. A. The concentrations of oil in sea water resulting from natural and chemically induced dispersion of oil slicks. *Int. Oil Spill Conf. Proc.* **1977**, 381–385.
- (117) Jeffery, P. G. Large-scale experiments on the spreading of oil at sea and its disappearance by natural factors. *Int. Oil Spill Conf. Proc.* **1973**, 469–474.
- (118) Gill, S. D. Dispersant field trials in Canadian waters. *Int. Oil Spill Conf. Proc.* **1977**, 391–394.
- (119) Fingas, M.; Brown, C. E. Oil spill remote sensing: A forensic approach. In *Oil Spill Environmental Forensics*; Wang, Z.; Stout, S. A., Eds.; Academic Press: Burlington, 2007; pp. 419–447.
- (120) Sivadier, H. O.; Mikolaj, P. G. Measurement of evaporation rates from oil slicks on the open sea. *Int. Oil Spill Conf. Proc.* **1973**, 475–484.
- (121) Lichtenthaler, R. G.; Daling, P. S. Dispersion of chemically treated crude oil in Norwegian offshore waters. *Int. Oil Spill Conf. Proc.* **1983**, 7–14.
- (122) Delvigne, G. A. L. Experiments on natural and chemical dispersion of oil in laboratory and field circumstances. *Int. Oil Spill Conf. Proc.* **1985**, 507–514.
- (123) Gill, S. D.; Goodman, R. H.; Swiss, J. Halifax '83 sea trial of oil spill dispersant concentrates. *Int. Oil Spill Conf. Proc.* **1985**, 479–482.
- (124) Lange, R. A 100 tons experimental oil spill at Halten Bank, off Norway. *Int. Oil Spill Conf. Proc.* **1985**, 503–505.
- (125) Buist, I. A.; Dickins, D. F. Experimental spills of crude oil in pack ice. *Int. Oil Spill Conf. Proc.* **1987**, 373–381.
- (126) McAuliffe, C. D. The weathering of volatile hydrocarbons from crude oil slicks on water. *Int. Oil Spill Conf. Proc.* **1989**, 357–363.
- (127) Hurford, N.; Buchanan, I. Results of the 1987 forties crude oil trial in the North Sea. *Int. Oil Spill Conf. Proc.* **1989**, 525–532.
- (128) Reed, M.; Turner, C.; Price, J. Implications of observations of intentional oil spills. *Int. Oil Spill Conf. Proc.* **1993**, 617–622.
- (129) Lunel, T. Dispersant effectiveness at sea. *Int. Oil Spill Conf. Proc.* **1995**, 147–155.
- (130) Rye, H.; Brandvik, P. J. Verification of subsurface oil spill models. *Int. Oil Spill Conf. Proc.* **1997**, 551–557.
- (131) Belore, R. C.; Trudel, B. K.; Lee, K. Correlating wave tank dispersant effectiveness tests with at-sea trials. *Int. Oil Spill Conf. Proc.* **2005**, 65–70.
- (132) Brekne, T. M.; Eide, G. A.; Skeie, G. M. Full scale implementation of state-of-the-art mechanical oil spill response technology on the Norwegian continental shelf. *Int. Oil Spill Conf. Proc.* **2005**, 831–836.

- (133) Dickins, D.; Brandvik, P. J.; Bradford, J.; Faksness, L.-G.; Liberty, L.; Daniloff, R. Svalbard 2006 experimental oil spill under ice: Remote sensing, oil weathering under Arctic conditions and assessment of oil removal by in-situ burning. *Int. Oil Spill Conf. Proc.* **2008**, 681–688.
- (134) Lewis, A.; Daling, P. S.; Strøm-Kristiansen, T.; Nordvik, A. B.; Fiocco, R. J. Weathering and chemical dispersion of oil at sea. *Int. Oil Spill Conf. Proc.* **1995**, 157–164.
- (135) Daling, P. S.; Aamo, O. M.; Lewis, A.; Strøm-Kristiansen, T. SINTEF/IKU oil-weathering model: Predicting oils' properties at sea. *Int. Oil Spill Conf. Proc.* **1997**, 297–307.
- (136) Short, J. W.; Irvine, G. V.; Mann, D. H.; Maselko, J. M.; Pella, J. J.; Lindeberg, M. R.; Payne, J. R.; Driskell, W. B.; Rice, S. D. Slightly weathered *Exxon Valdez* oil persists in Gulf of Alaska beach sediments after 16 years. *Environ. Sci. Technol.* **2007**, *41*, 1245–1250.
- (137) Irvine, G. V.; Mann, D. H.; Short, J. W. Multi-year persistence of oil mousse on high energy beaches distant from the *Exxon Valdez* spill origin. *Mar. Pollut. Bull.* **1999**, *38*, 572–584.
- (138) Boehm, P. D.; Neff, J. M.; Page, D. S. Assessment of polycyclic aromatic hydrocarbon exposure in the waters of Prince William Sound after the *Exxon Valdez* oil spill: 1989–2005. *Mar. Pollut. Bull.* **2007**, *54*, 339–356.
- (139) Chao, X.; Shankar, N. J.; Cheong, H. F. Two- and three-dimensional oil spill model for coastal waters. *Ocean Eng.* **2001**, *28*, 1557–1573.
- (140) Guo, W. J.; Wang, Y. X. A numerical oil spill model based on a hybrid method. *Mar. Pollut. Bull.* **2009**, *58*, 726–734.
- (141) Wang, J.; Shen, Y. Modeling oil spills transportation in seas based on unstructured grid, finite-volume, wave-ocean model. *Ocean Model.* **2010**, *35*, 332–344.
- (142) Short, J. W.; Heintz, R. A. Identification of *Exxon Valdez* oil in sediments and tissues from Prince William Sound and the Northwestern Gulf of Alaska based on a PAH weathering model. *Environ. Sci. Technol.* **1997**, *31*, 2375–2384.
- (143) Stiver, W.; Shiu, W. Y.; Mackay, D. Evaporation times and rates of specific hydrocarbons in oil spills. *Environ. Sci. Technol.* **1989**, *23*, 101–105.
- (144) Drivas, P. J. Calculation of evaporative emissions from multicomponent liquid spills. *Environ. Sci. Technol.* **1982**, *16*, 726–728.
- (145) Page, C. A.; Bonner, J. S.; Sumner, P. L.; Autenrieth, R. L. Solubility of petroleum hydrocarbons in oil/water systems. *Mar. Chem.* **2000**, *70*, 79–87.
- (146) Luk, G. K.; Kuan, H. F. Modelling the behaviour of oil spills in natural waters. *Can. J. Civ. Eng.* **1993**, *20*, 210–219.
- (147) French McCay, D. P.; Payne, J. R. Model of oil fate and water concentrations with and without application of dispersants. *Proc. 24th Arct. Mar. Oilspill Tech. Semin.* **2001**, 611–645.
- (148) Hibbs, D. E.; Gulliver, J. S. Dissolution rate coefficients for surface slicks on rivers. *Water Res.* **1999**, *33*, 1811–1816.
- (149) Southworth, G. R.; Herbes, S. E.; Allen, C. P. Evaluating a mass transfer model for the dissolution of organics from oil films into water. *Water Res.* **1983**, *17*, 1647–1651.
- (150) Mackay, D.; Leinonen, P. J. *Mathematical model of the behaviour of oil spills on water with natural and chemical dispersion*; EPS-3-EC-77-19; Department of Fisheries and the Environment, 1977.
- (151) Yang, W. C.; Wang, H. Modeling of oil evaporation in aqueous environment. *Water Res.* **1977**, *11*, 879–887.

- (152) Fingas, M. Chapter 3 - Introduction to oil chemistry and properties. In *Oil Spill Science and Technology*; Mervin Fingas, Ed.; Gulf Professional Publishing: Boston, 2011; pp. 51–59.
- (153) Reed, M.; Ekrol, N.; Daling, P.; Johansen, Ø.; Ditlevsen, M. K.; Swahn, I.; Myrhaug Resby, J. L.; Skognes, K. *SINTEF oil weathering model user's manual, Version 3.0*; SINTEF Materials and Chemistry: Trondheim, Norway, 2004.
- (154) *Crude oil assay, Grane*; Statoil: Norway, 2003; p. 18.
- (155) Mullins, O. C.; Ventura, G. T.; Nelson, R. K.; Betancourt, S. S.; Raghuraman, B.; Reddy, C. M. Visible–near-infrared spectroscopy by downhole fluid analysis coupled with comprehensive two-dimensional gas chromatography to address oil reservoir complexity. *Energy Fuels* **2008**, *22*, 496–503.
- (156) Schwarzenbach, R. P.; Gschwend, P. M.; Imboden, D. M. *Environmental Organic Chemistry*; 2nd ed.; John Wiley & Sons, Inc.: Hoboken, 2003.
- (157) Fick, A. Ueber Diffusion. *Ann. Phys.* **1855**, *170*, 59–86.
- (158) Einstein, A. Über die von der molekularkinetischen Theorie der Wärme geforderte Bewegung von in ruhenden Flüssigkeiten suspendierten Teilchen. *Ann. Phys.* **1905**, *322*, 549–560.
- (159) Fischer, H. B.; List, E. J.; Koh, R. C. Y.; Imberger, J.; Brooks, N. H. *Mixing in Inland and Coastal Waters*; Academic Press: London, 1979.
- (160) Brown, J. W.; Churchill, R. V. *Fourier Series and Boundary Value Problems*; 5th ed.; McGraw-Hill: New York, 1993.
- (161) Becker, J. J.; Sandwell, D. T.; Smith, W. H. F.; Braud, J.; Binder, B.; Depner, J.; Fabre, D.; Factor, J.; Ingalls, S.; Kim, S.-H.; Ladner, R.; Marks, K.; Nelson, S.; Pharaoh, A.; Trimmer, R.; Von Rosenberg, J.; Wallace, G.; Weatherall, P. Global bathymetry and elevation data at 30 arc seconds resolution: SRTM30_PLUS. *Mar. Geod.* **2009**, *32*, 355–371.
- (162) Xie, H.; Yapa, P. D.; Nakata, K. Modeling emulsification after an oil spill in the sea. *J. Mar. Syst.* **2007**, *68*, 489–506.
- (163) Xu, D.; Lu, H.; Yu, D. On the relationships between the mean wavelength and wave-period of wind waves in deep water. *Appl. Ocean Res.* **1999**, *21*, 127–131.
- (164) Ichiye, T. Upper ocean boundary-layer flow determined by dye diffusion. *Phys. Fluids* **1967**, *10*, S270.
- (165) Hu, H.; Wang, J. Modeling effects of tidal and wave mixing on circulation and thermohaline structures in the Bering Sea: Process studies. *J. Geophys. Res. Oceans* **2010**, *115*, C01006.
- (166) Brutsaert, W. *Evaporation into the Atmosphere*; Kluwer Academic Publishers: Dordrecht, Netherlands, 1982.
- (167) Ambaum, M. H. P. *Thermal Physics of the Atmosphere*; John Wiley & Sons: Chichester, UK, 2010.
- (168) Kumar, L.; Andrew K. S.; Knowles, E. Modelling topographic variation in solar radiation in a GIS environment. *Int. J. Geogr. Inf. Sci.* **1997**, *11*, 475–497.
- (169) Becker, G. A. Beiträge zur Hydrographie und Wärmebilanz der Nordsee. *Dt Hydrogr Z* **1981**, *34*, 167–262.
- (170) Pohlmann, T. Calculating the annual cycle of the vertical eddy viscosity in the North Sea with a three-dimensional baroclinic shelf sea circulation model. *Cont. Shelf Res.* **1996**, *16*, 147–161.
- (171) Wüest, A.; Carmack, E. A priori estimates of mixing and circulation in the hard-to-reach water body of Lake Vostok. *Ocean Model.* **2000**, *2*, 29–43.

- (172) Mackay, D.; Shiu, W. Y.; Ma, K.-C.; Lee, S. C. *Handbook of Physical-Chemical Properties and Environmental Fate for Organic Chemicals*; 2nd ed.; Taylor & Francis: Boca Raton, Florida, U.S.A., 2006.
- (173) Xie, W.-H.; Shiu, W.-Y.; Mackay, D. A review of the effect of salts on the solubility of organic compounds in seawater. *Mar. Environ. Res.* **1997**, *44*, 429–444.
- (174) Sharqawy, M. H.; Lienhard, J. H.; Zubair, S. M. Thermophysical properties of seawater: A review of existing correlations and data. *Desalination Water Treat.* **2010**, *16*, 354–380.
- (175) Tsonopoulos, C. Thermodynamic analysis of the mutual solubilities of normal alkanes and water. *Fluid Phase Equilibria* **1999**, *156*, 21–33.
- (176) Ferguson, A. L.; Debenedetti, P. G.; Panagiotopoulos, A. Z. Solubility and molecular conformations of *n*-alkane chains in water. *J. Phys. Chem. B* **2009**, *113*, 6405–6414.
- (177) McCain, W. D. Jr. *The Properties of Petroleum Fluids*; 2nd ed.; PennWell: Tulsa, 1990.
- (178) Sebastião, P.; Guedes Soares, C. Modeling the fate of oil spills at sea. *Spill Sci. Technol. Bull.* **1995**, *2*, 121–131.
- (179) Delvigne, G. A. L.; Sweeney, C. E. Natural dispersion of oil. *Oil Chem. Pollut.* **1988**, *4*, 281–310.
- (180) Yapa, P. Modeling oil spills to mitigate coastal pollution. In *Handbook of Environmental Fluid Dynamics*; CRC Press, 2012; Vol. 2, pp. 243–256.
- (181) Ezra, S.; Feinstein, S.; Pelly, I.; Bauman, D.; Miloslavsky, I. Weathering of fuel oil spill on the east Mediterranean coast, Ashdod, Israel. *Org. Geochem.* **2000**, *31*, 1733–1741.
- (182) Hiemenz, P. C.; Rajagopalan, R. *Principles of Colloid and Surface Chemistry*; 3rd ed.; Marcel Dekker: New York, 1997.
- (183) Irvine, G. V.; Mann, D. H.; Short, J. W. Persistence of 10-year old Exxon Valdez oil on Gulf of Alaska beaches: The importance of boulder-armoring. *Mar. Pollut. Bull.* **2006**, *52*, 1011–1022.
- (184) Mackay, D.; Buist, I.; Mascarenhas, R.; Paterson, S. *Oil spill processes and models*; EE-8; Environment Canada, 1980.
- (185) Thorpe, S. A. Langmuir circulation and the dispersion of oil spills in shallow seas. *Spill Sci. Technol. Bull.* **2000**, *6*, 213–223.
- (186) Aeppli, C.; Reddy, C. M.; Nelson, R. K.; Kellermann, M. Y.; Valentine, D. L. Recurrent oil sheens at the *Deepwater Horizon* disaster site fingerprinted with synthetic hydrocarbon drilling fluids. *Environ. Sci. Technol.* **2013**, *47*, 8211–8219.
- (187) Justwan, H.; Dahl, B.; Isaksen, G. H. Geochemical characterisation and genetic origin of oils and condensates in the South Viking Graben, Norway. *Mar. Pet. Geol.* **2006**, *23*, 213–239.
- (188) Fingas, M. F. Modeling evaporation using models that are not boundary-layer regulated. *J. Hazard. Mater.* **2004**, *107*, 27–36.
- (189) Fingas, M. Chapter 9 - Evaporation modeling. In *Oil Spill Science and Technology*; Fingas, Mervin, Ed.; Gulf Professional Publishing: Boston, 2011; pp. 201–242.
- (190) Middlebrook, A. M.; Murphy, D. M.; Ahmadov, R.; Atlas, E. L.; Bahreini, R.; Blake, D. R.; Brioude, J.; de Gouw, J. A.; Fehsenfeld, F. C.; Frost, G. J.; Holloway, J. S.; Lack, D. A.; Langridge, J. M.; Lueb, R. A.; McKeen, S. A.; Meagher, J. F.; Meinardi, S.; Neuman, J. A.; Nowak, J. B.; Parrish, D. D.; Peischl, J.; Perring, A. E.; Pollack, I. B.; Roberts, J. M.; Ryerson, T. B.; Schwarz, J. P.; Spackman, J. R.; Warneke, C.; Ravishankara, A. R. Air quality implications of the *Deepwater Horizon* oil spill. *Proc. Natl. Acad. Sci.* **2012**, *109*, 20280–20285.

-
- (191) *Aerial observations of oil at sea*; HAZMAT; 96-7; National Oceanic and Atmospheric Administration, Office of Ocean Resources Conservation and Assessment, Hazardous Materials Response and Assessment Division, Modeling and Simulation Studies Branch: Seattle, Washington, U.S.A., 1996.
- (192) Shaw, D. G.; Reidy, S. K. Chemical and size fractionation of aqueous petroleum dispersions. *Environ. Sci. Technol.* **1979**, *13*, 1259–1263.
- (193) Smith, K. E. C.; Thullner, M.; Wick, L. Y.; Harms, H. Dissolved organic carbon enhances the mass transfer of hydrophobic organic compounds from nonaqueous phase liquids (NAPLs) into the aqueous phase. *Environ. Sci. Technol.* **2011**, *45*, 8741–8747.
- (194) Fritt-Rasmussen, J.; Brandvik, P. J.; Villumsen, A.; Stenby, E. H. Comparing ignitability for in situ burning of oil spills for an asphaltenic, a waxy and a light crude oil as a function of weathering conditions under arctic conditions. *Cold Reg. Sci. Technol.* **2012**, *72*, 1–6.
- (195) Ross, A. S.; Farrimond, P.; Erdmann, M.; Larter, S. R. Geochemical compositional gradients in a mixed oil reservoir indicative of ongoing biodegradation. *Org. Geochem.* **2010**, *41*, 307–320.
- (196) *Crude oil assay, Grane*; Statoil: Norway, 2012; p. 18.
- (197) Welty, R. W.; Wicks, C. E.; Wilson, R. E.; Rorrer, G. L. *Fundamentals of Momentum, Heat, and Mass Transfer*; 5th ed.; John Wiley & Sons: Hoboken, 2008.
- (198) Lewis, W. K.; Whitman, W. G. Principles of gas absorption. *Ind. Eng. Chem.* **1924**, *16*, 1215–1220.
- (199) Bandara, U. C.; Yapa, P. D.; Xie, H. Fate and transport of oil in sediment laden marine waters. *J. Hydro-Environ. Res.* **2011**, *5*, 145–156.
- (200) Poling, B., E.; Prausnitz, J. M.; O’Connell, J. P. *The Properties of Gases and Liquids*; 5th ed.; McGraw-Hill, 2001.
- (201) Gill, A. E. *Atmosphere-ocean dynamics*; International Geophysics Series; Academic Press: New York, 1982.
- (202) Elias, V. O.; Cardoso, J. N.; Simoneit, B. R. T. Acyclic lipids in Amazon shelf waters. *Estuar. Coast. Shelf Sci.* **2000**, *50*, 231–243.
- (203) *Final report on the investigation of the Macondo well blowout*; Deepwater Horizon Study Group, 2011; p. 124.
- (204) Chanton, J.; Zhao, T.; Rosenheim, B. E.; Joye, S.; Bosman, S.; Brunner, C.; Yeager, K. M.; Diercks, A. R.; Hollander, D. Using natural abundance radiocarbon to trace the flux of petrocarbon to the seafloor following the *Deepwater Horizon* oil spill. *Environ. Sci. Technol.* **2015**, *49*, 847–854.
- (205) Valentine, D. L.; Fisher, G. B.; Bagby, S. C.; Nelson, R. K.; Reddy, C. M.; Sylva, S. P.; Woo, M. A. Fallout plume of submerged oil from *Deepwater Horizon*. *Proc. Natl. Acad. Sci.* **2014**, *111*, 15906–15911.
- (206) Ahmed, Tarek *Reservoir Engineering Handbook*; 4th ed.; Elsevier: Burlington, 2010.
- (207) Gautier, D. L.; Bird, K. J.; Charpentier, R. R.; Grantz, A.; Houseknecht, D. W.; Klett, T. R.; Moore, T. E.; Pitman, J. K.; Schenk, C. J.; Schuenemeyer, J. H.; Sørensen, K.; Tenyson, M. E.; Valin, Z. C.; Wandrey, C. J. Assessment of undiscovered oil and gas in the Arctic. *Science* **2009**, *324*, 1175–1179.
- (208) Speight, J. G. Offshore oil and gas. In *Handbook of Offshore Oil and Gas Operations*; Gulf Professional Publishing, 2014.
- (209) Zick, A. A. *Equation-of-state fluid characterization and analysis of the Macondo reservoir fluids*; Expert report prepared on behalf of the United States TREX-011490R; 2013.

- (210) de Hemptinne, J.-C.; Peumery, R.; Ruffier-Meray, V.; Moracchini, G.; Naiglin, J.; Carpentier, B.; Oudin, J. L.; Connan, J. Compositional changes resulting from the water-washing of a petroleum fluid. *J. Pet. Sci. Eng.* **2001**, *29*, 39–51.
- (211) Dhima, A.; de Hemptinne, J.-C.; Jose, J. Solubility of hydrocarbons and CO₂ mixtures in water under high pressure. *Ind. Eng. Chem. Res.* **1999**, *38*, 3144–3161.
- (212) de Hemptinne, J. C.; Dhima, A.; Zhou, H. The importance of water-hydrocarbon phase equilibria during reservoir production and drilling operations. *Rev. Inst. Francais Pet.* **1998**, *53*, 283–302.
- (213) Shakir, S.; de Hemptinne, J.-C. The effect of diffusion on the modeling of the water-washing phenomenon. *J. Pet. Sci. Eng.* **2007**, *58*, 403–412.
- (214) Krichevsky, I. R.; Kasarnovsky, J. S. Thermodynamical calculations of solubilities of nitrogen and hydrogen in water at high pressures. *J. Am. Chem. Soc.* **1935**, *57*, 2168–2171.
- (215) King, M. B. *Phase Equilibrium in Mixtures*; Danckwerts, P. V., Ed.; International series of monographs in chemical engineering; Pergamon press: Oxford, 1969.
- (216) Peng, D.-Y.; Robinson, D. B. A new two-constant equation of state. *Ind. Eng. Chem. Fundam.* **1976**, *15*, 59–64.
- (217) Gaines, R. B.; Frysinger, G. S.; Reddy, C. M.; Nelson, R. K. Oil spill source identification by comprehensive two-dimensional gas chromatography (GC×GC). In *Oil Spill Environmental Forensics*; Wang, Z.; Stout, S. A., Eds.; Academic Press: Burlington, 2007; pp. 169–206.
- (218) Frysinger, G. S.; Gaines, R. B.; Ledford Jr., E. B. Quantitative determination of BTEX and total aromatic compounds in gasoline by comprehensive two-dimensional gas chromatography (GC×GC). *J. High Resolut. Chromatogr.* **1999**, *22*, 195–200.
- (219) Frysinger, G. S.; Gaines, R. B.; Xu, L.; Reddy, C. M. Resolving the unresolved complex mixture in petroleum-contaminated sediments. *Environ. Sci. Technol.* **2003**, *37*, 1653–1662.
- (220) Mao, D.; Lookman, R.; Van De Weghe, H.; Van Look, D.; Vanermen, G.; De Brucker, N.; Diels, L. Detailed analysis of petroleum hydrocarbon attenuation in biopiles by high-performance liquid chromatography followed by comprehensive two-dimensional gas chromatography. *J. Chromatogr. A* **2009**, *1216*, 1524–1527.
- (221) Tran, T. C.; Logan, G. A.; Grosjean, E.; Ryan, D.; Marriott, P. J. Use of comprehensive two-dimensional gas chromatography/time-of-flight mass spectrometry for the characterization of biodegradation and unresolved complex mixtures in petroleum. *Geochim. Cosmochim. Acta* **2010**, *74*, 6468–6484.
- (222) *United States of America versus BP Exploration & Production, Inc., et al.*; 2015; Vol. Case 2:10-md- 02179-CJB-SS.
- (223) Robinson, D. B.; Peng, D.-Y. *The characterization of the heptanes and heavier fractions for the GPA Peng-Robinson programs*; Research Report 28; Gas Processors Association: Tulsa, 1978.
- (224) Michelsen, M. L.; Mollerup, J. M. *Thermodynamic Models: Fundamentals & Computational Aspects*; 2nd ed.; Tie-Line Publications: Holte, 2007.
- (225) Péneloux, A.; Rauzy, E.; Fréze, R. A consistent correction for Redlich-Kwong-Soave volumes. *Fluid Phase Equilibria* **1982**, *8*, 7–23.
- (226) Lin, H.; Duan, Y.-Y. Empirical correction to the Peng–Robinson equation of state for the saturated region. *Fluid Phase Equilibria* **2005**, *233*, 194–203.
- (227) Oliveira, M. B.; Coutinho, J. A. P.; Queimada, A. J. Mutual solubilities of hydrocarbons and water with the CPA EoS. *Fluid Phase Equilibria* **2007**, *258*, 58–66.

- (228) Lewan, M. D.; Warden, A.; Dias, R. F.; Lowry, Z. K.; Hannah, T. L.; Lillis, P. G.; Kokaly, R. F.; Hoefen, T. M.; Swayze, G. A.; Mills, C. T.; Harris, S. H.; Plumlee, G. S. Asphaltene content and composition as a measure of *Deepwater Horizon* oil spill losses within the first 80 days. *Org. Geochem.* **2014**, *75*, 54–60.
- (229) Zuo, J. Y.; Mullins, O. C.; Freed, D.; Elshahawi, H.; Dong, C.; Seifert, D. J. Advances in the Flory–Huggins–Zuo equation of state for asphaltene gradients and formation evaluation. *Energy Fuels* **2013**, *27*, 1722–1735.
- (230) Sander, R. Compilation of Henry's law constants, version 3.99. *Atmos Chem Phys Discuss* **2014**, *14*, 29615–30521.
- (231) Mathews, S. G. *Fluid analysis on Macondo samples*; Reservoir sample analysis report TREX-011575; Schlumberger: Houston, 2010; p. 50.
- (232) LeBlanc, J. *Volatile oil reservoir fluid study for BP*; TREX-130815; Pencor: Broussard, 2010.
- (233) Carmichael, C. A.; Arey, J. S.; Graham, W. M.; Linn, L. J.; Lemkau, K. L.; Nelson, R. K.; Reddy, C. M. Floating oil-covered debris from *Deepwater Horizon*: Identification and application. *Environ. Res. Lett.* **2012**, *7*, 015301.
- (234) Plyasunov, A. V.; Shock, E. L. Thermodynamic functions of hydration of hydrocarbons at 298.15 K and 0.1 MPa. *Geochim. Cosmochim. Acta* **2000**, *64*, 439–468.
- (235) Liu, H.; Ruckenstein, E. Aggregation of hydrocarbons in dilute aqueous solutions. *J. Phys. Chem. B* **1998**, *102*, 1005–1012.
- (236) Graziano, G. Partial molar volume of *n*-alcohols at infinite dilution in water calculated by means of scaled particle theory. *J. Chem. Phys.* **2006**, *124*, 134507.
- (237) Ni, N.; Yalkowsky, S. H. Prediction of Setschenow constants. *Int. J. Pharm.* **2003**, *254*, 167–172.
- (238) Weiss, R. F. Carbon dioxide in water and seawater: The solubility of a non-ideal gas. *Mar. Chem.* **1974**, *2*, 203–215.
- (239) Weiss, R. F. The solubility of nitrogen, oxygen and argon in water and seawater. *Deep Sea Res. Oceanogr. Abstr.* **1970**, *17*, 721–735.
- (240) Aवाल्ले, L.; Trassy, L.; Neau, E.; Jaubert, J. N. Thermodynamic modeling for petroleum fluids I. Equation of state and group contribution for the estimation of thermodynamic parameters of heavy hydrocarbons. *Fluid Phase Equilibria* **1997**, *139*, 155–170.
- (241) Gharagheizi, F.; Eslamimanesh, A.; Mohammadi, A. H.; Richon, D. Determination of critical properties and acentric factors of pure compounds using the artificial neural network group contribution algorithm. *J. Chem. Eng. Data* **2011**, *56*, 2460–2476.
- (242) Hine, J.; Mookerjee, P. K. Structural effects on rates and equilibria. XIX. Intrinsic hydrophilic character of organic compounds. Correlations in terms of structural contributions. *J. Org. Chem.* **1975**, *40*, 292–298.
- (243) Majer, V.; Sedlbauer, J.; Bergin, G. Henry's law constant and related coefficients for aqueous hydrocarbons, CO₂ and H₂S over a wide range of temperature and pressure. *Fluid Phase Equilibria* **2008**, *272*, 65–74.
- (244) Twu, C. H. An internally consistent correlation for predicting the critical properties and molecular weights of petroleum and coal-tar liquids. *Fluid Phase Equilibria* **1984**, *16*, 137–150.
- (245) Chen, D. H.; Dinivahi, M. V.; Jeng, C. Y. New acentric factor correlation based on the Antoine equation. *Ind. Eng. Chem. Res.* **1993**, *32*, 241–244.

- (246) Zuo, J. Y.; Zhang, D.; Dubost, F.; Dong, C.; Mullins, O. C.; O'Keefe, M.; Betancourt, S. S. EOS-based downhole fluid characterization. In *SPE 114702*; Society of Petroleum Engineers, 2008.
- (247) Pedersen, K. S.; Christensen, P. L.; Shaikh, J. A. *Phase Behavior of Petroleum Reservoir Fluids*; 2nd ed.; CRC Press: Boca Raton, 2014.
- (248) Katz, D. L.; Firoozabadi, A. Predicting phase behavior of condensate/crude-oil systems using methane interaction coefficients. *J. Pet. Technol.* **1978**, *30*, 1649–1655.
- (249) Privat, R.; Jaubert, J.-N. Addition of the sulfhydryl group (SH) to the PPR78 model: Estimation of missing group-interaction parameters for systems containing mercaptans and carbon dioxide or nitrogen or methane, from newly published data. *Fluid Phase Equilibria* **2012**, *334*, 197–203.
- (250) Xu, X.; Jaubert, J.-N.; Privat, R.; Duchet-Suchaux, P.; Braña-Mulero, F. Predicting binary-interaction parameters of cubic equations of state for petroleum fluids containing pseudo-components. *Ind. Eng. Chem. Res.* **2015**, *54*, 2816–2824.
- (251) Lyckman, E. W.; Eckert, C. A.; Prausnitz, J. M. Generalized reference fugacities for phase equilibrium thermodynamics. *Chem. Eng. Sci.* **1965**, *20*, 685–691.
- (252) Endo, S.; Pfennigsdorff, A.; Goss, K.-U. Salting-out effect in aqueous NaCl solutions: Trends with size and polarity of solute molecules. *Environ. Sci. Technol.* **2012**, *46*, 1496–1503.
- (253) Abdelrahim, M. Measurement of interfacial tension in hydrocarbon/water/dispersant systems at deepwater conditions. Master thesis, Louisiana State University, 2012.
- (254) *Oil budget calculator*; The Federal Interagency Solutions Group, Oil Budget Calculator Science and Engineering Team, 2010; p. 217.
- (255) Aliseda, A.; Bommer, P.; Espina, P.; Flores, O.; Lasheras, J. C.; Lehr, B.; Leifer, I.; Possolo, A.; Riley, J.; Savas, O.; Shaffer, F.; Wereley, S.; Yapa, P. *Deepwater Horizon release estimate by PIV*; National Incident Command Flow Rate Technical Group, 2010; p. 215.
- (256) Sawamura, S.; Kitamura, K.; Taniguchi, Y. Effect of pressure on the solubilities of benzene and alkylbenzenes in water. *J. Phys. Chem.* **1989**, *93*, 4931–4935.
- (257) Sawamura, S.; Suzuki, K.; Taniguchi, Y. Effect of pressure on the solubilities of *o*-, *m*- and *p*-xylene in water. *J. Solut. Chem.* **1987**, *16*, 649–657.
- (258) Sawamura, S.; Tsuchiya, M.; Ishigami, T.; Taniguchi, Y.; Suzuki, K. Effect of pressure on the solubility of naphthalene in water at 25°C. *J. Solut. Chem.* **1993**, *22*, 727–732.
- (259) Kujawinski, E. B.; Kido Soule, M. C.; Valentine, D. L.; Boysen, A. K.; Longnecker, K.; Redmond, M. C. Fate of dispersants associated with the *Deepwater Horizon* oil spill. *Environ. Sci. Technol.* **2011**, *45*, 1298–1306.
- (260) Clift, R.; Grace, J. R.; Weber, M. E. *Bubbles, Drops, and Particles*; Academic Press: New York, 1978.
- (261) Passow, U.; Ziervogel, K.; Asper, V.; Diercks, A. Marine snow formation in the aftermath of the *Deepwater Horizon* oil spill in the Gulf of Mexico. *Environ. Res. Lett.* **2012**, *7*, 035301.
- (262) Fisher, C. R.; Demopoulos, A. W. J.; Cordes, E. E.; Baums, I. B.; White, H. K.; Bourque, J. R. Coral communities as indicators of ecosystem-level impacts of the *Deepwater Horizon* spill. *BioScience* **2014**, *64*, 796–807.
- (263) Fu, J.; Gong, Y.; Zhao, X.; O'Reilly, S. E.; Zhao, D. Effects of oil and dispersant on formation of marine oil snow and transport of oil hydrocarbons. *Environ. Sci. Technol.* **2014**, *48*, 14392–14399.

- (264) Crone, T. J.; Tolstoy, M. Magnitude of the 2010 Gulf of Mexico oil leak. *Science* **2010**, *330*, 634–634.
- (265) Hsieh, P. *Computer simulation of reservoir depletion and oil flow from the Macondo well following the Deepwater Horizon blowout*; TREX 008615; 2010.
- (266) Dykhuizen, R. C. *Flow rates from Macondo MC252 well submitted on behalf of the United States*; TREX 011452; 2013.
- (267) Ratzel, A. C. III *DOE-NNSA flow analysis studies associated with the oil release following the Deepwater Horizon accident*; TREX 009361; Sandia National Laboratories: Albuquerque, 2011.
- (268) Hsieh, P. A. Application of MODFLOW for oil reservoir simulation during the *Deepwater Horizon* crisis. *Ground Water* **2011**, *49*, 319–323.
- (269) Socolofsky, S. A.; Bhaumik, T.; Seol, D.-G. Double-plume integral models for near-field mixing in multiphase plumes. *J. Hydraul. Eng.* **2008**, *134*, 772–783.
- (270) Socolofsky, S. A. *TAMOC*; College Station, 2015.
- (271) Lohrenz, J.; Bray, B. G.; Clark, C. R. Calculating viscosities of reservoir fluids from their compositions. *J. Pet. Technol.* **1964**, 1171–1176.
- (272) Burant, A.; Lowry, G. V.; Karamalidis, A. K. Measurement of Setschenow constants for six hydrophobic compounds in simulated brines and use in predictive modeling for oil and gas systems. *Chemosphere* **2016**, *144*, 2247–2256.
- (273) Zhao, L.; Boufadel, M. C.; Socolofsky, S. A.; Adams, E.; King, T.; Lee, K. Evolution of droplets in subsea oil and gas blowouts: Development and validation of the numerical model VDROD-J. *Mar. Pollut. Bull.* **2014**, *83*, 58–69.
- (274) Davies, C. S.; Loomis, N. *Deepwater Horizon oil spill (DWHOS) water column technical working group, Image data processing plan: Holocam, Description of data processing methods used to determine oil droplet size distributions from in situ holographic imaging during June 2010 on cruise M/V Jack Fitz 3*.
- (275) Li, Z.; Lee, K.; Kepkey, P. E.; Mikkelsen, O.; Pottsmith, C. Monitoring dispersed oil droplet size distribution at the Gulf of Mexico *Deepwater Horizon* spill site. *Int. Oil Spill Conf.* **2011**, 1–15.
- (276) Zhao, L.; Boufadel, M. C.; Adams, E.; Socolofsky, S. A.; King, T.; Lee, K.; Nedwed, T. Simulation of scenarios of oil droplet formation from the *Deepwater Horizon* blowout. *Mar. Pollut. Bull.* **2015**, *101*, 304–319.
- (277) Johansen, Ø.; Brandvik, P. J.; Farooq, U. Droplet breakup in subsea oil releases – Part 2: Predictions of droplet size distributions with and without injection of chemical dispersants. *Mar. Pollut. Bull.* **2013**, *73*, 327–335.
- (278) Bandara, U.; Yapa, P. Bubble sizes, breakup, and coalescence in deepwater gas/oil plumes. *J. Hydraul. Eng.* **2011**, *137*, 729–738.
- (279) Zheng, L.; Yapa, P. D.; Chen, F. A model for simulating deepwater oil and gas blowouts - Part I: Theory and model formulation. *J. Hydraul. Res.* **2003**, *41*, 339–351.
- (280) Johansen, Ø. Development and verification of deep-water blowout models. *Mar. Pollut. Bull.* **2003**, *47*, 360–368.
- (281) Socolofsky, S. A.; Adams, E. E. Multi-phase plumes in uniform and stratified crossflow. *J. Hydraul. Res.* **2002**, *40*, 661–672.
- (282) Socolofsky, S. A.; Adams, E. E.; Boufadel, M. C.; Aman, Z. M.; Johansen, Ø.; Konkel, W. J.; Lindo, D.; Madsen, M. N.; North, E. W.; Paris, C. B.; Rasmussen, D.; Reed, M.; Rønningen, P.; Sim, L. H.; Uhrenholdt, T.; Anderson, K. G.; Cooper, C.; Nedwed, T. J. Inter-comparison of oil spill prediction models for accidental blowout scenarios with and without subsea chemical dispersant injection. *Mar. Pollut. Bull.* **2015**, *96*, 110–126.

- (283) Dissanayake, A. L.; Jun, I.; Socolofsky, S. A. Numerical models to simulate oil and gas blowout plumes and associated chemical and physical processes of hydrocarbons. In *E-proceedings of the 36 th IAHR World Congress*; The Hague, 2015.
- (284) Socolofsky, S. A.; Dissanayake, A. L.; Jun, I.; Gros, J.; Arey, J. S.; Reddy, C. M. Texas A&M Oilspill Calculator (TAMOC) modeling suite for subsea spills. In *Proceedings of the Thirty-Eighth AMOP Technical Seminar*; Environment Canada: Ottawa, 2015; pp. 153–168.
- (285) Fan, L.-S.; Yang, G. Q.; Lee, D. J.; Tsuchiya, K.; Luo, X. Some aspects of high-pressure phenomena of bubbles in liquids and liquid–solid suspensions. *Chem. Eng. Sci.* **1999**, *54*, 4681–4709.
- (286) Johnson, A. I.; Besik, F.; Hamielec, A. E. Mass transfer from a single rising bubble. *Can. J. Chem. Eng.* **1969**, *47*, 559–564.
- (287) Kumar, A.; Hartland, S. Correlations for prediction of mass transfer coefficients in single drop systems and liquid–liquid extraction columns. *Chem. Eng. Res. Des.* **1999**, *77*, 372–384.
- (288) Jun, I.; Socolofsky, S. A. Effects of hydrates on the dissolution of rising hydrocarbon bubbles from natural gas seepage in the deep ocean. *J. Geophys. Res.* **in review**.
- (289) Hsu, C.-Y. Resonant near-inertial current response to land-sea breeze in the Gulf of Mexico. Ph.D. Dissertation, Texas A&M University: College Station, not submitted.
- (290) Hyun, K. H.; He, R. Coastal upwelling in the South Atlantic Bight: A revisit of the 2003 cold event using long term observations and model hindcast solutions. *J. Mar. Syst.* **2010**, *83*, 1–13.
- (291) Xue, Z.; Zambon, J.; Yao, Z.; Liu, Y.; He, R. An integrated ocean circulation, wave, atmosphere, and marine ecosystem prediction system for the South Atlantic Bight and Gulf of Mexico. *J. Oper. Oceanogr.* **2015**, *8*, 80–91.
- (292) COREXIT® Ingredients <http://www.nalcoesllc.com/nes/1602.htm> (accessed Dec 18, 2015).
- (293) Riehm, D. A.; McCormick, A. V. The role of dispersants' dynamic interfacial tension in effective crude oil spill dispersion. *Mar. Pollut. Bull.* **2014**, *84*, 155–163.
- (294) Danesh, A. *PVT and Phase Behaviour of Petroleum Reservoir Fluids*; Developments in Petroleum Science; Elsevier.; Amsterdam, 1998.
- (295) Firoozabadi, A.; Ramey, H. J. Surface tension of water-hydrocarbon systems at reservoir conditions. *J. Can. Pet. Technol.* **1988**, *27*, 41–48.
- (296) Hayduk, W.; Laudie, H. Prediction of diffusion coefficients for nonelectrolytes in dilute aqueous solutions. *AIChE J.* **1974**, *20*, 611–615.
- (297) Daniel-David, D.; Guerton, F.; Dicharry, C.; Torré, J.-P.; Broseta, D. Hydrate growth at the interface between water and pure or mixed CO₂/CH₄ gases: Influence of pressure, temperature, gas composition and water-soluble surfactants. *Chem. Eng. Sci.* **2015**, *132*, 118–127.
- (298) Rorick, R.; Nedwed, T.; DeMarco, G.; Cooper, C. Comment on “A tale of two spills: Novel science and policy implications of an emerging new oil spill model.” *BioScience* **2012**, *62*, 1009–1010.
- (299) *Matlab*; The MathWorks Inc.: Natick, 2014.
- (300) Bowman, A. W.; Azzalini, A. *Applied Smoothing Techniques for Data Analysis*; Oxford University Press: New York, 1997.
- (301) Hazen, T. C.; Dubinsky, E. A.; DeSantis, T. Z.; Andersen, G. L.; Piceno, Y. M.; Singh, N.; Jansson, J. K.; Probst, A.; Borglin, S. E.; Fortney, J. L.; Stringfellow, W. T.; Bill, M.; Conrad, M. E.; Tom, L. M.; Chavarria, K. L.; Alusi, T. R.; Lamendella, R.; Joyner, D. C.; Spier,

- C.; Baelum, J.; Auer, M.; Zemla, M. L.; Chakraborty, R.; Sonnenthal, E. L.; D'haeseleer, P.; Holman, H.-Y. N.; Osman, S.; Lu, Z.; Nostrand, J. D. V.; Deng, Y.; Zhou, J.; Mason, O. U. Deep-sea oil plume enriches indigenous oil-degrading bacteria. *Science* **2010**, *330*, 204–208.
- (302) Boehm, P. D.; Murray, K. J.; Cook, L. L. Distribution and attenuation of polycyclic aromatic hydrocarbons in Gulf of Mexico seawater from the *Deepwater Horizon* oil accident. *Environ. Sci. Technol.* **2016**, *50*, 584–592.
- (303) Payne, J. R.; Driskell, W. B. *Deepwater Horizon oil spill NRDA offshore adaptive sampling strategies and field observations*; 2015.
- (304) Material Safety Data Sheet, Docusate sodium, <https://www.spectrumchemical.com/MSDS/D3570.PDF>.
- (305) Hamme, R. C.; Emerson, S. R. The solubility of neon, nitrogen and argon in distilled water and seawater. *Deep Sea Res. Part Oceanogr. Res. Pap.* **2004**, *51*, 1517–1528.
- (306) Pilson, M. E. Q. *An Introduction to the Chemistry of the Sea*; 2nd ed.; Cambridge University Press: Cambridge, 2013.
- (307) Prince, R. C. Oil spill dispersants: Boon or bane? *Environ. Sci. Technol.* **2015**, *49*, 6376–6384.
- (308) Gray, J. L.; Kanagy, L. K.; Furlong, E. T.; Kanagy, C. J.; McCoy, J. W.; Mason, A.; Lauenstein, G. Presence of the Corexit component dioctyl sodium sulfosuccinate in Gulf of Mexico waters after the 2010 *Deepwater Horizon* oil spill. *Chemosphere* **2014**, *95*, 124–130.
- (309) Paris, C. B.; Hénaff, M. L.; Aman, Z. M.; Subramaniam, A.; Helgers, J.; Wang, D.-P.; Kourafalou, V. H.; Srinivasan, A. Evolution of the Macondo well blowout: Simulating the effects of the circulation and synthetic dispersants on the subsea oil transport. *Environ. Sci. Technol.* **2012**, *46*, 13293–13302.
- (310) Moghadamzadeh, H.; Maghsoodloorad, H.; Zarabpour, A.; Hemmati, A.; Shahsavari, S.; Shahsavari, S. Impact of lumping techniques for fluid characterization in gas condensate reservoir. *Aust. J. Basic Appl. Sci.* **2013**, *7*, 320–333.
- (311) Lee, S. T.; Jacoby, R. H.; Chen, W. H.; Culham, W. E. Experimental and theoretical studies on the fluid properties required for simulation of thermal processes. *Soc. Pet. Eng. J.* **1981**, *21*, 535–550.
- (312) Abraham, M. H.; Chadha, H. S.; Whiting, G. S.; Mitchell, R. C. Hydrogen bonding. 32. An analysis of water-octanol and water-alkane partitioning and the delta log P parameter of seiler. *J. Pharm. Sci.* **1994**, *83*, 1085–1100.
- (313) Battino, R.; Rettich, T. R.; Tominaga, T. The solubility of oxygen and ozone in liquids. *J. Phys. Chem. Ref. Data* **1983**, *12*, 163–178.
- (314) Redman, A. D.; McGrath, J. A.; Stubblefield, W. A.; Maki, A. W.; Di Toro, D. M. Quantifying the concentration of crude oil microdroplets in oil–water preparations. *Environ. Toxicol. Chem.* **2012**, *31*, 1814–1822.
- (315) Wang, Z.; Fingas, M.; Blenkinsopp, S.; Sergy, G.; Landriault, M.; Sigouin, L.; Foght, J.; Semple, K.; Westlake, D. W. S. Comparison of oil composition changes due to biodegradation and physical weathering in different oils. *J. Chromatogr. A* **1998**, *809*, 89–107.
- (316) Prince, R. C.; Walters, C. C. Biodegradation of oil hydrocarbons and its implications for source identification. In *Oil Spill Environmental Forensics*; Wang, Z.; Stout, S. A., Eds.; Academic Press: Burlington, 2007; pp. 349–379.
- (317) Prince, R. C.; Garrett, R. M.; Bare, R. E.; Grossman, M. J.; Townsend, T.; Suflita, J. M.; Lee, K.; Owens, E. H.; Sergy, G. A.; Braddock, J. F.; Lindstrom, J. E.; Lessard, R. R. The

- roles of photooxidation and biodegradation in long-term weathering of crude and heavy fuel oils. *Spill Sci. Technol. Bull.* **2003**, *8*, 145–156.
- (318) Sexstone, A.; Gustin, P.; Atlas, R. M. Long term interactions of microorganisms and Prudhoe Bay crude oil in tundra soils at Barrow, Alaska. *ARCTIC* **1978**, *31*, 348–354.
- (319) Brownawell, B. J.; Dick, J.; McElroy, A. E.; Reddy, C. M.; Nelson, R. K. *The environmental implications of the UCM in sediments of the New York Harbor complex*; A final report to the Hudson River Foundation on contract 002/003A; 2007.
- (320) Aeppli, C.; Carmichael, C. A.; Nelson, R. K.; Lemkau, K. L.; Graham, W. M.; Redmond, M. C.; Valentine, D. L.; Reddy, C. M. Oil weathering after the *Deepwater Horizon* disaster led to the formation of oxygenated residues. *Environ. Sci. Technol.* **2012**, *46*, 8799–8807.
- (321) Gough, M. A.; Rowland, S. J. Characterization of unresolved complex mixtures of hydrocarbons in petroleum. *Nature* **1990**, *344*, 648–650.
- (322) Prince, R. C.; Elmendorf, D. L.; Lute, J. R.; Hsu, C. S.; Haith, C. E.; Senius, J. D.; Dechert, G. J.; Douglas, G. S.; Butler, E. L. $17\alpha(H),21\beta(H)$ -hopane as a conserved internal marker for estimating the biodegradation of crude oil. *Environ. Sci. Technol.* **1994**, *28*, 142–145.
- (323) Wang, Z.; Fingas, M.; Owens, E. H.; Sigouin, L.; Brown, C. E. Long-term fate and persistence of the spilled *Metula* oil in a marine salt marsh environment: Degradation of petroleum biomarkers. *J. Chromatogr. A* **2001**, *926*, 275–290.
- (324) Guiliano, M.; El Anba-Lurot, F.; Doumenq, P.; Mille, G.; Rontani, J. F. Photo-oxidation of *n*-alkanes in simulated marine environmental conditions. *J. Photochem. Photobiol. Chem.* **1997**, *102*, 127–132.
- (325) Gesser, H. D.; Wildman, T. A.; Tewari, Y. B. Photooxidation of *n*-hexadecane sensitized by xanthone. *Environ. Sci. Technol.* **1977**, *11*, 605–608.
- (326) Charrié-Duhaut, A.; Lemoine, S.; Adam, P.; Connan, J.; Albrecht, P. Abiotic oxidation of petroleum bitumens under natural conditions. *Org. Geochem.* **2000**, *31*, 977–1003.
- (327) Wang, Z.; Fingas, M.; Sergy, G. Chemical characterization of crude oil residues from an Arctic beach by GC/MS and GC/FID. *Environ. Sci. Technol.* **1995**, *29*, 2622–2631.
- (328) Ventura, G. T.; Kenig, F.; Reddy, C. M.; Frysiner, G. S.; Nelson, R. K.; Mooy, B. V.; Gaines, R. B. Analysis of unresolved complex mixtures of hydrocarbons extracted from Late Archean sediments by comprehensive two-dimensional gas chromatography (GC×GC). *Org. Geochem.* **2008**, *39*, 846–867.
- (329) Garrett, R. M.; Rothenburger, S. J.; Prince, R. C. Biodegradation of fuel oil under laboratory and arctic marine conditions. *Spill Sci. Technol. Bull.* **2003**, *8*, 297–302.
- (330) Olson, J. J.; Mills, G. L.; Herbert, B. E.; Morris, P. J. Biodegradation rates of separated diesel components. *Environ. Toxicol. Chem.* **1999**, *18*, 2448–2453.
- (331) Mao, D.; Lookman, R.; Weghe, H. V. D.; Weltens, R.; Vanermen, G.; Brucker, N. D.; Diels, L. Combining HPLC-GCXGC, GCXGC/ToF-MS, and selected ecotoxicity assays for detailed monitoring of petroleum hydrocarbon degradation in soil and leaching water. *Environ. Sci. Technol.* **2009**, *43*, 7651–7657.
- (332) Miralles, G.; Grossi, V.; Acquaviva, M.; Duran, R.; Bertrand, J. C.; Cuny, P. Alkane biodegradation and dynamics of phylogenetic subgroups of sulfate-reducing bacteria in an anoxic coastal marine sediment artificially contaminated with oil. *Chemosphere* **2007**, *68*, 1327–1334.
- (333) Blumer, M.; Sass, J. Oil pollution: Persistence and degradation of spilled fuel oil. *Science* **1972**, *176*, 1120–1122.

- (334) Wenger, L. M.; Davis, C. L.; Isaksen, G. H. Multiple controls on petroleum biodegradation and impact on oil quality. *SPE Reserv. Eval. Eng.* **2002**, 375–383.
- (335) Wardroper, A. M. K.; Hoffmann, C. F.; Maxwell, J. R.; Barwise, A. J. G.; Goodwin, N. S.; Park, P. J. D. Crude oil biodegradation under simulated and natural conditions—II. Aromatic steroid hydrocarbons. *Org. Geochem.* **1984**, 6, 605–617.
- (336) Atlas, R. M.; Hazen, T. C. Oil biodegradation and bioremediation: A tale of the two worst spills in U.S. history. *Environ. Sci. Technol.* **2011**, 45, 6709–6715.
- (337) *ChromaTOF software instruction manual, Version 4.2x*; Leco Corporation: St-Joseph, U.S.A., 2009.
- (338) Farrington, J. W.; Teal, J. M.; Quinn, J. G.; Wade, T.; Burns, K. Intercalibration of analyses of recently biosynthesized hydrocarbons and petroleum hydrocarbons in marine lipids. *Bull. Environ. Contam. Toxicol.* **1973**, 10, 129–136.
- (339) Sutton, P. A.; Lewis, C. A.; Rowland, S. J. Isolation of individual hydrocarbons from the unresolved complex hydrocarbon mixture of a biodegraded crude oil using preparative capillary gas chromatography. *Org. Geochem.* **2005**, 36, 963–970.
- (340) Douglas, G. S.; Owens, E. H.; Hardenstine, J.; Prince, R. C. The OSSA II pipeline oil spill: The character and weathering of the spilled oil. *Spill Sci. Technol. Bull.* **2002**, 7, 135–148.
- (341) King, S. M.; Leaf, P. A.; Olson, A. C.; Ray, P. Z.; Tarr, M. A. Photolytic and photocatalytic degradation of surface oil from the *Deepwater Horizon* spill. *Chemosphere* **2014**, 95, 415–422.
- (342) Howard, P. H. Biodegradation. In *Handbook of Property Estimation Methods for Chemicals: Environmental and Health Sciences*; CRC Press: Boca Raton, Florida, 2000; p. 467.
- (343) Kwok, E.; Atkinson, R. Estimation of hydroxyl radical reaction-rate constants for gas-phase organic-compounds using a structure-reactivity relationship - an update. *Atmos. Environ.* **1995**, 29, 1685–1695.
- (344) Neeb, P. Structure-reactivity based estimation of the rate constants for hydroxyl radical reactions with hydrocarbons. *J. Atmospheric Chem.* **2000**, 35, 295–315.
- (345) Elordui-Zapatarietxe, S.; Rosell-Melé, A.; Moraleda, N.; Tolosa, I.; Albaigés, J. Phase distribution of hydrocarbons in the water column after a pelagic deep ocean oil spill. *Mar. Pollut. Bull.* **2010**, 60, 1667–1673.
- (346) Watson, J. S.; Jones, D. M.; Swannell, R. P. J.; van Duin, A. C. T. Formation of carboxylic acids during aerobic biodegradation of crude oil and evidence of microbial oxidation of hopanes. *Org. Geochem.* **2002**, 33, 1153–1169.
- (347) Wang, Z.; Fingas, M. Differentiation of the source of spilled oil and monitoring of the oil weathering process using gas chromatography-mass spectrometry. *J. Chromatogr. A* **1995**, 712, 321–343.
- (348) Lemkau, K. L.; Peacock, E. E.; Nelson, R. K.; Ventura, G. T.; Kovacs, J. L.; Reddy, C. M. The M/V *Cosco Busan* spill: Source identification and short-term fate. *Mar. Pollut. Bull.* **2010**, 60, 2123–2129.
- (349) Hall, G. J.; Frysinger, G. S.; Aeppli, C.; Carmichael, C. A.; Gros, J.; Lemkau, K. L.; Nelson, R. K.; Reddy, C. M. Oxygenated weathering products of *Deepwater Horizon* oil come from surprising precursors. *Mar. Pollut. Bull.* **2013**, 75, 140–149.
- (350) Jones, D.; Scarlett, A. G.; West, C. E.; Rowland, S. J. Toxicity of individual naphthenic acids to *vibrio fischeri*. *Environ. Sci. Technol.* **2011**, 45, 9776–9782.
- (351) *Standard test method for boiling range distribution of petroleum fractions by gas chromatography*; D2887 – 13; ASTM: West Conshohocken, 2014.

- (352) Reichenbach, S. E.; Rempe, D. W.; Tao, Q.; Bressanello, D.; Liberto, E.; Bicchi, C.; Balducci, S.; Cordero, C. Alignment for comprehensive two-dimensional gas chromatography with dual secondary columns and detectors. *Anal. Chem.* **2015**, *87*, 10056–10063.

Chapter 9 Curriculum Vitae

Address: Boulevard Henri-Plumhof 6, CH-1800 Vevey, Switzerland

E-mail: gros.jonas@gmail.com

Telephone: 0041 (0)21 922 19 56

Date of Birth: 6.4.1987

Employment History: Ph.D. student, LMCE, EPFL, (currently, since 2012)

Scientific assistant, LMCE, EPFL, (2011)

Qualifications: Master in environmental sciences and engineering at the EPFL with specialization in environmental chemistry and bioprocesses (2010)

Bachelor in environmental sciences and engineering at the EPFL (2008)

Main publications: **Gros, J.**; Nabi, D.; Dimitriou-Christidis, P.; Rutler, R.; Arey, J. S., "Robust algorithm for aligning two-dimensional chromatograms", *Anal. Chem.*, **84**, 9033-9040, **2012**.

Gros, J.; Reddy, C. M.; Aeppli, C.; Nelson, R. K.; Carmichael, C. A.; Arey, J. S., "Resolving biodegradation patterns of persistent saturated hydrocarbons in weathered oil samples from the *Deepwater Horizon* disaster", *Environ. Sci. Technol.*, **48**, 3, 1628-1637, **2014**.

Gros, J.; Nabi, D.; Würz, B.; Wick, L. Y.; Brussaard, C. P. D.; Huisman, J.; van der Meer, J. R.; Reddy, C. M.; Arey, J. S., "First day of an oil spill on the open sea: Early mass transfers of hydrocarbons to air and water", *Environ. Sci. Technol.*, **48**, 16, 9400-9411, **2014**.

Co-authorship: Hall, G. J.; Frysinger, G. S.; Aeppli, C.; Carmichael, C. A.; **Gros, J.**; Lemkau, K. L.; Nelson, R. K.; Reddy, C. M., "Oxygenated weathering products of *Deepwater*

Horizon oil coming from surprising precursors”, *Mar. Pollut. Bull.*, 75, 1–2, 140-149, **2013**.

Nabi, D.; **Gros, J.**; Dimitriou-Christidis, P.; Arey, J. S., “Mapping environmental partitioning properties of non-polar complex mixtures by use of GC×GC”, *Environ. Sci. Technol.*, 48, 12, 6814-6826, **2014**.

Dimitriou-Christidis, P.; Bonvin, A.; Samanipour, S.; Hollender, J.; Rutler, R.; Westphale, J.; **Gros, J.**; Arey, J. S., “GC×GC quantification of priority and emerging nonpolar halogenated micropollutants in all types of wastewater matrices: Analysis methodology, chemical occurrence, and partitioning”, *Environ. Sci. Technol.*, 49, 13, 7914-7925, **2015**.

Samanipour, S.; Dimitriou-Christidis, P.; **Gros, J.**; Grange, A.; Arey, J. S., “Analyte quantification with comprehensive two-dimensional gas chromatography: Assessment of methods for baseline correction, peak delineation, and matrix effect elimination for real samples”, *J. Chromatogr. A*, 1375, 123-139, **2015**.

Bartha, A.; De Nicolais, N.; Sharma, V.; Roy, S. K.; Srivastava, R.; Pomerantz, A. E.; Sanclemente, M.; Perez, W.; Nelson R. K.; Reddy, C. M.; **Gros, J.**; Arey, J. S.; Lelijveld, J.; Dubey, S.; Tortella, D.; Hantschel, T.; Peters, K. E.; Mullins, O. C., “Combined petroleum system modeling and comprehensive two-dimensional gas chromatography to improve understanding of the crude oil chemistry in the Llanos basin, Colombia”, *Environ. Fuel*, 29, 8, 4755-4767, **2015**.

Nelson, R. K.; Aeppli, C.; Arey, J. S.; Chen, H.; de Oliveira, A. H. B.; Eiserbeck, C.; Frysinger, G. S.; Gaines, R. B.; Grice, K.; **Gros, J.**; Hall, G. J.; Koolen, H. H. F.; Lemkau, K. L.; McKenna, A. M.; Reddy, C. M.; Rodgers, R. P.; Swarthout, R. F.; Valentine, D. L.; White, H. K., “Applications of comprehensive two-dimensional gas chromatography (GC×GC) in studying the source, transport, and fate of petroleum hydrocarbons in the environment”, *In* “Standard Handbook of Oil Spill Environmental Forensics”, Wang, Z.; Stout, S. A., Eds.; Elsevier: **2016**; pp. 339-448.

Swarthout, R. F.; Arey, J. S.; **Gros, J.**; Nelson, R. K.; Reddy, C. M.; Valentine, D. L., “Comprehensive two-dimensional gas chromatography to assess petroleum product weathering”, *In* “Lipid Microbiology Protocols,

Volume 3: Chemical and Physical Analysis of Hydrocarbons and Petroleum”, Springer, *submitted on 31 Dec. 2015*.

Awards: EDCE mobility award for a stay of two months at Texas A&M University, **2013**.

Conferences: **Gros, J.**; Reddy, C. M.; Nelson, R. K.; Arey, J. S., “Quantifying composition alteration through biodegradation for *Deepwater Horizon* oil in surface environments using GC×GC”, Gulf of Mexico Oil Spill & Ecosystem Science Conference, January 21-23, **2013**. *Talk*.

Gros, J.; Reddy, C. M.; Aeppli, C.; Nelson, R. K.; Carmichael, C. A.; Arey, J. S., “Developing a new saturates biodegradation index for weathered oils, based on samples from the *Deepwater Horizon* disaster”, Society of Environmental Toxicology and Chemistry (SETAC) Europe 24th Annual Meeting, Basel, Switzerland, May 11-14, **2014**. *Poster*.

Gros, J., “Oil fate investigation and modeling using GC×GC-FID”, 2nd Workshop on Marine Oil Spill & Its Biological Effects, Busan, South Korea, December 3-5, 2014. *Talk*.

Gros, J.; Nelson, R. K.; Reddy, C. M.; Socolofsky, S. A.; Arey, J. S., “Predicting the state and properties of *Deepwater Horizon* oil under pressure using the Peng-Robinson equation of state”, Gulf of Mexico Oil Spill & Ecosystem Science Conference, Houston, United States, February 16-19, 2015. *Poster*.

Gros, J.; Jun, I.; Reddy, C. M.; Socolofsky, S. A.; Arey, J. S., “Validating formulas for the prediction of ascent speed and mass transfer coefficient for liquid oil droplets and gas bubbles under pressure”, Gulf of Mexico Oil Spill & Ecosystem Science Conference, Houston, United States, February 16-19, 2015. *Poster*.

Socolofsky, S. A.; Dissanayake, A. L.; Jun, I.; **Gros, J.**; Arey, J. S.; Reddy, C. M., “Texas A&M Oilspill Calculator (TAMOC): Modeling suite for subsea spills”, 38th AMOP Technical Seminar on Environmental Contamination and Response, Vancouver, Canada, June 2-4, 2015.

Gros, J.; Reddy, C. M.; Nelson, R. K.; Socolofsky, S. A.; Arey, J. S., "Thermodynamic modeling of gas-liquid-water partitioning and fluid properties for Macondo reservoir fluid at deep-water conditions", Gulf of Mexico Oil Spill & Ecosystem Science Conference, February 2-4, **2016**. *Talk*.

Field work: Sampling of oil residues on several beaches in the Gulf of Mexico during a stay at Woods Hole Oceanographic Institution (2012).

Languages: French, mother tongue
English, working knowledge (level C1),
German, good scholar level (level B1-C1)

